The Integrity of Geosynthetic Elements of Waste Containment Barrier Systems Subject to Seismic Loading

by

Mohamed Arab

A Dissertation Presented in Partial Fulfillment
of the Requirements for the Degree
Doctor of Philosophy

Approved July 2011 by the
Graduate Supervisory Committee:

Edward Kavazanjian, Chair
Claudia Zapata
Sandra Houston

ARIZONA STATE UNIVERSITY

August 2011

ABSTRACT

A method for evaluating the integrity of geosynthetic elements of a waste containment system subject to seismic loading is developed using a large strain finite difference numerical computer program. The method accounts for the effect of interaction between the geosynthetic elements and the overlying waste on seismic response and allows for explicit calculation of forces and strains in the geosynthetic elements. Based upon comparison of numerical results to experimental data, an elastic-perfectly plastic interface model is demonstrated to adequately reproduce the cyclic behavior of typical geomembrane-geotextile and geomembrane-geomembrane interfaces provided the appropriate interface properties are used. New constitutive models are developed for the in-plane cyclic shear behavior of textured geomembrane/geosynthetic clay liner (GMX/GCL) interfaces and GCLs. The GMX/GCL model is an empirical model and the GCL model is a kinematic hardening, isotropic softening multi yield surface plasticity model. Both new models allows for degradation in the cyclic shear resistance from a peak to a large displacement shear strength.

The ability of the finite difference model to predict forces and strains in a geosynthetic element modeled as a beam element with zero moment of inertia sandwiched between two interface elements is demonstrated using hypothetical models of a heap leach pad and two typical landfill configurations. The numerical model is then used to conduct back analyses of the performance of two lined municipal solid waste (MSW) landfills subjected to strong ground motions in the Northridge earthquake. The modulus reduction "backbone curve" employed with the Masing criterion and 2% Rayleigh damping to model the cyclic behavior of MSW was established by back-analysis of the response of the Operating Industries Inc. landfill to five different

earthquakes, three small magnitude nearby events and two larger magnitude distant events. The numerical back analysis was able to predict the tears observed in the Chiquita Canyon Landfill liner system after the earthquake if strain concentrations due to seams and scratches in the geomembrane are taken into account. The apparent good performance of the Lopez Canyon landfill geomembrane and the observed tension in the overlying geotextile after the Northridge event was also successfully predicted using the numerical model.

DEDICATION

This thesis is dedicated to my Mother and Father who have supported me all the way since the beginning of my life.

Also, this thesis is dedicated to my wife Fatima and my daughter Maria who have been a great source of motivation and inspiration.

ACKNOWLEDGMENTS

The time I have spent at Arizona State University has been a rewarding experience both academically and personally. I want to thank all my colleagues and friends that made these years a joyful and beneficial time. I would like to thank some people in particular.

First of all, I would like to begin by thanking my advisor Professor Edward Kavazanjian, Jr. for his invaluable guidance during the course of my studies. I am grateful that he provided the encouragement and patience that I needed. I would like to thank Dr. Neven Matasovic of GeoSyntec Consultants, who provided many valuable suggestions during the course of my research. I also would like to thank Dr. Liping who shared with me his subroutine for multi yield surface constitutive model. I also would like to thank Dr. Fowmes who shared his subroutine for beam mesh interface for interface softening.

The work in this thesis is part of a joint Arizona State University / University of California at San Diego research program titled GOALI, Collaborative Research: The Integrity of Geosynthetic Elements of Waste Containment Barrier Systems Subject to Large Settlements or Seismic Loading. This project is funded by the Geomechanics and Geotechnical Systems, Geoenvironmental Engineering, and Geohazards Mitigation program of the National Science Foundation (NSF) Division of Civil, Mechanical, and Manufacturing Innovation under grant number CMMI-0800873. I am grateful for this support as well as the support from the project's industrial partners, GeoSyntec Consultants, Inc.

TABLE OF CONTENTS

Page

Page

Page

Page

Page

Page

Page

Page

LIST OF TABLES

Table Page

Table Page

LIST OF FIGURES

Figure Page

Figure Page

Figure Page

Figure Page

Figure Page

Figure Page

Figure Page

Figure Page

Figure Page

Figure Page

Figure Page

Figure Page

Figure Page

Figure Page

Figure Page

Figure Page

Figure Page

Figure Page

Figure Page

CHAPTER 1 INTRODUCTION

1.1 Introduction

Landfills, sites for the disposal of waste materials by burial, are considered the oldest form of waste treatment. Landfilling has long been the most common method of waste disposal and remains so in most places around the world. In 1997, the United States has 3,091 active landfills and over 10,000 old municipal landfills, according to the Environmental Protection Agency (EPA website: http://www.epa.gov/).

Modern sanitary landfills are different from old unengineered, unlined dump sites. Landfills for solid wastes disposal nowadays are required to meet very stringent federal and state standards to protect public health and the environment. In the United States, these standards have been established under the Resource Conservation and Recovery Act (RCRA), initially promulgated in 1970. RCRA governs the location, design, construction, operation, and final closure of the landfills. RCRA sets minimum standards for landfills in the United States. In addition to RCRA requirements, landfills must meet any additional state requirements. Solid waste landfills, regulated under Subtitle C of RCRA (for hazardous wastes) and Subtitle D of RCRA (for municipal solid wastes), must be lined, at a minimum, with single composite or double liners, depending on the type of waste, and a leachate collection and removal system above and between the liners.

On October 9, 1993, the current version of the RCRA Subtitle D regulations (40 CPR Part 258) went into effect. These regulations are applicable to new or lateral expansion of existing municipal solid waste (MSW) landfills, including the entire waste containment system, liners, leachate collection systems, and surface water control systems. Section 258.14 of the subtitle D regulations identifies areas where seismic

analysis and design is required; deemed seismic impact zones are based on earthquake probability maps prepared by the United States Geological Survey (USGS). Seismic impact zones are defined in subtitle D regulations as those regions having peak ground acceleration (PGA) in bedrock exceeding 0.1 g with a 90% probability of not being exceeded over a 250 year time period. Within seismic impact zones, the regulations require that the waste containment system for new MSW landfills and for lateral expansions of existing MSW landfills be designed to resist the maximum horizontal acceleration (MHA). The MHA is defined as the maximum expected horizontal acceleration either depicted on a seismic hazard map with a 90 percent probability of not being exceeded in 250 years (i.e. the USGS maps prepared under the National Earthquake Hazard Reduction Program) or based upon a site-specific seismic risk assessment. The 2008 seismic hazard map for the peak ground acceleration in bedrock with a 90 percent probability of not being exceeded in 250 years from the National Earthquake Hazard Reduction Program is presented in Figure 1-1. The seismic impact zones, areas on the map with a PGA of 0.1g and higher (darker colors); encompass nearly half of the continental United States.

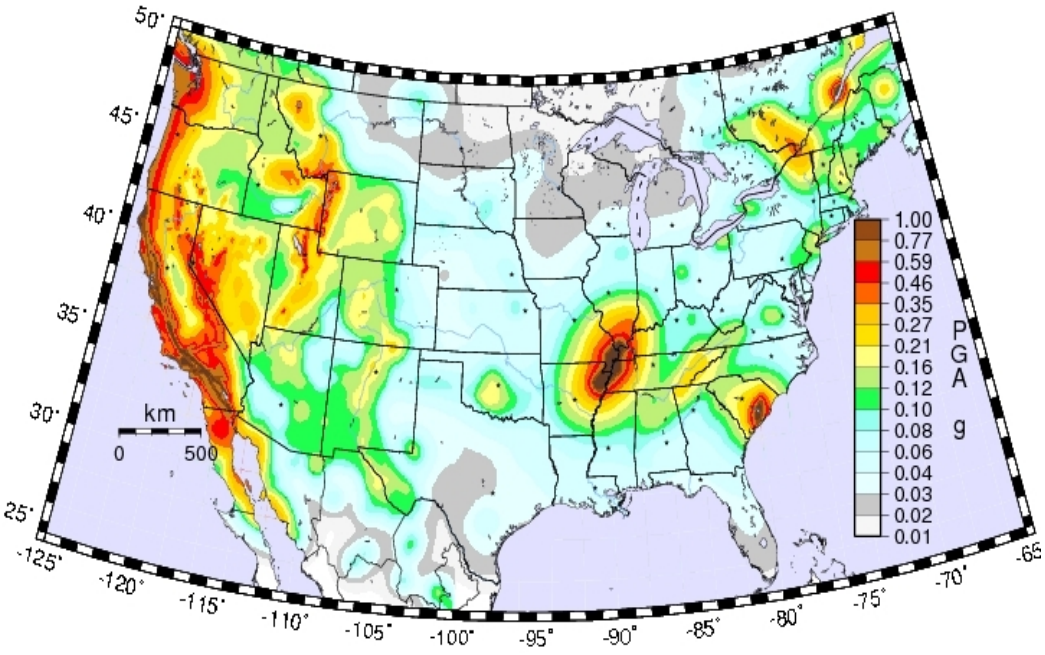

Figure 1-1 Seismic hazard map with a 90 percent probability of not being exceeded in 250 years (source: www.USGS.org)

1.2 Background and Motivation

Except in areas of very low seismicity, seismic design of landfill liner systems is typically based on a Newmark-type seismic displacement analysis (Bray et al. 1998). While engineers may sometimes assume that a Newmark analysis provides a realistic assessment of cumulative permanent seismic deformation, among engineers with expertise in seismic design the displacement calculated in a Newmark analysis is generally recognized as merely an index of seismic performance (Augello et al. 1995; Matasovic et al. 1995). The calculated seismic displacement is used to evaluate the potential for damage to geosynthetic elements of landfill containment systems quantitatively based upon correlation with observed performance of landfills in

earthquakes (Anderson and Kavazanjian 1995; Kavazanjian et al. 1998). This type of analyses ignores the stresses and strains that may develop in the liner system.

The effectiveness of geomembrane and geosynthetic clay liner (GCL) barriers in landfill liner systems can be threatened by the development of tensile stresses (or strains) beyond the tensile capacity of these geosynthetic elements. Current landfill design practice does not explicitly consider the development of tension in these containment system elements, despite analyses and field observations indicating that tensile stresses induced by seismic loading can exceed the tensile strength of these materials (Anderson and Kavazanjian 1995; Augello et al. 1995 and Dixon and Jones 2005). Threats to the integrity of geosynthetic elements of waste containment systems are exacerbated by the fact that damage to these elements may be hidden beneath the waste, with no surface expression to alert the engineer, operator, owner, or regulator to the problem. One mechanism of integrity failure of a geosynthetic liner system due to seismic loading is illustrated in Figure 1-2.

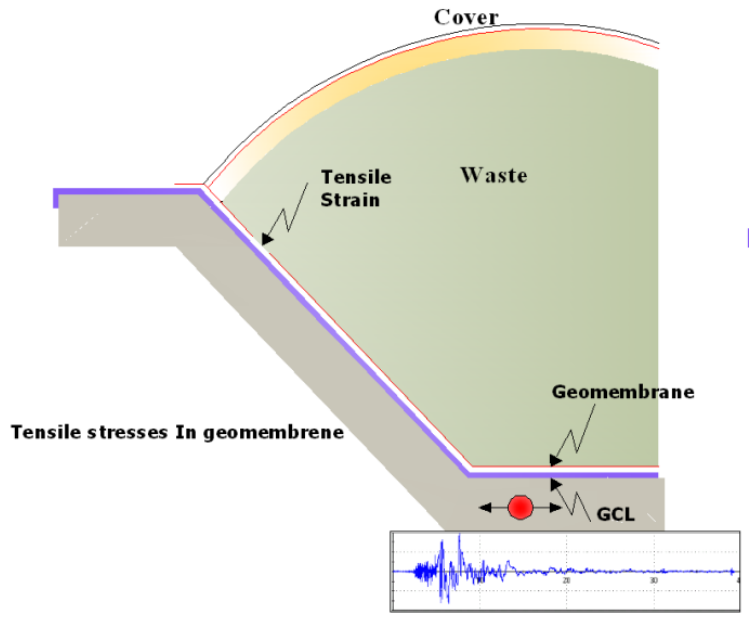

Figure 1-2 Mechanisms of local side slope integrity failure due to seismic loading

Figure 1-3 is a picture of damage to the exposed portion of the liner system at the Chiquita Canyon landfill after 1994 Northridge earthquake. Several tears in the exposed liner at this facility started at or near anchor trenches. While there was no surface evidence tears in the liner beneath the waste, excavation many years later for lateral expansion of the liner system are reported to have revealed another tear in the geomembrane beneath the waste further down the slope (personnel communication, Edward Kavazanjian, Jr.). This case history illustrates the concern about stresses developed in the liner system due to seismic loading that can threaten the effectiveness of the liner system after an earthquake.

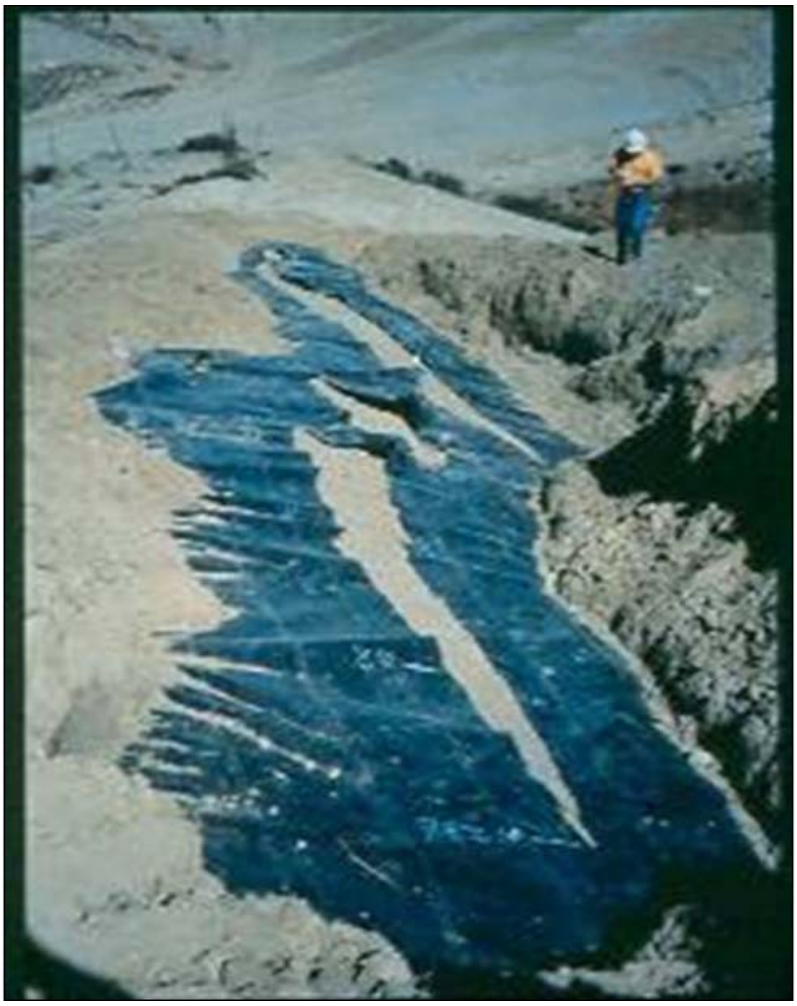

Figure 1-3 Tear in geomembrane liner system, Cell C, Chiquita Canyon Landfill after 1994 Northridge earthquake (photo courtesy of Calif. EPA, Integrated Waste Management Board)

Due to the relatively low in-plane (internal and interface) shear strength of geosynthetic elements in landfill liner barrier systems, it is often impossible to establish unconditional seismic stability for landfills, i.e. to have a yield acceleration greater than the seismically-induced acceleration of the waste mass. To provide a practical means of assessing the seismic performance of the geosynthetic elements of landfill liners, a criterion based upon the permanent seismic displacement calculated using a Newmark type analysis of the waste mass is typically employed, as discussed above. The typical

criterion employed in practice states that, based upon observations of the performance of landfills in earthquake, if the calculated seismic displacement in a Newmark-type analysis is less than between 150 to 300 mm, the design is considered adequate, i.e. that there is no threat to the integrity of the geosynthetic elements of the waste containment system (Seed and Bonaparte 1992).

The design criterion of 150 to 300 mm of allowable calculated seismic displacement commonly used in seismic design of geosynthetic liner systems can be traced back to a 1992 survey of consulting firms conducted by Seed and Bonaparte (1992). However, these investigators simply reported that this range of values was typically used as the seismic design criterion for geomembrane liners in practice. No firm basis was given for the choice of this range of values. Despite the absence of any firm proof of its adequacy, this criterion was recommended as the seismic performance criterion in the 1995 EPA guidance document RCRA Subtitle D (258) Seismic Design Guidance for Municipal Solid Waste Landfill Facilities (Richardson et al. 1995). This guidance document has never been updated and 150 to 300 mm of calculated seismic displacement is still the generally accepted performance criterion used for design of geosynthetic liner systems.

Using conventional methods to conduct back analyses of landfills that survived major earthquakes events without any visible damage, researchers have subsequently found that Newmark-type analyses can yield up to 300 mm of calculated seismic displacement (e.g., Anderson and Kavazanjian 1995 and Augello et al. 1995). These analyses lend some confidence to the Seed and Bonaparte performance criterion, despite the fact that these conventional analyses do not provide an assessment of actual seismically induced stresses and strains in the geosynthetic elements of a liner or final cover system. However, many engineers fail to realize that the 150 to 300 mm criterion is

empirical and is valid only for conventional analysis methods due to the inherent conservatism in such methods. Furthermore, even though there is no visible damage, transient seismic loads and displacements in the liner system may have overstressed system components without any visible indications at the ground surface.

1.3 Research Objectives

The objective of the research is to develop guidelines for identifying the conditions under which seismic loading may threaten the integrity of geosynthetic elements of a waste containment barrier system.

Seismically-induced stresses and strains can impair the integrity of geomembrane (GM) and geosynthetic clay liner (GCL) barrier layers and impact the effectiveness of other geosynthetic elements of the containment system (e.g. the leachate collection and removal system). For example, GM and GCL barrier layers can be torn due to excessive tensile strain and geotextile filters can also be torn by tensile loading, allowing fine particles to infiltrate and clog drainage or leachate collection systems. Current landfill design practices usually do not explicitly consider the tensile stresses induced in geosynthetic elements of the waste containment system, despite analyses and field observations which indicate that large settlement or seismic loading can induce stresses that exceed the strength of the geosynthetic materials (Kavazanjian et al. 2006). Furthermore, damage to the geosynthetic elements of the containment system may be hidden, with no surface expression to alert the engineer, operator, owner, or regulator to the integrity failure of these geosynthetic elements.

The work described herein has three main tasks: 1) Development and calibration of a numerical model to predict the seismic performance a waste containment system subject

to seismic loading using data available in the literature; 2) Development and implementation, within the numerical model environment, of advanced constitutive relationships for the behavior of geosynthetics and geosynthetics interfaces based on the available test data for different geosynthetic materials; and 3) Numerical analysis of the behavior of geosynthetic liner systems subject to seismic loading using the calibrated numerical model and the advanced constitutive relationships.

1.4 Organization

This dissertation is organized as follows. In Chapter 2, a review of the literature on the seismic design methods for landfills is presented. This chapter will briefly review the methods that have been used historically to analyze landfills under dynamic loading.

In Chapter 3, the engineering characteristics of the various components of a landfill (e.g. solid waste, geosynthetic lining material) are presented. This chapter will briefly review static and dynamic characteristics of the different components of landfills that will be used in the subsequent numerical modeling.

In Chapter 4, the numerical schemes in the software used in this study are presented. FLAC6.0 (Itasca 2008) was used for the numerical analyses in this research. Some general concepts about this software package are presented in this chapter. The Cam Clay constitutive model used to model solid waste behavior is also discussed briefly.

In Chapter 5, the development of a constitutive model for the in plane shear behavior of a GM and GCL composite barrier layer is presented. This model is based upon cyclic testing of GCL/GM system conducted at the University of California, San Diego by Professor Patrick Fox and his students. This constitutive model was developed to account

for degradation of the in plane shear strength of GCL/GM components. A subroutine is developed under FLAC6.0 environment for use of this constitutive model for geosynthetic in plane behavior (e.g. interfaces behavior in landfill).

In Chapter 6, a constitutive model for the internal shear behavior of GCLs is developed. The model is a multi yield surface kinematic hardening plasticity model developed to simulate GCL cyclic behavior. The model also handles the strain softening behavior of the GCLs.

In Chapter 7, the validation of the interface elements available in FLAC6.0 using laboratory testing data is presented. Several laboratory shaking table tests, conducted on rigid and flexible blocks, have been used to validate the numerical models.

In Chapter 8, the seismic analysis of a heap leach pad, including the calculation of the strains and forces in the geomembrane component of the liner system is presented. A simple heap leach pad configuration is analyzed under seismic loading as a prelude to more complicated analysis of MSW landfill liner system. The analysis demonstrates calculations of the forces developed by the dynamic loading in the geosynthetic liner system element.

In Chapter 9, seismic analyses of the liner system for two typical landfill geometries, including the calculation of the strains and forces in the geomembrane is presented.

In Chapter 10, calibration of the material properties for solid waste subject to dynamic loading using the case history of the seismic response of an unlined landfill is presented. The case history employed in this chapter is for the Operating Industries, Inc. (OII) landfill in southern California, the only landfill to date instrumented with strong motion recording stations. The strong ground motion instruments recorded several

earthquakes between 1988 and 1994. This chapter describes back analysis of the seismic response of the OII landfill using five of these records.

In Chapter 11, the results of back-analyses of the performance of two lined landfills during the Northridge earthquake are presented. Back analyses presented in this chapter include analyses of the Chiquita Canyon and Lopez Canyon landfills.

In Chapter 12, the results of sensitivity analyses were conducted using the Chiquita Canyon landfill model to investigate the influence of interface parameters on the seismic response of the model.

Chapter 13 contains the summary and conclusions draw from this study, including the implications for engineering practice and recommendations for future research and development.

CHAPTER 2 SEISMIC DESIGN OF LANDFILLS: REVIEW

2.1 Current US Practice for Seismic Design of Landfills

Current US practice for the seismic stability of landfills is based upon either pseudostatic limit equilibrium slope stability analyses or analyses of seismically induced permanent deformations. Pseudostatic slope stability analysis is generally performed using a seismic coefficient estimated from procedures developed for earth embankments.

Seed and Bonaparte (1992) conducted a survey of five leading landfill engineering firms to determine the methods they used to perform seismic analysis of landfills. A majority of these firms said (in 1991) that they "virtually never perform response analyses for the actual (or proposed) waste fill materials" because of the difficulties associated with estimating their properties. The firms said they generally perform one-dimensional dynamic response analysis to evaluate local site effects. In most cases, the maximum horizontal acceleration (MHA) or acceleration time history calculated at the ground surface for the site soil profile, without the waste fill in place, was used to estimate the seismic loading. Either the MHA value was used as the seismic coefficient in pseudostatic slope stability analyses (sometimes with a reduction factor applied to it) or the calculated ground surface acceleration-time history was used in a seismically induced permanent deformation analysis. The design was judged to be acceptable in terms of seismic performance if the calculated pseudostatic factor of safety was at least 1.5 or if the calculated seismically induced permanent displacement was no more than 150 mm to 300 mm. The basis for this displacement criterion was engineering judgment with regard to the tolerable amount of permanent displacement lined landfills could sustain without

major damage to the containment system. The methods commonly used to estimate the seismic permanent displacement in landfills are discussed in the next section.

2.2 Rigid Block Analogy (Newmark Analysis)

Newmark (1965) proposed using a block in a plane as an analog to an earthen embankment to estimate seismic permanent displacement. This method has been commonly extended to estimate the seismic displacement of landfills. In a Newmark analysis of the seismic displacement of a landfill, the sliding block is analogous to the displacing waste mass, the plane on which the block sits is analogous to the slip surface from a limit equilibrium analysis, and the coefficient of friction between the sliding block and the underlying plane is analogous to the yield acceleration from a limit equilibrium analysis (i.e. to the seismic coefficient for a pseudo-static factor of safety of 1.0). The acceleration time history of the underlying plane is assumed to be equal to the time history of the shear stress ratio, τ_{eq}/σ_v, at the base of the sliding mass, where τ_{eq} is the earthquake induced shear stress and σ_v is the total vertical stress. Note that τ_{eq}/σ_v is equal to the average acceleration of the mass of a vertical column of soil above the base of the sliding mass.

In a Newmark analysis, the block and the plane initially move together and the block is assumed to begin moving relative to the plane when the acceleration of the plane exceeds the yield acceleration of the block (i.e. when it exceeds the friction coefficient of the block-plane interface assuming to adhesion between the block and the plane). The block begins to decelerate when the acceleration of the plane falls below the yield acceleration of the block and ceases movement after the subsequent deceleration of the block brings the velocity of the block relative to the plane back to zero (see Figure 2-1).

The relative displacement between the block and the plane is calculated by double integrating the acceleration of the block relative to the plane.

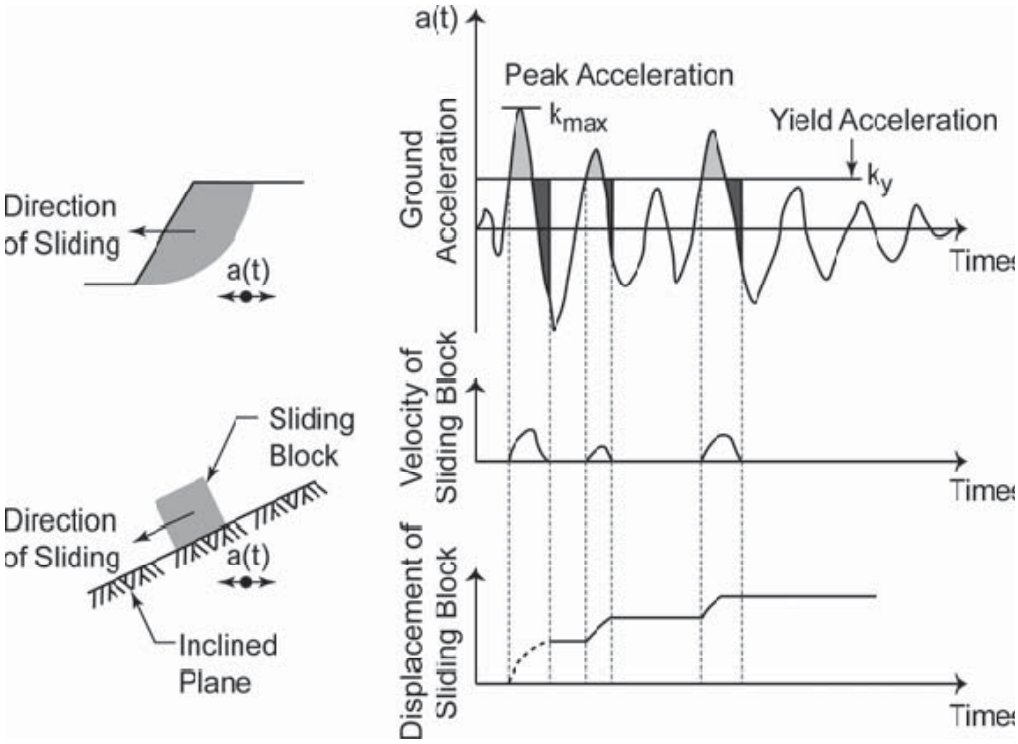

Figure 2-1 Cumulative seismic permanent deformation of embankments (Anderson et al. 2009)

Displacements in a Newmark analysis are typically calculated considering excursions above the yield acceleration on only one side of the acceleration time history to account for a preferred direction of sliding during slope instability. However, in some cases the analysis may consider excursions above the yield acceleration on both sides of the acceleration time history, e.g. for analysis of frictional base isolation. Cases where excursions above the yield acceleration on both sides of the case history are considered may include both cases where the yield acceleration is the same on both sides of the time history and cases where the yield acceleration in one direction is greater than the yield acceleration in the other direction. The case where the yield acceleration is the same in

both directions (e.g. frictional seismic base isolation) is analogous to a block on a horizontal plane. The case where the yield acceleration differs on either side of the time history may represent a slope or retaining wall and is analogous to a block on an inclined plane.

In a conventional Newmark analysis the block is assumed rigid, i.e. the deformability of the sliding mass is ignored, which perhaps makes this type of analysis more suitable for analysis of short retaining wall, than for slope stability of landfill design, as many retaining wall systems with heights less than 6 m can reasonably be assumed to behave as a rigid block without sacrificing the accuracy of the results. Using Newmark-type of analysis to estimate the permanent deformation in cases of slope stability or landfill design is subject to inaccuracies introduced by the rigid block assumption, as discussed subsequently.

Wartman et al. (2003) conducted shaking table tests of both rigid and deformable soil columns on an inclined plane. The shaking table tests on deformable soil columns were used to examine the validity of the Newmark (1965) sliding block procedure analysis with respect to non rigid block. In the Wartman et al. (2003) study, the soil columns were not intended to model an actual prototype slope, but rather simply to examine the effects of soil deformability on sliding displacements. By comparing the displacement from the rigid block experiments to the displacements from the soil column experiments, Wartman et al. (2003) concluded that the rigid sliding block procedure is unconservative when the predominant frequency of the input motion is between 80% less than to about 30% more than the natural frequency of the sliding mass ($0.2 <$ tuning ratio < 1.3). Conversely, the sliding block procedure is generally conservative when the predominant frequency of the input motion is less than 20 percent of the natural

frequency of the mass (tuning ratio < 0.2) or more than 30% greater than the natural frequency of the mass (tuning ratio >1.3). These investigators found that, while sliding surfaces might limit transmission of energy in the case of a rigid block, high inertial forces could, nonetheless, develop in a sliding mass in the case of flexible soil column because of its dynamic response.

2.3 Modified Newmark Analysis with Peak and Residual Shear Strength

Matasovic et al. (1998) extended the Newmark-type analysis to include the effects of two-way sliding, degradation of the yield acceleration, and vertical accelerations. Matasovic et al. (1998) demonstrated that the conventional Newmark-type seismic deformation analysis in which the yield acceleration is based upon the residual or large deformation shear strength can be conservative when applied to composite liner and cover interfaces with a pronounced difference between peak and residual shear strengths. The degree of conservatism depends to a large extent upon the difference between the peak and residual strength and the value of the calculated seismic deformation compared to the threshold deformation at which the peak and residual strengths are mobilized. Figure 2-2 schematically compares the conventional Newmark analysis and modified Newmark analysis with degrading yield acceleration.

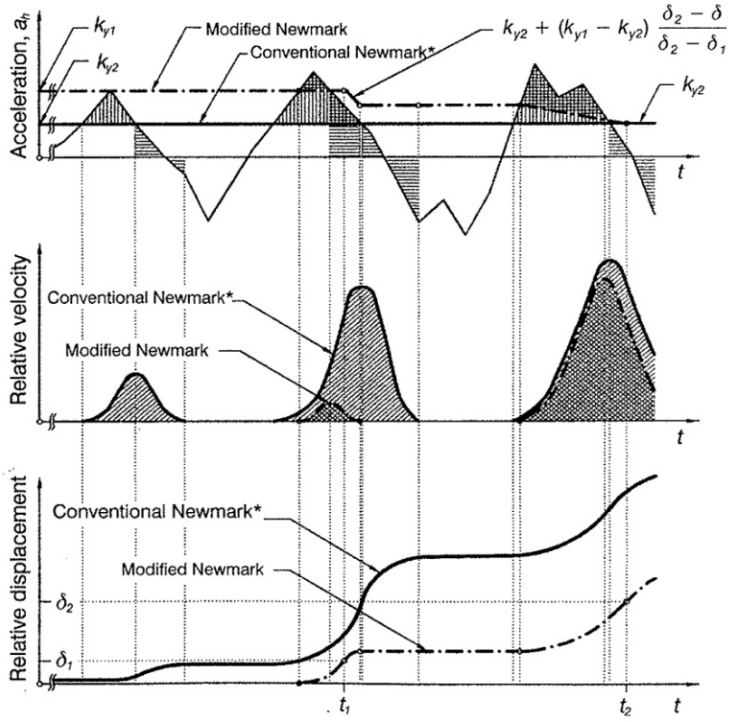

Figure 2-2 Comparison of the classical and modified (degrading yield acceleration) Newmark-type integration schemes (Matasovic et al. 1998)

2.4 Decoupled Newmark Analysis

Makdisi and Seed (1978) first proposed modifying the Newmark analysis to account for the deformability of earthen structures. As opposed to the original Newmark (1965) rigid sliding block model, which ignores the dynamic response of a deformable sliding mass, Makdisi and Seed (1978) introduced the concept of an equivalent acceleration time history to represent the seismic loading of a potential sliding mass. They proposed using the horizontal equivalent acceleration (HEA) time history of the potential failure mass instead of the original earthquake record. The HEA when applied to a rigid potential sliding mass produces the same dynamic shear stresses along the potential sliding surface that is produced when a dynamic analysis of the deformable waste structure is performed.

Makdisi and Seed (1978) employed a decoupled analysis to calculate the HEA time history. The analysis was considered decoupled because the dynamic response analysis was performed assuming that no relative displacement occurs along the potential sliding failure plane to evaluate the HEA time history. While Makdisi and Seed (1978) used equivalent linear two-dimensional finite element analysis to calculate the HEA time history, one-dimensional equivalent linear site response analyses is often used in practice to calculate the HEA time history. In Makdisi and Seed (1978) approach, to estimate seismic displacement, a Newmark type analysis is conducted using the HEA time history as the input motion

A simplified seismic displacement methodology was developed by Bray et al. (1998) to calculate the seismic displacement of landfill liner and cover systems. The method of Bray et al. (1998) is similar to the Makdisi and Seed (1978) method, but the HEA time history in the Bray et al. (1998) method is based on the results of fully nonlinear decoupled one-dimensional seismic response analyses using the computer program D-MOD (Matasovic and Vucetic 1995) instead of an equivalent linear analysis as in the Makdisi and Seed (1978) method. A large number of scaled and unmodified recorded earthquake bedrock input motions with PGAs ranging from 0.2 g to 0.8 g were used by Bray et al. (1998) to develop a series of design charts for the seismic displacement of landfill liner and cover systems. The Bray et al. (1998) method was calibrated against several case histories of waste fill performance during the 1989 Loma Prieta and 1994 Northridge earthquakes.

The Bray et al. (1998) procedure provides a more comprehensive assessment of the earthquake ground motions, seismic loading, and seismic displacement than the Makdisi

and Seed (1978) method but it also requires more effort than the Makdisi and Seed (1978) procedure.

In the first step of the Bray et al. (1998) method, the ground motion is characterized by estimating the MHA or PGA in lithified rock for the design earthquake, the mean period of the design earthquake, T_m, and the significant duration of the design earthquake, D_{5-95}, for an outcropping rock at the site based upon the design moment magnitude and site-to-source distance for the seismic sources considered in the analysis. Guidance is given on evaluating these parameters using empirical ground motion parameter relationships. The rock site condition used for the input parameters is consistent with the Site Class B weak sedimentary rock site condition used in the development of probabilistic National Earthquake Hazard Reduction Program national ground motion seismic hazard maps developed by the United States Geological Survey (USGS). For the base sliding (landfill liner) case, the initial fundamental period of the potential sliding mass, T_s, is estimated as:

$$T_s = 4H/V_s \tag{1}$$

where H is the height of the landfill, and V_s is the shear wave velocity of the MSW waste. With the ratio of T_s/T_m, the normalized maximum seismic loading (MHEA)/(MHA rock)(NRF),is calculated where *MHEA* is the maximum horizontal equivalent acceleration and *NRF* is a nonlinear response factor. The normalized maximum seismic loading can be found from a chart presented by Bray et al. (1998) or it can be estimated with the equation provided below when $T_s/T_m > 0.5$

$$\ln(MHEA/(MHA_{rock}\,NRF)) = -0.624 - 0.7831\ln(T_S/T_m) \pm \varepsilon \tag{2}$$

where ε is the standard deviation and is equal to 0.298. The seismic coefficient, k_{max}, can then be found as *MHEA/g* and the normalized seismic displacement can be estimated as a function of k_y/k_{max} as:

$$\log_{10}(U/(k_{\max} D_{5-95})) = 1.87 - 3.477(k_y / k_{\max}) \pm \varepsilon \quad (3)$$

where ε = 0.35 and U is the seismic displacement (in cm). The normalized seismic loading and displacement values estimated using $+\varepsilon$ represent the values at the 16% probability of exceedance levels (assuming a log normal distribution for U). It is important to note that the Bray et al. (1998) method is also limited by the decoupled seismic response approximation employed in the Newark sliding blocks calculations.

2.5 Coupled Analysis

Lin and Whitman (1983) proposed using the single-degree-of freedom (SDOF), one-dimensional lumped mass system shown in Figure 2-3 and linear elastic soil properties to calculate coupled seismic permanent displacements. The model employed by Lin and Whitman can be characterized as a shear beam type model with one degree-of-freedom (DOF) during the nonsliding phase of motion and two DOFs during the sliding phase (stick–slip model). Lin and Whitman (1983) calculated the permanent displacement for harmonic motions and synthetic earthquake motions using their proposed coupled formulation. Lin and Whitman (1983) compared the response predicted using the decoupled approximation to the response of the proposed coupled formulation for shallow, deep, and intermediate sliding surfaces. Lin and Whitman (1983) concluded that deep sliding is most affected by the decoupled assumption. A comparison of the decoupled and coupled displacements from their study is shown in Figure 2-3, where the

ratio of the displacement calculated using the decoupled model to the displacement calculated decoupled model (referred to as the exact solution in Figure 2-3) is presented as a function of the ratio of the k_y to the k_{max}. At k_y/k_{max} equal to 0.5 with a material damping ratio of 15%, the decoupled approximation overestimates the coupled permanent displacement of the shear beam system by an average of 20%.

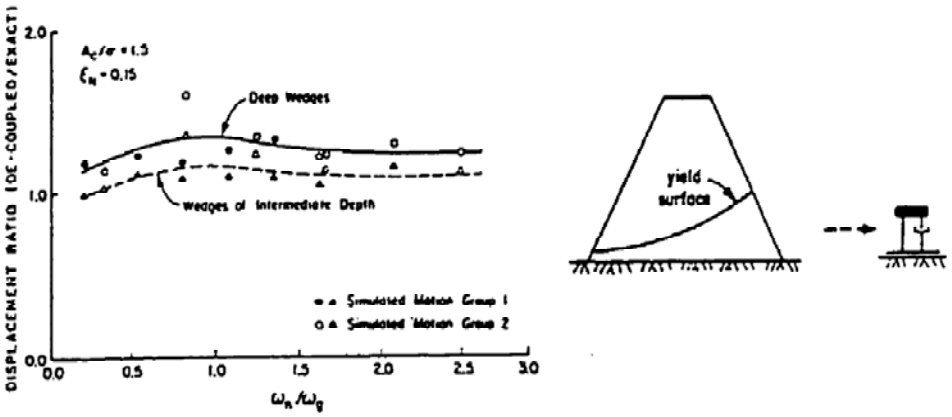

Figure 2-3 Results from Decoupled approximation (Lin and Whitman 1983)

Gazetas and Uddin (1994) investigated the sliding response of failure masses in earth dams using a finite element model. Figure 2-4 shows the finite-element mesh employed by Gazetas and Uddin (1994). The Gazetas and Uddin (1994) model employed a Coulomb friction law along a sliding tensionless interface to represent the sliding behavior of a failure mass. It was assumed that all irreversible shear distortion occurs along this sliding interface, the behavior of which is ideally rigid-plastic. These assumptions limit the amount of shear stress that can be transmitted into the sliding mass (as does a Newmark-type analysis).

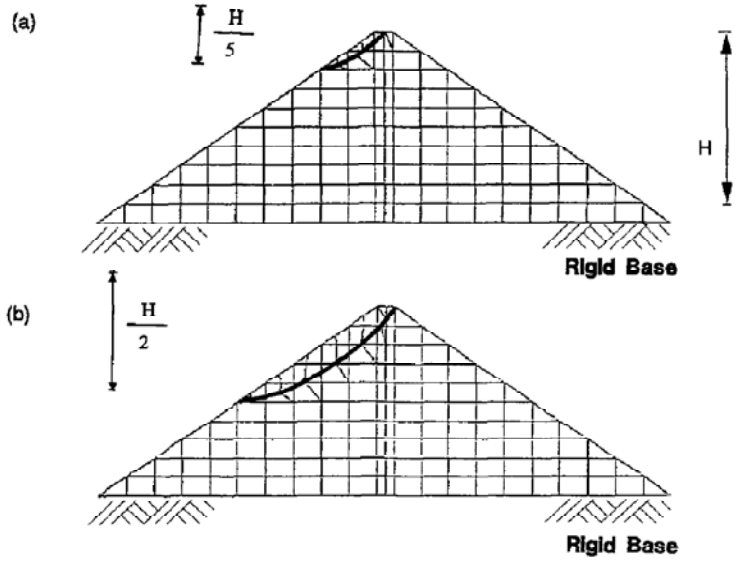

Figure 2-4 Mesh used in the study by Gazetas and Uddin (1994): (a) k_y =0.30 g (Interface 1); and (b) k_y = 0.50 g (Interface 2) (Gazetas and Uddin 1994)

Figure 2-5 show some details of typical results Gazetas and Uddin (1994) obtained from sinusoidal excitation using the mesh shown in Figure 2-4 at a frequency ratio f/f_1 = 0.75 , where f is the excitation frequency and f_1 is the fundamental frequency of the dam, for a PGA at the toe of the embankment equal to 0.40 g. Figure 2-5 (a) shows the acceleration history of a point inside the sliding block and Figure 2-5 (b) shows the acceleration history of a point just outside the sliding block for the dam. The time history in Figure 2-5 (b) is rather similar to the time history for the intact dam without a sliding interface shown in Figure 2-5 (c). However, some high-frequency spikes are generated at point "b" during the half-cycles where the failure mass tends to move inward relative to the dam the sticking phase of the motion. Displacements calculated by this procedure and by the decoupled procedure developed by Makdisi and Seed (1978) were compared using a harmonic input motion. The decoupled approach overestimated sliding displacement with respect to the coupled procedure when the frequency of the input motion was close

to the first fundamental frequency of the dam. However, results also indicated that the decoupled procedure underpredicts displacements at a frequency ratio (f/f_1) less than 0.5. Gazetas and Uddin (1994) concluded that the decoupled displacements are generally reasonable and conservative, but that underestimation of sliding displacement is possible. They also noted that the frequency is the important parameter when comparing the permanent deformation calculated from the decoupled analysis to the finite element (coupled analysis) results.

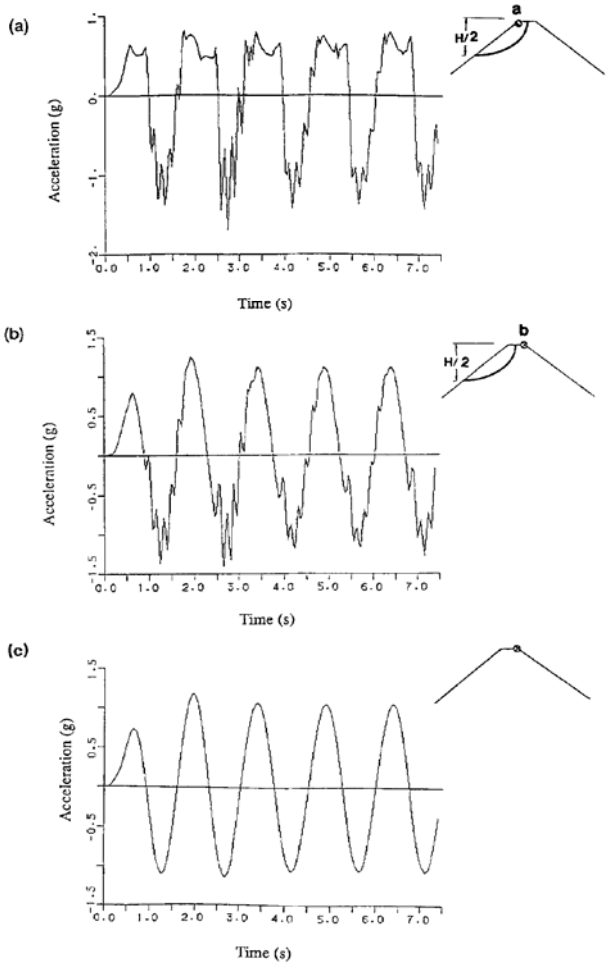

Figure 2-5 dynamic response at the crest of the dam a) within sliding mass b) just outside the sliding mass c) crest acceleration of the intact dam (Gazetas and Uddin 1994)

Kramer and Smith (1997) developed a modified lumped mass model for the sliding behavior of a flexible (compliant) block on a plan. In the Kramer and Smith (1997) model, the discrete two mass system rests on an inclined plane. Frictional sliding occurs between the lower mass and the base plane, as illustrated in Figure 2-6.

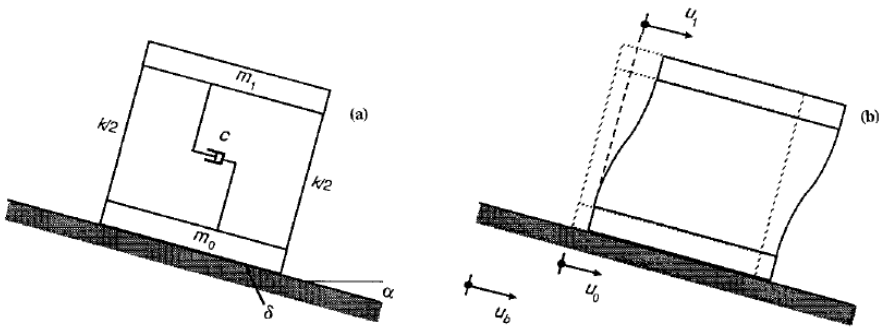

Figure 2-6 Schematic diagram of the model used: (a) Schematic Illustration; (b) Notation Used to Describe Displacements of Modified Newmark Model (Kramer and Smith 1997)

Comparing the results from a coupled formulation accounting for the sliding at the base of the system illustrated in Figure 2-6 to a decoupled Newmark procedure, Kramer and Smith (1997) concluded that the decoupled procedure provides good to substantially overconservative estimates of permanent displacement for relatively thin or stiff failure masses. For thick or flexible failure masses however, these investigators showed that the decoupled procedure may underpredict permanent displacements. They found the factor by which displacements are underpredicted varies for different ground motions but appears to be on the order of 1.5-1.7 for many cases. Consequently, Kramer and Smith (1997) concluded that the decoupled procedure may produce unconservative estimates of permanent displacement for many landfills.

Rathje and Bray (2000) presented a nonlinear, coupled, stick-slip analytical formulation for sliding of a compliant mass that uses fully nonlinear soil properties to model the dynamic response of the potential sliding mass. This model may be considered to be a generalized SDOF system with the mass and stiffness distributed along the height of the system, as illustrated in Figure 2-7. To develop their model, Rathje and Bray (2000) implemented a coupled, stick-slip response into the nonlinear dynamic response program, DMOD (Matasovic 1993). D-MOD employs a lumped mass formulation for the one-dimensional column in which the soil stiffness is modeled by nonlinear shear springs. In D-MOD, the modified Kondner-Zelasko (MKZ) hyperbolic stress-strain relationship is used to represent the nonlinear hysteretic response of the soil (Matasovic 1993; Matasovic and Vucetic 1995). The Rathje and Bray (2000) model was validated using results from the shaking table experiments of a sliding, deformable soil column conducted by Wartman (1999). In Wartman (1999) tests, the shaking-induced sliding displacement of a deformable soil column on a plane inclined at 11.37 degrees from the horizontal was measured. Theses shaking table tests were performed with sinusoidal input motions of varying frequencies and intensities.

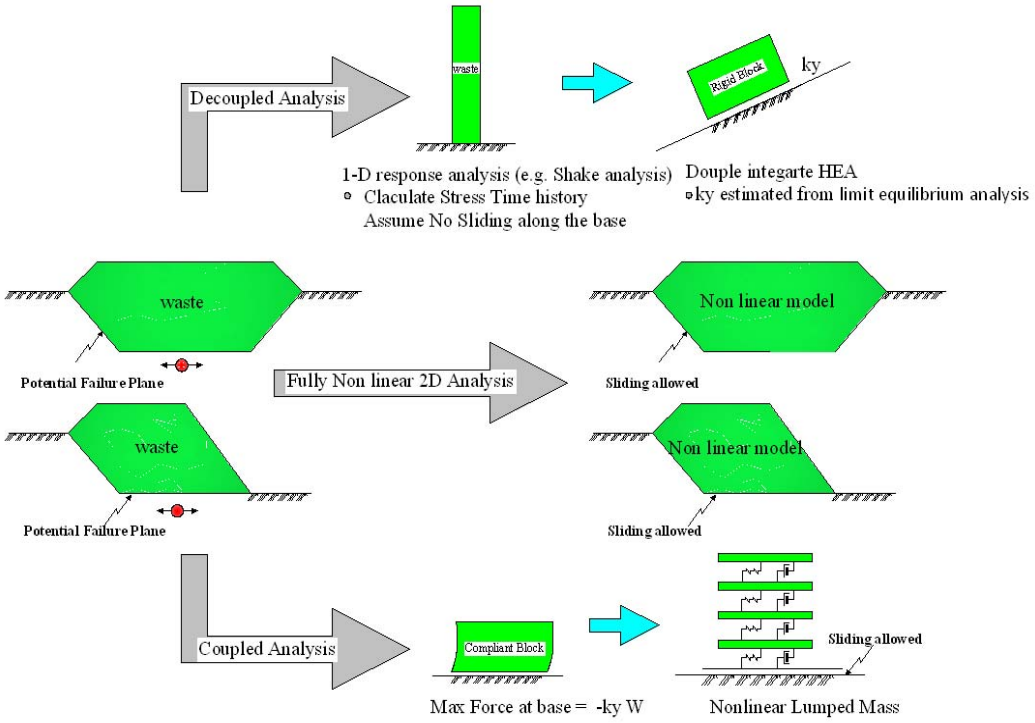

Figure 2-7 Decoupled dynamic response/rigid sliding block analysis, fully non linear 2D analysis and fully coupled analysis

A comparison between the recorded sliding displacement of the soil column in Wartman's tests and the sliding displacement calculated using the coupled sliding model developed by Rathje and Bray (2000) is shown in Figure 2-8(a). The coupled analysis accurately predicts the initiation of sliding at 0.6 s and the final calculated displacement is within 1% of the experimental value. Figure 2-8(b) compares measured and calculated displacements for the same soil column subjected to input motions of varying frequency and with intensities ranging from 0.14*g* to 0.18*g*. The coupled analyses shown in Figure 2-7(b) incorporated a sliding velocity-dependent interface friction angles varying from 16.57^{o} and 17.57 ^{o}. These friction angles were chosen based on a relationship between interface friction angle and sliding velocity developed by Wartman (1999).

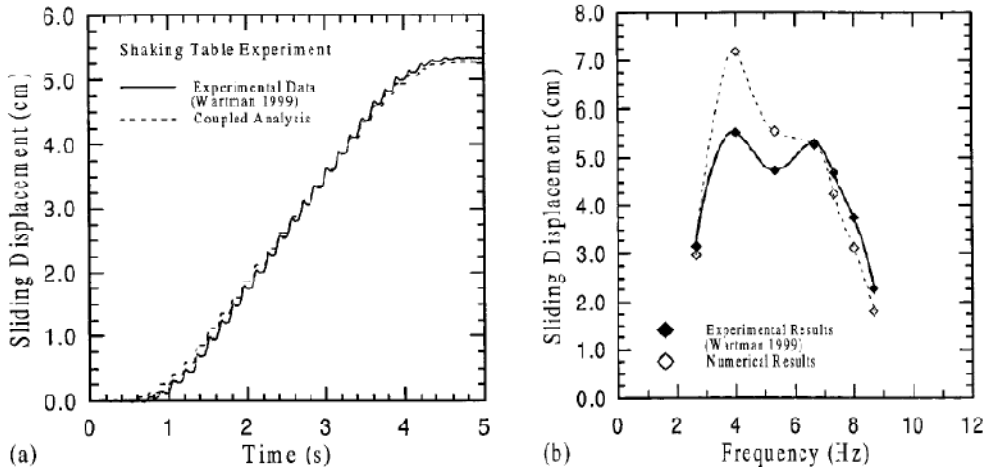

Figure 2-8 Comparison of Experimental Results from Wartman (1999) and Numerical Results from Rathje and Bray (2000) (a) Sliding Displacement Time Histories for 0.18g, 6.7-Hz Input Motion; (b) Experimental and Numerical Sliding Displacement versus Input Frequency (Rathje and Bray 2000)

In Figure 2-9, measured acceleration time histories at the top of the soil column for the Wartman (1999) experiment displayed in Figure 2-8 (a) are compared to calculated values from Bray and Rathje (2000). The maximum accelerations from the coupled analysis and shaking table test compare favorably, with both sets of data revealing high frequency pulses during sliding. The Rathje and Bray (2000) coupled formulation, however, did not accurately predict the high frequency response during sliding in the shaking table tests.

The calculated acceleration-time history at the top of the deformable soil column shown in Figure 2-9 has similar amplitudes in the positive and negative directions, unlike the results of the shaking table results shown in the figure and results of similar shaking table tests using a rigid block on inclined plane performed by Elgamal et al. (1990). The observations from the Elgamal et al. (1990) shaking table tests using a rigid sliding block and other shaking table tests using sliding blocks on a horizontal plane (e.g. Kavazanjian et al. 1991; Yegian and Lahlaf 1992) show that the acceleration transmitted to the rigid

block is limited by the yield acceleration of the sliding interface. However, unlike a rigid sliding block, a deformable soil column vibrates during sliding. Therefore, accelerations greater than the yield acceleration may occur within the sliding mass of a deformable soil column. Also, unlike the rigid block dynamic response, the acceleration at the base of a deformable sliding soil column is not constant because the limiting force at the sliding interface is not directly related to the acceleration directly above the sliding interface but is related to the mass-weighted average of the entire non-uniform acceleration distribution within the soil column.

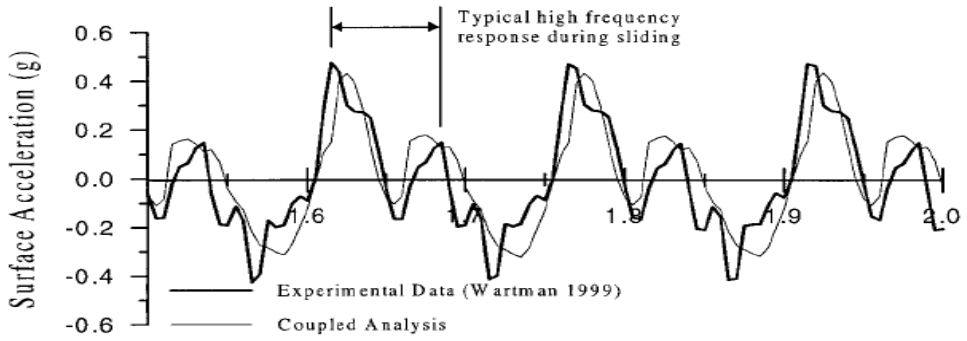

Figure 2-9 Comparison of Surface Accelerations from Shaking Table Experiment from Wartman (1999) and Coupled Analysis (Rathje and Bray 2000)

Figure 2-10 compares the acceleration response spectra at 5% damping calculated at the top of a landfill using the coupled formulation proposed by Rathje and Bray (2000) for a 30 m-high landfill subjected to the Loma Prieta Earthquake Corralitos input motion for sliding at a yield accelerations, k_y, of 0.05 and 0.1 g to the response calculated with D-Mod but with no sliding allowed. Bray and Rathje (2000) concluded that the response between periods of 0.3 and 1.0 s is generally reduced as a result of sliding, particularly for k_y = 0.05. The reduction of spectral acceleration amplitudes at longer periods is a direct result of the change in response characteristics of the soil column that occurs

during sliding. These investigators note that the change in intensity and frequency content of the surface motion of a sliding system could possibly affect the assessment of cover stability for a solid-waste landfill. Rathje and Bray (2000) concluded that, although sliding can reduce the peak acceleration at the top of the landfill by as much as 30%, a substantial amount of sliding must take place before the surface response is significantly affected. When base sliding displacements are maintained below the generally accepted displacement limit used in engineering practice for synthetic liner systems of 150 mm (k_y = 0.1 for this case studied by Bray and Rathje (2000)), the surface response is not significantly modified by the sliding episodes. Therefore, their conclusion was that the response of landfills will only be moderately affected by sliding at allowable levels of base displacement.

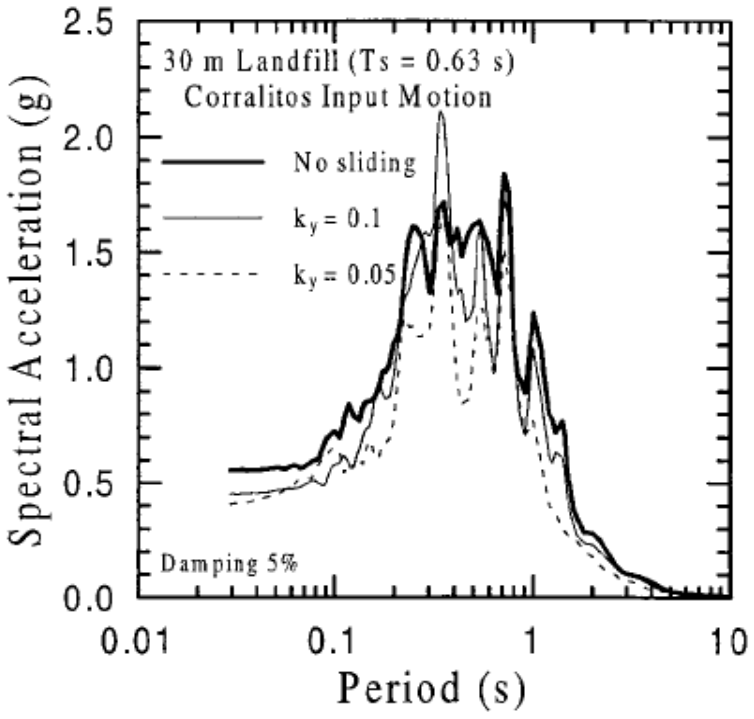

Figure 2-10 Response Spectra of Surface Motions for Sliding and Nonsliding Model of 30-m-High Solid-Waste Landfill (Rathje and Bray 2000)

An important observation from the Bray and Rathje (2000) analysis and the deformable column shaking table experiments by Wartman (1999) is that the acceleration directly above the sliding plane is not limited to a value of k_y, as is observed in rigid block tests as presented in Figure 2-11. In fact, it is the average acceleration of the entire column above the base that is limited by k_y. Furthermore, it can be shown that this average acceleration is equal to the shear stress at the interface divided by the normal stress on the interface.

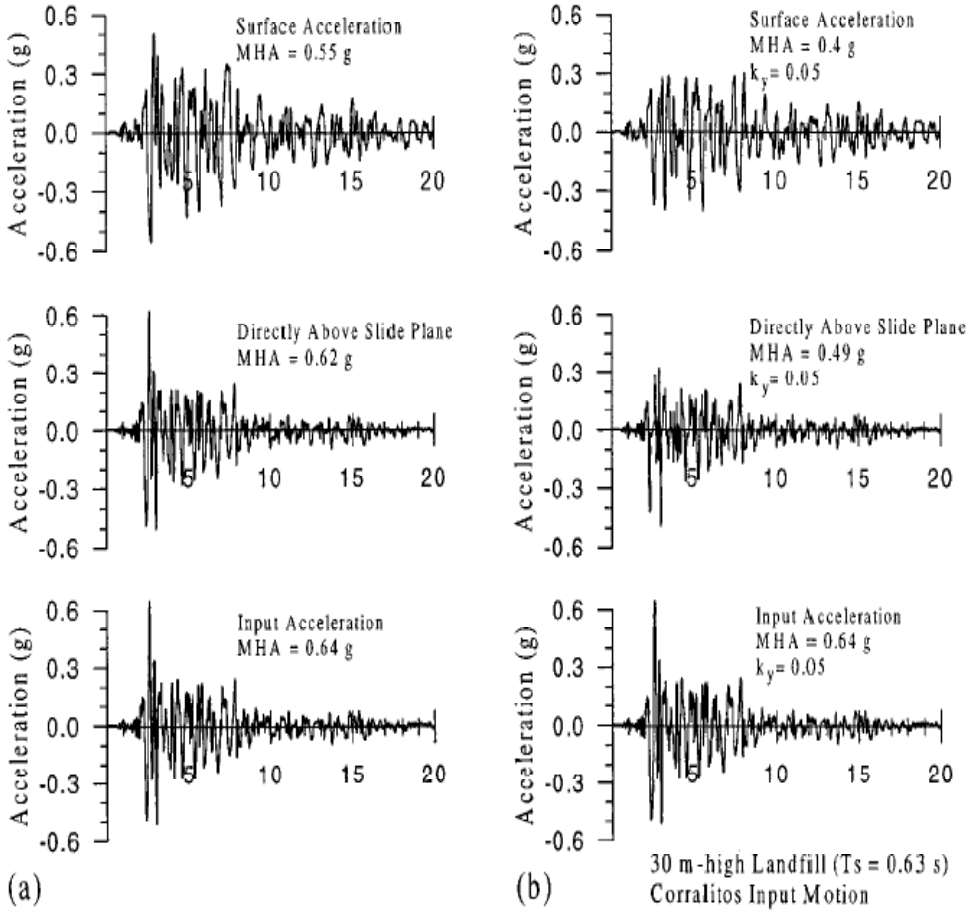

Figure 2-11 Acceleration-Time Histories within: (a) Nonsliding; (b) Sliding (k_y = 0.05) of 30 m high landfill (Rathje and Bray 2000)

Rathje and Bray (2000) studied the effect of the ratio T_s/T_m on the accuracy of displacement predictions for the coupled, decoupled and rigid block methods where T_s is the initial undamped natural period of the soil column and T_m is the mean period of the earthquake motion as defined by Rathje et al. (1998). Rathje and Bray (2000) used a soil column with a changing height while keeping the shear-wave velocity above the sliding interface equal to 240 m/s and assuming a modulus reduction and damping for a soil with a plasticity index, PI, equal to 30. The Superstition Mountain strong motion record (135 component) from the 1987 Superstition Hills earthquake Moment magnitude, M_w, 6.7 was used as the input motion for the comparison study. An interface yield acceleration, k_y, equal to 0.05 was used as input for these analyses. The trend of permanent displacement for both coupled and decoupled models for linear elastic and fully nonlinear seismic response analyses, along with the calculated displacement from a rigid sliding block analyses are presented in Figure 2-12.

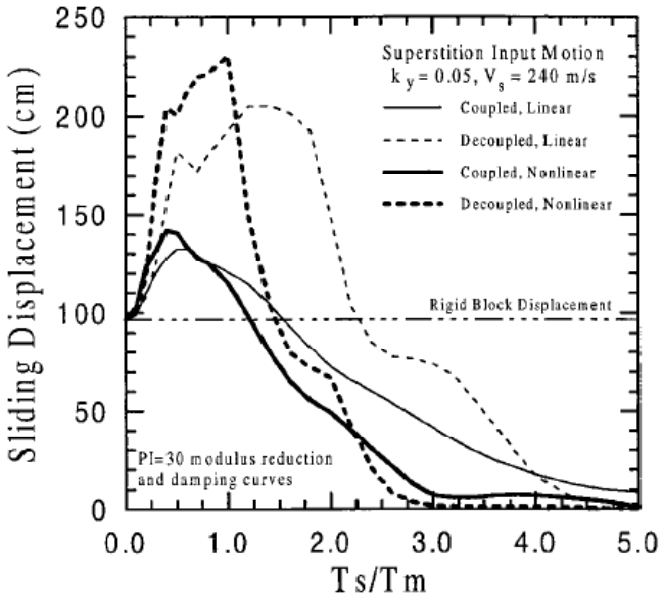

Figure 2-12 Coupled and Decoupled Sliding Displacements Calculated from Linear and Nonlinear Analysis (Rathje and Bray 2000)

Rathje and Bray (2000) distinguished between three different ranges in Figure 2-12 for period ratios T_s/T_m on the trend of the seismic displacements predicted from different methods.

For $T_s/T_m < 0.2$ the results in Figure 2-12 shows that all of the numerical procedures (coupled, decoupled sliding displacements for linear elastic and fully nonlinear seismic response analyses) provide similar sliding displacements. This agreement attributed to the stiffness of the system (short soil columns) with respect to the input motion.

For $0.2 < T_s/T_m < 1.5$, the results in Figure 2-12 shows that decoupled displacements predictions are larger than coupled displacements predictions, which means that the decoupled analysis overpredict the seismic displacements in this range. Rathje and Bray (2000) showed that in this period ratio range the rigid sliding block analysis is significantly unconservative and should not be used.

For $T_s/T_m > 1.5$ the results in Figure 2-12 shows that the rigid sliding block analysis overpredicts the seismic displacements compared to analyses for a compliant mass. For the nonlinear analyses, the decoupled analyses predict higher seismic displacement than coupled analyses in the range $1.5 < T_s/T_m < 2.2$. For period ratios of $T_s/T_m > 2.2$ coupled non-linear analyses show a slightly higher seismic displacement than nonlinear decoupled analyses. For the linear elastic analyses, the decoupled analyses predict higher seismic displacement than coupled analyses in the range $1.5 < T_s/T_m < 4.0$. For period ratios of $T_s/T_m > 4.0$, coupled elastic analyses shows a slightly higher seismic displacement than decoupled elastic analyses.

CHAPTER 3 LANDFILL COMPONENTS CHARACTERISTICS

3.1 Introduction

Landfills that accept MSW typically do not accept hazardous waste, except of incidental quantities mixed with MSW. This thesis will restrict its focus to the MSW landfills. In order to perform static or seismic analyses of landfills the cyclic and static properties of the various landfill components must be characterized. Modern landfills almost always contain several layers of geosynthetics. The potential for in-plane slip or relative displacement at the interfaces has a crucial rule in the assessment of the dynamic and static stability of landfills. These and other relevant characteristics of the behavior of these geosynthetics layers will be reviewed in this chapter, including internal and interface behavior of geosynthetics under shear stress.

Uncertainty in the value of MSW properties and the variability of these properties make it challenging to evaluate the static and the dynamic behavior of the waste. This chapter will review laboratory and field testing conducted to characterize static and dynamic material properties of MSW.

3.2 Static Shear Strength of Geosynthetic Interfaces

The stability of liner systems in landfills is often controlled by the interface and internal in-plane shear strength of the various components of the liner system. The importance of interface strengths was illustrated by the slope-stability failure in Phase IA of Landfill B-19 at the Kettleman Hills facility in Kettleman City, California in 1988. The landfill was constructed in an oval-shaped bowl carved into an existing valley to a depth of approximately 30 m and covered an area of approximately 120,000 m^2. A stability failure

occurred during filling of Phase IA on 19 March 1988 that resulted in 11 m of lateral displacement of the waste fill and 4.3 m vertical settlement around the crest of the fill. Byrne et al. (1992) concluded that sliding primarily occurred along the 1.1 m thick secondary clay liner/secondary high-density polyethylene (HDPE) geomembrane interface in the double composite liner system. This led both landfill designers and researchers to pay more attention to the interface shear strength of the geosynthetic components of landfill liner systems and the potential for failure along those interfaces. List of typical interfaces in modern MSW landfill liner system are presented in Table 3-1.

Table 3-1 Typical interfaces in MSW landfill liner and cover systems

Interface	Comments
GM/clay	Textured or smooth geomembrane / clay liner
GM/geotextile	Textured or smooth geomembrane / geotextile
GM/GCL	Textured or smooth geomembrane / geosynthetic Clay Liner
GM/Drainage aggregate	Textured or smooth geomembrane / sand or gravel aggregate
GM/Geonet	Textured or smooth geomembrane / drainage geonet
Geotextile/Soil	Woven or Non woven Geotextile /soil
GCL/Soil	Cover only

Notes: Geomembrane may be smooth, textured, or smooth textured
Geotextiles may be woven or non woven
GCLs are typically needle-punched reinforced
Soil may be sand silt or clay

3.2.1 **Shear strength of GM HDPE/GCL liner interface**

A common interface in landfill liner systems is between a geomembrane (GM) and a (GCL). Triplett and Fox (2001) conducted interface shear tests between smooth and textured high density polyethylene (HDPE) GMs and woven/nonwoven needle-punched GCL. The interfaces tested in this program are summarized in Table 3-2. The tests were performed using a large direct shear machine capable of measuring peak shear strength and large displacement shear strength at 200 mm. Table 3-3 lists the peak shear strength

parameters, large displacement shear strength parameters, and their applicable stress range for each interface tested by Triplett and Fox (2001). Peak shear strengths for the textured GM/nonwoven geotextile interfaces were consistently higher than those measured for the textured GM/woven geotextile interfaces.

Triplett and Fox (2001) also conducted testing to evaluate the effect of the shear rate on the shear strength parameters of the interfaces shown in Table 3-2. The effect of the horizontal displacement rate on the peak and large displacement shear strengths of the SM/W, LM/W, and CX/W interfaces (σ_n = 72.2 kPa) is shown in Figure 3-1.

Table 3-2 GM/GCL Interfaces Tested by Triplett and Fox (2001)

GM/GCL interface	Geomembrane	GCL
SM/W	Smooth HDPE (40 mil)	Woven geotextile of woven/ nonwoven NP GCL
SM/NW	Smooth HDPE (40 mil)	Nonwoven geotextile of woven/ nonwoven NP GCL
LM/W	Laminated textured HDPE (40 mil)	Woven geotextile of woven/ nonwoven NP GCL
LM/NW	Laminated textured HDPE (40 mil)	Nonwoven geotextile of woven/ nonwoven NP GCL
CX/W	Coextruded textured HDPE (40 mil)	Woven geotextile of woven/ nonwoven NP GCL
CX/NW	Coextruded textured HDPE (40 mil)	Nonwoven geotextile of woven/ nonwoven NP GCL

Table 3-3 Peak and Large Displacement Shear Strength Parameters (Triplett and Fox 2001)

GM/GCL interface	Normal stress range (kPa)	Peak strength parameters		Normal stress range (kPa)	Large displacement strength parameters	
		c_p (kPa)	Φ_p (degrees)		c_{ld} (kPa)	Φ_{ld} (degrees)
SM/W	6.9-486	0.3	9.8	6.9-127	0.3	8.1
				127-486	3.0	6.9
LM/W	6.9-124	2.2	21.3	6.9-134	1.0	12.7
	124-486	22.0	13.3	134-486	15.7	6.6
CX/W	6.9-279	0	23.7	6.9-72	0	15.0
				72-279	4.9	11.3
SM/NW	6.9-486	0.4	9.9	6.9-127	06	9.2
				127-486	5.8	6.9
LM/NW	6.9-279	7.4	31.7	6.9-70	2.3	18.5
				70-279	11.8	11.2
CX/NW	6.9-279	7.2	28.3	6.9-135	3.4	14.4
				135-279	16.0	9.3

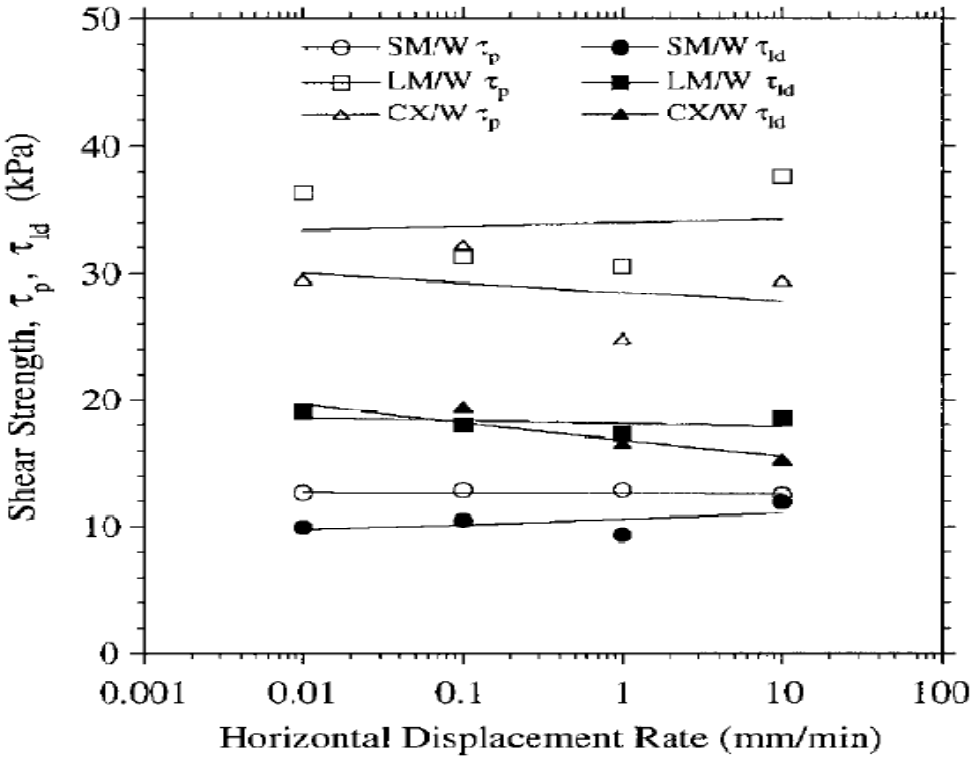

Figure 3-1 Effect of Horizontal Displacement Rate on Shear Strength of GM/GCL Interfaces (Triplett and Fox 2001)

3.2.2 **Shear strength of HDPE geomembrane/geotextile interface**

Another common interface in landfill liner systems is between the geomembrane and a geotextile. Stark et al. (1996) conducted torsional ring shear tests on high density polyethylene (HDPE) GM/Geotextile interfaces to determine the shear strength of the interface. In their testing they investigated the effect of geomembrane texturing on the interface shear strength. In addition, the effects of the geotextile fiber type and mass per unit area on the HDPE geomembrane interface strength were also investigated.

Figure 3-2 shows typical failure envelopes for a geomembrane/ nonwoven geotextile interface. It can be seen that the failure envelope is fairly linear. Figure 3-3 presents a

comparison of failure envelopes for smooth and textured geomembrane/nonwoven geotextile interfaces. It can be seen that the peak and residual shear strengths are increased by 200% to 300% by the use of textured geomembrane instead of smooth geomembrane.

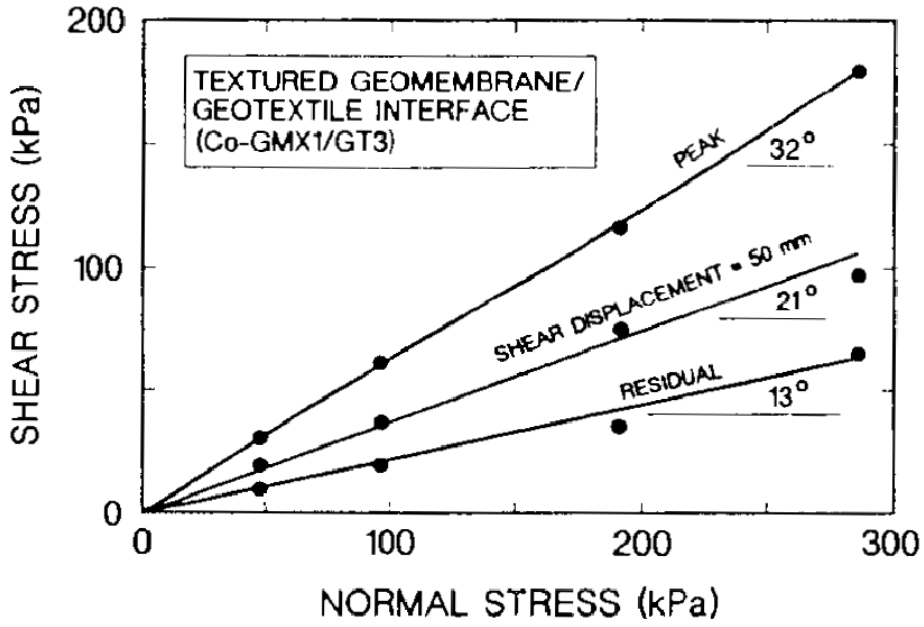

Figure 3-2 Typical failure envelope for textured geomembrane/ nonwoven geotextile interface (Stark et al. 1996)

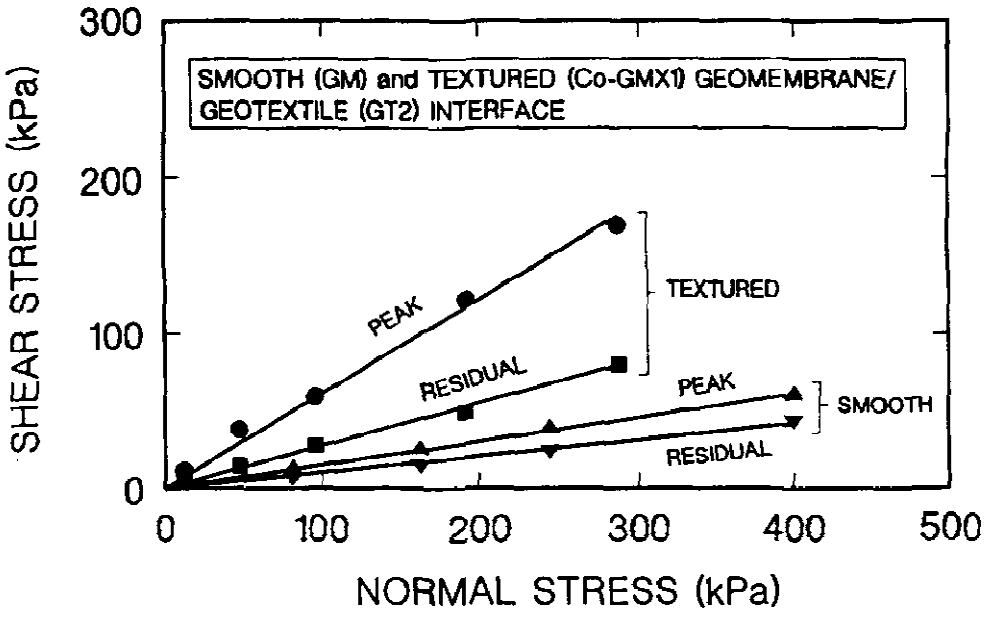

Figure 3-3 Comparison of the failure envelopes for smooth and textures geomembranes/geotextile interfaces (Stark et al. 1996)

Stark et al. (1996) also investigated the effect of the displacement rate on the textured geomembrane/nonwoven geotextile interface. Figure 3-4 shows the peak and residual shear stresses for a textured GM/geotextile interface tested at 5 different strain rates at normal stress of 96 kPa. The figure shows that the shear strength of this interface did not change significantly as a result of changing the shear rate.

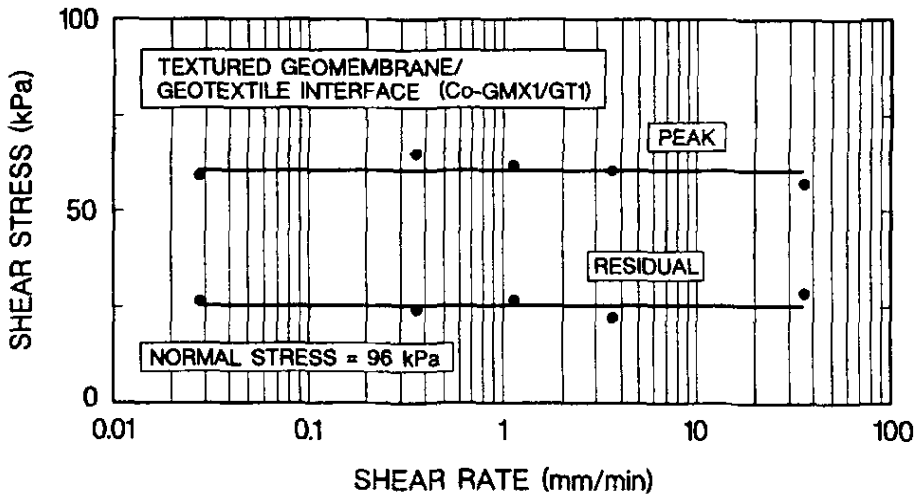

Figure 3-4 Effect of the shear displacement rate on textured Geomembrane/Nonwoven Geotextile interface (Stark et al. 1996)

The inclined plane (tilt table) test is used when studying the stability of sloping geosynthetic liner systems under conditions of low normal stress. The inclined plane offers the dual advantage of enabling testing at low normal stresses at the interface and simplicity in the test setup.

Gourc et al. (2004) present the results of a large scale inclined plane test where the tensile forces and strains in the geomembrane liner and overlaying geotextile were measured as a function of increasing the length L_c, of the granular soil layer placed on top of the geomembrane (Figure 3-5). The geosynthetic lining system was supported by a clay base layer and consisted of an HDPE geomembrane overlain by a non-woven (NW) geotextile and a 0.30 m thick granular cover soil layer. The friction angles measured in laboratory shear box tests for the various interfaces were 9° for GM/clay interface, 12° for NW geotextile/GM interface, and 29° for the granular soil/NW geotextile interface. The forces acting on the geosynthetics at top of the slope were measured by force sensors positioned between the geotextile sheet clamps and the fastening posts used to anchor the

geosynthetic at the top of the slope. Gourc et al. (2004) measured the displacements of the geosynthetics and the cover granular layer by means of cable-type displacement sensors linked to the fastening posts and regularly spaced on the geosynthetic sheets and in the granular soil layer.

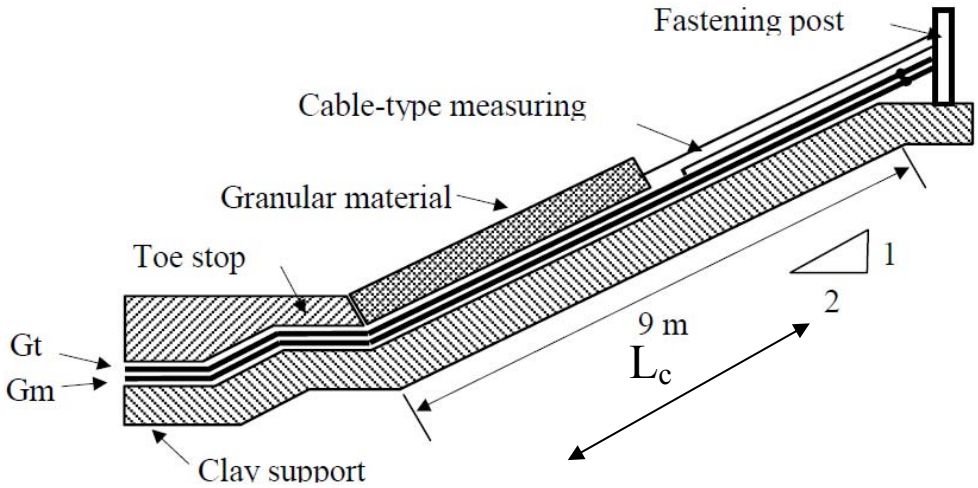

Figure 3-5 Monitoring on a slope barrier of the Montreuil landfill (Gourc et al. 2004)

The experimental procedure used by Gourc et al. (2004) involved monitoring the forces and displacements in the various layers of the liner while loading the granular material layer meter by meter on the slope over a total loading length, L_c, of 6 m. Figure 3-6 presents the increase in the tensile forces in the geotextile and geomembrane measured at the top of the slope with placement the soil cover (i.e. with increasing L_c). The plots of the strains in the GM and geotextile sheets with increasing L_c, in Figure 3-6 show that both the geotextile and GM a subjected to positive tensile strains (elongation) at the top of the slope but that the tension decreases with decreasing L_c. The plots in Figure 3-7 show that the geotextile develops compressive strains at the toe of the slope. The formation of wrinkles as a mechanism for accommodating these compressive strains was postulated by Gourc et al. (2004) as illustrated in Figure 3-8. As the slope length is

constant, the elongation of the sheet at the top of the slope should be compensated by compression at the bottom of the slope. However, as non-woven geotextile is a very compressible material it is not clear that the compressive strains shown in Figure 3-7 are sufficient to generate wrinkles in the geotextile. Gourc et al. (2004) noted that this complex behavior is generally not taken in consideration in design and numerical calculations.

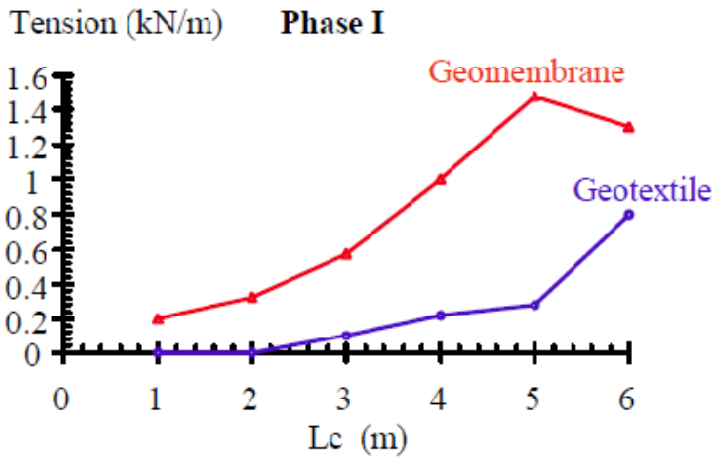

Figure 3-6 Montreuil landfill slope: tensile forces in the geotextile and geomembrane (Gourc et al. 2004)

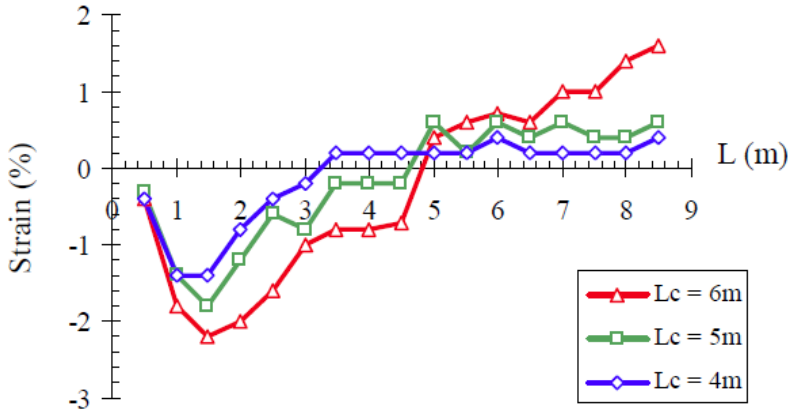

Figure 3-7 Montreuil landfill slope: Distribution of strains in the geotextile (elongation positive) (Gourc et al. 2004)

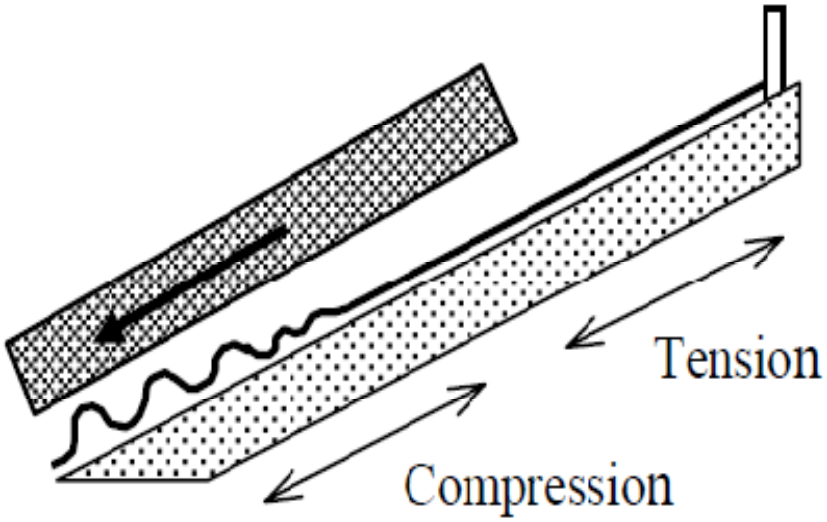

Figure 3-8 Mechanism inducing wrinkles at the base of the slope (Gourc et al. 2004)

3.3 Geosynthetics Internal Behavior

3.3.1 Internal axial behavior of geotextiles

In-soil tests are often conducted to assess the axial stress-strain behavior of geotextiles in tension, particularly nonwoven geotextiles. The results of this type of tests are influenced by the normal stress (i.e. confinement) on the geosynthetic element. The influence of confinement on the mechanical behavior of mechanically bonded nonwoven geotextiles was studied by McGown et al. (1982). Figure 3-9 shows schematically the test device and some of the results from McGown et al. (1982) in tests on nonwoven geotextiles. Confinement increases interlocking and friction among geotextile fibers, yielding a stiffer response of the geotextile with increasing confinement. It is important to point out that in this type of test arrangement does not directly measure the in-plane tensile properties of the geotextile: friction between geotextile and confining soil takes place and influences the magnitude of the applied tensile load and measured tensile stiffness (Palmeira 2009).

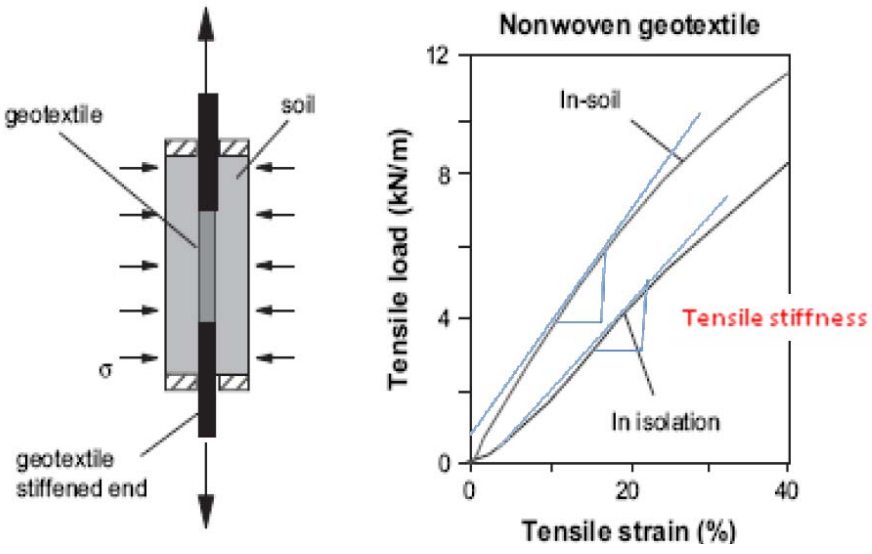

Figure 3-9 Effect confinement on geotextile stiffness (after Palmeira 2009)

An improved version of the geosynthetic tensile loading test was developed by Palmeira (2009) to avoid the friction effect. In Palmeira (2009) test, illustrated in Figure 3-10 (a) lubricant is applied to the sides of the geotextile to minimize friction between soil and the geotextile. The plot presented in Figure 3-10 (b) shows that the secant tensile stiffness obtained for this arrangement is significantly greater than that obtained with the geotextile in isolation (without confinement), but smaller than the value obtained when friction between the confining soil and geotextile specimen is allowed.

Figure 3-10 (c) shows that the tensile load along the geotextile specimen length for the lubricated geotextile type of test arrangement is constant, in contrast to what is observed in the traditional apparatus, where the tensile load in the geotextile varies due to friction between the soil and the geotextile.

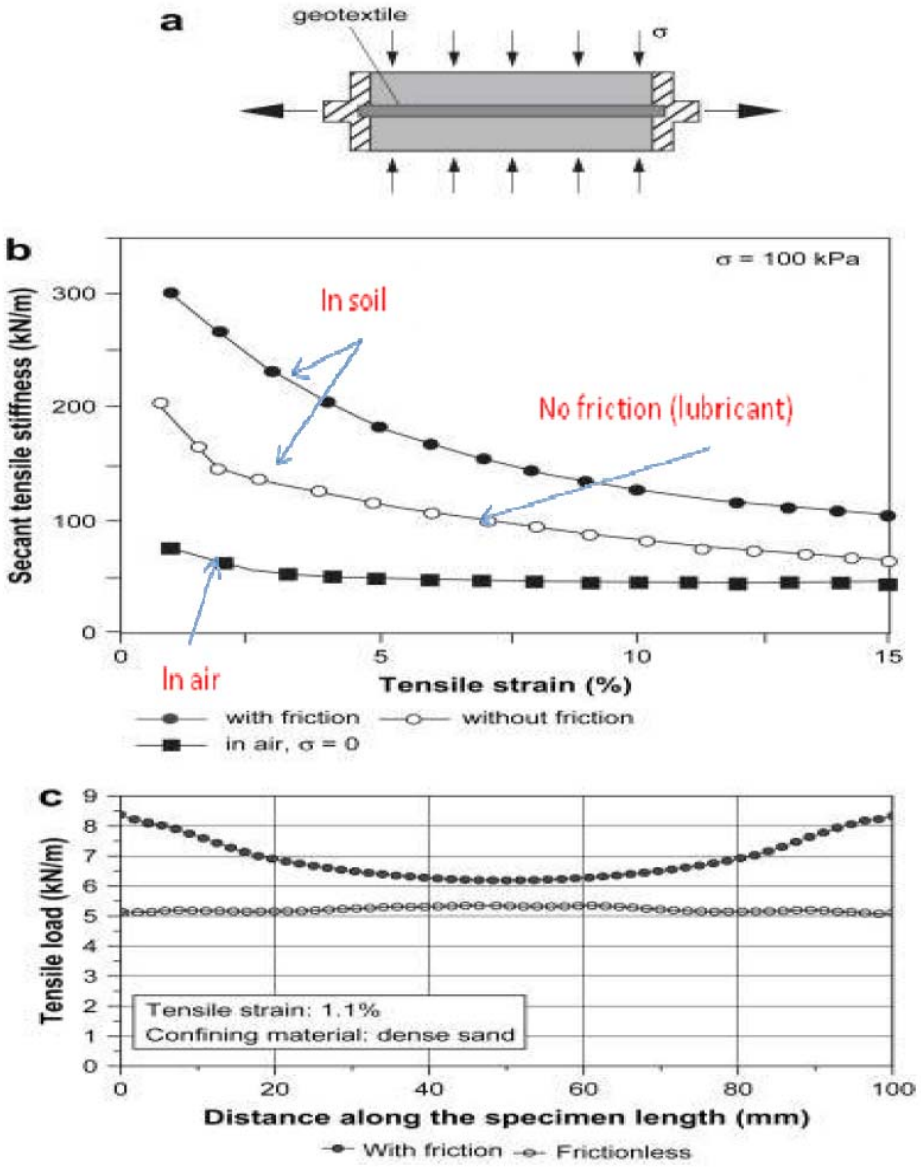

Figure 3-10 Results of in-soil tensile tests with and without friction between soil and geotextile (a) Frictionless in-soil tensile test. (b) Comparison between test arrangements. (c) Variation of tensile load along the geotextile specimen length (after Palmeira 2009)

3.4 In Situ Strain Measurement of HDPE GM system in Northern California

Yazdani et al. (1995) presented three years of in situ measurements from strain gauges installed on a 1.5 mm (60 mil) HDPE geomembrane used as a liner for a municipal solid waste landfill in Northern California. The instrumented MSW cell is located at the Yolo County Central landfill (YCCL), situated 5 kilometers northeast of Davis, California, USA.

The Yazdani et al. (1995) measurements were conducted on Module A, the first 8 hectare HDPE composite lined landfill cell at the YCCL, constructed to meet US EPA Subtitle D standards. The composite liner system consisted of 0.6 m of $1x10^{-7}$ cm/s compacted clay overlain sequentially by a 60 mil (1.5 mm) HDPE geomembrane, a geonet, a non-woven geotextile, and 0.3 m of a soil operations layer. Strain gauges and thermocouples were installed at seven locations along the north and east side slopes of Module A. In total, 19 locations within the module were instrumented with a half-bridge Wheatstone strain gauge configuration. Figure 3-11 shows the YCCL site plan and the location of the seven strain gauge stations (A through G) within Module A. Figure 3-12 shows a typical cross-section of Module A indicating the locations of the strain gauges and the thermocouples, examples of the measurements recorded at the site are shown in figures Figure 3-13 to Figure 3-15.

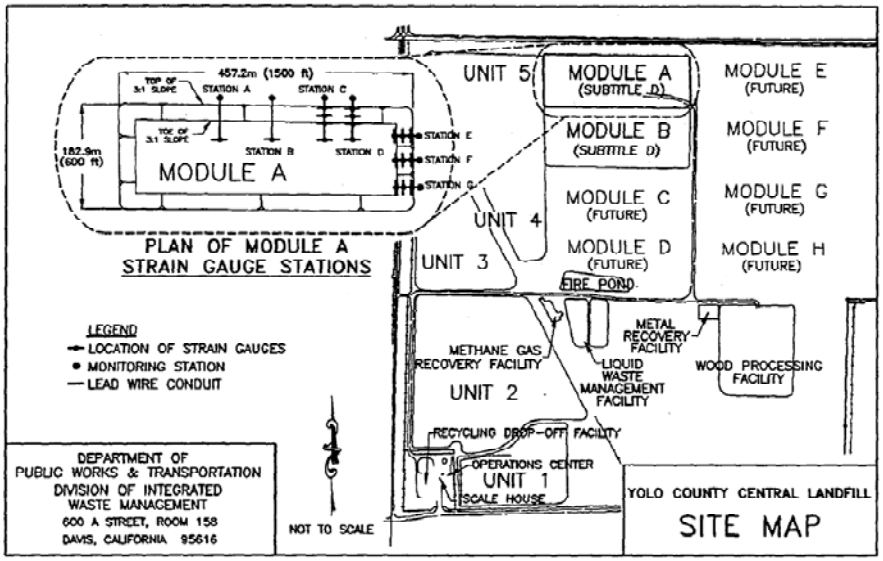

Figure 3-11 site plan and location of the seven strain gauge stations in Module A (Yazdani et al. 1995)

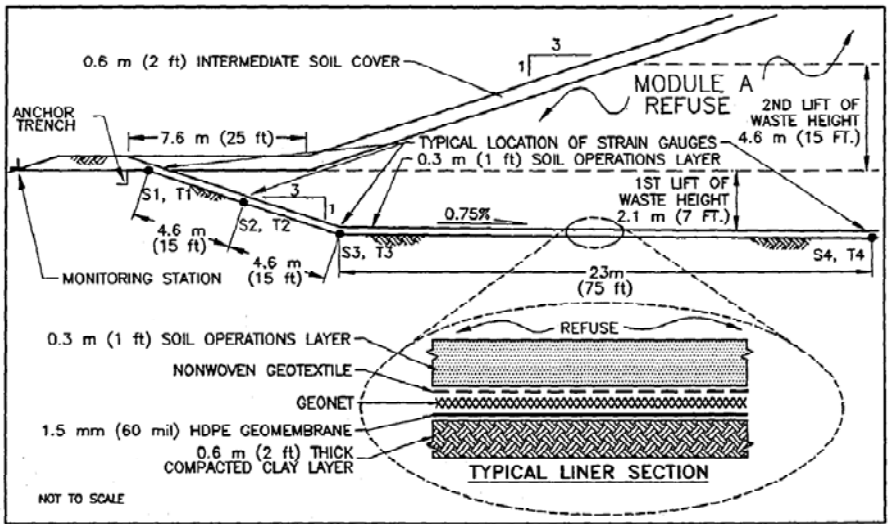

Figure 3-12 Typical Cross-Section of the Instrumented Landfill liner (Yazdani et al. 1995)

Figure 3-13 presents plots of the strain response at two locations within Module A, both at the bottom of the landfill cell and located beneath 12.2 m of waste. Strain gauge A experienced an initial peak compressive strain of over 0.1% immediately after the placement of the operation soil layer and the first layer of waste. The GM at strain gauge

A relaxes to a residual compressive strain of 0.07% at the end of loading. The tension in strain gauge B increased to a value of approximately 0.09% tensile strain and then relaxed to approximately 0.06% tensile strain at the end of loading.

The strain responses of all four gauges at station C are presented in Figure 3-14. The initial peaks of strain at all four locations are attributed the placement of the first lift of waste. Two gauges of the top (S1C) and the middle (S2C); both showed a residual tensile strain in range of 0.12% to 0.19%. The gauge at the toe of the slope (S3C) was on tensile strain of 0.02%, while the gauge at the bottom of the cell (S4C) was in compression strain of about 0.08%.

The strain responses of three gauges installed at station G are presented Figure 3-15. The gauge at the top of the slope (S1G) was strained at about 0.27% tensile strain at the end of the monitoring period. After a year and half the tensile strain at station G jumped from 0.14% to 0.3%; this increase attributed to adding a second lift of waste above this station (G). The gauge at the toe of the slope (S3G) was in compression all the time and reached 0.13% compression strain at the end of the testing program.

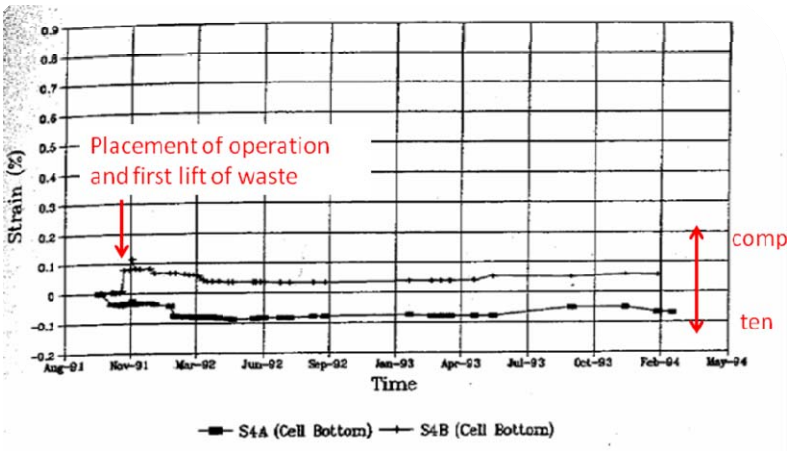

Figure 3-13 Strain response of the station A and B gauges (Yazdani et al. 1995)

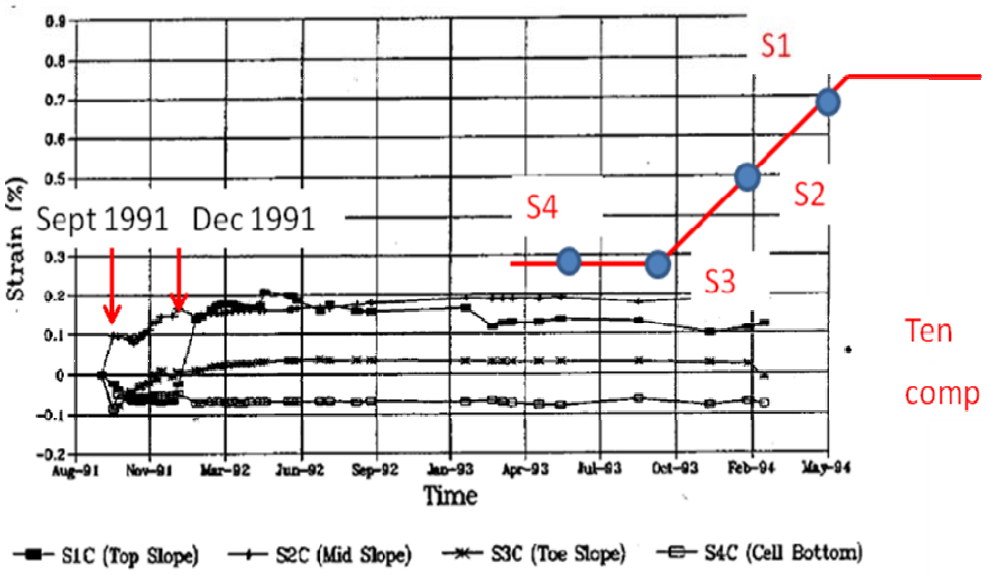

Figure 3-14 Strain response of the station C gauges (Yazdani et al. 1995)

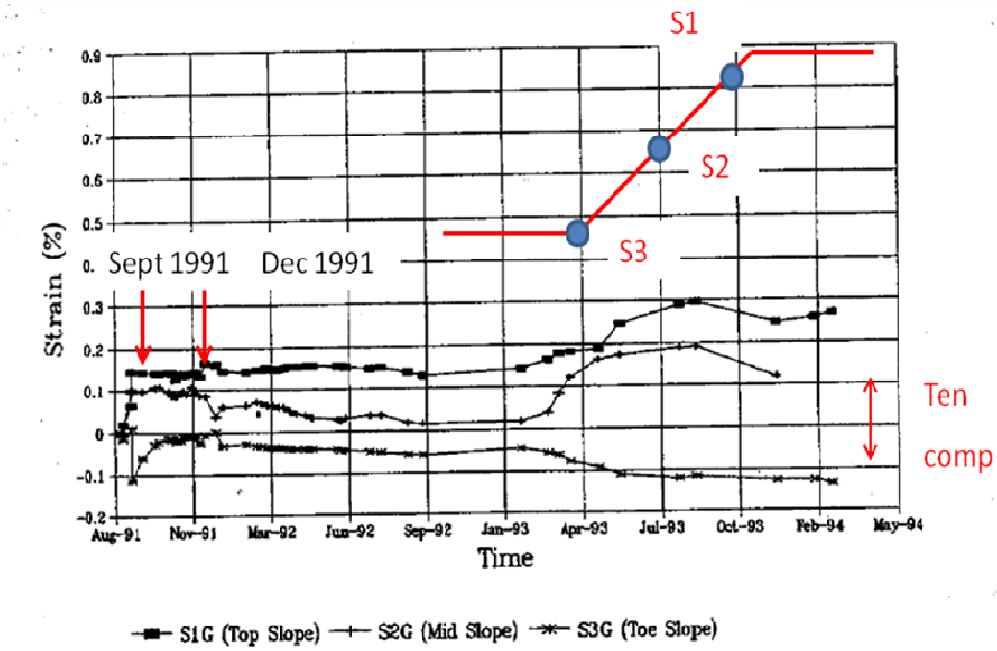

Figure 3-15 shows strain response of the station G gauges (Yazdani et al. 1995)

3.5 Internal axial behavior of HDPE geomembrane

Merry and Bray (1996) performed a series of wide strip tension tests on HDPE geomembrane. This type of test provides test from which the tensile stress-strain response of the geomembrane may be calculated. In their calculations Merry and Bray (1996) accounted for the volumetric response of the geomembrane. The volumetric response was evaluated by measuring the lateral response of the geomembrane.

Figure 3-16 shows the test apparatus, used by Merry and Bray (1996), the HDPE specimen clamped into apparatus prior to the start of tension test. Figure 3-16 shows the test specimen at different stages of the tension test (at 5%, 10%, 20% and 50% axial strain). Up to 10% strain the grid lines on the specimen still appear as straight lines, although a small amount of deformation can be detected along the vertical edges of the specimen, particularly near the top and bottom of the specimen. At higher strains, the thinning and deformation in the lateral direction is more distinct than at lower strains.

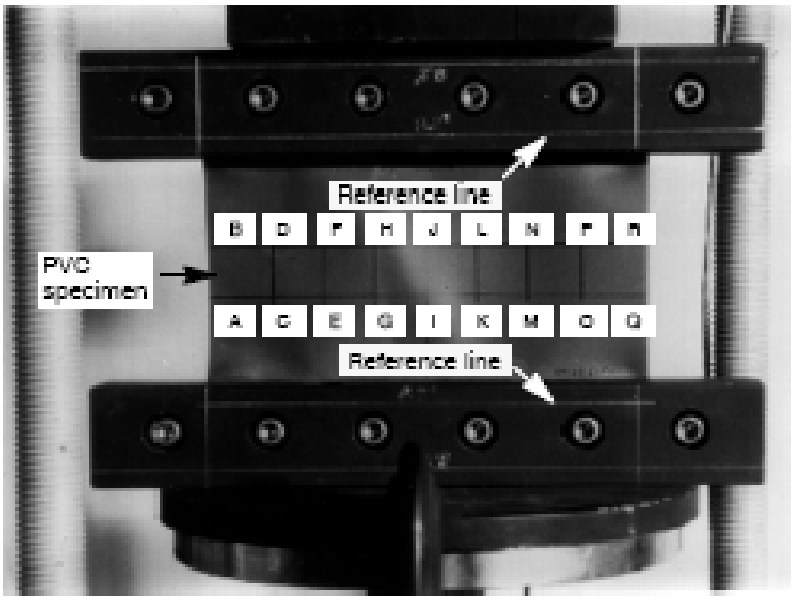

igure 3. Initial setup of geomembrane wide strip tension test.

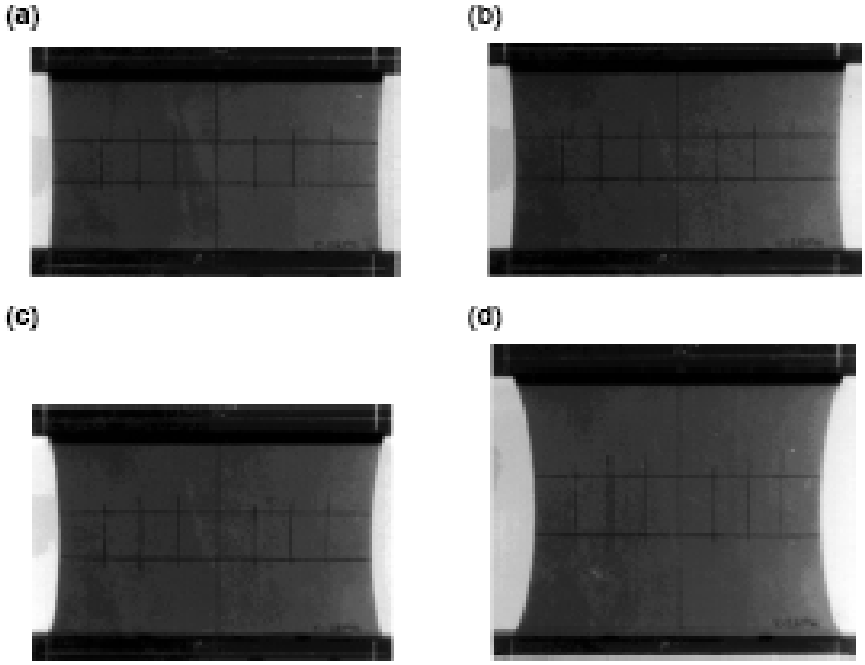

Figure 3-16 Clamps to clamp the test specimens, PVC specimen in wide strip tension at approximately: (a) 5% strain; (b) 10% strain; (c) 20%strain; (d) 50%strain (Merry and Bray 1996)

Merry and Bray (1996) investigated the effects of the aspect ratio of the HDPE geomembrane specimens on their tensile stress-strain response. Figure 3-17 shows the stress-strain results from tests performed on specimens with aspect ratio from 5.5 (304.8 mm wide × 55.8 mm long) to 0.10 (25.4 mm wide × 254.0 mm long). Merry and Bray (1996) concluded that there was no systematic variation in the stress-strain response due to changes in the specimen aspect ratio, indicating that all of the tests results yielded the true stress-strain response of the HDPE GM. It is worth noting that the initial tensile stiffness (Modulus) of the HDPE GM is 3-4 times greater the secant modulus at yield of the specimen as toted by Giroud (1994).

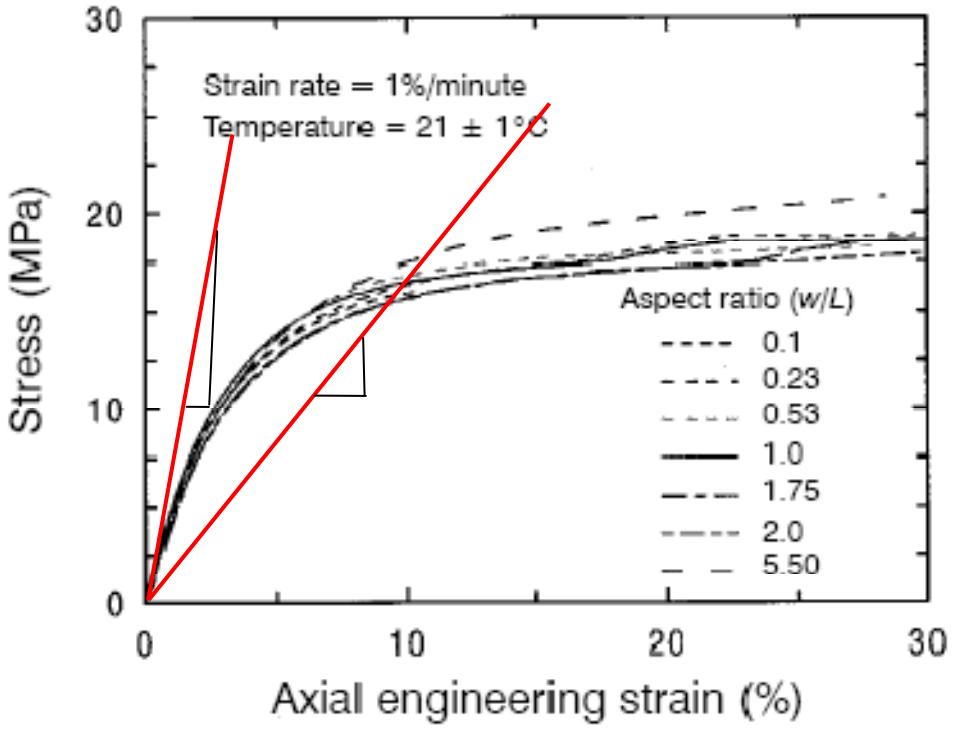

Figure 3-17 Comparison of uniaxial tension test results with different aspect ratios for HDPE geomembrane specimens (Merry and Bray 1996)

Giroud (1993) conducted more than 500 uniaxial tensile tests on HDPE geomembrane specimens from five US manufacturers at temperatures ranging from 20^{o} C to 70^{o} C. The tests did not show large differences between the stress–strain curves for HDPE geomembranes from different manufacturers (Giroud 2005). Figure 3-18 (a) presents the average uniaxial stress–strain curves obtained from the testing program conducted by Giroud (1993) for HDPE geomembranes at different testing temperatures (only the portion of the curve between the origin and the yield peaks are shown). Giroud (2005) indicated that the relationship between the geomembrane yield stress (σ_y) and temperature is linear as shown graphically in Figure 3-18 (b). The relationship between the yield strain and the temperature is shown in Figure 3-18 (c).

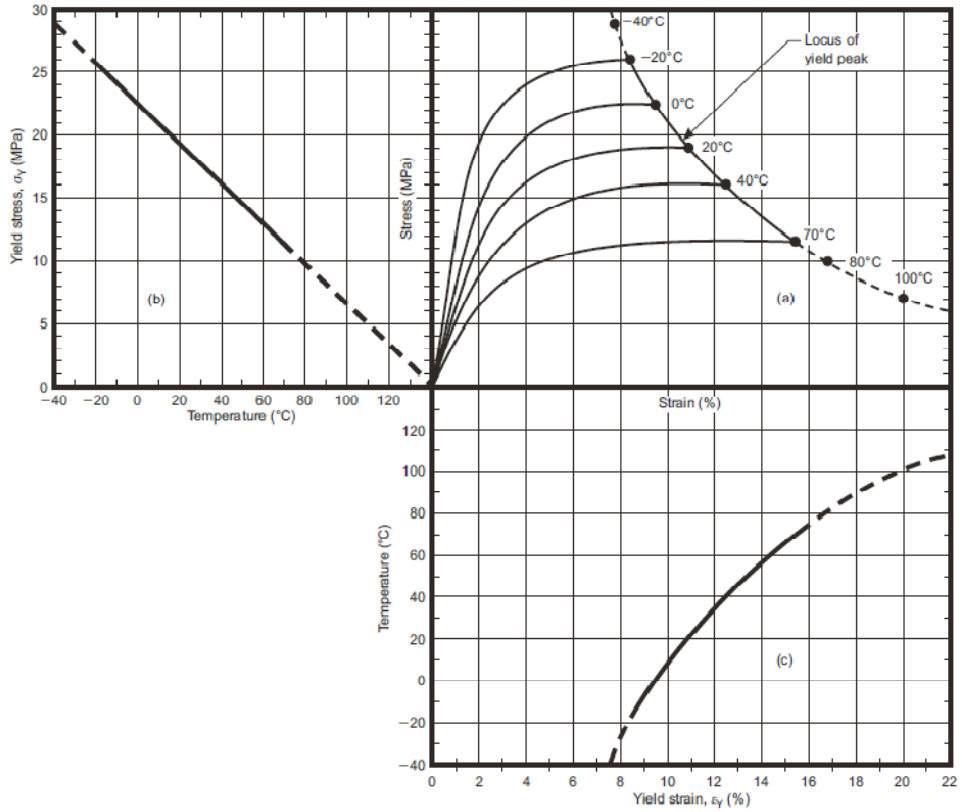

Figure 3-18 Average tensile characteristics of HDPE geomembranes as a function of temperature: (a) uniaxial stress–strain curves from the origin to the yield peak; (b) yield stress as a function of temperature; (c) yield strain as a function of temperature (Giroud 2005)

Giroud (2005) showed that an N-order parabola, where N = 4, was a good approximation of a unique normalized stress–strain curve for all tested HDPE geomembranes regardless of temperature. This parabola is shown in Figure 3-19. The equation for the N-order parabola is given by Giroud (2005) as:

$$\frac{\sigma}{\sigma_y} = 1 - \left(1 - \frac{\varepsilon}{\varepsilon_y}\right)^N \tag{4}$$

where σ_y is the uniaxial stress at yield, ε_y is the uniaxial strain at yield, and N is an exponent equal to 4 for HDPE.

Using this equation, only the stress and strain at the yield peak need be known for a given HDPE geomembrane at a given temperature to develop the uniaxial stress–strain curve of the geomembrane between the origin and the yield peak.

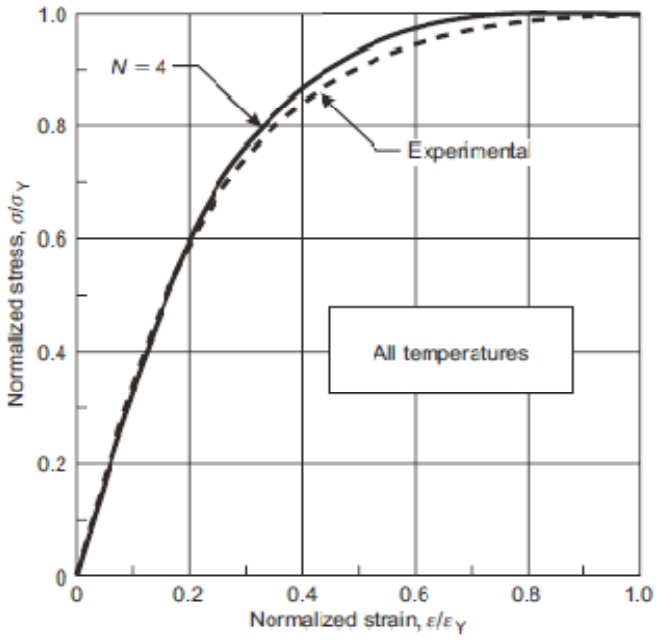

Figure 3-19 HDPE geomembrane normalized uniaxial stress– strain curve, for all temperatures (Giroud 2005)

From Eq. (4), Giroud (1994) derived the relationships between the tangent moduli, E_{tan}, for any strain below the yield strain as:

$$E_{\tan} = \frac{N\sigma_y}{\varepsilon_y}\left(1-\frac{\varepsilon}{\varepsilon_y}\right)^{n-1} \tag{5}$$

The tangent modulus as a function of axial strain is presented in Figure 3-20. An important aspect of the Giroud (1994) N-order parabola is that the initial modulus of an HDPE geomembrane, E_o, is N times the secant modulus at yield as follows:

$$E_o = N\frac{\sigma_y}{\varepsilon_y} = 4\frac{\sigma_y}{\varepsilon_y} \tag{6}$$

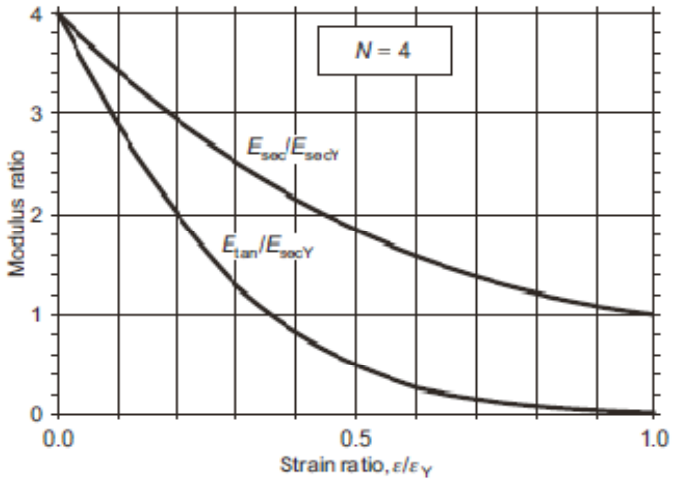

Figure 3-20 geomembrane uniaxial secant and tangent moduli at any strain below the yield strain (Giroud 2005)

All the results presented above were obtained from uniaxial tests. In the field, geomembranes are generally subjected to biaxial or triaxial stress states. For the case of the axial strain in a plane strain biaxial stress states, Giroud (2005) conducted an analysis based on energy conservation that led to the following relationships between the uniaxial

yield strain, ε_y, and the plane strain biaxial yield strain, ε_{yps} in the geomembrane as a function of the Poisson's ratio, ν, as follows:

$$\varepsilon_{yps} = \varepsilon_y \frac{(1-\nu^2)}{\sqrt{1-\upsilon+\nu^2}} \tag{7}$$

Assuming nearly incompressible properties for the geomembrane a Poisson's ratio of 0.48 is a reasonable assumption. This means that based upon Eq. (7), the yield strain in the plain strain condition, ε_{yps}, (representative of conditions in the field) would be 0.91 ε_y.

3.5.1 **Geomembrane stress concentration**

Failure in a geomembrane may occur due to stress concentration even though the average stress on the geomembrane itself is not enough to cause failure. Giroud (2005) divided the different causes for stress concentration in a geomembrane into two main categories: stress concentration due to scratches in geomembranes and stress concentration due to bending at the seams. In both cases, the first cause of stress concentration is an abrupt change in geometry, i.e. an abrupt change in thickness due to the seam overlap or due to the penetration of the scratch into the geomembrane. Figure 3-21 and Figure 3-22 illustrate these two sources of abrupt geometry change.

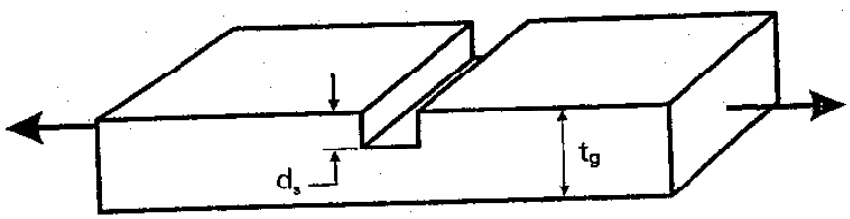

Figure 3-21 Geomembrane with scratch (Giroud 1993)

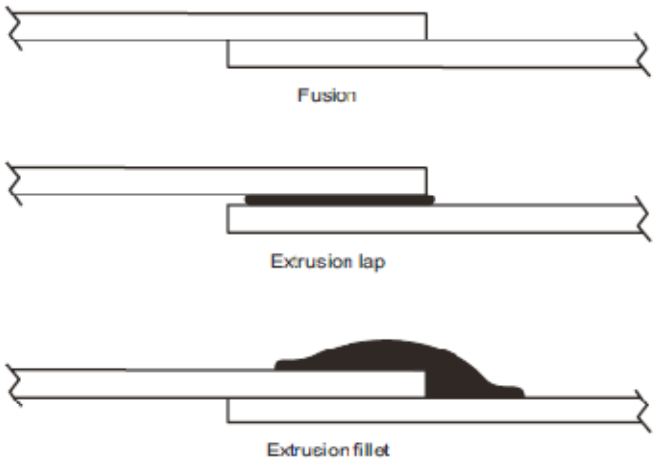

Figure 16. Seam types, with the extrudate shown in black

Figure 3-22 Seam types, with the extrudate shown in black (Giroud 2005)

3.5.1.1 Strain concentration due to bending at seams

Giroud (2005) shows that, seams rotate perpendicular to the loading direction when a geomembrane is loaded in tension. Giroud (2005) also indicates that the rotation of the seam is due to equilibrium of the tensile forces applied on the geomembrane, which requires a portion of the geomembrane on one side of the seam to be in the same plane with a portion of the geomembrane on the other side. As a result, bending axial strain builds in the geomembrane as it bends on each side of the seam, as illustrated in Figure 3-23.

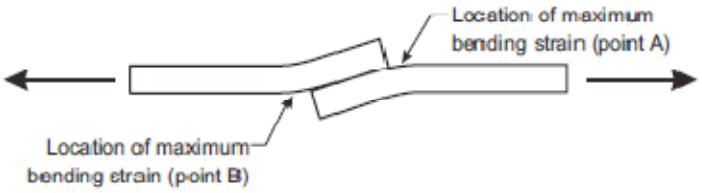

Figure 3-23 Bending strain due to rotation in the seam (Giroud 2005)

Giroud et al. (1995) performed a detailed analysis of the additional strain in the geomembrane due to bending of the seam. The main finding of the Giroud et al. (1995) analysis was the determination of the maximum additional strain due to bending, ε_b, referred to as the 'additional strain due to bending' in Figure 3-24. The analysis showed that the maximum additional strain due to bending occurs at the connection between the geomembrane and the seam a point A or B in Figure 3-23. As shown in Figure 3-26, at 2% axial strain denoted as ε_{GM} in Figure 3-26), the additional bending strain, ε_b, can range from 1.6% to 2.5% depending on the weld type and thickness. This means that the strain at the weld will be on the order of 2 to 2.25 times the axial strain developed in the geomembrane.

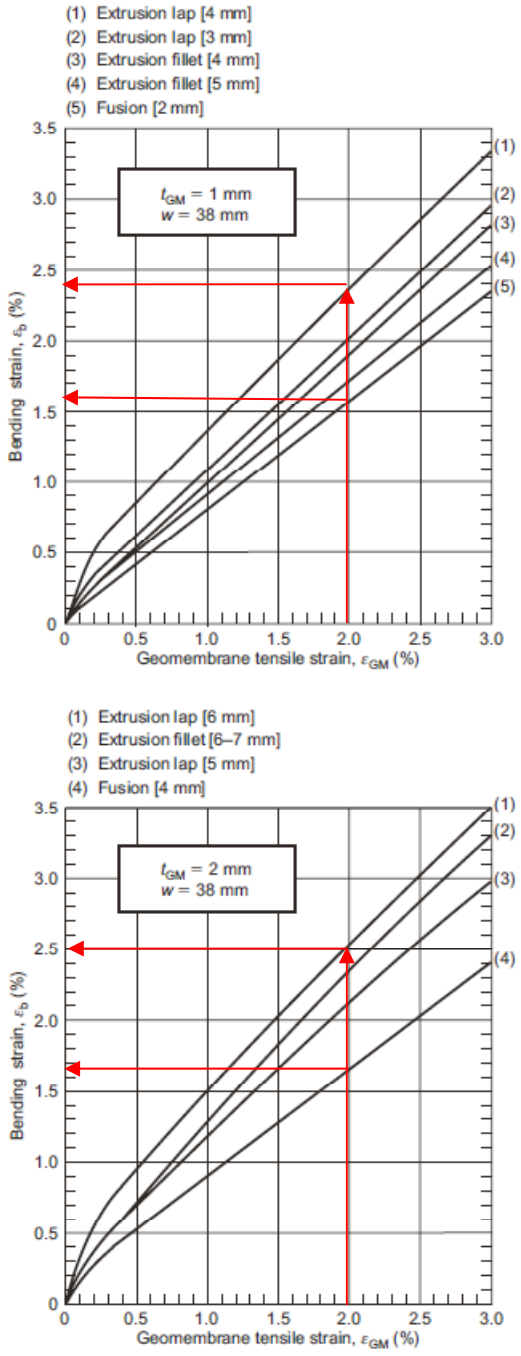

Figure 3-24 Additional strain due to geomembrane bending next to a seam, ε_b, as a function of the tensile strain in the geomembrane away from the seam, ε_{GM} (after Giroud 1993) (Notes: The value indicated in square brackets is the total seam thickness, which is the thickness of extrudate, if any, plus the thickness of the two geomembrane layers.

3.5.1.2 Strain concentration due to scratches

The stress concentration around a scratch is proportional to the geomembrane thickness reduction due to the scratch. Giroud (1994) have shown that the ratio between the yield strain of a scratched HDPE geomembrane, ε_{ys}, and the yield strain of an intact HDPE geomembrane, ε_y, is given by the following equation:

$$\varepsilon_{ys} = \varepsilon_y \left(1 - \left(\frac{d_s}{t_{GM}} \right)^{1/N} \right) \tag{8}$$

where d_s is the depth of scratch or any other type of thickness reduction, t_{GM} is the geomembrane thickness (outside the zone of thickness reduction), and $N = 4$ for HDPE. This relationship is shown graphically in Figure 3-25.

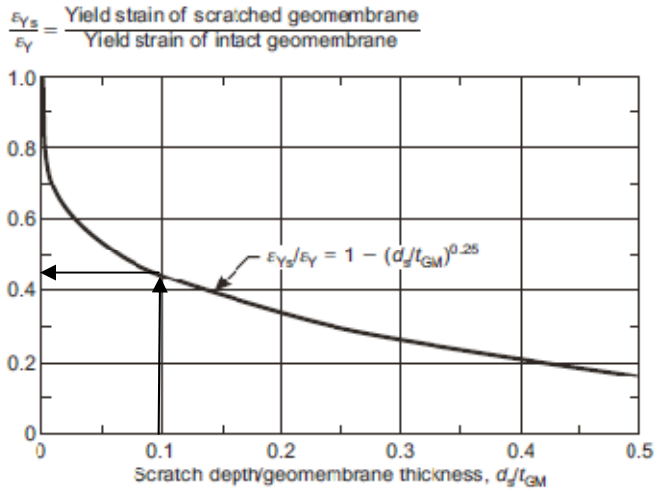

Figure 3-25 Ratio of the yield strains of an HDPE geomembrane with a scratch, or any other type of thickness reduction, and an intact HDPE geomembrane (Giroud 1993)

3.5.2 **Internal shear strength of GCL**

The in-plane shear resistance of a GCL may be governed by either the interface shear strength or its internal shear strength. Figure 3-26 shows a typical relationship between shear stress (τ) and shear displacement (Δ) for internal shear loading of a GCL at constant normal stress from Fox and Stark (2004). In the test shown in Figure 3-26 the shear stress increases rapidly to a peak shear strength (τ_p) at the beginning of the test. The data presented by Fox and Stark (2004) indicates that the corresponding displacement at the peak (Δ_p) is usually less than 50 mm (but not always). As displacement continues, all GCLs and (most GCL interfaces) experience post-peak strength reduction in which the measured shear resistance decreases and ultimately reaches a residual shear strength (τ_r), after which no further strength reduction occurs. The displacement at residual shear strength (Δ_r) may be 0.1 - 0.5 m, or more. In cases in which the test is not run to large enough strains that the shear resistance drops to a constant minimum value, a "large displacement" shear strength (τ_{ld}) is often reported (Fox and Stark 2004). GCLs are generally tested hydrated based upon the assumption that, due to the high affinity of bentonite for water, hydration is inevitable unless special measures are taken to prevent hydration (e.g. the GCL is encapsulated by a geomembrane on both sides).

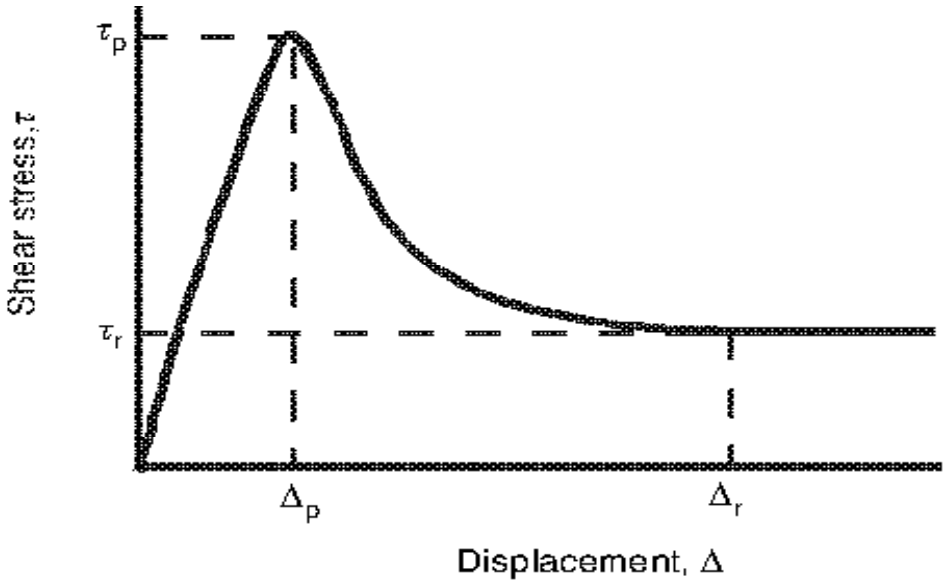

Figure 3-26 Typical shear stress-displacement relationship for an internal shear test of a hydrated GCL (Fox and Stark 2004)

Unreinforced GCL: For a hydrated unreinforced GCL, the internal shear strength should be equal to the strength of the bentonite used to manufacture the GCL (generally a sodium bentonite). The drained shear strength of hydrated sodium bentonite is the lowest of any natural soil. Fox et al (1998) measured friction angles on the order of $\phi_p = 10.2^o \; and \; \phi_r = 4.7^o$ for a hydrated unreinforced geotextile-supported GCL, as shown in Figure 3-27.

Reinforced GCL: Geosynthetic reinforcement can greatly increase the peak shear strength of hydrated GCLs. The failure mode in reinforced GCLs generally makes a transition from an interface failure to an internal failure as normal stress increases. However, reinforced GCL in-plane strength envelopes of ten often do not distinguish between these two different failure modes. Figure 3-27 shows peak and residual failure envelopes for a GCL employing woven geotextiles on both sides (WW) and reinforced

by stitched bonding (SB) and a GCL employing a woven geotextile on one side, a non woven geotextile on the other side (W/NW), and reinforced by needle punching (NP). The shear strength parameters for the NP reinforced GCLs were developed for two different products. One product, designated 85N (having peel strengths, F_p, of 85 N/10 cm), had shear strength parameters of $c_p = 98.2\,kPa \;and\; \phi_p = 32.6^o$. The other product, designated 160N (F_p of 160 N/10 cm), were had shear strength parameters of $c_p = 42.3\,kPa \;and\; \phi_p = 41.9^o$ (Fox and Stark 2004). The peak shear strength of the NP reinforced GCL increases sharply with increasing normal stress and shows good correlation with the peel strength of the carrier geotextile (the force required to peel off one of the carrier geotextiles). The residual failure envelope for all GCLs reported by Fox and Stark (2004), regardless of the type of reinforcement and the peel strength, was equal to that of hydrated bentonite ($c_r = 1.0$ kPa and $\phi_r = 4.7^o$), as shown in Figure 3-27. Thus the residual shear strength of hydrated GCLs can only be improved by increasing the residual shear strength of the hydrated bentonite. However, it is not clear that a NP reinforced GCL in a landfill liner or cover is likely to be subjected to enough internal deformation to mobilize the residual shear strength.

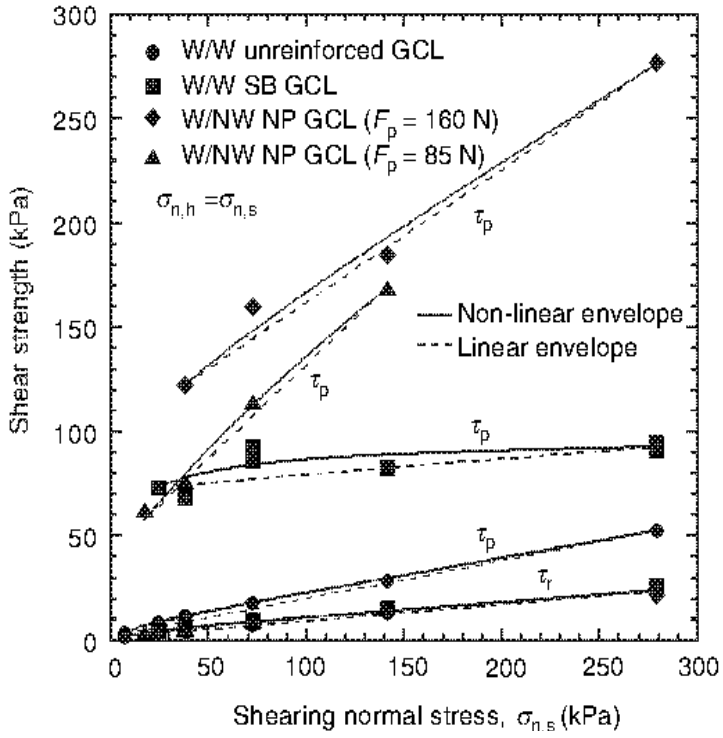

Figure 3-27 Peak and residual failure envelops for hydrated unreinforced, stitch bonded and needle-punched GCLS (Fox et al. 1998)

3.6 Cyclic Shear Properties of Geosynthetics

3.6.1 Geosynthetics Liners as Base-Isolation

The interface behavior of geosynthetic materials subject to cyclic loading was investigated by Kavazanjian et al. (1991), Yegian and Lahlaf (1992), Yegian et al. (1998), and Yegian and Kadakal (2004) for the use as frictional base isolation materials. In most cases, these investigators use rigid block on a horizontal plane shaking table tests to investigate the interface behavior of geosynthetic material subject to cyclic loading.

Kavazanjian et al. (1991), Yegian et al. (1998), and Yegian and Kadakal (2004) conducted testing using a rigid block with a geosynthetic layer glued to one of its faces

and with another geosynthetic layer fixed to the shaking table. The shaking table was excited with either sinusoidal or earthquake like motions. These groups of researchers monitored both the acceleration of the block and the slip of the block relative to the shaking table.

Kavazanjian et al. (1991) conducted shaking table tests on four different geosynthetic interfaces under different sinusoidal wave frequencies and peak accelerations and with an earthquake like motion. They also conducted one centrifuge test with a similar block on plane setup, applying an earthquake like motion under a 5g centrifugal acceleration. Figure 3-28 shows a sample of the results from Kavazanjian et al. (1991) from a shaking table test with a sinusoidal input motion with a peak acceleration of 0.4 g. The figure shows the acceleration of the block is cut off at a relatively constant threshold of 0.16g. This threshold coincides with the dynamic friction coefficient of the interface used in this test. Figure 3-29 shows similar behavior for the 5 g centrifuge test with an earthquake like input motion. Kavazanjian et al. (1991) reported a slight decrease in the coefficient of friction of the interface subject to dynamic loading (sinusoidal wave) compared to the static coefficient of friction (as measured in tilt table tests). They also reported a slight change in the coefficient of dynamic friction with changes in the frequency of the sinusoidal input motion. The results of the centrifuge test also suggested that the dynamic friction coefficient may depend on the normal stress under the block as well. They attributed the apparent trend of a decrease in the coefficient of dynamic friction with increasing frequency to an increase in velocity of sliding. Kavazanjian et al. (1991) concluded that the shaking table results and centrifuge shaking tests demonstrated the potential for a smooth geomembrane to provide effective frictional seismic base isolation.

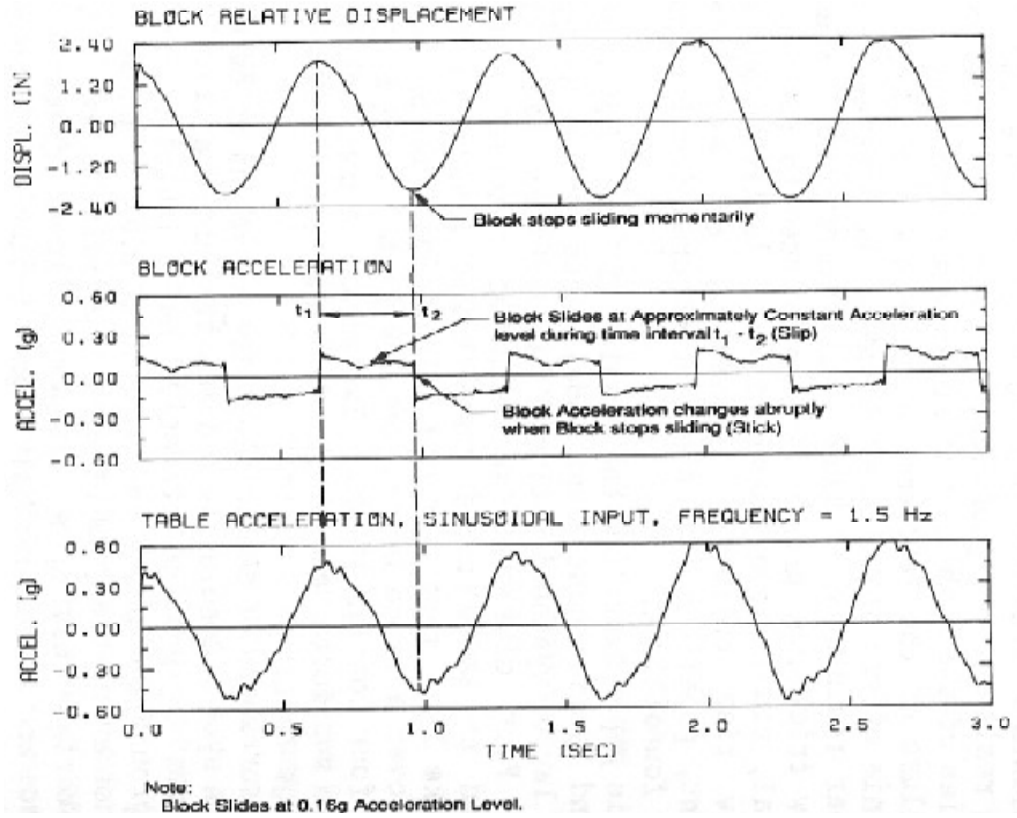

Figure 3-28 Example of the displacement and acceleration time histories results from sinusoidal shaking table tests (Kavazanjian et al. 1991)

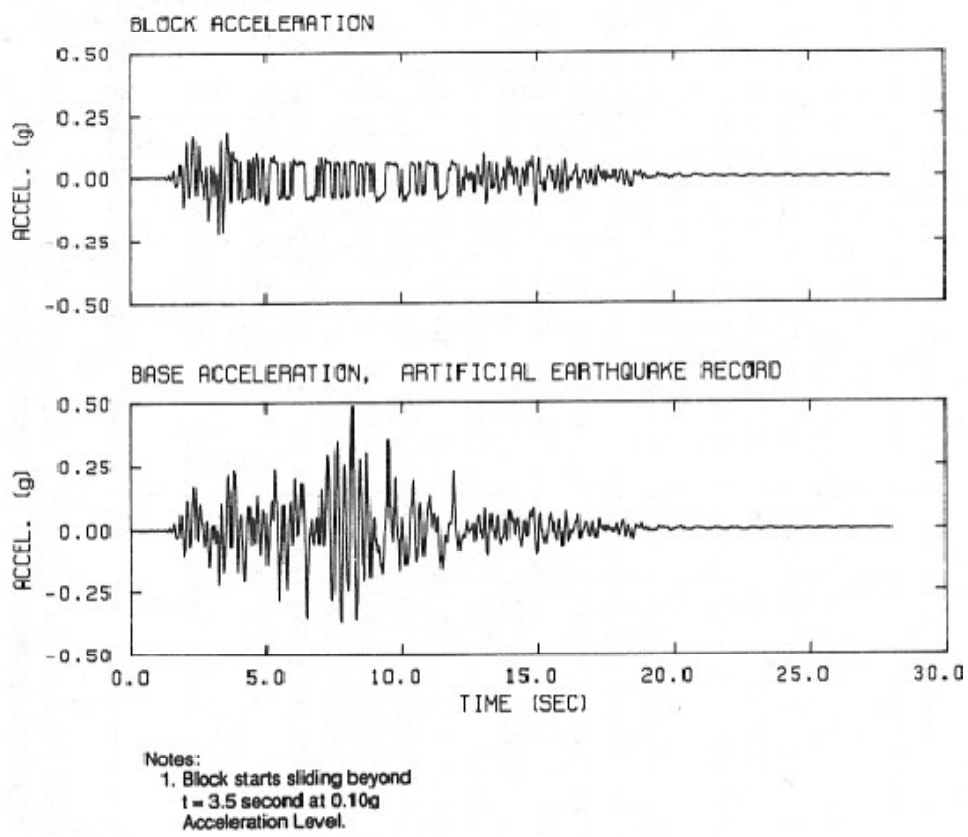

Figure 3-29 Example of the time histories results from earthquake like motion input centrifuge shaking tests (Kavazanjian et al. 1991)

Yegian and Kadakal (2004) also conducted a series of shaking table tests of the sliding of a geosynthetically lined rigid block. These investigators used both sinusoidal acceleration input and earthquake acceleration-like input in their testing program. A schematic of the rigid block testing setup they used is presented in Figure 3-30. In their testing program, Yegian and Kadakal (2004) used four different geosynthetic types. They concluded that only one of these interfaces (geotextile/ultrahigh molecular weight polyethylene liner (UHMWPE)) was suitable for base isolation because this geotextile/

UHMWPE interface shows a constant coefficient of friction under varying frequency, normal stress, and velocity of sliding.

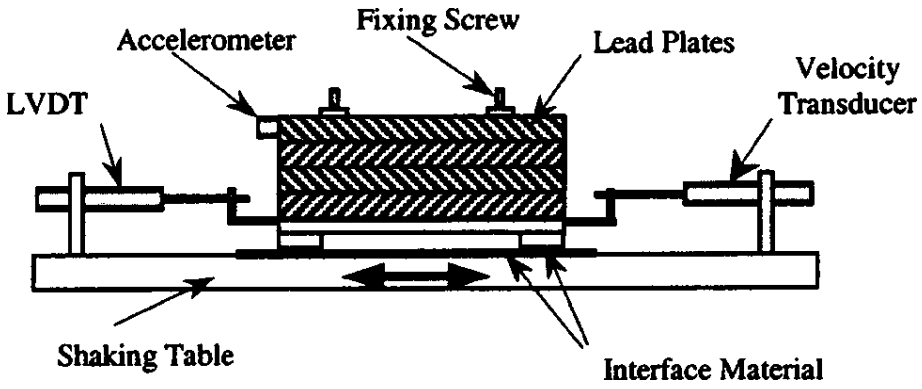

Figure 3-30 Schematic of the rigid block test setup Complaint block response (Yegian and Kadakal 2004)

Figure 3-31 presents plots showing the typical response of geosynthetically isolated block with a geotextile/UHMWPE to an earthquake-like excitation from Yegian and Kadakal (2004). As in all tests reported by these investigators, truncation of the transmitted acceleration to the block at an acceleration expressed as a fraction of gravity equal to the dynamic friction coefficient of the interface was clearly observed during the test. Because of the difference in the block and table accelerations, transient slip displacements of up to 5 cm were recorded in the test shown in Figure 3-31. In Figure 3-32 the peak transmitted acceleration from three different earthquake records scaled to peak table input motions to 0.4 g are plotted versus of the peak table acceleration for the geotextile/UHMWPE interface. The results shown in Figure 3-32 suggest that the transmitted accelerations are independent of the frequency content of the earthquake as well as its peak acceleration of the input motion for the geotextile/UHMWPE interface.

Yegian and Kadakal (2004) also used a 1 story building model to demonstrate the ability of the geosynthetics to serve as a frictional seismic base isolator. Yegian and Kadakal (2004) concluded, based on their shaking table results, that a geotextile / smooth geosynthetic liner may provide effective frictional seismic base isolation.

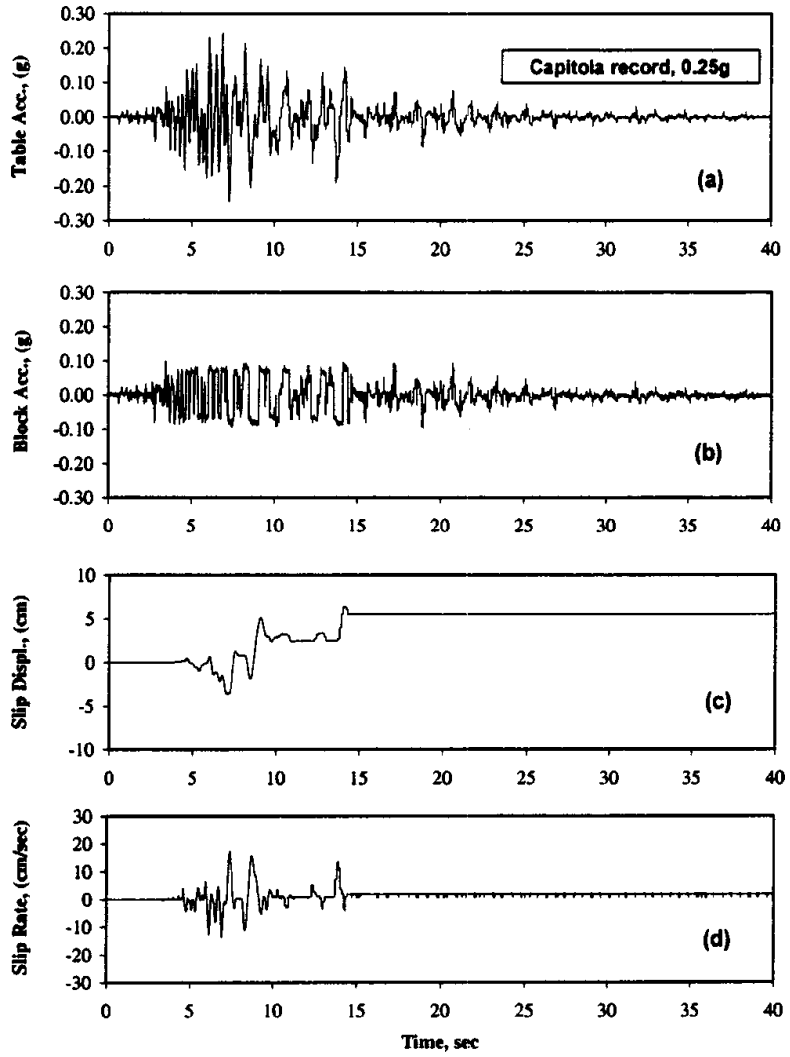

Figure 3-31 Measurements from rigid block tests on geotextile/ UHMWPE interface when subjected to the Capitola record scaled to 0.25*g*: (a) table acceleration, (b) block acceleration, (c) slip displacement, and (d) slip rate (Yegian and Kadakal 2004)

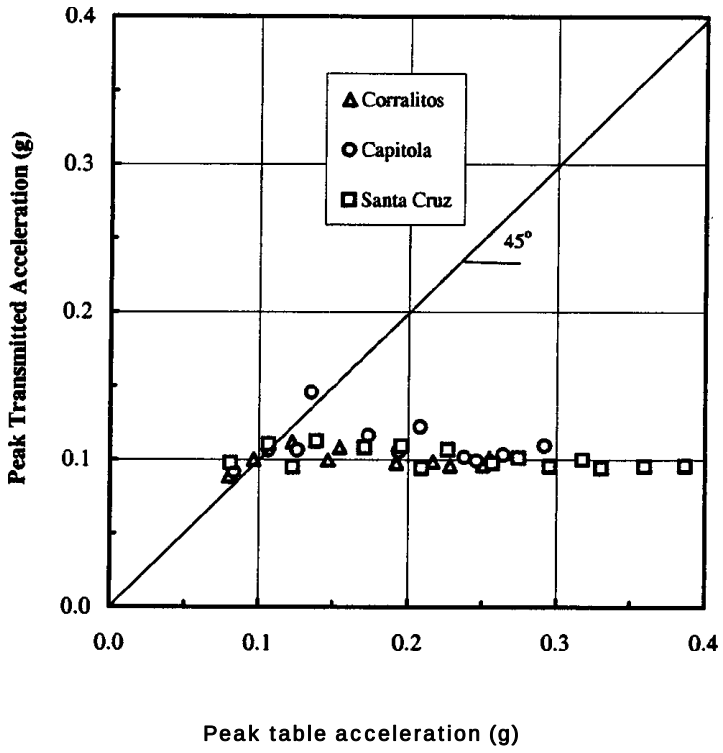

Figure 3-32 Variation of peak transmitted acceleration with peak table acceleration from rigid block tests with earthquake excitations, using geotextile/UHMWPE interface (Yegian and Kadakal 2004)

3.6.2 **Cyclic Shear Behavior of Geosynthetic / Geosynthetic Interfaces**

Yegian and Kadakal (2004) conducted tests to examine the effect of the number of cycles of loading, sliding velocity, normal stress, and geosynthetic surface condition on the interface friction coefficient for various geomembrane interfaces using shaking table tests. Table 3-4present a list of the interfaces tested by Yegian and Kadakal (2004) and the range of friction coefficient measured by these investigators in their cyclic testing.

Table 3-4 list of geotextiles interfaces tested (Yegian and Kadakal 2004)

Interface	Description	Friction coefficient
Geotextile/HDPE	A high-strength nonwoven geotextile, "Typar 3601" against 1.5 mm smooth HDPE (high density polyethylene)	0.15–0.3
PTFE/PTFE	Two sheets of 1.5 mm thickness PTFE (polypropylene)	0.08– 0.15
UHMWPE/UHMWPE	Two layers of 6.4 mm thick UHMWPE (ultrahigh molecular weight polyethylene) "TIVAR 88-2 AntiStatic"	0.09–0.25
Geotextile/UHMWPE	Typar 3601 geotextile against TIVAR 88-2, 6.4 mm thick UHMWPE	0.06–0.08

Figure 3-33 presents a summary plot showing the variation of the friction coefficient as a function of the number of cycles for a sliding velocity of ±2.5 cm/s at a frequency of 0.25 Hz. The combination of this slip velocity and frequency induced a relative displacement of 5 cm per cycle. During the first 10 cycles, the friction coefficient varied by about ±30% from its initial value, depending on the interface tested. However, in some cases the friction coefficient increased and in other cases it decreased. Beyond 10 cycles, the variation in friction coefficient for a given interface was negligible. Figure 3-34 shows the friction coefficients reported by Yegian and Kadakal (2004) as a function of normal stress. Generally, the friction coefficient of the interfaces slightly decreased with increasing normal stress up to about 80 kPa, beyond which the friction coefficient remained constant. Figure 3-35 presents the results of testing done by Yegian and Kadakal (2004) to measure friction coefficients over the range of sliding velocity from 0.01 and 10 cm/s. The geotextile/HDPE and PTFE/PTFE interfaces exhibited a significant increase in the friction coefficient with increase in sliding velocity. The friction coefficient for the UHMWPE/UHMWPE interface decreased significantly with sliding velocity. The friction coefficient of the geotextile/UHMWPE interface was independent of the sliding velocity.

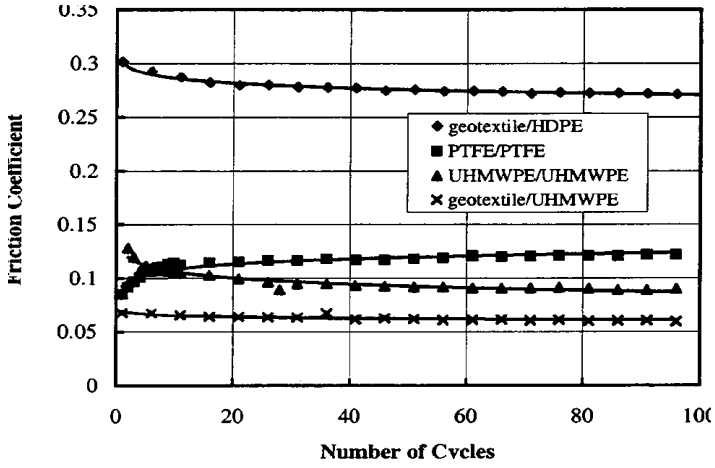

Figure 3-33 Effect of number of cycles of application of interface shear on the friction coefficient of the tested interfaces (Yegian and Kadakal 2004)

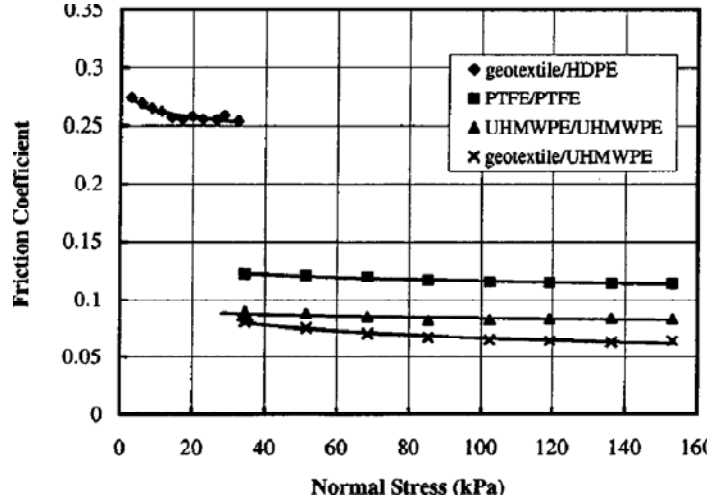

Figure 3-34 Effect of normal stress on the friction coefficient of the tested interfaces (f =0.25 Hz, sliding velocity=±2.5 cm/ s) (Yegian and Kadakal 2004)

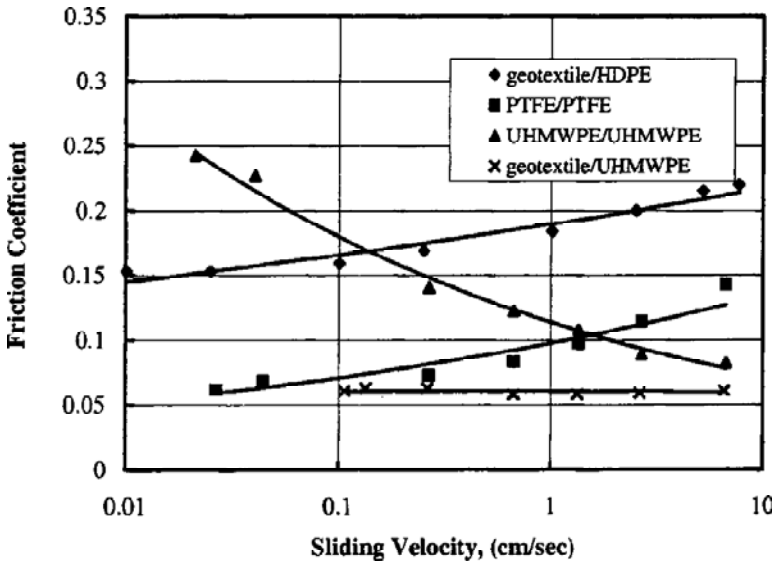

Figure 3-35 Effect of number of cycles of application of interface shear on the friction coefficient of the tested interfaces (f =0.25 Hz, sliding velocity=±2.5 cm/ s) (Yegian and Kadakal 2004)

Kim et al. (2005) conducted an experimental study of geosynthetic interface shear strength on a shaking table to investigate the dynamic friction resistance characteristics of geosynthetic materials. These investigators conducted their testing on 8 different types of geosynthetic interfaces. Three different types of smooth high-density polyethylene (HDPE) geomembranes (designated hereafter as Geomembrane 1, Geomembrane 2, and Geomembrane 3, respectively) were tested. The first two geomembranes were 1.5mm (60 mil) thick and the third was 0.5mm (20 mil) thick. Two different types of polypropylene geotextiles made of continuous filament, non-woven needle punched fabrics (designated as Geotextile 1 and Geotextile 2, respectively) were employed in the testing. A medium-density polyethylene geonet of 5.1mm (200 mil) thickness (designated hereafter as Geonet 1) was also employed in the testing. The geonet had openings of 10mm by 5mm in a diamond shape. Finally, a GCL made of two needle-punched nonwoven geotextiles (designated hereafter as GCL 1) was also employed in the

testing. Kim et al. (2005) concluded that interfaces involving geotextiles have unique shearing characteristics that are different from the interfaces involving only non-geotextiles based on their testing.

The typical behavior of interfaces involve geotextiles are presented in Figure 3-36. The peak friction angle (and thus peak friction resistance) develops at a relatively small shear displacement amplitudes for this interface (typically less than 2 mm). At the displacement larger than the displacement at the peak strength, the shear resistance decreases continuously. Kim et al. (2005) concluded for such interfaces (involve geotextiles) that the friction angle at a displacement of 254 mm are typically 2–3° less than the peak friction angle (i.e., about 80–90% of the peak values). Kim et al. (2005) found that the large displacement friction angle fell between a low of 12.3° and a high of 16.5° for a geomembrane/dry geotextile interface, depending on the displacement rate.

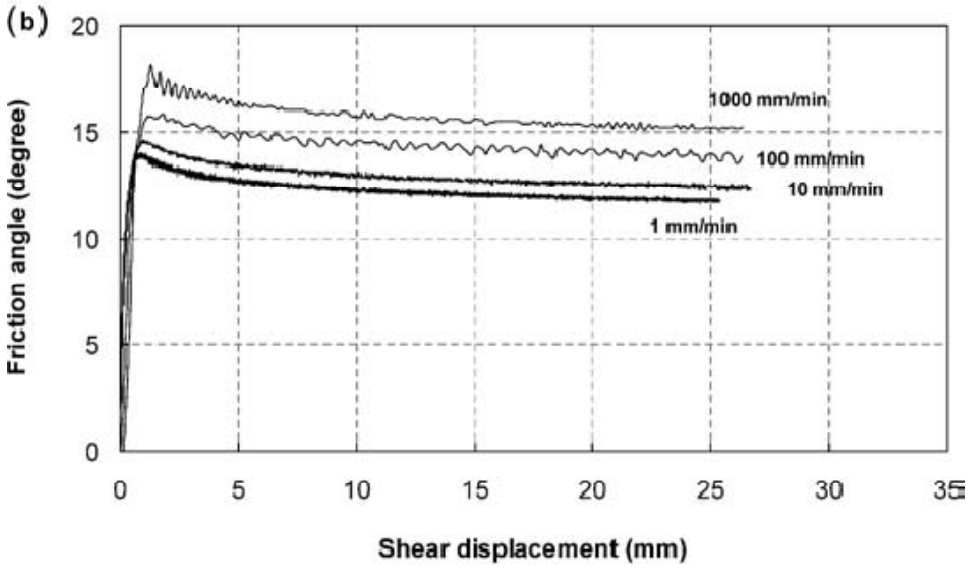

Figure 3-36 Typical plots of friction angle versus shear displacement of four different displacement rates at a normal stress of 10.94 kPa for interfaces involve geotextiles (Kim et al. 2005)

The typical behavior of interfaces including non geotextiles is presented in Figure 3-37 as reported by Kim et al. (2005). The shear strength of these interfaces increases with cumulative shear displacement until it stabilizes at some relatively constant level. Kim et al. (2005) speculated that this phenomenon as specimen being roughen with cumulative shear displacement. They also speculated that the increase in roughness occurs because the tips of the geonet strands dig into and cut the surface of the geomembrane.

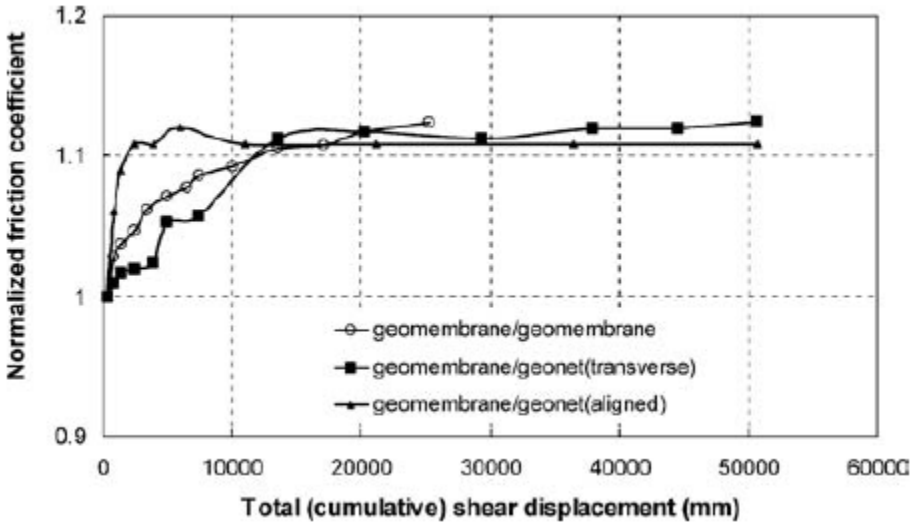

Figure 3-37 Typical variation of peak frictional resistance (or shear resistance) during the pre-shearing cycles for non-geotextile-involved geosynthetic interfaces (Kim et al. 2005)

3.6.3 GCL internal cyclic shear behavior

Nye and Fox (2007) investigated the effects of displacement rate, displacement amplitude, number of cycles, frequency, and motion waveform on GCL internal response using cyclic displacement-controlled shear tests conducted at a normal stress of 141 kPa. Figure 3-38 presents the response of a hydrated W/NW NP reinforced GCL subjected to

50 cycles of sinusoidal displacement with amplitude of ±10 mm at a frequency equal to1.0 Hz. The figure shows degradation in the shear resistance of the GCL during cyclic loading. Nye and Fox (2007) speculated that the needle-punched fibers become increasingly engaged as displacement increased in the first quarter cycle of loading. During the second quarter of each cycle, shear resistance is essentially constant when the reinforcement is relaxed. The shear resistance increases sharply towards the peak resistance at the end of the third quarter cycle, and then remains relatively constant again in the fourth quarter. They suggest that the reinforcement experiences additional damage with every cycle of loading, leading to the progressive decrease of shear resistance observed in the testing. Nye and Fox (2007) concluded from a comparison between the initial GCL response during cyclic loading and the monotonic shear response of the GCL presented in Figure 3-39 that the load-displacement curves are similar for the first quarter-cycle of loading and that monotonic shear data may provide a reasonable approximation for the initial cyclic response of the GCL prior to displacement reversal.

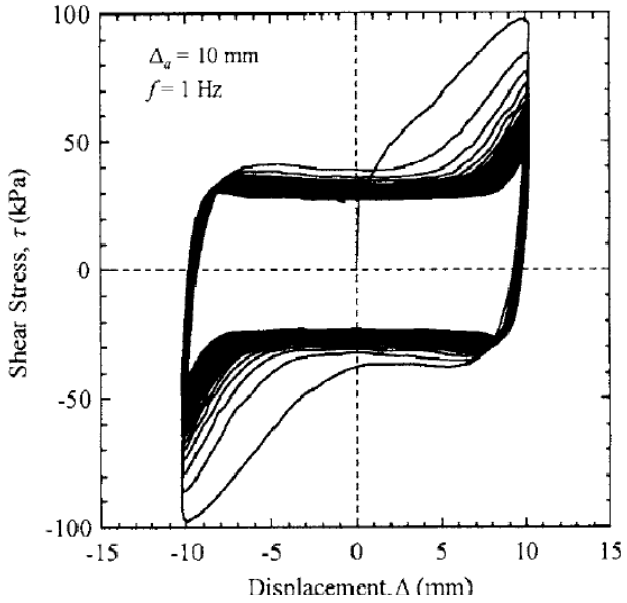

Figure 3-38 Shear stress versus displacement for ±10 mm cyclic shear test (Nye and Fox 2007)

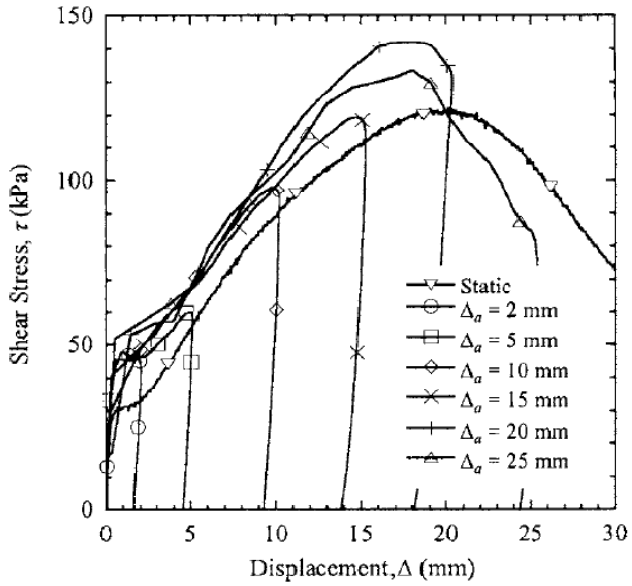

Figure 3-39 Comparison of first cycles for six cyclic shear tests with varying displacement amplitude with the static shear response (Nye and Fox 2007)

As shown by the hysteresis loops presented in Figure 3-40, in the Nye and Fox (2007) experiments the cyclic shear load-displacement response is generally symmetrical for displacement amplitudes of up to 15 mm. However, the hysteresis loops in the ±20 and ±25 mm displacement amplitude tests were not symmetrical. Nye and Fox (2007) concluded that lack of symmetry was due to reinforcement failure, which resulted in a marked decrease in shear strength during the second half-cycle of loading. After the reinforcement broke, the shear resistance of the GCL is essentially controlled by the hydrated bentonite. So, for subsequent cycles of loading in the ±20 and ±25 mm displacement amplitude tests, the shear resistance remained nearly constant until the shear stress reversed.

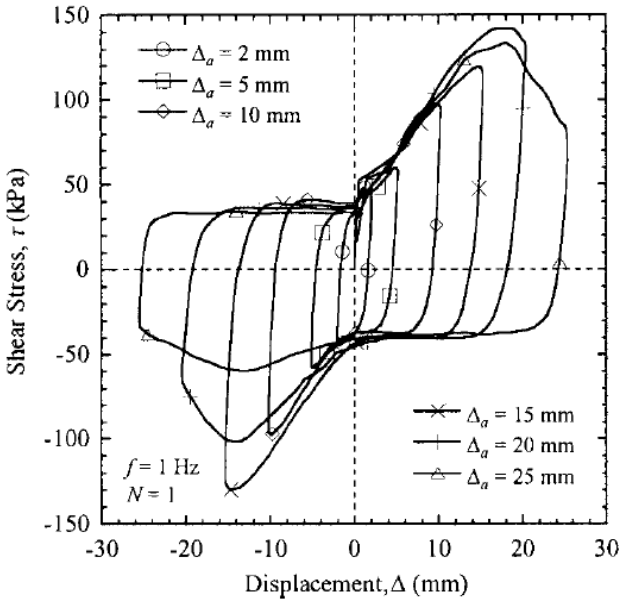

Figure 3-40 Comparison of first cycles for six cyclic shear tests with varying displacement amplitude (Nye and Fox 2007)

Nye and Fox (2007) investigated the effect of the number of cycles of loading (N) with respect to the degradation index of the GCL in-plane stiffness (δ). Figure 3-41 illustrates this degradation of stiffness with a plot of $log\,\delta$ versus $log\ N$ for various displacement amplitudes. This plot shows a linear relationship between $log\,\delta$ and $log\ N$ that passes through zero except for the 20 mm and 25 mm amplitudes. The deviation of the tests with the displacement amplitudes of 20 mm and 25 mm from this pattern of behavior is likely related to the damage to the fibers in the first cycle of these tests. Nye and Fox (2007) reported that the frequency of the cyclic load had an insignificant effect on cyclic shear behavior based on testing conducted with several different sinusoidal wave frequencies.

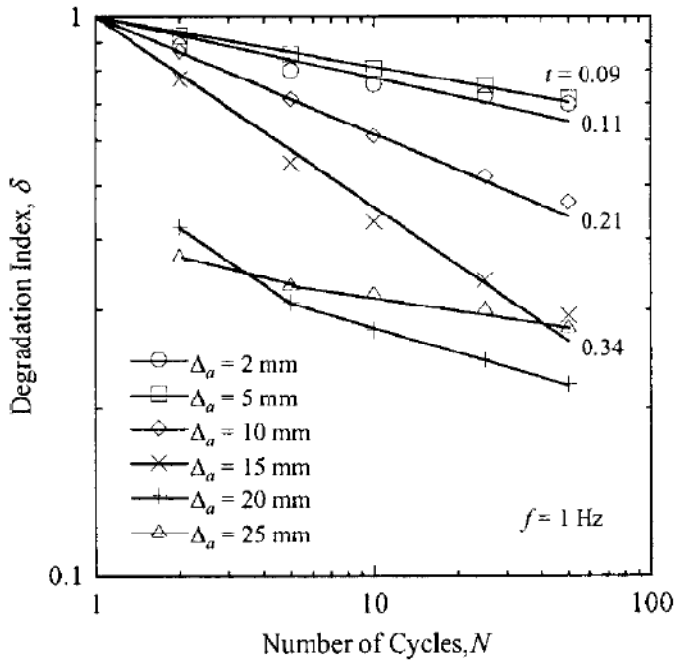

Figure 3-41 Degradation index for six cyclic shear tests (Nye and Fox 2007)

Sura (2009) tested the cyclic internal shear behavior of GCLs under high normal stresses. The hysteresis loops from the testing by Sura (2009) at 692 kPa normal stress are similar in shape to the GCL hysteresis loops reported by Nye and Fox (2007) for testing at 141 kPa. Figure 3-42 shows the shear stress versus the shear displacement for a NP reinforced GCL at 692 kPa normal stress for a displacement amplitude of 5 mm. Figure 3-43 shows the shear stress versus the shear displacement a NP reinforced GCL 692 kPa normal stress with a displacement amplitude of 25 mm. In Figure 3-42, the shear strength versus displacement curve for the NP reinforced GCL at a normal stress of 692 kPa and displacement amplitude of 5 mm experience the same three stages behavior as observed by Nye and Fox (2007) discussed subsequently.

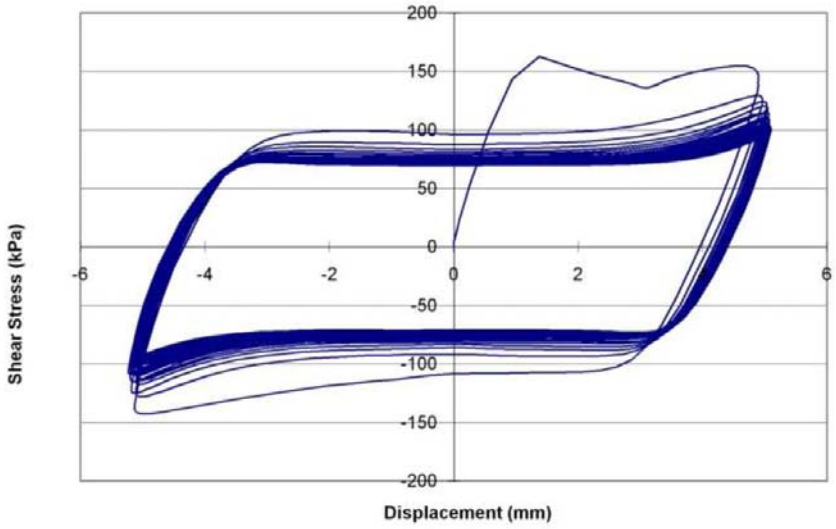

Figure 3-42 Cyclic shear test, Δ_a = 5 mm, σ_n = 692 kPa (Sura 2009)

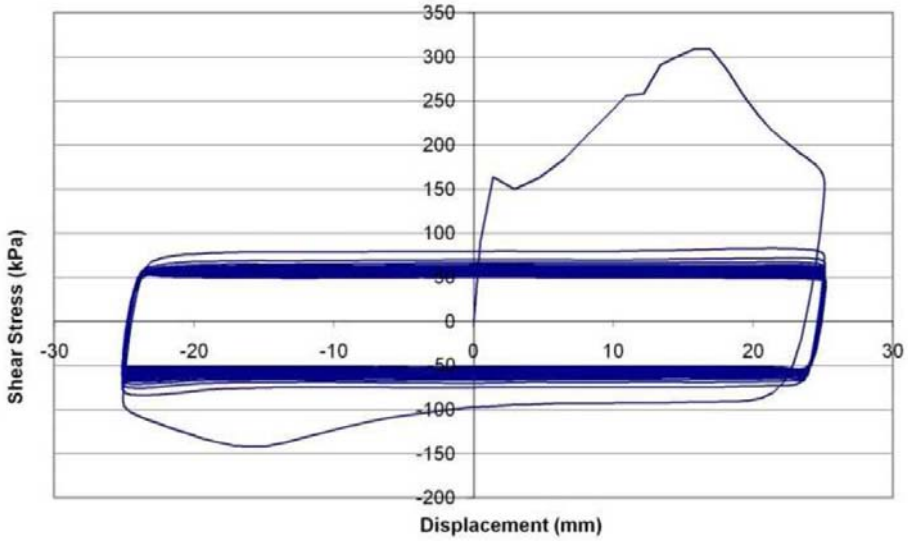

Figure 3-43 Cyclic shear test, Δ_a = 25 mm, σ_n = 692 kPa (Sura 2009)

3.6.4 **Cyclic shear behavior of GM / NP GCL**

Stern (2009) conducted both monotonic and cyclic tests on GCL/HDPE GM interfaces under high normal stress. Figure 3-44 presents shear stress-displacement plots for the monotonic shear testing of a GCL/HDPE GM combination sheared at different shearing rates. The shearing rate effect on the GCL/HDPE GM interface is similar to the shearing rate effect on the internal shear behavior of a NP reinforced GCL. In Figure 3-44 the largest peak strength is from internal shear test of needle punch reinforced GCL and the lowest residual strength is also from the internal shear test of needle punch reinforced GCL.

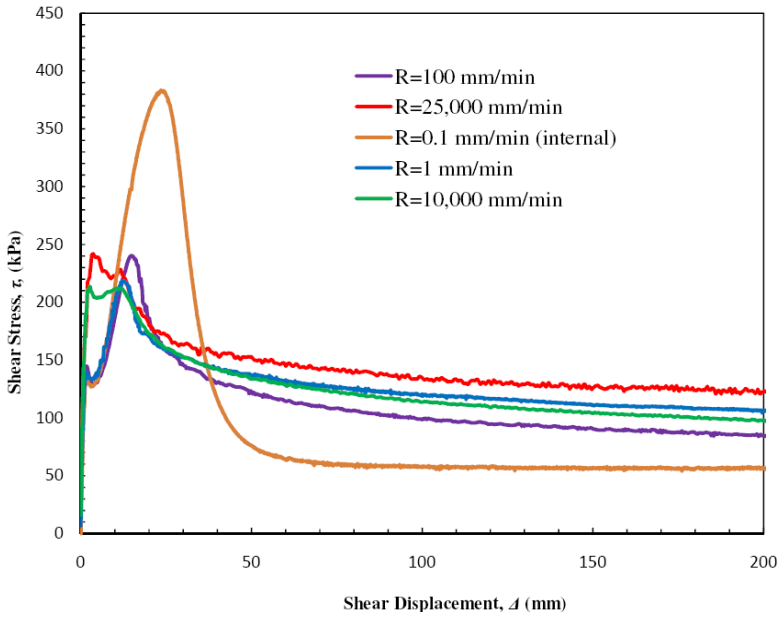

Figure 3-44 Shear stress-displacement relationships for GCL/GM interface under σ_n=962 kPa (Stern 2009).

Stern (2009) presented results of 7 cyclic tests on GM/GCL interfaces at a normal stress of 692 kPa. The displacement amplitudes for the 7 tests were 2, 10, 15, 20, 30, 60, and 120 mm. The cyclic testing was performed using a sinusoidal wave form with a

frequency of 1 Hz and carried out for 25 cycles of loading. Figure 3-45 presents a plot of shear stress versus displacement for all seven tests. In this figure it can be observed that the peak shear stress occurs during the first half of the first cycle, and then the peak shear stress decreases with each additional cycle of loading. The greatest decrease in shear stress generally occurs between the first and tenth cycle of loading. After the tenth cycle the stress reduction from each additional cycle of loading is very small. This suggests that after 10 cycles of loading the strength reduction during additional cyclic loading may be ignored. This finding agrees with the findings of Nye and Fox (2007) for GCL internal loading.

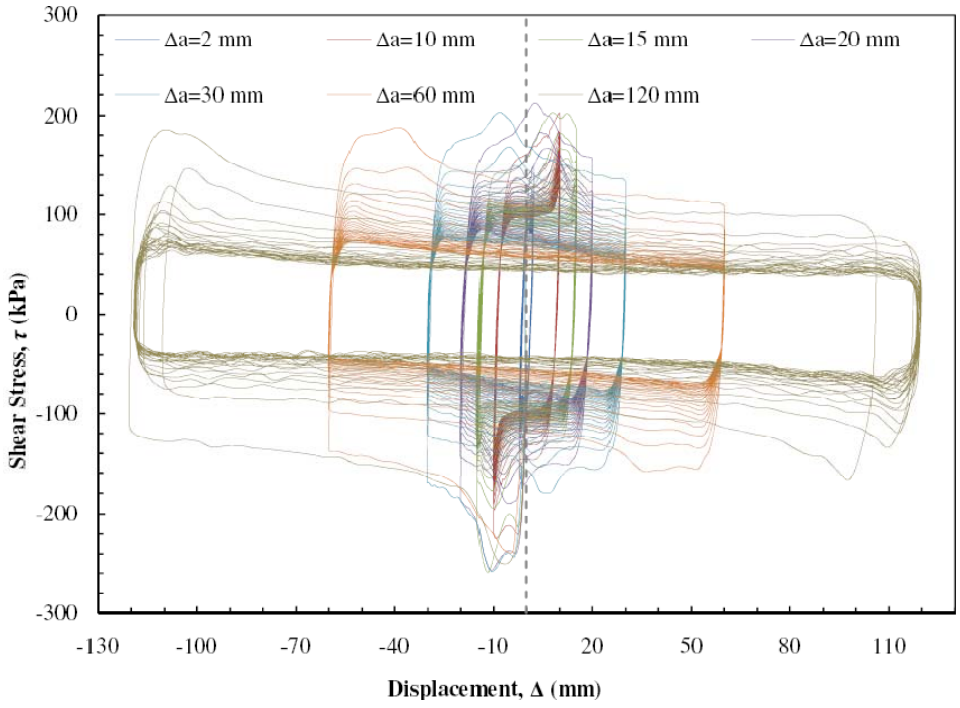

Figure 3-45 Shear stress versus displacement for seven cyclic shear tests (Stern 2009)

Stern (2009) plotted the results from the first quarter-cycle of each hysteresis loop in his tests against the monotonic stress-displacement curve from a test conducted at a shear rate of 1 mm/min. This plot is presented in Figure 3-46. Stern (2009) attributed the

observed increase of peak shear strength for the first quarter cycle of the cyclic tests compared to the monotonic test to the fact that the 1 Hz cyclic frequency results in a loading rate much faster than the rate of 1 mm/min employed for the monotonic loading test.

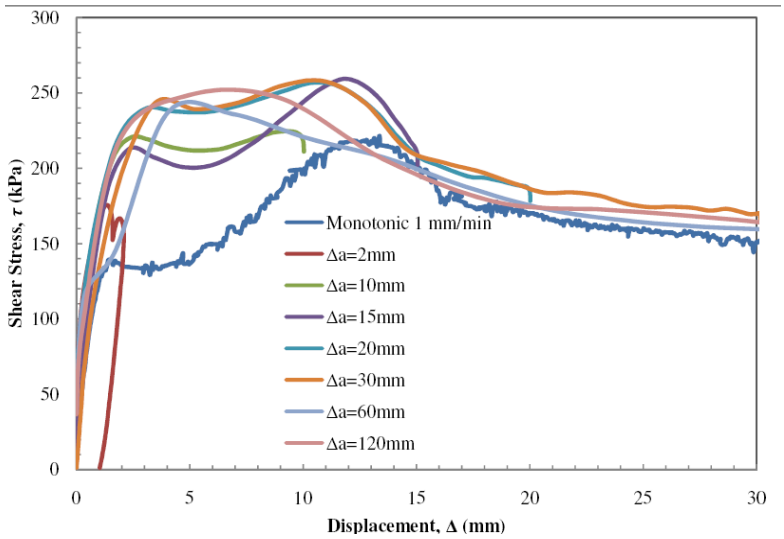

Figure 3-46 Shear stress versus displacement for first quarter cycle of seven cyclic tests (Stern 2009)

3.7 Static Shear Strength of the Municipal Solid Waste (MSW)

3.7.1 Introduction

The heterogeneous nature of MSW makes the task of characterizing of its properties a challenge. The obstacles to evaluating the shear strength of the MSW include obtaining and testing representative samples, degradation of the waste over time, and the variability of the composition of waste from one landfill to another. These make characterizing MSW shear behavior more challenging than characterizing the shear behavior of soils. MSW also usually contains material that can sustain large tensile strains and act as reinforcement to the waste. Therefore, due care must be taken in applying regular soil

mechanics rules and constitutive models to waste. Using the Mohr-Coulomb shear strength criterion to characterize waste shear strength is common. However, this does not necessarily mean that waste is a frictional material. It may merely reflect an increase in waste strength with increasing confining pressure. To characterize the in-place shear strength of MSW, information like the age of the waste, leachate circulation in the landfill and temperature of the waste may be important pieces of information, as these factors may affect the constituents of the waste and the amount of degradation in the waste, which in turn affects the shear strength of the waste. Methods used to evaluate the static and dynamic shear strength of MSW are covered in this section, including laboratory testing and back calculation from field performance.

3.7.2 **Direct shear testing on MSW**

Dixon and Jones (2005) presented a comparison between the different testing techniques used to get information on the shear strength of the MSW. They concluded that the most appropriate laboratory technique is the direct shear test. Figure 3-47 shows a summary of range of recommended values for the shear strength parameters of MSW from different research groups as presented by Dixon and Jones (2005). Dixon and Jones (2005) distinguished between three different normal stress ranges or "zones of normal stresses", in their summary as follows:

- Zone A, corresponding to very low normal stress (0 kPa to 20 kPa); Dixon and Jones (2005) recommended MSW shear strength to be characterized as a cohesive material in this zone ($\phi = 0$), with c = 20 kPa in this zone.

- Zone B, corresponding to low to moderate normal stresses (20 kPa to 60 kPa); Dixon and Jones (2005) recommended MSW shear strength be characterized by c = 0 kPa and $\varphi = 38^{o}$ in this zone.

- Zone C, corresponding to higher normal stresses (higher than 60 kPa); In this case, Dixon and Jones (2005) recommended MSW shear strength be characterized by c=20 kPa and $\varphi = 30^{o}$ in this zone.

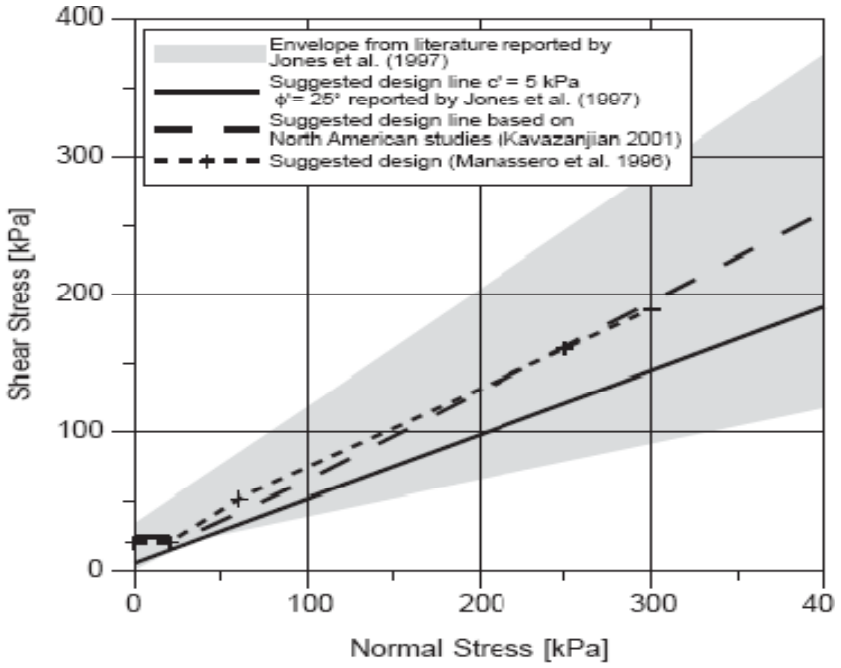

Figure 3-47 Suggested MSW shear strength envelopes for design (Dixon and Jones 2005)

Bray et al. (2009) present the results of a direct shear testing program on reconstituted MSW samples using waste recovered from the Tri-cities landfill in northern California. To investigate the effects of waste composition on shear strength, direct shear tests on specimens with varying fractions of less than 20 mm (soil-like), and larger than 20 mm (fibrous) waste materials were conducted. Specimens were prepared with 100%, 62–76%, and 8–25% of the material smaller than 20 mm, by weight. Bray et al. (2009)

prepared the specimens with the long axis of the fibrous particles generally oriented horizontally. Bray et al. (2009) concluded from the direct shear testing that waste that contained 100, 62, and 12% soil-like material revealed similar shear strength characteristics and that this may be attributed to the orientation of the fibrous material parallel to the shear plane in the test. As shown in Figure 3-48 (a), the fibrous material did not appear to contribute significantly to the waste shearing resistance in this test series. Bray et al. (2009) also showed that the secant friction angle from direct shear tests decreases with increasing normal stress, as illustrated in Figure 3-48 (b).

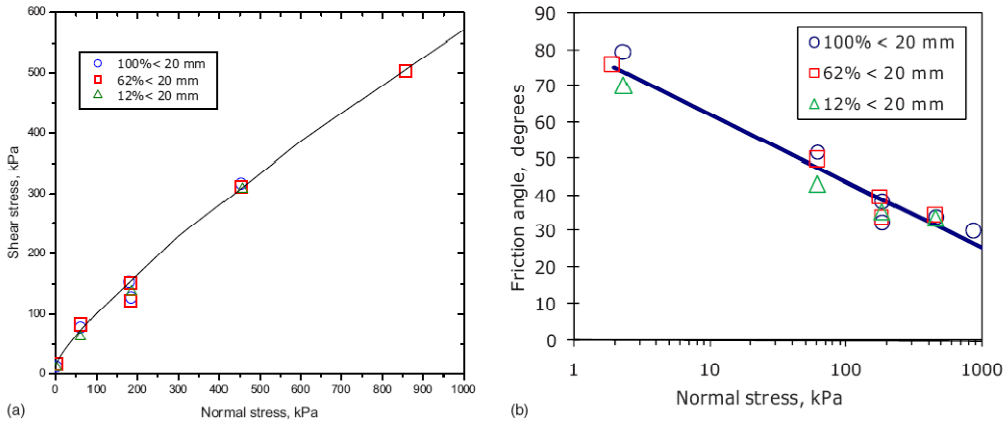

Figure 3-48 Direct shear strength of Tri-Cities landfill MSW: (a) curved strength envelope for samples with varying waste composition; (b) decrease in secant friction angle with increasing normal stress assuming c=5 kPa (Bray et al. 2009)

Bray et al. (2009) concluded that the Direct Shear (DS) strength of the waste materials from this test series may be defined by the Mohr-Coulomb equation as:

$$\tau = c + \sigma_n \tan(\phi_d) \tag{9}$$

where τ =shear strength; σ_n=total normal stress; c =cohesion intercept; and ϕ_d = a normal stress dependent friction angle given by:

$$\phi_d = \phi_o - \Delta\phi \cdot \log\left(\frac{\sigma_n}{p_a}\right) \tag{10}$$

where ϕ_o = friction angle measured at a normal stress of 1 atmosphere; $\Delta\phi$ = the change of the friction angle over 1 log-cycle change of normal stress; and p_a =atmospheric pressure (i.e., 101.3 kPa).

Bray et al. (2009) collected a database of available direct shear test data for MSW to evaluate ϕ_o and $\Delta\phi$. Data from a total of 103 large-scale direct shear tests were collected from eight studies and combined with the large-scale direct shear tests conducted on MSW from the Tri-Cities landfill in the San Francisco Bay area by Bray et al. (2009) as part of the study. Figure 3-49 shows the collected data on a Mohr-Coulomb plot with the best fit failure envelope to the data. Bray et al. (2009) concluded that the shear static shear strength of MSW tested in direct shear could be characterized by c =15 kPa, ϕ_o =36°, and $\Delta\phi$ =5° based upon this data.

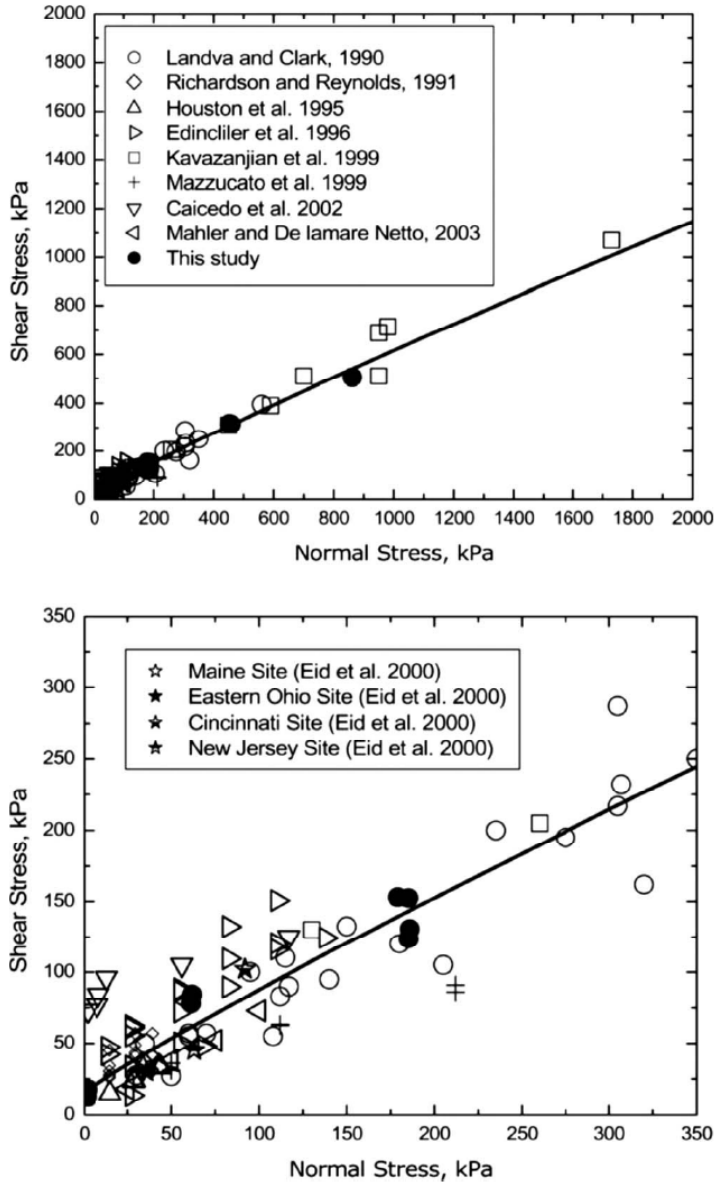

Figure 3-49 Recommended static shear strength of MSW based primarily on direct shear tests and field observations of static slope stability (Bray et al. 2009)

3.7.3 **Triaxial testing**

Bray et al. (2009) presented the results of a series of triaxial compression tests conducted on reconstituted specimens of MSW recovered from the Tri-Cities Landfill in the San

Francisco Bay area. Specimens were prepared with the same different percentages of fibrous waste particles used in the previously cited direct shear testing program conducted by these investigators. Representative results of the Bray et al. (2009) triaxial compression test are shown in Figure 3-50. The specimens for the tests reported on Figure 3-50 were prepared with the same compaction effort, subjected to an isotropic confining stress of 75 kPa, and sheared at an axial strain rate of 0.5%/min. One specimen, containing 100% soil-like (<20 mm) material, reached a peak shear stress at an axial strain of about 22% and then exhibited a post-peak reduction in shear resistance. The other two specimens, which contained 38 and 86 percent of fibrous material (>20 mm) by weight, exhibited initially a softer response than the specimen with no fibrous material but exhibited an increasing upward curvature at strains greater than 5% without reaching a peak shear stress, as shown in Figure 3-50.

Most of the samples tested in the triaxial compression by Bray et al. (2009) did not show a pronounced peak in the stress-strain response (in fact, only the one test shown in Figure 2-55 did), which coincides with results shown by Dixon and Jones (2005). Due to the absence of a peak stress, determining the failure point from triaxial testing has to be based upon a strain criterion. A shear strain of 10% is commonly used as the strain-based failure criteria for isotropic triaxial tests. However, Bray et al. (2009) argued that the failure strain should be based upon the strain developed from an anisotropic K_o consolidation state. Figure 3-51 shows shear strength envelopes and secant friction angle from triaxial compression test data for assumed K_o values of 0.3, 0.6, and 1.0 for incremental strain levels of 5 and 10%. As these results show, as the assumed value of K_o decreases, the mobilized shear strength increases for a specified incremental axial strain. Furthermore, as expected, the mobilized shear strength increases as the incremental axial

strain increases. However, even for a K_o value of 1.0 and an incremental strain of 5%, a friction angle of 34^o degrees seemed reasonable (with a value as high as 48^o for K_o = 0.3 and an incremental strain of 10%).

Based upon triaxial data from their own testing and from a variety of different investigations available in the literature, Bray et al. (2009) recommended that the shear strength of MSW in triaxial compression be described based upon a K_o value of 0.6 and an incremental strain of 5% by a secant friction angle of 35 degrees.

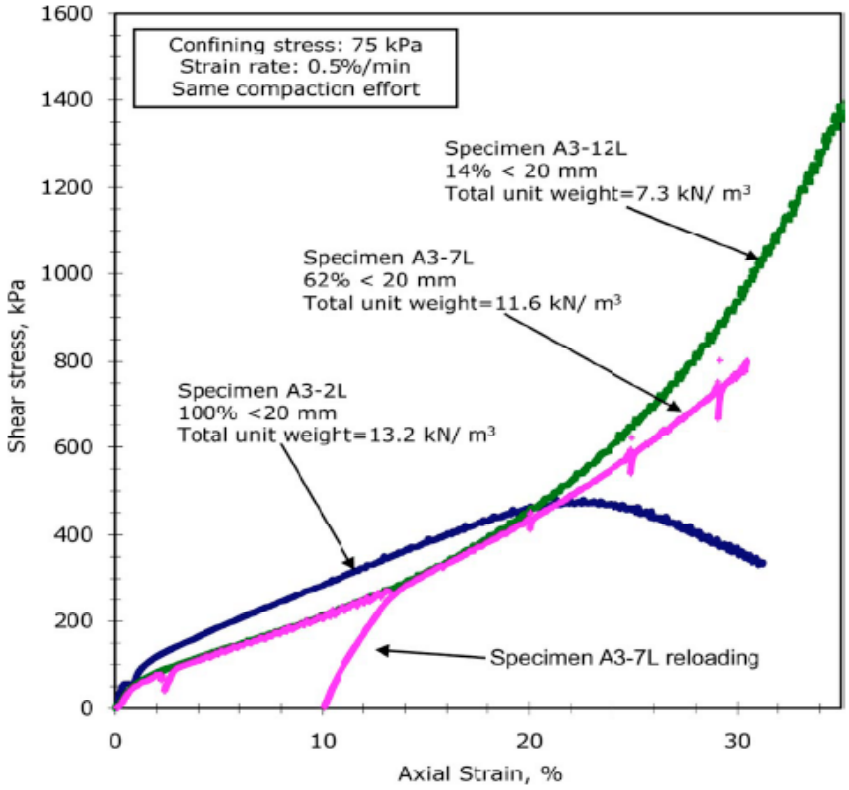

Figure 3-50 Responses of MSW in monotonic triaxial compression testing for specimens with varying waste compositions (Bray et al. 2009)

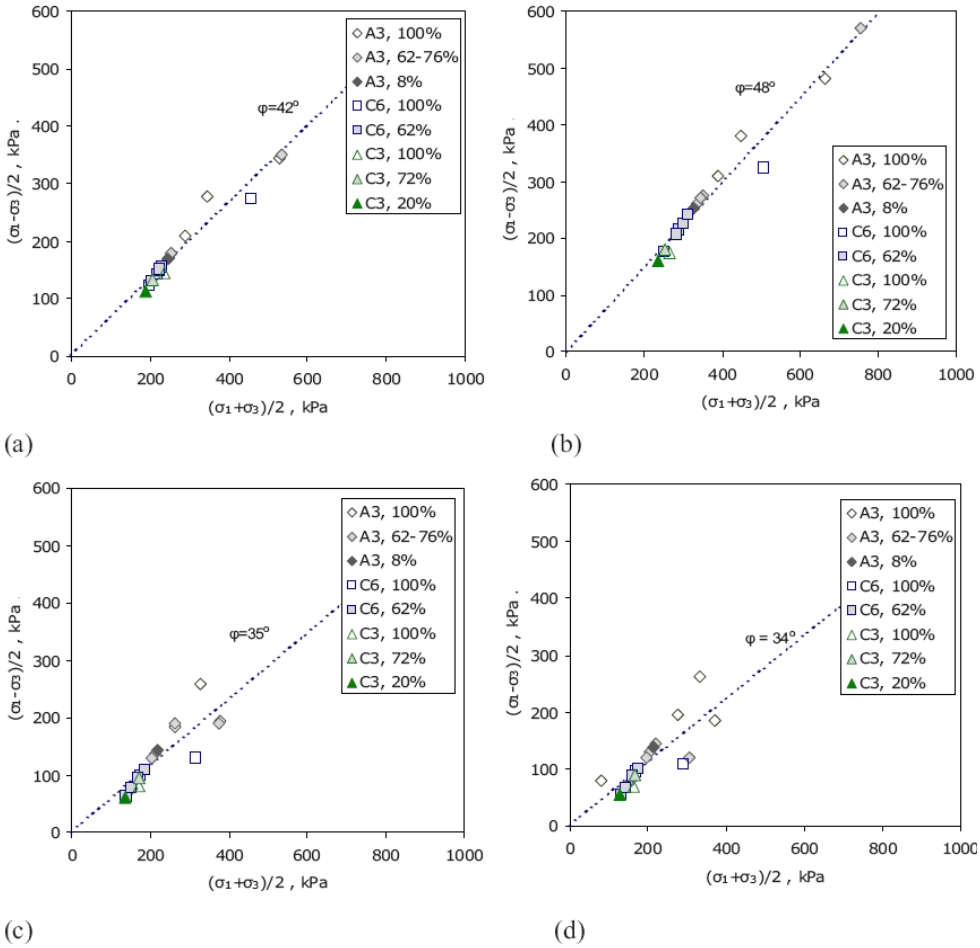

Figure 3-51 Mobilized TX stress-based friction angles: (a) K_o=0.3 and 5% axial strain; (b) K_o=0.3 and 10% axial strain ; (c) K_o=0.6 and 5% axial strain; and (d) K_o=1 and 5% axial strain; the sample group and percent of material smaller than 20 mm is provided in the legends (Bray et al. 2009)

3.7.4 Simple shear testing

Results of simple shear tests on MSW are limited. In interpreting this test, an assumption on the orientation of the failure surface or on the value of the horizontal normal stress is required. Assuming the failure plane to be horizontal and interpreting the simple shear test as a direct shear test results in the lowest possible shear strength estimate from a simple shear test. Assuming the normal stress on the vertical plane to be the K_o stress or

that the normal stress on the vertical plane is the mean normal stress results in a significantly higher strength estimate. Using K_o= 0.6, Kavazanjian et al. (1999) estimated a lower bound shear strength envelope of c=16 kPa and φ =33° and an upper bound envelope of c=30 kPa and φ =59° from simple shear tests on reconstituted MSW. Figure 3-52 shows results from three monotonic loading SS tests conducted on reconstituted specimens of MSW from the Tri-Cities landfill: one using 100% smaller than 20 mm material compacted to a unit weight of 14.9 kN/m^3, the second using 62% less than 20 mm compacted to a unit weight of 9.6 kN/m^3 using the same compaction energy used to compact the first specimen, and the third using 62% less than 20 mm but compacted with less energy than the first two specimens to a unit weight of 8.2 kN/m^3. All three tests were sheared under a vertical normal stress of 75 kPa at a shear strain rate of approximately 0.6% per min (Bray et al. 2009). Using the direct shear interpretation method, the secant friction angle at a shear strain of 10% varied from 32° for the low unit weight specimen with 62% less than 20 mm to 42° for the specimen with 100% less than 20 mm.

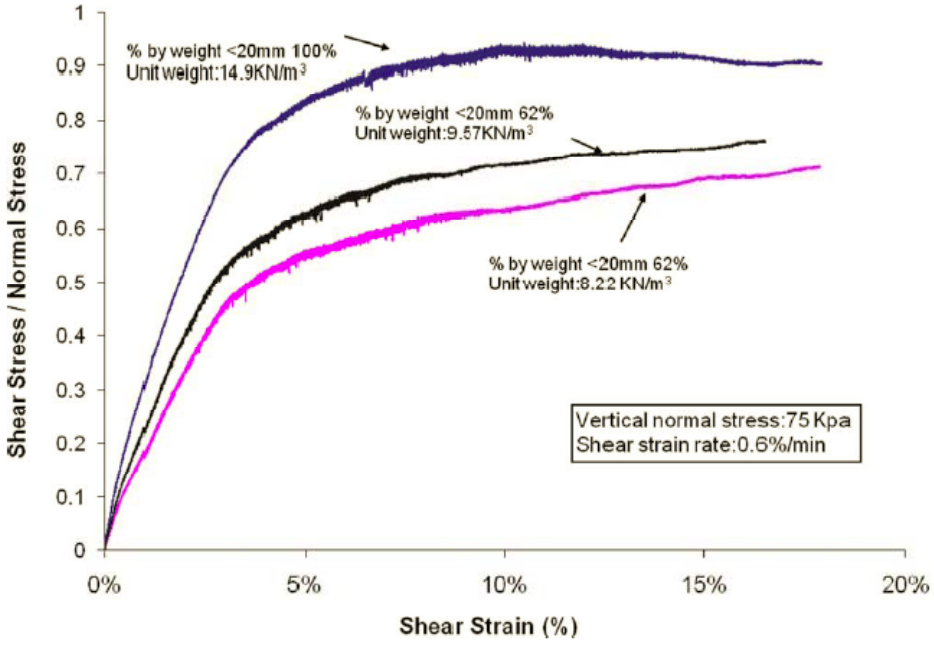

Figure 3-52 Results of simple shear tests on reconstituted Tri-Cities landfill MSW (Bray et al. 2009)

3.7.5 Back analysis of the MSW static shear strength

Field performance of failed and stable landfills provides a valuable source of information for back calculating MSW shear strength. Kavazanjian et al., (1995) evaluated available data on steep but stable landfill slopes to back calculate the shear strength of the MSW. Table 3-5 shows a list of the cases analyzed by these investigators to back calculate the shear strength parameters of the MSW (Kavazanjian et al., 1995). These researchers conducted limit equilibrium analyses of the cases identified in Table 3-5 using the modified Bishop method of slices. Table 3-5 shows the friction angle calculated assuming 5 kPa cohesion for factors of safety of 1.1, 1.2, and 1.3. As all of the landfill slopes used in the back analysis had been stable for at least 15 years without any signs of static instability, and two of the landfills had survived seismic loading, the values for a

factor of safety of 1.2 were considered appropriate to characterize a lower bound for the shear strength of MSW.

Table 3-5 Back Analysis of Exciting Landfill Slopes (Kavazanjian et al. 1995)

Landfill	Average Slope		Maximum Slope		Waste Strength		
	Height (m)	Slope (H:V)	Height (m)	Slope (H:V)	FS=1.0	FS=1.1	FS=1.2
Lopez Canyon, CA	120	2.5:1	35	1.7:1	25	27	29
OII, CA	75	2:1	20	1.6:1	28	30	34
Babylon, NY	30	1.9:1	10	1.25:1	30	34	38
Private landfill, OH	40	2:1	10	1.2:1	30	34	37

In addition to the back analyzed data shown in Table 3-5, Kavazanjian et al. (1995) considered evidence drawn from field observations of vertical excavated trenches at landfills (i.e. that vertical trenches in waste remained stable up to a height of at least 6m) and from large diameter direct shear tests to draw conclusions regarding MSW shear strength. This data led Kavazanjian et al. (1995) to recommend using a bilinear relationship to characterize MSW shear strength. A Mohr-Coulomb strength envelope with Φ=0.0^o and c=24 kPa for normal stresses less than 32 kPa and Φ=33^o and c=0.0 kPa for higher normal stresses was recommended by Kavazanjian et al. (1995) to characterize the shear strength of MSW, as shown in Figure 3-53.

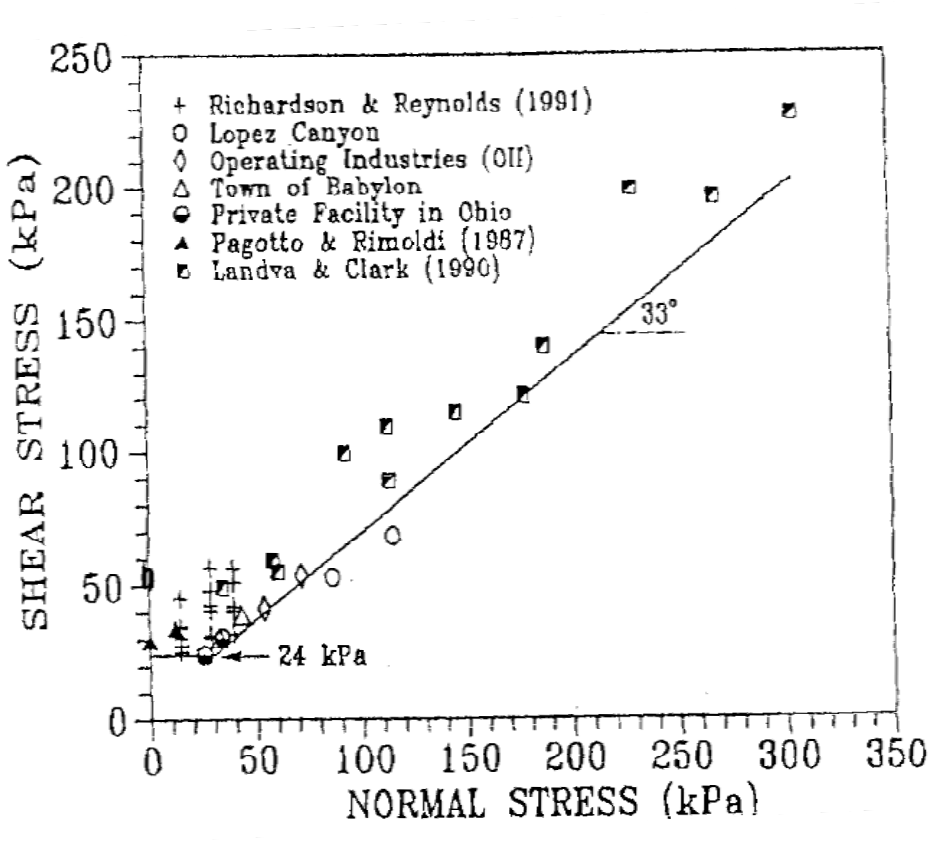

Figure 3-53 Bilinear Mohr- coulomb shear stress envelop for MSW (Kavazanjian et al. 1995)

3.8 Municipal solid waste unit weight

Estimating MSW unit weight is often the first step in performing seismic analyses of landfill systems. In particular Zekkos et al. (2006) have shown that an appropriate MSW unit weight profile is important for performing reliable seismic analyses of landfill. Zekkos et al. (2006) developed a characteristic shape for the profile MSW unit weight versus depth by a hyperbolic equation based upon analysis of laboratory and field data. This characteristic profile was developed using field data and large-scale laboratory data. Zekkos et al. (2006) indicated that MSW unit weight is principally governed by waste composition and landfill operational practices (i.e., compaction effort, cover soil

placement, and liquids management) during waste placement. Using their characteristic shape, Zekkos et al. (2006) developed a family of representative MSW unit weight profiles depending on the compaction effort used in constructing the landfill shown in Figure 3-54.

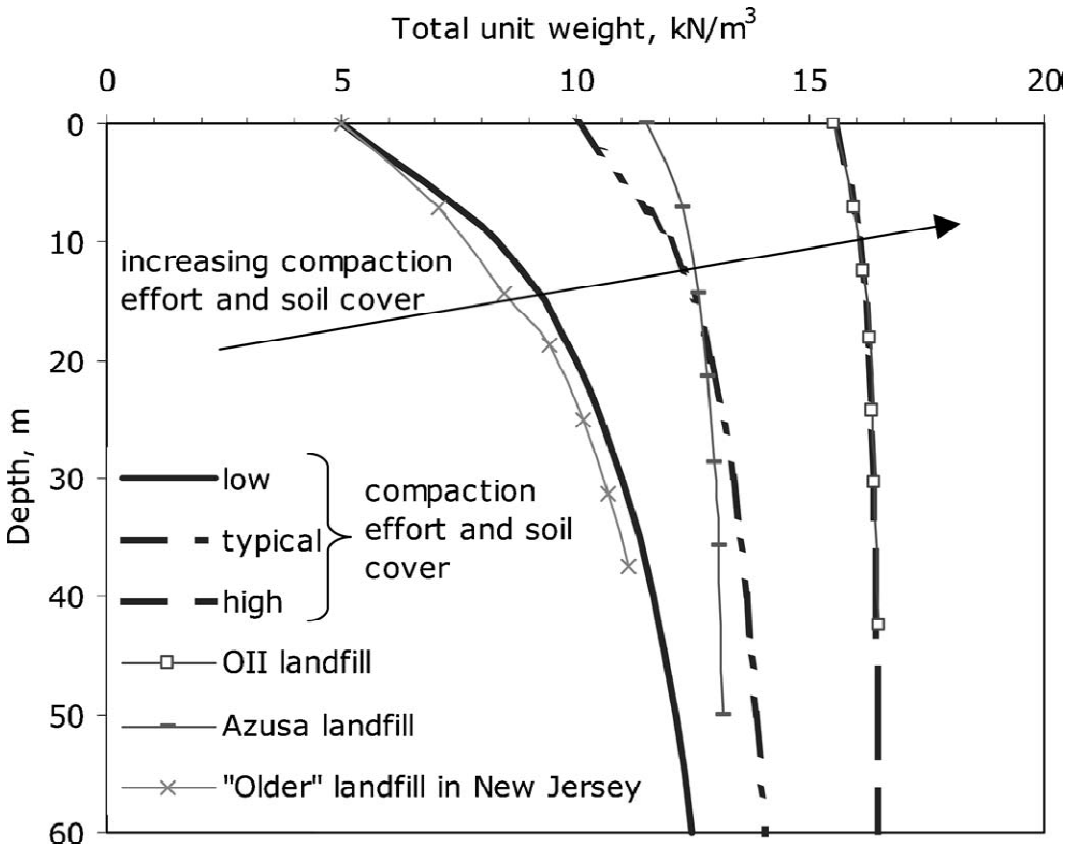

Figure 3-54 Recommended unit weight profiles for conventional municipal solid-waste landfills (Zekkos et al. 2006)

3.9 MSW Shear Wave Velocity

Kavazanjian et al. (1996) investigated the performance of several landfills at the southern California area after 1994 Northridge earthquake. As part of this investigation, in situ

shear wave velocity was measured using the spectral analyses of surface waves (SASW) method at six MSW landfills.

Figure 3-55 presents a summary of the shear wave velocity profiles, presented by Kavazanjian et al. (1996) as derived from SASW testing at the six landfills. The plot in Figure 3-55 provides the mean, the mean plus standard deviation, and the mean minus standard deviation shear velocity versus depth for the entire data set. Based on these measurements, Kavazanjian et al. (1996) recommended the range for typical the shear wave velocity profile for southern California landfills shown in Figure 3-56. It should be noted that the recommended curve of Kavazanjian et al. (1995) shown in Figure 3-56 was developed using limited data compared to the data employed in the Kavazanjian et al. (1996) work.

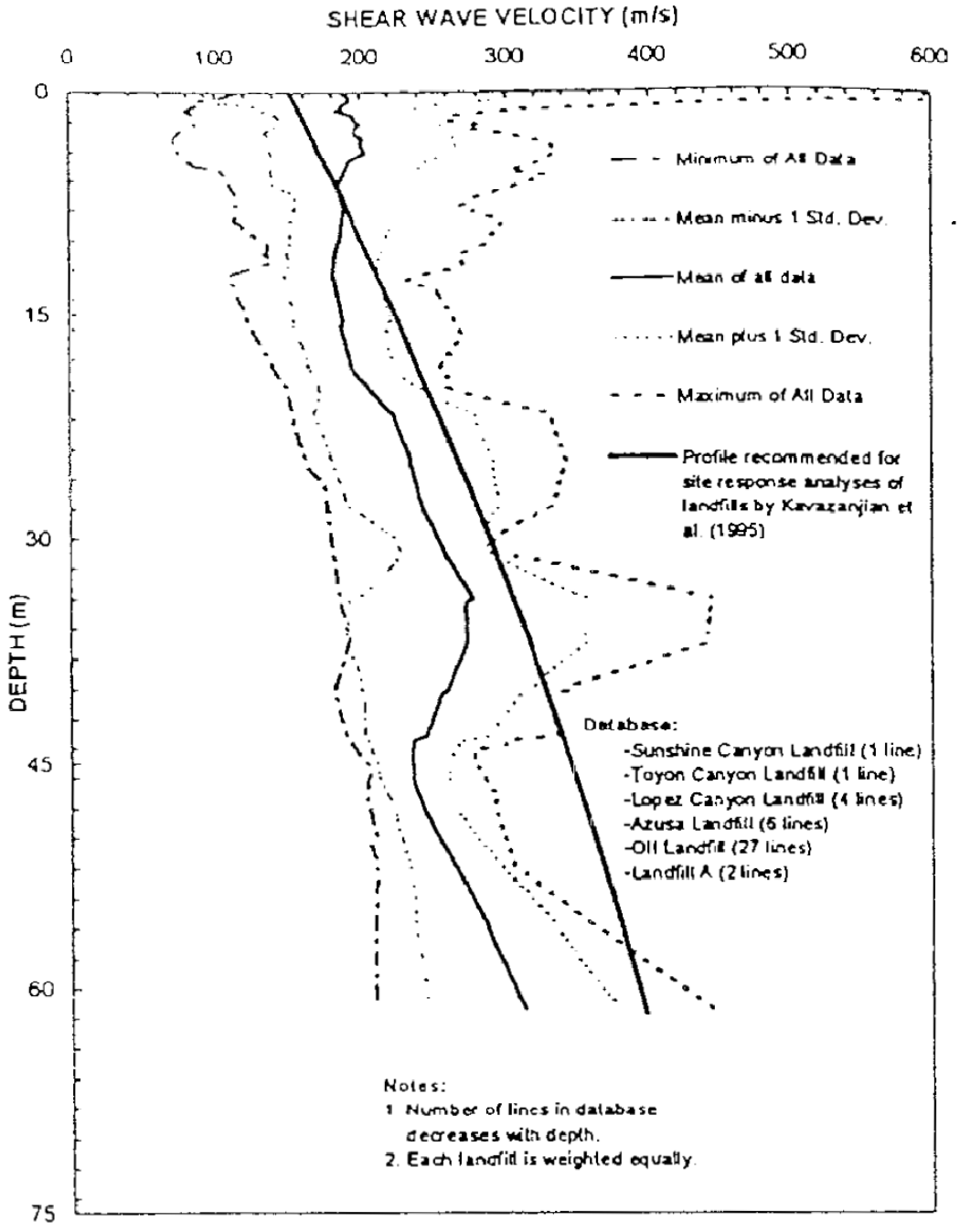

Figure 3-55 Summary of all six landfills shear wave velocity profile (Kavazanjian et al. 1996)

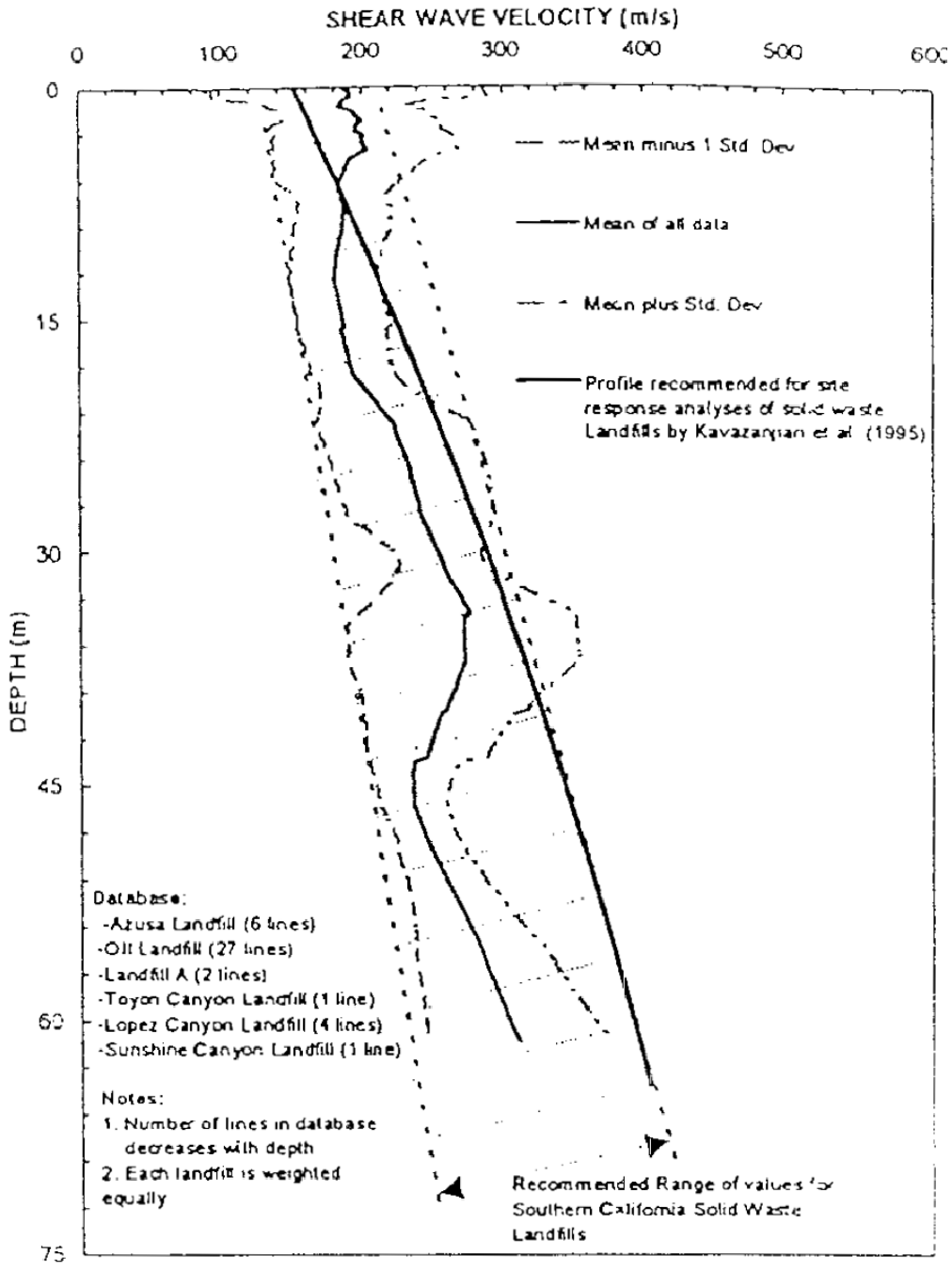

Figure 3-56 recommended range for MSW shear wave velocity (Kavazanjian et al. 1996)

3.10 Shear Modulus and Material Damping of MSW

The strain dependant modulus and damping properties of MSW are of great importance in seismic analysis. In order to accurately analyze the seismic performance of landfills, the shear modulus reduction and increase in damping due with the increase in shear strain must be accurately characterized. Several groups of researchers have conducted a back analysis of field data from the OII landfill in order to characterize strain dependent normalized shear modulus (G/G_{max}) and damping ratio curves (Kavazanjian and Matasovic 1995; Idriss 1995; Matasovic and Kavazanjian 1998; Augello et al. 1998 and Zekkos et al. 2008). Laboratory testing on reconstructed specimens to develop MSW modulus reduction and damping curves has been reported by Zekkos et al. (2008) and Matasovic and Kavazanjian (1998).

Zekkos et al. (2008) conducted more than 90 cyclic shear tests on large diameter reconstructed MSW samples (300mm diameter specimens) using waste from the Tri-cities landfill in northern California. Specimens were reconstructed with different waste composition ratios and different unit weights then subjected to cyclic loading. These investigators identified the waste composition as an important factor in characterizing the modulus and damping curves for MSW. They also concluded that the modulus reduction and damping curves are not significantly affected by the unit weight, time under confinement or loading frequency.

Figure 3-57 (a) compares the results from the testing program conducted by Zekkos et al. (2008) to several G/G_{max} of the curves recommended in the literature. The Augello et al. (1998) curve falls between the G/G_{max} curves from Zekkos et al. (2008) specimens with 100% and 62%-75% smaller than 20 mm material. The G/G_{max} curve recommended

by Matasovic and Kavazanjian (1998) falls close to the G/G_{max} from Zekkos et al. (2008) for specimens with 8%-25% smaller than 20 mm material. Augello et al. (1998) and Matasovic and Kavazanjian (1998) curves provide reasonable bounds to the laboratory data produced by Zekkos et al. (2008).

As shown in Figure 3-57 (b), the material damping curve recommended by Augello et al. (1998) captures the laboratory data from Zekkos et al. (2008) well at intermediate strains, but lies below the Zekkos et al. (2008) data at higher strains. Both the Matasovic and Kavazanjian (1998) and Idriss et al. (1995) damping curves capture the Zekkos et al. (2008) data at small strains, but fall above the Zekkos et al. (2008) data at larger strains.

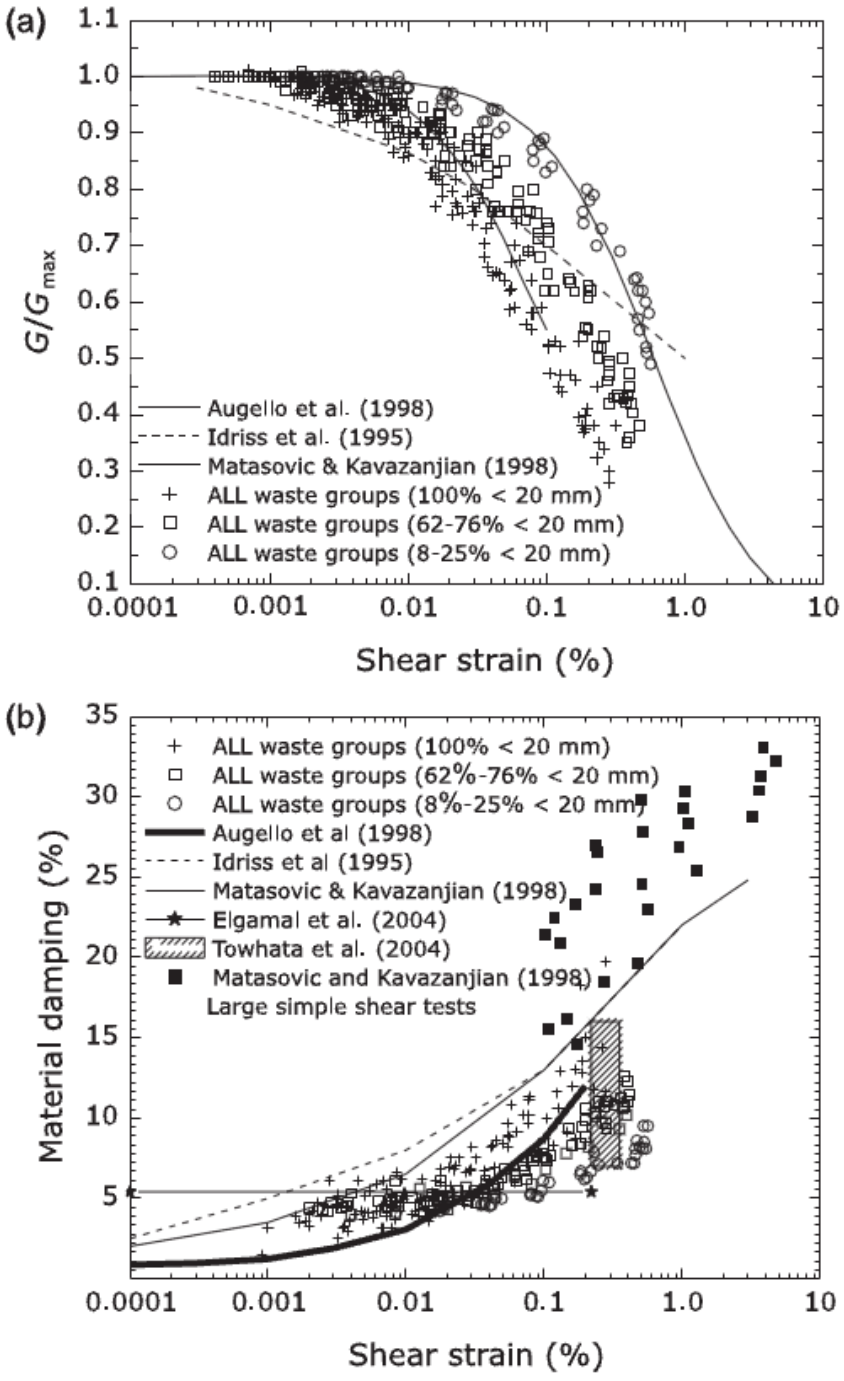

Figure 3-57 Cyclic triaxial test results by Zekkos et al. (2008) and comparison with the literature: (a) normalized shear modulus reduction curve, and (b) material damping curve as a function of shear strain (Zekkos et al. 2008)

More recently, Yuan et al. (2011) performed 15 large-scale cyclic simple shear tests in the Arizona State University (ASU) laboratory on reconstituted specimens of MSW from the Tri-Cities landfill. These tests will be referred herein as the ASU curves. The specimens were reconstituted using 100%, 65%, and 35% material that passed through a 20 mm screen (i.e. 100%, 65%, and 35% < 20 mm material). All tests were conducted at a normal stress of 75 kPa. Figure 3-58 compares the G/G_{max} curves from Yuan et al. (2011) to results from Zekkos et al. (2008). Results of the tests presented by Yuan et al. (2011) are consistent with results of the large scale cyclic triaxial tests on reconstituted specimens of the same waste reported by Zekkos et al. (2008) except that the damping ratio from the Zekkos et al. (2008) cyclic simple shear tests appeared to be systematically lower than the damping ratio from the ASU tests as presented in Figure 3-59.

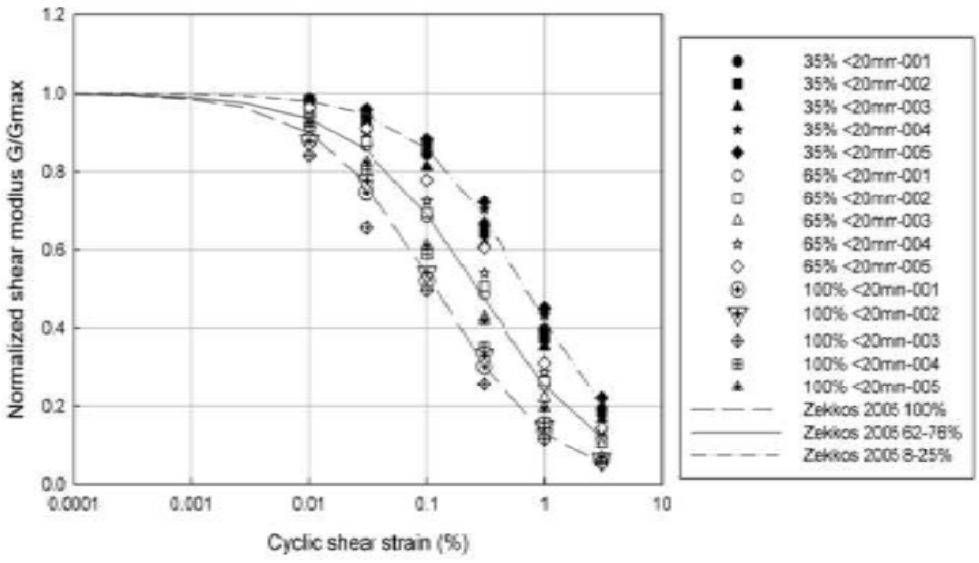

Figure 3-58 Comparison of ASU G/G_{max} curve with data from Zekkos et al. (2008) values for reconstituted Tri-Cities MSW (Yuan et al. 2011)

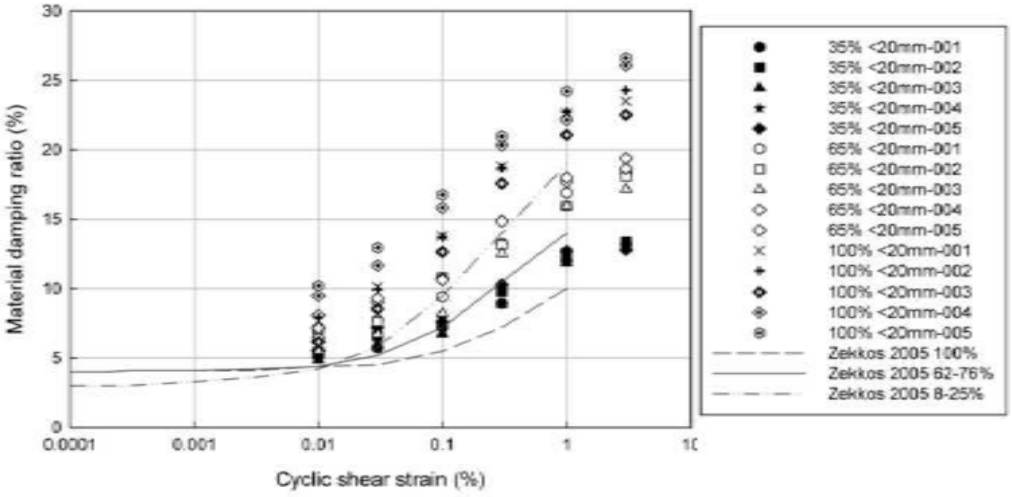

Figure 3-59 Comparison of ASU and Zekkos et al. (2008) strain-dependent damping ratio values for reconstituted Tri-Cities MSW (Yuan et al. 2011)

CHAPTER 4 COMPUTATIONAL TOOL AND NUMERICAL ISSUES

4.1 Introduction

The primary computational tool used in this dissertation is a commercial software program called FLAC 6.0 (**F**ast **L**agrangian **A**nalysis of **C**ontinua Version 6.0). This chapter describes briefly some of the features and numerical schemes used in FLAC 6.0 . The content of this chapter closely follows the FLAC 6.0 User's Manual for FLAC Version 6.0 (Itasca 2008).

4.2 Finite Difference Computer Software: FLAC 6.0

FLAC 6.0 is a two-dimensional explicit finite difference program designed specifically to model the behavior of structures built of soil, rock or other materials that may undergo plastic flow when their yield limits are reached (Itasca 2008) in response to applied forces and boundary restraints. Materials are represented by elements, or zones, which form a grid that is adjusted by the user to fit the shape of the object to be modeled. Each element behaves according to a prescribed constitutive model. In addition to the constitutive models built in FLAC 6.0, user defined constitutive models can be employed. The material within an element can yield and flow and the grid deforms (in large-strain mode) according to the movement of the material within it. An explicit Lagrangian calculation scheme and the mixed-discretization zoning technique is used in FLAC 6.0 to ensure that plastic collapse and flow are numerically stable and modeled accurately.

4.3 FLAC 6.0 Mechanics and Numerical Schemes

FLAC 6.0 uses a dynamic relaxation method to find the solution to a static problem. An explicit time-marching scheme is used to solve the equation of motion. In the finite difference method, every derivative in the set of governing equations is replaced directly by an algebraic expression written in terms of the state variables (e.g., stress or displacement) at discrete points in space. These state variables are undefined within the elements. This scheme ensures that the numerical model stays stable when the physical system is unstable (i.e. in a failure state).

Figure 4-1 shows the general computational procedure embedded in FLAC 6.0. In the first step in solving for displacements due to an applied load, new velocities and displacements from the applied stresses and forces are generated after invoking the equation of motion. Then, strain rates are derived from the velocities. In the next step, the new stresses are generated from the strain rates generated from the previous step using the prescribed constitutive law(s). In this manner, as illustrated in Figure 4-1, the state variables are calculated in every step from known values and these state variables remain fixed over the step. Since this scheme does not require forming a global stiffness matrix, it is possible to update coordinates at each time step in the large-strain mode. The incremental displacements from each step are added to the coordinates of the grid so that the grid moves and deforms. This process of updating the coordinates of the grid is referred to in the continuum mechanics as a "Lagrangian" formulation as it describes a process in which the material moves and deforms relative to a fixed grid. Although, the "Lagrangian" formulation is used to model large deformations in FLAC 6.0, the constitutive formulation at each step is a small-strain one.

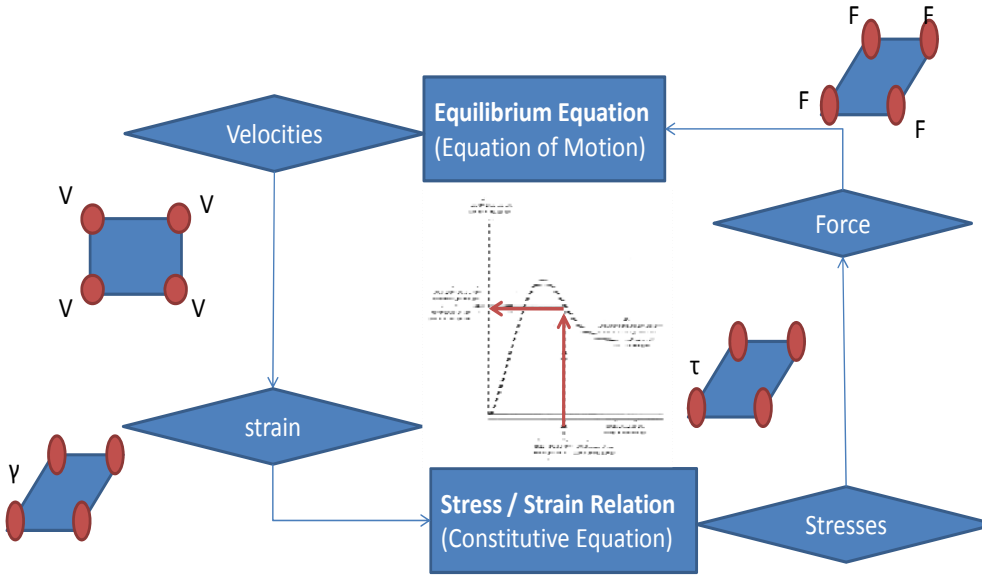

Figure 4-1 Explicit computational cycle

4.4 Material Models

FLAC 6.0 has the following built-in constitutive material models: the isotropic and transversely isotropic elastic models, and nine plasticity models (Drucker-Prager, Mohr-Coulomb, Ubiquitous-Joint, Strain-Hardening/Softening, Bilinear Strain-Hardening/Softening Ubiquitous-Joint, Double-Yield, Modified Cam-Clay, Hoek-Brown, and Cap-Yield (Cysoil). The model that was used in this study to model waste settlement is the Modified Cam-Clay (MCC) model.

4.5 Modified Cam-Clay (MCC)

The Modified Cam-Clay model is an incremental elasto-plastic constitutive model developed to model soft compressible soils. The model's features include a particular form of nonlinear elasticity and hardening behavior governed by volumetric plastic strain.

The Cam Clay model employs three state variables: the mean effective pressure, p, the deviator stress, q, and the specific volume (void ratio plus unit), v. In the FLAC 6.0 implementation of this model, the principal stresses, σ_1, σ_2 and σ_3 are used to define p and q and, by convention, traction and dilation are positive. The state variables p and q are defined as:

$$q = -\frac{1}{\sqrt{2}}\sqrt{(\sigma_1 - \sigma_2)^2 + (\sigma_2 - \sigma_3)^2 + (\sigma_1 - \sigma_3)^2} \tag{11}$$

$$p = -\frac{1}{3}(\sigma_1 + \sigma_2 + \sigma_3) \tag{12}$$

4.5.1 **Virgin consolidation line and swelling lines**

In the Cam-clay model, isotropic or one dimensional compression test results are used to define the relationship between the normal stress and the specific volume. The results of a typical isotropic compression test are presented in the semi-logarithmic plot shown in Figure 4-2. The compression curve in Figure 4-2 can be characterized by two lines: the virgin consolidation line (or the K_o compression line and the swelling line)

The virgin consolidation line in Figure 4-2 is defined by the equation

$$\upsilon = \upsilon_\lambda - \lambda \ln p \tag{13}$$

The equation for a swelling line has the form

$$\upsilon = \upsilon_\kappa - \kappa \ln p \tag{14}$$

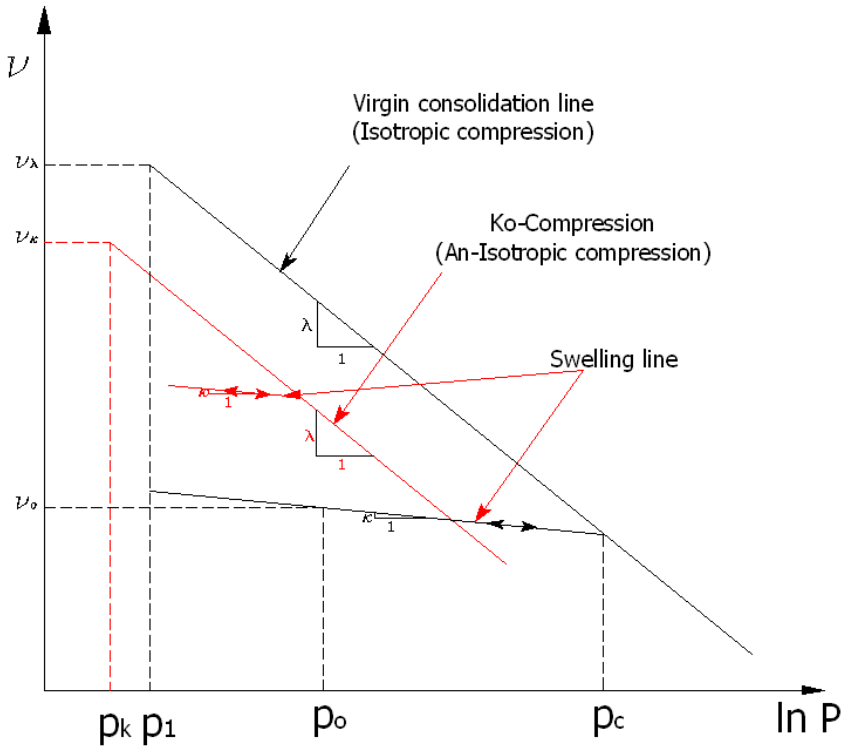

Figure 4-2 Isotropic compression curve used in Cam-Clay and the relationship with the 1-D K_o compression test constitutive model

4.6 Yield Functions

Under increasing shear loading, q, soils in the Modified Cam-Clay model behave elastically until the yield value of q is attained. The yield value of q is determined from the following equation:

$$f = q^2 + M^2 p(p - p_c) \tag{15}$$

where M is a material constant and p_c is the preconsolidation pressure (illustrated in Figure 3-2). The yield condition $f = 0.0$ is represented on a p-q plot by an ellipse

oriented with one axis along the horizontal (p) axis and with a peak located along a line through the origin with a slope of M, as illustrated in Figure 4-3.

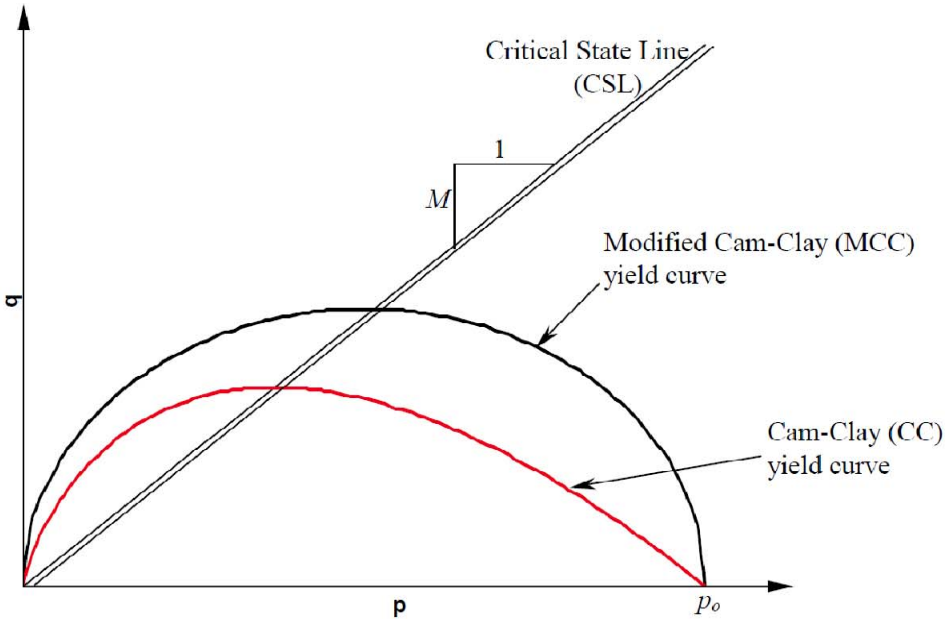

Figure 4-3 Cam-Clay and Modified Cam-Clay yield surfaces (in p-q) space. The parameter M is the slope of the CSL (Rockscience 2005)

4.7 Hardening and Softening Behavior

The line through the origin with a slope of M (the locus of the peak points of all yield ellipses) is referred to as the critical state line (CSL). If yielding occurs to the right the CSL, hardening behavior accompanied by volumetric compression is exhibited. This side of the yield surface is known as the wet or subcritical side.

Figure 4-4 (a) illustrates soil behavior on the wet side for the case of direct simple shear loading. When a sample is loaded in direct simple shear, it behaves elastically until it hits the initial yield surface. From then on the yield surface begins to isotropically

expand and exhibits hardening behavior (yielding and plastic strain is accompanied by an increase in yield stress). Figure 4-4 (b) shows the stress-strain hardening deviatoric stress strain behavior that occurs for a sample loaded in simple shear on the wet side.

If yielding occurs to the left of the CSL line, the soil exhibits softening behavior accompanied by dilatancy (volume expansion), as shown in Figure 4-5 (a). In softening the yield surface contracts after the stress state point touches the initial yield surface. The deviatoric stress-strain curve for softening behavior is shown in Figure 4-5 (b).

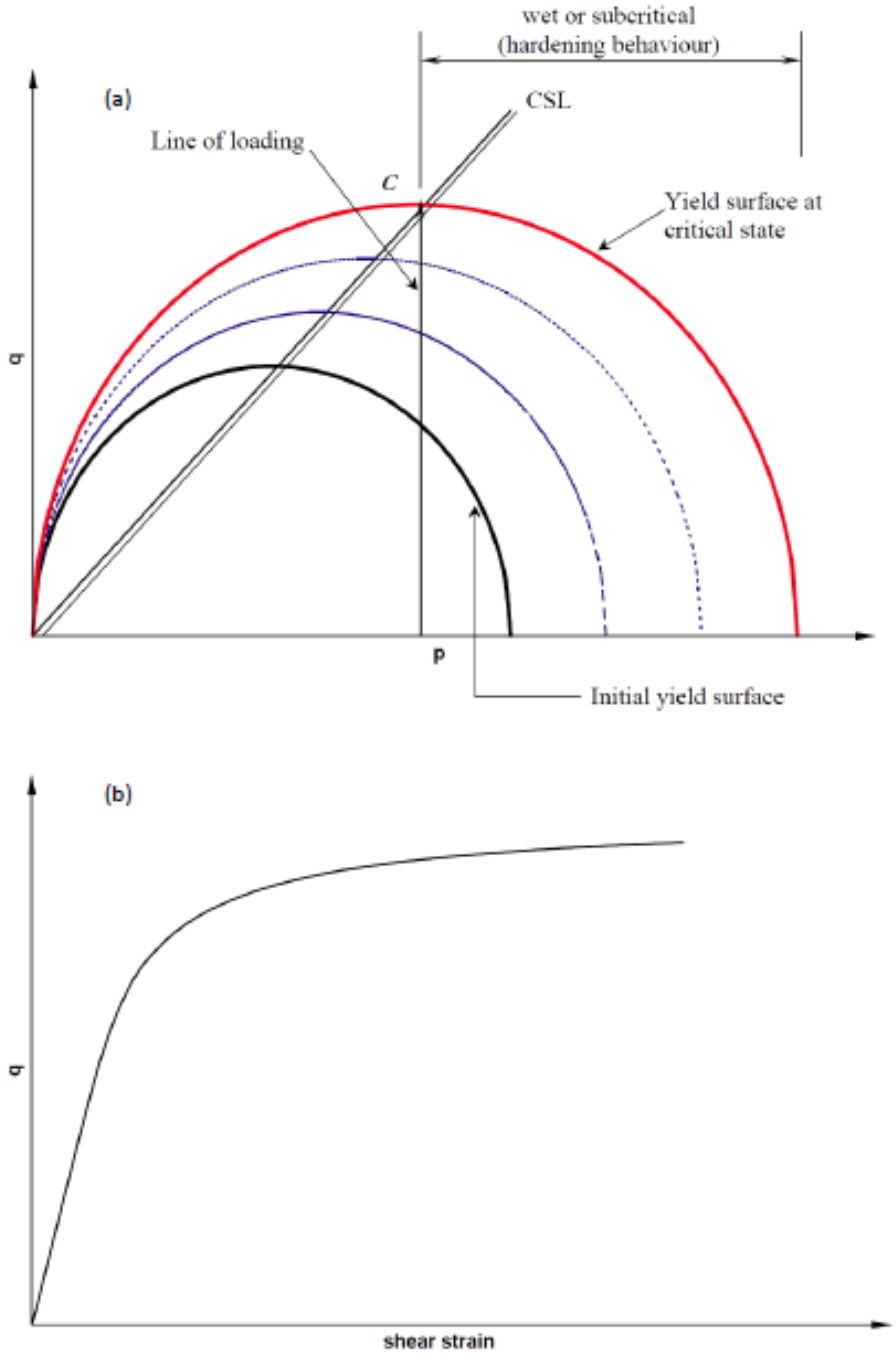

Figure 4-4 Hardening stress behavior, (a) stress path; (b) stress strain behavior (Rockscience 2005)

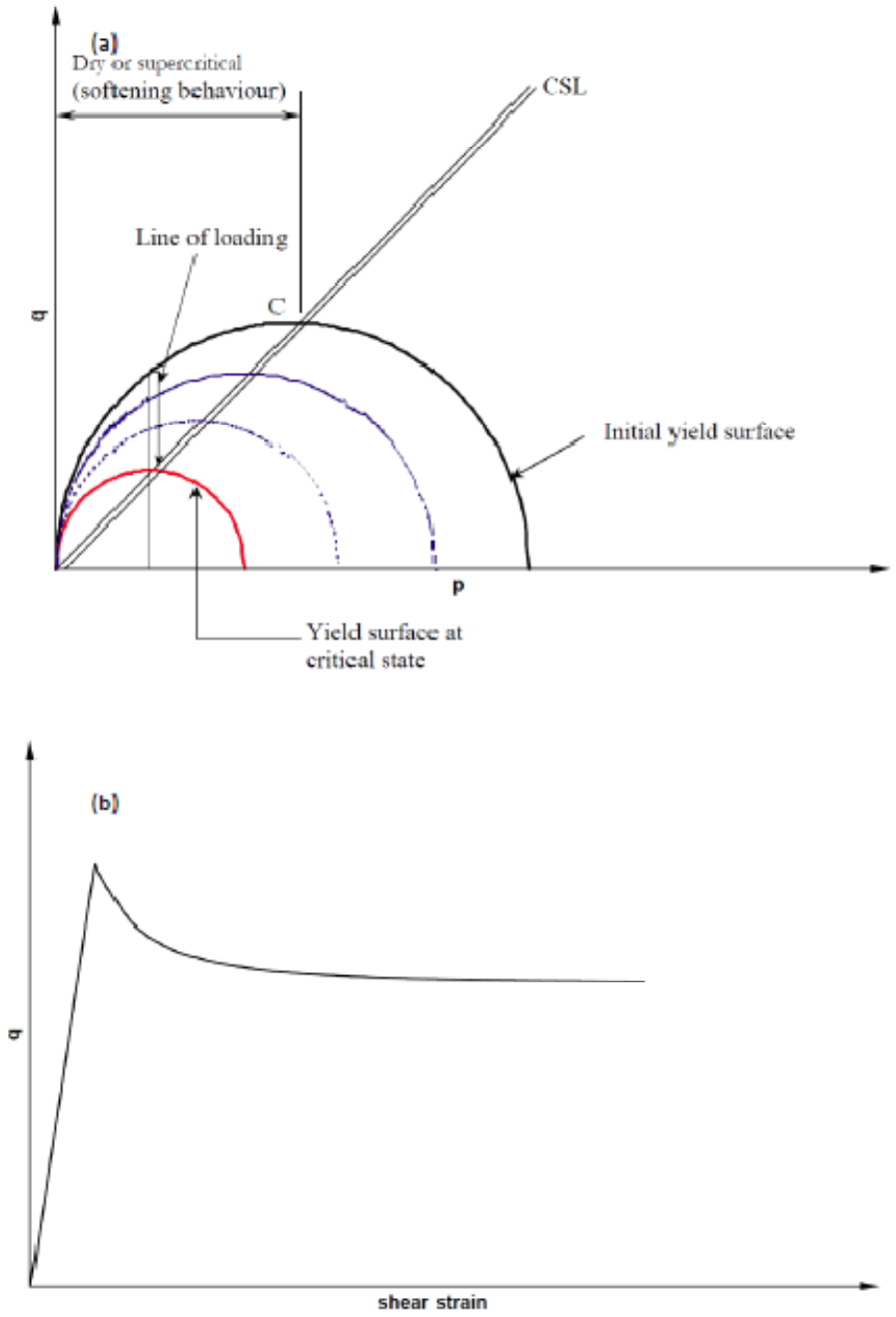

Figure 4-5 Softening Stress behavior, (a) stress path; (b) stress strain behavior (Rockscience 2005)

4.7.1 **Elastic material constants for Modified Cam-Clay**

For Modified Cam-Clay soils, the bulk modulus, *K*, is not a constant but instead depends on mean stress, p, the specific volume, v, and the swelling line slope, κ. The bulk modulus is calculated at any point in the soil as

$$K = \frac{vp}{\kappa} \tag{16}$$

Modified Cam-Clay formulations require specification of either the shear modulus G or Poisson's ratio υ, but not both. When G is supplied, υ is no longer a constant but is calculated from K and G as:

$$\upsilon = \frac{3K - 2G}{2G + 6K} \tag{17}$$

When υ is specified, G is calculated from ν and *K* using the relationship:

$$G = \frac{K(3 - 6\upsilon)}{2(1 + \upsilon)} \tag{18}$$

4.7.2 **Summary of input parameters**

The parameter *M* can be related to the friction angle of the soil in triaxial testing, ϕ from the Mohr-Coulomb criterion as measured in triaxial compression as:

$$M = \frac{6\sin\phi}{3 - \sin\phi} \tag{19}$$

The slope of the virgin consolidation and swelling lines (λ and κ) can be derived from an isotropically consolidated triaxial test or from a one-dimensional compression

test. Note that the slope of the v vs $\ln p$ line will be equal to the slope of the e versus $\ln p$ line, where e is the void ratio and is related to ν as:

$$e = v - 1 \tag{20}$$

The slope of the e vs. $\log p$ virgin compression curve, sometimes called the compression index, C_c is related to λ and the slope of the e vs. log p swelling curve C_s, sometimes called the recompression or swilling index, is related to κ as：

$$\lambda = \frac{C_c}{\ln(10)} \tag{21}$$

$$\kappa = \frac{C_s}{\ln(10)} \tag{22}$$

4.8 Fish Programming Language

FLAC 6.0 contains a powerful built-in programming language called FISH (short for FLACish). With FISH, user defined constitutive models can be implemented in lieu of using one of the material models already available in FLAC 6.0. FISH was used to code the two new constitutive models (described subsequently) into FLC 6.0.

4.9 Interface and Beam Elements

4.9.1 FLAC 6.0 interface elements

FLAC 6.0 contains interface elements that join two separate grids or structural elements together. These interface elements have zero thickness. Large relative shear displacements, e.g. relative displacements of several meters that may occur between the waste mass and the lining system in a landfill, can be handled in FLAC 6.0 using interface elements. As the Lagrangian calculations are performed, the relative displacement across the interface is accommodated by movement of the modeling grid, and as such the points of reference for calculation are updated after each increment to account for the large movements (Fowmes 2007).

4.9.2 FLAC 6.0 interface logic

In FLAC 6.0, an interface element joins two faces (grid to grid or structural beam to grid) with two springs, one in the normal direction and one in the transverse direction, as illustrated in Figure 4-6. The interface shear stiffness controls the initial stress displacement response of an interface until a limiting shear stress value, controlled by the interface strength, is reached. The limiting shear stress of an interface, F_{max}, is defined by the Mohr-Coulomb criterion as follows:

$$F_{s\max} = cL + \tan\phi F_n \tag{23}$$

where c = cohesion (in stress units) along the interface, L = effective contact length of the interface (illustrated in Figure 4-6), and ϕ = friction angle of interface surface. If the

yield criterion is satisfied (i.e., if $|F_s| \geq F_{s\max}$), then $F_s = F_{s\max}$, with the sign of shear preserved, where F_s is the shear force at the interface.

Choosing the interface shear and normal stiffness is not a trivial a task. Choosing too small a stiffness may result in instability due to unrealistically high relative displacement at the interface. However, choosing too large a stiffness will result in lengthening of the convergence time.

Interface interpenetration is one of the numerical issues that can occur when using interface elements in FLAC 6.0. In this phenomenon, one side of the interface moves into the other side of the interface such that an overlap is created. Even small interpenetration may cause errors in interface displacement calculations. This process is controlled by the normal stiffness of the interface. For this reason, it is recommended that the normal stiffness of the interface to be assigned 10 times the stiffness of the adjacent material (Itasca 2008). If there is a significant difference between the material stiffness across the interface, the material with the lower stiffness should be considered when assigning the interface normal stiffness. While slight interpenetration will occur even with very high normal stiffness, it is greatly reduced by selection of the correct normal stiffness (Fowmes 2007).

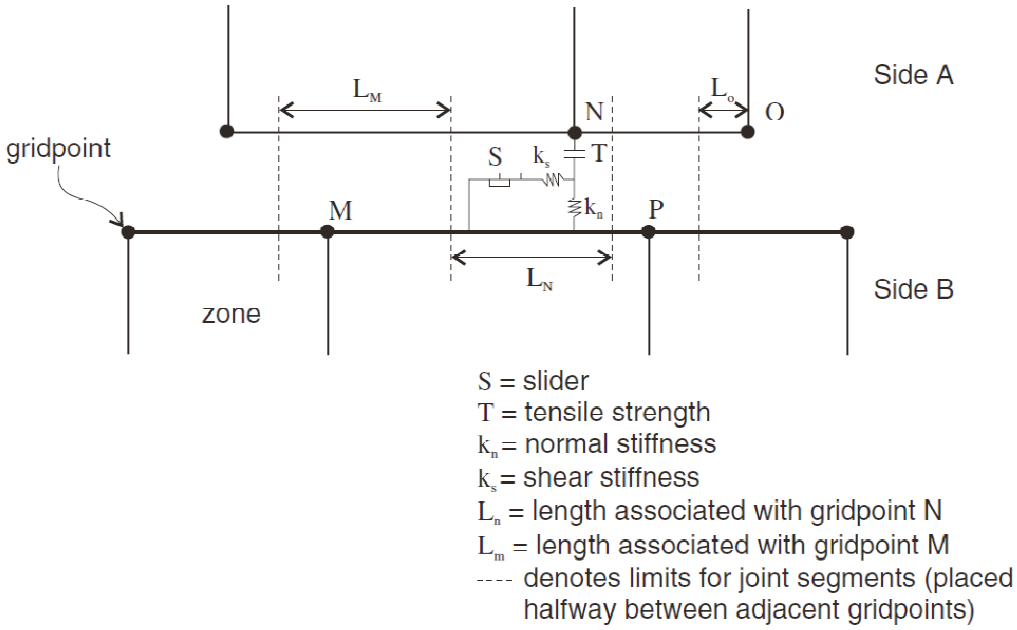

Figure 4-6 FLAC 6.0 interface logic: Sides A and B are connected by shear (k_s) and normal (k_n) stiffness springs (Itasca 2008)

Fowmes (2007) demonstrated the influence of the shear stiffness of the interface on the stress-strain response in case of a textured LLDPE geomembrane against a nonwoven geotextile tested at 10 kPa normal stress using the FLAC 6.0 interface model. Based on the measured data from direct shear tests presented in Fowmes (2007), the initial tangential modulus was found to be 10 MPa/m, while the secant modulus at 10mm displacement was found to be 1MPa/m (Figure 4-7). Fowmes (2007) varied the shear stiffness of the interface from (10MPa/m to 0.1MPa/m). Fowmes (2007) concluded that using initial tangential modulus or the secant modulus at 10 mm displacement as the interface shear stiffness did not make difference in predicting the behavior of the interface. However, using lower values for the interface shear stiffness (i.e. values lower

than the secant modulus at 10mm displacement) did not accurately predict the behavior of the interface.

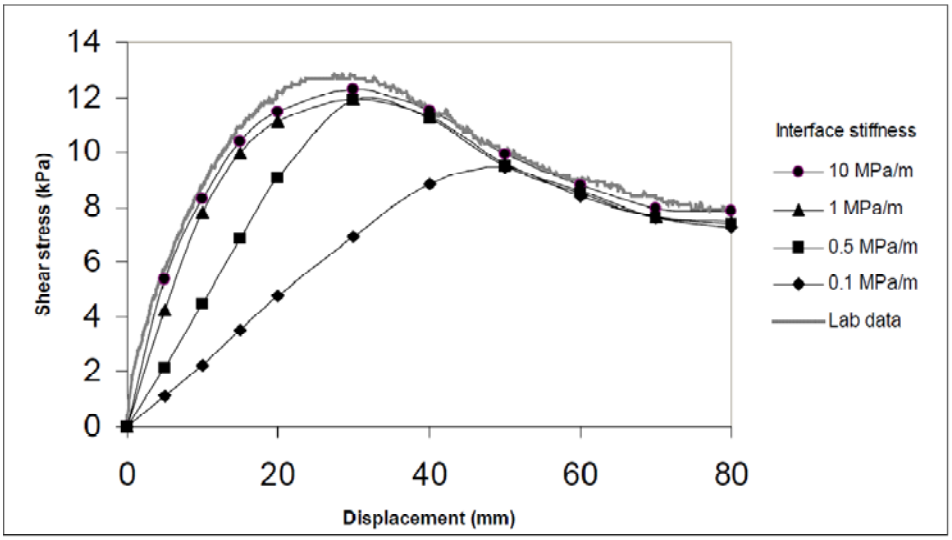

Figure 4-7 Influence of interface shear stiffness (Fowmes 2007)

4.9.3 **FLAC 6.0 beam element**

Fowmes et al. (2005), Fowmes et al.(2006) and Fowmes (2007) used FLAC 6.0 beam elements to represent geosynthetic materials in a landfill liner system, assuming a moment of inertia of zero to the beam element to represent a flexible sheet that cannot support any bending moment. This enabled the calculation of the in-plane forces and strains developed in geomembranes and geotextiles on a landfill side slope due to waste settlement. Beam elements are defined in FLAC 6.0 outside of the continuum and can interact with the continuum through interfaces.

In the Fowmes et al. (2006) analysis of the in-plane forces and strains developed in a lining system on a landfill side slope, a user defined code that allowed for displacement dependant friction was used to account for softening at the interfaces. In this analysis, the

lining system was consisted of three geosynthetic layers that interacted through interfaces. Fowmes et al. (2006) also developed a user defined code to allow varying the Young's Modulus as a function of the axial strain in the beam element, as the FLAC 6.0 beam element is linear elastic.

Fowmes et al. (2005) modeled the lining of a reinforced sand body on a benched hard rock quarry slope using FLAC 5.0. A 0.5m thick clay barrier layer was placed in direct contact with an incompressible stable rock subgrade and then an engineered reinforced sand body was placed against the clay to provide stability. In this analysis Fowmes et al. (2005) modeled a two geosynthetic layer lining system using two layers of beam elements with three interfaces defined between them. In these analyses, the geomembrane was placed on the top expanded polystyrene panels on the side slope. Overlying the geomembrane is a geotextile protection layer. The waste was then placed directly in contact with the geotextile protection layer for simplicity.

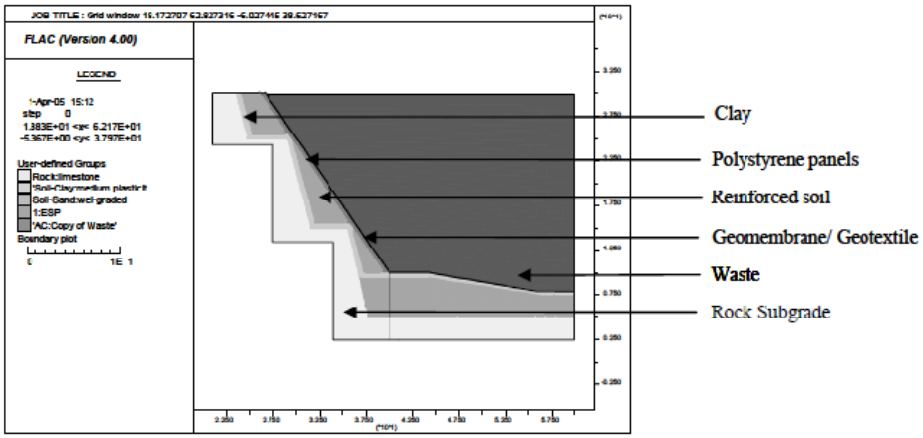

Figure 4-8 Lining system model (Fowmes et al. 2005)

Fowmes et al. (2005) investigated the influence of the waste modulus (stiffness) on the downdrag i.e. the stresses developed in the lining system due to the waste settlement. In these analyses, the waste was modeled as elastic linear material with variable modulus, the waste was placed in 10 m height and vertical normal stress was applied on the top of the layer to force this layer to settle. Figure 4-9 shows the influence of the reduced waste stiffness (downdrag) on the strain developed in the geosynthetic layers.

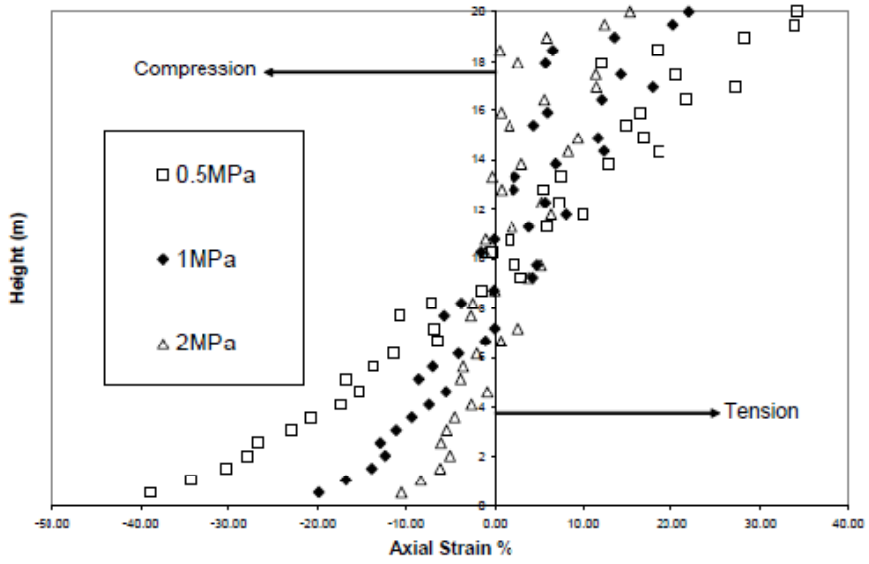

Figure 4-9 Influence of waste stiffness properties on geotextile axial strain. (N.B. Tensile strain is positive) (Fowmes et al. 2005)

Fowmes et al. (2005) also investigated the influence of increasing the (geomembrane/geotextile) interface friction on the maximum tensile stresses developed in the geomembrane. The max tensile strain developed on geomembrane increased from 1.6% to 12.7% when the interface friction angle increased from (9 to 36 degrees). Also, softening of the GM/geotextile interface was modeled using a FISH subroutine developed by Fowmes et al. (2005) for the FLAC 5.0. The subroutine decreased the friction angle from peak friction angle of (20 degrees) to a residual friction angle of (15 degrees)

depending on the relative displacement. Maximum tensile strain of 4.5% was reported for this type of analysis.

CHAPTER 5 GM/GCL CONSTITUTIVE MODELING

5.1 Introduction

Comprehensive modeling of the cyclic shear behavior of landfill liner and cover systems used in waste containment facilities requires a suitable constitutive model for geosynthetic interfaces. Modeling of liner and cover system cyclic shear behavior can be important in the assessment of the long-term performance of waste containment facilities subjected to earthquakes or other dynamic loading. Although a significant body of research has been conducted on the static shear modeling of geosynthetic interfaces (e.g., Byrne 1994, Esterhuizen et al. 2001, Triplett and Fox 2001), only very limited work has been published on modeling the shear behavior of geosynthetic interfaces under cyclic loads (Desai and Fishman 1991, LoGrasso et al. 2002, Kim et al. 2005).

This chapter presents a constitutive model for modeling the in-plane cyclic shear behavior of textured geomembrane/geosynthetic clay liner (GMX/GCL) interfaces. This model is based upon experimental data from uniform cyclic tests. Comparison between model predictions and experimental results is good, as the model captures the progressive degradation of the hysteresis loops deemed the most important facet of the observed behavior. The model has been implemented in a finite-difference program for predicting the response of landfill liner and cover systems to earthquake loading. This constitutive model can be extended to predict other in plane behavior of other elements in landfills (e.g. GM/clay, GM/Geotextile, etc.).

A strain softening interface code (SSint.fis) was developed by Itasca (2002) (SSint.fis). However, this is code is unsuitable for dynamic loading purposes and also is not usable if the interfaces involve structure elements such as beams. Fowmes (2005)

adapted the original Itasca code to handle beam elements subject to static loading, if a beam element is involved; the code employs the nodal velocity, to calculate the relative shear displacement. In the code developed herein Fowmes (2005) work was extended it to consider cyclic loading. Initially, a simple grid to grid interface code labeled (SSint_eqn_com.fis), was developed to model GM/GCL interface behavior. This code is provided in Appendix A. The code implements the model presented in this chapter for (GM/GCL) interfaces.

The code was then extended to include interfaces involve beam elements. The final code, labeled (SSint_eqn_beams_com.fis), is provided in Appendix A.

5.2 Experimental Data from Cyclic Shear Testing of GM/GCL Interface

The constitutive model presented herein was developed using the results of a series of cyclic direct shear tests on GMX/GCL specimens described by Ross (2009) and Ross et al. (2010). These tests were conducted using the cyclic direct shear device described by Fox et al. (2006). GMX/GCL specimens are sheared between the floor of the test device and a horizontal pullout plate. Both test device floor and the pullout plate are configured to prevent specimen slippage and related progressive failure effects (Fox and Kim 2008). Each GMX/GCL specimen was free to fail at the interface or internally (within the GCL).

Ross et al. (2010) describe the experimental program employed to develop the constitutive model described herein. Testing was conducted in the geotechnical laboratory, as part of joint Arizona State University (ASU) / University of California at San Diego (UCSD) funded by the National science foundation (NSF), at UCSD using two geosynthetic products: a double non-woven (NW) needle-punched (NP) GCL with no thermal bonding and a 60 mil, HDPE GM with single-sided structured (Micro Spike®)

texturing. All specimens were 1320 x 305 mm in plan dimension. Each GCL specimen was hydrated under the shearing normal stress using the two-stage accelerated hydration procedure developed by Fox and Stark (2004). Ross (2009) conducted twenty-nine displacement-controlled cyclic shear tests on this GMX/GCL combination to determine the effects of the displacement amplitude, Δ_a, on material response. The loading consisted of 25 cycles of sinusoidal displacement with a frequency, *f,* equal to 1 Hz. Tests were conducted at five normal stress levels (13, 348, 692, 1382 and 2071 kPa) and seven displacement amplitudes (±2, 10, 15, 20, 30, 60, and 120 mm).

After each test was completed, the pullout plate and GCL were carefully removed from the shear machine. The observed failure mode was recorded along with any indications of localized stress, tearing, or GMX slippage.

5.2.1 **Results**

Inspection of the cyclic shear stress-displacement curves indicated that that the displacement at which the peak shear resistance was mobilized was typically between ±10 and ±15 mm. Therefore, cyclic testing done with displacement amplitudes of (±2, 10 and 15 mm) were considered pre-peak tests and cyclic testing done with displacement amplitudes of (±20, 30, 60 and 120 mm) were considered post-peak tests (Ross 2009). The differences between pre- and post-peak response were not as clear at a normal stress, σ_n, equal to 13 kPa as they were at the larger normal stresses (e.g., 348, 692, and 1382 kPa). Ross (2009) concluded that the 13 kPa normal stress was too small to create intimate contact at the GMX/GCL interface.

In the cyclic interface shear strength tests conducted by Ross (2009), interface failures were consistently observed at the three smallest normal stresses (13, 348, and 692 kPa).

The only cyclic test in which a partial internal failure was observed was at σ_n = 1382 kPa for a displacement amplitude of ±10 mm. All tests at ±15 mm and greater caused interface failures.

Figure 5-1 and Figure 5-2 show the pre-peak (±10 mm) and post-peak (±20 mm) response, respectively, of the GMX/GCL interface at σ_n = 1382 kPa. In the post-peak case, presented in Figure 5-2, a continuous degradation in shear strength is observed over the 25 cycles of the test. However, most of the shear strength degradation occurs within the first five cycles of loading in the pre-peak tests.

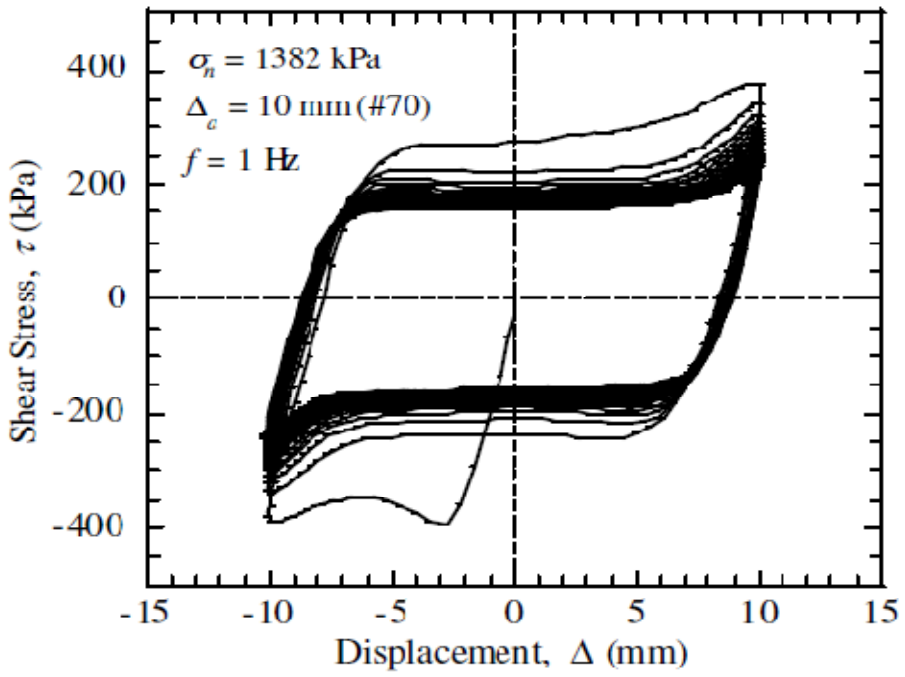

Figure 5-1 Pre-peak shear stress vs. displacement for ±10 mm cyclic shear test at σ_n = 1382 kPa (Ross 2009)

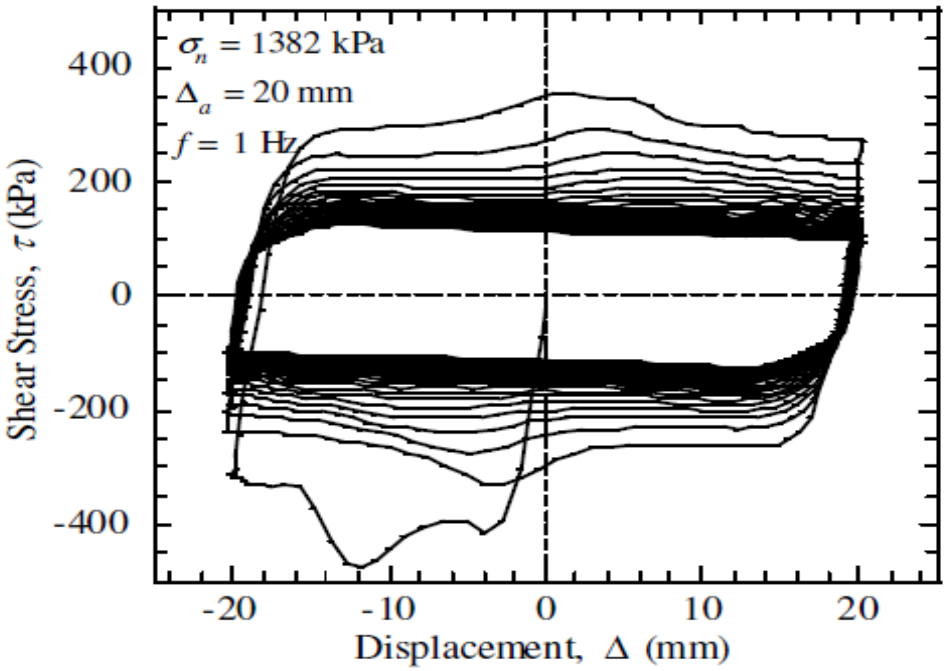

Figure 5-2 Post-peak shear stress vs. displacement for ±20 mm cyclic shear test at σ_n = 1382 kPa (Ross 2009)

The post-peak test results from Ross (2009) for cyclic testing of the GMX/GCL combination at normal stresses of 1382 kPa and 2071 kPa are shown in Figure 5-3 and Figure 5-4, respectively, for four displacement amplitudes (±20, 30, 60, and 120 mm). For these post-peak cyclic tests, a peak in the shear stress may be observed in the third quadrant of the plot. Both Figure 5-3 and Figure 5-4 show a continuous degradation in shear strength with cyclic loading until the cyclic strength reaches a stable minimum value near the end of the test (i.e. reaches a large displacement shear strength).

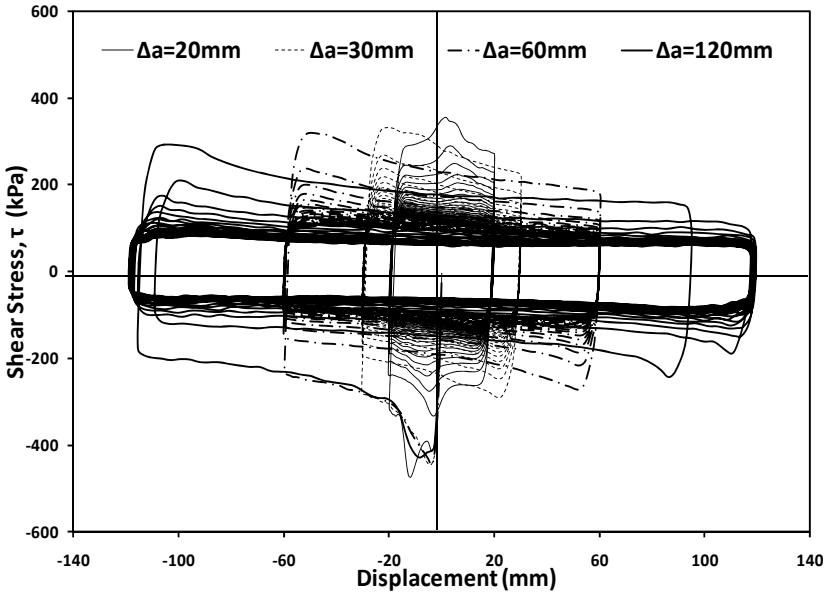

Figure 5-3 Shear stress vs. displacement for ±20, 30, 60, and 120 mm amplitudes cyclic shear tests at σ_n = 1382 kPa

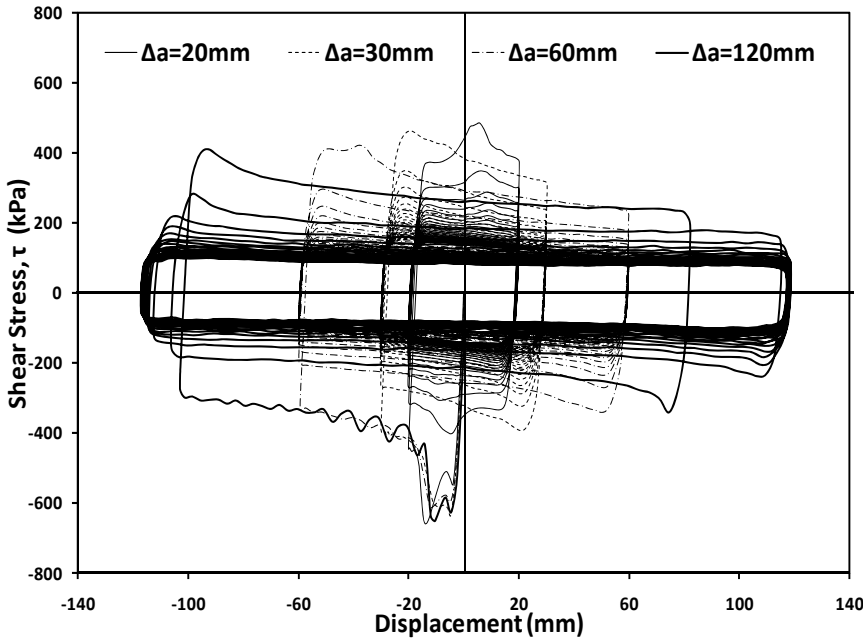

Figure 5-4 Shear stress vs. displacement for ±20, 30, 60, and 120 mm amplitudes cyclic shear tests at σ_n = 2071 kPa

5.3 Interpretation of Test Results

The progressive degradation of the hysteresis loops in Figure 5-2 through Figure 5-4 was deemed the most important aspect of the observed interface behavior with respect to modeling the in plane shear behavior of the GMX/GCL combination. To illustrate the typical post peak degradation behavior of the GMX/GCL combination modeled in this paper, the shear stress time history over 25 cycles of loading with a constant displacement amplitude of ± 120 mm under σ_n = 692 kPa is presented in Figure 5-5. The first five cycles experience most of the degradation in mobilized shear strength and after 10 cycles the mobilized shear strength is almost constant. Based upon the shear stress time history presented in Figure 5-5, it was hypothesized that the observed degradation in the mobilized shear strength may be related to the cumulative relative shear displacement.

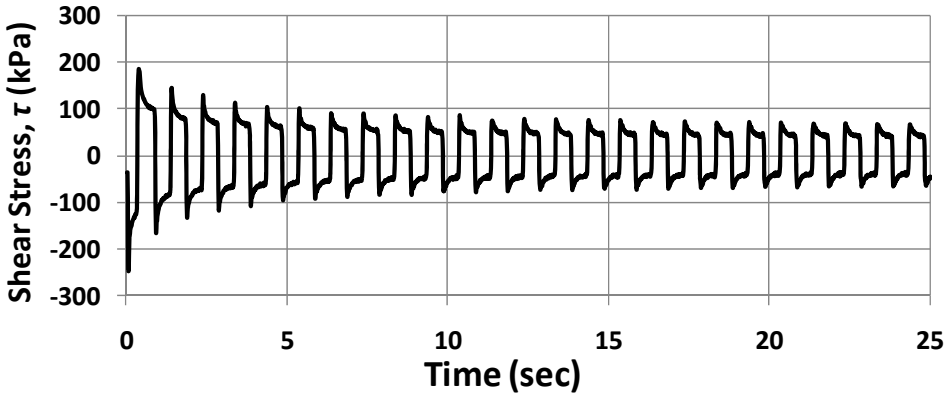

Figure 5-5 Shear stress vs. time for displacement amplitude ± 120 mm cyclic shear tests at σ_n = 692 kPa.

A plot of the absolute value of the mobilized shear stress at the peak displacement versus the cumulative relative shear displacement for post-peak displacement amplitudes of 20, 30, 60 and 120 mm at σ_n = 692 kPa is presented in Figure 5-6. A distinctive trend

of mobilized shear stress versus cumulative relative shear displacement may be observed in the figure. As the cumulative displacement increases, it appears that a stable minimum value of mobilized shear strength (i.e. a large displacement shear strength) is reached, after which further degradation is negligible. The relationship between mobilized shear strength and cumulative relative shear displacement illustrated in Figure 5-6 indicates that the reduction in GMX/GCL mobilized shear strength may reasonably be expressed as a function of cumulative relative shear displacement. Relating the reduction in mobilized interface shear strength to the relative shear displacement is not a new concept. Esterhuizen et al. (2001) developed a hyperbolic model for interface behavior under monotonic loading that relates the reduction in interface shear strength to relative shear displacement based on monotonic interface direct shear test results.

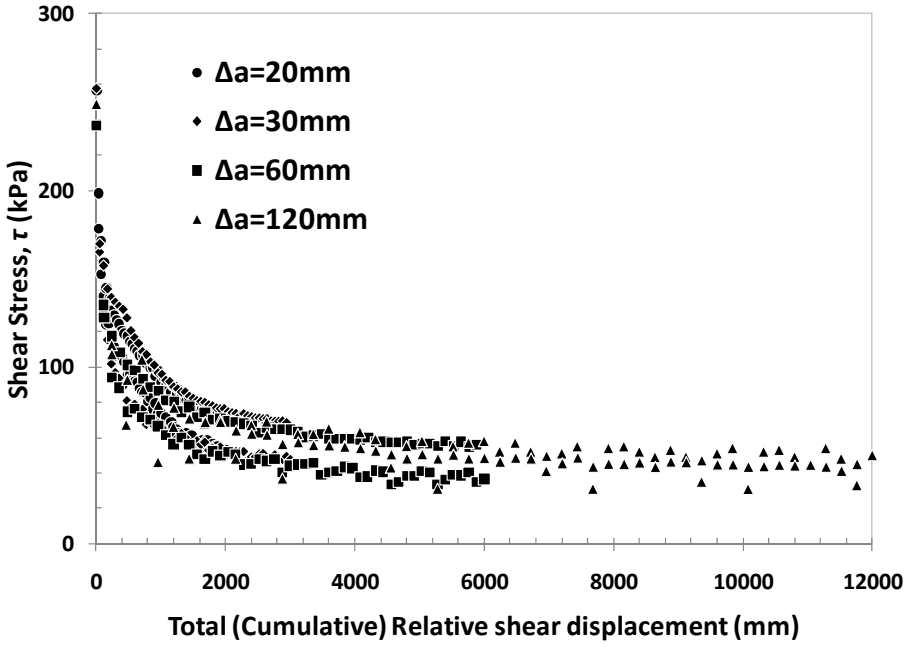

Figure 5-6 Mobilized shear strength vs. cumulative relative shear displacement for ± 20, 30, 60 and 120 mm amplitudes cyclic shear tests at σ_n = 692 kPa.

The peak and large displacement shear-strength failure envelopes for the in-plane shear strength of the GMX/GCL combination modeled herein subject to cyclic loading are shown in Figure 5-7.

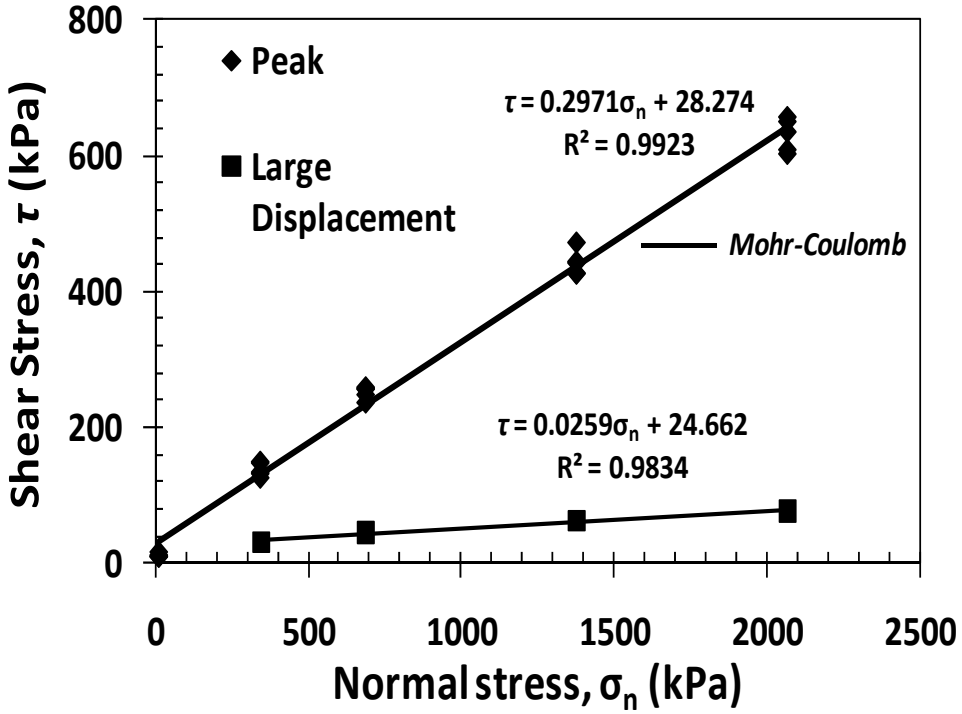

Figure 5-7 Peak and large displacement failure envelopes for the in-plane strength of a GMX/GCL combination

Both the peak and large displacement shear strength envelopes can be represented by the Mohr-Coulomb model as follows:

$$\tau = c + \sigma_n \tan\phi \tag{24}$$

where c is the in-plane cohesion and ϕ is the in-plane friction angle. Table 5-1 presents the best fit parameters for both the peak and large displacement Mohr-Coulomb envelopes.

Table 5-1 Peak and large displacement shear strength failure envelope parameters.

Failure Envelope	Mohr Coulomb Parameters	
	c (kPa)	ϕ (degrees)
Peak	28.20	16.5
Large Displacement	24.70	1.5

The peak strengths in Figure 5-7 and Table 5-1 were mobilized at shear displacements of 10.0-15.0 mm. If the cohesion is assumed to be constant, the friction angle at any stage during degradation can be related to the mobilized shear strength,τ, at the peak displacement amplitude according to Eq. 24 as:

$$\phi = \tan^{-1}\left(\frac{\tau - c}{\sigma_n}\right) \tag{25}$$

The friction angle evaluated using Eq. 25 and the large-displacement cohesion from Figure 5-8 is plotted versus the cumulative relative shear displacement for post-peak tests at four different normal stresses in Figure 5-8. The trends of the four curves are quite similar over the range of normal stresses from 348 kPa to 2071 kPa. At each normal stress, the peak friction angle (and thus peak shear resistance) develops at a relatively small cumulative shear displacement (i.e. 10.0-15.0 mm). Then, as cumulative shear displacement increases the friction angle reduces until it reaches a stable large displacement friction angle. The data in Figure 5-8 display a higher variability at lower normal stresses. The data in Figure 5-8 also show a distinctive trend between in-plane friction angle and cumulative relative displacement. This trend may change slightly with normal stress. However, the hypothesis of using cumulative relative displacement as the governing variable to estimate the reduction in in-plane shear strength that accompanies cyclic loading of a GMX/GCL combination is clearly supported by the data in Figure 5-8.

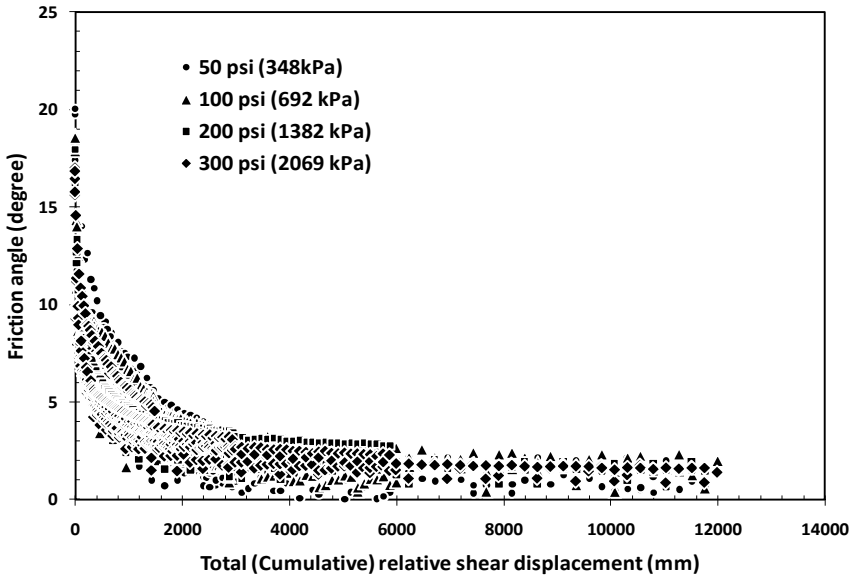

Figure 5-8 Friction angle versus cumulative relative shear displacement at normal stresses of 348, 692, 1382 and 2069 kPa for post-peak tests only

5.4 Displacement-Softening Relationship

To model the in-plane behavior of a GMX/GCL specimen subject to cyclic shear loading, a nonlinear displacement-softening model was been developed. The model assumes that a unique relationship exists between the in-plane friction angle and the cumulative relative shear displacement, as suggested by the data in Figure 5-8. The formulation presented herein results in hysteresis loops representative of those presented in Figure 5-3.

5.4.1 Constitutive relationship

The generalized shear strength-displacement relationship for the in-plane mobilized friction angle, $\emptyset$, of a GMX/GCL combination is illustrated in Figure 5-9. Key parameters in this relationship include for the plastic cumulative relative shear

displacement (δ^p), the peak friction angle ($\emptyset_p$), the large displacement friction angle ($\emptyset_r$), the cumulative displacement at the peak friction angle (δ_p^e) and cumulative displacement at the large displacement friction angle (δ_r^p). This formulation assumes elastic behaviour at relative shear displacements less than δ_p^e and plastic behaviour after the shear displacement exceeds δ_p^e.

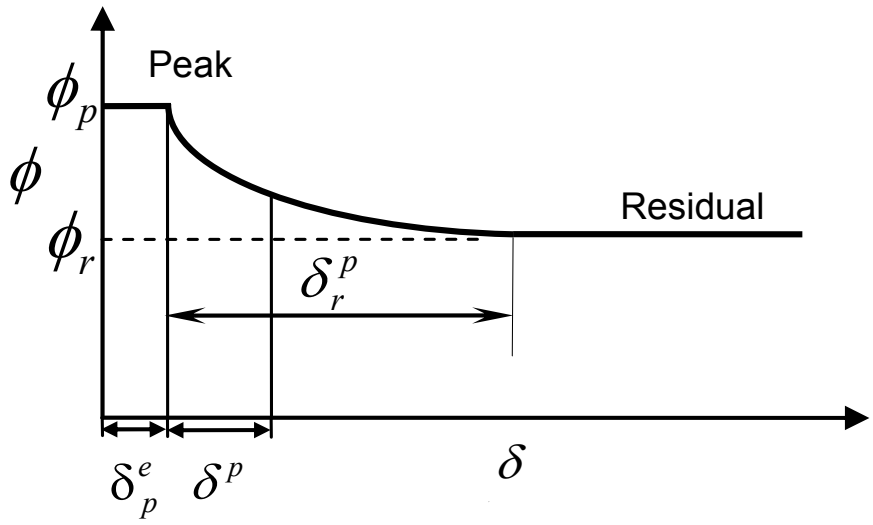

Figure 5-9 Generalized interface friction angle versus cumulative shear displacement relationship

The assumption that the mobilized friction angle decreases as the cumulative displacement increases once $\delta_{\mathrm{p}}^{\mathrm{e}}$ is exceeded and continues to decrease until it reaches a stable residual value (the large displacement friction angle), as illustrated in Figure 5-9, is the basis for the displacement-softening model developed herein. This relationship can be represented mathematically as follows:

$$\phi = \begin{cases} \dfrac{1}{a + b\left(\delta^{p}\right)^{k}} & 0 < \delta^{p} \le \delta_{r}^{p} \\ \phi_{r} & \delta^{p} > \delta_{r}^{p} \end{cases} \tag{26}$$

where a, b and k are model parameters and are assumed to be constant for a particular GMX/GCL combination. These parameters can be defined using the coordinates (δ_{r}^{p},$\emptyset_{r}$), (δ_{p}^{e},$\emptyset_{p}$), and (0, $\emptyset_{p}$) from the cumulative shear displacement relationship in Figure 5-9. The shear strength of the specimen is equal to $\emptyset_{p}$ until the cumulative deformation exceeds δ_{p}^{e}. At this point, the mobilized friction angle starts to degrade until it reaches a value of $\emptyset_{r}$ at a displacement equal to δ_{r}^{p}. The rate of decay of the mobilized friction angle is described by the exponent k. The relationship between the mobilized friction angle and the cumulative plastic shear displacement δ^{p} at displacements greater than δ_{p}^{e} can be written as:

$$\phi = \frac{1}{\left(a + d\left(\dfrac{\delta^{p}}{\delta_{r}^{p}}\right)^{k}\right)} \tag{27}$$

where,

$$d = \frac{1}{\phi_{p}}\left(\frac{\phi_{p}}{\phi_{r}} - 1\right) \tag{28}$$

$$a = \frac{1}{\phi_{p}} \tag{29}$$

5.5 Cyclic Behavior

The hysteretic behavior for post-peak cyclic loading predicted by Eq. 28 is illustrated in Figure 5-10. The model will initially behave elastically until the cumulative displacement exceeds the displacement at the peak friction angle (δ_p^e), at which point cumulative plastic shear displacements will start to accumulate. Once plastic shear displacements begin to accumulate, the mobilized friction angle (or shear strength) will follow Eq. 28 until unloading begins. Plastic shear displacements begin to accumulate in the reverse direction when the shear stress exceeds the mobilized shear strength from any prior loading cycle. This model will generate shear hysteresis loops similar to the post-peak behavior presented in Figure 5-3 and Figure 5-4. The displacement-softening model assumes elastic behavior for pre-peak loading, so the model does not correctly predict the pre-peak hysteresis loops presented in Figure 5-1.

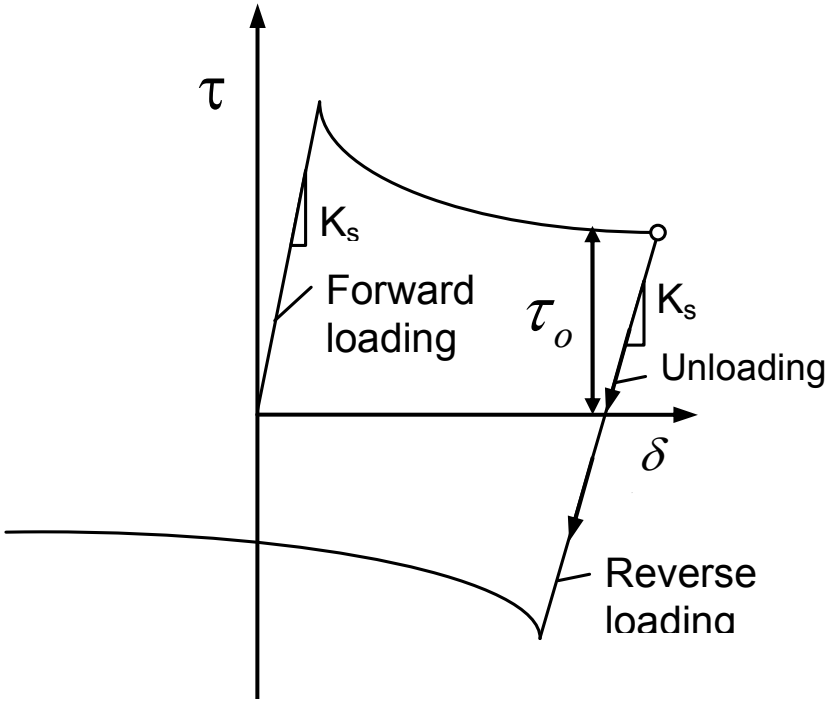

Figure 5-10 Generalized shear stress versus cumulative shear displacement relationship

5.6 Implementation

An elasto-plastic formulation of the new constitutive model was implemented in FLAC 6.0 (Itasca, 2008), a finite difference software package for solving general stress-deformation problems in geotechnical engineering. Elastic behavior was assumed for stress conditions below failure. Elastic behavior is governed by the unload-reload stiffness, K_s. For post-failure stress conditions, the new constitutive model described above was used to model softening and degradation of the in-plane shear strength of an interface element.

A simple numerical model, illustrated in Figure 5-11, was used to test the performance of the new constitutive model. The single element rigid block in Figure 5-11 represents the upper pull out plate and the five element base in Figure 5-11 represents the base of the direct shear device employed by Fox et al. (2006). Values of bulk and shear modulus representative of structural steel were used to model both the rigid block and base. Interface elements were used between the rigid block and the base to represent the GMX/GCL combination. The constitutive model described above was used to model the shear behavior of the interface elements. Table 5-2 presents the parameters used for the constitutive model in the numerical analysis. The interface elements were assigned an elastic shear stiffness equal to $5x10^7$ Pa/m (calculated from the test results shown in Figure 5-4 and Figure 5-5). The code (SSint_eqn_com.fis) was used to amend the friction angle of the interface according to the cumulative relative displacement. A velocity time history was applied to the base of the mesh to model the cyclic test input motion (25 cycles of sinusoidal displacement with f = 1 Hz).

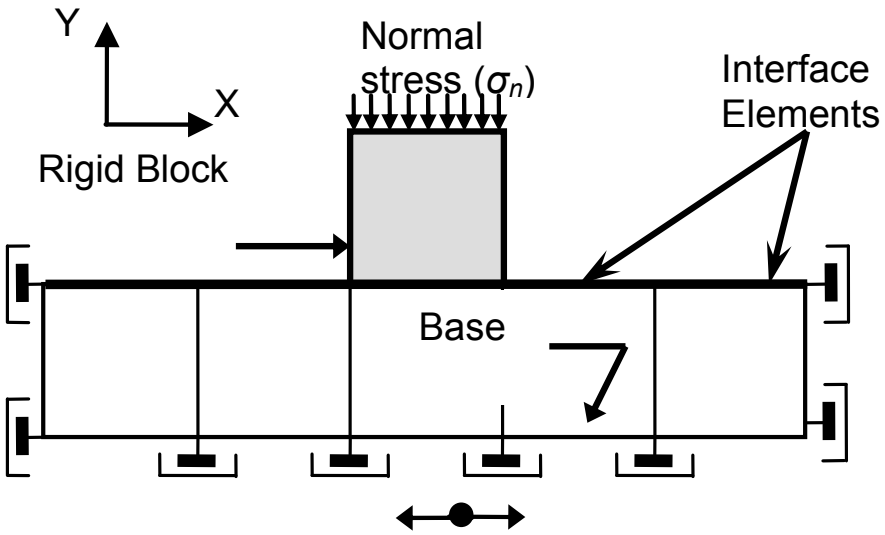

Figure 5-11 Finite difference model (macro elements shown)

Table 5-2 Model parameters values for model verification

Shear strength			Plastic parameters			Elastic parameters
c kPa	ϕ_p degree	ϕ_r degree	δ_p^e mm	δ_r^p m	k	K_s pa/m
26	16.5	1.5	10.6	12.0	0.52	$5x10^7$

The results calculated using the numerical model are compared to the experimental results from Ross (2009) for a normal stress of 2071 kPa and a 120 mm displacement amplitude in Figure 5-12. While there is some discrepancy with respect to the initial stiffness and peak shear strength, the numerical model appears to accurately predict the degradation in shear stress.

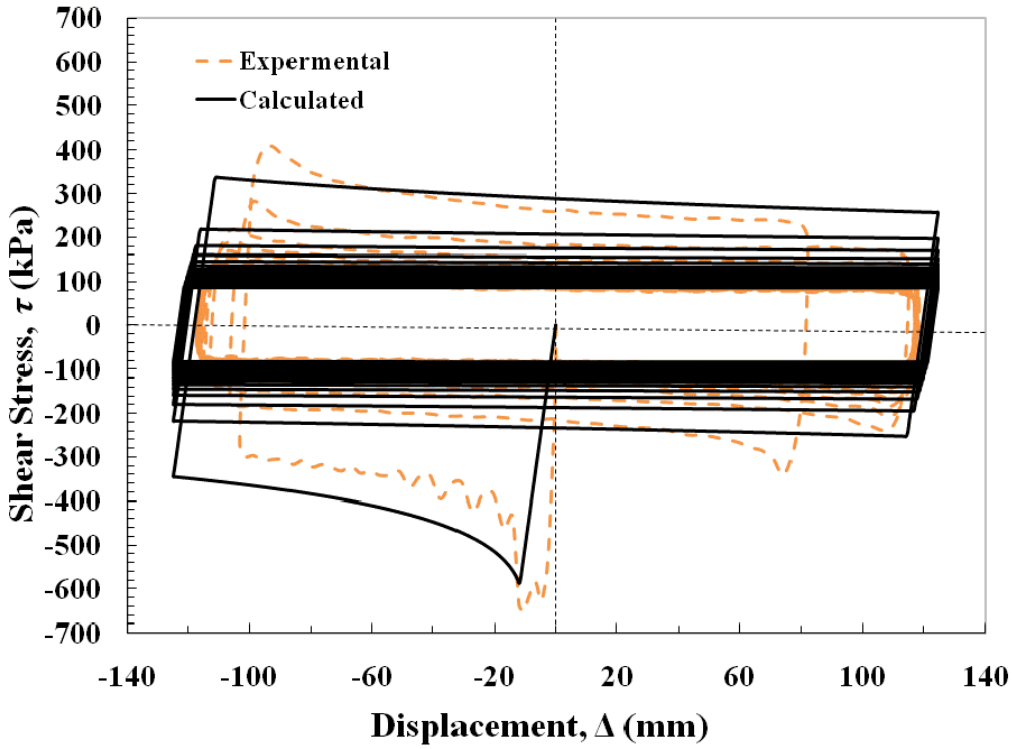

Figure 5-12 Comparison of test data to prediction using new constitutive model for ± 120 mm displacement amplitude at σ_n = 2071 kPa

The numerical and experimental results under the same normal stress as in Figure 5-12 (2071 kPa) but for a 60 mm displacement amplitude (instead of 120 mm) are compared in Figure 5-13. While the numerical model still seems a little off with respect to the initial stiffness, in this case it accurately predicts the peak shear stress upon initial loading and the shear strength at the point of stress reversal. However, the numerical model does not capture the peak in the shear stress at the beginning of every cycle.

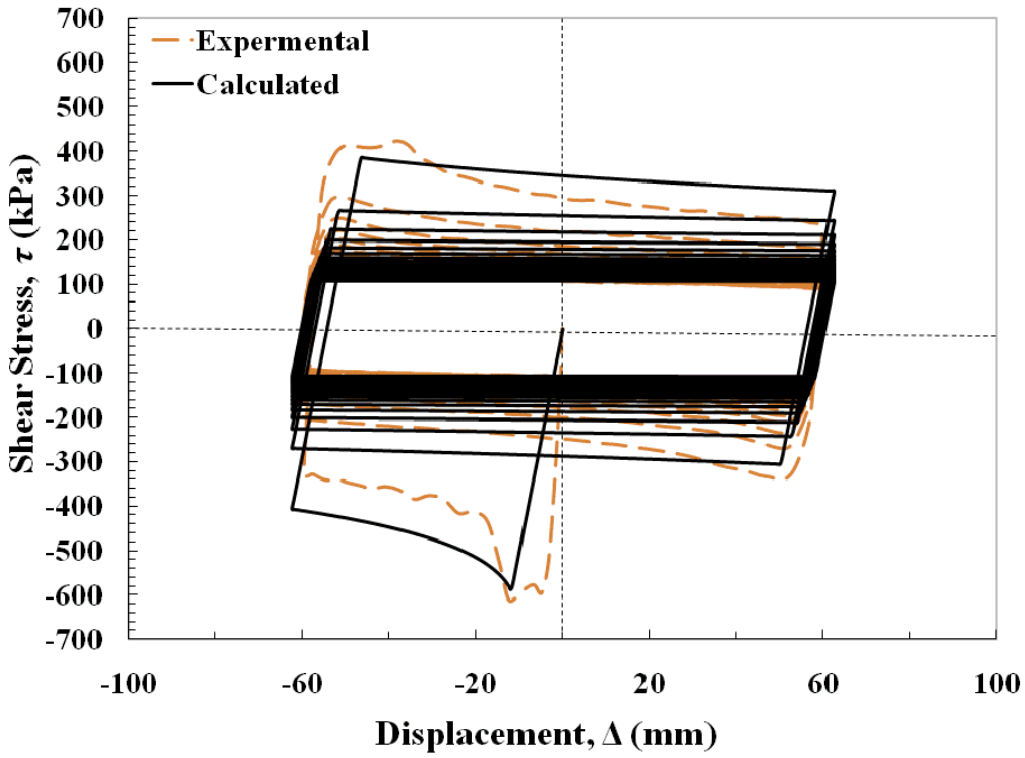

Figure 5-13 Comparison of test data to prediction using new constitutive model for ± 60 mm displacement amplitude at σ_n = 2071 kPa

In Figure 5-14, the shear stress time history calculated using the numerical model is compared to the results for the test with a displacement amplitude of 120 mm at a normal stress of 692 kPa (the test results presented in Figure 5-5). The general trend of the shear stress time history is captured well by the numerical model results presented in Figure 5-14. However, similar to the discrepancy between the numerical model and test results presented in Figure 5-13, the peak at the beginning of every stress cycle was not captured by the numerical model. The shear stress spikes observed in the test data at the begging of every cycle may be related to the internal shear behavior of the GCL, as opposed to the behavior of the GMX/GCL interface.

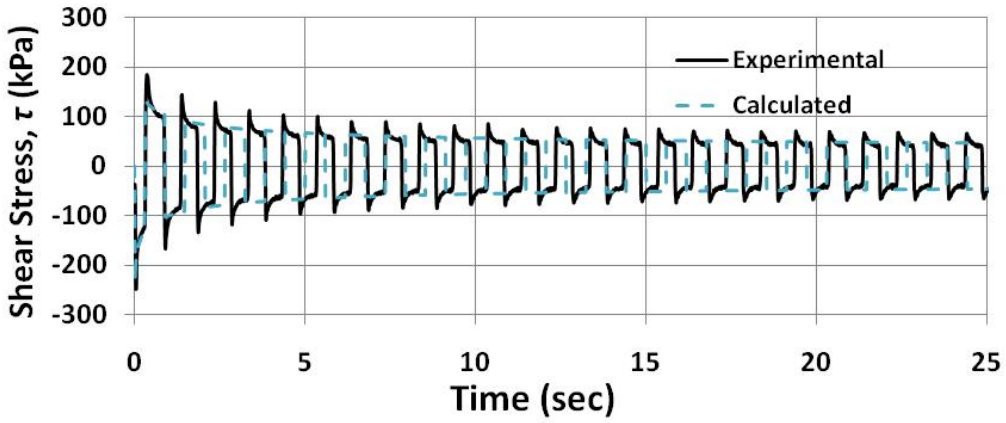

Figure 5-14 Shear stress vs. time calculated for (± 120 mm) displacement amplitudes cyclic shear tests at σ_n = 692 kPa

5.7 Implementation with structural elements

Using beam elements to model geomembrane in FLAC 6.0 was recommended by Itasca (2002). Fowmes (2005) used the same concept to test the effect of the down drag on geomembranes in landfills. In order to use softening interfaces to FLAC 6.0, Fowmes (2005) wrote a code to use softening with interfaces involve structural elements. The code written by Fowmes (2005) was implemented along with the new constitutive model developed in this thesis. The code (SSint_eqn_com_ Beams.fis), provided in Appendix A, was used to amend the friction angle of the interface according to the constitutive model shown earlier in case of beam elements are involved. To test the performance of the code, beam elements were introduced to the model in Figure 5-11. The beam elements as in Figure 5-15 attached to the grid elements through two interfaces, upper and lower. The upper interface was modified according to the code (SSint_eqn_com_ Beams.fis) while the lower interface was glued to the grid.

Similar to the model in Figure 5-11, the upper layer, in Figure 5-15, represents a rigid block and the lower layer represents a base, values of bulk and shear modulus representative of structural steel were used to model both the rigid block and base. Table 5-2 presents the parameters used for the constitutive model in the numerical analysis. The beam elements were assigned elastic stiffness equal to $2x10^8$Pa/m with a thickness of 60mil and a zero moment of inertia to account for the geomembrane flexibility. A velocity time history was applied to the base of the mesh to model the cyclic test input motion (25 cycles of sinusoidal displacement with f = 1 Hz).

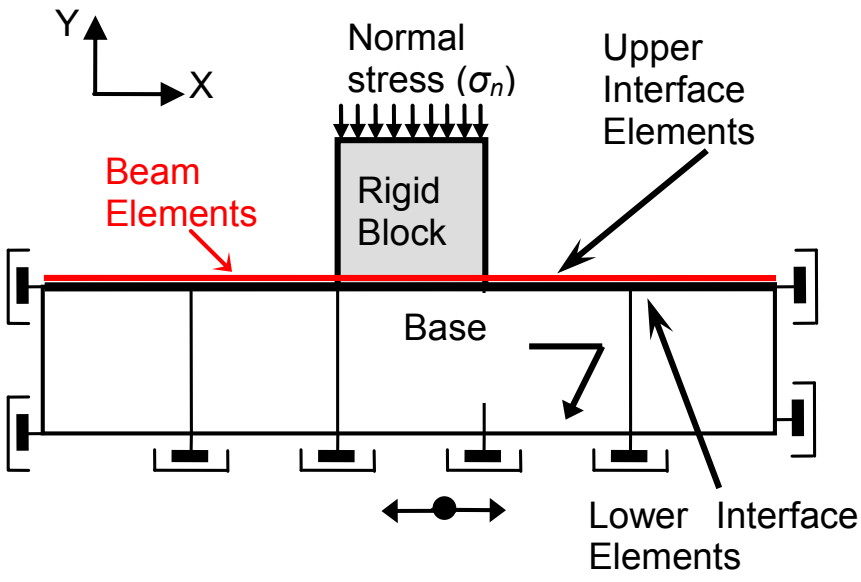

Figure 5-15 Finite difference model (macro elements shown) with beam elements representing geomembrane.

Normal stress in Figure 5-15 was assigned a value of 2071 kPa and 692 kPa for 120 mm displacement amplitudes. Figure 5-16 shows the reduction in the shear stress developed at the interface with time. Unlike the model with no beam elements, the shear stress at the interface after the displacement reversal is higher than the shear stress before reversal. This increase in shear stress may be attributed to the response of the geomembrane and the second interface (lower interface) which simulates the real experiment setup. Figure 5-16 shows that constitutive model accurately predicts the behavior in the cyclic testing of GM/GCL in-plane shear stresses. The discrepancy in Figure 5-16 is attributed to the inaccuracy in the testing as the peak amplitude (120 mm) was not achieved in all the cycles. Figure 5-17 shows a similar comparison for the in plan shear stress versus time in case of 692 kPa.

In conclusion, this model accurately predicts the degradation of the shear strength at the interface with accumulative relative shear displacement for high normal stresses.

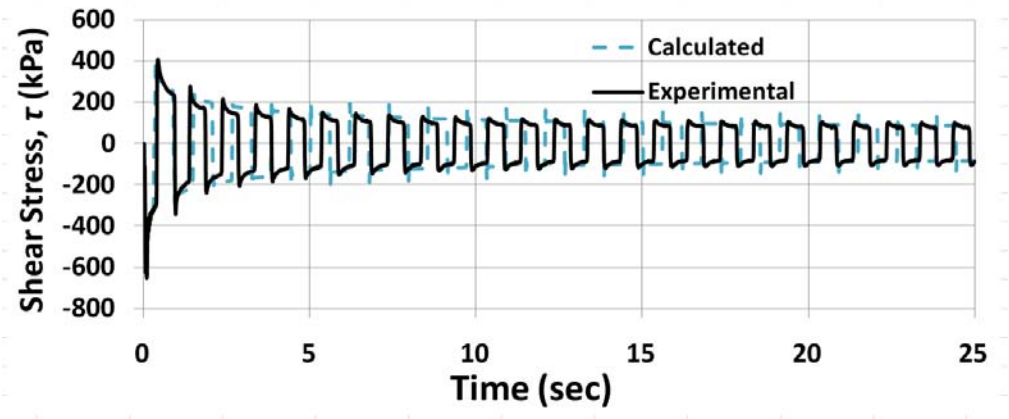

Figure 5-16 Shear stress vs. time calculated for (± 120 mm) displacement amplitudes cyclic shear tests at σ_n = 2071 kPa

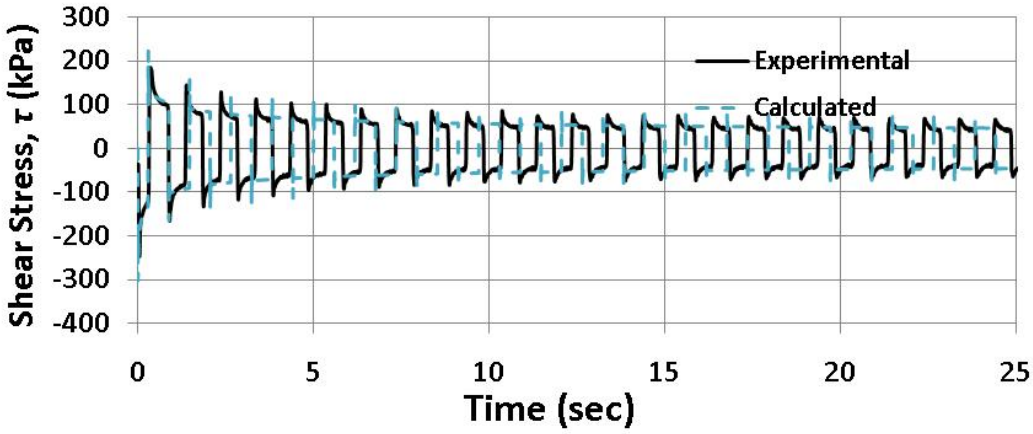

Figure 5-17 Shear stress vs. time calculated for (± 120 mm) displacement amplitudes cyclic shear tests at σ_n = 692 kPa

5.8 Non-uniform Loading

Due to lack of experimental testing of geosynthetic interfaces with Non-uniform (earthquake like input motion), it is not possible to calibrate the model presented herein for non-uniform loading. As an attempt to show the performance of the new constitutive model, in case earthquake loading, the model shown in Figure 5-11was used with an earthquake like input motion instead of sinusoidal wave as in the first case. The El Centro Site Imperial Valley Irrigation District record from the 1940 M 7.1 Elcentro earthquake scaled to 0.8 g was used as input motion at the base of the model. The new constitutive model was used to modify the interface element between the rigid block and the base. The same parameters in Table 5-2 was used for the interface constitutive model. Figure 5-18 shows a comparison between the base acceleration and the rigid block acceleration. The block transmitted acceleration in limited by the friction coefficient of the interface. Figure 5-18 shows a degradation in the block transmitted acceleration with time due to the increase in the cumulative relative displacement.

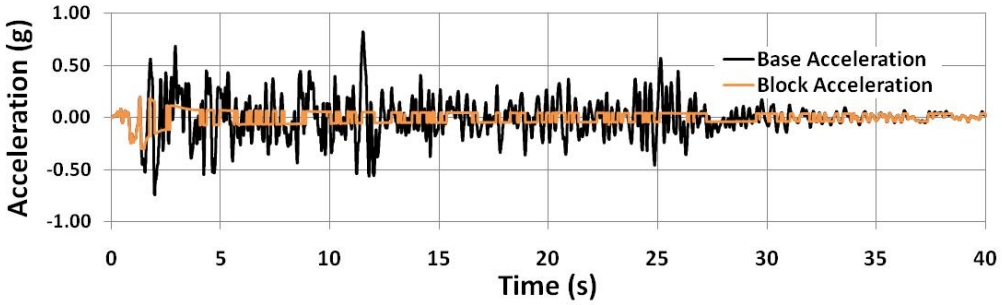

Figure 5-18 Comparison between base input motion and block acceleration in case of using the new constitutive model

For the sack of comparison, the model in Figure 5-11was used with an earthquake like input motion with constant friction angle of 16.5 degrees. Comparison between the

base and the block acceleration in case of constant friction angle with relative displacement is shown in Figure 5-19.

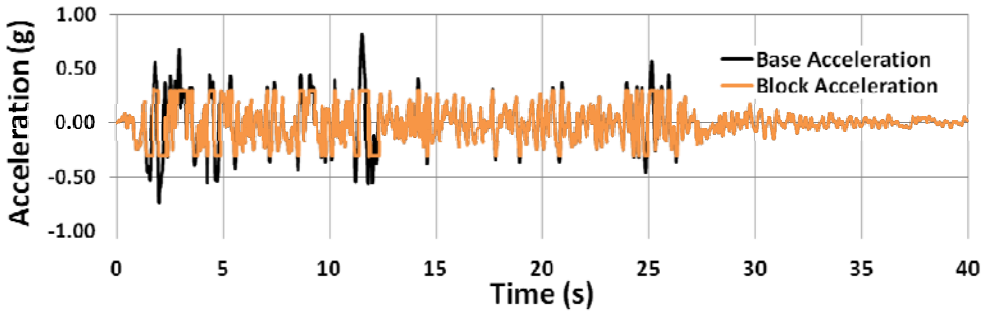

Figure 5-19 Comparison between base input motion and block acceleration in case of constant friction angle.

5.9 Summary

An elasto-plastic constitutive model for the in-plane shear behavior of a GMX/GCL combination has been developed to simulate the degradation in mobilized shear strength accompanying cyclic loading that exceeds the peak shear strength of the material. The model uses the Mohr- Coulomb shear strength criterion for both peak and post-peak shear strength characterization. When implemented in a finite difference computer program, the model is shown to capture the degradation of hysteresis loops (i.e. the degradation in mobilized shear strength) observed in direct shear testing of a GMX/GCL combination. Comparison of numerical and experimental results indicates that the model has some shortcomings with respect to the initial shear stiffness and the shear stress immediately after shear stress reversal. However, capturing the degradation of the mobilized shear strength is considered to be of paramount importance in modeling the behavior of a GMX/GCL combination subject to earthquake loading.

The framework of the model can be expanded to any geosynthetic interface that follows the same trend of strength reduction, i.e. a strength reduction dependent upon the cumulative relative shear displacement during cyclic loading. A shortcoming of the model is that it is based solely upon the results of uniform cyclic loading tests. However, no data was available on the behavior of a GMX/GCL combination subject to non-uniform cyclic loading. Additional experimental data is needed to assess the performance of the model under non-uniform cyclic loading, e.g. under loading conditions representative of seismic loading. Furthermore, additional work is needed to improve model performance during initial loading and immediately following stress reversal.

CHAPTER 6 GCL CONSTITUTIVE MODEL

6.1 Introduction

Geosynthetic Clay liners (GCL) are common elements of liner systems in modern landfills. A GCL is a thin layer of sodium montmorillonite, or bentonite, clay encapsulated between two layers of geosynthetic fabrics. The GCL in-plane shear strength can be very low when the bentonite is hydrated. Nye and Fox (2007) and Sura (2009) conducted laboratory tests on the in-plane shear cyclic behavior of GCLs. These cyclic direct shear tests were conducted using the cyclic direct shear device described by Fox et al. (2006) as part of a joint National Science Foundation funded Arizona State University / University of California at San Diego research program titled GOALI: Collaborative Research: The Integrity of Geosynthetic Elements of Waste Containment Barrier Systems Subject to Large Settlements or Seismic Loading.

The results of the GCL testing conducted by Nye and Fox (2007) were discussed earlier in Chapter 3. Figure 3-42 and Figure 3-43 present examples of the in-plane cyclic behavior of the GCL. The hysteresis loops Figure 3-42 and Figure 3-43 exhibit two main characteristics depending on whether or not the peak in-plane shear strength of the GCL has been exceeded. Pre-peak hysteresis loops have an unusual shape, showing strain hardening behavior at the end of the first and the third quarter cycles of loading. The post peak hysteresis loops exhibit softening behavior, with the mobilized shear strength decreasing with increasing number of cycles of loading. To simulate the observed in-plane cyclic behavior of GCL, a kinematic hardening multi yield surface plasticity model was employed. This chapter describes the development of the model.

Multiple yield surface (MYS) kinematic hardening plasticity model was first developed by Iwan (1967) and Mroz (1967). Prevost (1985) popularized this type of model for use in soil mechanics. MYS constitutive models produce a non-linear backbone curve for the material with hysteresis loops that obeys the Masing (1926) criterion for cyclic loading. The original MYS theory developed by Mroz (1967) can be described as a nonlinear perfectly plastic model that does not handle softening behavior. Salah-Mars (1989) extended the theory to include softening behavior by adding an outermost isotropic yield surface. One of the shortcomings of the MYS models is the difficulty in mapping the stress state at specific time step relative to the multi yield surfaces, Salah-Mars and Kavazanjian (1992) developed the concept of virtual yield surfaces to facilitate this process. A brief description of the Salah-Mars (1989) MYS constitutive model and the implementation of that model in FISH is presented in this chapter.

Salah-Mars (1989) developed his MYS model to simulate the behavior of dry soils without considering pore water pressure generation. The Salah-Mars Constitutive model has two main characteristics that make it suitable to reproduce the GCL hysteresis loops observed in laboratory testing. First, because the model belongs to the multi yield surface family, it provides the flexibility of the multi yield surface to produce a piecewise linear approximation of a backbone curve of any arbitrary shape. Second, the model has the capability to exhibit softening after the material reaches its peak strength. These two characteristics make the model a perfect fit for modeling GCL in-plane cyclic shear behavior. The Salah-Mars (1989) constitutive model was not available in FLAC 6.0, so a FISH subroutine was written to implement the model in FLAC 6.0.

Yan (1998) used the virtual surface concept introduced by Salah-Mars and Kavazanjian (1992) to code a constitutive model in FLAC 6.0 for seismic modeling of bridge abutments. However, Yan (1998) did not include the softening formulation proposed by Salah-Mars and Kavazanjian (1992) in his constitutive model. Yan (1998) coded two separate FISH subroutines for the constitutive model, one to initialize the backbone curve called (Y_INI_F.FIS) and another one for the constitutive model labled (Y_MYS_F.FIS).

Similar to the approach taken by Yan (1998), two subroutines were written to implement Salah-Mars (1989) constitutive model in FLAC 6.0. The Subroutine (M_INI.FIS) is used to initialize the backbone curve parameters, including the softening behavior, and the subroutine (M_MYSS.FIS) is used to implement the Salah-Mars (1989) constitutive model. Both (M_INI.FIS) and (M_MYSS.FIS) are presented in Appendix B along with the flowchart developed by Salah-Mars (1989) for the constitutive model.

6.2 Theoretical Background

The main components of any plasticity-based constitutive model are: (1) the yield condition; (2) the flow rule; and (3) the hardening rule. In the case of a MYS model, a family of nested yield surfaces is employed instead of a single yield surface. The theoretical formulation of a MYS model follows the classical theory of associated plasticity for each yield surface (Morz 1967). An illustration of the MYS approach developed by Morz (1967) is shown in Figure 6-1. Figure 6-1 (a) presents the stress-strain response (i.e. the backbone curve) from a MYS model. The backbone curve in Figure 6-1consises of n linear segments, each segment with a constant elastic tangent modulus E_i and a plastic modulus E_p associated with a corresponding yield surface. The

relationship between E_i and E_p is obtained by assuming that the increment of total strain $d\varepsilon$ can be expressed as the sum of the increment of the elastic strain, $d\varepsilon^e$, and the plastic strain, $d\varepsilon^p$, components:

$$d\varepsilon = d\varepsilon^e + d\varepsilon^p \tag{30}$$

Since by definition:

$$d\varepsilon = \frac{d\sigma}{E}, \qquad d\varepsilon^e = \frac{d\sigma}{E^e} \qquad d\varepsilon^p = \frac{d\sigma}{E^p} \tag{31}$$

Then

$$\frac{1}{E} = \frac{1}{E^e} + \frac{1}{E^p} \tag{32}$$

where, $d\sigma$ is the increment of stress and E^e is the elastic modulus.

A representation of the yield surfaces associated with Figure 6-1 (a) in a three-dimensional principal stress space is shown in Figure 6-1 (b). In a MYS model, these yield surfaces are kinematic surfaces that translate with the stress state once the stress state engages the yield surface. A new yield surface becomes active after being touched by the translating yield surface (or yield surfaces) and then these yield surfaces move together until they touch the next surface in the series (see Figure 6-1). Note that f_0 represents the initial yield surface beyond which plastic strain starts to accumulate. Furthermore, in the Morz-type of model after the last yield surface is engaged (f_n in Figure 6-1) the material behavior in a perfectly plastic manner.

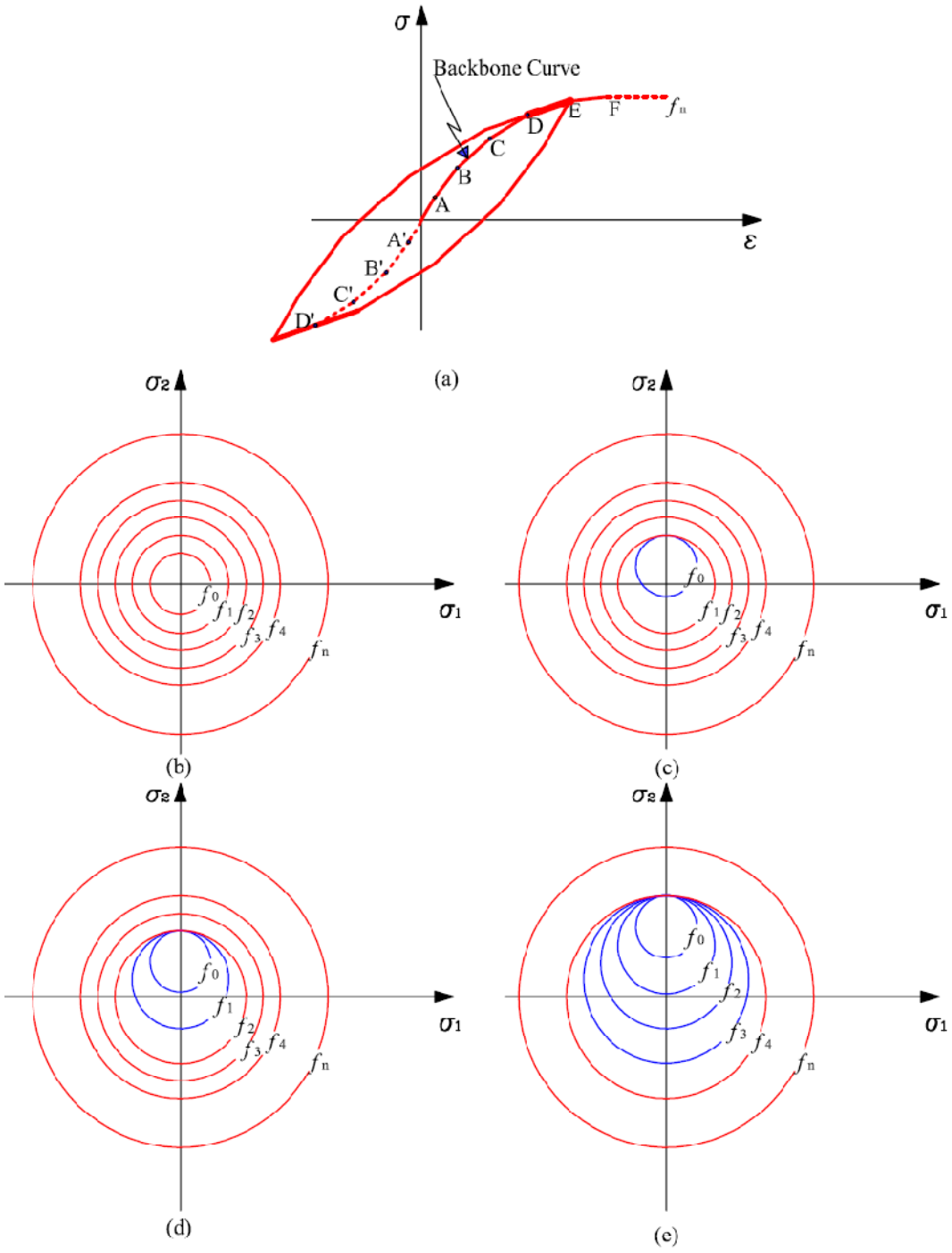

Figure 6-1 MYS model: (a) stress-strain curve; (b) before loading; (c) loading A to B; (d) loading from B to C; (e) loading C to D to E (after Morz 1967)

6.3 Yielding Criterion

A Drucker-Prager yield function was chosen by Salah-Mars (1989) to represent the states of stress at which plastic flow occurs in the MYS model:

$$f = \frac{1}{2}\underline{\xi} \cdot \underline{\xi} - \left[l\left(k + 3\alpha p\right)\right]^2 = 0 \tag{33}$$

where

$\underline{\xi} = \underline{s} - \underline{\alpha} =$ relative stress tensor

$\underline{s} = \underline{\sigma} - \bar{\sigma}\underline{\delta} =$ deviatoric stress tensor

$\underline{\alpha} =$ back stress tensor

$\bar{\sigma} = \frac{1}{3} tr(\underline{\sigma}) =$ mean normal stress

$k =$ *cohesion coefficient*

$\alpha =$ *cone angle*

$p = -\bar{\sigma} =$ *mean pressure*

$l =$ *yield surface size coefficient*

As shown in Figure 6-2, the Dracker Prager criterion can be represented as a straight line on a J_1 versus $\sqrt{J_{2D}}$ plot, where, J_1 is the first invariant of the stress tensor and J_{2D} is the second invariant of the deviatoric stress tensor.

The relative stress function in this formulation measures the position of the stress tensor as illustrated in Figure 6-2 with respect to the yield surface, with the back stress tensor $\underline{\alpha}$ defining the coordinates of the center of the yield surface in deviatoric stress subspace. The initial position of a yield surface given by the tensor $\underline{\alpha}$ reflects the material's memory of its fabric or past loading history. A particular stress point corresponding to the current stress state has to lie inside or on the active yield surface but cannot be outside the active yield surface: this condition is known as the consistency condition.

According to the Drucker-Prager yield criterion, the radius of the yield surface (R) can be presented as:

$$R = \|\underline{s} - \underline{\alpha}\| = \sqrt{2}(k + 3\alpha p)l \tag{34}$$

Siriwardane and Desai (1983) showed that α and k could be expressed in terms of Mohr-Column criteria parameters c and ϕ as follows:

For triaxial compression:

$$\alpha = \frac{2\sin\phi}{\sqrt{3}(3 - \sin\phi)} \tag{35}$$

$$k = \frac{6c\cos\phi}{\sqrt{3}(3 - \sin\phi)} \tag{36}$$

For plane strain:

$$\alpha = \frac{\tan\phi}{\left(9 + 12\tan\phi^2\right)^{1/2}} \tag{37}$$

$$k = \frac{3c}{\left(9 + 12\tan\phi^2\right)^{1/2}} \tag{38}$$

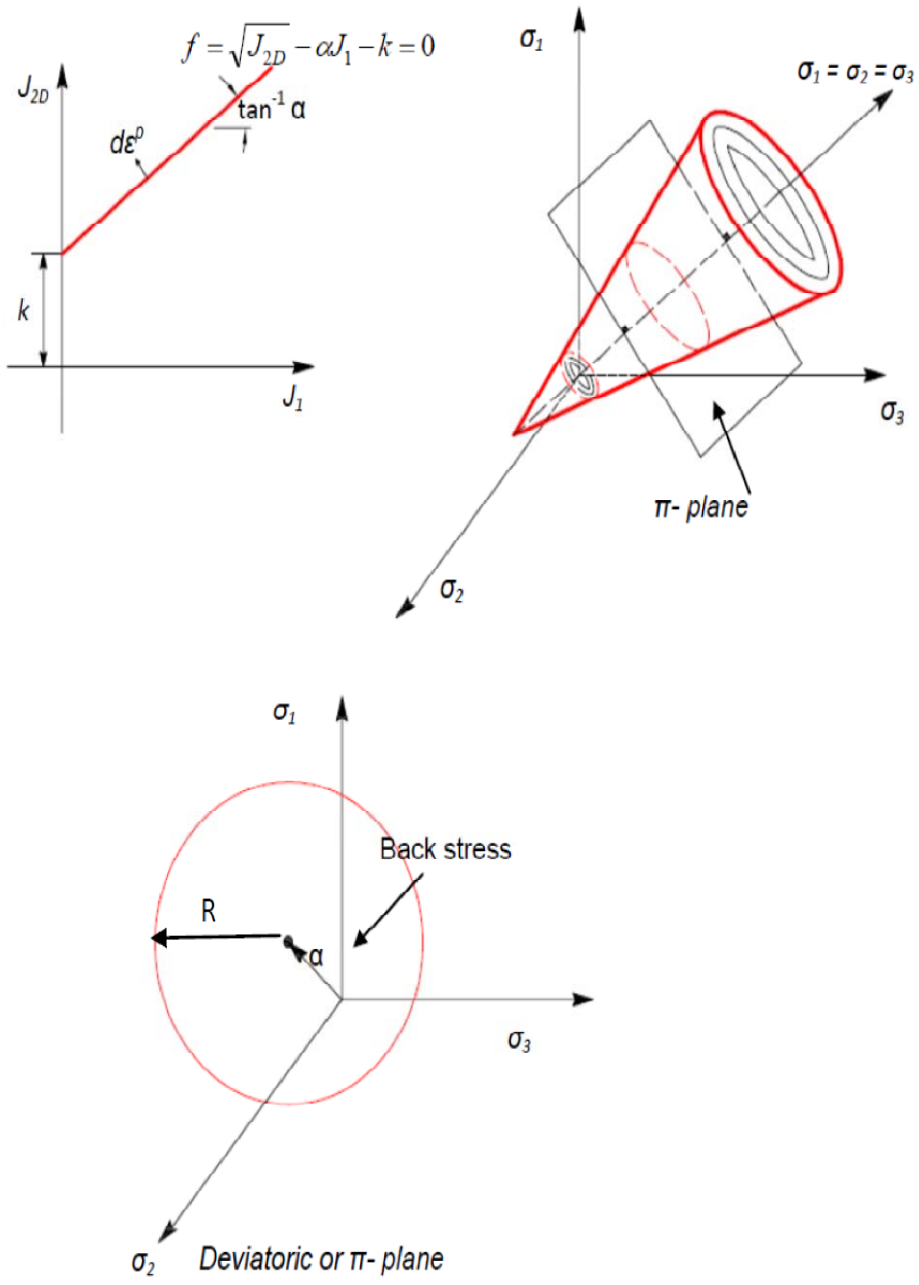

Figure 6-2 Drucker and Prager Failure criterion (after Salah-Mars 1989; Yan 1998)

6.4 Flow Rule

The flow rule defines the behavior of the material after it reaches the yield surface. In the MYS formulation, after the stress state reaches the first yield surface, the soil undergoes plastic strains: this process is called plastic flow. The flow rule determines the direction of the plastic strain vector by assuming the normality of the incremental strain vector to the plastic potential function. In associated plasticity, the plastic potential function is also the yield surface.

The increment of the elastic strain during plastic flow is expressed as:

$$d\varepsilon_{ij}^{p} = \lambda \frac{\partial Q}{\partial \sigma_{ij}} \tag{39}$$

where Q is the plastic potential function and λ is a positive scalar factor. In matrix form the plastic strain increment can be expressed as follows:

$$\dot{\underline{\varepsilon}}^{p} = \Lambda \underline{N} \tag{40}$$

where $\underline{N}$ is the outward normal to the potential surface and Λ is the hardening parameter.

An associated flow rule was chosen in the MYS formulation presented herein. Thus the plastic potential surface coincides with the yield surface. Based on this assumption, Yan (1998) came up with the following expression for the normal tensor:

$$\underline{N} \cdot \dot{\underline{\alpha}} = \sqrt{1 + 6\alpha^{2} l^{2}}\, H' \Lambda \tag{41}$$

6.5 Hardening Criterion

The hardening rule specifies the shape of the stress strain curve after yield has been triggered. Two types of hardening rule are usually used in plasticity theory: an isotropic hardening rule, where the yield surface expands (or shrinks in the case of softening) after the soil undergoes yield deformation, as illustrated in Figure 6-3 (a); and a kinematic hardening rule where, the yield surface moves with the stress state after reaching the state of yielding, as illustrated in Figure 6-3 (b). In the MYS constitutive model developed herein, all the yield surfaces can move except the last yield surface.

In kinematic hardening plasticity, the yield surfaces translate in the stress space without changing form and they continuously touch and push each other. Yield surfaces in kinematic hardening can be tangent to each other but cannot intersect (Yan 1998). In the Salah-Mars (1989) formulation, both types of hardening rules were used. The inner yield surfaces are kinematic yield surfaces that translate without changing its shape until outmost isotropic the softening yield surface is activated. The isotropic softening yield surface then shrinks to accommodate softening until it encounter a final fixed perfectly plastic yield surface (representing the residual, or large displacement shear strength). A description of the softening yield surface is shown in next section.

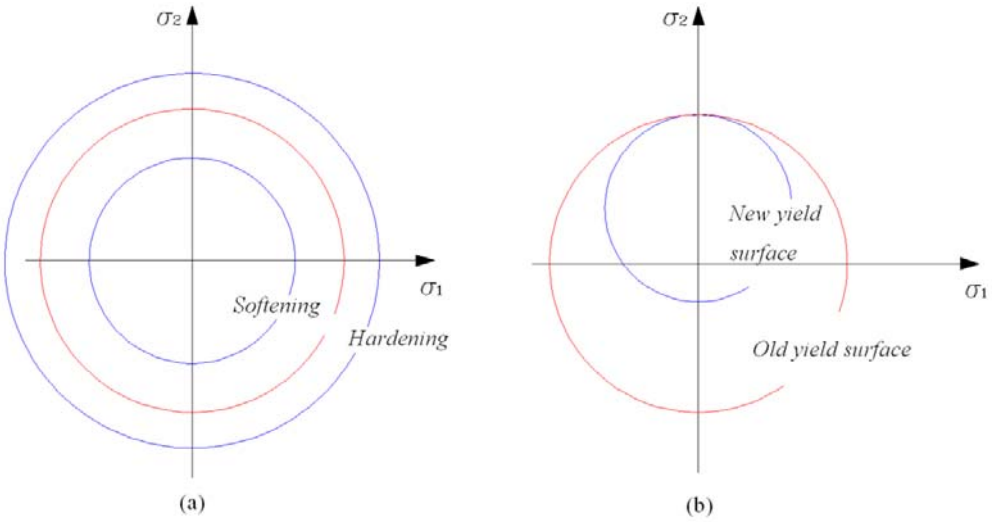

Figure 6-3 Hardening criteria (a) isotropic hardening rule, (b) kinematic hardening rule

Based upon Prager's hardening rule, which assumes that the change in the rate of the back stress is linearly proportional to the rate of the plastic strain tensor, Yan (1998) found that the back stress evolution of the outer most yield surface follows the expression:

$$\underline{\dot{\alpha}_{nys}} = \sqrt{1+6\alpha^2 l_{nys}^2}\, H'_{nys}\, \Lambda_{nys}\, \underline{N}_{nys} \tag{42}$$

For all inner yield surfaces except nys-1 (the softening yield surface), the yield surfaces translates along the direction of tensor $\underline{\mu}_i$. Therefore:

$$\underline{\dot{\alpha}_i} = M_i \underline{\mu}_i, \qquad i \le nys-2 \tag{43}$$

where $\underline{\dot{\alpha}_i}$ is the change rate of the back stress tensor for the active yield surface and M_i is a scalar parameter that scales the rate of change along $\underline{\mu}_i$. Morz (1967) proposed an

evolution scheme that follows direction tensor $\underline{\mu}_i$ as illustrated in Figure 6-4. According to Morz's definition $\underline{\mu}_i$ takes the form of the following expression:

$$\underline{\mu}_i = \left(\underline{\alpha}_{i+1} - \underline{\alpha}_i\right) + \left(\underline{R}_{i+1} - \underline{R}_i\right)\underline{N}_m \tag{44}$$

Morz (1967) derived the expression for M_i based on the flow rule and consistency condition as:

$$M_i = \frac{\sqrt{1 + 6\alpha^2 l_i^2}\, H'_i \Lambda_i}{\underline{N}_i \cdot \underline{\mu}_i} \tag{45}$$

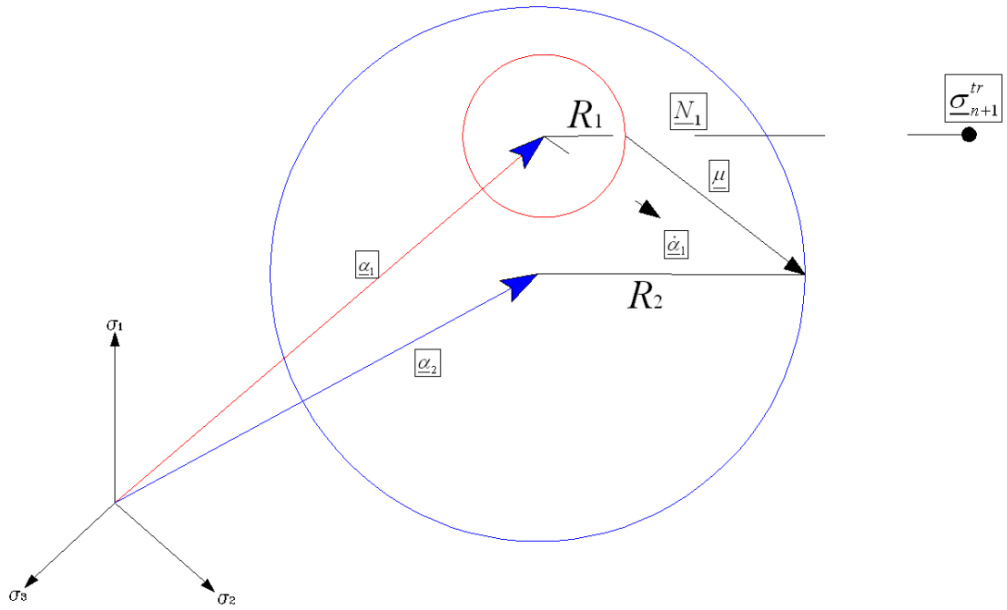

Figure 6-4 Evolution to the inner back stress according to (Morz 1967)

In order to determine the tangent modulus of the yield surfaces on stress strain curve, Salah-Mars (1989) introduced the concept of plastic modulus H'. Figure 6-5 shows a representation of uniaxial compression stress loading: the slope of the elastic part

of the stress-strain curve is equal to initial elastic Young's modulus, E, and the slope of the second linear segment of the stress-strain curve is the tangent modulus E^t. The plastic modulus H' corresponding to the second segment of the stress-strain curve can be defined as follows:

$$H' = \frac{E^t}{1 - \frac{E}{E^t}} \tag{46}$$

The sign of the plastic modulus will determine the state of the hardening process: if H' > 0 the model undergoes strain hardening; if H' = 0.0 then the model undergoes perfect plasticity; and if H' < 0.0 then the model undergoes strain softening.

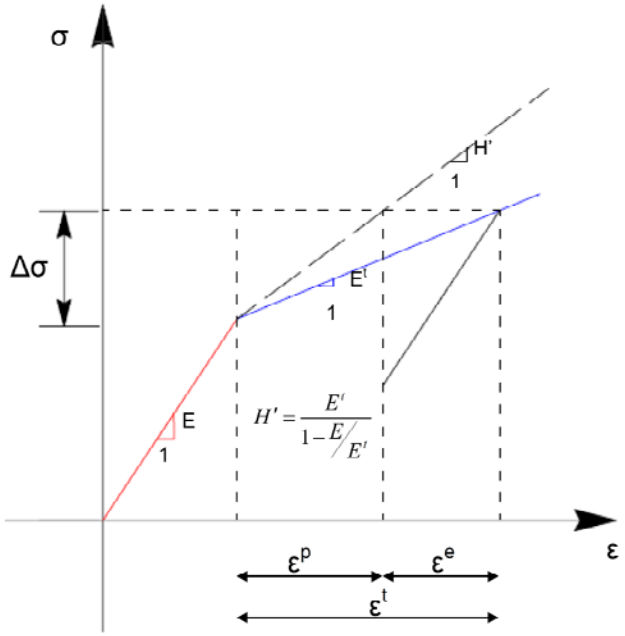

Figure 6-5 1-D definition of the plastic modulus H'

6.6 Softening Criteria

Salah-Mars and Kavazanjian (1992) characterized the last two yield surfaces in their MYS surface as an isotropic softening yield surface and a perfectly plastic yield surface to characterize the softening and subsequent perfect plasticity behavior of a geomaterial in a numerically stable manner. The next to last softening yield surface shrinks isotropically as the material softens until it collapses into the last perfectly plastic yield surface. The last yield surface represents the residual shear strength (perfect plasticity plateau) and therefore is motionless. The isotropically softening yield surface is allowed to change its radius without changing its center. This leads to the following evolution equation for the radius of the softening yield surface:

$$\dot{R} = \frac{2}{3} H' \Lambda \tag{47}$$

and

$$\Lambda = \frac{1}{2\mu} \frac{1}{\left(1 + \frac{H'}{3\mu}\right)} \underline{N} \cdot \underline{\dot{\sigma}}^{tr} \tag{48}$$

If the value of H' is negative, the above equations produce an isotropic shrinking of the corresponding yield surface. In Figure 6-6 yield surface number 5 is used to represent the isotropic softening yield surface, while yield surface number 6 which is motionless with constant radius, represents the perfect plasticity yield surface. When the isotropic yield surface is active the evolution of its radius follows the following equation according to Salah-Mars and Kavazanjian (1992):

$$R_m = R_m + \frac{2}{3} H'_m \Lambda_m \tag{49}$$

One important condition in the Salah-Mars and Kavazanjian (1992) formulation is that as the radius R_m shrinks, it may become smaller than some of the inner yield surface radii. When this occurs, the yield surfaces that have been crossed by the isotropic yield surface are deactivated and collapse to the isotropic yield surface. Also, the radius R_m cannot be smaller that of the first yield surface.

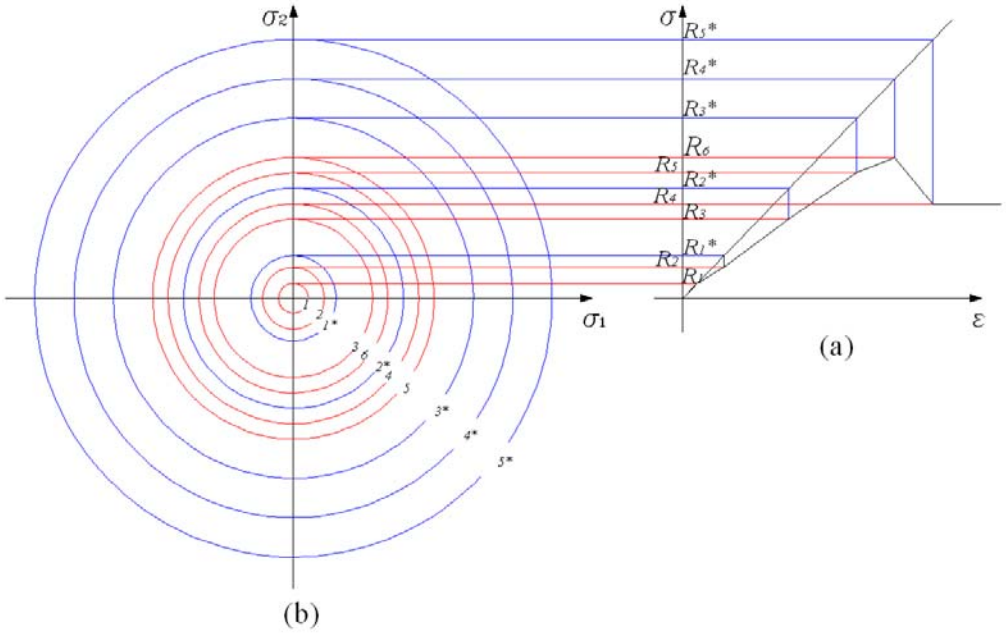

Figure 6-6 Schematic representation of the multi yield surface constitutive model proposed by Salah-Mars and Kavazanjian (1992) (a) Stress strain relationship represented by 6 yield surfaces, (b) Yield surfaces and corresponding virtual surface in π plane (After Salah-Mars 1989)

6.7 GCL Model Parameters

In the previous sections, a multi yield surface kinematic hardening isotropic softening constitutive model following the proposed formulation by Salah-Mars and Kavazanjian (1992) was developed. There are four types of parameters involved in this MYS model: (1) parameters describing the elastic behavior of the material; (2) parameters describes the plastic behavior of the material; (3) parameters related to the evolution of the model constants with the changes in confining pressure; and (4) parameters related to the softening behavior of the model.

6.7.1 **Elastic parameters**

Only two parameters are needed to describe the elastic behavior of the model, as the material is assumed to be isotropic material. These parameters can be the shear modulus, G, and the bulk modulus, B, or Young's modulus, E, and Poisson ratio, υ.

6.7.2 **Backbone curve**

Soil nonlinearity is represented by a nonlinear stress-strain backbone curve. In the MYS model, this nonlinearity is modeled by a piecewise linear approximation modulus as shown in Figure 6-7. Each segment of this piecewise linear approximation represents a yield surface f_i, which is characterized by an elastoplastic modulus H_i and size l_i where i 1, 2, ..., *nys*. where *nys* is the total number of yield surfaces. The maximum number of yield surfaces can be used with the code presented herein is 10. It is worth to note here that an increase of the number of surfaces may lead to more accuracy but will also lead to an increase in computing time.

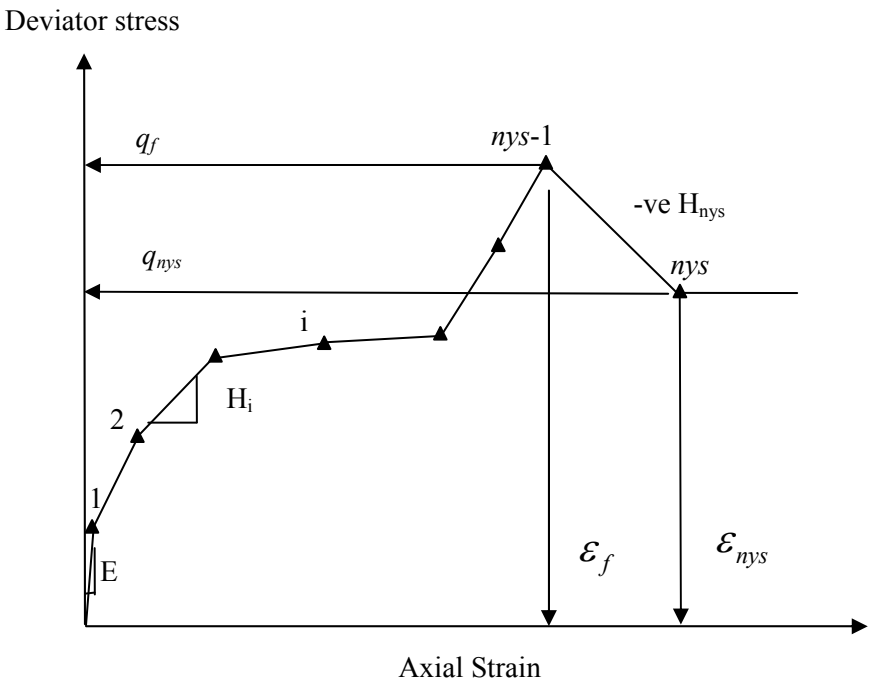

Figure 6-7 A stress-Strain Backbone Curve

To define the parameters for the MYS model for GCLs, discrete stress strain laboratory values were used. The required parameters were derived from the cyclic simple shear testing on GCLs by Sura (2009) described previously in chapter 3.

The maximum deviator stress q_f can be evaluated according to Dracker-Prager criterion as:

$$q_f = \frac{2c\cos\phi + 2p_r \sin\phi}{1 - \sin\phi} \tag{50}$$

where c is cohesion, ϕ is the friction angle and p_r is the reference normal pressure.

Knowing the q_i at a specific strain level, the corresponding yield surface size coefficient l_i is given by :

$$l_i = \frac{q_i}{q_f} \tag{51}$$

The radius of the yield surface *i* for the mean pressure p is given by:

$$R_i = \sqrt{2}(k + 3\alpha p) l_i \tag{52}$$

The elastoplastic modulus H_i can be evaluated as:

$$H_i = \frac{q_{i+1} - q_i}{\varepsilon_{i+1} - \varepsilon_i} \tag{53}$$

Note that H_{nys} is equal to zero (perfectly plastic yield) and H_{nys-1} is a negative value (representing softening behavior).

6.7.3 **Confining pressure parameters**

The moduli required for the model vary depending on the mean normal pressure. Duncan et al. (1980) assumed variation of modlui with mean pressure as follows:

$$E = E_r \left(\frac{p}{p_r} \right)^{n_e} \tag{54}$$

$$B = B_r \left(\frac{p}{p_r} \right)^{n_b} \tag{55}$$

$$H = H_r \left(\frac{p}{p_r} \right)^{n_h} \tag{56}$$

Where E_r, B_r and H_r are the young's, bulk and bulk moduli measured at the mean normal confining pressure p_r; n_e, n_b and n_h are the modulus exponents defined from the

laboratory tests. Due to the lack of comprehensive database for the GCL behavior a values used herein for these factors are typical values for clay material.

6.7.4 **Softening parameters**

The softening of the model is fully described by the deviator stress for the yield surface *nys* (q_{nsf}) and the strain associated with yield surface *nys*, ε_{nys}. These values can be related to the stress and strain values at the peak stress as follows:

$$rf_s = \frac{q_{nys}}{q_f} \tag{57}$$

$$ss = \frac{\varepsilon_{nys}}{\varepsilon_f} \tag{58}$$

where rf_s is the reduction in deviator stress due to the softening, and ss is the ratio of the strain associated with the yield surface *nys*, ε_{nys}, to the strain at the peak stress, ε_f.

6.8 Virtual Surface Concept

The virtual surface concept proposed by Salah-Mars and Kavazanjian (1992) was used to overcome the ambiguity in mapping the stress location in MYS model. Using this concept, only one-step is needed to evaluating the final update stress for each load increment in the numerical solution.

The virtual surface concept may be described as follows and as illustrated in Figure 6-8. Consider an initial stress that lies on the first yield surface (elastic). Next, assume an elastic trial deviator stress that moves the stress to point V. Point V is past the first yield

surface, so a radial return from point V produces a stress located on the yield surface. The change in the stress from point 1 to 2 (the stress increment) is equivalent to the back stress increase by the amount equal to:

$$\Delta\underline{\alpha} = \sqrt{1+6\alpha^2 l_1^2}\, H_1' \Lambda_1 \underline{N}_1 = (R_2 - R_1)\underline{N}_1 \tag{59}$$

where R_1 and R_2 are the radii of the inner and the outer yield surfaces respectively and $\underline{N}_1$ is the unit outward normal tensor of the potential surface associated with the inner yield surface. The hypothetical yield surface passing through point V is the virtual surface. The trial stress reduced by the amount equal to:

$$\Delta\sigma = 2G\Lambda_1 \underline{N}_1 = (R_1^* - R_2)\underline{N}_1 \tag{60}$$

The radius of the virtual surface can be formulated as:

$$R_1^* = R_1 + (R_2 - R_1)\left(1 + \frac{2G}{h_1'}\right) \tag{61}$$

$$R_i^* = R_{i-1} + (R_{i+1} - R_i)\left(1 + \frac{2G}{h_i'}\right), \quad 2 \le i \le nys - 2 \tag{62}$$

$$h_i' = H_i' \sqrt{1+6\alpha^2 l_i^i}\ , \ 1 \le i \le nys - 2 \tag{63}$$

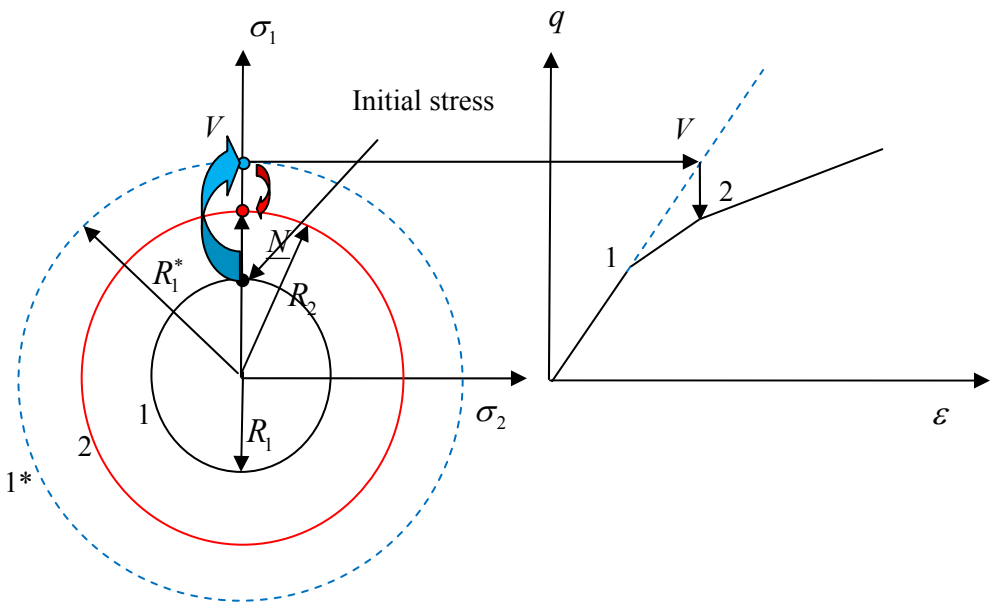

Figure 6-8 Virtual surface concept

6.9 Constitutive Model Algorithm

A FISH subroutine developed to implement the MYS model in FLAC 6.0. The code developed was adapted from the flow chart developed by Salah-Mars (1989). In the FLAC 6.0 finite difference formulation, the incremental strain is known for every specific time step. There, the fish subroutine will provide the final value of the stress state $\underline{\sigma}_{n+1}$ and the new position of the yield surface and the virtual surface as well. The algorithm developed by Salah-Mars (1989) requires four stages to reach the final update for the stress in each load step.

The first step in the algorithm is to estimate the trial stress using an elastic formulation as follows:

$$\underline{\sigma}_{n+1}^{tr} = \underline{\sigma}_n + \underline{C}^e . \Delta\underline{\varepsilon} \tag{64}$$

where $\underline{\sigma}_{n+1}^{tr}$ is the trial stress state, $\underline{\sigma}_n$ is the initial stress state before calling the subroutine, $\underline{C}^e$ is the elastic stiffness matrix, and $\Delta\underline{\varepsilon}$ is the strain increment. As described in the example, the inner yield surface is active which makes the virtual surface active as well. Both surfaces start moving with the stress increment, but the virtual stress moves in the opposite direction as the inner yield surface. As result of this movement, the stress state evolves until both yield surfaces touch the outer yield surface at the same contact point. The evolution of the back stress of the virtual surface was described by Salah-Mars (1989) as follows:

$$\Delta\underline{\alpha}_1^* = -\frac{2G}{h_i'}\Delta\underline{\alpha}_1 \tag{65}$$

If the initial trial stress lies outside the virtual surface, then Salah-Mars and Kavazanjian (1992) proposed a second correction called the intermediate update to account for a possible gap between the inner and the outer yield surfaces. The inner yield surface is adjusted as follows:

$$\Delta\underline{\alpha}_1 = (\underline{\alpha}_2 - \underline{\alpha}_1) + (R_2 - R_1)\underline{N}_1 \tag{66}$$

The corresponding trial deviatoric stress correction for the intermediate update as obtained as:

$$\underline{s}_{n+1}^{tr} = \underline{s}_{n+1}^{tr} - \frac{2G}{H_1'}(\Delta\underline{\alpha}_1 \cdot \underline{N}_2)\underline{N}_2 \tag{67}$$

where $\underline{N}_2$ is the unit normal tensor associated with the active outer yield surface.

Finally, the final stress update is performed with the evolution of the outer yield surface determined as:

$$\underline{\alpha}_2^{n+1} = \underline{\alpha}_2^{n} + H_2' \sqrt{1 + 6\alpha^2 l_2^2}\, \Lambda_2 \underline{N}_2 \tag{68}$$

$$\underline{s}_{n+1} = \underline{\alpha}_2^{n+1} + R_2 \underline{N}_2 \tag{69}$$

$$\Lambda_2 = \left(\frac{1}{H_2' \sqrt{1 + 6\alpha^2 l_2^2} + 2G} \right) \left(\left\| \underline{\zeta}_{n+1,1}^{tr} \right\| - R_2 \right) \tag{70}$$

During the final update, the inner yield surfaces are in active although they translate with both the outer yield surface and the virtual surfaces. The position of the inner yield surface at the end of the timestep is as follows:

$$\underline{\alpha}_1^{n+1} = \underline{\alpha}_2^{n+1} + (R_2 - R_1) \underline{N}_2 \tag{71}$$

The position of the virtual surface at the end of the time step will be

$$\underline{\alpha}_1^{*n+1} = \underline{\alpha}_2^{n+1} + (R_2^* - R_1) \underline{N}_2 \tag{72}$$

In a case in which one of the yield surfaces m is active (the initial stress point is not in the linear elastic zone), the stress update is a combination of the intermediate update of the yield surfaces *1* to *m-1* and the final update for the evolution of the active yield surface m. During the intermediate update, the stress tensor is corrected according to:

$$\underline{s}_{n+1,1}^{tr} = \underline{s}_{n+1,0}^{n+1} - \sum_{i=1}^{m-1} \frac{2G}{h_i'} (\Delta \underline{\alpha}_i . \underline{N}_{m,0}) \underline{N}_{m,0} \tag{73}$$

where $\underline{s}_{n+1,0}^{n+1}$ is the initial trial deviatoric stress at time t_{n+1}, $\underline{s}_{n+1,1}^{tr}$ is the intermediate trial deviatoric stress the same step, and $\underline{N}_{m,0}$ is the unit normal tensor associated with the active yield surface m during the intermediate update $\underline{N}_{m,0}$ is evaluated as:

$$\underline{N}_{m,0} = \frac{\underline{\zeta}_{m,0}^{tr}}{\left\| \underline{\zeta}_{m,0}^{tr} \right\|} \tag{74}$$

$$\underline{\zeta}_{m,0}^{tr} = \underline{s}_{n+1,0}^{n+1} - \underline{\alpha}_{m}^{n} \tag{75}$$

The values of the inner back stress evolution are known to be equal to:

$$\Delta\underline{\alpha}_{i} = (\underline{\alpha}_{i+1} - \underline{\alpha}_{i1}) + (R_{i+1} - R_{i})\underline{N}_{i} \tag{76}$$

During the final update, the evolution of the active yield surface back stress is obtained from:

$$\underline{\alpha}_{m}^{n+1} = \underline{\alpha}_{m}^{n} + M_{m}\underline{\mu}_{m} \tag{77}$$

where M_m is equal to

$$M_{m} = \frac{h'_{m}\Lambda_{m}}{\underline{N}_{m} \cdot \underline{\mu}_{m}} \tag{78}$$

$$\Lambda_{m} = \frac{1}{h'_{m} + 2G}\left(\left\| \underline{\zeta}_{m,1}^{tr} \right\| - R_{m} \right) \tag{79}$$

$$\underline{\zeta}_{m,1}^{tr} = \underline{s}_{n+1,1}^{tr} - \underline{\alpha}_{m}^{n} \tag{80}$$

$$R_m = \sqrt{2} l_m \left(k - \alpha \, tr\left(\underline{\sigma}_{n+1}^{tr} \right) \right) \tag{81}$$

The final stress update is obtained as:

$$\underline{s}_{n,1}^{tr} = \underline{\alpha}_m^{n+1} + R_m \underline{N}_{m,F} \tag{82}$$

where $\underline{N}_{m,F}$ is the unit normal associated with the yield surface m in its new position. The virtual surfaces $j \geq m$ are also updated to the account for the effect of the evolution of all yield surfaces equal or less than active yield surface in the following manner:

$$\underline{\alpha}_j^{*n+1} = \underline{\alpha}_j^{*n} - \sum_{i=1}^{m-1} \frac{2G}{h_i'} \Delta \underline{\alpha}_i \,, \quad j = m, ..., nys - 2 \tag{83}$$

At this point, the active yield surface and the trial stress have been updated to their final state. All yield surfaces interior to the active one along with their corresponding virtual surfaces are tangent to each other along with the active surface m at the final stress point as described by the following equations:

$$\underline{\alpha}_i^{n+1} = \underline{\alpha}_m^{n+1} + (R_m - R_i) \underline{N}_{m,F} \tag{84}$$

$$\underline{\alpha}_i^{*n+1} = \underline{\alpha}_m^{n+1} + (R_i^* - R_m) \underline{N}_{m,F} \,, \qquad 1 \leq i \leq m - 2 \tag{85}$$

6.10 Model performance

To test the general performance of the FISH subroutine for the MYS model, analyses were performed to simulate the cyclic simple shear tests conducted by Sura (2009) on GCLs. Sura (2009) conducted a series of simple shear cyclic tests on GCL specimens at four different normal stresses (114, 348, 692 and 1382 kPa) and at five different displacement levels (±2, 5, 10, 15, 25 mm maximum amplitude). Shear stress versus displacement curves developed by Sura (2009) for GCLs are presented in Figure 6-9 to Figure 6-15.

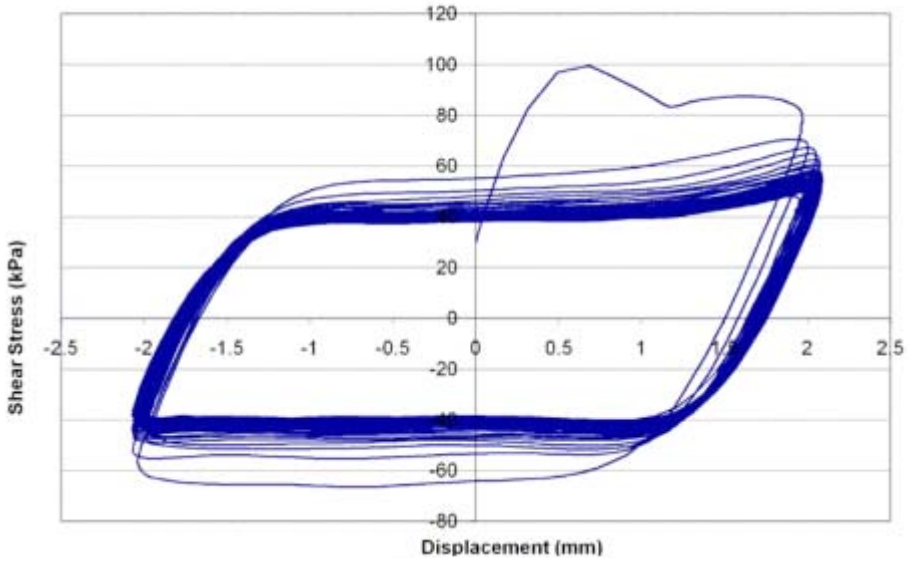

Figure 6-9 Cyclic shear test, Δ_a = 2 mm, σ_n = 348 kPa (Sura 2009)

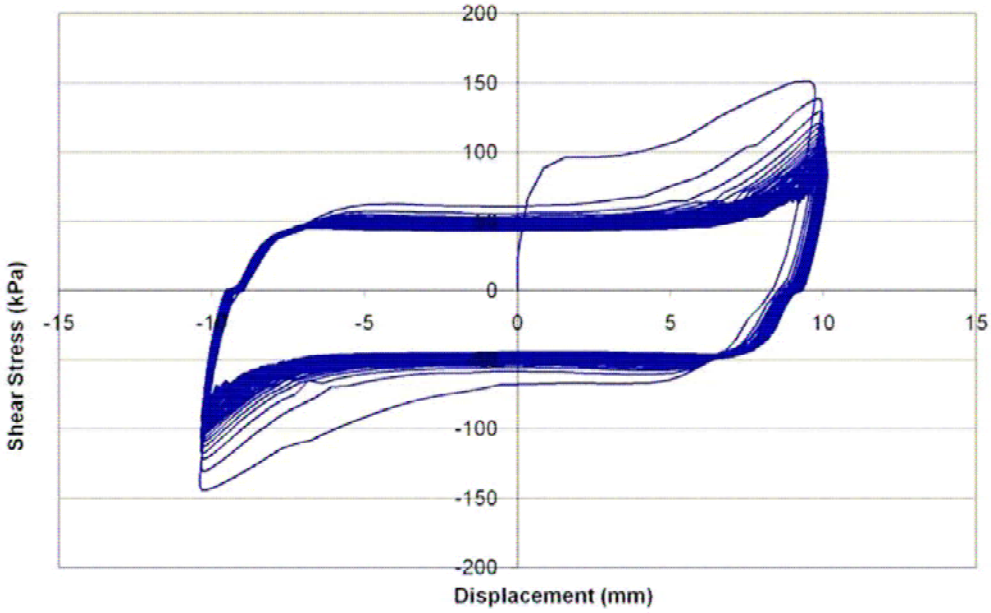

Figure 6-10 Cyclic shear test, Δ_a = 10 mm, σ_n = 348 kPa (Sura 2009)

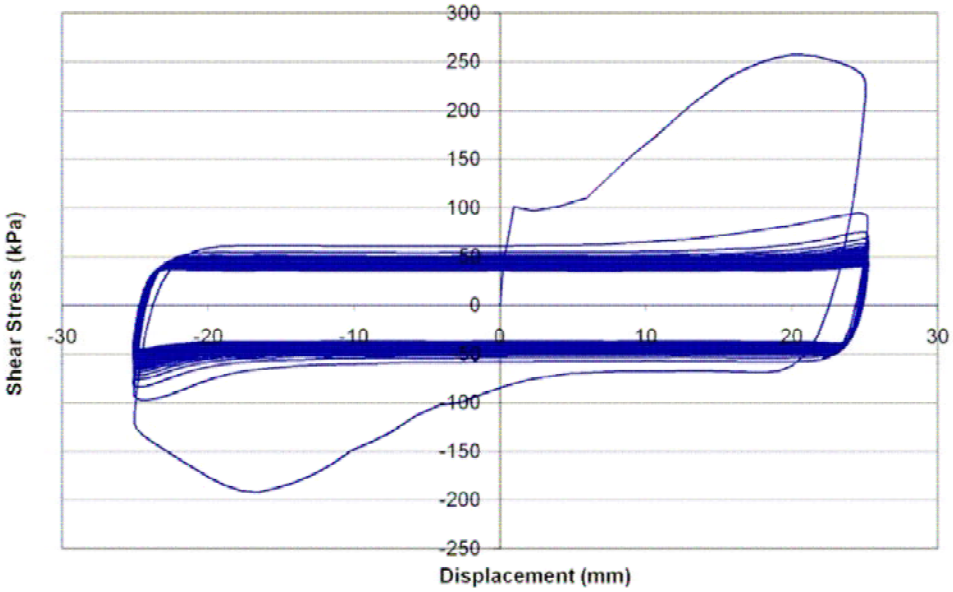

Figure 6-11 Cyclic shear test, Δ_a = 25 mm, σ_n = 348 kPa (Sura 2009)

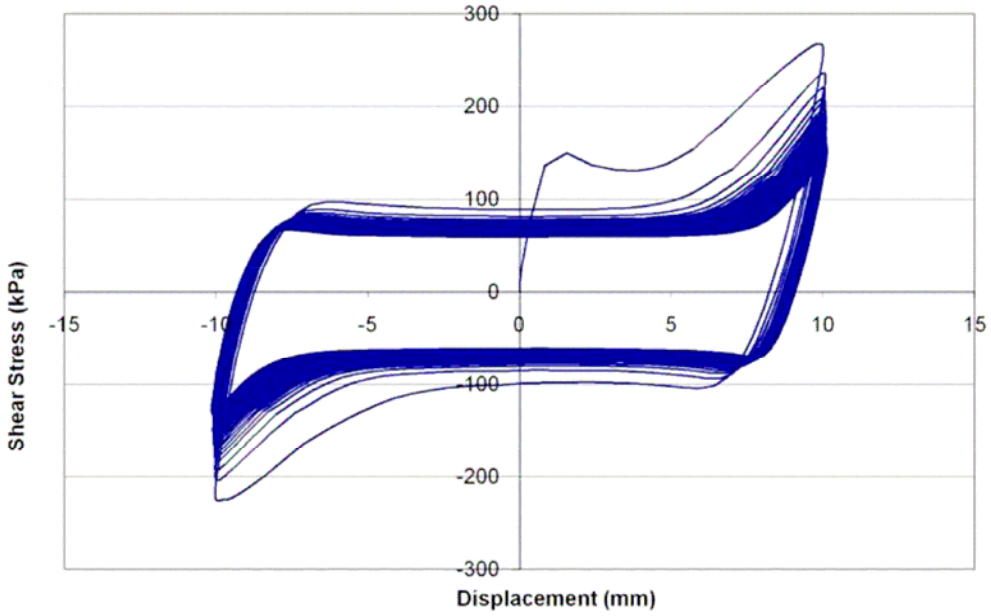

Figure 6-12 Cyclic shear test, Δ_a = 10 mm, σ_n = 692 kPa (Sura 2009)

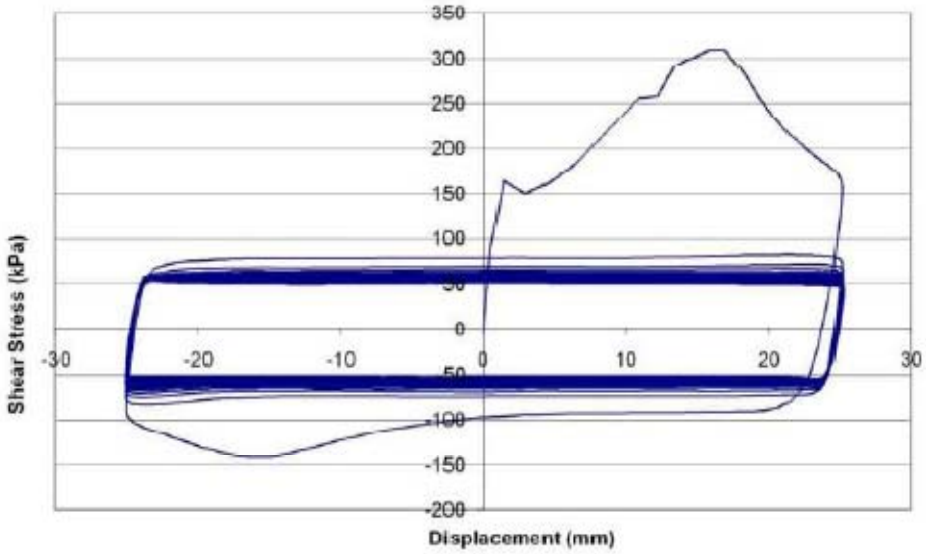

Figure 6-13 Cyclic shear test, Δ_a = 25 mm, σ_n = 692 kPa (Sura 2009)

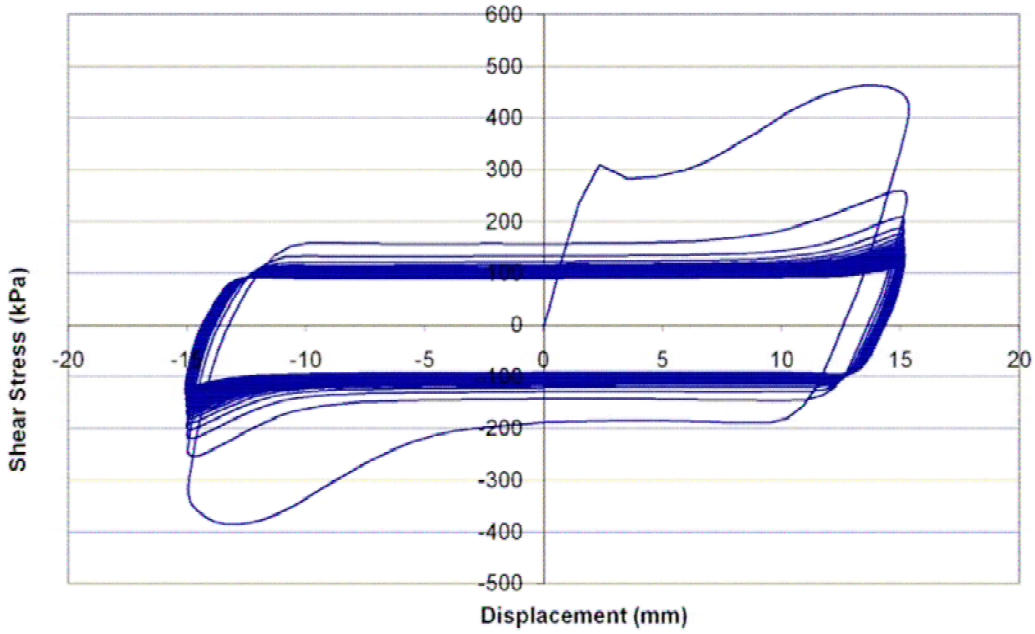

Figure 6-14 Cyclic shear test, Δ_a = 15 mm, σ_n = 1382 kPa (Sura 2009)

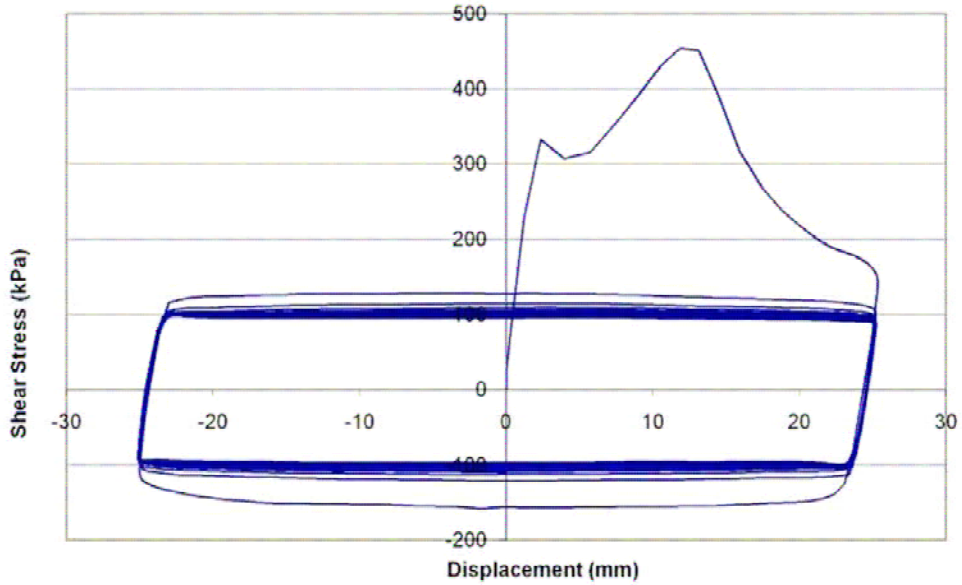

Figure 6-15 Cyclic shear test, Δ_a = 25 mm, σ_n = 1382 kPa (Sura 2009)

The backbone curve for cyclic loading at a normal stress of 1382 kPa, shown in Figure 6-16, was used to develop model parameters for nine hardening yield surfaces and one softening yield surface (*nys*=10). The stress and strain points used to discretize the back bone curve are presented in Table 6-1. The backbone curve was initialized using subroutine (M_INI.FIS). The rest of the GCL model parameters are listed in Table 6-2. The constitutive model was then enabled in (M_MYSS.FIS). Both Subroutines are provided in Appendix B.

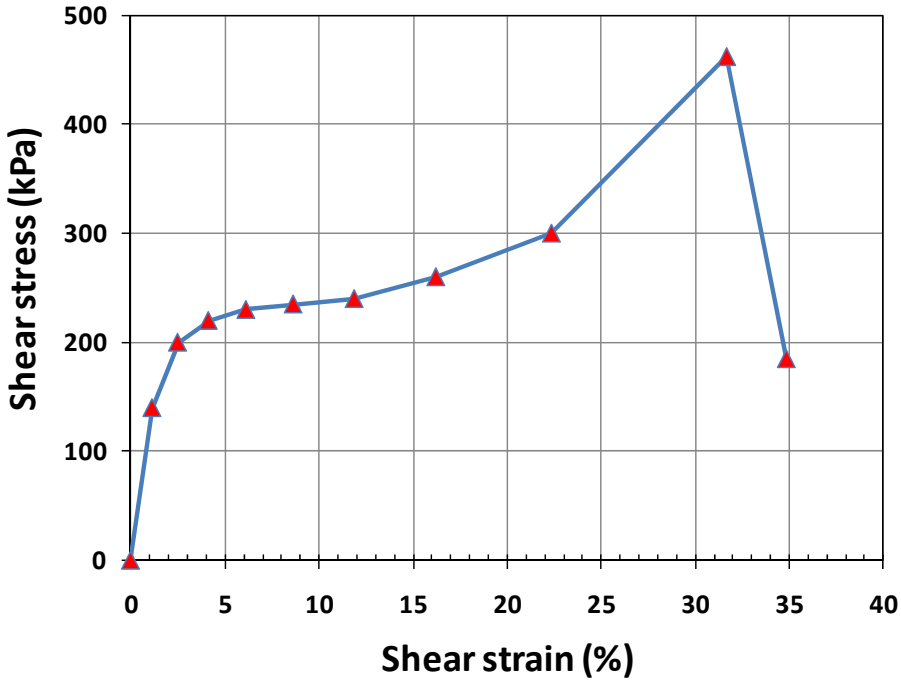

Figure 6-16 Discrete stress strain laboratory values for GCL backbone curve at σ_n = 1382 kPa

Table 6-1 Discrete stress strain laboratory values for GCL backbone curve at σ_n = 1382 kPa.

Deviatoric Stress, q (kPa)	Shear Strain, ε (%)
0	0
140	1.14
200	2.50
220	4.13
230	6.13
235	8.64
240	11.88
260	16.22
300	22.36
462	31.67

Table 6-2 Model parameters for the GCL material

K	n	K_b	m	C (kPa)	ϕ (degrees)	rf_s	ss
425	0.58	205	0.44	160	14	0.4	1.3

Analyses were performed using the FLAC 6.0 constitutive model to simulate the cyclic behavior of GCLs under different normal stresses. The results of the analyses are shown in Figure 6-17 to Figure 6-21 along with the measured hysteresis loops. Comparing the numerical results with the experimental results, we can find that the numerical model does a good job reproducing the key aspects of the behavior of the GCLs, i.e. the computed hysteresis reproduce the general patterns of behavior for the measured hysteresis loops and the model exhibits peak and residual behavior similar to the measured behavior.

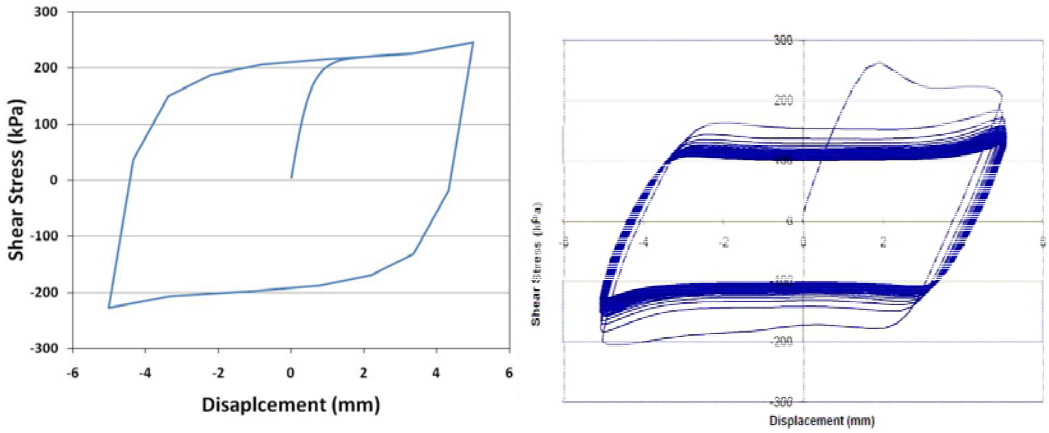

Figure 6-17 Cyclic shear response for GCL under normal stress σ_n = 1382 kPa for amplitude ±5mm (left) computed; (right) measured

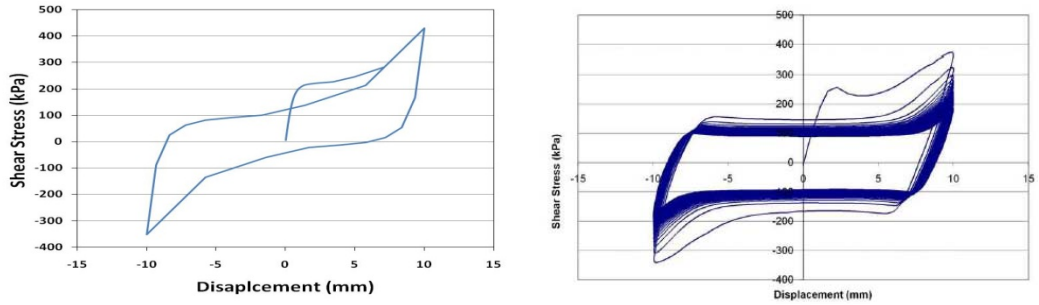

Figure 6-18 Cyclic shear response for GCL under normal stress σ_n = 1382 kPa for amplitude ±10mm (left) computed; (right) measured

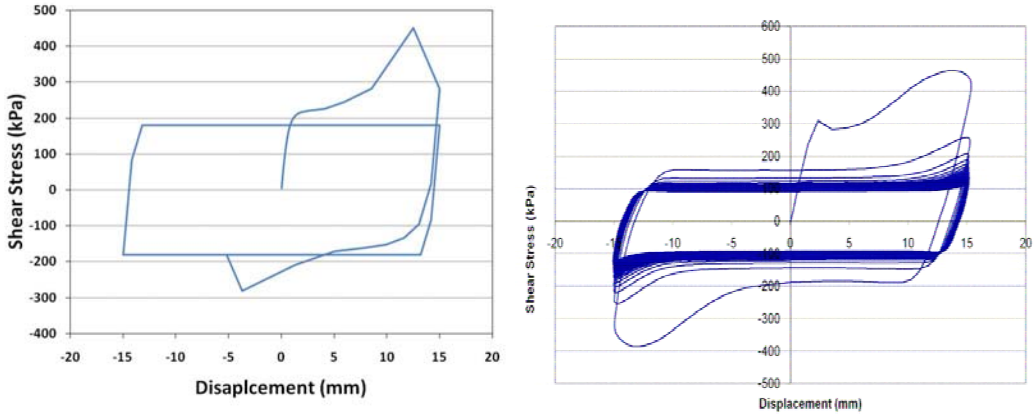

Figure 6-19 Cyclic shear response for GCL under normal stress σ_n = 1382 kPa for ±15mm amplitude (left) computed; (right) measured

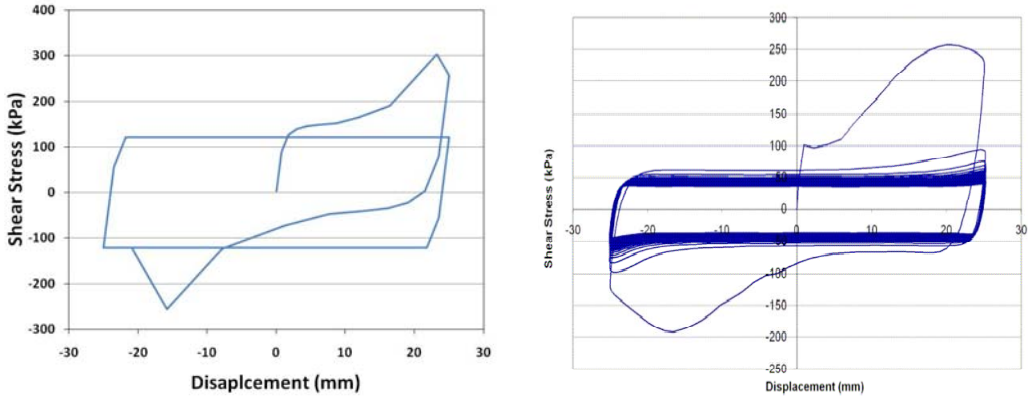

Figure 6-20 Cyclic shear response for GCL under normal stress σ_n = 348 kPa for amplitude at ±25mm (left) computed; (right) measured

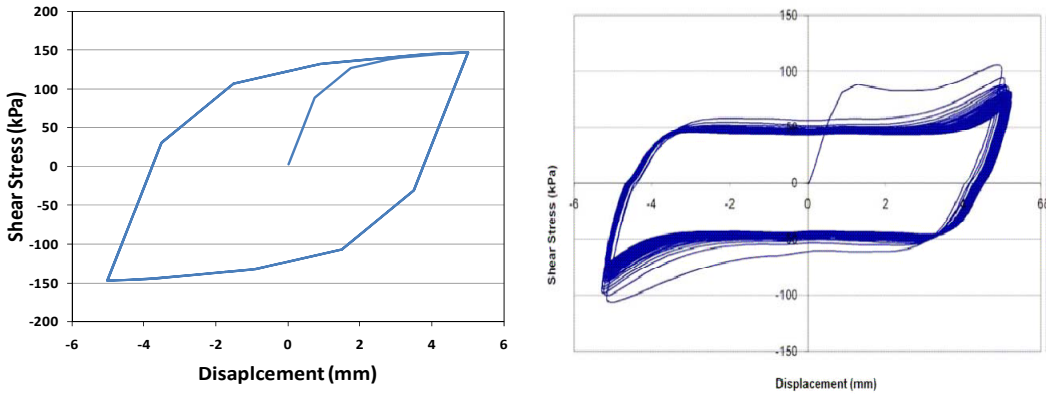

Figure 6-21 Computed cyclic shear for with normal stress σ_n = 348 kPa for amplitude at ±5mm

CHAPTER 7 CALIBRATION OF THE INTERFACE ELEMENTS

7.1 Introduction

FLAC 6.0 provides elastic-perfectly plastic interface elements in which the interface shear strength is characterized by the Mohr-Coulomb failure criterion. These elements allows for displacement of contacting grids relative to each other (slip at the interface). Interface elements can be also used with structural elements. These interface elements are a very powerful tool for modeling shear behavior when there is a distinguished discontinuity between two different materials, as in case of geosynthetic liner system element. It is very important to calibrate the behavior of these interface elements for accurate prediction of relative displacement at the interface as well as the effect of slip at the interface on seismic response. A time domain finite difference numerical model of a rigid block on a plane with a frictional interface was developed using the large strain formulation coded in FLAC 6.0 for the purpose of calibrating of the interface elements. The frictional interface was modeled using a simple elastic-perfectly plastic stress-strain relationship and the Mohr-Coulomb failure criterion already available in FLAC 6.0. The numerical model was validated using a series of shaking table tests of a sliding block on a horizontal plane and inclined plane. In these tests, a rigid block with one geosynthetic material glued to its bottom side was placed on a shaking table that had a second geosynthetic material secured to it. Different combinations of geotextile and geomembrane materials were subject to uniform sinusoidal motions of varying amplitude. The acceleration of the block and the displacement of the block relative to the shaking table were monitored during these tests. The results presented in this chapter are

also presented in two conference publications (Arab and Kavazanjian 2010; Arab et al. 2010).

7.2 Rigid Block on an Horizontal Plane

Kavazanjian et al. (1991) conducted a series of shaking table tests of a sliding block on a horizontal plane. In these tests, a rigid block with one geosynthetic material glued to its bottom side was placed on a shaking table that had a second geosynthetic material secured to it. Four different combinations of geotextile and geomembrane materials were subject to uniform sinusoidal motions of varying amplitude. Three of the geosynthetics combinations were also subjected to a non-uniform earthquake-like motion based upon the S90W component of the 1940 El Centro strong motion record. The acceleration of the block and the displacement of the block relative to the shaking table were monitored during these tests.

To model the Kavazanjian et al. (1991) shaking table tests in FLAC 6.0, the two-layer, nine macro-element mesh shown in Figure 7-1 was used. The upper layer of the mesh represents the rigid block and the lower layer represents the shaking table.

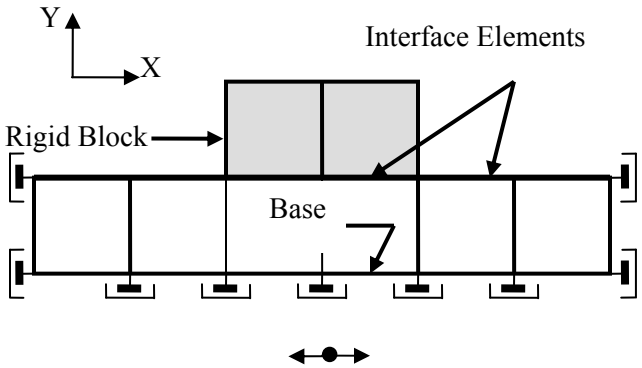

Figure 7-1 Finite difference model (macro elements shown) of the horizontal shaking table test

Values of bulk and shear modulus representative of structural steel were used to model both the rigid block and shaking table. An interface element was used between the upper and lower layers of the mesh to model the geosynthetic /geosynthetic interface. The interface was assigned an elastic shear and normal stiffness approximately equal to ten times the bulk modulus of the mesh elements. The interface shear strength was initially based upon the static interface strength of the interface as measured in a tilt-table test and then adjusted as necessary to find the best fit with the experimental results. A shear stress time history was applied to the base of the mesh to model the shaking table input motion.

Figure 7-2 shows a comparison between the block acceleration measured in one of the uniform sinusoidal loading tests and the results calculated in the FLAC 6.0analysis. The test was conducted using a geomembrane/geotextile interface with a measured static coefficient of friction equal to 0.16. However, analysis conducted with a friction coefficient of 0.15 resulted in better agreement between the measured values and the numerical analysis results. The best-fit numerical analysis results, calculated using a friction coefficient of 0.15 in the Mohr-Coulomb interface model, are shown in Figure 7-2. These results suggest that the dynamic coefficient of friction for the interface may be somewhat different from the static interface friction coefficient. The same conclusion was reached by Kavazanjian et al. (1991) based solely on the experimental results (i.e. by comparison of the yield acceleration of the block to the static coefficient).

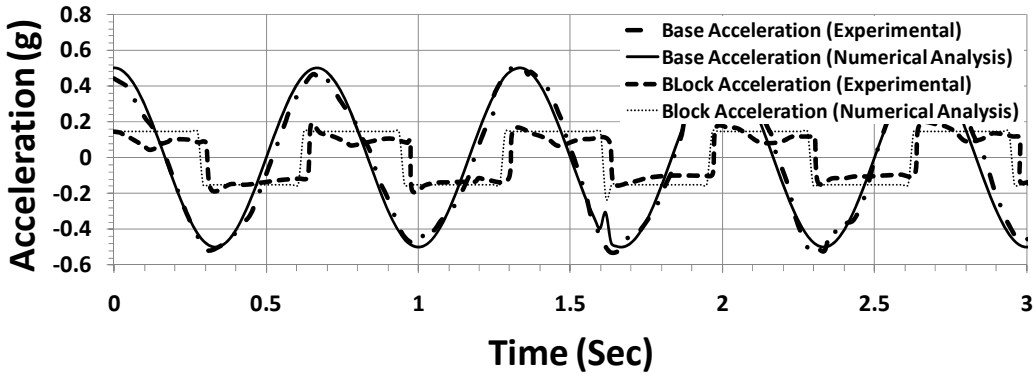

Figure 7-2 Comparison between best-fit numerical analysis and acceleration response measured by Kavazanjian et al. (1991) uniform sinusoidal excitation

Figure 7-3 presents a comparison of the relative displacement of the rigid block as measured in the shaking table test to that calculated in the numerical analysis. The small discrepancies between the experimental results and the numerical analysis (e.g. the steady drift of the experimental relative displacement towards the negative side of the displacement scale) may be attributed to the somewhat asymmetrical behavior in the yielding behavior: note the somewhat non-uniform acceleration behavior of the block in Figure 7-2.

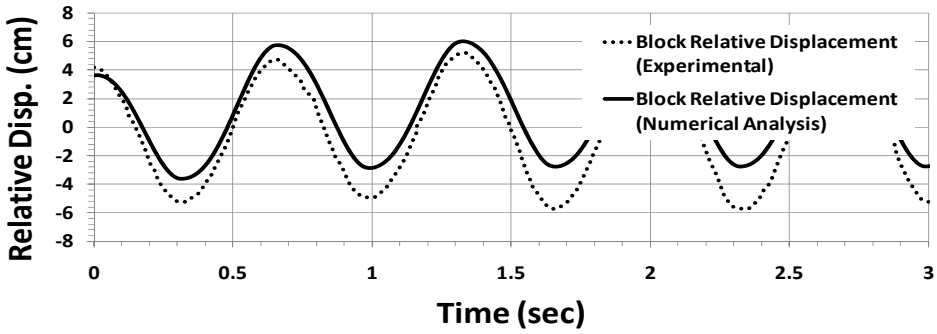

Figure 7-3 Comparison between best-fit numerical analysis and displacements measured by Kavazanjian et al. (1991) during uniform sinusoidal loading

Figure 7-4 shows a comparison between the transmitted acceleration of the block from numerical analyses using the coefficient of friction from the tilt table tests and from physical testing of Kavazanjian et al. (1991). The numerical analysis shows the same acceleration for the block for all the base frequencies. For some of the interface types, the dynamic interface friction coefficient changed with the base frequency. This behavior suggests that the interface friction coefficient may be both material and frequency (or velocity) dependent.

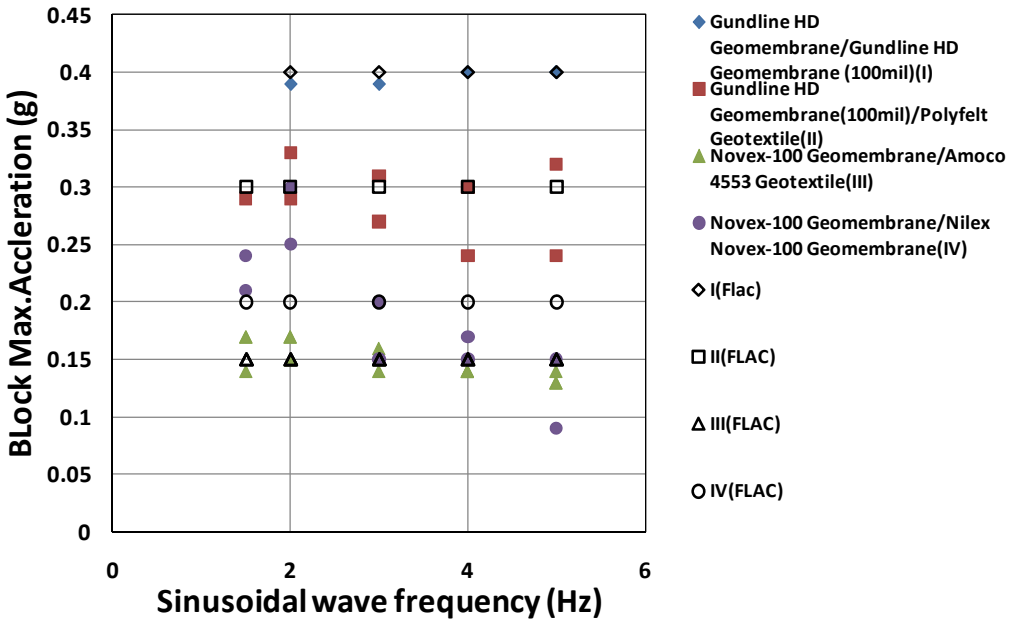

Figure 7-4 Comparison between transmitted block acceleration from the numerical analysis and transmitted block acceleration measured by Kavazanjian et al. (1991) during uniform sinusoidal loading with different wave frequency

The time domain numerical model shown in Figure 7-1 was also used to simulate rigid block on a horizontal plane shaking table tests conducted by Yegian et al. (1998) and Yegian and Kadakal (2004) that used earthquake time histories as input. Yegian et al. (1998) used the Los Angeles University Hospital Grounds record from the 1994 M_w 6.7

Northridge earthquake scaled to 0.9 g. Yegian and Kadakal (2004) used the Corralitos, Capitola, and Santa Cruz records from 1989 M 7.1 Loma Prieta earthquake scaled to peak accelerations of 0.1 g to 0.4 g. Because earthquake motions are asymmetric, both the shaking table tests and the numerical analyses using earthquake time histories yielded a residual (permanent) displacement. Figure 7-5 presents a comparison between the residual displacement reported by Yegian et al. (1998) and Yegian and Kadakal (2004) and the residual displacement calculated using the numerical model.

The comparison of residual displacements from the experimental results of Yegian et al. (1998) and Yegian and Kadakal (2004) to the numerical analysis in Figure 7-5 shows generally good agreement. The primary discrepancy is for the Corralitos record from the Loma Prieta event. The calculated permanent displacement for the Corralitos record is less than the displacement measured experimentally in the 0.1 g to 0.25 g range. However, both calculated and experimental results show a similar trend of increasing residual displacement with increasing base peak acceleration. One interesting aspect of the results is that in some cases the residual displacement decreases as base acceleration increases.

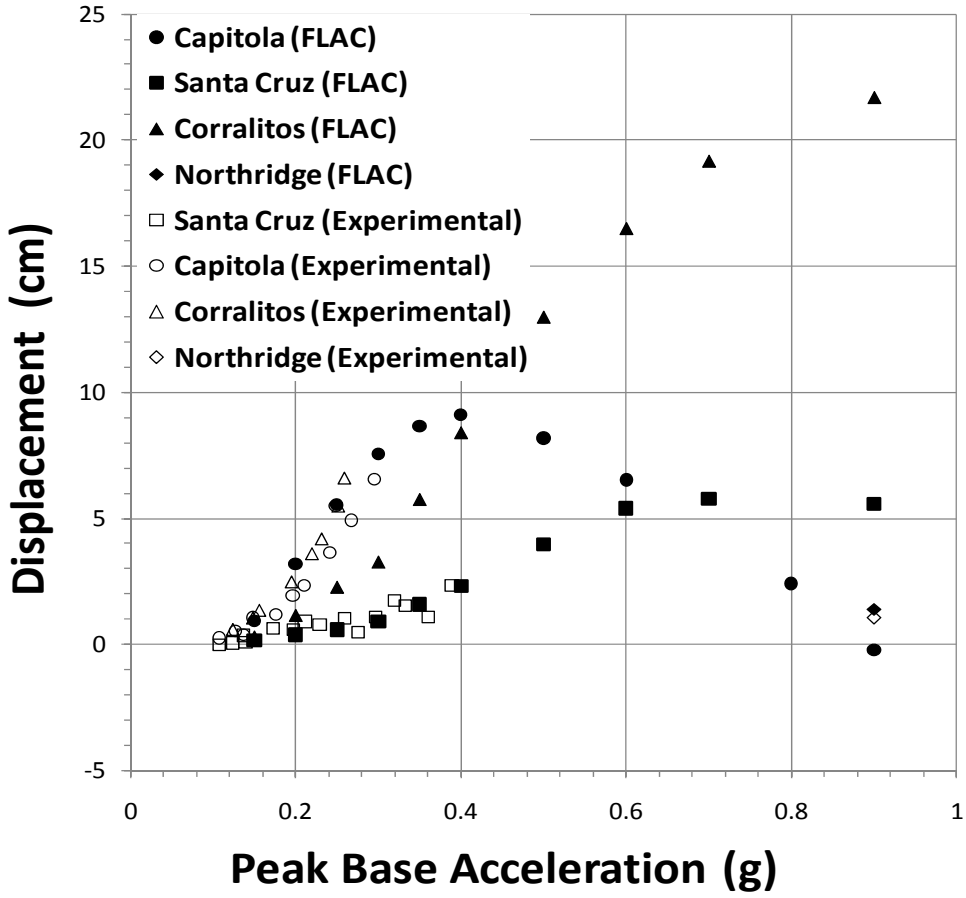

Figure 7-5 Residual permanent displacement from the numerical model compared to the experimental results of Yegian et al. (1998) and Yegian and Kadakal (2004)

Despite small differences between experimental and numerical results, the analyses shown in Figure 7-2 through Figure 7-5 suggest that the elasto-plastic Mohr-Coulomb interface model is capable of reproducing the dynamic behavior of a block on a horizontal plane with a frictional interface if the appropriate interface dynamic shear strength is employed.

7.3 Westermo and Udwadia Analytical Solution

Westermo and Udwadia (1983) presented an analytical solution for a rigid mass resting on a flat horizontal surface with an interface friction coefficient, μ, excited with a simple harmonic motion of amplitude a_o. They showed that the system experienced two different slippage conditions that were independent of the frequency of the harmonic motion and depended only on a non-dimensional parameter η, where:

$$\eta = \frac{\mu g}{a_o} \tag{86}$$

and g is the acceleration of gravity. The quantity μg is the yield acceleration of the block, i.e., the acceleration at which the block begins to slide relative to the plane.

Westermo and Udwadia (1983) identified two different slippage conditions. These two conditions were referred to as the slip-stick and slip-slip conditions. At the end of a sliding cycle the block will either stick before moving again or immediately start to slide in the opposite direction. Westermo and Udwadia showed that if η was greater than 0.53, the block will stick before the base acceleration exceeds the threshold for movement (μg) for the next half cycle. In this case, the motion of the block will consist of two sliding and two non-sliding intervals per cycle, as illustrated in Figure 7-6 (a). This mode of motion was referred to as slip-stick behavior. However, for η equal to or less than 0.53, the end of the slip interval converges on the time of initiation of sliding in the opposite direction. In this case, the block begins to slide in the opposite direction immediately and the block never comes to a complete stop (except for the instantaneous moment during reversal of the direction of motion when the relative velocity between the block and the plane is zero). This pattern of displacement, illustrated in Figure 7-6 (b), was referred to

as the slip-slip condition. Note that if η is greater than, the block will not slip relative to the plan (i.e. a stick-stick condition exist).

The numerical model illustrated in Figure 7-1 was also employed to reproduce the slip-stick and stick-stick modes of behavior predicted analytically by Westermo and Udwadia (1983). An interface friction angle corresponding to a friction coefficient of 0.3 was employed in the numerical analyses and the numerical model was excited with a harmonic sinusoidal motion of a frequency of 1 Hz using two different peak accelerations. A peak acceleration of 0.4g, corresponding to a value of η = 0.75, was used in one analysis and a peak acceleration of 0.9 g, corresponding to a value of η = 0.33, was used in a second analysis. In the first case, since $0.53 < \eta < 1.0$, stick-slip behavior is expected. In the second case, since $\eta < 0.53$, slip-slip behavior is expected. The results of the numerical analysis are shown in Figure 7-6. Figure 7-6 (a) shows the calculated acceleration, velocity and displacement of the rigid block for the slip-stick case (0.4 g peak acceleration, η = 0.75). Looking at the relative velocity of the block, the block experiences three modes of displacement per cycle. The block first sticks to the base until the acceleration exceeds μg. The block then starts to slide and the relative velocity increases until the acceleration of the base has decreased to μg. At this point, the relative velocity decreases until it reaches zero and the block sticks to the plane again. Figure 7-6 (b) illustrates the slip-slip behavior for the second case (0.9 g peak acceleration, η = 0.33). In this case the block slides in one direction until the block passes the μg threshold and the relative velocity decreases to zero, at which point the block immediately begins sliding in the other direction and never comes to rest on the plane.

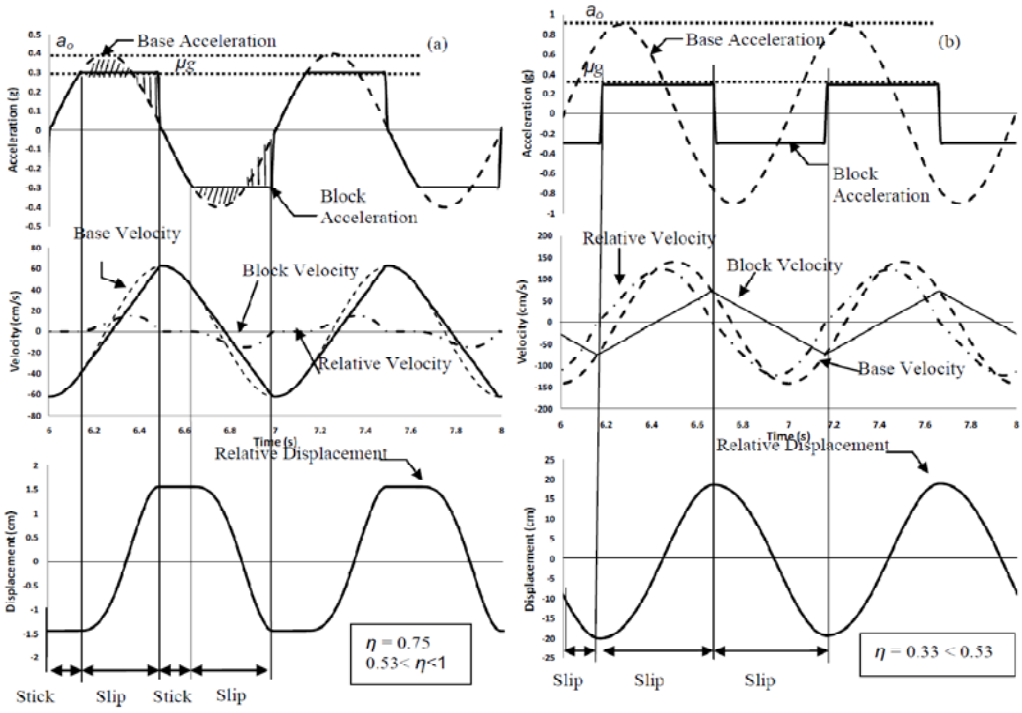

Figure 7-6 The influence of η on the response of a rigid block on a horizontal plane (a) slip-stick response, (b) slip-slip response

7.4 Rigid Block on an Inclined Plane

7.4.1 Sand-Sand interface

Elgamal et al. (1990) conducted a shaking table test of a rigid block on a plane inclined at 10^{o} to assess the accuracy of the Newmark (1965) procedure for calculating permanent seismic displacement. An inclined plane coated with sandpaper was mounted on a shake table and a solid-metal block with sand glued to the base was placed on the plane. Accelerometers were attached to both the sliding block and the shaking table. A harmonic sinusoidal excitation at a frequency of 1 Hz with amplitude sufficient to induce the block to slide down slope was applied to the base for 12 seconds. In addition to the acceleration

of the block and the plane, the relative slip between the block and the plane was measured over the course of the test.

To model the Elgamal et al. (1990) shaking table tests in the time domain analyses, a two-layer, nine macro element mesh similar to the one used to simulate the horizontal shaking table tests was used. However, in this case the block, the base, and the interface were inclined at an angle at an angle $\beta = 10^o$. As in the horizontal plane model shown in Figure 7-1, in the inclined plane model, illustrated in Figure 7-7, the upper layer represents the rigid block and the lower layer represents the shaking table with $\beta = 10^o$. The same values for bulk and shear modulus of the block and plane and for the elastic stiffness of the interface used in the model in Figure 7-1 were assigned to the inclined plane model in Figure 7-7. A shear stress time history was applied to the base of the mesh to model the shaking table input motion.

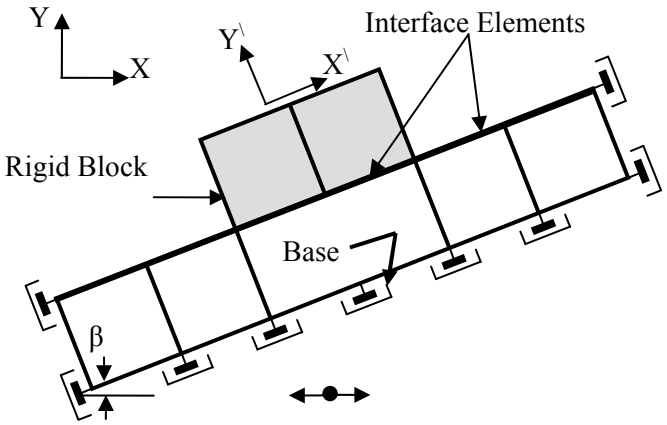

Figure 7-7 Finite difference model (macro elements shown) of an inclined shaking table test

Figure 7-8 shows a comparison between the block acceleration measured in the uniform sinusoidal loading test of Elgamal et al. (1990) and the results calculated in the

FLAC 6.0 analysis using a friction angle based upon the static friction coefficient of 0.36 reported by Elgamal et al. (1990).

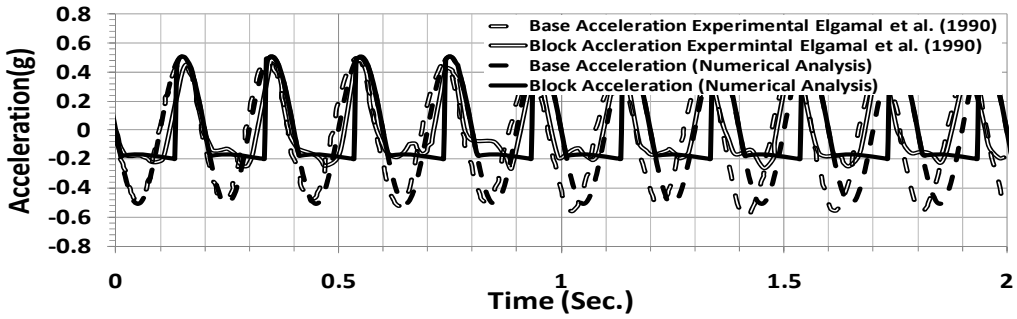

Figure 7-8 Acceleration from the numerical model compared to the experimental results of Elgamal et al. (1990)

Figure 7-9 presents a comparison of the relative displacement of the rigid block as reported by Elgamal et al. (1990) for the shaking table test and as calculated in the numerical analysis. The primary discrepancy between the experimental results and the numerical analysis is at the start of shaking, when there is a delay in the initiation of relative displacement in the shaking table test. Note that the experimental results suggest that the block sticks for a little less than 2 seconds, i.e., for the first one and a half cycles of motion (the excitation frequency was 1 Hz) before it starts to move relative to the plane. This delay in the initiation of relative movement suggests that there may have been some initial adhesion at the interface (perhaps due to interlocking of sand grains) that had to be overcome before the block began to slide. However, once the block began to move, relative displacement accumulated at approximately the same rate in the numerical analysis as ob-served in the model, as evidenced by the nearly parallel displacement curves in Figure 7-9.

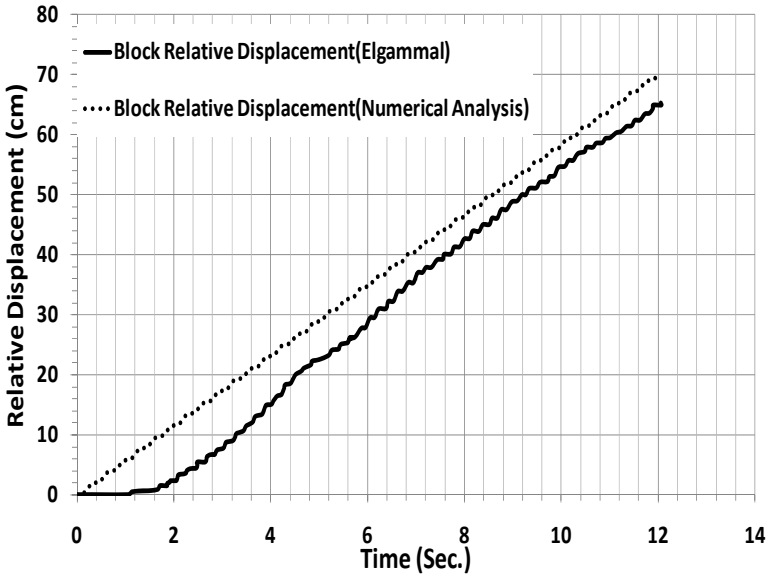

Figure 7-9 Displacement from the numerical model compared to the experimental results of Elgamal et al. (1990)

The generally good agreement shown in Figure 7-8 and Figure 7-9 between the model test results reported by Elgamal et al. (1990) and the numerical analysis suggests that the numerical model is capable of reproducing the behavior of a rigid block on an inclined plane subject to dynamic excitation. Furthermore, the good agreement shown in these two figures, once the initial resistance to sliding was overcome in the physical model, suggests that in this case the dynamic sliding resistance is similar to the static sliding resistance. In this respect, the sand-sand interface tested by Elgamal et al. (1990) is different from the geomembrane-geotextile interfaces tested by Kavazanjian et al. (1991), which showed a difference between the dynamic and static sliding resistance.

7.4.2 **Geosynthetic-Geosynthetic interface**

Wartman (1999) and Wartman et al. (2003) reported shaking table tests of a rigid block on a plane inclined at 11.37^{o}. A steel block, 2.54 cm thick with a cross sectional

area of 25.8 cm^2 and mass of 1.6 kg, was positioned on top of the plane. The interface between the block and the plane was a smooth high-density polyethylene (HDPE)/non-woven geotextile interface similar to one that might be found in a side-slope geosynthetic liner system for a landfill. Figure 7-10 illustrates the test setup employed by these investigators. Accelerometers were fitted to both the sliding block and the inclined plane. Displacement transducers were employed to measure the absolute displacement of the sliding block and absolute displacement of the shaking table. Relative displacement was calculated from the two absolute displacement measurements.

The input motions used in the tests described by Wartman (1999) and Wartman et al. (2003) were a suite of 22 uniform sinusoidal motions, three sinusoidal frequency sweep motions, and one earthquake-like motion. The input type, excitation frequency, peak acceleration of the input motion, and cumulative relative displacement between the block and the plane for these tests are presented in Table 7-1.

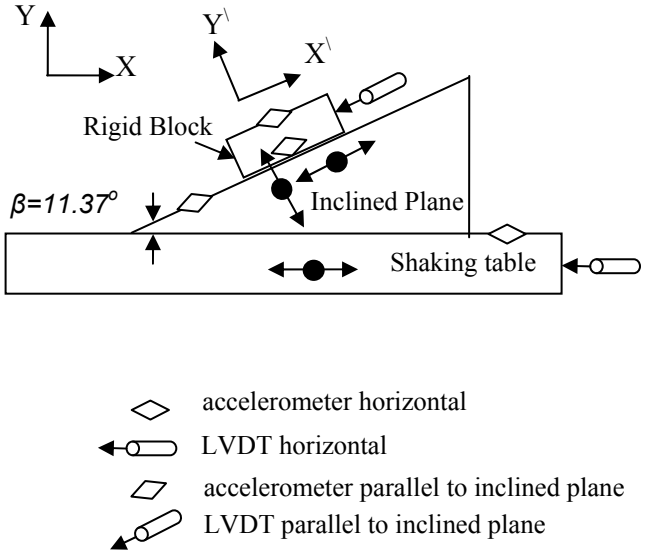

Figure 7-10 Schematic representation of the shaking table setup and the instrumentation used by Wartman (1999) and (after Wartman1999)

Table 7-1 Input motions used in the tests reported by Wartman et al. (2003)

Type	Frequency (Hz)	Input Motion Peak Acceleration (g)	Cumulative relative Displacement (cm)
Uniform	1.33	0.01	0.19
Uniform	2.66	0.09	0.12
Uniform	2.66	0.15	2.42
Uniform	2.66	0.2	12.64
Uniform	4.0	0.07	0.12
Uniform	4.0	0.13	2.51
Uniform	4.0	0.17	2.51
Uniform	4.0	0.25	6.60
Uniform	6.0	0.07	0.45
Uniform	6.0	0.1	0.83
Uniform	6.0	0.12	1.39
Uniform	6.0	0.19	3.65
Uniform	8.0	0.04	0
Uniform	8.0	0.07	0.13
Uniform	8.0	0.11	0.54
Uniform	8.0	0.16	1.20
Uniform	10.92	0.05	0.17
Uniform	10.92	0.06	0.21
Uniform	10.92	0.09	0.46
Uniform	10.92	0.21	3.20
Uniform	12.8	0.07	0.20
Uniform	12.8	0.23	3.01
Sweep	-	0.25	3.43
Sweep	-	0.35	4.90
Sweep	-	0.58	11.78
Earthquake like	Kobe	2.0	8.22

The uniform sinusoidal loading tests were conducted for duration of 6 seconds at frequencies varying from 1.33 to 12.76 Hz with acceleration amplitudes varying from 0.01 g to 0.23 g. The inability of the shaking table to instantaneously apply or terminate the full amplitude of sinusoidal motion led to the use of a motion in these so-called uniform loading tests that linearly ramped up to the peak amplitude for 1.5 seconds followed by the full amplitude of motion for 3 seconds and then 1.5 seconds of ramping down. The frequency sweep motion linearly increased in both frequency (from 1 to 16 Hz) and acceleration over a 5 second duration.

To back analyze his test results, Wartman (1999) employed the computer program YSLIP_PM developed by Matasovic et al. (1998) for Newmark-type displacement analysis. The interface friction angle was varied in the YSLIP_PM analysis until calculated acceleration and displacement time histories of the block matched the measured values as closely as possible. However, interface friction angles back calculated in these analyses were consistently greater than the value of $12.7^{o} \pm 0.7^{o}$ determined for the interface employed in these tests by tilt tests reported in Wartman et al. (2003).

Wartman (1999) postulated that the friction angle of the interface during dynamic loading was controlled by two factors: 1) the amount of displacement; and 2) sliding velocity. Figure 7-12 shows the friction angle back calculated from the table acceleration at the initiation of sliding plotted versus the average sliding velocity of the block as calculated by Wartman et al. (2003). The calculated friction angles were in the range of 14^{o}–19^{o} and appeared to increase linearly with increasing average sliding velocity. Wartman (1999) cites an increase in the threshold acceleration for the initiation of sliding in the sweep frequency test with an amplitude of 0.58 g from approximately 0.1 g at the

beginning of the test to 0.2 g at the end the test as additional evidence of an interface friction angle proportional to sliding velocity for the HDPE / non-woven geotextile interface that was tested.

The numerical model shown in Figure 7-7 was used to simulate the shaking table tests reported in Table 7-1 using $\beta = 13.37^{o}$. For each test, the interface friction angle was varied until a calculated cumulative relative displacement approximately equal to the one reported in the test was achieved. Figure 7-11 shows the variation in the calculated permanent deformation with two variables: interface friction angle and frequency of the input motion. Similar to the trend obtained by Wartman et al. (2003), the best-fit friction angle from the numerical analysis increased with average velocity. The open symbols in Figure 7-12 show the best-fit friction angle from the numerical analysis plotted versus average sliding velocity. The average sliding velocity was calculated as the cumulative relative displacement divided by the total sliding time for the block. The total sliding time was determined assuming that the block was sliding when the relative velocity exceeded 0.01cm/s. As illustrated in Figure 7-12, the friction angle back calculated from the numerical analysis was consistently less than the friction angle reported by Wartman et al. (2003) for these tests.

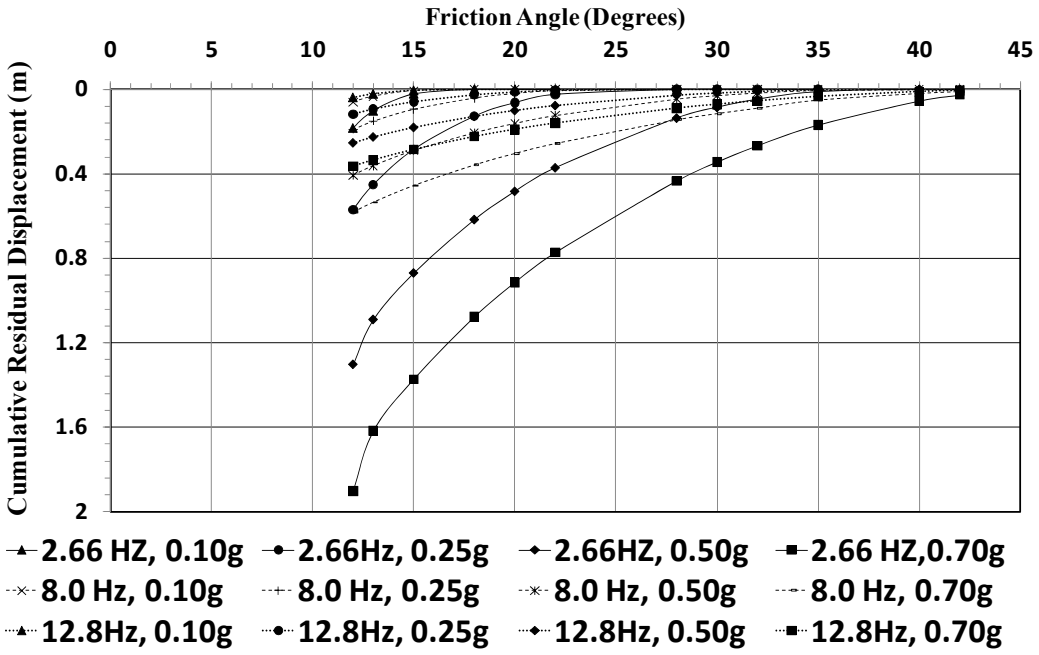

Figure 7-11 Cumulative residual changing as a function of input frequency, input peak acceleration, and interface friction angle calculated using FLAC 6.0.

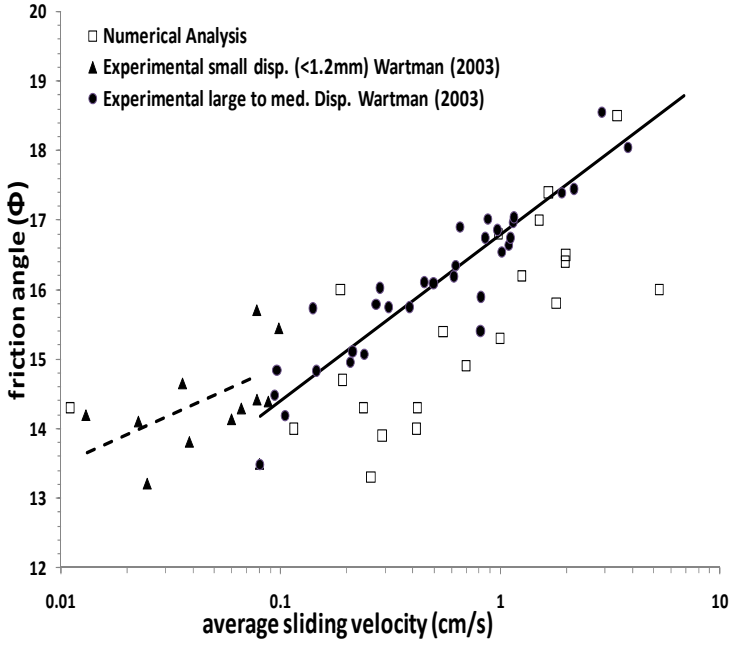

Figure 7-12 Interface friction angle as a function of average sliding velocity of the block (after Wartman et al., 2003)

The discrepancy shown in Figure 7-12 between the numerical analysis results and the friction angle reported by Wartman et al. (2003) may be attributed to the use by Wartman et al. (2003) of the acceleration parallel to the plane rather than the acceleration in the horizontal direction to predict the friction angle between the block and the plane.

Yan et al. (1996) present the following equation for the horizontal acceleration at yield at the initiation of movement in the downslope direction of a rigid block on a plane:

$$\ddot{X}_y = g\left(\tan(\phi - \beta)\right) \tag{87}$$

where $\ddot{X}_y$ is the horizontal acceleration at yield, ϕ is the friction angle between the block and the plane, and β is the angle of the plane. The free body diagram is illustrated in Figure 7-13. Prior to yield, the vertical acceleration of the block is zero and the acceleration of the block parallel to the plane at yield, $\ddot{X}'_y$, is given by:

$$\ddot{X}'_y = \ddot{X}_y \cos\beta \tag{88}$$

However, once the block yields there is a downward vertical acceleration induced in the block and the acceleration of the block parallel to the plane increase accordingly. Thus, using the acceleration parallel to the plane of a yielding block to predict the yield acceleration according to equations above results in overprediction of the block friction angle.

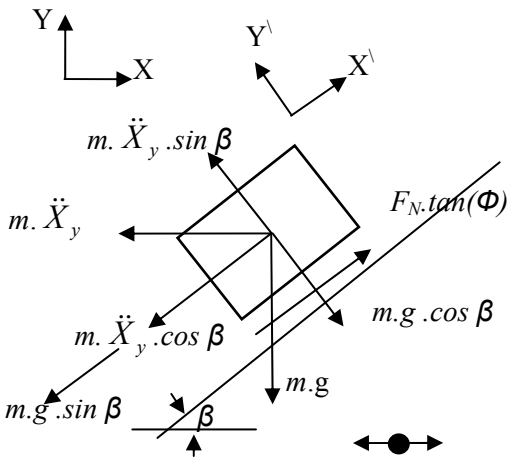

Figure 7-13 Free body diagram of a block on an inclined plane subject to horizontal excitation at the initiation of downslope sliding

This phenomenon is illustrated in Figure 7-14, which shows results from the numerical model for a frequency sweep test for a friction coefficient of 0.1 g. Note that downslope accelerations are positive in this figure. Figure 7-14 (a) shows the calculated horizontal acceleration of the block from the frequency sweep analysis. Figure 7-14 (b) shows the corresponding calculated vertical acceleration of the block while Figure 7-14 (c) shows the calculated acceleration of the block parallel to the plane. Note that Figure 7-14 (a) shows that the horizontal acceleration at yield in this numerical analysis is constant and equal to 0.10 g, the value that would be predicted from equation above using the input friction angle. However, Figure 7-14(c) shows the acceleration of the block parallel to the plane increases from 0.1g to 0.15 g as the horizontal acceleration of the base increases over the duration of the test. Thus, use of the acceleration parallel to the plane as the friction coefficient of the block over-predicts the value of the friction coefficient.

The numerical analysis predicted an increase in acceleration from 0.1 g to 0.15 g in the frequency sweep tests assuming a constant friction coefficient of 0.10 g. In the shaking table test conducted by Wartman (1999) that corresponds to the numerical analysis shown in Figure 7-14, an increase in the acceleration parallel to the plane from 0.1g to 0.2g was observed. The additional 0.05 g in acceleration at yield parallel to the plane observed in the shaking table test may still be attributed to an increase in average velocity of the block as the frequency and amplitude of the excitation increased.

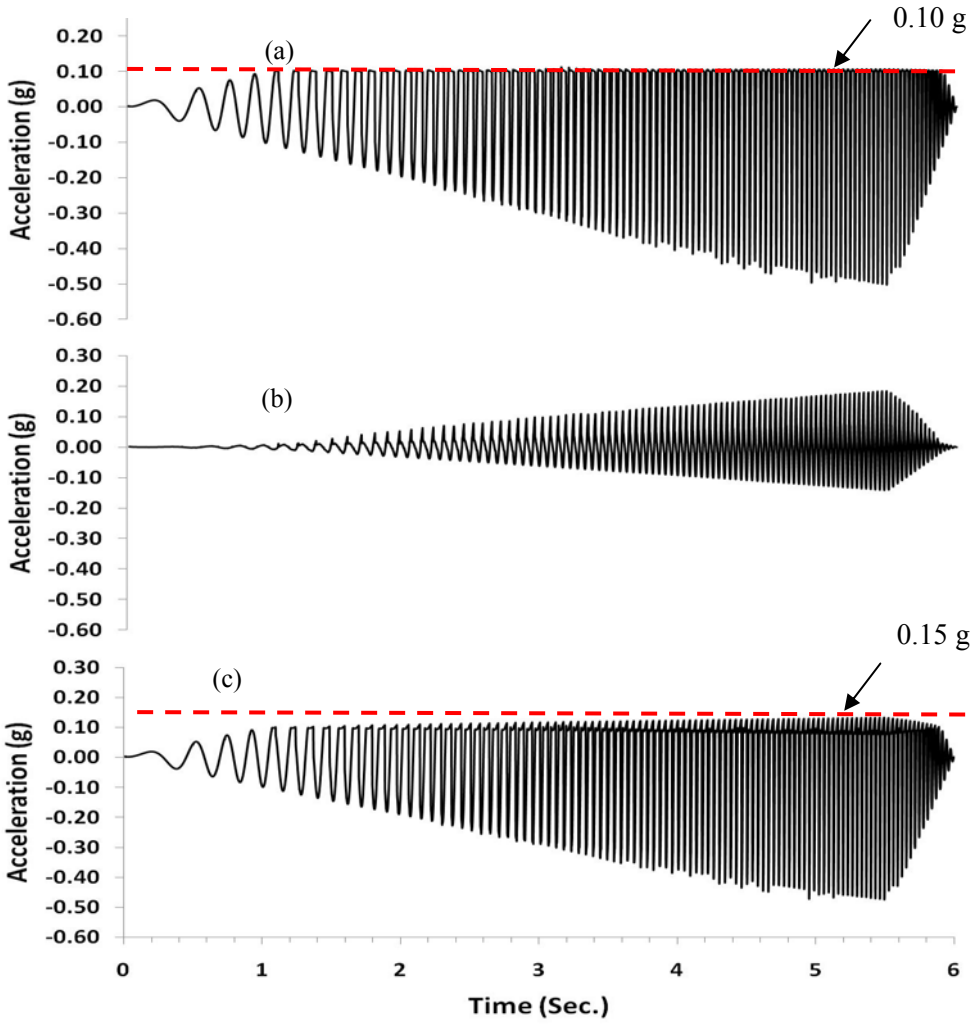

Figure 7-14 Frequency sweep motion (a) Horizontal block acceleration (b) Block acceleration normal to the plane (c) Block acceleration parallel to the plane.

Wartman (1999) also reported shaking table tests conducted using the same physical model described above and a scaled version of a Hyogoken Nanbu (Kobe) earthquake recording (Kobe Port Island array, depth = 79 m) as input. The peak acceleration of the scaled record was 2.0 g. The same numerical model described in the previous paragraphs of a rigid block on a plane was also used to model this test.

Figure 7-15 presents a comparison of the relative displacement of the rigid block as measured in the shaking table test and as calculated in the numerical analysis for the Kobe acceleration input. Once again, the interface friction angle in the numerical model was varied until the maximum relative displacement matched the measured value. The best fit interface friction angle from this analysis was 16.2^{o}. The relative displacement time history from the numerical analysis closely matches the relative displacement time history observed in the laboratory test, including episodes of upslope relative displacement at around 5 seconds. Furthermore, the best fit friction angle of 16.2^{o} and the average sliding velocity between 5 and 8 seconds of 2.67 cm/s plots in the middle of the band of results from the numerical analysis of the uniform sinusoidal loading tests reported in Figure 7-12. Figure 7-16 shows the acceleration time history calculated using in case of the Kobe earthquake input motion and the acceleration of the block as measured by Wartman (2001). The maximum acceleration measured experimentally is little higher in both the upslope and downslope directions than the calculated acceleration using the numerical model.

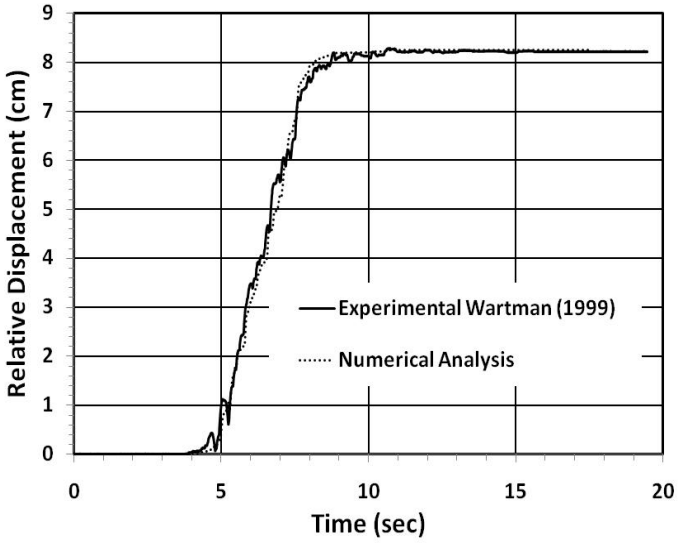

Figure 7-15 Measured and calculated block relative displacement for the Kobe earthquake acceleration input

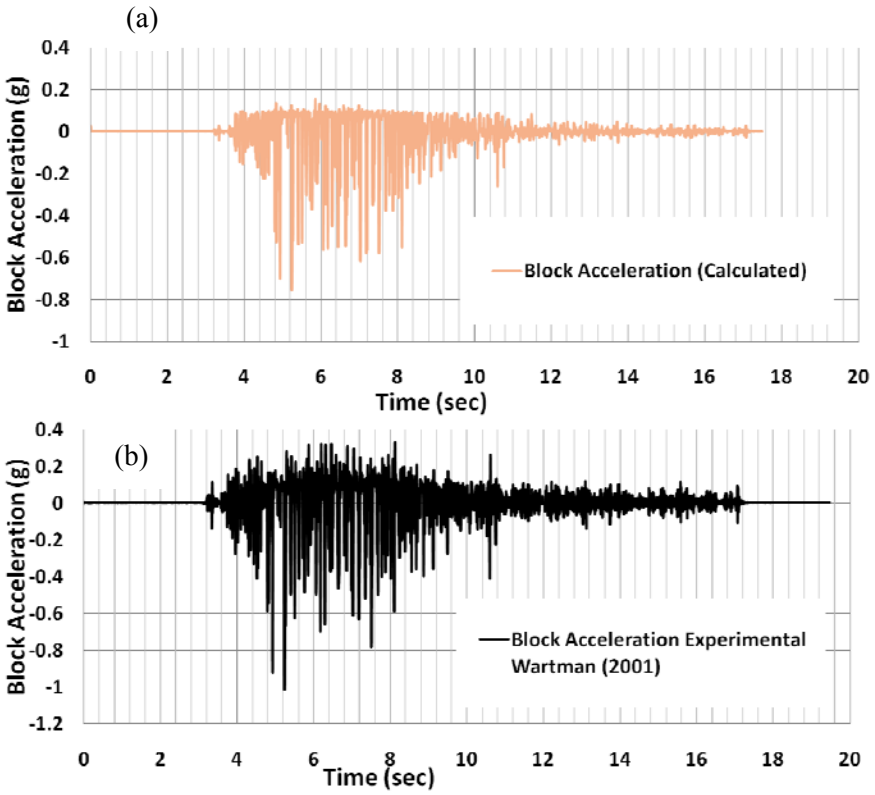

Figure 7-16 Block acceleration (a) Calculated; (b) Experimental (Wartman 2001)

7.5 Stick-Slip and Slip-Slip Behavior

The numerical model was also used to investigate the potential for slip-stick and slip-slip conditions for an inclined plane, where the threshold acceleration is different in the downslope and upslope directions. A plane inclined at 11.37^{o} with an interface friction coefficient of 0.29 was used in the analysis, corresponding to a downslope yield acceleration of 0.08 g and an upslope yield acceleration of 0.52 g. Figure 7-17(a) shows the calculated block acceleration, relative velocity and relative displacement for an input sinusoidal acceleration with an amplitude of 0.2g and a frequency of 2.66 Hz. In this case, block response is in a stick-slip mode. Figure 7-17 (b) shows the calculated block acceleration, relative velocity and relative displacement between the base and the block for an input sinusoidal acceleration with amplitude of 2.0g and a frequency of 2.66Hz. In this case, a slip-slip mode of response is observed, but the upslope movement is relatively small compared to the downslope movement.

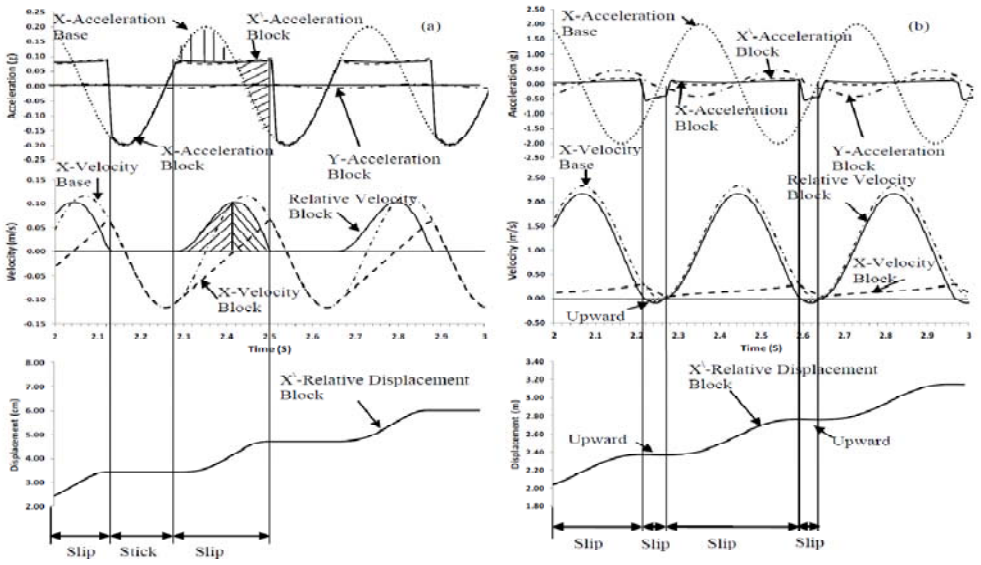

Figure 7-17 The calculated acceleration, velocity and the displacement of the rigid block on an inclined plane (a) slip-stick response, (b) slip-slip response

7.6 Soil Column

Wartman (1999) and Wartman et al. (2003) reported shaking table tests of a soil columns on a plane inclined at 11.37^{o} (Figure 7-18). Two 25.4 cm diameter clay soil columns with different moisture contents were used in the Wartman (1999) inclined plane studies. In the Wartman (1999) experiments, the clay mixture was highly plastic (plasticity index 105%) and the soil column was ‘‘sandwiched’’ between two lightweight 1.7-cmthick, 25.4 cm diameter Lucite plastic disks. A stiff soil column with a moisture content of 133.0 % and a soft soil column with a moisture content of 147.0 % were used in the testing. A textured 1.5 mm HDPE geomembrane was glued to the top and bottom surfaces of the lower and upper disks to minimize movement between the soil and disks during testing. A geotextile was secured to the bottom of the lower disk using two-sided carpet tape. The soil container was 25.4 cm diameter and was 16 cm and 14 cm height for the stiff and soft soil columns respectively. A 0.5-mm-thick latex membrane was attached to the perimeter of the disks to contain the soil.

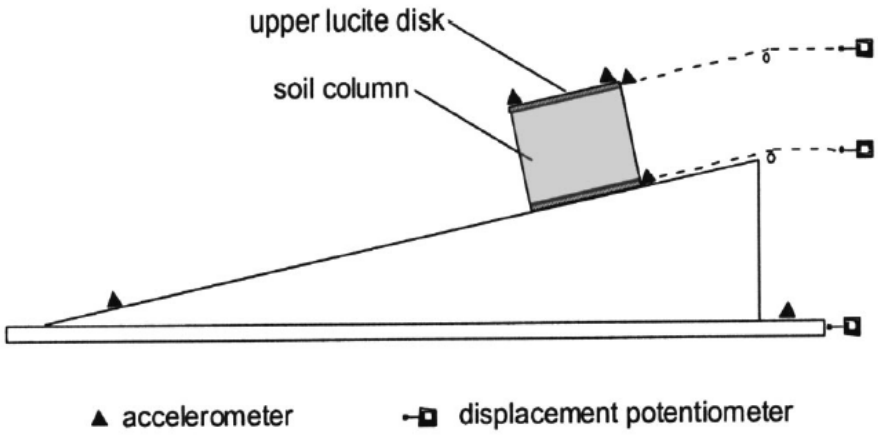

Figure 7-18 Shaking table experiment with clay soil columns (Wartman et al. 2003)

Wartman (1999) measured the shear wave velocity as 6.4 m/s and 4.3 m/s, corresponding to fundamental frequencies of 9.6 and 7.8 for the stiff and soft soil columns respectively. An average-damping ratio of 3.3 and 3.9 %, for the stiff and soft soil columns respectively, were measured using free vibration test.

The interface between the block and the plane was a smooth high-density polyethylene (HDPE)/non-woven geotextile interface similar to the interface was used in the rigid block experiments conducted by the same investigator. Accelerometers were fitted to both the sliding block and the inclined plane. Displacement transducers were employed to measure the absolute displacement of the sliding block and absolute displacement of the shaking table. Relative displacement was calculated from the two absolute displacement measurements. The input motions used in the tests described by Wartman (1999) and Wartman et al. (2003) were the suite of 22 uniform sinusoidal motions presented in Table 7-1. Typical accelerations measured at the top and the bottom of the soil column are shown in Figure 7-19 to Figure 7-22.

Figure 7-19 presents the results for the acceleration in the stiff soil column for the case of a sinusoidal input motion with frequency of 2.66 Hz. In the test presented in Figure 7-19, the maximum acceleration at the bottom of the soil column in the upslope direction was smaller than the input motion. However, the acceleration at the top of the soil column in this test was higher in the down slope direction than the base acceleration. Figure 7-20 shows the acceleration of the soil column for the case of a sinusoidal input motion with a frequency of 4.0 Hz. For the case illustrated in the case in Figure 7-20, the maximum acceleration at the base of the soil column is higher than the input base acceleration. Figure 7-21 shows acceleration of the soil column for case of a sinusoidal input motion with a frequency of 8.0 HZ. For the case illustrated in Figure 7-21, the

maximum acceleration at the base of the column was similar to maximum acceleration of the input motion but the maximum acceleration at the top of the column was higher than that of the input motion. Furthermore, the motion of the top and bottom of the column is slightly out of phase in the case illustrated in Figure 7-21. Results for case of sinusoidal input with a frequency of 12.8 HZ are presented in Figure 7-22.The recorded displacement suggests that the soil column did not move relative to the base in this case (i.e. the relative displacement between the base and bottom of the soil column is zero). The recorded displacements show that the top and bottom of the soil column move approximately 180° out of phase. A similar observation can be made from the acceleration records.

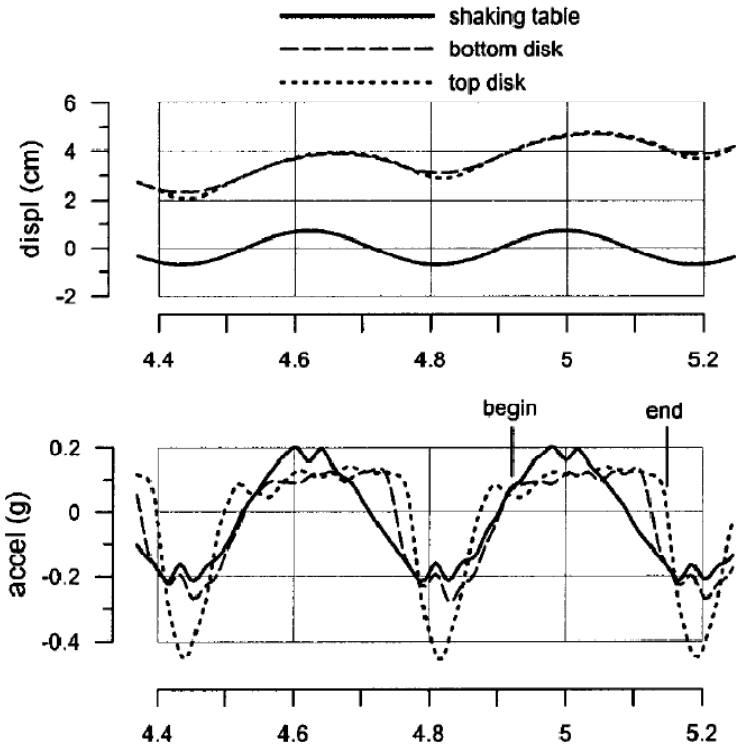

Figure 7-19 Acceleration of top and bottom of the stiff soil column for 2.66 Hz sinusoidal input motion, positive acceleration is in upslope direction (Wartman et al. 2003).

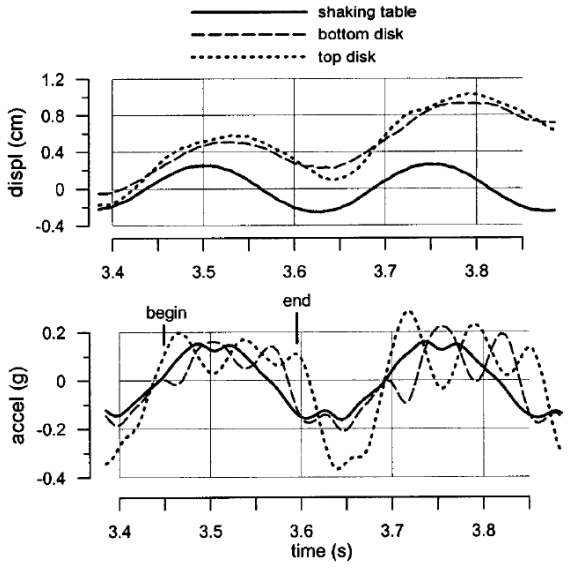

Figure 7-20 Acceleration of top and bottom of the stiff soil column for 4 Hz sinusoidal input motion, positive acceleration is in upslope direction (Wartman et al. 2003).

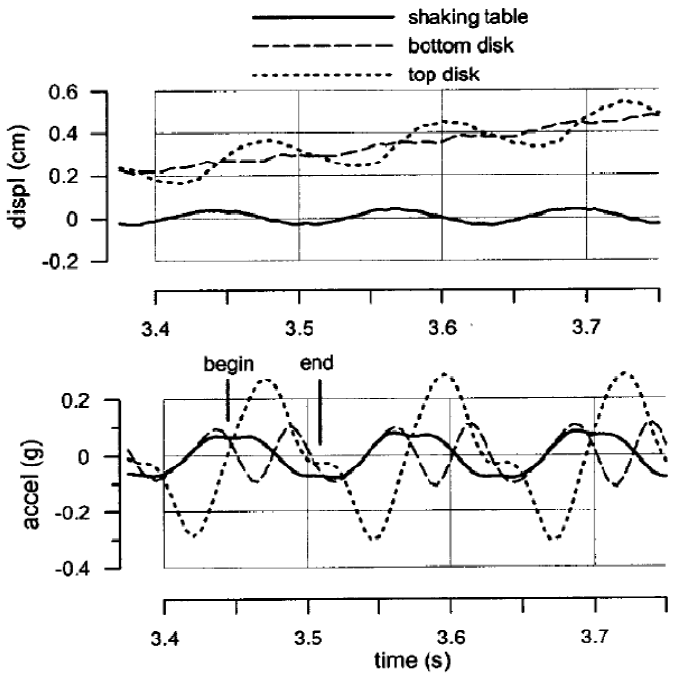

Figure 7-21 Acceleration of top and bottom of the stiff soil column for 8 Hz sinusoidal input motion, positive acceleration is in upslope direction (Wartman et al. 2003).

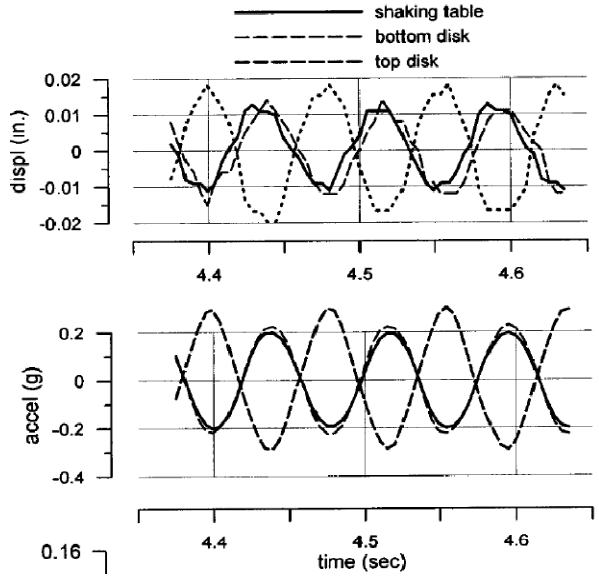

Figure 7-22 Acceleration of top and bottom of the stiff soil column for 12.8 Hz sinusoidal input motion, positive acceleration is in upslope direction (Wartman et al. 2003).

The numerical model shown in Figure 7-7 was used to simulate the shaking table tests for the stiff columns tested by Wartman (1999). The properties (V_s = 6.5 m/s and density of 1678 kg/m^3) and dimensions of the soil column were assigned to the grid elements above the interface. The input motions reported in Table 7-1 and $\beta = 13.37^o$ were used in the numerical analysis. The backbone curve developed by Vucetic and Dobry (1991) for clays with a plasticity index, PI of 100%, was assigned to soil column with the Masing rule was used to define the shape of the hysteresis loops. The interface friction angle was changed until the computed displacement fit the measured displacement as closely as possible. The acceleration, velocity and displacement at the top and the bottom of the soil column were calculated relative to the base.

Typical results of this analysis are presented in Figure 7-23 (b) to Figure 7-28 (b). Figure 7-23 (b) shows typical results for the sinusoidal motion at 2.66 Hz. Similar to the experimental results shown in Figure 7-23(a), the results presented in Figure 7-23 (b) show the soil column behaving much like a rigid block, with upslope accelerations for the bottom of the soil column limited to 0.18 g during sliding (in this case a friction angle of 19 degrees was used for the interface). However, the top of the soil column did experience acceleration amplification in the downslope direction. The relative displacement computed between the bottom of the soil column and the base is shown in Figure 7-24 (b) for the 2.66 Hz sinusoidal motion. The trend measured experimentally is similar to the computed relative displacement between the bottom of the soil column and the base. The bottom of the soil column experienced stick-slip behavior, similar to the rigid block case.

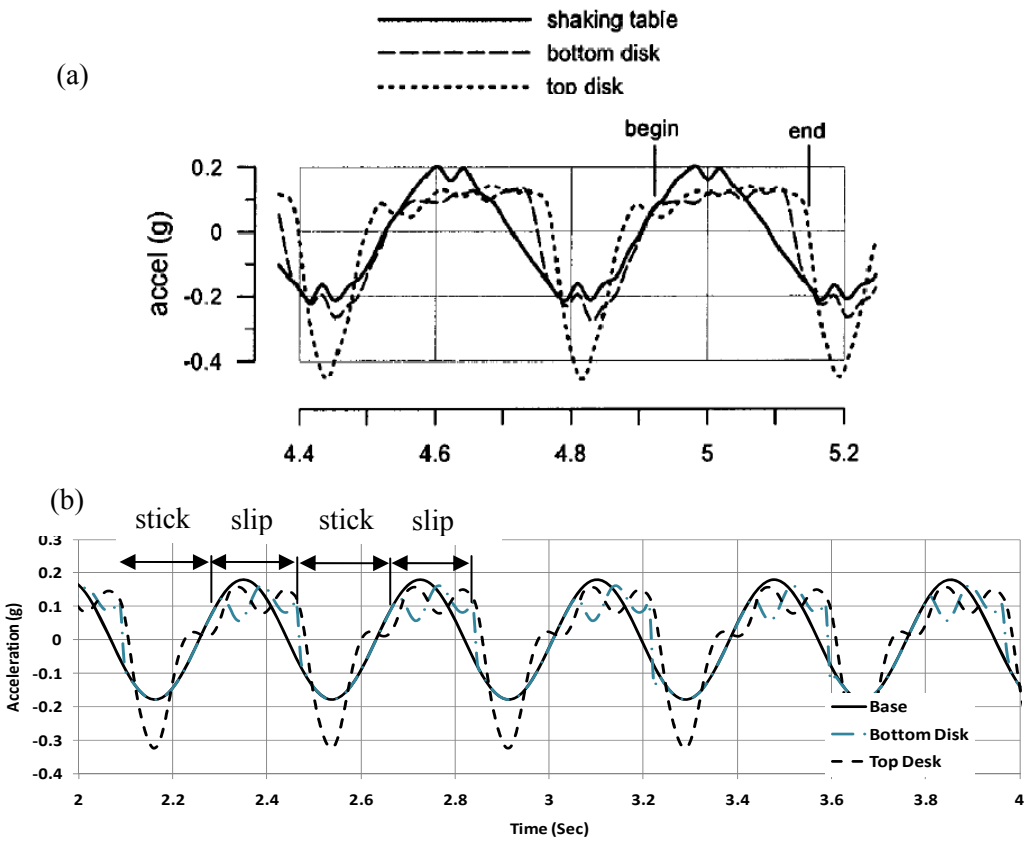

Figure 7-23 Measured and calculated acceleration for stiff soil column for 2.66 Hz sinusoidal input motion, positive acceleration is in upslope direction (a) measured, (b) calculated

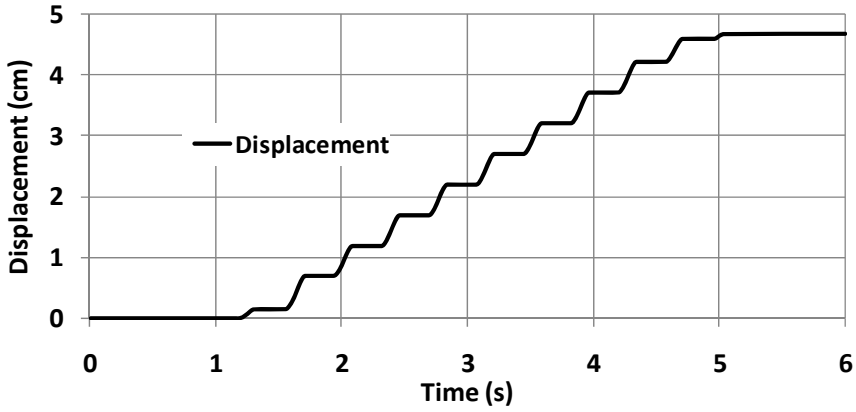

Figure 7-24 Calculated relative displacement between the bottom plate and the base for (stiff soil column), for 2.66 Hz sinusoidal input motion, positive acceleration is in upslope direction.

Typical numerical results for the sinusoidal motion at 4.0 Hz are presented in Figure 7-25 (b). The calculated acceleration at the bottom of the soil column in case of 4.0 Hz input illustrated in Figure 7-25 (b) is different in shape to the measured acceleration in the slip episode at the bottom of the soil column shown in Figure 7-25 (a). However, the calculated upslope peak acceleration at the bottom of the soil column is very similar to the upslope peak acceleration measured at the bottom of the soil column. The acceleration calculated at the top of the soil column in Figure 7-25 (b) was very similar in shape to the measured acceleration at the top of the soil column in Figure 7-25 (a), with very similar peak accelerations. The calculated acceleration at bottom of the soil column at the end of the slip episode goes momentarily from positive acceleration (upslope) to negative acceleration similar to the measured acceleration of the bottom of the soil column. In contrast to the rigid block, accelerations in excess of the yield acceleration (assuming a friction angle of 17 degrees for the interface) are computed for both the top and the bottom of the soil column. The bottom of the soil column shows stick slip behavior, the base and the bottom of the soil column have the same acceleration and after the slip initiates, the lower disk momentarily reverses acceleration to negative acceleration. Figure 7-26 shows the calculated relative displacements between the bottom of the soil column and the base. The displacement trend in Figure 7-26 is similar to the trend measured in the experiment by Wartman (1999).

(a)

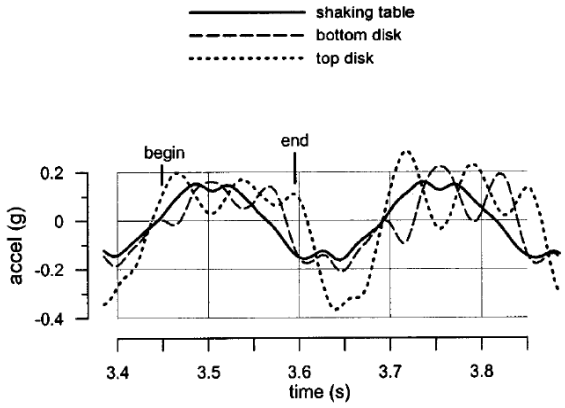

(b)

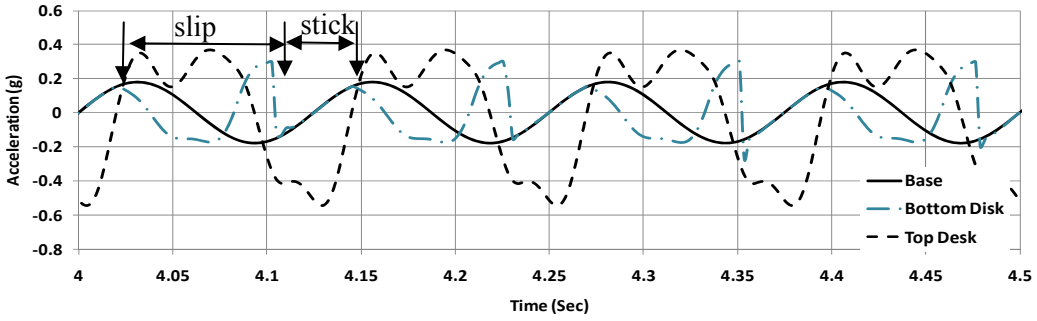

Figure 7-25 Calculated acceleration for (stiff soil column) top and bottom and input motion, for 4.0 Hz sinusoidal input motion, positive acceleration is in upslope direction.

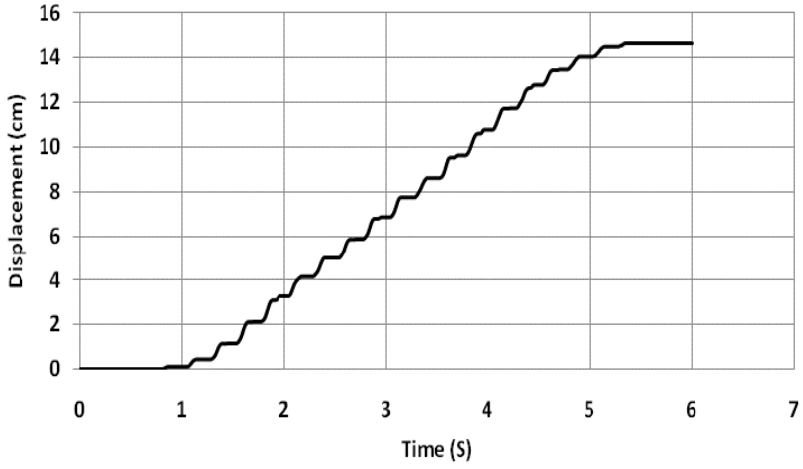

Figure 7-26 Calculated relative displacement between the bottom plate and the base for (stiff soil column), for 4.0 Hz sinusoidal input motion, positive acceleration is in upslope direction.

The calculated acceleration responses of stiff soil column for 8 Hz sinusoidal input motion are presented in Figure 7-27 (b). In this case, the calculated acceleration at the bottom of the soil column showed a stick-slip behavior, where the acceleration of the bottom of the soil column is the same as the input motion until slip initiated. In the slip mode the acceleration of the bottom of the soil column exceeds the maximum acceleration of the base input motion. These results are very consistent with the experimental results in Figure 7-27 (a).

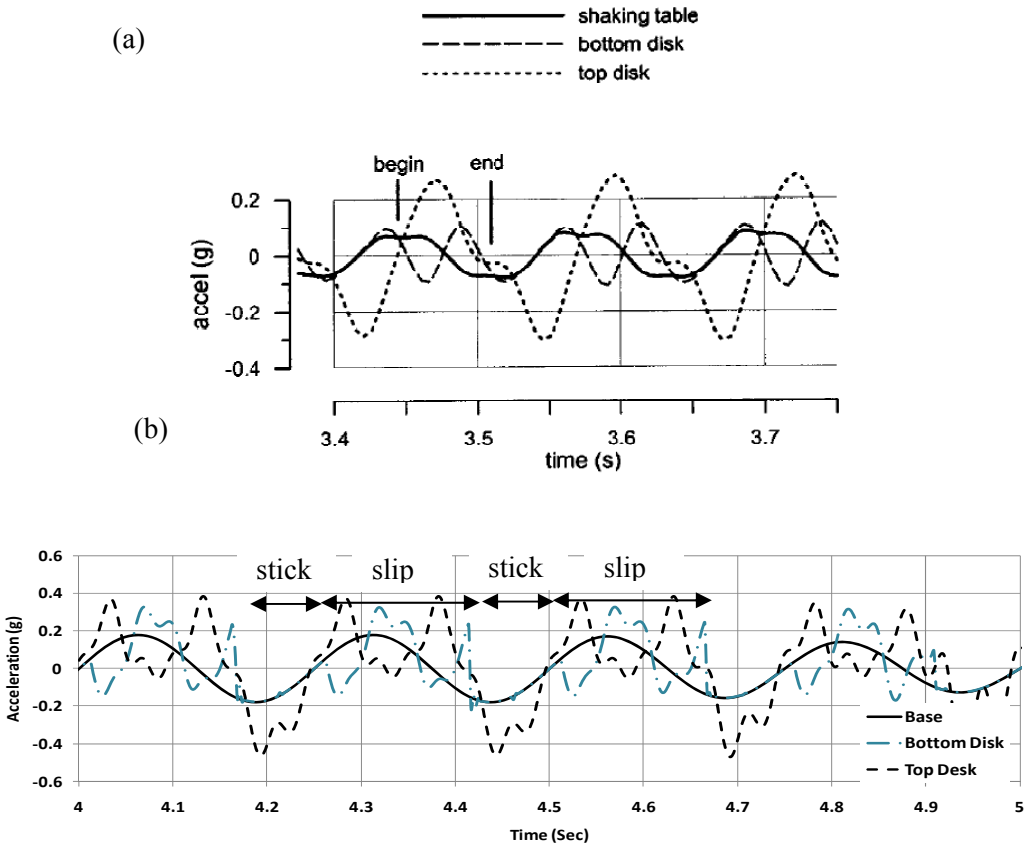

Figure 7-27 Calculated acceleration for (stiff soil column) top and bottom and input motion, for 8.0 Hz sinusoidal input motion, positive acceleration is in upslope direction

The calculated acceleration responses of the stiff soil column for the case at 12.8Hz sinusoidal motion are presented in Figure 7-28 (b). In this case, the calculated acceleration at the bottom of the soil column was identical to the acceleration at the base (Input motion), no relative movement between the lower plate and the upper plate. The calculated accelerations in Figure 7-28 (b) show that the top and bottom disks move approximately 90° out of phase. A similar observation is made from the Wartman (1999) experimental results in Figure 7-28 (a) except that the top and bottom disks move approximately 180° out of phase in the experimental results.

(a)

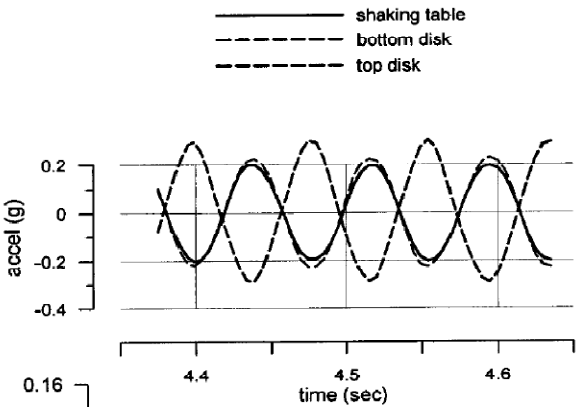

(b)

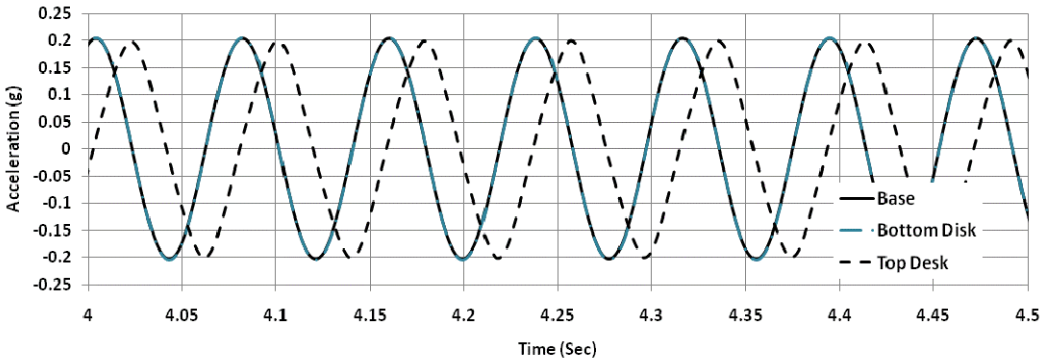

Figure 7-28 Calculated acceleration for complied block (stiff soil column) top and bottom and input motion, for 12.8 Hz sinusoidal input motion, positive acceleration is in upslope direction

7.7 Summary

A FLAC 6.0 model of a rigid block and soil column sliding along an interface on a plane subject to dynamic excitation has been developed using a simple elastic-perfectly plastic constitutive model for the interface and the Mohr-Coulomb failure criterion to characterize the load-displacement behavior of the interface. This numerical model has been shown to accurately reproduce the slip-stick and slip-slip behavior described by Westermo and Udwadia (1983) for frictional sliding of a rigid block on a horizontal plane. The numerical model has also been shown to accurately predict shaking table tests of a sliding block on horizontal and inclined planes subject to uniform and non-uniform motions provided the appropriate friction angle is used to characterize the interface. Comparison of physical model test results to the results of best-fit numerical analyses demonstrates that the appropriate friction angle depends upon the velocity of sliding. However, the rate dependence appears to be less than deduced in a previous study using a simpler back analysis.

Also, the numerical model has also been shown to predict the general trend of shaking table tests of a compliant soil column on an inclined planes subject to uniform cyclic loading provided the appropriate friction angle is used to characterize the interface. It is important to note that, in contrast to the rigid block, accelerations in excess of the interface yield acceleration may be induced in both the top and bottom of the compliant soil column. Unlike a rigid sliding block, a compliant soil column vibrates during sliding. Therefore, acceleration greater than the yield acceleration may occur within the sliding mass of the compliant soil column. Also, unlike the rigid block dynamic response, the acceleration at the base of the compliant soil column is not constant during sliding, as the limiting force at the sliding interface is not directly related to the acceleration directly

above the sliding interface but is instead related to the mass-weighted average of the entire acceleration distribution within the soil column.

CHAPTER 8 SEISMIC ANALYSIS OF HEAP LEACH PAD LINER SYSTEMS

8.1 Introduction

A two-dimensional (2-D) non-linear time-domain numerical model of heap leach pad seismic response was developed using the interface model described in the previous sections to demonstrate the ability of the model to predict forces and strains in geosynthetic liner systems and the impact of slip (relative displacement) at the liner interface. The 2-D model was also compared to different types of one-dimensional (1-D) analyses to evaluate differences among the results from the 2-D model and current methods for modeling the performance of geosynthetic liner systems. The 2-D model includes interface elements that account for slip at liner system interfaces and beam elements that allow for computation of stresses and strains in liner system components. The 1-D analysis methods include two methods proposed in the literature to model the impact of slip at a geosynthetic liner system interface: an equivalent linear method proposed by Yegian et al. (1998) and a nonlinear method proposed by Kavazanjian and Matasovic (1995). Yegian et al. (1998) proposed a set of damping and modulus values to model the impact of slip at a geosynthetic liner interface on landfill seismic response using 1-D frequency domain equivalent linear response analysis. Kavazanjian and Matasovic (1995) proposed using a weak soil layer with a shear strength equal to the interface shear strength of the liner system to model the impact of slip at a geosynthetic interface in a 1-D time domain nonlinear seismic analysis. Neither of these 1-D analyses is able to predict stresses or strains in the liner system. The 2-D time domain non-linear analysis described herein not only explicitly accounts for slip at the liner interface but

also computes the stresses and strains induced in the liner system elements by seismic loading.

8.2 Non-Linear 2-D Time Domain Analyses

The heap leach pad model analyzed in this study illustrated in Figure 8-1, in was representative of a 50 m high leach pad with 2H:1V (Horizontal: Vertical) side slopes and a 3% base slope. Three cases were analyzed using the non-linear 2-D model. In Case I, the impact of slip at the liner interface was modeled using a single interface connecting the foundation to the waste but with no element representing the liner itself. In Case II, the liner was modeled as a beam element with two interfaces (one on each side) connecting the beam (liner) to the underlying foundation and the overlying ore pile. The beam element was assigned a zero moment of inertia in order to consider the potential for buckling of the geomembrane under compressive loads. In Case III, neither interfaces nor a beam element were employed in order to provide a basis for evaluating the impact of the liner system models used in Cases I and II on seismic response.

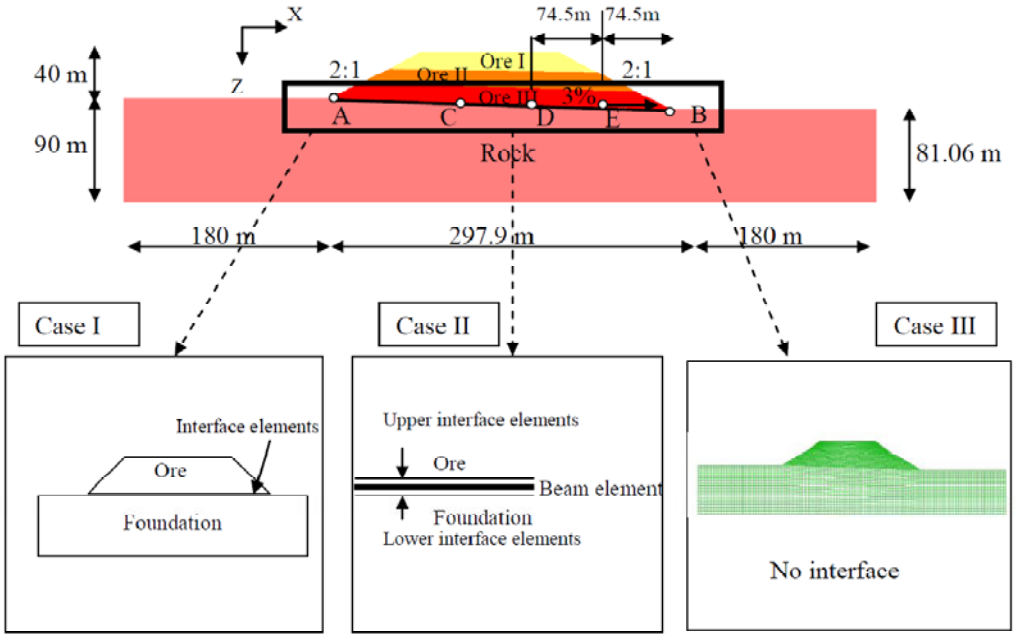

Figure 8-1 Leach pad 2-D models

The 2-D non-linear analyses were conducted using FLAC 6.0. The finite difference grid for the leach pad model consisted of 3,899 mesh zones. An increased mesh density was employed around the interface. Ore and foundation material properties used in the study are summarized in Table 8-1. The initial elastic modulus and unit weight assigned to the ore were based upon typical properties for granular materials. The ore was assigned a friction angle of 37^{o}. The weak rock foundation was modeled as a linear elastic material. The properties of the geomembrane beam element were assigned based upon typical properties for a 1.5 mm high density polyethylene geomembrane. For simplicity, and due to the lack of any other information, the Young's modulus from manufacturer's literature (i.e., the tensile modulus under zero normal stress) was employed for the membrane in both tension and compression, with no adjustment made for normal stress on the geomembrane. The Young's modulus assigned to the geomembrane (i.e. the beam element) was 117 MPa, the yield tensile strength of the geomembrane was assumed to be

23 kN/m based upon typical values for 1.5 mm thick HDPE geomembranes (GSE 2010). The beam element was pinned at both ends, as recommended by Fowmes et al. (2005).

Table 8-1 Ore and foundation material properties

Layer	Depth	Unit weight	Shear wave velocity	Poisson's ratio
Ore Layer I	0-19.4	19.0	350	0.25
Ore Layer II	19.4-30	19.0	375	0.25
Ore Layer III	30-50	19.0	400	0.25
Rock	50-∞	20.0	700	0.25
Equivalent	50-51	0.16	1365.5	
Equivalent	50-51	9.7	1421.96	

In some of the analyses, interface elements were attached to the top and bottom of the beam element were employed to model the geomembrane / foundation soil and geomembrane / leachate collection layer interfaces. However, no low permeability soil layer beneath the geomembrane was included in the model and the leachate collection layer on top of the geomembrane was ignored in the analyses to simplify the model. Therefore, for the analyses described herein, the upper interface was assigned an interface shear strength represented by a friction angle of 20 degrees $(\phi = 20^o)$ and the lower interface was assigned an interface shear strength represented by a friction angle of 15 degrees $(\phi = 15^o)$. The shear and normal stiffness of the interfaces were assigned a value 10 times greater than the corresponding stiffness in the adjacent elements to prevent the mesh from penetrating the beam element. The free-field bedrock strong ground motions selected for input to the analyses were converted to upward histories in the bedrock 90 m below the ground surface using the equivalent linear computer program SHAKE2000 for input to the 2-D analyses. The quiet boundary condition in FLAC 6.0 was employed at the bottom and the sides of the numerical model to absorb the reflected seismic motion (instead of reflecting the downward propagating seismic waves back into the model).

The ore in the FLAC analyses was treated as a nonlinear geo-material using the equivalent linear model. An equivalent linear material is characterized as a visco-elastic material with a constant linear elastic shear modulus and a constant fraction of critical damping ratio. The modulus and damping ratio assigned to each element (or mesh zone) depends upon the peak shear strain in the element. The behavior of the ore under cyclic loading was based upon the equivalent linear damping curve for gravel. FLAC uses a backbone curve and the Masing criterion to model cyclic behavior with hysteretic damping. Therefore, in developing equivalent linear properties for numerical analysis the modeler must decide whether it is more important to match the damping curve or the modulus reduction curve (since both cannot be satisfied simultaneously). Figure 8-2 (a) compares the mean, mean plus one standard deviation, and mean minus one standard deviation damping curves for gravel from Rollins et al. (1998) to the damping curve based upon the backbone curve that gives the best fit to the Rollins et al. (1998) modulus reduction curve and best-fit damping curve established by varying the backbone curve. Figure 8-2 (b) presents the mean, mean plus one standard deviation, and mean minus one standard deviation modulus reduction curves for gravel from Rollins et al. (1998) and the best fit modulus reduction developed by varying the backbone curve to give the best fit to the Rollins et al. (1998) modulus reduction curve and the modulus reduction curve established using the backbone curve for the best fit damping curve. The best fit damping curve and the associated modulus reduction curve were used in the 2-D non-linear (FLAC) analyses described in this chapter.

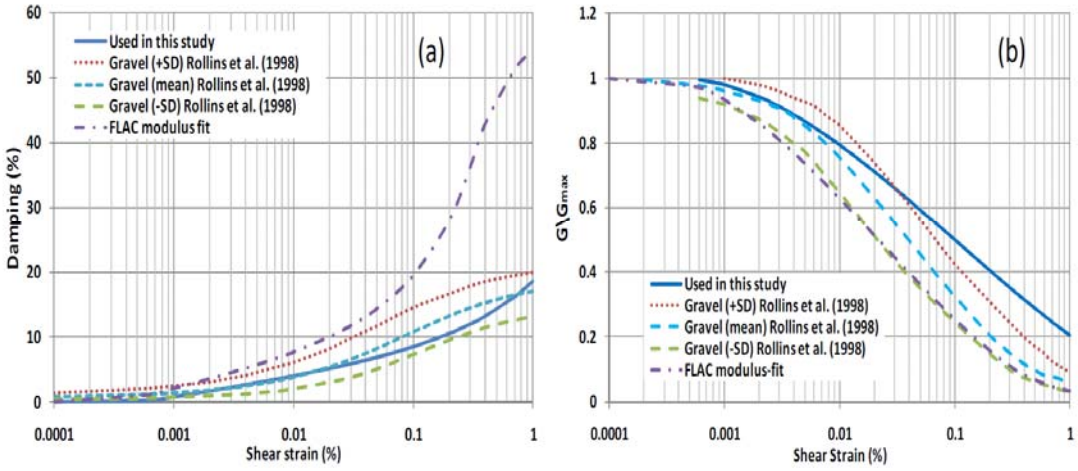

Figure 8-2 Comparison of (a) damping and (b) modulus reduction curves used in this study to Rollins et al. (1998)

8.3 1-D Equivalent Linear Analyses

In the1-D equivalent linear analyses, a representative vertical column through the ore pile was subject to analysis. Each layer within the column is characterized as a strain-dependent equivalent linear material. Shear deformations are continuous across layer boundaries, prohibiting explicit consideration of slip at an interface. However, Yegian et al. (1998) proposed a procedure to model slip at a geosynthetic interface in a 1-D equivalent linear analysis. The procedure proposed by Yegian et al. (1998) called for use of an "equivalent layer" of unit thickness with 0.16 kN/m^3 unit weight, a fraction of critical damping of 0.45, and an equivalent shear modulus curve obtained from back analysis of shaking table tests using a rigid block on a plane with geosynthetic interface. Yegian et al. (1998) proposed different initial shear modulus values for the "equivalent layer" (G_{max}) depend on the interface shear strength. For a HDPE/geotextile interface a value of 36σ was recommended for initial shear modulus of the "equivalent layer"

(G_{max}), where σ is the normal stress on top of the liner. Yegian et al. (1998) found the dynamic friction coefficient of the HDPE/geotextile interface he tested to be about 0.26, equivalent to an interface friction angle of 15 degrees.

Figure 8-3 (a) shows the 1-D cross section used to represent a 50 m high heap leach pad in the equivalent linear analysis. The ore and foundation material properties used in the study are summarized in Table 8-1. Figure 8-3 (b) shows the 1-D cross section used to represent a 50 m high heap leach pad in the equivalent linear analysis with a unit thickness equivalent layer represents the interface according to Yegian et al. (1998) procedure.

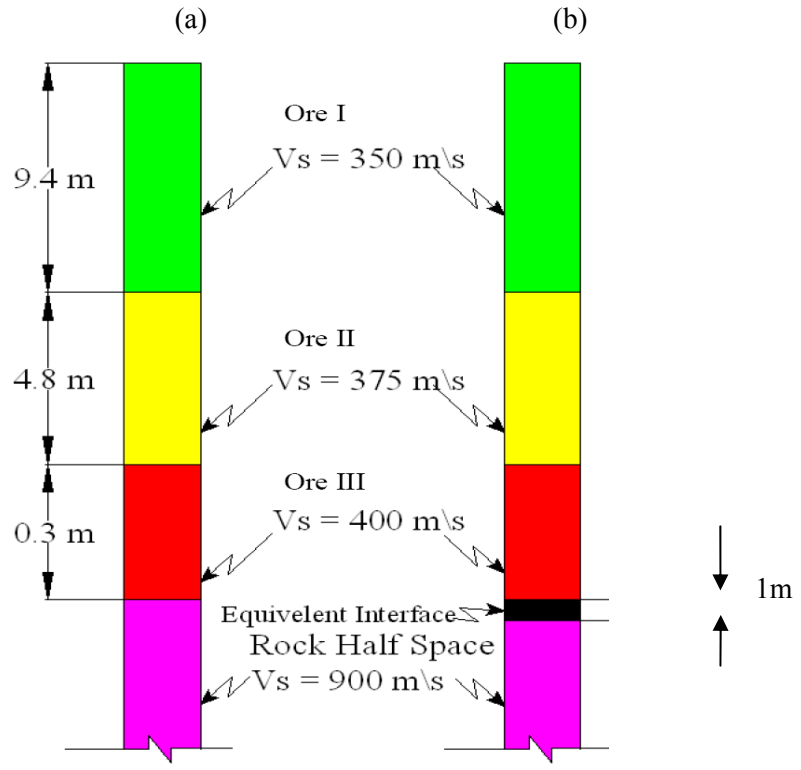

Figure 8-3 1-D profile used in the analysis a) no liner included b) including a liner layer

8.4 Nonlinear 1-D Time Domain Analysis

1-D non-linear time domain analyses of seismic response were conducted using the computer program D-MOD2000 (Matasovic**,** 2010). Like the 1-D equivalent linear analyses, the 1-D non-linear analyses analyze a representative vertical column through the ore pile. D-MOD2000 uses the MKZ constitutive model (Matasovic and Vucetic 1993; 1995) to define an initial backbone curve (which can be fitted to match an equivalent linear backbone curve) and to describe unloading and reloading (in a manner that can be fitted to an equivalent linear damping curve with the addition of a constant viscous damping. As described by Kavazanjian and Matasovic (1995), a thin soil layer with shear strength equal to the interface shear strength of the liner was used to model slip at the liner interface in the D-MOD2000 analyses. For comparison purposes, the stress-strain behavior of the equivalent layer was represented by the linear elastic-perfectly plastic constitutive relationship shown in Figure 8-4, with the same elastic modulus used for the interface in the FLAC 6.0 analyses and a shear strength characterized by the interface friction angle of 15 degrees. The 1-D column analyzed in this manner is shown in Figure 8-3 (b). 1-D non-linear analyses were also conducted without the weak soil layer for comparison purposes. The 1-D column used for the 1-D nonlinear analysis without employing the interface is shown in Figure 8-3 (a).

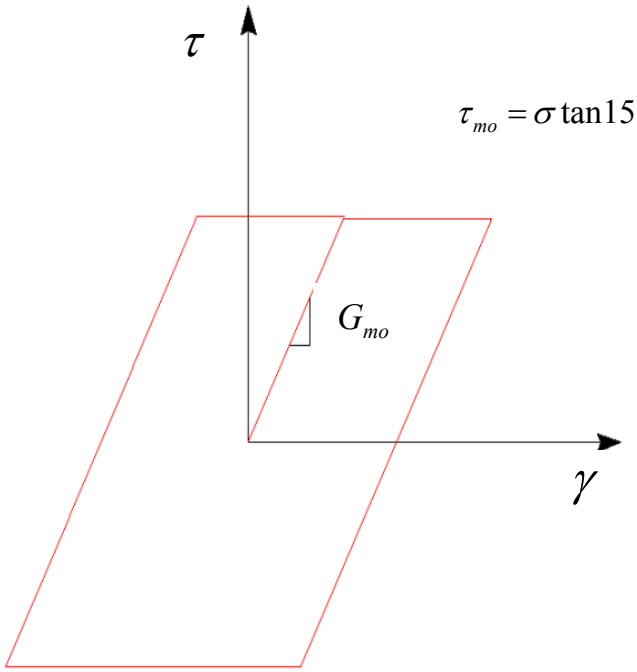

Figure 8-4 Stress strain curve used in D-MOD2000 to represent the interface behavior

8.5 Strong Motion Records

Three pairs of strong motion records from earthquakes of moment magnitude from 6.4 to 7.4 were used in this analysis. Each pair of records was scaled to a different PGA. PGA values of 0.25g, 0.45g and 0.6g were employed to investigate the influence of PGA on the seismic response. The 0.25g PGA was employed corresponding to the 0.26 friction coefficient of the interface with a friction angle of 15 degrees, so that there was no slip at the interface. The higher PGA values were used to study the effect of slip at the interface on seismic response. Table 8-2 shows the characteristics of the six records used in the analysis.

Table 8-2 Characteristics of the strong earthquake records used in the analysis

Earthquake	Record	Moment Magnitude, M_w	PGA (g)
Coalinga (1983)	Pleasant Valley P.P., YARD, 045	6.4	0.6
Loma Prieta (1989)	LGPC, 090	6.9	0.6
Imperial Valley (1979)	2316, Bonds Corner, 140	6.5	0.45
Kobe (1995)	Kakogawa, 000 (CUE)	6.9	0.45
Landers (1992)	Joshua Tree, 090	7.3	0.25
Tabas (1978)	Iran, 9102 Dayhook, Ln.	7.4	0.25

8.6 Acceleration Response Spectra

8.6.1 **2-D nonlinear FLAC 6.0 analyses**

The three configurations shown in Figure 8-1 were loaded with the six earthquake records presented in Table 8-2. Figure 8-5 (a) to (d) compares the acceleration response spectrum (ARS) from the 2-D nonlinear analysis for a point in the middle of the top deck of the leach pad model from case III, where there is no interface, to case I (interface element no beam element) for the four earthquake records used in this comparison. Figure 8-5 (a) shows the comparison for the Coalinga (1983) earthquake input motion. At long periods (greater than 1 sec) the interface shows no effect on the spectral response but in the vicinity of the resonant period of the ore body (at around 0.5 s) the spectral response in case I is lower than in case III. At short periods (periods less than 0.1 s) the spectral acceleration is similar for both cases. Figure 8-5 (b) shows the comparison for the Loma Prieta (1989) earthquake input motion. At long periods (greater than 1.0 s), the interface shows no effect on the spectral response but in the vicinity of the resonant period of the ore body the spectral response in case I is lower than in the case III at periods (between 0.2 and 0.1 s), the spectral acceleration in case I is interestingly higher

than case III where there no interface elements were used. Figure 8-5 (c) shows the comparison for the Tabas (1978) earthquake input motion. Figure 8-5 (c) shows small differences in the response spectra except at around a period of 0.2 s, where case I gives a higher spectral acceleration than case III. Figure 8-5 (d) shows the comparison for the Landers (1992) earthquake input motion. Figure 8-5 (d) shows small differences in the response spectra except in the vicinity of the resonant period of the ore body (0.5 s), where the spectral response for case I is lower than for case III. In Figure 8-5 (a) and (b) the effect of slip at the liner interface is more pronounced due to the higher PGA of the input motion. In Figure 8-5 (c) and (d), the acceleration response spectra are very similar because the PGA of the input motion is very close to the interface friction coefficient at the interface. One important observation from the results shown in Figure 8-5 is that introducing the interface element (case I) into the model did not affect the PGA at the top deck of the leach pad.

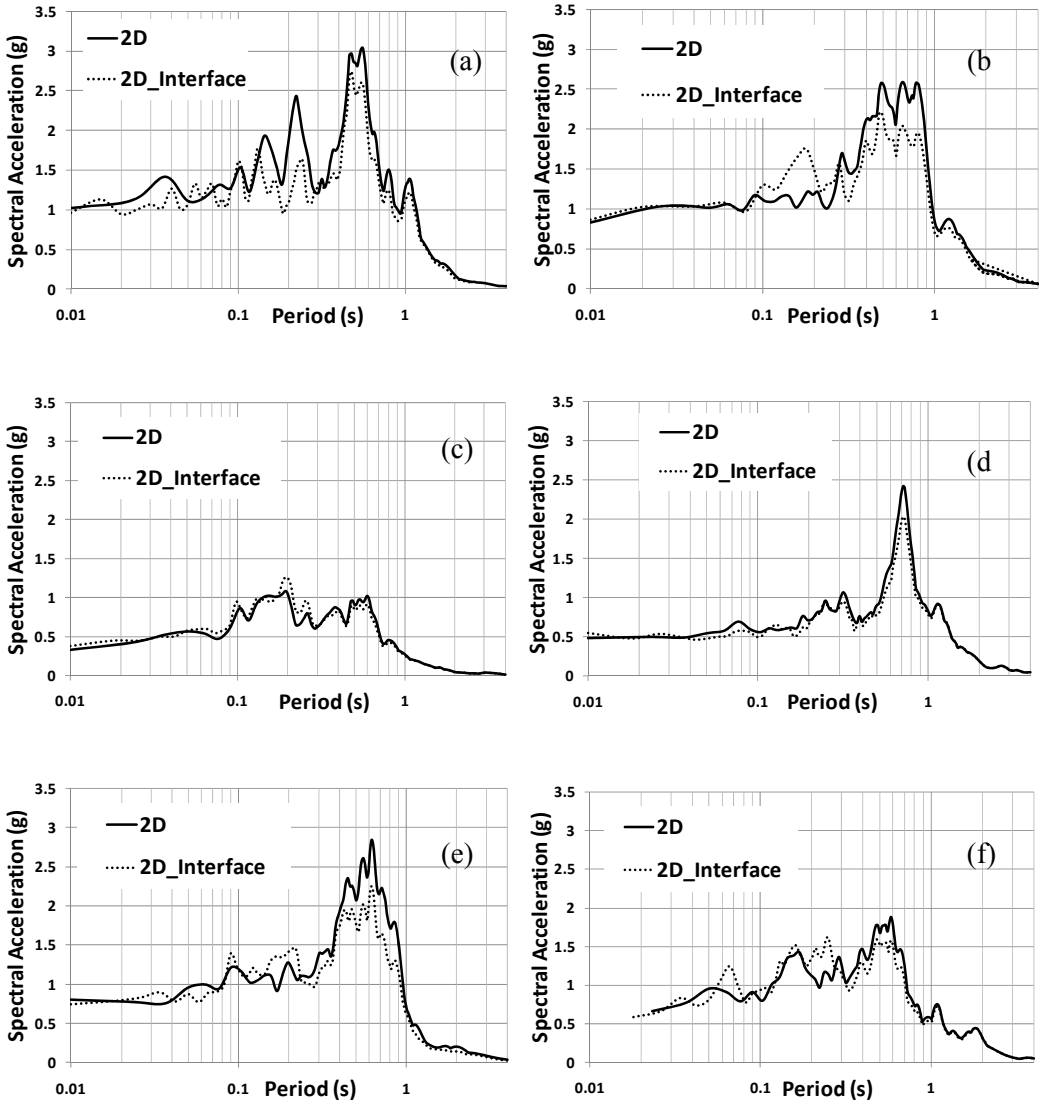

Figure 8-5 ARS on the top deck from 2-D analysis for Case I and Case III (a) Coalinga (1983), (b) Loma Prieta (1989), (c) Tabas (1978), (d) Landers (1992), (e) Imperial Valley (1979) and (f) Kobe (1995)

Figure 8-6 (a) and (b) compares the ARS from the 2-D non-linear analysis for a point in the middle of the top deck of the leach pad model for case I, where there a single interface is used to model the liner, to the ARS for the same point for case II, where the liner was modeled as a beam element with interface in both sides. Figure 8-6 (a)

represents the comparison for the Coalinga (1983) earthquake input motion. At long periods (greater than 1 sec) the response is identical but, at short periods (periods less than 0.1 s) the spectral acceleration shows some differences. Figure 8-6 (c) to (f) also show identical response at long periods (greater than 1 sec) the response but some differences at short periods (periods less than 0.1 s) in the spectral acceleration. In Figure 8-6 (b) the comparison for the Tabas (1983) earthquake record, the spectral response is almost identical over the entire range of spectral periods.

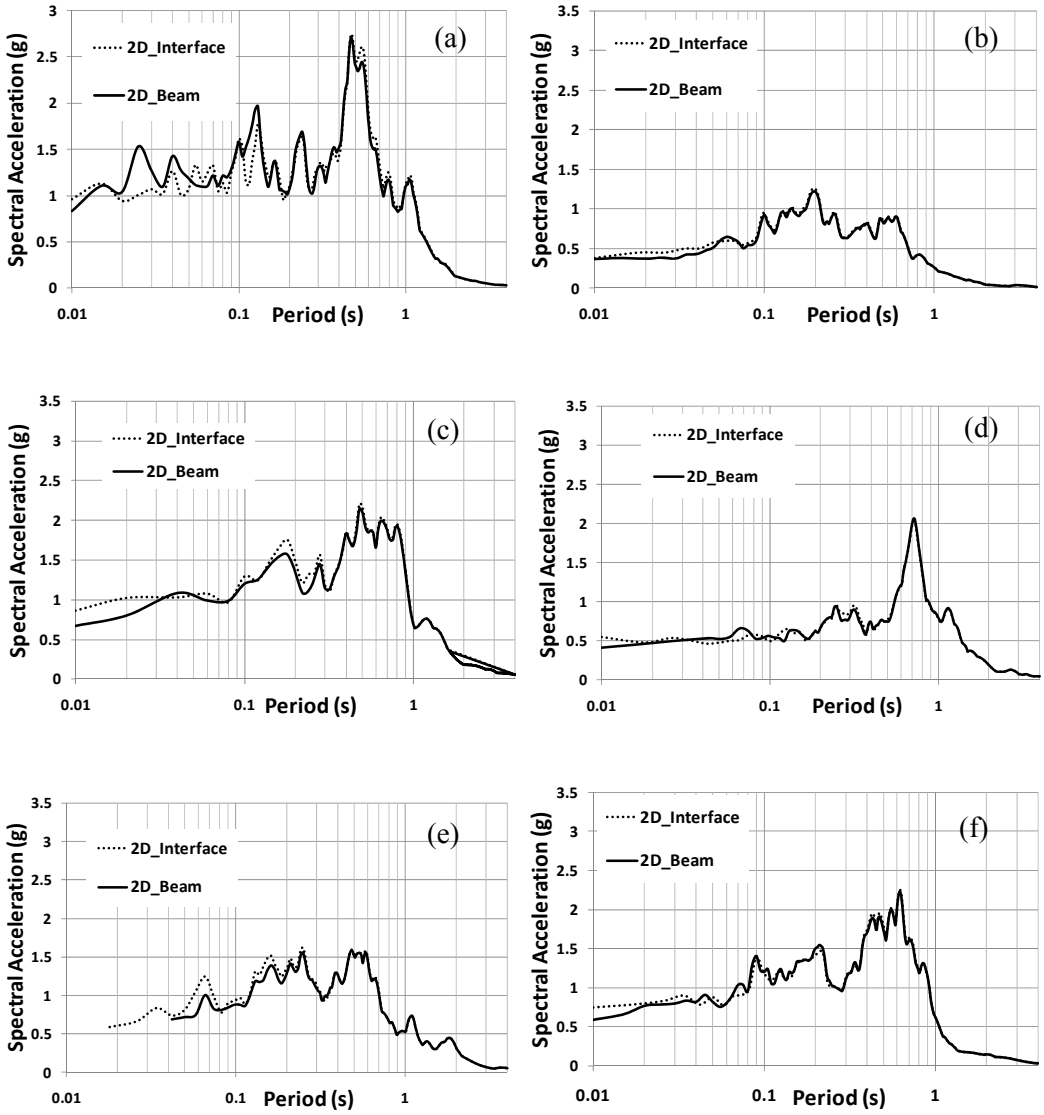

Figure 8-6 Comparison of ARS on the top deck from nonlinear 2-D analysis from Case I and Case II (a) Coalinga, (b) Tabas (1978), (c) Loma Prieta (1989), (d) Landers (1992), (e) Kobe (1995) and (f) Imperial Valley (1979).

8.7 1-D Equivalent Linear and Nonlinear Analyses

The two configurations shown in Figure 8-3 were loaded with the six earthquake records presented in Table 8-2 using the equivalent linear computer code SHAKE2000 (Ordonez, 2008). The two configurations presented in Figure 8-3 were also loaded with the six earthquake records shown in Table 8-2 using the nonlinear computer code D-MOD2000 (Matasovic, 2010). Figure 8-7(a) to (d) compare the ARS at the top of the column from the 1-D non-linear analysis with and without a weak layer at the base to simulate liner response to the ARS from the equivalent linear analysis without consideration of the liner and using the method of Yegian et al. (1998) to consider liner. For the cases where the impact of the liner is ignored (Column 3a), the ARS from the 1-D nonlinear analysis and the1-D equivalent linear analyses are identical at long periods (greater than 0.3 sec). However, at shorter periods the 1-D nonlinear spectral accelerations are generally higher than the 1-D equivalent linear values. For the cases where the impact of the liner is considered the models that consider the presence of the liner generally result in a lower PGA when the input motion PGA is high enough to induce slip at the interface, as shown in Figure 8-7 (a) to (c). However, the only the Kobe record Figure 8-7 (c) provides a substantial lower PGA when slip is considered in the 1-D analyses, only for nonlinear D-Mod 2000 analyses. In Figure 8-7 (d), where the input motion PGA is not high enough to induce slip at the interface result, the PGA at the top of the column is similar to the PGA whether or not an interface layer is employed.

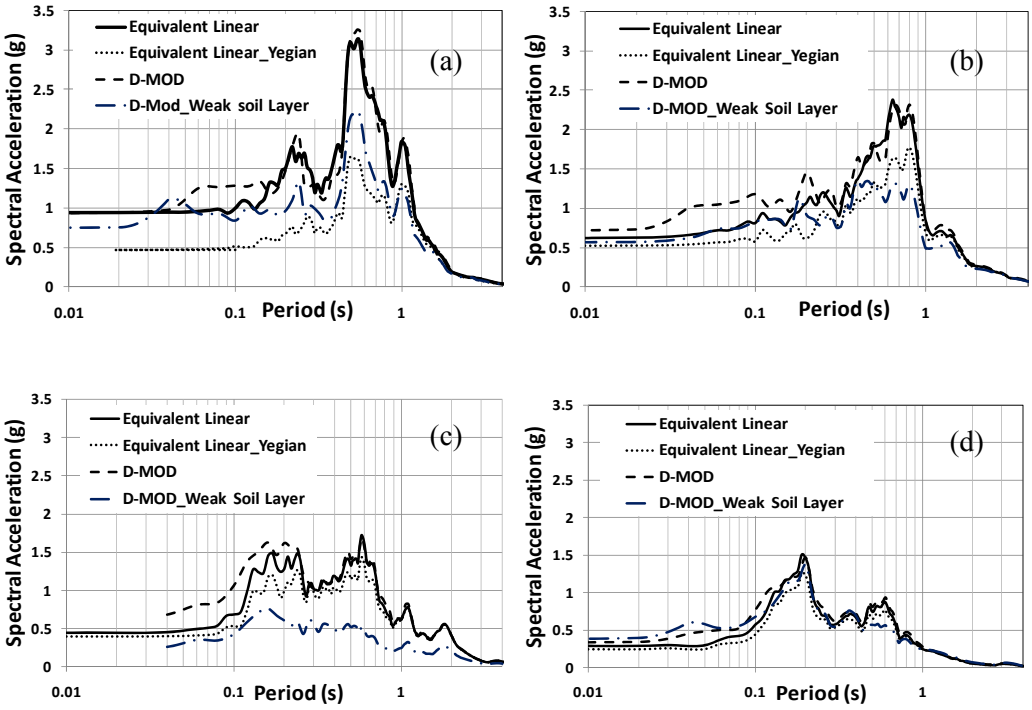

Figure 8-7 Comparison of ARS from 1-D analyses with and without liner elements (a) Coalinga (1983), (b) Loma Prieta (1989), (c) Kobe (1995), and (d) Tabas (1978)

8.8 Comparison between the 1-D Response Spectra and 2-D Response Spectra

Figure 8-8 (a) to (f) compares the (ARS) from the 2-D non-linear analysis for a point in the middle of the top deck to the ARS for the top deck (i.e. at the top of the column) from the 1-D equivalent linear analysis and nonlinear analyses for cases with and without consideration of the liner interface.

The 1-D models that include consideration of the element consistently give the lowest response, though in Figure 8-8 (f) (Tabas record scaled to 0.25 g) there is no significant difference among any of the analyses. Furthermore, the equivalent linear model that includes an interface (the Yegian et al. (1998) model) always underpredict the response at the high frequencies, including the PGA at the top of the column. This result

is consistent with the finding of Rathje and Bray (2000), who found that the response at the top of the landfill is not significantly modified by the sliding episodes at the base liner interface is the sliding displacements are maintained below a certain displacement limit. The 2-D model without an interface tends to give the greatest spectral response. However, the 2-D interface model and the 1-D non-linear models occasionally have higher spectral accelerations than the 2-D model without an interface.

8.9 Seismic Deformation Behavior

8.9.1 Permanent deformation from 2-D analyses

Permanent deformations calculated in the 2-D FLAC 6.0 analyses at four different locations (A, B, C and D) for the case I model (a single interface to represent the liner) are shown in Table 8-3 (see Figure 8-1 for the point locations). Point A represents the heel of the leach pad while point B represents the toe. Point C represents the point at the center of the leach pad and point D is in between point B and C. The calculated permanent displacements at the center of the leach pad (points C and D) were negligibly small in all cases. However, except for the Tabas record, the analyses consistently show extension at the heel of the leach pad and compression at the toe. The results for case II (using the beam and two interfaces to model the liner) are similar (with minor differences) to the results reported in Table 8-2 for the Case I (using single interface to model the liner).

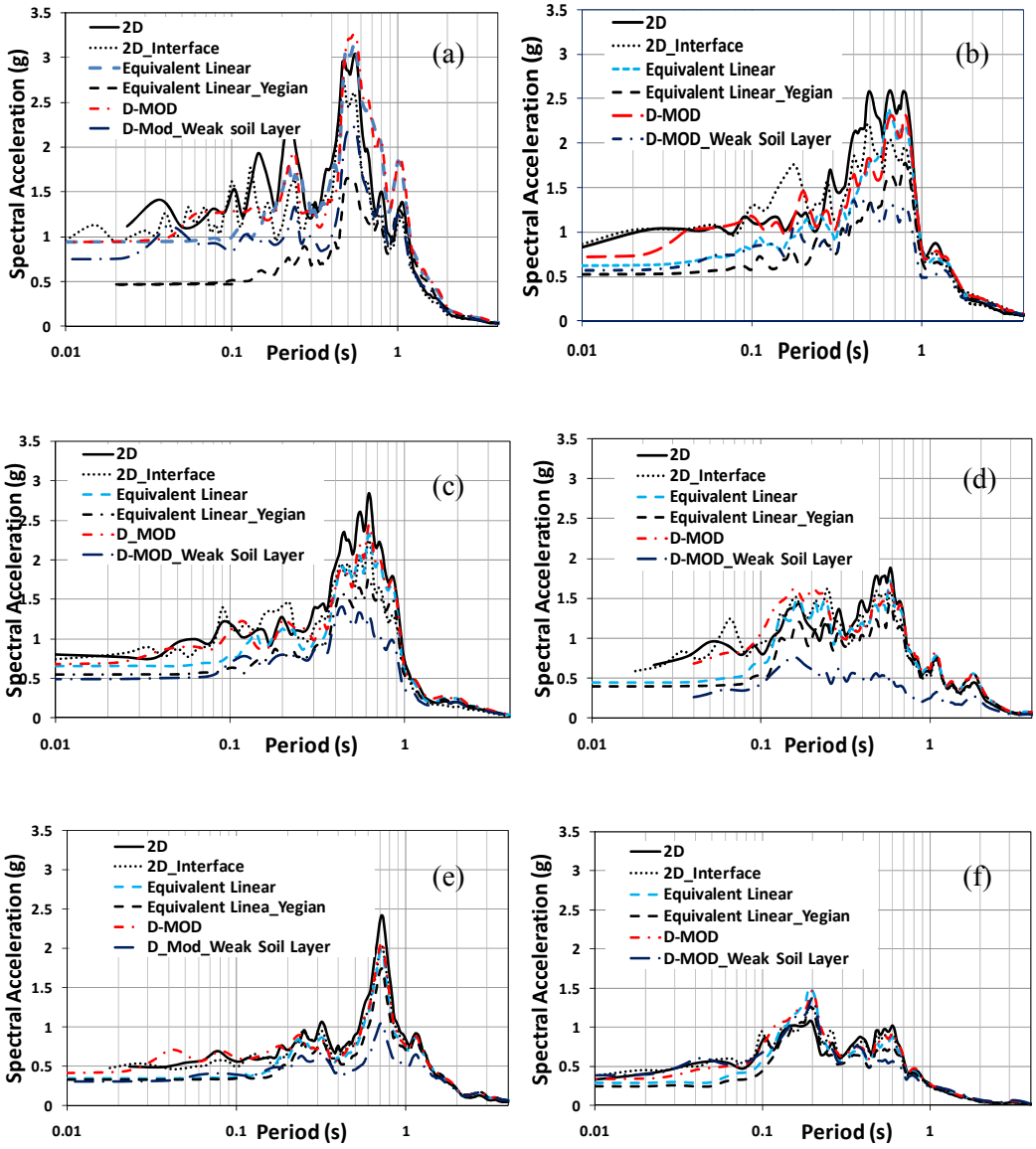

Figure 8-8 ARS at center of the top deck (a) Coalinga, (b) Loma Prieta (1989), (c) Imperial Valley (1979), (d) Kobe (1995), (e) Landers (1992) and (f) Tabas, Iran (1978)

Table 8-3 Permanent Deformation at the geosynthetic liner interface

Q Motion	Calculated permanent seismic displacement (cm)				
	2-D FLAC 6.0 analysis (Case I)				Decoupled (Newmark) analysis
	A	B	D	C	
Coalinga (1983)	-105	167	16	1.5	64.0
Loma Prieta (1989)	-108.9	154	19.3	4.7	125.32
Imperial Valley (1979)	-97.6	120	13.5	3.2	34.6
Kobe (1995)	-77.5	121	4.07	0.23	25.53
Landers (1992)	-130	207	3.7	0.0	46.4
Tabas (1978)	-13.7	23	0	0	0.936

Note: For location of points A, B, D and C refer to Figure 8-1.

8.10 Newmark Displacements from 1-D Analyses

A conventional decoupled Newmark seismic deformation analysis was conducted using the 1-D equivalent linear analysis results (with no interface layer) for comparison to the results of 2-D analyses. The decoupled procedure described by Bray et al. (1995) for seismic analysis of lined landfills was employed. First, a limit equilibrium analysis was used to determine the yield acceleration of the ore mass / liner system using SLIDE 5.0 (Rockscience 2005). Next, the time history of shear stress at the liner level from the SHAKE2000 equivalent linear analysis was converted to an average acceleration time history for the ore mass by dividing the shear stress by the total normal stress acting on the liner. Excursions of one side of the average acceleration time history above the yield acceleration were then double-integrated (using Y-Slip subroutine in the SHAKE2000 program) to calculate the permanent seismic displacement for the decoupled analysis method. A yield acceleration of 0.08 g was found for the leach pad model shown in Figure 8-1 (interface friction angle equal to 15 degrees). It is important to note that the

surfaces with the lowest yield acceleration were relatively small wedges at the toe of the ore mass. There is also a small wedge with low yield acceleration at the heel of the ore mass (explaining the large relative displacement at this location). Table 8-3 presents the results of the decoupled permanent seismic displacement analysis. The permanent deformation at the heel and toe from the 2-D FLAC 6.0 analyses were always bigger than the permanent deformation calculated in the decoupled Newmark analysis. The Newmark displacement at points A to B consistently exceeded the common employed allowable displacement limit of 15-30 cm for all records except Tabas record.

8.11 Geomembrane Stresses and Strains

A significant advantage of the 2-D (FLAC 6.0) analysis compared to the 1-D analyses is the ability to predict the stresses and strains in the geomembrane liner. Figure 8-9 shows the axial stresses and strains in the geomembrane predicted using the beam model (case II) for the liner, i.e., for a case where the lower interface shear strength was less than the upper interface shear strength, using the Landers (1992) input motion, i.e., the motion that produced the largest permanent displacement at the liner interface, possibly due to its long duration and long period content. The axial tensile strain at the end of the record (which was also the maximum axial strain) at the base liner for the case illustrated in Figure 8-9 is approximately 12.8%, which is below the yield strain of the liner but not an insignificant value.

Table 8-4 presents a summary of the maximum tensile and compressive forces and tensile and compressive strains in the liner system for the 2-D analyses for Case II using the six records in Table 8-3, where the interface friction angle below the geomembrane was five degrees less than interface friction angle above the geomembrane. The

maximum tensile strains and forces were approximately at a point in between points D and B. In all of the analyses, the maximum compressive forces and strains were at the toe of the leach pad, where the geomembrane element was pinned. Except for the aforementioned (Landers case), maximum tensile strains and forces are well below values at yield for the geomembrane despite calculated permanent displacement as high as 150 cm (5 to 10 times the generally accepted limiting value).

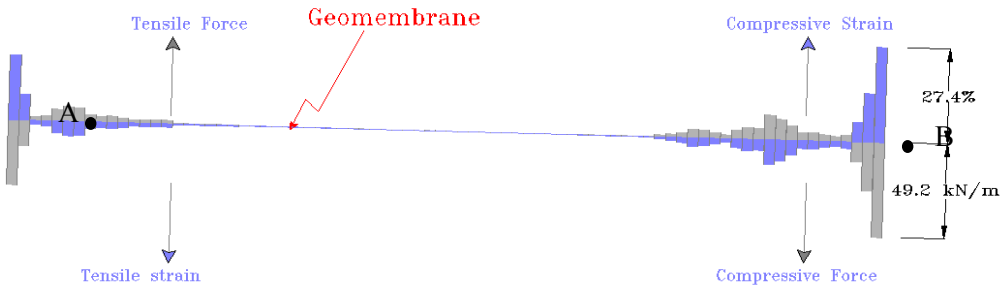

Figure 8-9 Axial strains and axial force in the base liner geomembrane calculated at the end of earthquake record (Landers (1992).

Table 8-4 Summary of stresses on the linear - results from time domain analysis

EQ Motion	Max Force and strain in developed GM			
	Tensile force (kN)	Tensile strain (%)	Compressive force (kN)	Compressive strain (%)
Coalinga (1983)	3.92	2.18	36.56	21.3
Loma Prieta (1989)	5.37	2.99	39.79	22.14
Imperial Valley (1979)	4.21	2.38	36.42	20.62
Kobe (1995)	3.98	2.21	33.57	18.67
Landers (1992)	7.096	12.76	49.22	27.38
Tabas (1978)	1.19	0.65	8.5	4.7

8.12 Summary

Site response analyses have been conducted using 2-D nonlinear and 1-D equivalent-linear and nonlinear analyses with and without liner elements. In the 2-D analyses the liner system was modeled: 1) solely as a weak interface; and 2) as a beam element with interface with interfaces on each side. In the 1-D non-linear analyses, the liner was modeled as weak soil layer. In the 1-D equivalent linear analyses, the liner was modeled using the recommendations of Yegian et al. (1998). Results of the analyses with the 2-D models show that there are only minor differences between the two means of modeling the liner (i.e. interface and beam element with two interfaces). However, the beam model allows for the explicit computation of the stresses and strains in the liner. The 2-D model without a liner element generally produced greater spectral acceleration than the model with a liner, though in one case the model with the liner produced higher spectral acceleration in the 0.1 to 0.3 second spectral period range. Comparison of the 2-D and 1-D models shows that: 1) based upon comparison to the 2-D analysis with slip elements (which are believed to be more accurate, but which are also more complicated to perform than 1-D analyses), use of a weak layers in the non-linear 1-D models is an improvement with respect to conventional 1-D analysis without slip elements; 2) additional calibration of the non-linear 1-D models is required to improve the accuracy of this type of modeling; 3) the 1-D equivalent linear model proposed by Yegian et al. (1998) is not reliable; and 4) as the calculated maximum permanent seismic displacement varies along the liner, 1-D models using a weak layer cannot fully account for the impact of slip at a liner interface on seismic response.

CHAPTER 9 SEISMIC ANALYSIS OF TYPICAL LANDFILL GEOMETRIES

9.1 Introduction

Two-dimensional (2-D) non-linear time-domain numerical models of the seismic response of two typical landfill geometries, a quarry-fill model and a canyon-fill model, were developed using FLAC 6.0. The model includes interface elements that account for slip at liner system interfaces and beam elements allow for computation of stresses and strains in liner system elements. Two different landfill configurations were analyzed in this study: a symmetrical configuration representative of a quarry fill and an asymmetrical configuration representative of a canyon fill. The geometry of the two models is presented in Figure 9-1. The performance of the liner system in terms of liner stresses, strains and permanent displacement from the 2-D FLAC6.0 analyses was compared to the liner system performance as evaluated in conventional 1-D decoupled seismic deformation analyses.

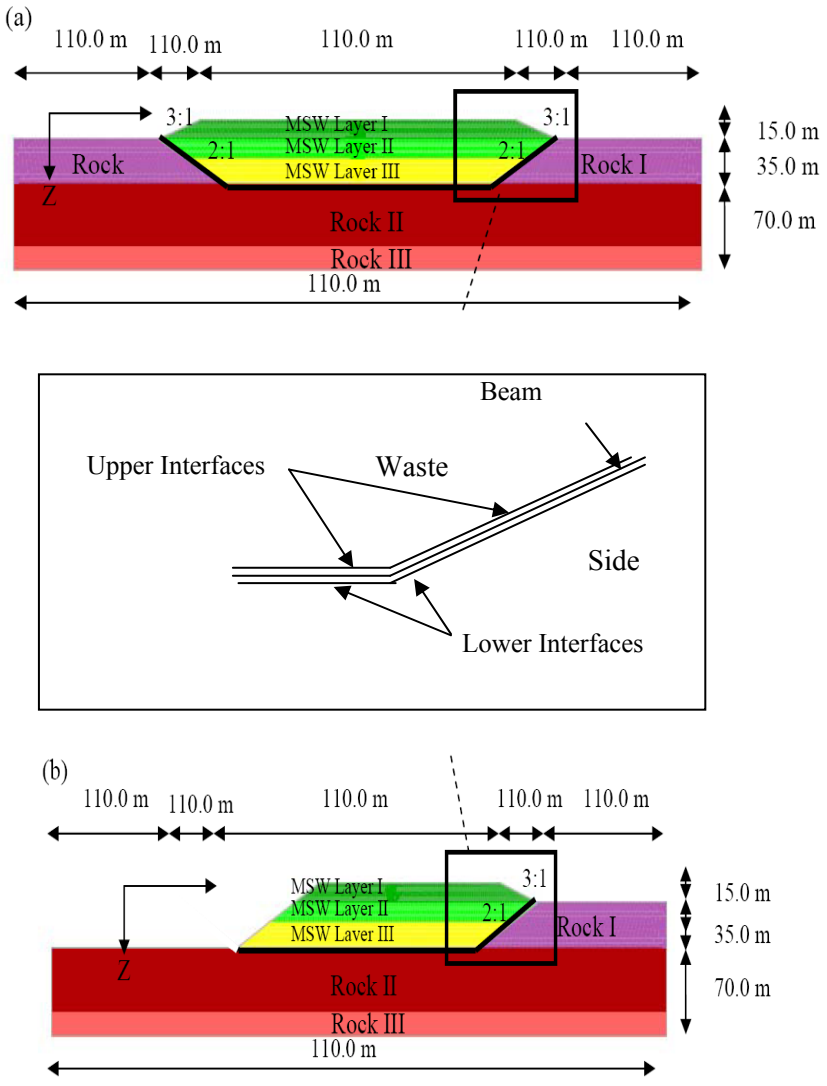

Figure 9-1 Landfill models used in the numerical analysis: (a) Quarry-fill model; (b) Canyon-fill model

9.2 Liner System Interaction Modeling

Interface elements were attached to each side of the beam element (geomembrane elements) to allow for relative displacement at the interface while accounting for the transfer of stresses through the lining system. This configuration also allows for different interface shear strengths on either side of a liner element. The interface elements were modeled as linear elastic-perfectly plastic materials. The Mohr-Coulomb criterion was used to model the interface shear strength. The ability of this type of model to accurately represent slip at the liner interface has been demonstrated by modeling of shaking table tests of a rigid block on both horizontal and inclined planes in Chapter 7. The beam element used to represent the geosynthetic materials was modeled as a linear elastic material with zero moment of inertia. The zero moment of inertia allows the geosynthetic element to buckle (wrinkle). The FLAC 6.0 software package has provisions to numerically handle cases when the moment of inertia is assigned a zero value, allowing the beam element to buckle.

9.3 Seismic Analyses

9.3.1 Non-Linear Analyses

The finite difference grid for the quarry-fill, shown in Figure 9-1 (a), consisted of 5808 mesh zones. The finite difference grid for the canyon-fill, shown in Figure 9-1 (b), consisted of 5398 mesh zones. An increased mesh density was employed around the side slope liner. Waste and foundation material properties used in this study are summarized in Table 9-1. The initial elastic modulus and unit weight assigned to waste were based upon shear wave velocities from Kavazanjian et al. (1996) and unit weights reported by

Zekkos et al. (2006). The waste was assigned a shear strength represented by cohesion of 24 kPa for the top 3 meters and a friction angle of 33^o at greater depths based upon the bi-linear strength envelope of Kavazanjian et al. (1995).

Table 9-1 Waste and foundation material properties

Layer	Depth (m)	Unit weight (kN/m^3)	Shear wave velocity (m/s)	Poison's ratio
Waste Layer I	0-15	16.0	240	0.33
Waste Layer II	15-30	16.5	285	0.33
Waste Layer III	30-50	16.9	345	0.33
Rock I	50-70	18	500	0.25
Rock II	70-100	18	700	0.25
Rock III	100-120	18	884	0.25

The waste was modeled as a linear visco-elastic material with Rayleigh damping and the foundation rock was modeled as a linear elastic material. The center frequency for the Rayleigh damping for the waste was established as the resonant frequency from an undamped 2-D linear elastic analysis of the model. A 1-D column in the center of the landfill was analyzed using equivalent linear analyses with SHAKE2000 (Ordonez 2010) to determine the strain-compatible damping ratio and elastic modulus for the waste in the FLAC analysis. Table 9-2 shows the damping ratio and the modulus reduction factor assigned to each waste layer in the FLAC analysis based upon the results of the SHAKE2000 analysis.

Table 9-2 Fraction of critical damping and modulus reduction for waste in the FLAC analyses

Layer	Damping Ratio	Modulus reduction factor
Waste Layer I	0.13	0.76
Waste Layer II	0.18	0.51
Waste Layer III	0.17	0.58

The elastic properties of the geomembrane beam element were assigned based upon typical properties for a 1.5 mm (60 mil) high density polyethylene geomembrane (GSE 2011). For simplicity, and due to the lack of any other information, the Young's modulus from manufacturer's literature (i.e. the tensile modulus under zero normal stress) was employed for both tension and compression, with no adjustment made for normal stress on the geomembrane. The beam element was pinned at the top of the slope to account for anchoring, as recommended by Fowmes et al. (2005). The Young's modulus assigned to the beam element was 117 MPa. The yield tensile strength of the geomembrane was assumed to be 23 kN/m based upon typical values.

Interface elements were attached to the top and bottom of the beam element to model the geomembrane / low permeability soil and geomembrane / leachate collection layer interfaces. However, the low permeability layer underlying the geomembrane and the leachate collection layer on top of the geomembrane were ignored in the analyses to simplify the model. To investigate the influence of the lower interface shear strength on the stresses and strains in the geomembrane, analyses were conducted using different interface shear strengths, as discussed subsequently. The shear and normal stiffness of the interfaces were assigned a value 10 times greater than (using the largest of the values of either side of the interface) the adjacent elements to prevent the mesh from penetrating the beam element. Bedrock motions selected for input to the FLAC 6.0 analysis were

converted to shear stress time histories at the base of the model using SHAKE2000. The quiet boundary condition in FLAC was employed at the bottom and the sides of the models to absorb the reflected seismic waves (instead of reflecting the seismic waves back into the model).

9.4 Equivalent Linear Analyses

The 1-D equivalent linear seismic response analyses used to develop the waste material properties and the shear stress time histories for input to the FLAC 6.0 analyses and required for the decoupled Newmark-type seismic displacement analyses were conducted using SHAKE2000. The equivalent linear site response analyses were conducted for representative columns extending from the bottom of the bedrock layer in the FLAC 6.0 models to the top deck of the landfill. As the waste thickness was the same in each landfill model, the same column was employed for the equivalent linear analysis of both landfill models. The properties presented in Table 9-1 were employed in the equivalent linear analyses along with the modulus reduction and damping curves for waste developed by Matasovic and Kavazanjian (1998) from back analysis of the OII landfill seismic response. Equivalent linear analysis does not consider interface behavior. Therefore, no interface properties were required for the equivalent linear analysis. Earthquake acceleration time histories were input as free field bedrock outcrop motions in the equivalent linear analyses.

9.5 Landfill Response to Seismic Loading

The landfill models shown in Figure 9-1 were loaded with the Pleasant Valley P.P. - YARD, 045 record from the 1983 moment magnitude (M_w) 6.7 Coalinga earthquake

scaled to a peak horizontal ground acceleration (PHGA) of 0.4 g. This "outcrop" acceleration-time history was converted to an "upward" rock motion using SHAKE2000. The corresponding "upward" shear time histories were applied at the base of the model in FLAC as the design ground motion (Mejia and Dawson 2006)

Figure 9-2 (a) compares the acceleration response spectrum (ARS) from the 2-D non-linear analysis for a point in the middle of the top deck to the ARS for the top deck from the 1-D equivalent linear analysis for the quarry-fill model. Figure 9-2 (b) makes the same comparison for the canyon-fill model. In both figures, Case A refers to an analysis in which the upper and lower interface shear strength were the same, with a friction angle of 20^{o} assigned to the base and a friction angle of 15^{o} assigned to the side slope. Case B refers to the case when the upper interface shear strength is higher than the lower interface shear strength, with a value of 15^{o} used for the lower interface friction angle on the base and 10^{o} used for the lower interface friction angle on the side slope (the upper interface friction angles were unchanged from Case A).

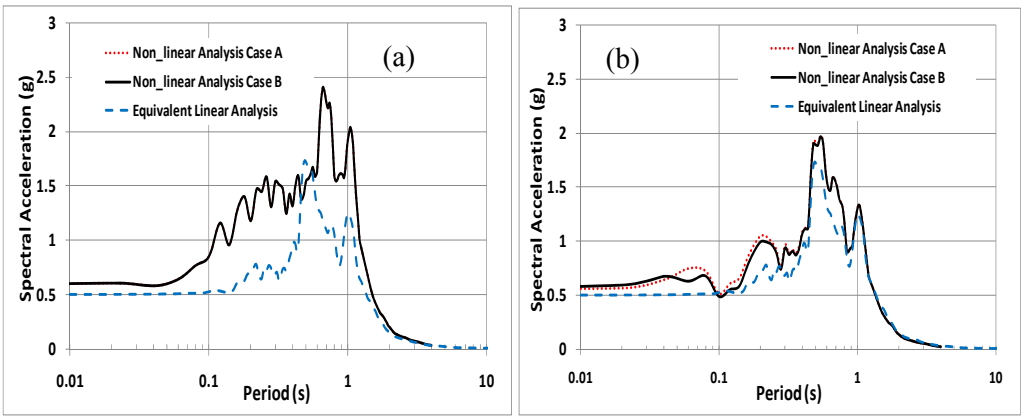

Figure 9-2 Acceleration response spectra on the top deck from non-linear and equivalent linear analysis (a) Quarry-fill model; (b) Canyon-fill model

For the quarry fill analysis, the ARS for the 2-D non-linear (FLAC 6.0) analysis shows significantly greater spectral response at short periods (periods less than 0.5 s) than the equivalent linear model and in the vicinity of the resonant period of the waste mass (at around 0.8 s). The ARS for the 2-D non-linear (FLAC) analyses for the canyon fill is remarkably similar to ARS for the 1-D equivalent linear (SHAKE2000) results. Interestingly, neither the quarry fill nor the canyon fill non-linear analyses showed the expected "base-isolation" effect, i.e. neither of the 2-D non-linear analyses shows a significant reduction in the peak ground acceleration due to slip at the liner interface. In fact, the spectral response of the canyon fill at short periods is significantly greater in the 2-D non-linear analysis than in the equivalent linear analysis. This is consistent with the behavior observed by Wartman (1999) in his analysis on the seismic response of geosynthetically lined slopes.

9.6 Geomembrane Forces and Strains

In total, six 2-D non-linear analyses were conducted. In all cases the input motion was scaled to 0.4 g. In two of the analyses, the interface strength was the same above and below the geomembrane and the tensile forces and strains in the geomembrane were minimal. Table 9-3 presents a summary of the maximum tensile forces and tensile strains in the liner system for the four 2-D non-linear analyses in which the interface strength differed between the top and bottom of the geomembrane. In analyses 1 and 3, the interface friction angle below the geomembrane was five degrees less than above the geomembrane for both the base and the side slope. In analyses 2 and 4, the weaker interface was above the geomembrane on the side slope but transitioned to below the geomembrane at the base. While there was little difference in the overall seismic

response, the tensile strain and the tensile force at point A were greater for cases 2 and 4 than in cases 1 and 3. In all cases, the maximum tensile forces and strains were at the crest of the landfill, where the geomembrane element was pinned, and were significantly below yield. Also, the strains and forces at point C (the toe of the side slope) were compressive at all cases.

Figure 9-3 shows the axial stresses and strains in the geomembrane predicted for one side of the quarry-fill model for the case where the lower interface shear strength was less than the upper interface shear strength (the liner response for the quarry-fill model is essentially symmetric). Only the Case A where the upper and lower interface strengths are different, is shown because when the upper and lower interface shear strengths were equal the stresses and strains on the geomembrane were very low. Figure 9-3 shows that there are compressive strains generated at the toe of the slope and on the base of the landfill for this case.

Table 9-3 Forces and strains in the liner from FLAC analysis

Side Slope Lower Interface angle (^{O})	Side Slope Upper Interface angle (^{O})	Base Upper Interface angle (^{O})	Base Lower Interface angle (^{O})	GM Tensile Force (kN/m) Point A	GM Tensile Strain (%) Point A
Quarry-fill model					
10	15	20	15	+3.09	+1.7
15	10	20	15	+3.49	+1.94
Canyon-fill model.					
10	15	20	15	+2.96	+1.6
15	10	20	15	+3.40	+1.8

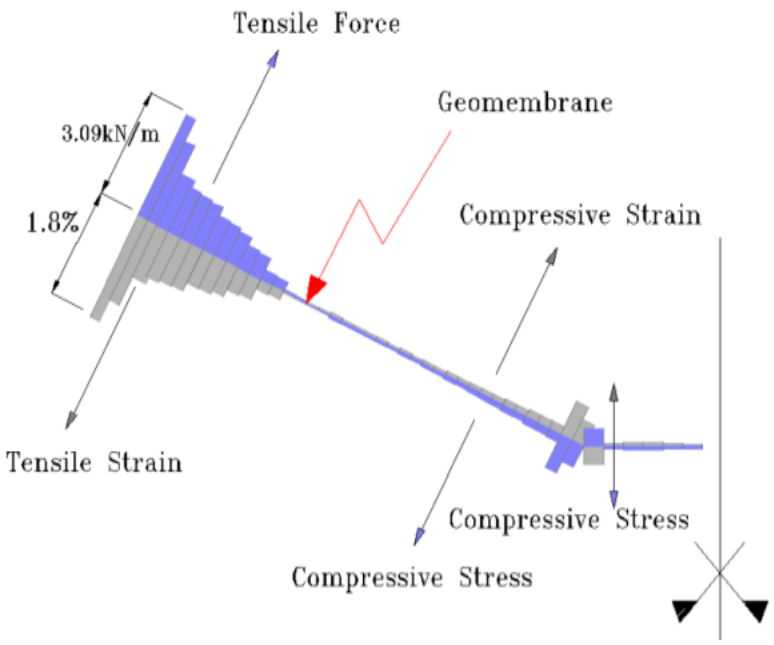

Figure 9-3 Axial strains and axial force at the end of the record in the geomembrane for the quarry-fill model

The behavior shown in Figure 9-3 is consistent with strains measured by Yazdani et al. (1995) in a 1.5 mm HDPE geomembrane side slope liner subject to waste settlement and downdrag over a period of three years in a landfill in Northern California. The axial tensile strain at the end of the record (which is also the maximum axial strain) in the side slope liner for the case illustrated in Figure 9-3 is approximately 1.8%, well below the yield strain of the liner.

Figure 9-4 shows the relative displacement between the geomembrane and the underlying foundation material at five points on the side slope and base of the landfill for the quarry-fill (Figure 9-4 (a)) and at six points for the canyon-fill (Figure 9-4 (b)). Points A through E are common to the two geometries. Point A is at the crest of the side slope, point B is at the middle of the side slope, and point C is the toe of the side slope. Point D is one half of the distance from the toe of the slope to the center of the base and

point E is in the center of the base. Point F is only applicable to the canyon-fill and is located at the toe of the waste. The maximum permanent displacement for the quarry-fill was at the top of the slope (point A) and was about 0.15 m. At mid slope, the quarry fill experienced about 0.06 m of permanent displacement but had a maximum transient relative displacement of about 0.09 m during the earthquake. The top of slope for the canyon-fill experienced a permanent displacement of about 0.11 m while the mid slope experience about 0.05 m in permanent displacement and a maximum transient displacement of 0.09 m for the canyon-fill. The maximum permanent displacements at point A-E in both models were equal to or less than the generally accepted allowable calculated displacement limits of 0.15 m to 0.3 m for geomembrane liners subjected to seismic loading. However, point F for the canyon-fill, located at the toe of the landfill, experienced a permanent displacement of about 0.81 m, exceeding the generally accepted allowable value, despite the fact that tensile strains and forces remained well below yield.

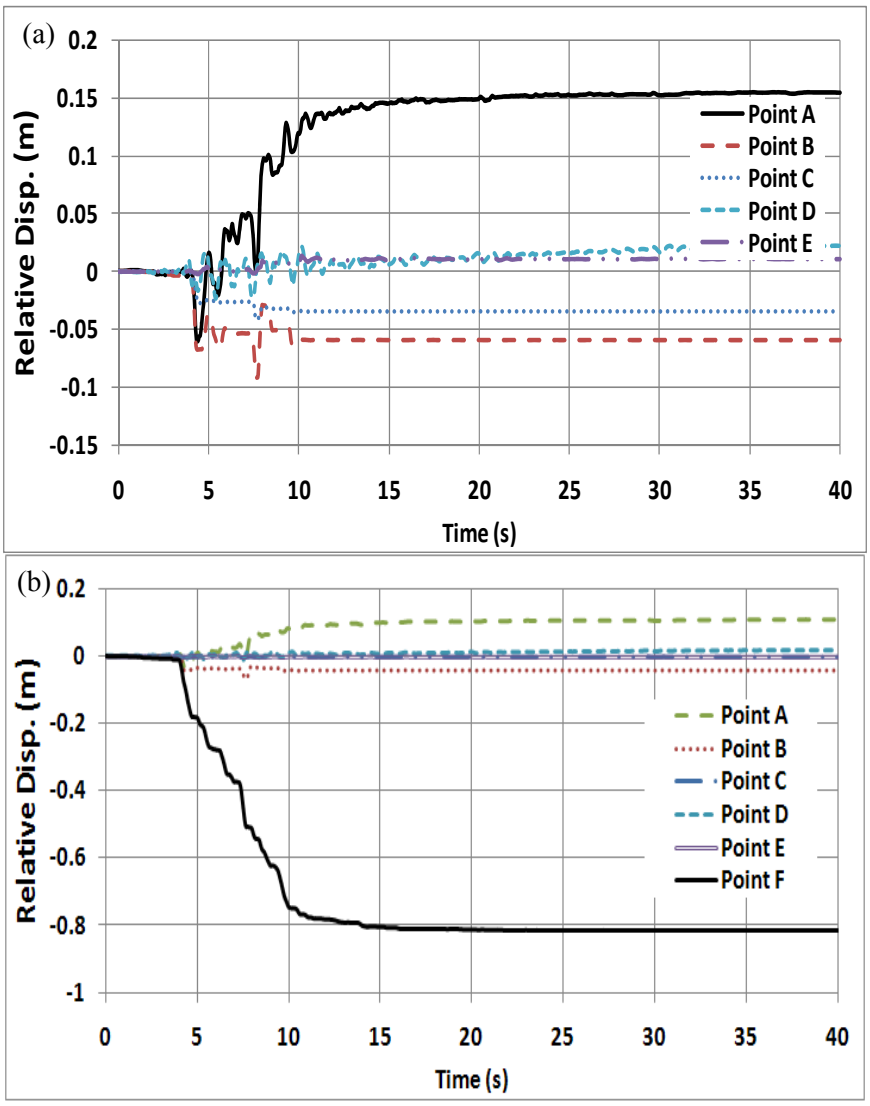

Figure 9-4 Displacement of waste relative to foundation rock (a) quarry-fill model; (b) canyon-fill model.

9.7 Decoupled Newmark Displacement Analysis

A conventional 1-D decoupled seismic displacement analysis was conducted for comparison to the results of 2-D nonlinear analysis. The decoupled procedure described by Bray et al. (1998) for seismic analysis of lined landfills was employed to evaluate liner performance in accordance with current practice. First, the time history of shear stress at the liner level from the SHAKE2000 analysis was converted to an average acceleration time history for the waste mass by dividing the shear stress by the normal stress acting on the membrane. Next, limit equilibrium analysis was used to determine the yield acceleration waste mass / liner system using SLIDE 5.0 (Rockscience 2005). A yield acceleration of 0.26 g was found for the quarry-fill and 0.1 g for the canyon-fill. Excursions of one side of the average acceleration time history above the yield acceleration were then double-integrated (using the Y-Slip subroutine in the SHAKE2000 program) to calculate the permanent seismic displacement for the decoupled analysis method.

Table 9-4 presents the results of the decoupled permanent seismic displacement analysis. The calculated permanent displacement for the quarry fill was negligibly small due to the relatively large yield acceleration. However, in the 2-D analysis a permanent displacement of 15 cm was calculated at the crest of the slope for the quarry-fill. The calculated permanent displacement of 7.2 cm for the canyon-fill from the decoupled analyses is similar to the displacement of 9 cm at the crest of the side slope calculated for the canyon fill in the 2-D analysis. However, the displacement at the toe of the waste for the canyon-fill calculated in the nonlinear analysis was 81 cm, significantly higher than the displacement calculated in the decoupled analysis.

Table 9-4 Decoupled (Newmark) displacement analysis summary

Quarry-fill	Canyon-fill
Permanent displacement (cm)	Permanent displacement (cm)
0.0	7.2

9.8 Summary

Two-dimensional non-linear numerical analyses have been conducted of the seismic response of idealized quarry-fill and canyon-fill landfills using interface elements that allow for slip at the geomembrane interface and computation of liner strains and forces. Response analyses were also conducted using conventional 1-D equivalent linear analysis. The analyses were conducted using a record from the M_w 6.7 Coalinga earthquake scaled to 0.4 g. Surprisingly, slip at the liner interface in the non-linear analyses did not significantly reduce the peak ground acceleration or the spectral response for either landfill configuration compared to the results of the equivalent liner analysis. The non-linear analyses indicated that the tensile forces and strains in the geomembrane were minimal when the interface shear strength was the same or greater on the bottom than on the top of the geomembrane. When the interface friction angle was five degree greater on the top than on the bottom of the geomembrane, the seismically-induced tensile stresses were still well within the allowable values. The permanent seismic displacement at the crest of the side slope from the non-linear analysis compared favorably to the calculated permanent displacement from a conventional decoupled analysis. However, the permanent displacement at the toe of the canyon fill was

significantly greater in the 2-D non-linear analysis compared to the decoupled analysis for both landfill configurations.

Additional analyses are required to determine if the findings reported herein are generally applicable to geosynthetically-lined landfills or are an artifact of the landfill geometry and earthquake ground motion used in these analyses. Furthermore, the tensile forces and strains calculated in this type of analysis must be added to static forces and strains induced in the liner by waste settlement and the impact of benches and interim anchorage for the geomembrane must be considered to determine if the geomembrane can withstand the seismic forces without damage.

CHAPTER 10 CALIBRATION OF MSW DYNAMIC PROPERTIES

10.1 Introduction

The ability to conduct an accurate seismic response analysis of a municipal solid waste (MSW) landfills depends to some extent upon reliable data on the strain dependent dynamic properties of the waste. Chapter 3 presented a summary of previous studies conducted to evaluate the dynamic properties of the MSW. Most of these studies employed data on the Operating Industries, Inc. (OII) landfill, perhaps the most studied landfill with respect to seismic response. In 1988, EPA installed three-component strong motion instruments at the base and top deck of the landfill. Inclinometers and survey monuments were also installed to monitor landfill deformations. The OII landfill is the only case history of a landfill subject to seismic shaking with actual strong motion records on and adjacent to the waste.

As part of predesign studies for closure of the OII landfill, the behavior of the OII solid waste when subject to earthquake-induced cyclic loading was extensively studied (Hushmand et al. 1990, Anderson et al. 1992, Kavazanjian and Matasovic 1995, Idriss et al. 1995, Matasovic et al. 1995, Matasovic and Kavazanjian 1998 and Augello et al. 1998). Matasovic and Kavazanjian (1998) presented results of field and laboratory testing to characterize cyclic behavior of the OII solid waste. These results include shear wave velocity, unit weight, and Poisson's ratio profiles from field testing and modulus reduction and damping curves developed using a combination of back analysis of strong motions recorded at the landfill and large-diameter cyclic direct simple shear laboratory tests on reconstituted solid waste specimens. Several other investigators also used back

analysis of strong motions recorded at the landfill to develop modulus reduction and damping curves for the OII waste (e.g. Idriss et al. 1995, Augello et al. 1998).

This chapter presents the results of back analysis of the recorded response of OII landfill to establish the dynamic properties of the waste for seismic analyses in FLAC 6.0.

10.2 Site Conditions

The OII landfill is located in southern California, approximately 16 km east of downtown Los Angeles (Figure 10-1). The landfill site was originally a sand and gravel quarry pit and was filled with solid waste over a 40-year period. There is no evidence that any subgrade preparation or liner installation took place prior to the disposal of solid waste at the site. California State Road 60 (the Pomona Freeway) divides the landfill into a relatively small level north parcel and the steep-slope 58-ha south parcel which is the subject of study in this chapter. The maximum thickness of solid waste on the south parcel is approximately 100 m. The top of the landfill ranges from 21 to 76 m above the ground surface (Matasovic and Kavazanjian 1998).

Figure 10-1 Aerial View of OII Landfill (Matasovic and Kavazanjian 1998)

10.3 Recorded Ground Motions

Two three-component strong motion instruments were installed at OII landfill site. The locations of the strong motion instruments are shown in the aerial view in Figure 10-1 and plan view presented in Figure 10-2. The first instrument labeled SS1 was installed adjacent to the base of the landfill, while the second instrument, labeled SS2, was installed on the top deck of the landfill. From their installation in 1988, Through April 1994, 34 earthquakes and aftershocks were recorded by these instruments at the OII site. The 34 events recorded at the OII site included both nearby small magnitude events and distant large magnitude events. Exclusive of the January 17, 1994 M_w 6.7 Northridge earthquake, the largest peak horizontal ground acceleration (PHGA) recorded at the top deck of the landfill was 0.10 g in the M_w 7.3 Landers earthquake of June 28, 1992 and the

largest PHGA recorded at the base of the landfill was 0.22 g in the M_w 5.0 Pasadena earthquake of December 3, 1988. The M_w 7.3 Landers earthquake was the largest magnitude event captured by the instrumentation at the site. The Northridge earthquake was the largest intensity earthquake recorded at the site. A PHGA of 0.25g was recorded at the top deck and a PHGA of 0.26 g was recorded at the base of the landfill in the M_w 6.7 Northridge event (Matasovic and Kavazanjian 1998).

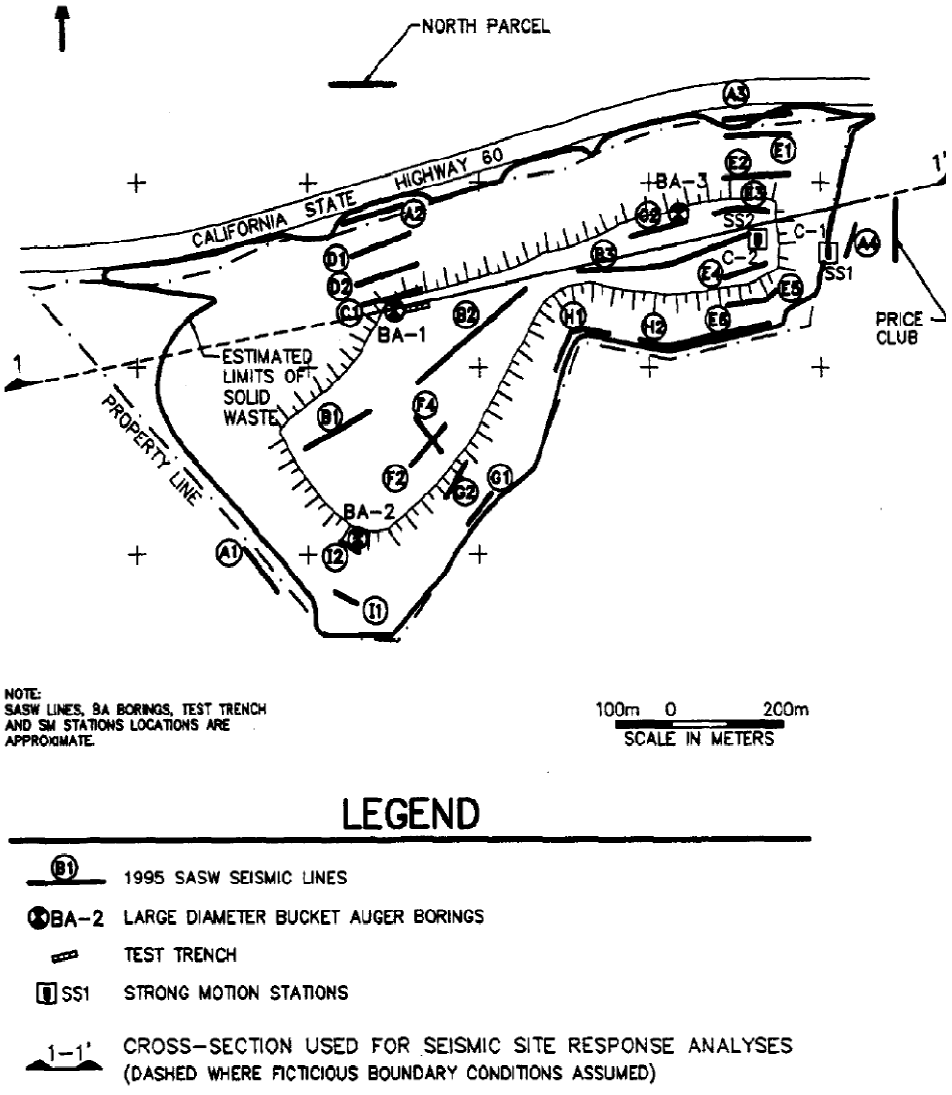

Figure 10-2 Plan view of the OII landfill showing the testing brings (Matasovic and Kavazanjian 1998)

A set of five strong ground motion acceleration time histories (accelerograms) were selected for use in this study for back analyses of the seismic response of the landfill based on the Matasovic and Kavazanjian (1998) selection criteria. Matasovic and Kavazanjian (1998) used an intensity criteria to select accelerograms for use in back analysis, where the intensity measures were the PHGA recorded at the top deck of the landfill, the energy content, and the duration of strong shaking of the east-west component of the ground motion. The recorded motions were provided to the author by Dr. Neven Matasovic of GeoSyntec consultants through personnel communication. The recorded acceleration response spectra used in the back analyses are presented in Figure 10-3 to Figure 10-7.

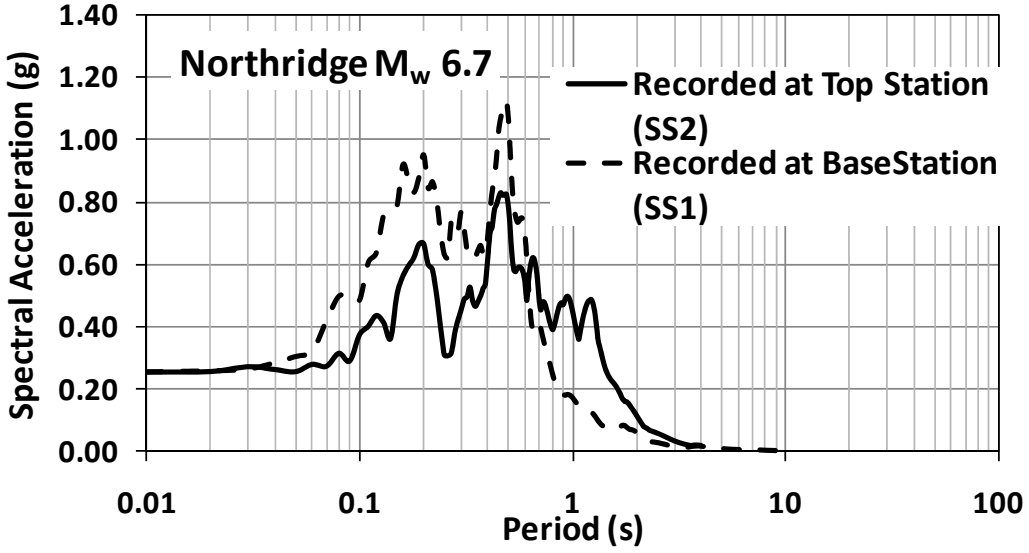

Figure 10-3 Acceleration response spectra for the recorded motion from the Mw 6.7 Northridge earthquake at OII landfill in the East-West direction

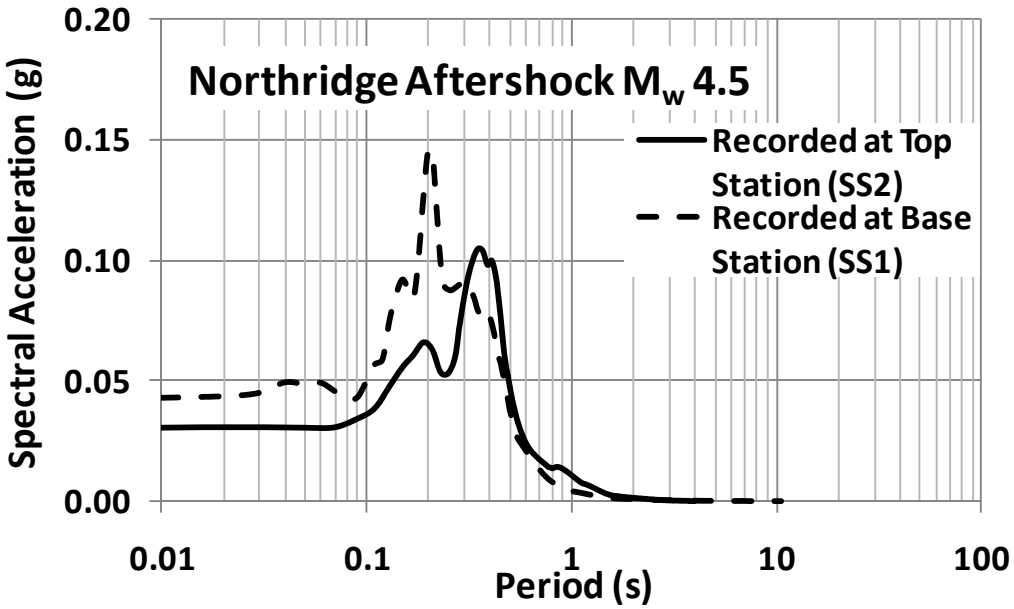

Figure 10-4 Acceleration response spectra for the recorded motion from the M_w 4.5 Northridge earthquake aftershock at OII landfill in the East-West direction

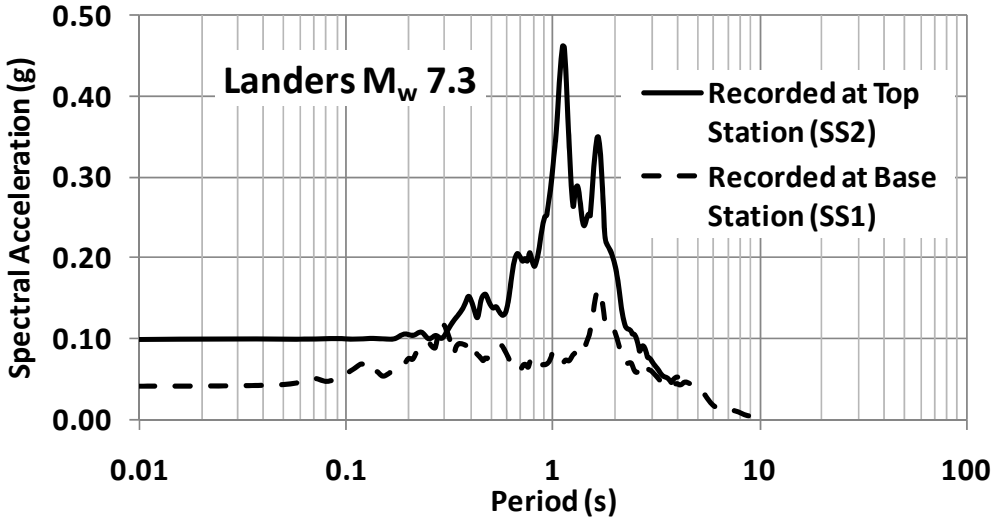

Figure 10-5 Acceleration response spectra for the recorded motion from the M_w 7.3 Landers earthquake at OII landfill in the East-West direction

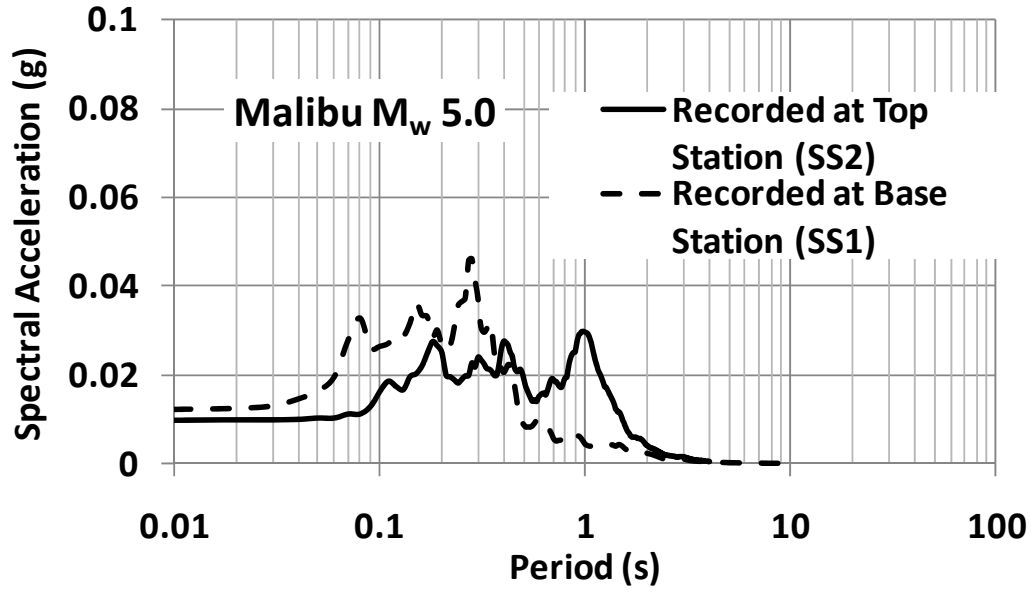

Figure 10-6 Acceleration response spectra for the recorded motion from the M_w 5.0 Malibu earthquake at OII landfill in the East-West direction

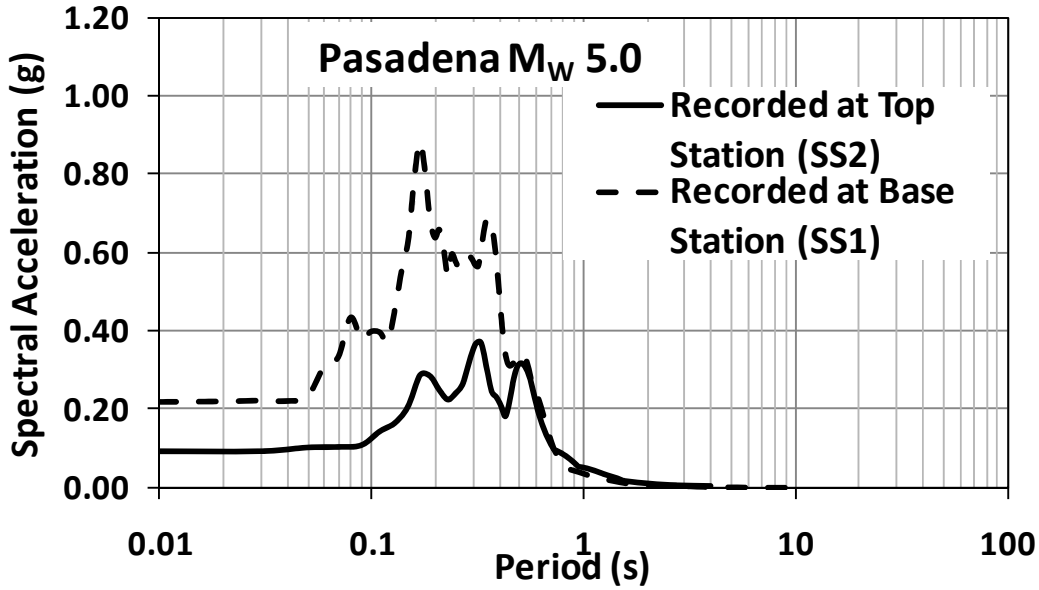

Figure 10-7 Acceleration response spectra for the recorded motion from the M_w 5.0 Pasadena earthquake at OII landfill in the East-West direction

10.4 1-D Deconvolution Analyses

Back analysis of the ground motions recorded at the OII landfill is complicated by the observation that the base station SS1 is located on compacted fill (not the bed rock) and therefore the base station records are not representative of free-field outcrop ground motion Matasovic and Kavazanjian (1998). The effect of the compacted fill on the free field ground motions at SS1 was evaluated using one-dimensional equivalent-linear deconvolution analyses to develop outcrop time histories suitable to use as input to the back analyses studies in the FLAC 6.0 finite difference model. Deconvolution analyses were done using SHAKE2000. As the back analyses the deconvolution analyses were one dimensional, the effect of topography was not considered in the analyses. Topographic effects were evaluated qualitatively by comparison of the response spectra for the motions predicted at SS1 in the two-dimensional finite difference back analysis to the response spectra of the recorded motions.

The idealized shear wave velocity profile for SS1 presented in GeoSyntec (1996), based upon the results of a downhole velocity survey at the location of SS1 was used in the deconvolution analysis. This shear wave velocity profile is presented in Figure 10-8. Unit weight, small strain shear modulus, and shear wave velocity profile used in the deconvolution analyses for the compacted fill, weak rock, and elastic half-space are presented in Figure 10-9. The Vucetic and Dobry (1991) modulus reduction and damping curves for a plasticity index (PI) of 15% were employed for the compacted fill as this soil was classified as low plasticity silty clay to clayey silt. The Shibuya et al. (1990) modulus reduction and damping curves for gravel were used for the weak rock at the base of the landfill.

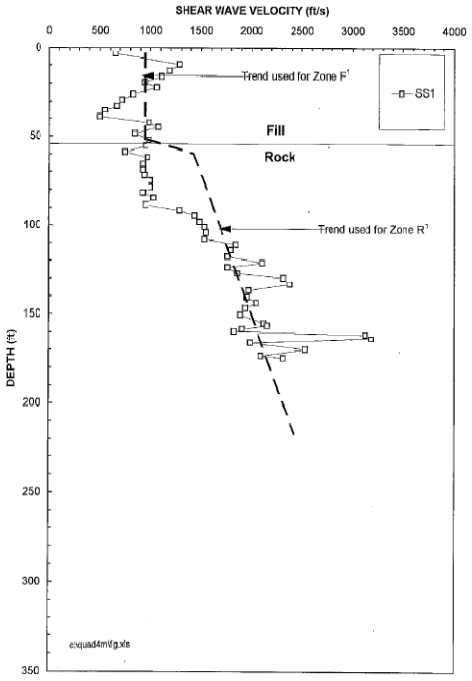

Figure 10-8 Idealized shear wave velocity in SS1 location (GeoSyntec 1996)

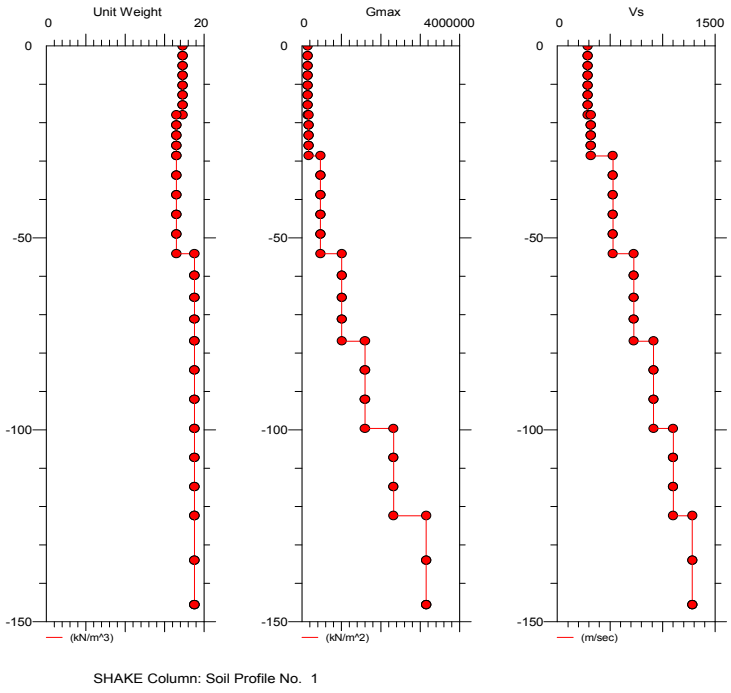

Figure 10-9 Material properties used in the deocnvolution analysis at SS1

In a deconvolution analysis the recorded input motion at the top of the column is used to predict (the deconvoluted) motion at the base of the column. Figure 10-10 to Figure 10-14 show the deconvoluted motion acceleration response spectra along with the recorded motion acceleration response spectra at SS1 for the five accelerograms used in the analysis. The figures show that the deconvoluted motion acceleration response spectra is much lower in amplitude than the recorded response spectra at the ground surface of the base of the landfill in all cases for all periods.

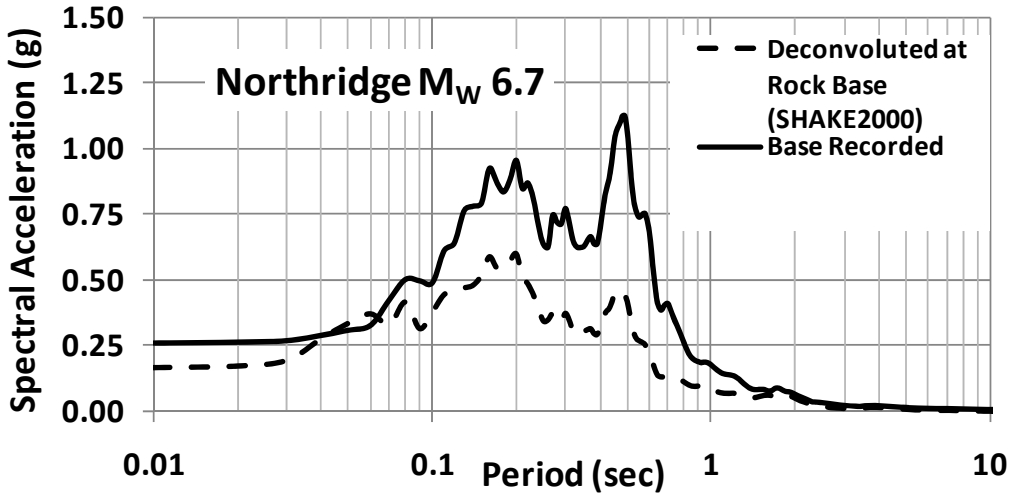

Figure 10-10 Acceleration response spectra for recorded motion and the deconvoluted motion at the base SS1 for the M_w 6.7 Northridge earthquake

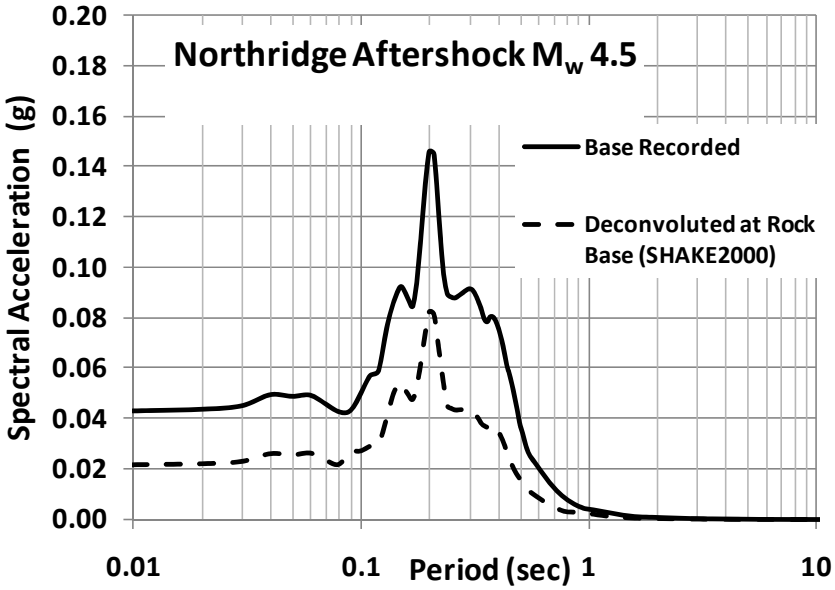

Figure 10-11 Acceleration response spectra for recorded motion and the deconvoluted motion at the base SS1 for the M_w 4.5 Northridge aftershock earthquake

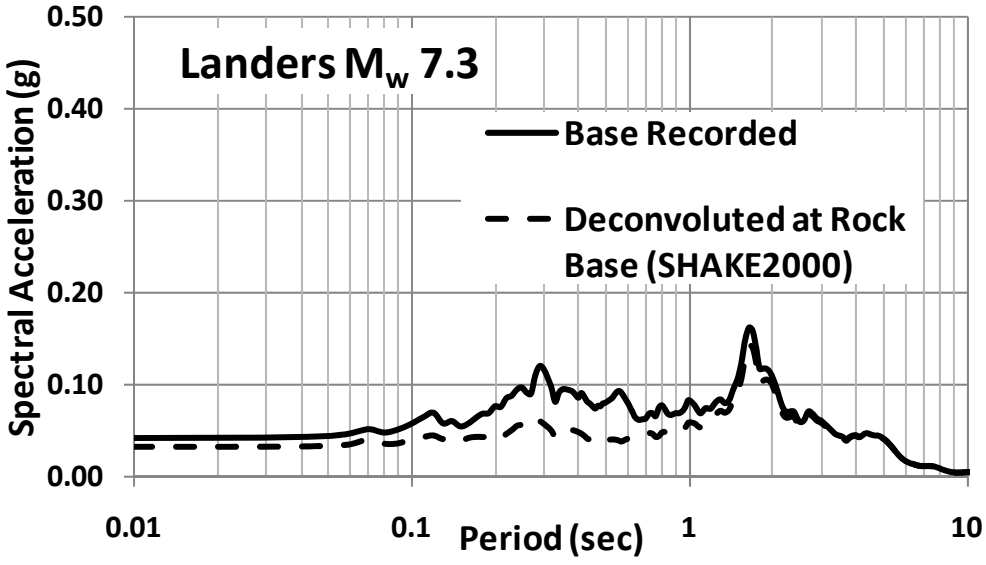

Figure 10-12 Acceleration response spectra for recorded motion and the deconvoluted motion at the base SS1 for the M_w 7.3 Landers earthquake

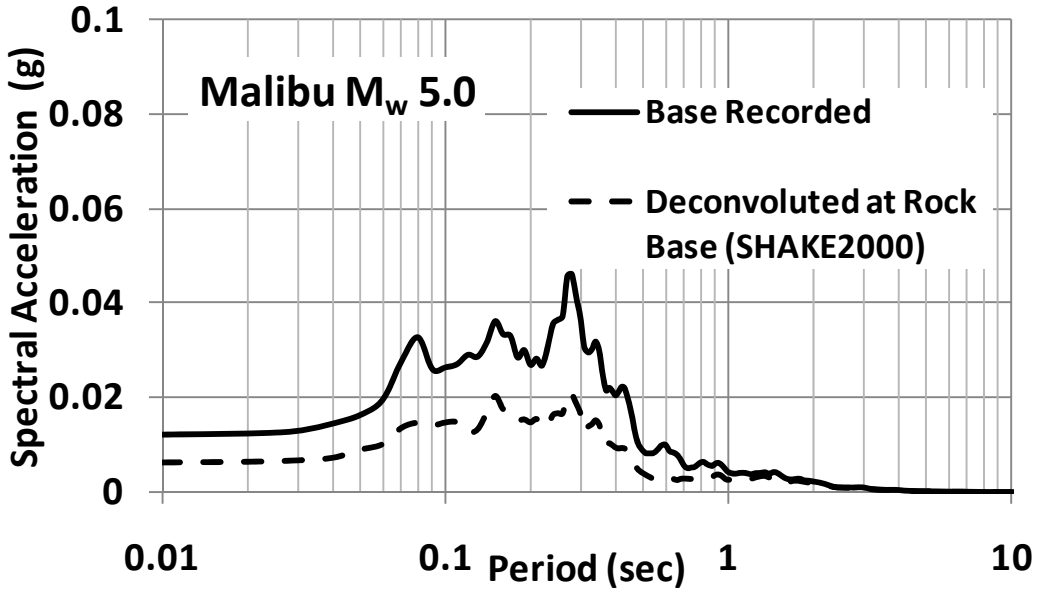

Figure 10-13 Acceleration response spectra for recorded motion and the deconvoluted motion at the base SS1 for the M_w 5.0 Malibu earthquake

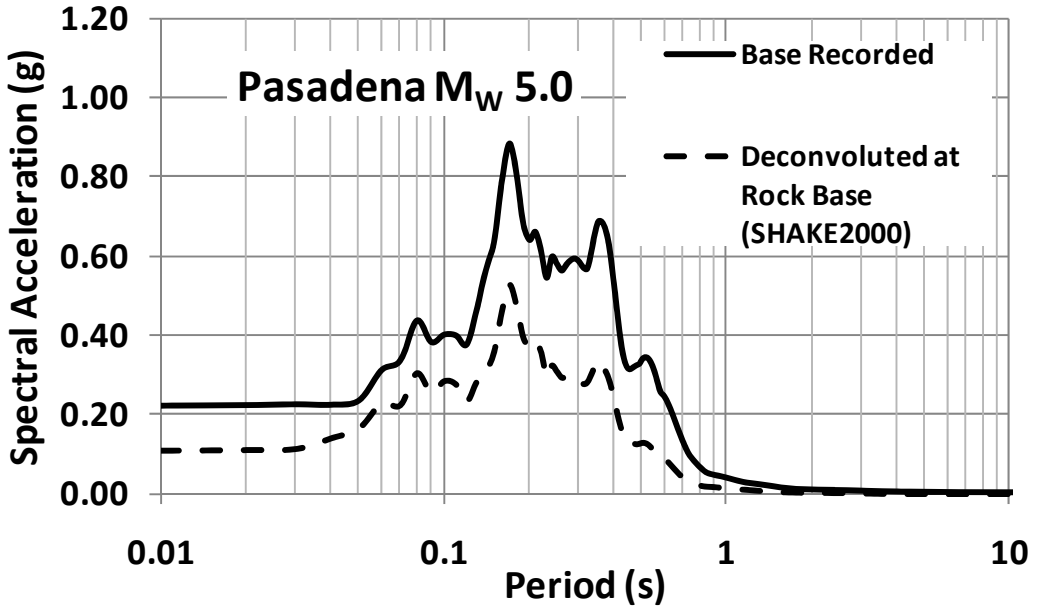

Figure 10-14 Acceleration response spectra for recorded motion and the deconvoluted motion at the base SS1 for the M_w 5.0 Pasadena earthquake

10.5 Solid Waste Material Properties

The field exploration program at OII landfill included the spectral analysis of surface wave (SASW) surveys at 27 locations on top of the waste at four locations on native material adjacent to the landfill, three 840 mm-diameter bucket auger borings with in situ unit weight measurements to depths of up to 45 m, and an approximately 6-m long by 6-m deep test trench with in situ unit weight measurement. The test results are presented in detail in (GeoSyntec 1996). The exploration locations from these field studies are presented in Figure 10-2.

A summary of the in situ unit weight results for MSW at the OII site is presented in Figure 10-15. The data in Figure 10-15 suggest that the average unit weight at the site is essentially constant with depth. Therefore a constant unit weight of 15.7 kN/m^3 was used for the waste in the back analysis. Matasovic and Kavazanjian (1998) used the shear and compressional wave velocities measured in a borehole at strong motion station SS2 were used to calculate Poisson's ratio, ν, for the solid waste (based upon basic equations from linear elasticity). Figure 10-16 shows the Poisson's ratio values calculated in this manner. Based on the data Figure 10-16 a value of ν equal to 0.33 was adapted for the solid waste in the back analyses.

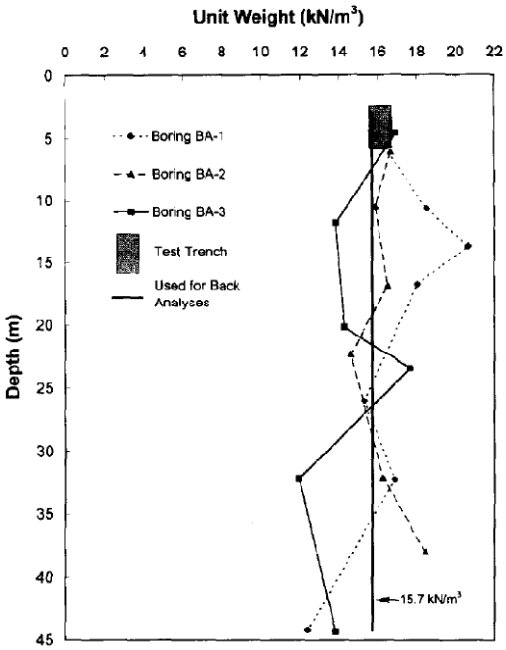

FIG. 5. Unit Weight of OII Landfill Solid Waste

Figure 10-15 MSW unit weight measured in situ at OII landfill (Matasovic and Kavazanjian 1998)

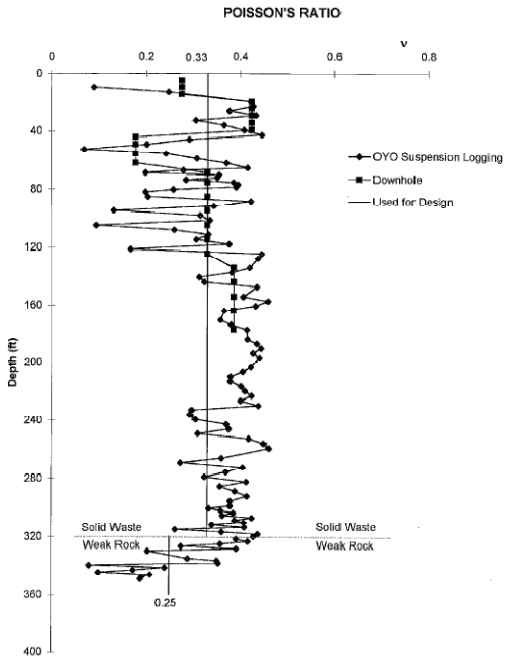

Figure 10-16 Poisson's ratio measures in situ at SS2 at OII landfill (Matasovic and Kavazanjian 1998)

For the use in their seismic analysis, Matasovic and Kavazanjian (1998) developed Cross Section 1-1', shown in Figure 10-17, using a topographic map prepared prior to the Northridge earthquake, the spectral analyses of the shear wave (SASW) velocity surveys at the site, and a base-of-the-landfill contour map developed from the SASW results the and the other site characterization and field investigation studies (GeoSyntec 1996). For the seismic analyses, Matasovic and Kavazanjian (1998) extended the cross section to elevation 55 m msl, approximately 130 m below the top deck of the landfill. Elevation 55 m mean sea level represented the lowest elevation reached by the SASW measurements.

As illustrated in Figure 10-17, Matasovic and Kavazanjian (1998) divided Cross Section 1-1' for modeling purposes into zones of four materials: cover soil, compacted fill, weak rock, and solid waste. Each zone was assigned an idealized linear relationship for shear wave velocity that increased linearly with depth based upon the SASW measurements. The idealized shear wave velocity for the compacted fill and the weak rock is shown in Figure 10-8. The idealized shear wave velocity for the zones W^1 (MSW) and the weak rock zone $R^1$are shown in Figure 10-18 and Figure 10-19, respectively.

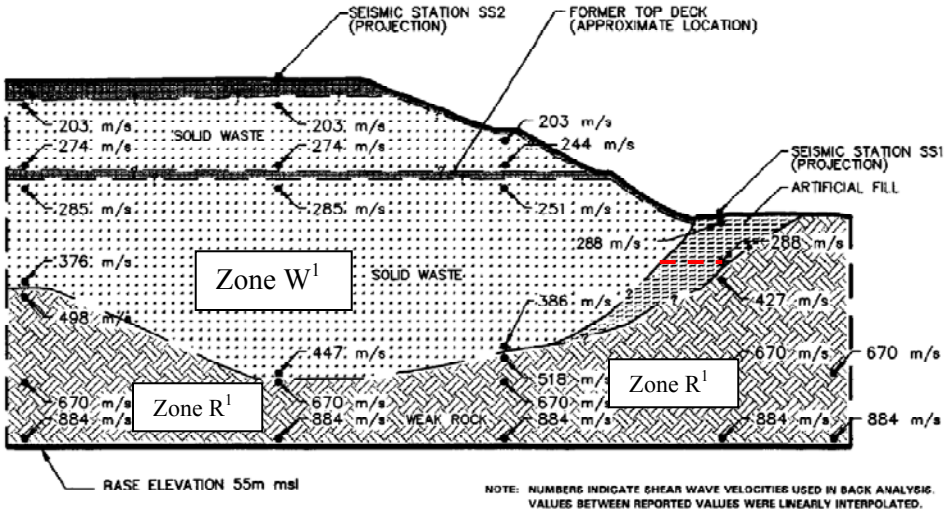

Figure 10-17 OII landfill cross section showing measures shear wave velocity (Matasovic and Kavazanjian 1998)

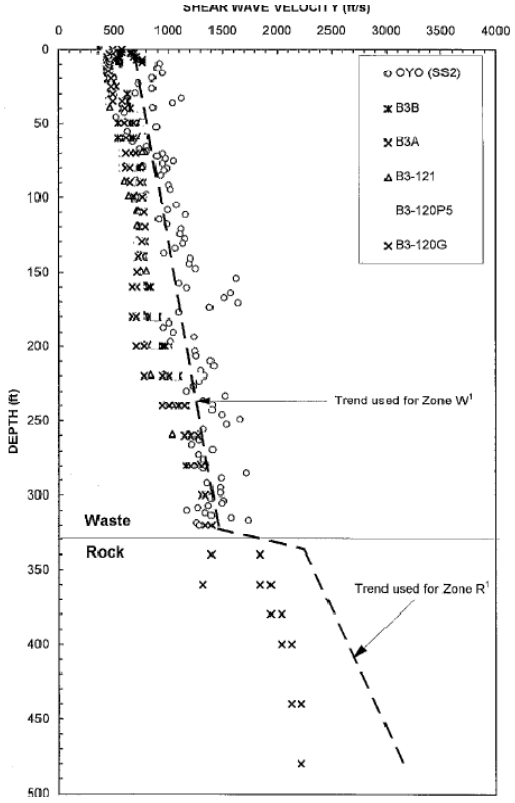

Figure 10-18 Idealized shear wave velocity profile for OII waste and underlying bedrock (GeoSyntec 1996)

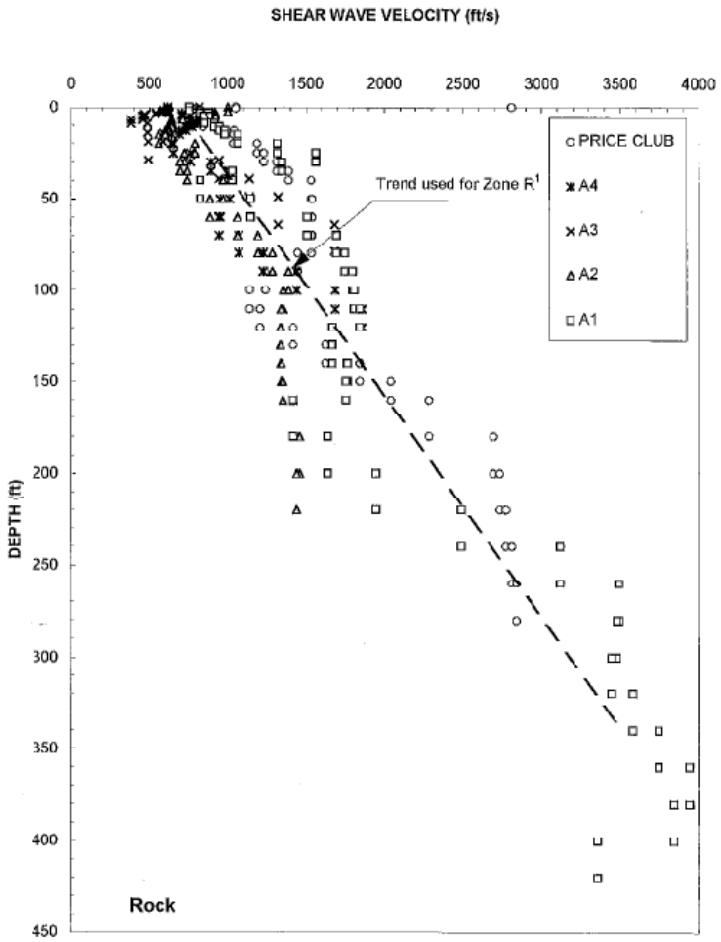

Figure 10-19 Idealized shear wave velocity profile for the rock at the OII site (GeoSyntec 1996)

10.6 Two Dimensional Calibration Analysis

10.6.1 **OII model**

A finite difference mesh was developed to back analyze the seismic response of Cross Section 1-1'. The mesh is shown in Figure 10-20. The mesh has more than 7,500 zones, with a higher density towards the waste body. Lateral boundaries of the mesh were extended more than 10 times the mesh thickness beyond the boundaries of the waste fill to minimize the influence of the lateral boundaries on the computed response in addition to the use of quite boundaries on the vertical sides and the bottom of the model for the same reason. The idealized material parameters described earlier provided the basis for choosing the initial elastic properties of the MSW, compacted fill and weak rock. The waste and the rock are divided into layers to account for increasing in shear wave velocity with depth resulting in an increase in maximum shear modulus with depth. Table 10-1 presents unit weight, shear wave velocity, small strain modulus, and poisson's ratio used in the back analysis.

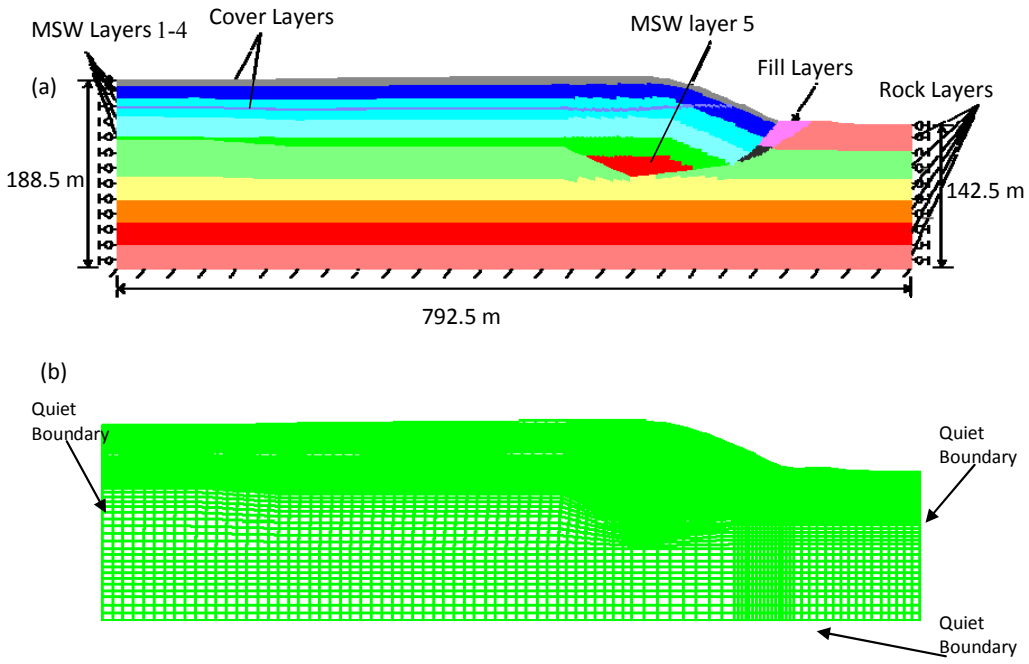

Figure 10-20 Finite difference mesh for Cross Section 1-1'

Table 10-1 OII Landfill material properties

	Layer	γ (kN/m^3)	ν	V_s (m/s)	G_{max} (Pa)
Cover	Layer 1	17.3	0.3	400	2.82E+08
	Layer 2	17.3	0.3	288	1.46E+08
Fill	Layer 1	17.3	0.3	288	1.46E+08
	Layer 2	19.6	0.3	288	1.66E+08
Waste	Layer 1	15.7	0.33	237.60	9.04E+07
	Layer 2	15.7	0.33	286.21	1.31E+08
	Layer 3	15.7	0.33	334.82	1.79E+08
	Layer 4	15.7	0.33	383.43	2.35E+08
	Layer 5	15.7	0.33	432.04	2.99E+08
Rock	Layer 1	16.5	0.25	318.28	1.70E+08
	Layer 2	16.5	0.25	528.07	4.69E+08
	Layer 3	18.8	0.25	726.99	1.01E+09
	Layer 4	18.8	0.25	914.16	1.60E+09
	Layer 5	18.8	0.25	1101.32	2.32E+09
	Layer 6	18.8	0.25	1282.81	3.15E+09

10.7 Nonlinear Analysis

Most nonlinear seismic response computer programs employ Masing rule in order to simulate the hysteretic stress-strain behavior in soils. Philips and Hashash (2009) showed that the Masing unloading–reloading rules provide greater hysteretic damping for medium to large strains compared to the damping values obtained in dynamic tests when the constitutive model backbone curve is based on the modulus reduction curve (MR) of the soil, as illustrated in Figure 10-21.

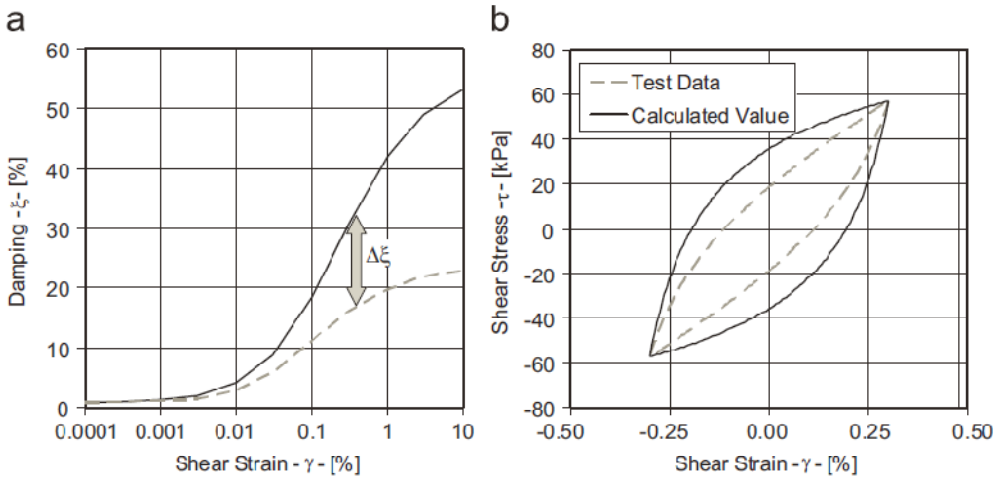

Figure 10-21 Overestimation of hysteretic damping using Masing rules, (a) Damping curve. (b) Hysteretic loop (Philips and Hashash 2009)

Philips and Hashash (2009) identified three options to determine constitutive parameters for non-linear analyses from modulus reduction and damping curves.

1- The modulus reduction curve is closely matched to the target curves but the damping curve is not matched due to the inherent limitation in the Masing load–unload criteria (MR);
2- A balance is struck between matching the modulus reduction and damping curves with neither curve closely matched (MRD);
3- The damping curve is very well matched to the target curves but the modulus reduction curve is not matched due to the inherent limitation in the Masing load–unload criteria (MD).

These three different procedures for fitting the modulus reduction and damping curve from experimental results are illustrated in Figure 10-22. Matasovic (1993) proposed a method to provide a good match for both modulus reduction and damping curves, combining the Masing rules with Raleigh (MRR).

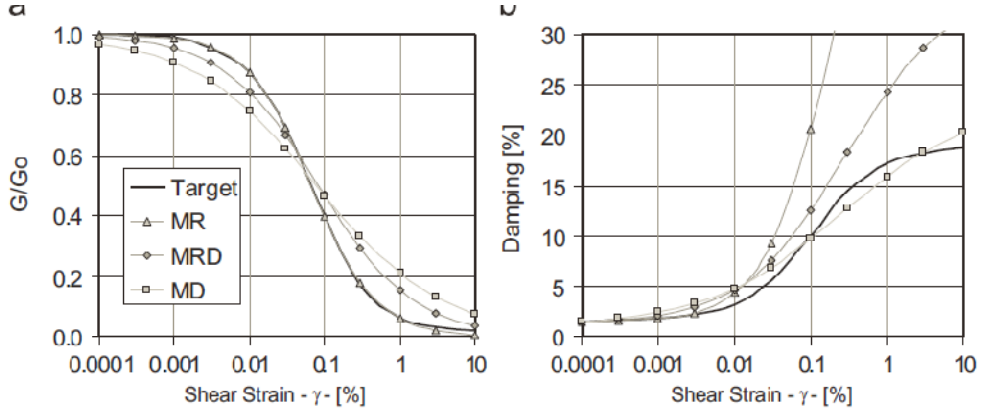

Figure 10-22 Hyperbolic model fitting procedure (a) modulus reduction; (b) damping curve (Philips and Hashash 2009).

10.8 Modulus Reduction and Damping Curves

Based on back analysis of the response of the OII landfill and lab testing of reconstituted specimens off OII solid waste, Matasovic and Kavazanjian (1998) proposed upper bound, average and lower bound modulus reduction curve and damping curves for municipal solid waste. Matasovic and Kavazanjian (1998) recommended using the upper bound for the modulus reduction and lower bound for the damping curve for seismic response analyses based upon the best fit with the back analyses and consistency with the Masing rules. This family of curves is presented in Figure 10-23 along with an earlier set of curves proposed by Kavazanjian and Matasovic (1995) without the benefit of the OII field studies. The upper bound modulus reduction and lower bound damping curves of Matasovic and Kavazanjian (1998) were used as initial input to the FLAC 6.0 back analyses.

Yuan et al. (2011) conducted simple shear testing on reconstituted waste specimens from Tricities landfill in the San Francisco Bay area. From their testing, Yuan et al.

(2011) developed a modulus and damping curves for waste with 65% of its constituents passing a 20mm sieve (the typical compositional for the waste in the field). These curves, labeled as ASU curves, are shown in Figure 10-23. The modulus curve recommended by Yuan et al. (2011) matches the upper bound modulus reduction curve recommended by Matasovic and Kavazanjian (1998) at lower and medium shear strain range, while in high shear strain range the Yuan et al. (2011) modulus reduction curve is higher than the Matasovic and Kavazanjian (1998) upper bound curve. The damping curve recommended by Yuan et al. (2011) is significantly lower than the lower bound damping curve recommended by Matasovic and Kavazanjian (1998) at high shear strain range. Modulus and damping curves used for the compacted fill and weak rock in the back analyses are presented in Figure 10-24.

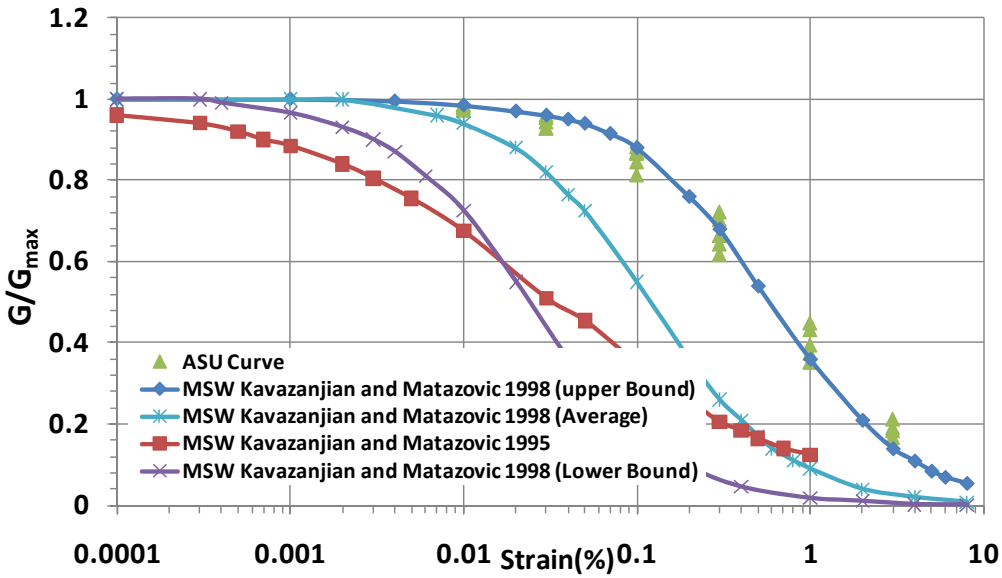

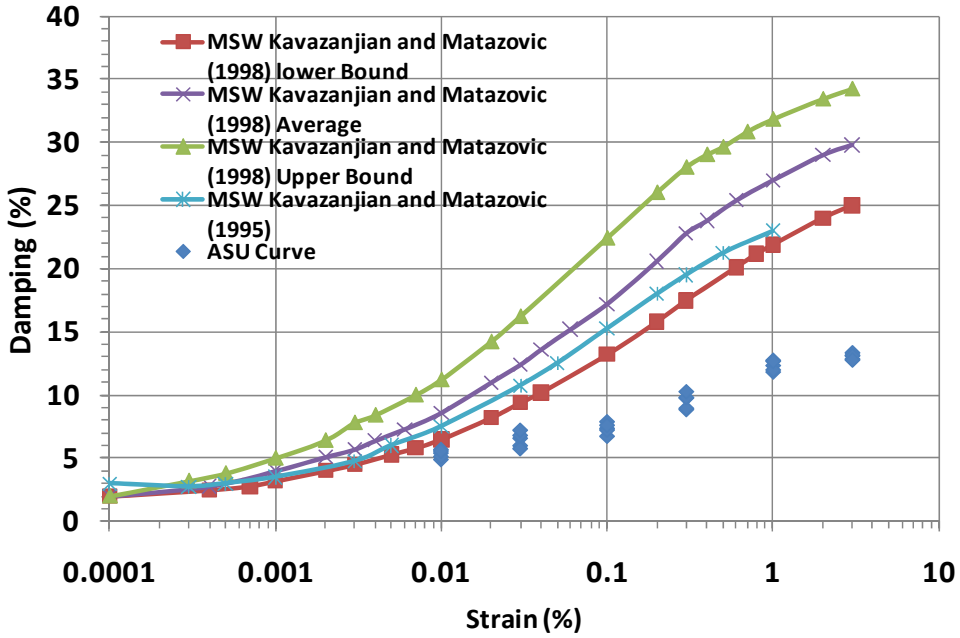

Figure 10-23 MSW modulus reduction and damping curves from Kavazanjian and Matasovic (1995), Matasovic and Kavazanjian (1998) and Yuan et al. (2011)

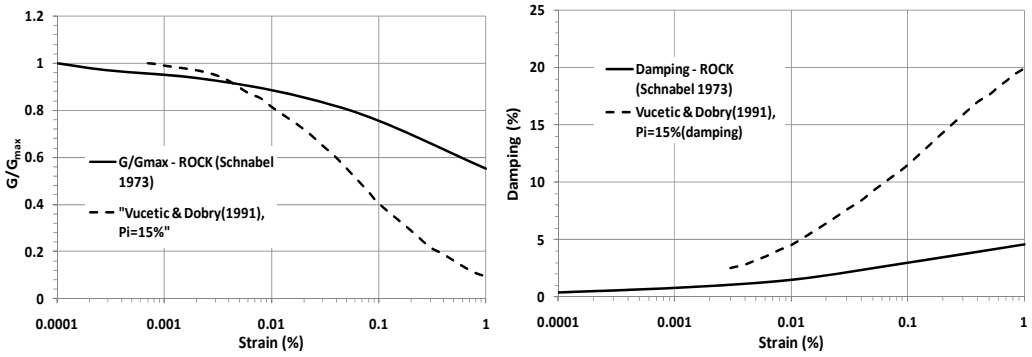

Figure 10-24 Compacted fill and weak rock modulus reduction and damping curves

10.9 OII Case History Calibration

The back analyses of the seismic response of the OII landfill were carried out using the computer program FLAC 6.0. There are varieties of constitutive models available in the program to account for nonlinearity of soil or waste, including hysteretic damping model which uses a backbone curve and the Masing criterion to model cyclic behavior. The hysteretic damping model can work side by side with a Mohr-Coulomb model or any other failure criterion. The hysteretic model will generate hysteresis loops based on the backbone for the soil before failure and behaves as fully plastic material when the material fails. The hysteretic model was used to account for the MSW and compacted fill nonlinearity. The material parameters used in the back analysis are summarized in Table 10-2. The modulus reduction and damping curves were varied until the best fit with the monitoring data at SS2 was obtained to calibrate the waste model.

Table 10-2 Initial material properties for the OII landfill back analyses

Layer	ϕ degree	Modulus reduction and damping curves
Waste	33	Varied
Fill	30	Vucetic and Dobry (1991) (PI =15)
Cover	30	Vucetic and Dobry (1991) (PI =15)
Rock	-	Shibuya et al. (1990)

A gravity turn-on analysis was conducted to establish the initial stresses in the numerical model before the dynamic response analyses were conducted. At this stage of analysis, the bottom boundary was fixed in both the vertical and horizontal directions and the side boundaries in the horizontal direction as presented in Figure 10-20 (a).

The back analyses were performed using the deconvoluted ground motions shown in Figure 10-10 through Figure 10-14. The quiet boundary condition in FLAC 6.0 was employed at the bottom and the sides of the numerical model to absorb the reflected seismic motion (instead of reflecting the downward propagating seismic waves back into the model), replacing the boundary conditions in the gravity on analysis as presented in Figure 10-20 (b).

The hysteretic damping model is based on Masing rule and therefore inherits the shortcomings associated with this model. Initially, a MR type of analysis was conducted using a back bone curve derived from the modulus reduction curve with the damping curve produced automatically.

Three cases were analyzed in the back analyses:

1- MR: The ASU curve was used as input for the modulus reduction curve, which pretty much agrees with the Matasovic and Kavazanjian (1998) lower bound modulus reduction curve except at the high shear strain values, presented in Figure 10-25.
2- MD: Matasovic and Kavazanjian (1998) upper bound damping curve was matched, as presented in Figure 10-25.
3- MRR: The ASU curve was used as input for the modulus reduction curve, adding 2% of Raleigh damping to enhance the damping fitting at low shear strain range presented in Figure 10-25.

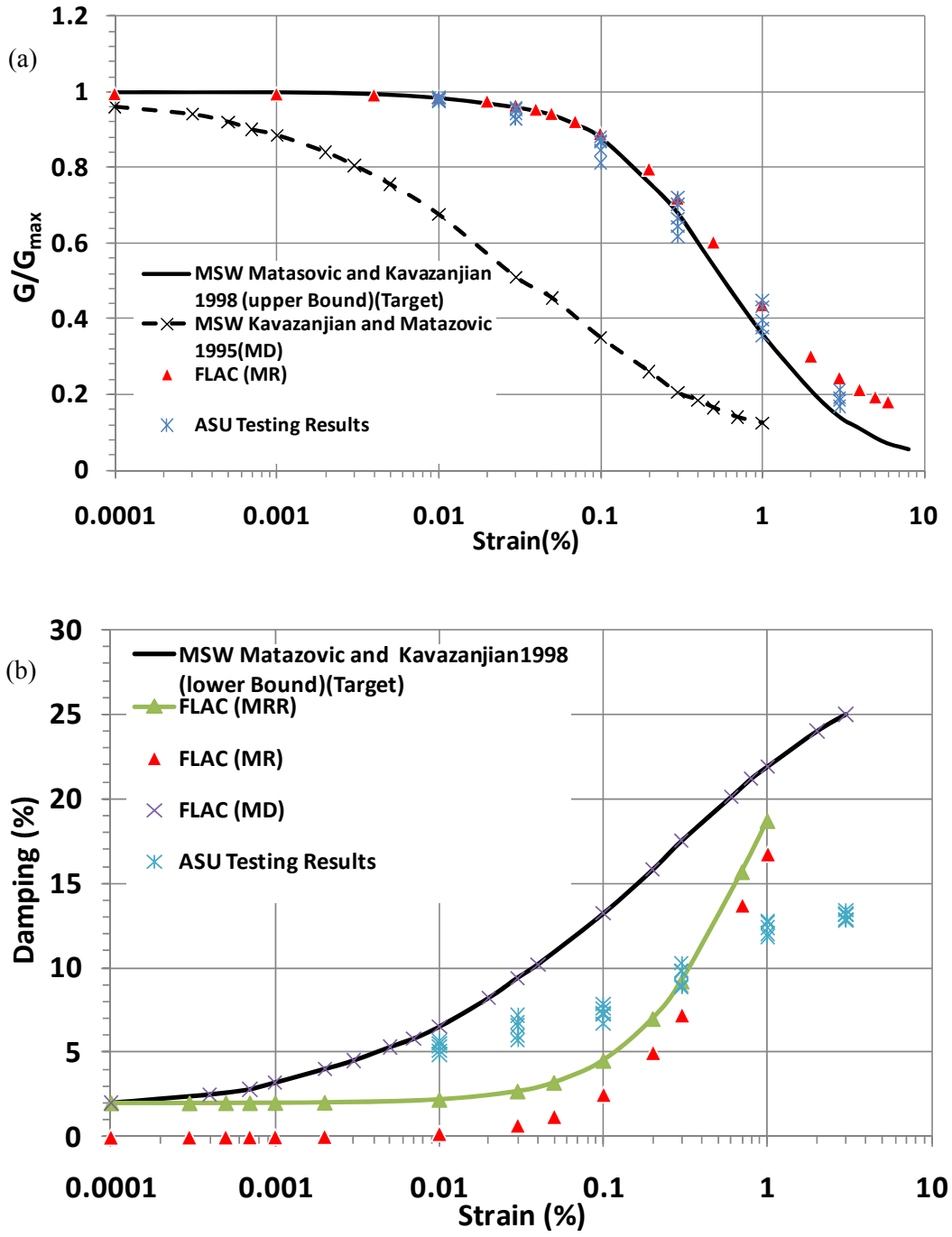

Figure 10-25 Model fitting procedure for MSW: (a) modulus reduction; (b) damping curve.

A set of nonlinear site response analyses were conducted using the Cross Section 1-1' of the OII landfill, presented in Figure 10-20, to evaluate the influence of the changing the backbone curve in the hysteretic material model on the seismic response at the top deck station (station SS2) of the landfill, in terms of response spectra. The analysis results are presented in Figure 10-26 to Figure 10-30 for the MR analyses. Except for the Northridge earthquake case history the calculated response spectra at the base station was under predicted compared to the recorded response spectra. This under prediction may be related to the 2-D geometric effect as the deconvolution study used to establish the base rock input motion was carried with the 1-D computer program.

The results for the MR analyses for Northridge earthquake input motions presented Figure 10-26 give a similar response at the top deck for the short periods, a higher response for the mid-period (0.1–0.4 s) range, and lower response at the longer periods than measured. The Northridge Aftershock earthquake input the MR analyses presented in Figure 10-27, give a similar response to the measured motion at all periods, except in the mid-period range from 0.2 to 0.3 s. Considering the uncertainties in the analyses, the response of the landfill in the in the case of MR analyses is considered acceptable for the Northridge earthquake and Northridge aftershock earthquake case histories.

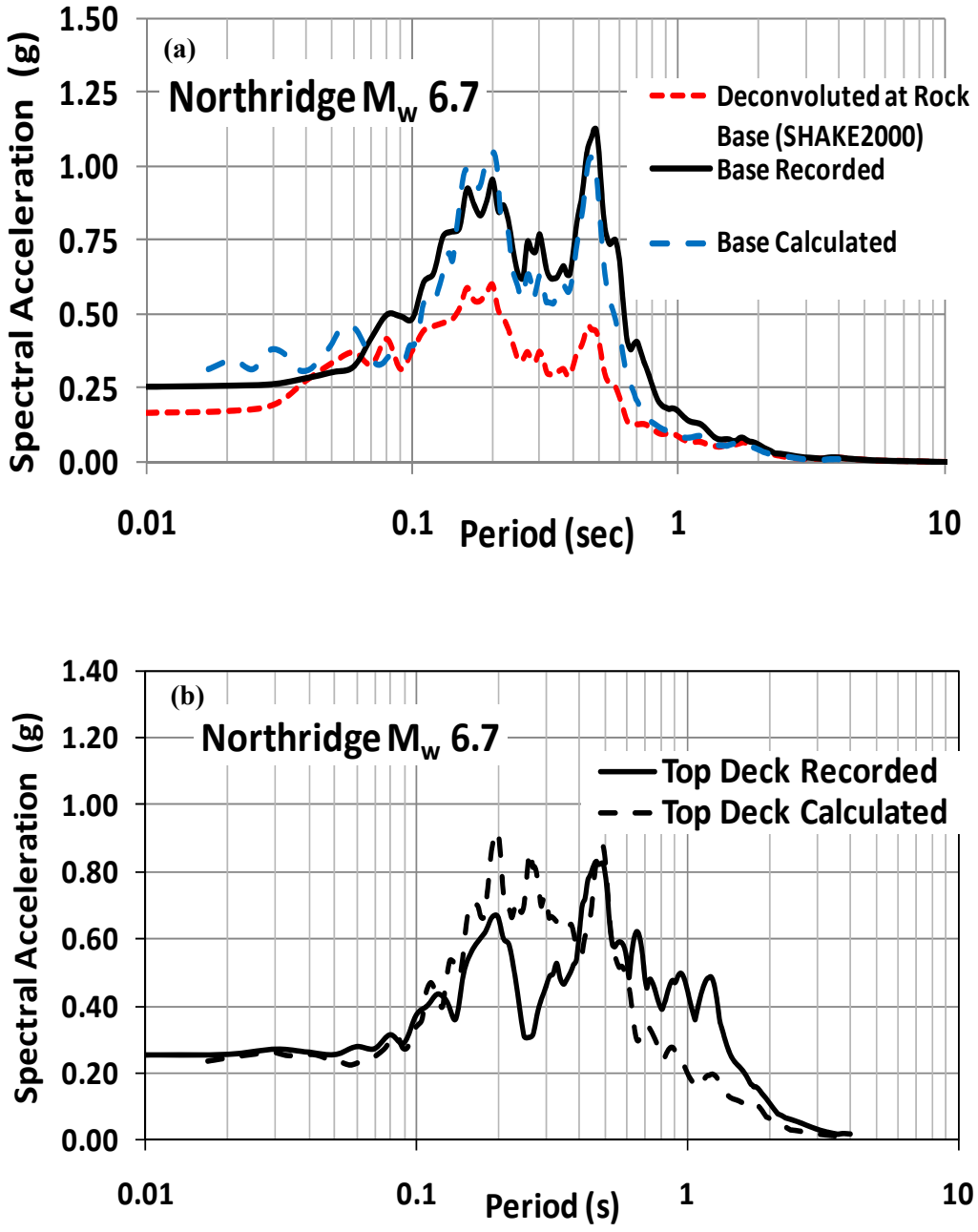

Figure 10-26 Comparison between the calculated (MR) and recorded response spectra of the OII landfill for Northridge earthquake (a) base and (b) top deck.

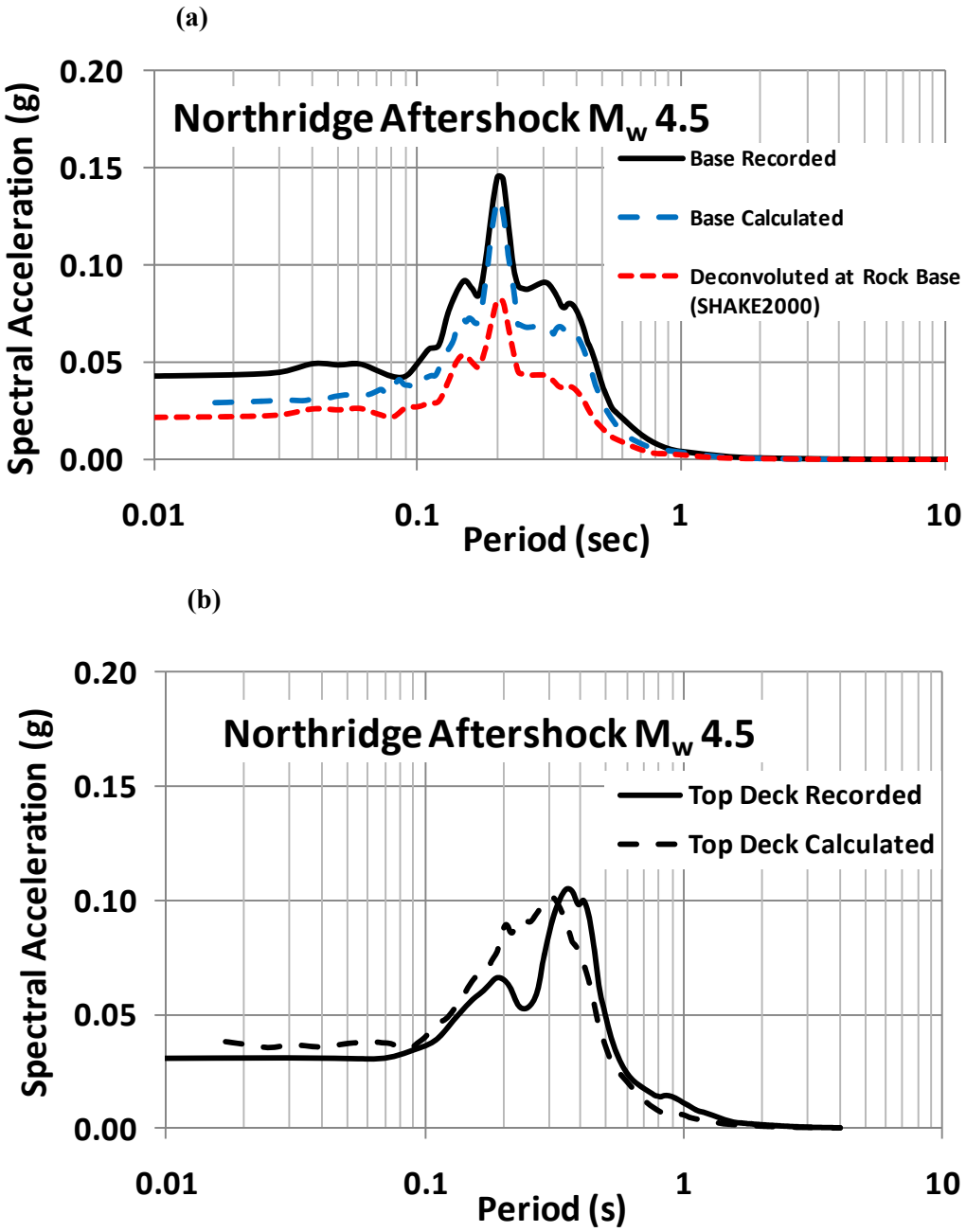

Figure 10-27 Comparison between the calculated (MR) and recorded response spectra of the OII landfill for Northridge aftershock earthquake (a) base and (b) top deck.

The MR analysis results for Pasadena earthquake are shown in Figure 10-28. For this case, the numerical analyses gives a similar response at long periods and a higher

response in the lower to mid-period range (0.01–0.4 s) at the top deck compared to the recorded response at the top of the landfill.

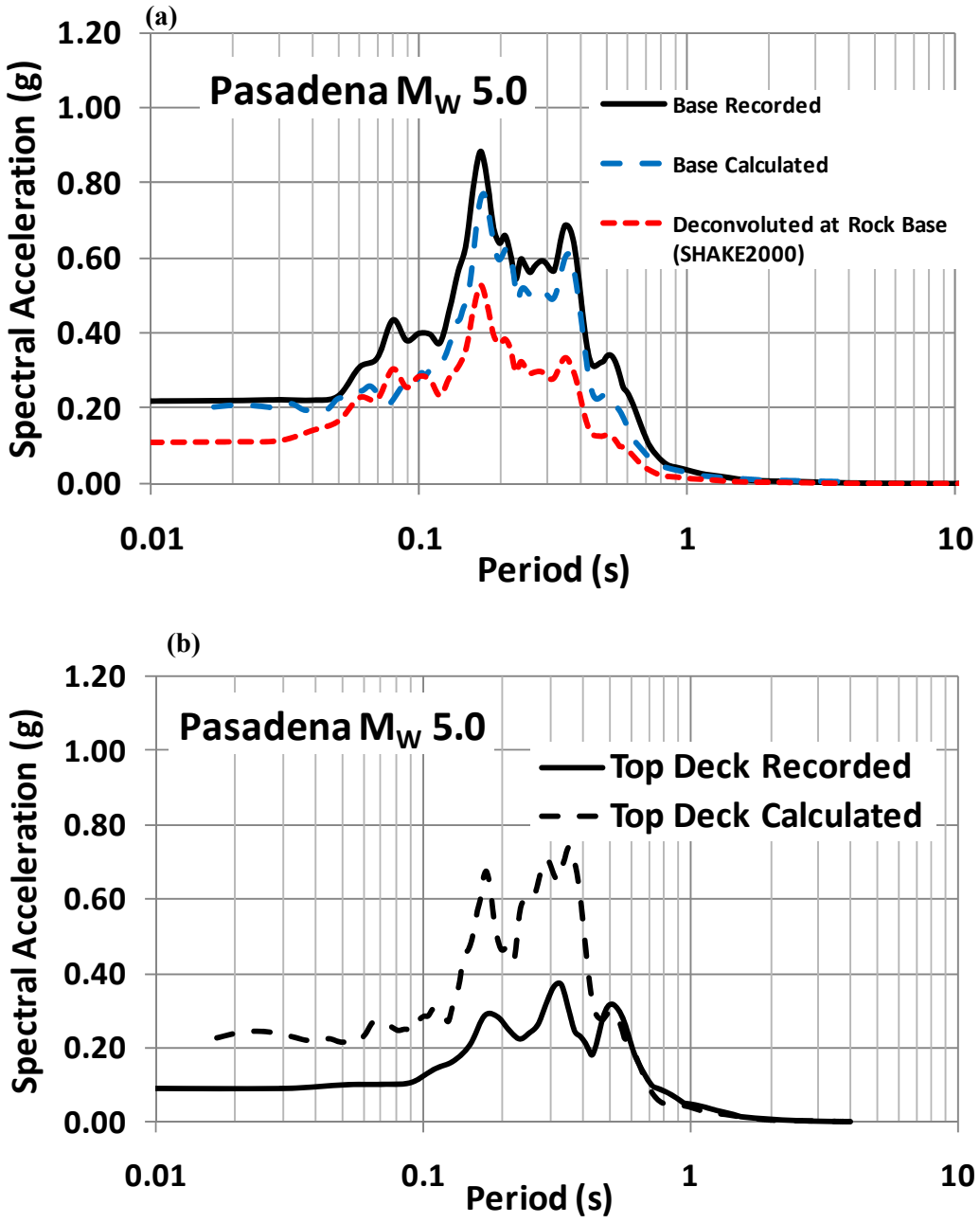

Figure 10-28 Comparison between the calculated (MR) and recorded response spectra of the OII landfill for Pasadena earthquake (a) base and (b) top deck

The MR analysis results for Malibu earthquake are presented in Figure 10-29. At the top of deck, the numerical analysis gives a lower response at short and long periods and a higher peak response at about 0.3 s than the recorded response at the top deck.

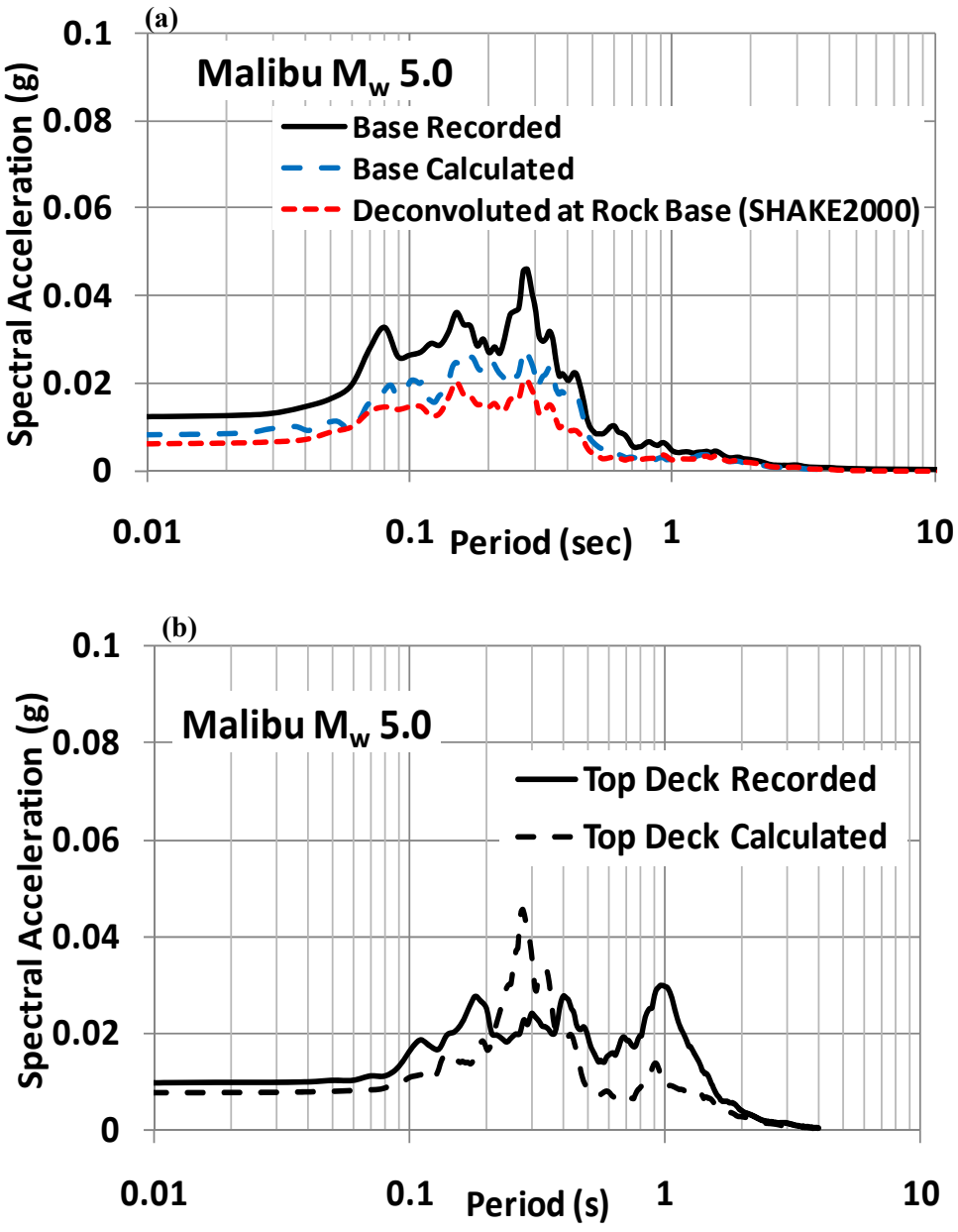

Figure 10-29 Comparison between the calculated (MR) and recorded response spectra of the OII landfill for Malibu earthquake (a) base and (b) top deck

The MR analysis results for the Landers earthquake are presented in Figure 10-30. For the Landers earthquake, the numerical analysis gives a lower response at the top deck in all periods, with the peak response shifted from 1 sec in the recorded response to 2 sec in the calculated response.

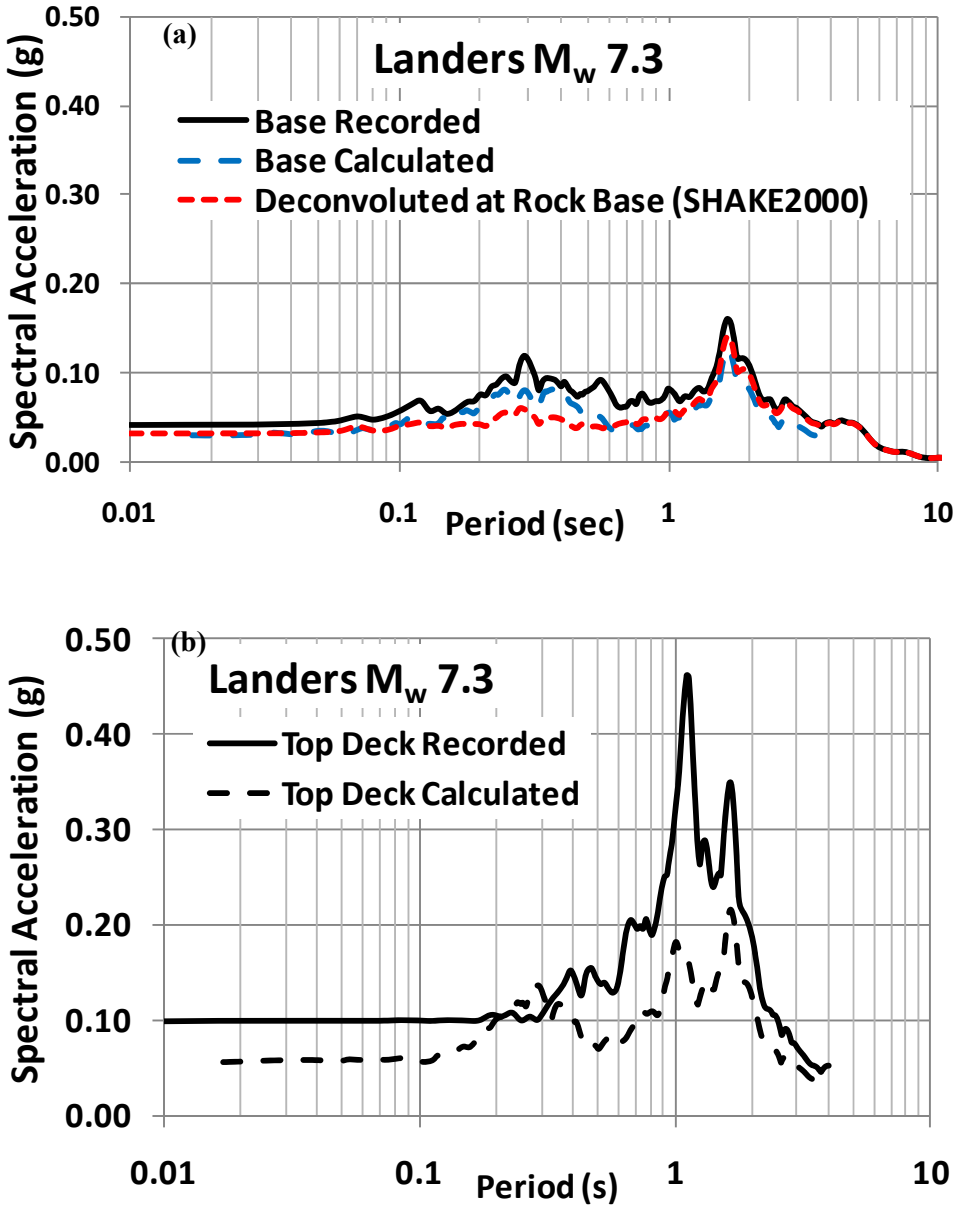

Figure 10-30 Comparison between the calculated (MR) and recorded response spectra of the OII landfill for Landers earthquake (a) base and (b) top deck

The case history analyses were repeated with the Matasovic and Kavazanjian (1998) lower bound curve for backbone curve and adding 2% of Raleigh damping (MRR analysis) to enhance the damping fitting. For the Northridge earthquake, the calculated Peak response in case of MRR analysis presented in Figure 10-31 approximately equal to and at the same period as the recorded motion of 0.5 sec and slightly lower response was calculated at shorter and longer periods for the top deck.

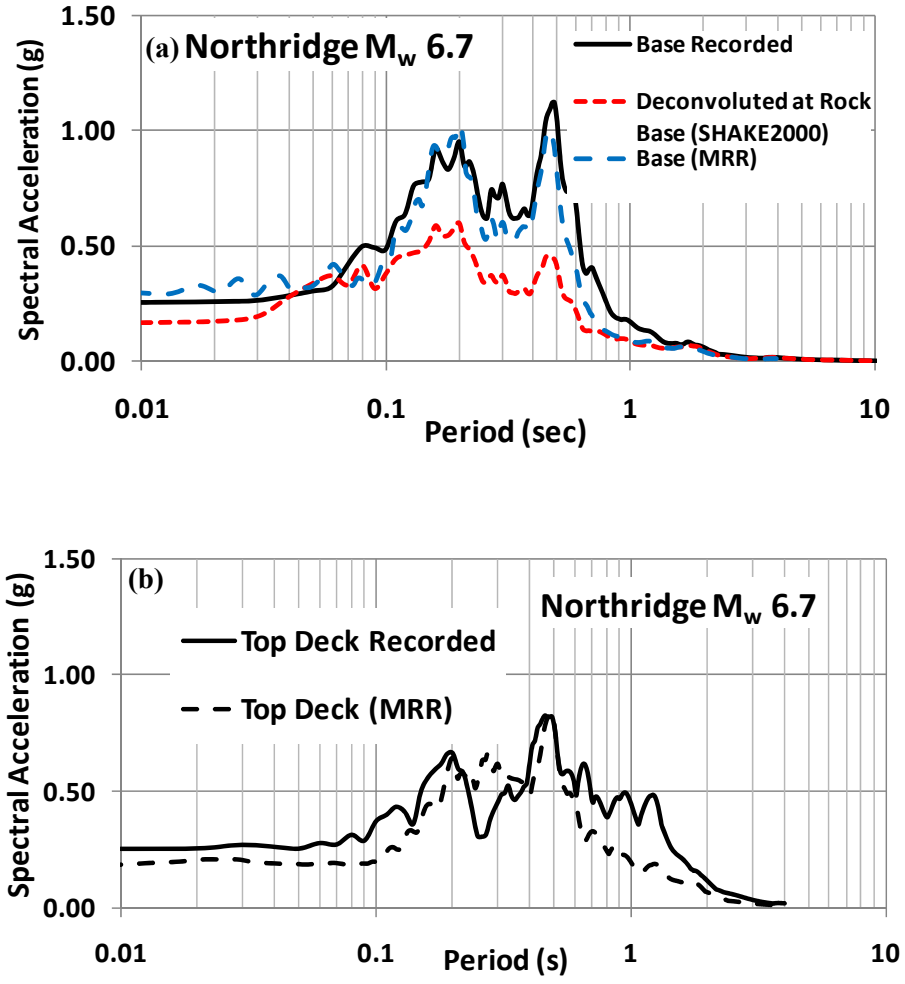

Figure 10-31 Comparison between the calculated (MRR) and recorded response spectra of the OII landfill for Northridge earthquake (a) base and (b) top deck

In case of the Northridge aftershocks presented in Figure 10-32 the calculated response is slightly lower than recorded response in the mid periods range (0.1-0.4) sec. Also, the peak spectral acceleration is shifted slightly to a lower period in the calculated response.

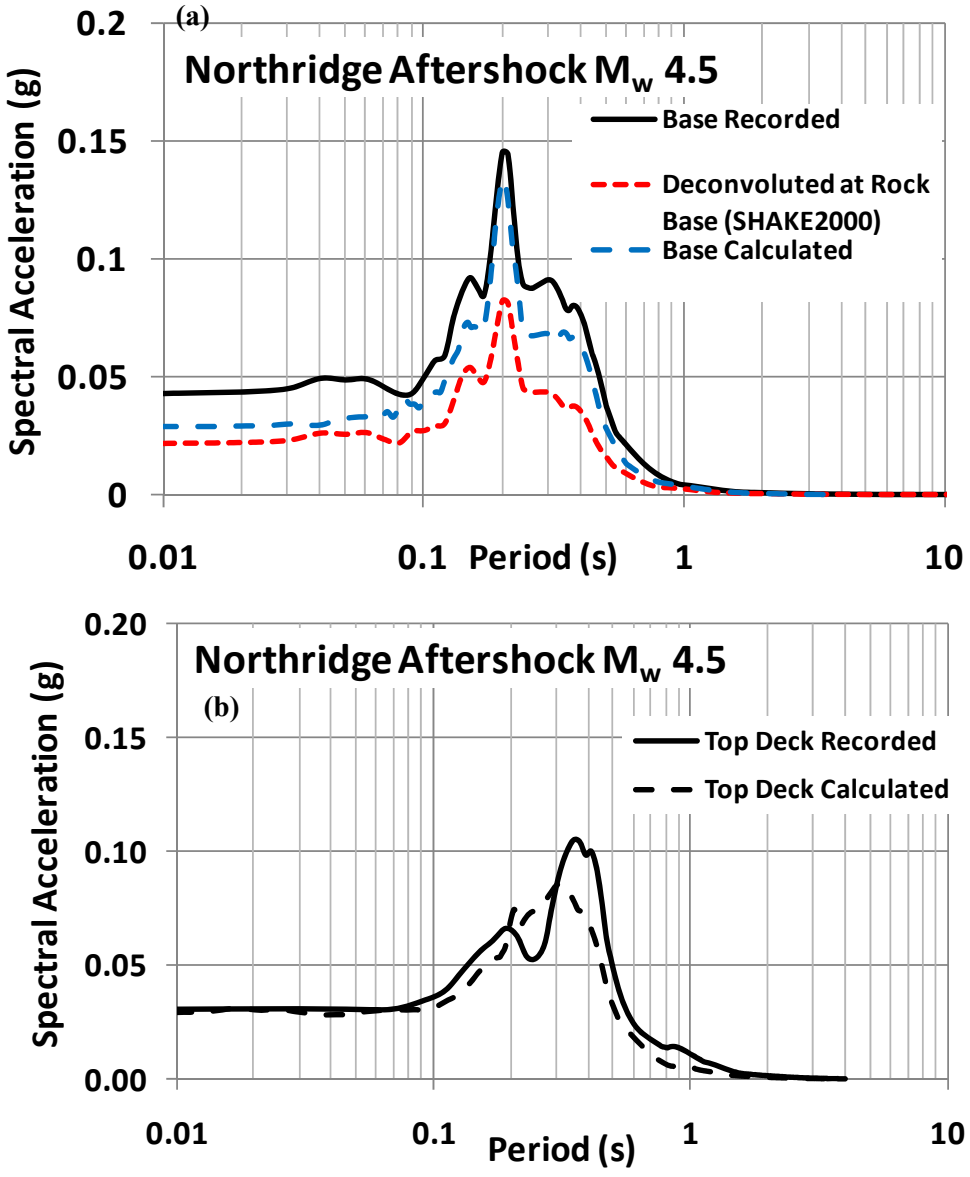

Figure 10-32 Comparison between the calculated (MRR) and recorded response spectra of the OII landfill for Northridge Aftershock earthquake (a) base and (b) top deck

In case of the Pasadena aftershocks presented in Figure 10-33 the calculated response is slightly higher than recorded response in the mid periods range (0.2-0.3) sec. Also, the peak spectral acceleration is shifted slightly to a higher period in the calculated response.

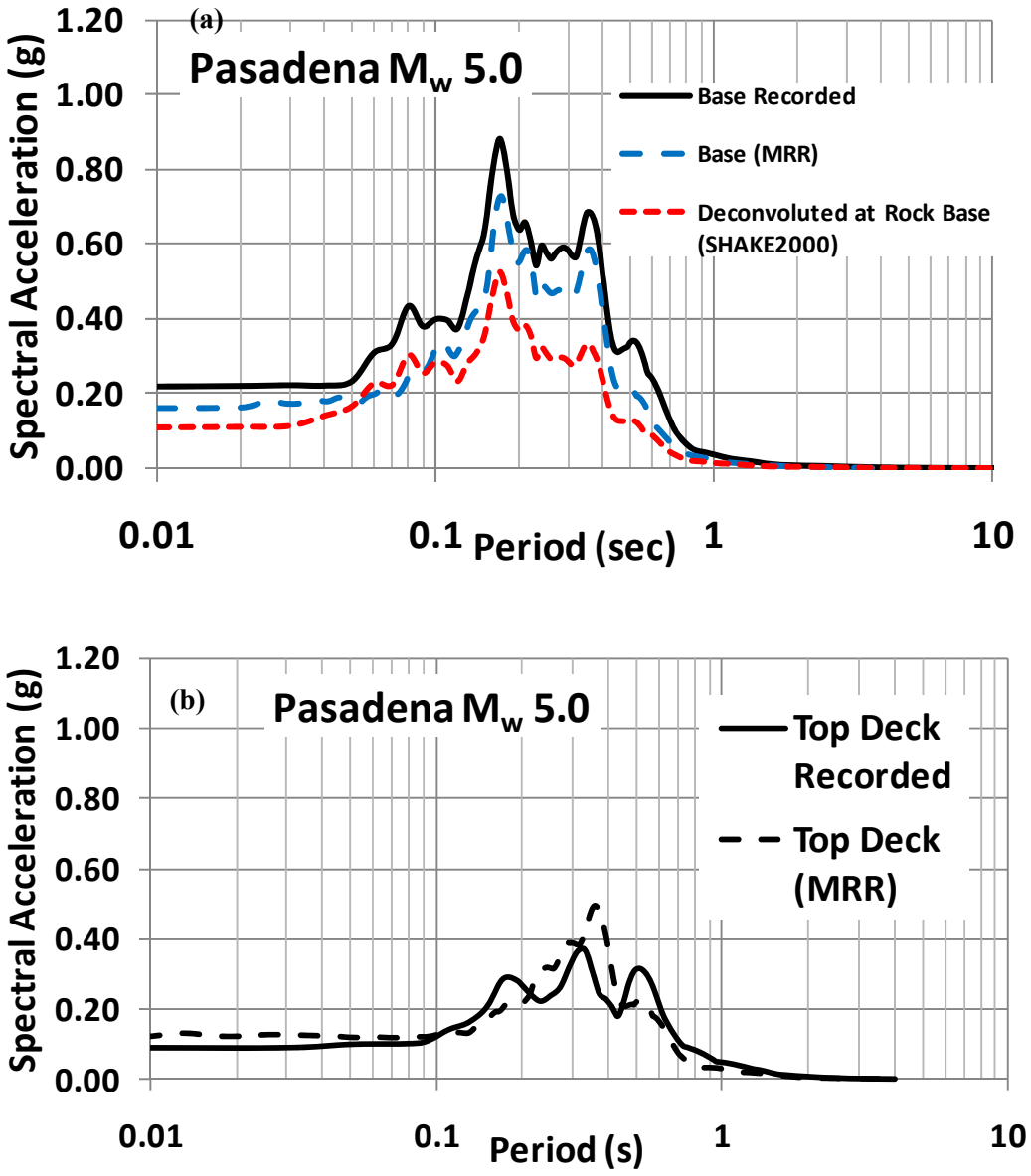

Figure 10-33 Comparison between the calculated (MRR) and recorded response spectra of the OII landfill for Pasadena earthquake (a) base and (b) top deck

Figure 10-34 shows the results for the MRR analyses for the Malibu earthquake input. In this earthquake, the calculated response at the top deck is lower at long and short periods and higher in mid range periods (0.2s-0.3s). Peak acceleration response was calculated at 0.3s as 0.042g versus 0.03g at 1 sec for the recorded peak response acceleration.

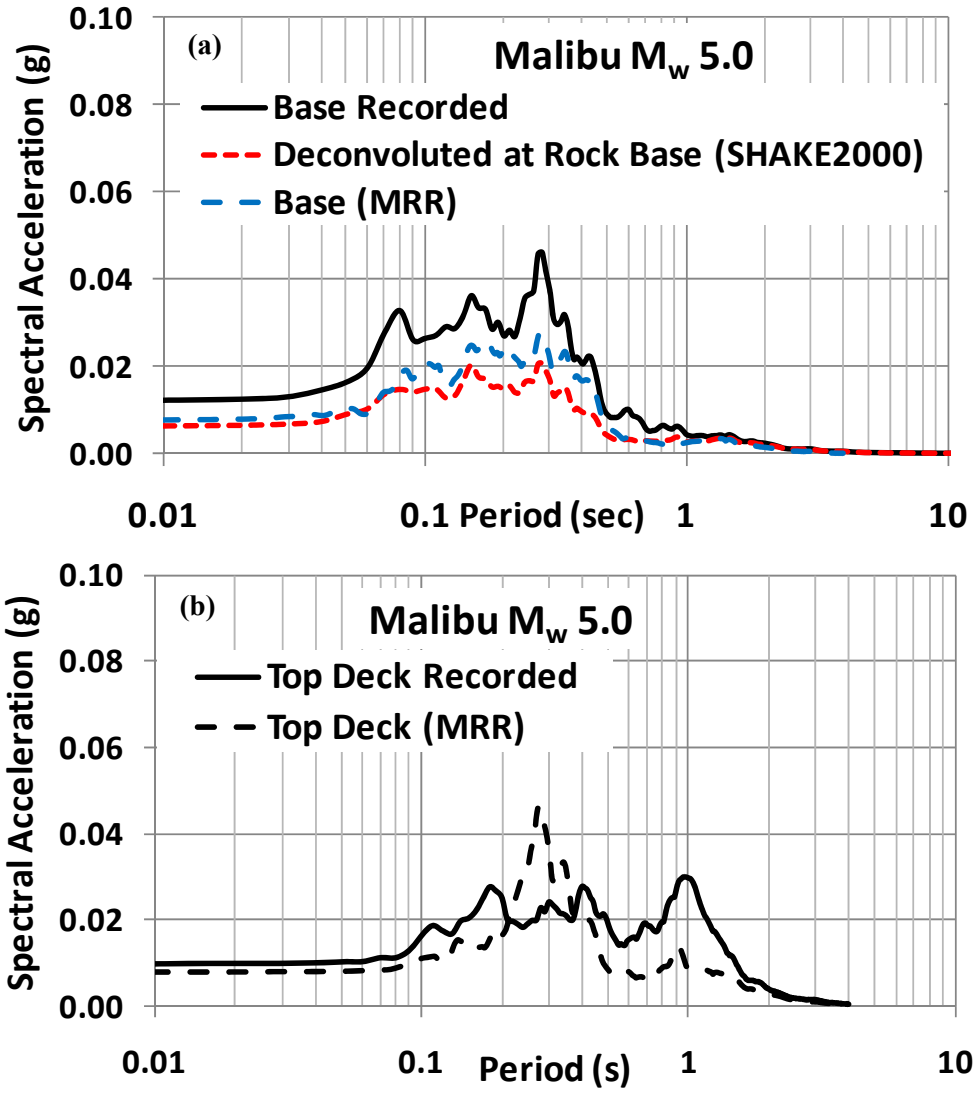

Figure 10-34 Comparison between the calculated (MRR) and recorded response spectra of the OII landfill for Malibu earthquake (a) base and (b) top deck

Figure 10-35 shows the results for the MRR analyses for the Landers earthquake input. The calculated response at the top deck in the Landers earthquake is lower than recorded response at all periods except at 0.2 s and 0.3 s.

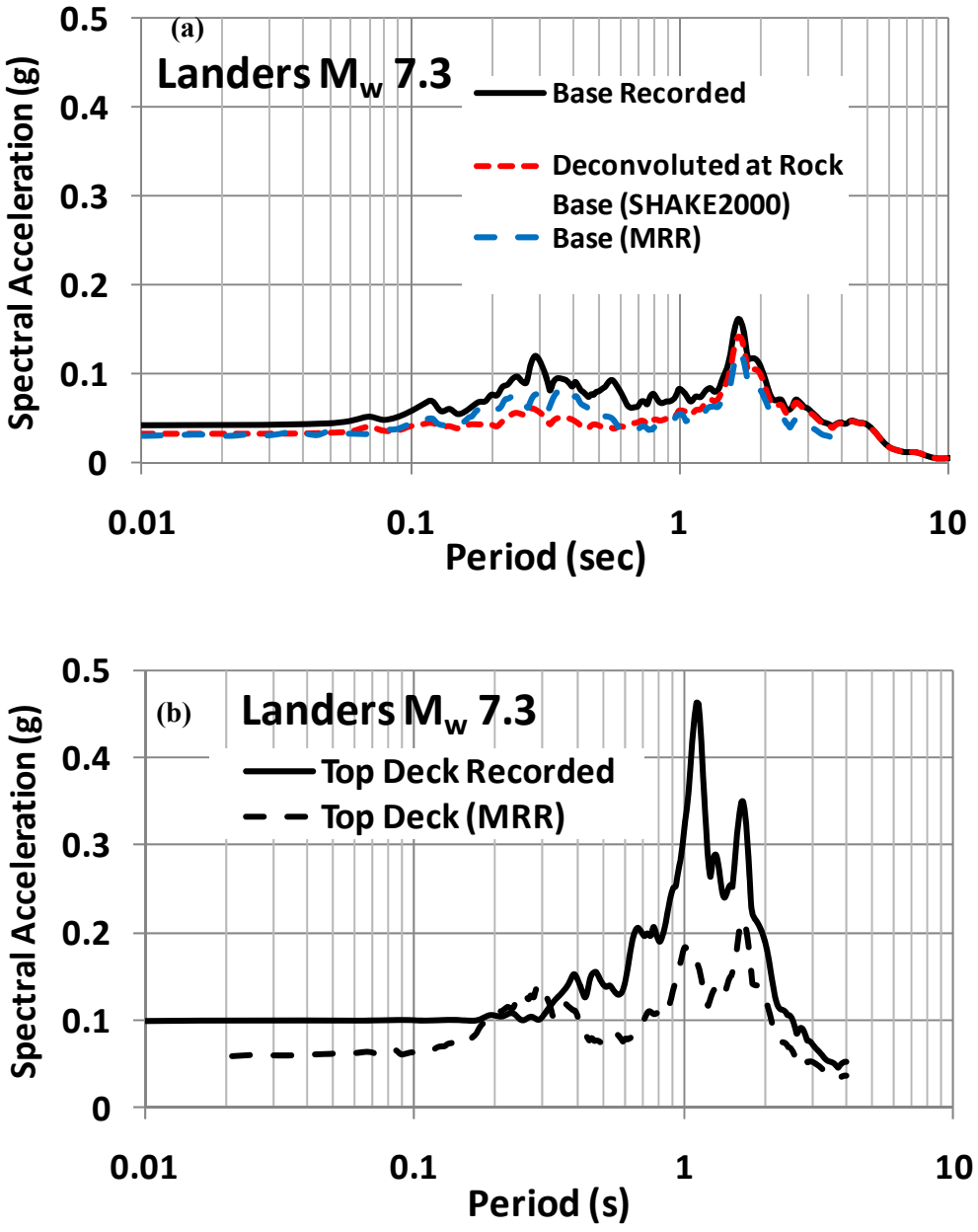

Figure 10-35 Comparison between the calculated (MRR) and recorded response spectra of the OII landfill for Landers earthquake (a) base and (b) top deck

The analyses were repeated with in which a damping curve fit to the Matasovic and Kavazanjian (1998) damping curve (MD). Results from the MD analysis are compared to both the MR analyses and the recorded response. Figure 10-36 shows the response at the top deck station for the Northridge earthquake. For the Northridge earthquake, the calculated response in the MD analysis is lower than recorded response in short to mid periods and is similar at very long periods (greater than 2 s). The calculated response for the MD analysis is much lower than the calculated response for the MR analysis for periods up to 0.6 s.

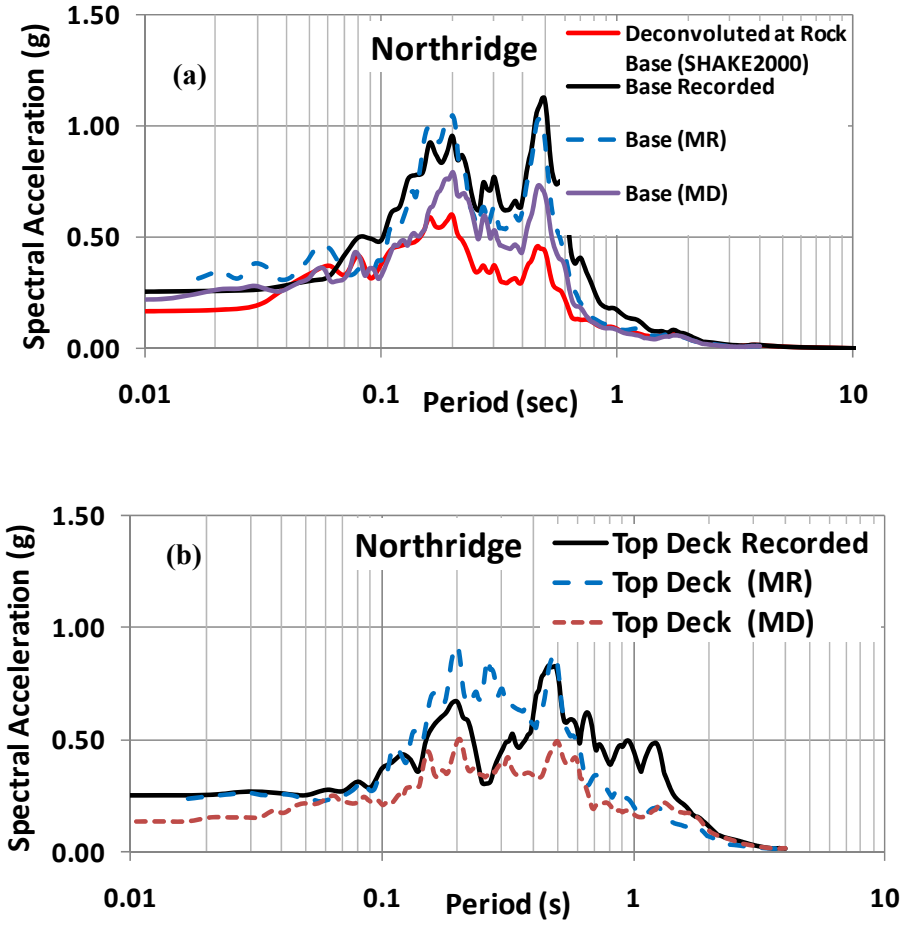

Figure 10-36 Comparison between the MR and MD calculated response and the recorded response spectra for the Northridge earthquake (a) base and (b) top deck.

Figure 10-37 shows the results for the MD analysis for the Northridge Aftershock. The results for the Northridge Aftershock are similar to the recorded response at long periods (greater than 0.5 s), slightly lower at short periods, and the peak spectral acceleration is shifted towards a shorter period.

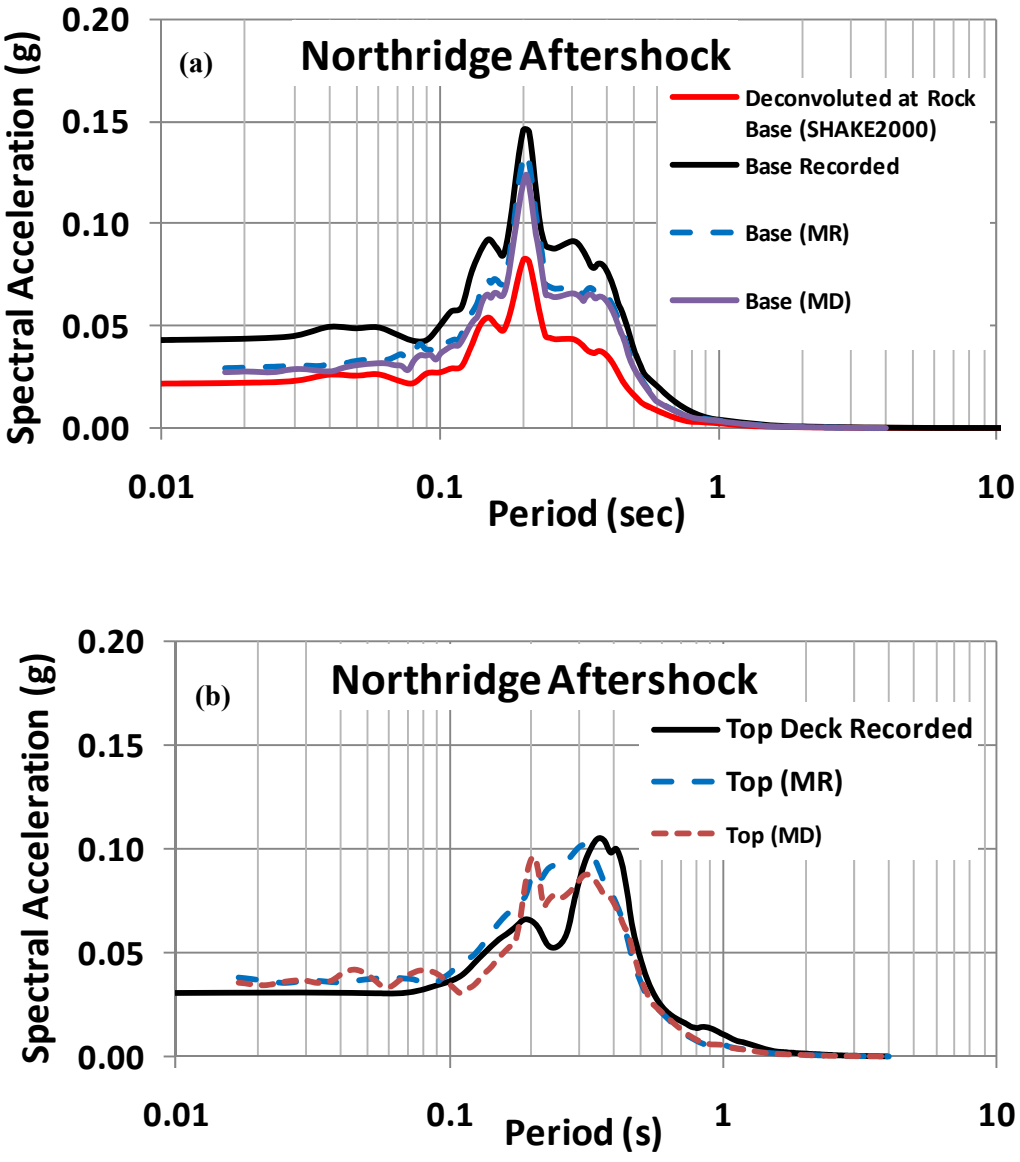

Figure 10-37 Comparison between the MR and MD calculated response and the recorded response spectra for the Northridge Aftershock earthquake (a) base and (b) top deck.

Figure 10-38 (b) shows the results for the MD analysis for the Pasadena earthquake. The results for the Pasadena earthquake show improvement with respect to agreement with the recorded motion compared to results from the MR analysis. The response for the MD analysis at long and short period is similar to recorded response at the top deck, while the calculated response in the mid period range (0.2s-0.4s) is higher than recorded response. The peak for the calculated response is at the same period (0.3 s) as recorded response but is higher in amplitude.

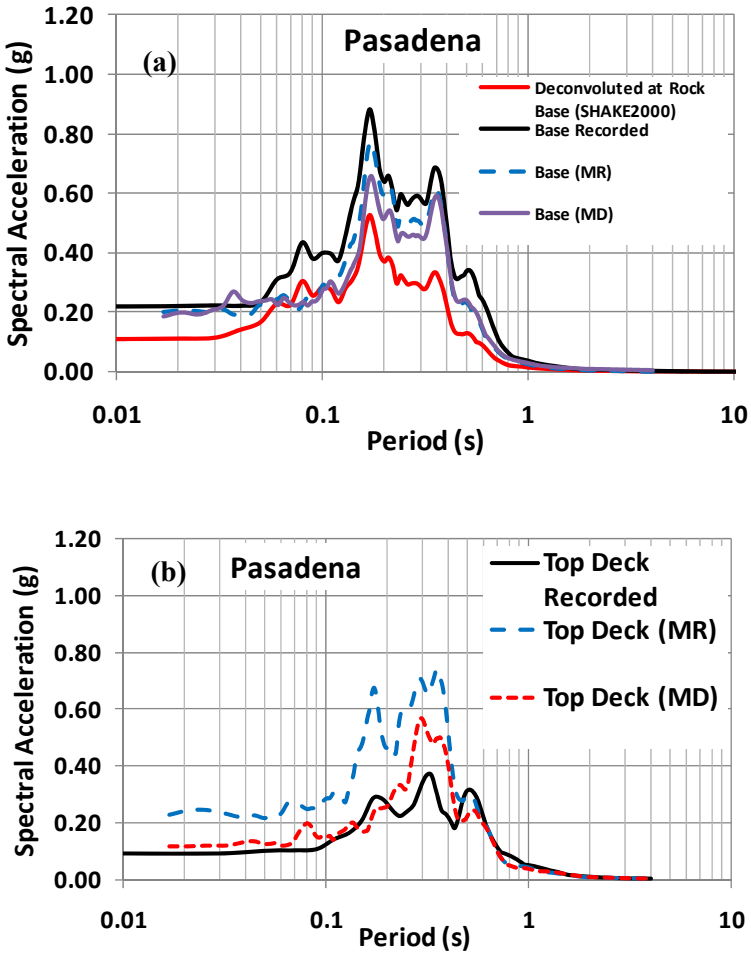

Figure 10-38 Comparison between the MR and MD calculated response and the recorded response spectra for the Pasadena earthquake (a) base and (b) top deck

Figure 10-39 shows the results for the MD analysis for Malibu earthquake input. The calculated results for the MD analyses are similar to the results for the MR analysis, with a peak spectral acceleration at 0.3s but overestimate the recorded response at this period and underestimate the recorded response at longer periods.

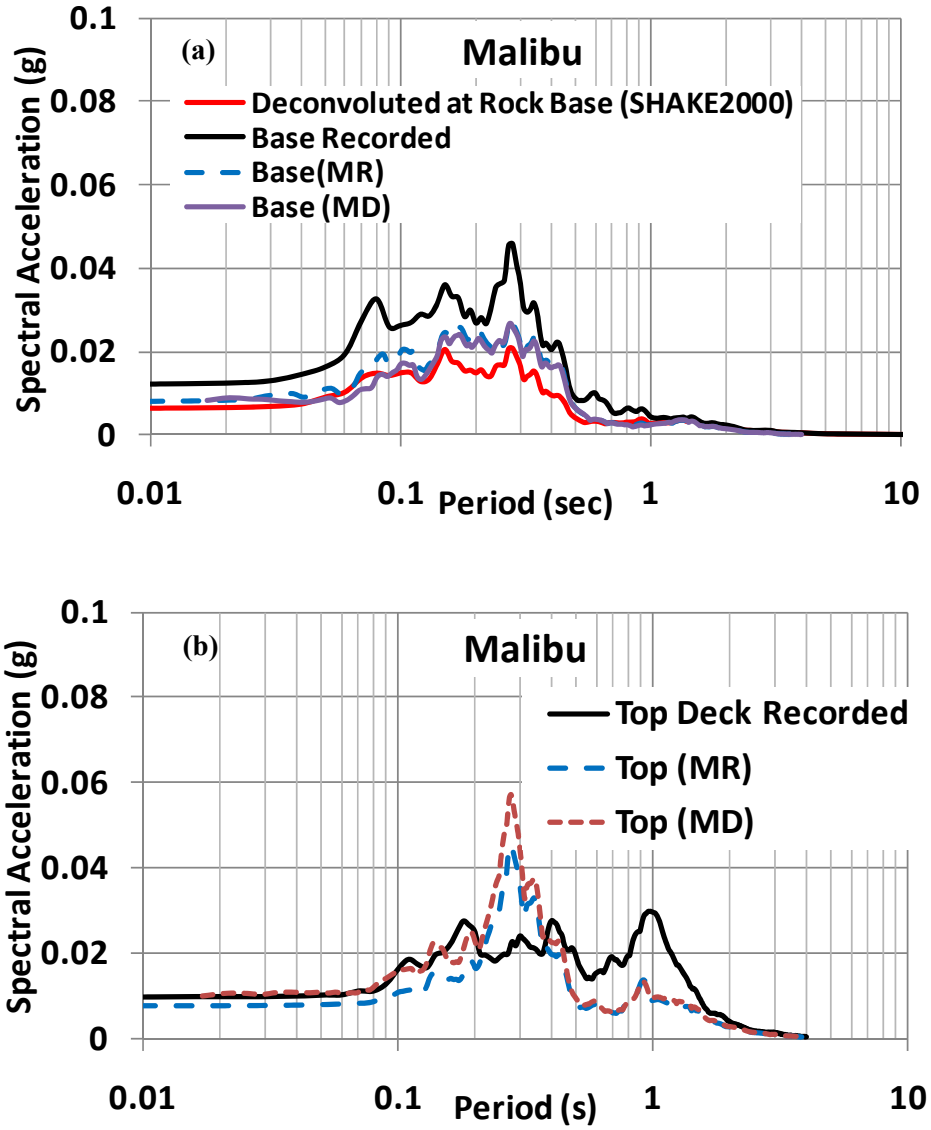

Figure 10-39 Comparison between the MR and MD calculated response and the recorded response spectra for the Malibu earthquake (a) base and (b) top deck

Figure 10-40 shows the results for the MD analysis for Landers earthquake input. The calculated results from the MD analysis for the Landers event are similar to the results from MR analysis, except that the MD analysis provides a somewhat higher peak spectral acceleration at 2.0s. But the MD and MR analyses significantly underpredict the recorded response at the top deck at periods between 0.4 s and 1.5 s.

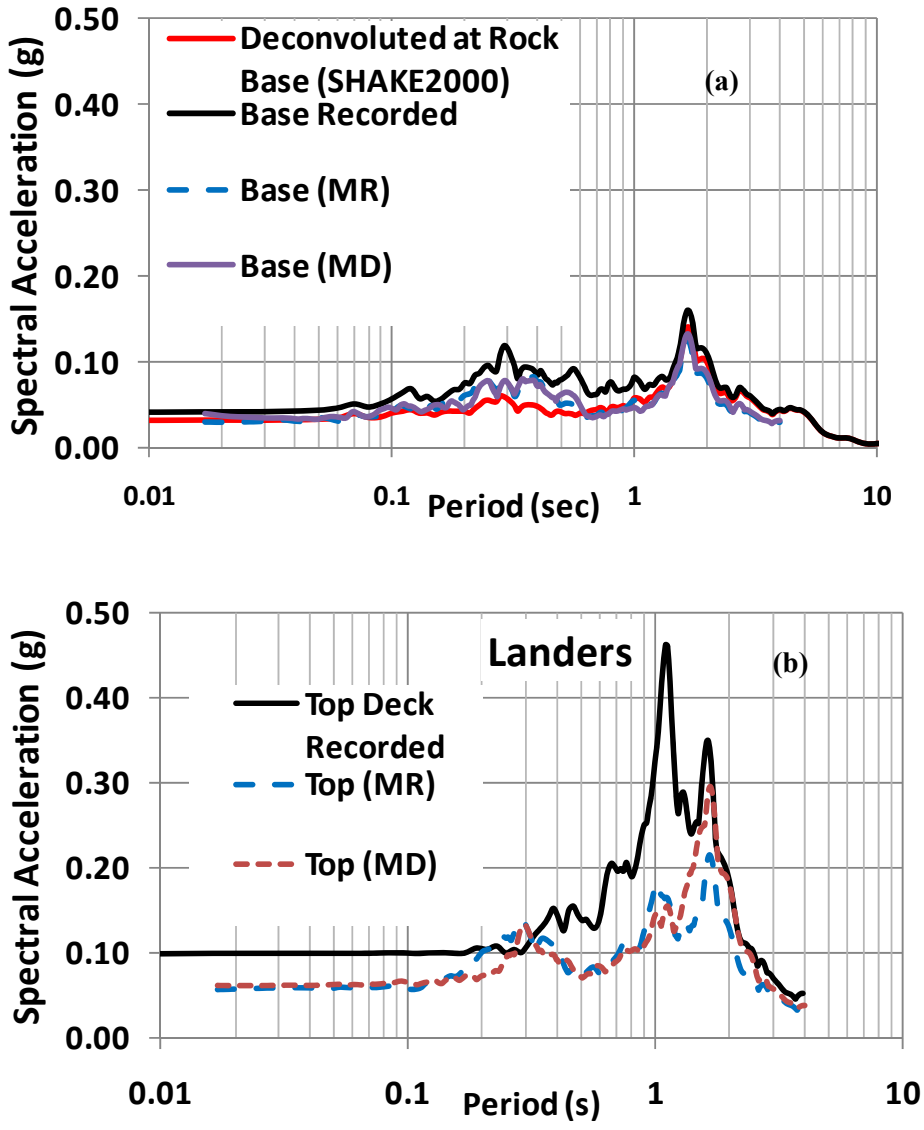

Figure 10-40 Comparison between the MR and MD calculated response and the recorded response spectra for the Landers earthquake (a) base and (b) top deck

To determine which analysis approach is more suitable for using in future MSW modeling, the calculated and recorded responses for the top deck of the OII landfill is plotted together in Figure 10-41 to Figure 10-44. Inspection of these figures suggests that the MRR analysis predicts the response at the top deck of the landfill better than the MR or MD analyses. Figure 10-41 shows the comparison for the case of the Northridge earthquake. The comparison in Figure 10-41 shows that the MRR analysis predicts the response at the top of the deck better than the other two approaches. However, the MRR does slightly underpredict analysis the peak ground acceleration at the top deck. Figure 10-42 shows the comparison for the case of Northridge aftershock. For the case of Northridge aftershock the MRR analysis slightly underpredicts the peak spectral acceleration but in general is reasonably accurate. Figure 10-43 shows the comparison of calculated and measured response of the top deck for the Pasadena. The MRR analysis predicts the response at station on the top deck of the OII landfill fairly well except in the mid period range (0.2-0.4s). The peak spectral acceleration in case of MRR analysis is slightly shifted to a higher period compared to the measures response. Figure 10-44 shows the comparison between the calculated and measured response for the Landers earthquake. None of the analyses produced a response comparable to the measured response, especially in the short period range.

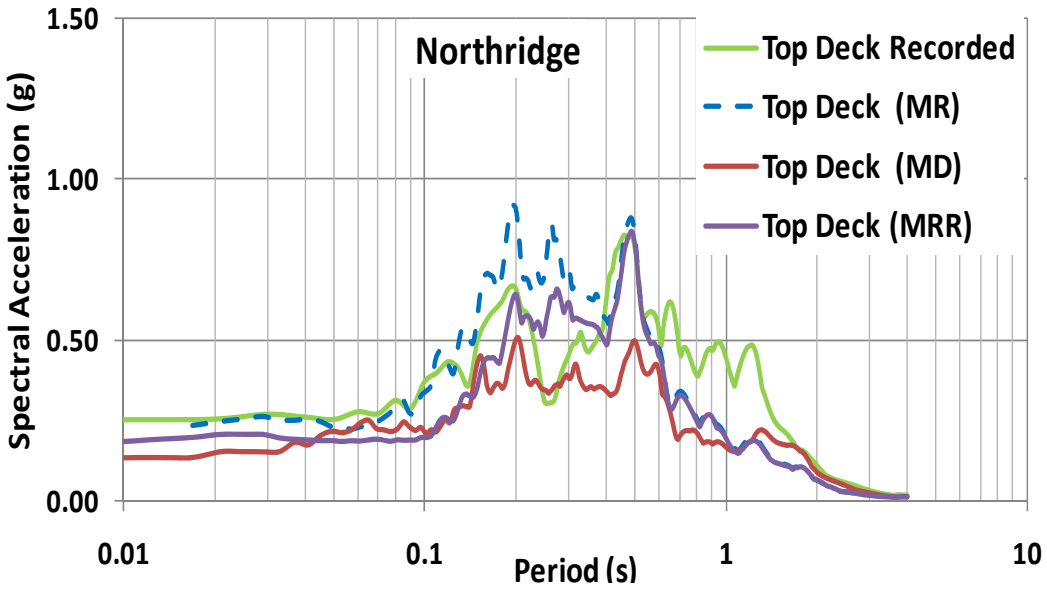

Figure 10-41 Comparison among the calculated and recorded response spectra for the Northridge earthquake at the top deck of the OII landfill

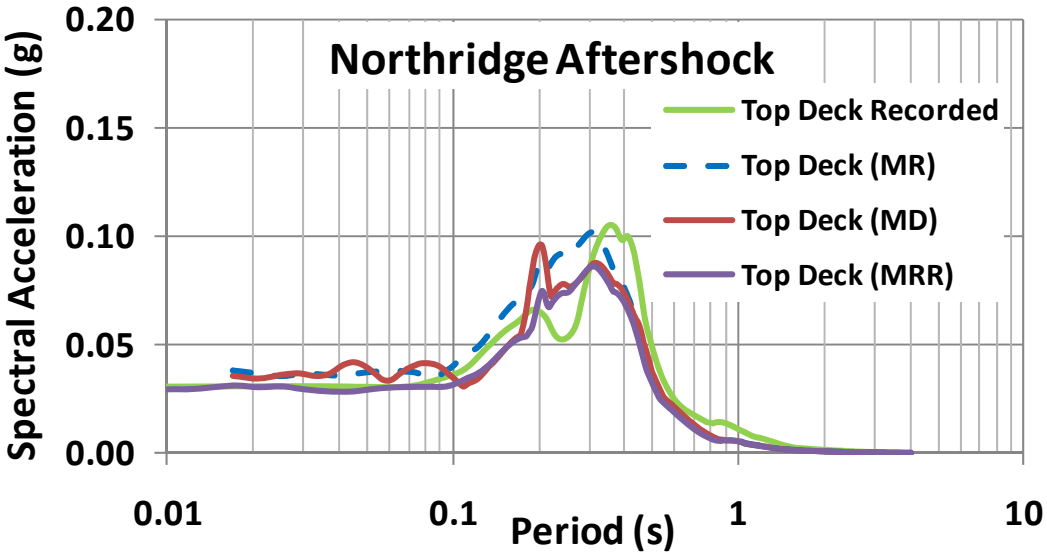

Figure 10-42 Comparison among the calculated and recorded response spectra for the Northridge Aftershock earthquake at the top deck of the OII landfill

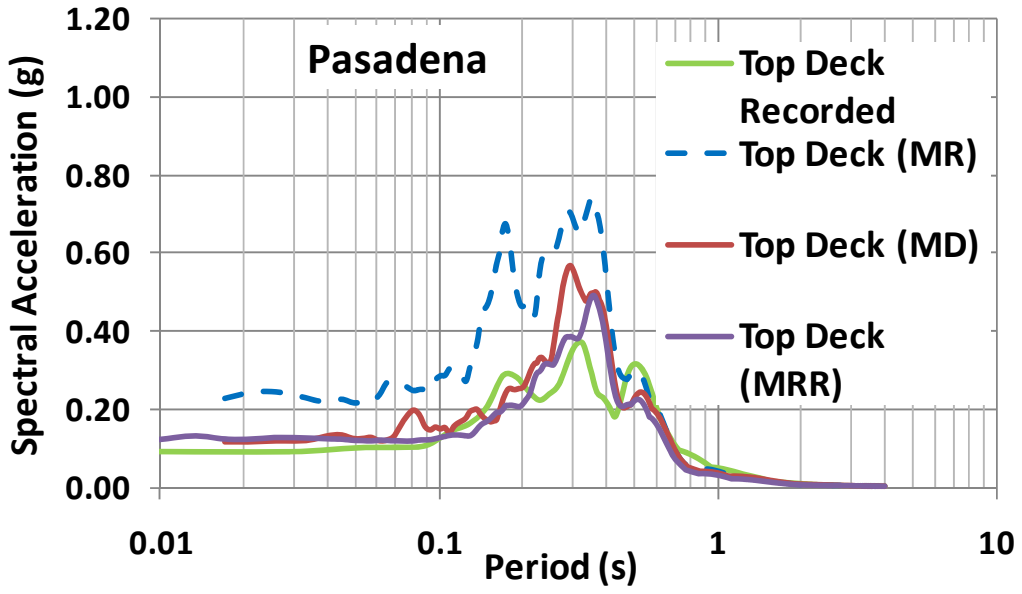

Figure 10-43 Comparison among the calculated and recorded response spectra for the Pasadena earthquake at the top deck of the OII landfill

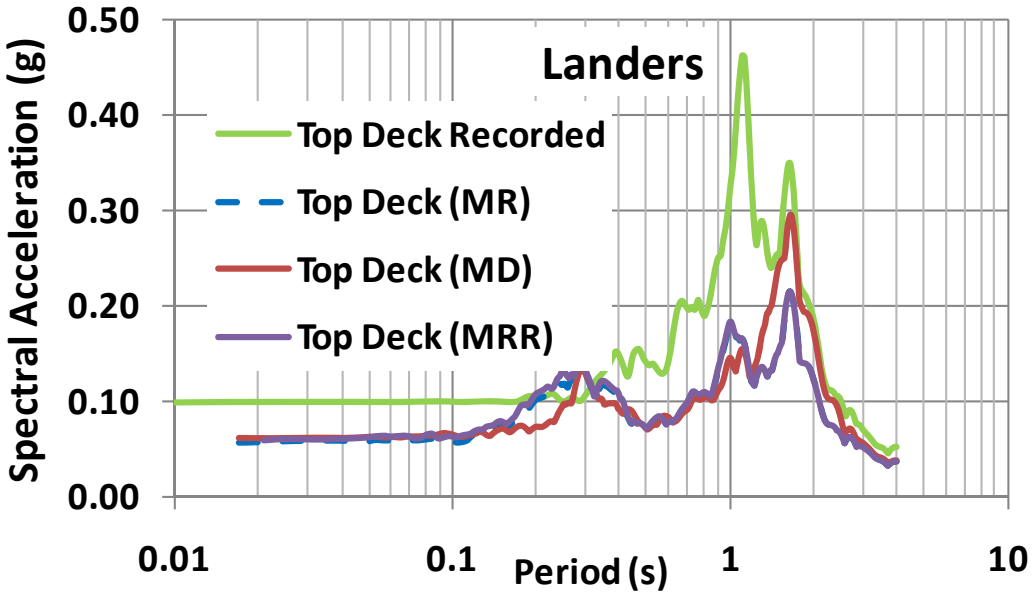

Figure 10-44 Comparison among the calculated and recorded response spectra for the Landers earthquake at the top deck of the OII landfill

10.10 Summary

The mechanical properties of the OII landfill solid waste were characterized based upon field and laboratory testing and back analyses of strong motion data recorded at the base and top deck of the OII landfill for use in subsequent numerical studies. Shear wave velocity and unit weight profile were established based upon data from field studies at the site (GeoSyntec 1996). The modulus reduction "backbone curve" was varied until the best match for the measured response at the landfill top deck in a series of five earthquakes was attained using Masing criteria for the hysteresis damping and adding 2% Raleigh damping. The geometry of the waste, soil, and weak rock materials used in the back analysis was based upon borings, topographic maps, and other information on the history of landfill development provided in Matasovic and Kavazanjian (1998) and GeoSyntec (1996). The properties of the soil and weak rock materials were based upon the results of the field investigation and typical properties described in GeoSyntec (1996).

The numerical analysis of landfill seismic response was performed using two-dimensional nonlinear time domain response analyses with the computer program FLAC 6.0. However, as the base strong motion station was located on fill, the "outcrop" input motions for the two-dimensional back analyses had to be determined by deconvolution of the recorded base station motions. The deconvolution analyses were performed using the one-dimensional equivalent-linear frequency domain computer program SHAKE2000.

Results of the landfill seismic response analysis using the deconvoluted motions indicated that the ASU curve for 65% ≤ 20mm material with 2% Raleigh damping give the best results for the response at the top deck of the OII landfill compared to the

recorded data. For subsequent numerical studies this curve along with Masing rule and 2% Raleigh damping will be used along to characterize the cyclic stress-strain behavior of MSW.

CHAPTER 11 LINED LANDFILL CASE HISTORIES

11.1 Introduction

The 1994 Mw 6.7 Northridge earthquake (Northridge earthquake) provided an excellent opportunity to study the performance of landfills subject to strong levels of earthquake shaking. Several groups of researchers investigated the seismic performance of landfills located within 100 km of the epicenter of the 1994 Northridge earthquake (Augello et al. 1995, Matasovic et al. 1995, Stewart et al. 1994). Matasovic et al. (1995) summarize the seismic performance of twenty-two landfills within 100 km of the epicenter subjected to ground motions with an estimated free field PGA in excess of 0.05 g. Nine of these landfills had geosynthetic liner systems over at least part of the waste disposal area. Only one of these landfills, the Chiquita Canyon landfill, was reported to have experienced significant damage to the geomembrane component of the lining system. A small tear (150 to 200 mm in length) in the geotextile overlying the side slope liner of Lopez Canyon landfill was reported by the California Integrated Waste Management Board (CIWMB). However, this tear was attributed to operating equipment and not to the earthquake by the landfill engineer (GeoSyntec 1994). The rest of the lined landfills addressed by Matasovic et al. (1995) were not reported to have experienced any damage to the lining system. Other reported damage at the twenty one landfills ranged from moderate to none, where moderate typically referred to minor cracks in soil cover without any major impact on the integrity of the landfill systems.

In this chapter two case histories from the Northridge earthquake will be back analyzed: the Chiquita Canyon landfill and the Lopez Canyon landfill. At the Chiquita Canyon landfill damage to the lining system was observed after the earthquake. In the

case of the Lopez Canyon landfill, only minor damage was observed, with no apparent damage to the waste containment system, despite very strong shaking at the landfill site. Each case history in this chapter begins with a brief review of the landfill's characteristics, including a summary of its performance during the Northridge earthquake. Next, a description of the analytical techniques employed in the case history analysis is provided along with a summary of the dynamic properties of the soil and waste fill materials employed in the back-analysis. Finally, the back-analysis of landfill performance in the Northridge event is presented.

11.2 Back Analysis of Chiquita Canyon Landfill

11.2.1 Landfill description

The Chiquita Canyon landfill was the only landfill that was reported to have experienced significant damage to the geosynthetic components of the lining system in the 1994 Northridge earthquake (Matasovic et al. 1995). EMCON Associates (1994) conducted an assessment of the damage to the Chiquita Canyon landfill lining system after the 1994 Northridge earthquake. The EMCON report provides a detailed description of the site and the damage observed at two different cross sections of the landfills.

The Chiquita Canyon landfill is located at the western edge of the Santa Clara Valley. Topography to the north, east and west of the site is characterized by east-west orientated steep-sided canyons with slopes that typically approach 1H:1V. The Chiquita Canyon landfill consists of five waste disposal units designated as the Primary Canyon and Canyons A, B, C and D. The landfill began operations in 1972 with the opening of the Primary Canyon landfill. Canyon D was partially filled and only used for landfilling

during wet weather at the time of 1994 Northridge earthquake. Canyon C, which consists of two cells, was the active area of the landfill at the time of the earthquake. The geosynthetic liner systems for Cell I in Canyon C was completed in 1991 and Cell I was actively receiving waste at the time of the earthquake. Cell II in Canyon C was not constructed at the time of the earthquake (EMCON Associates 1994).

Chiquita Canyon is regulated as a California Class 3 (municipal solid waste) landfill and received mostly municipal solid waste. However, the facility also received some construction and demolition debris and a small amount of sewage sludge with a solids content of greater than 50% (EMCON Associates 1994). The refuse deposited in Canyons C and D is relatively recent in age, with most of the waste being placed in the 8 years leading up to the Northridge earthquake (EMCON Associates 1994).

At the time of Northridge earthquake, the free face of the Canyon C landfill had a slope of about 2H:1V, while the lined side slopes, cut into the canyon wall, varied from 1.5H:1V to 2H:1V. The Canyon C landfill side slopes were lined with a 1.5 mm (60mil)-thick smooth HDPE geomembrane liner placed directly on a prepared subgrade. The base of the landfill was lined with a composite liner consisting of a 0.6 m thick low permeability soil-bentonite admixture underlying a 1.5 mm single-sided textured HDPE geomembrane (textured side down). The base of the Canyon C landfill has a leachate collection layer which consists of a network of polyvinyl chloride (PVC) pipes within a 0.3 m-thick gravel layer. The maximum refuse depth at the time of the earthquake was approximately 30 m. Figure 11-1 shows a plan view and cross section through the Canyon C landfill at the time of the earthquake in the area in which the geomembrane liner tear was observed.

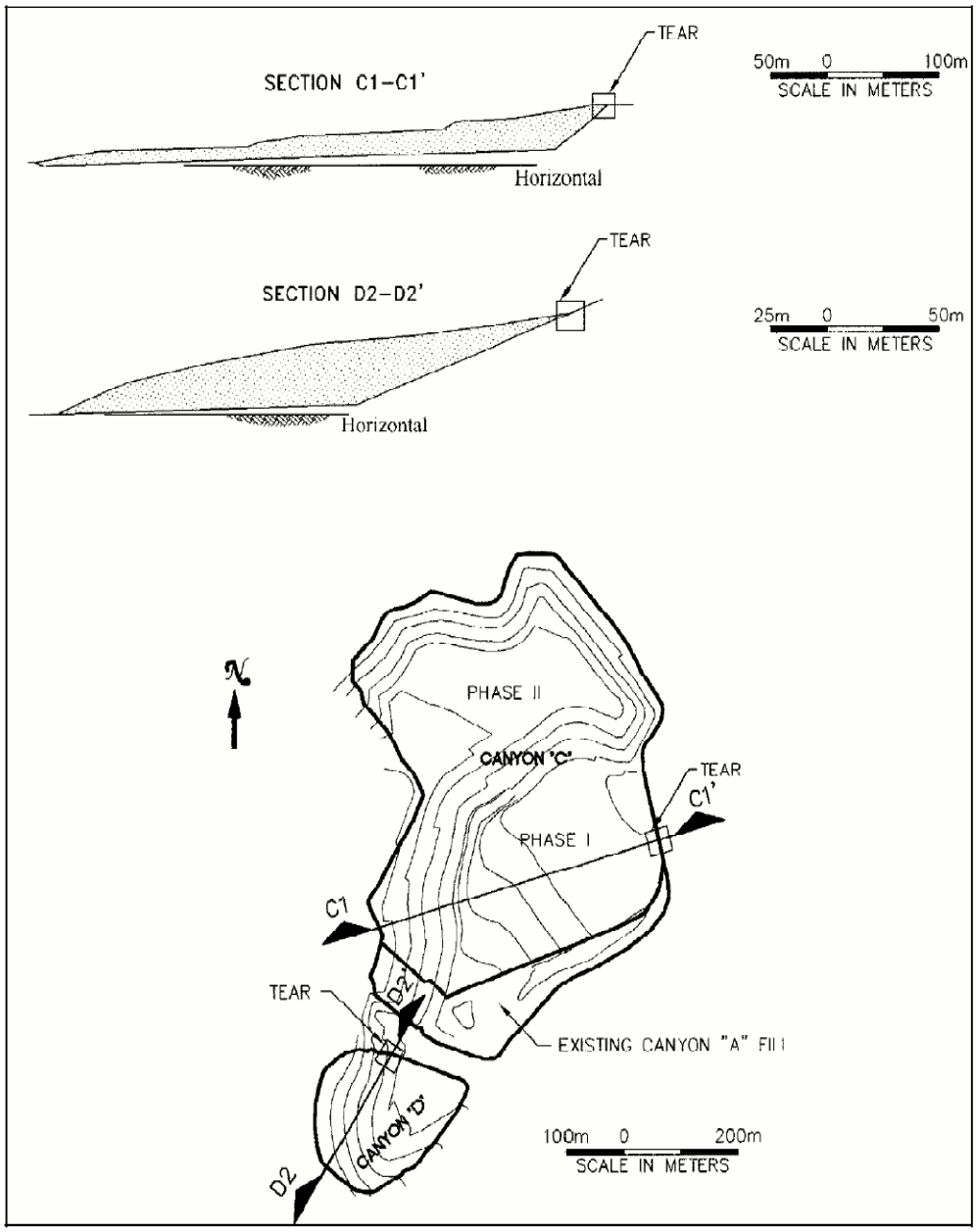

Figure 11-1 Plan view and cross sections through the Chiquita Canyon landfill (Augello et al. 1995).

In 1994 (at the time of the earthquake), the Canyon D landfill had a free face slope of approximately 3H:1V. The inclination of the cut side slopes in Canyon D was

2.5H:1V. The side slopes in Canyon D are lined with a 1.5 mm (60 mil)-thick smooth HDPE geomembrane placed directly over the subgrade and covered with 0.6 m of protective soil cover. The base of the Canyon D area is lined with only a 0.3 m-thick soil liner consisting of a mixture of alluvium and 9 percent bentonite (by dry weight) without a geomembrane. The leachate collection system in Canyon D consists of a 150 mm sand layer over the base soil liner. A cross section of Canyon D is also presented in Figure 11-1.

11.2.2 **Landfill damage**

Tears in the geomembrane side slope liner occurred in both Canyons C and D near the top of the slope at the locations shown in Figure 11-1. The damage observed at these locations included limited downslope movement of the waste, cracks in the soil cover, and tears in the geomembrane liner system. There was also a temporary shutdown of the gas extraction system at the landfill due to a loss of external power (Augello et al. 1995). Cracks in the soil cover were observed in all areas of the landfill after the earthquake.

In Canyon C, longitudinal cracks approximately 300 mm wide with vertical offsets of 150 to 300 mm were observed at the top of the slope along the interface between the landfill liner and the waste fill. One localized tear, at the top of the slope near the anchor trench, was observed in Canyon C after the earthquake. The tear was approximately 4 m long and 0.24 m wide (Augello et al. 1995). Figure 11-2 shows a picture of the tear after Northridge earthquake.

Figure 11-2 Tear in HDPE geomembrane liner system, Canyon C, Chiquita Canyon Landfill (photo courtesy of Calif. EPA, Integrated Waste Management Board)

The earthquake-induced cracks in Canyon D were as wide as 300 mm, with 200 mm of vertical offset, exposing the landfill liner in some areas. While no tear was noticed immediately after the earthquake in January 1994, several tears in the geomembrane liner were found in Canyon D during landfill gas monitoring one month later, in February 1994. The damage uncovered in February 1994 in Canyon D consisted of three parallel tears, each approximately 0.3 m wide, with a total length of 27 m at the top of the side slope near the anchor trench (EMCON Associates 1994).

Less pronounced cracks than observed in Canyons C and D were observed in cover soils of the Primary Canyon A and Canyon B after the earthquake. In Canyon A, typical

cracks were at the top of the slope and were on the order of 150 mm wide with approximately 130 mm of vertical offset.

11.2.3 **Post-Earthquake investigation**

As a part of the post-earthquake investigation, EMCON Associates (1994) obtained samples of geomembrane from the two tear areas beneath and above the liner. EMCON Associates (1994) also conducted in situ density measurements using the sand cone method and sampled the soil above and below the tear areas. Laboratory testing was conducted to classify the soil above and below the geomembrane. Table 11-1 presents a summary of the soil classification test results.

Table 11-1 Soil classification for the soil above and below torn geomembrane at the Chiquita Canyon landfill (data from EMCON Associates, 1994)

Sample ID	Sample location	Dry density (Kg/m^3)	Classification	Liquid limit	Plastic Limit
CA	Above Canyon C geomembrane	1717.18	Clayey Sand	-	-
CB	Below Canyon C geomembrane	1774.8	Sandy Clay	24	2
DA	Above Canyon D geomembrane	1566.6	Clayey sand	-	-
DB	Below Canyon D geomembrane	1968.7	Gravelly sand	-	-

EMCON Associates (1994) also conducted a series of interface shear tests on the geomembrane/ soil interfaces for the side slope liners in Canyon C and Canyon D. These tests were conducted in a 304.8 mm by 304.8 mm direct shear device. Geomembrane samples recovered from the landfill were used in the interface shear testing. All the testing was done using soil compacted to the in situ dry density at 2% above the in situ moisture content (i.e. on unsaturated soil). Interface shear test results are summarized in

Table 11-2. EMCON Associates (1994) repeated the direct shear tests using wetted interfaces and saturated soil with one degree decrease in interface shear strength. EMCON Associates (1994) reported an undrained shear strength for the low permeability soil-bentonite admixture of about 62.2 kPa.

Table 11-2 Interface shear test results from EMCON Associates (1994)

Sample ID	Sample location	Peak friction angle (degree)	Large displacement friction angle (degree)	Initial stiffness, E_i (Pa/m)
CA	Above Canyon C geomembrane	27	24	8e7
CB	Below Canyon C geomembrane	24	22	5.5e7
DA	Above Canyon D geomembrane	26	24	4.7e7
DB	Below Canyon D geomembrane	29	28	4.5e7

As part of the post-earthquake investigation, a study on the fracture morphology of the geomembrane was conducted by researchers at Drexel University using a scanning electron microscope to investigate the tear initiation and growth mechanism (EMCON Associates 1994). Six specimens from the Canyon C side slope geomembrane liner (S-1 to S-6) were sampled from locations adjacent to two tear faces in Canyon C at the locations indicated in the sketch presented in Figure 11-3. Based on the fracture morphology, it was concluded that the tear likely initiated from location of samples S-3 and S-4, i.e. at the fillet extrusion used to weld the patch at this location, and then propagated perpendicular to the dual hot wedge seam, i.e. perpendicular to the loading direction (EMCON Associates 1994).

As part of the post-earthquake investigation, eight 203.2 mm wide-width geomembrane specimens were tested under axial tensile loading conditions. Two sets of tests were performed at two different strain rates (50 mm/min & 500 mm/min). An

average yield stress of $2.0x10^4$ kPa was measured at a yield strain of 14% and a break strain of 64% was measured at the break point for the 50 mm/min strain rate. An average yield stress of $2.34x10^4$ kPa was measured at a yield strain of 12% and a break strain of 46% was measured at the break point for the 500 mm/min strain rate. These results indicate that the yield and break strain decreased due to the increase in the strain rate (EMCON Associates 1994). EMCON Associates (1994) noted that failure was always initiated at the location of surface defects in the wide width tensile tests.

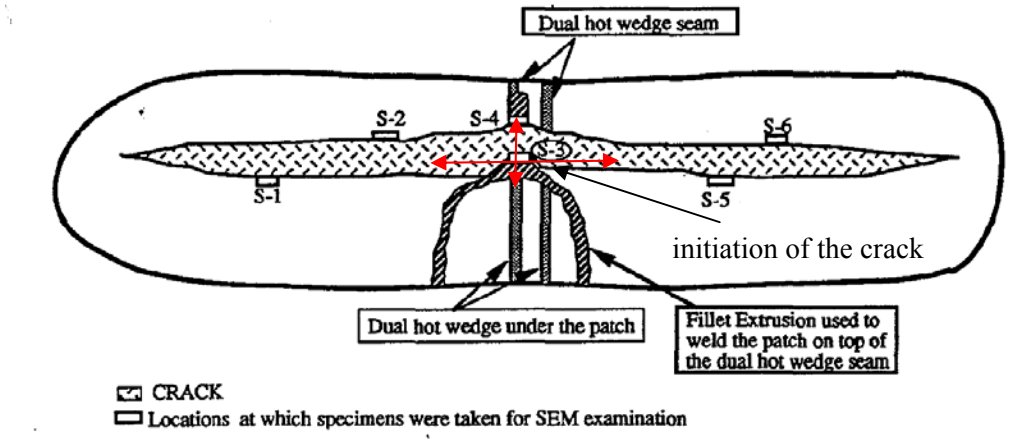

Figure 11-3 Geomembrane tear in Canyon C (after EMCON Associates 1994)

A similar fracture morphology study was conducted for the tears in Canyon D, (EMCON Associates 1994). Six coupons were recovered at locations adjacent to the tear faces in Canyon D at the locations indicated in Figure 11-4 and evaluated using a scanning electron microscope. Three major tears were observed in Canyon D. Tear #1 took place along the edge of a rib and proceeded across a fillet extrusion Seam 1 and then changed direction extending to the adjacent rib. Tear #2 took place along the edge of two extrusion seams and a section of the tear propagated along the seamed edge of a patch (EMCON Associates 1994). A large part of Tear #3 occurred in the geomembrane rather

than along a rib. One end of Tear #3 propagated along the edge of Seams 2 and 4 for almost 305 mm. The location and geometry of these tears are shown in Figure 11-4.

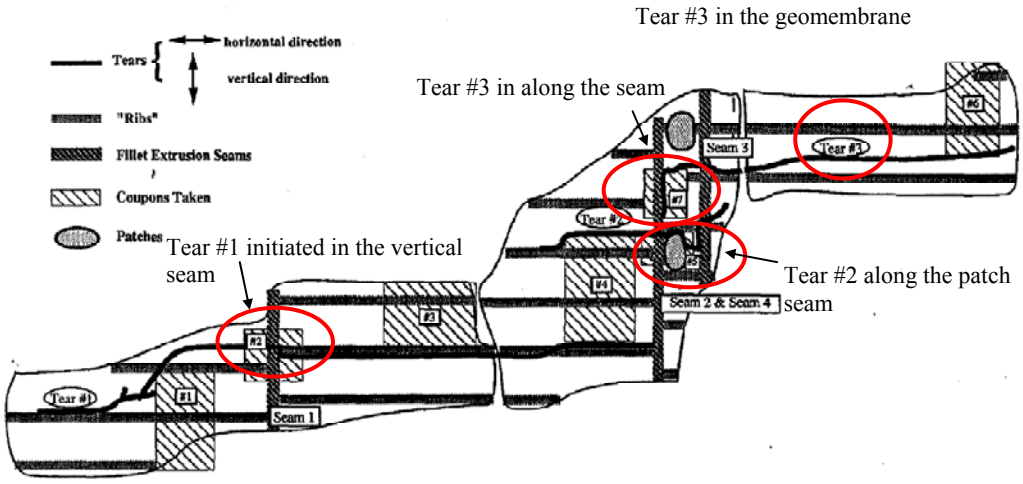

Figure 11-4 Geomembrane tears in Canyon D (after EMCON Associates 1994)

The fracture morphology study revealed that Tear #1, a long horizontal tear, initiated from two locations, the vertical seam and the grind lines adjacent to the seam. As the tear grew longer, the stress acting on the seam became so great that it pulled the seam apart via a ductile failure according to EMCON Associates (1994).

According to EMCON Associates (1994), Tear # 2 was initiated in a defect or a void in fillet extrusion seam as shown in the sketch in Figure 11-5. The failure began at the defect and radiated outward. EMCON Associates (1994) concluded that this failure was characterized by rapid crack propagation in a brittle material during the earthquake.

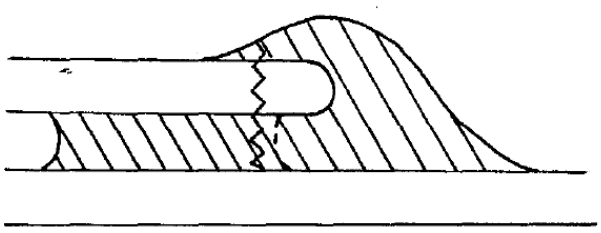

Figure 11-5 Crack through a doubly seamed region consisted of a fillet extrusion seam on top of a flat extrusion seam (EMCON Associates 1994).

Similar to Tear #1, EMCON Associates (1994) hypothesized that Tear #3 was initiated at a stress concentration at the vertical seam caused by the grinding lines. In a similar fashion to Tear #1, the major horizontal tear associated with Tear #3 began at one end of the vertical seam and then propagated to the right hand side of the seam.

As part of the evaluation of the geomembrane tears in Canyon D, eight 203.2 mm wide-width geomembrane specimens were tested under axial tensile loading. Two sets of tests were performed at strain rates of both 50 mm/min and 500 mm/min. An average yield stress of 1.93×10^4 kPa was measured at a yield strain of 14% and a break strain of 64% was measured for the 50 mm/min strain rate. An average yield stress of 2.07×10^4 kPa was measured at a yield strain of 13% and a break strain of 50% was measured for the 500 mm/min strain rate. Once again, the yield and break strains decreased due to the increase in the strain rate (EMCON Associates 1994).

The measured geomembrane stress and strain at yield from wide width tensile test on the specimens from both canyons C and D along with secant modulus at yield are summarized in Table 11-3.

Table 11-3 Strain, stress, and secant modulus at yield for Chiquita Canyon geomembrane (data from EMCON Associates 1994)

Cross Section	Strain at yield, ε_y (%)		stress at yield, σ_y (kPa)		Secant modulus at yield, E_y (pa)	
	Strain rate 50mm/min	Strain rate 500mm/min	Strain rate 50mm/min	Strain rate 500mm/min	Strain rate 50mm/min	Strain rate 500mm/min
C1-C1	14	12	2.0e4	2.3e4	1.4e8	1.9e8
D1-D1	14	13	1.93e4	2.1e4	1.4e8	1.6e8

11.2.4 **Waste properties for the Chiquita Canyon landfill**

No testing was done to characterize waste properties at the Chiquita Canyon landfill. So, typical profiles for both unit weight and shear wave velocity from literature were used for the seismic analyses of performance of the Chiquita Canyon in the Northridge earthquake. The unit weight profile for MSW developed by Zekkos et al. (2006) for typical compaction effort, presented in Figure 3-54, and the shear wave velocity for typical MSW landfills in southern California developed by Kavazanjian et al. (1996), presented in Figure 3-55, were used in the seismic analysis of the Chiquita Canyon Landfill. The best estimate shear modulus degradation and damping curves from the back analyses for the OII landfill described in Chapter 10, presented in Figure 10-25, were used to represent the waste material in the analyses presented herein. A Poisson's ratio of 0.33 was used for the waste, similar to average measured value at the OII site.

The shear strength of the waste was characterized using the bilinear envelope for MSW developed by Kavazanjian et al. (1995), presented in Chapter 4., and represented

by ϕ = 0 with c = 24 kPa at normal stresses below 30 kPa and ϕ =33 degrees with c = 0 at higher normal stresses.

11.2.5 **Input motions**

There was no strong motion station in the immediate vicinity of the landfill, so representative accelerograms from one of the closest stations to the site had to be used to represent the strong motions at the landfill. Chiquita Canyon is a rock site located between the Newhall and Castaic Dam strong motion stations. The Castaic Dam records were chosen by EMCON Associates (1994) to represent the rock motion at the Chiquita canyon landfill site. Two reasons for choosing the Castaic Dam records were presented by EMCON Associates (1994). First, the strong directivity of the Northridge earthquake makes the Castaic Dam records more suitable as they are oriented on a similar azimuth as the landfill. Second, the Castaic Dam recording station is rock site, similar to the landfill site, while the Newhall site is a soil site. Therefore, the two horizontal acceleration time histories from the Castaic Dam station (90- and 360-degree components) were used in the seismic analyses.

The recorded peak ground acceleration for the Castaic Dam records are 0.56 g and 0.5 g for the 90- and 360-degree components, respectively. However, these acceleration time histories were scaled to the mean PGA predicted using four of the 2008 NGA (Next Generation Attenuation) relationships as presented in the spread sheet developed by Al Atik (2009). The Abrahamson and Silva, Chiou and Youngs, Boore and Atkinso, and Campbell and Borzorgnia NGA relationships were employed in this study. The NGA 2008 spread sheet predicted a mean PGA of 0.28 g and a mean plus one standard deviation PGA of 0.48 g at the Chiquita Canyon landfill for the Northridge earthquake.

The scaled strong motion records are assumed to be outcrop motions, i.e. ground motions at the surface of a horizontal rock outcrop at the landfill site. To transform these strong motion records into ground motions that can be applied at the base of the 2-D models used in this analysis a deconvolution procedure was employed. The deconvolution procedure used SHAKE2000 to calculate the upward propagating motion at the base of the 2-D models according to the procedure described by Mejia and Dawson (2006) and illustrated in Figure 11-6.

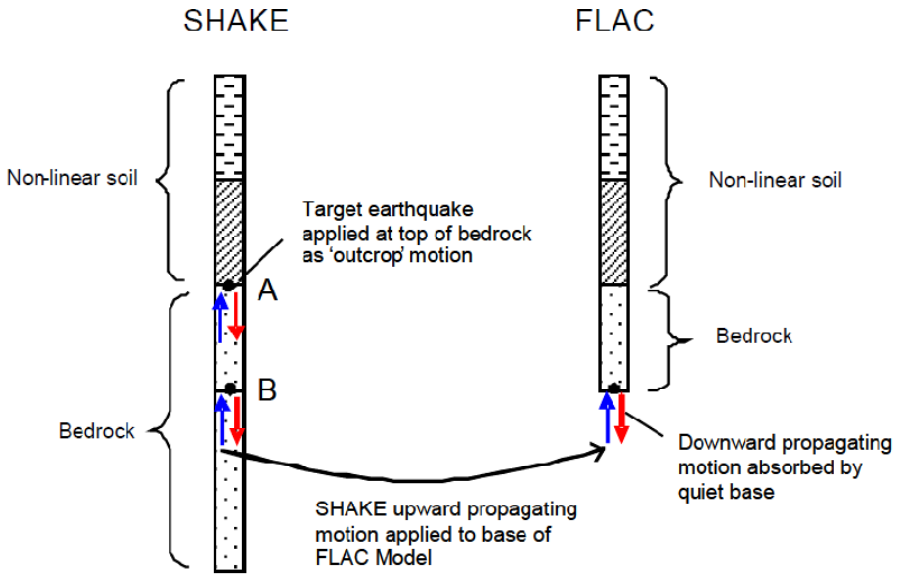

Figure 11-6 The deconvolution procedure for FLAC 6.0 (Mejia and Dawson 2006)

Figure 11-7 and Figure 11-8 show the acceleration response spectra (ARS) for the deconvoluted motion versus the ARS for the scaled outcrop motion for the two components of the Castaic Dam record scaled to a PGA of 0.28 g. The figures shows that the deconvoluted spectral accelerations are little lower than the outcrop spectral accelerations in all cases.

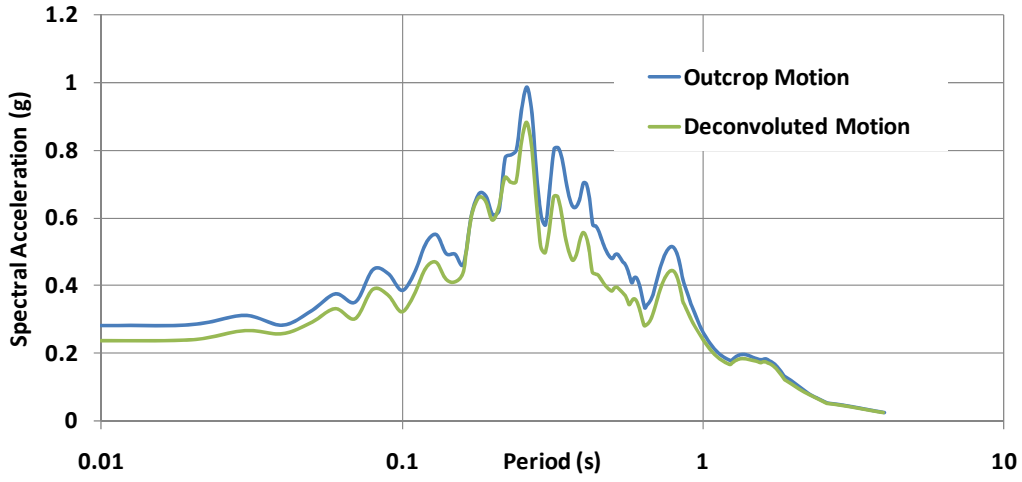

Figure 11-7 Comparison of acceleration response spectra for -90^{o} component at Castaic Dam scaled to 0.28 g versus the deconvoluted motion

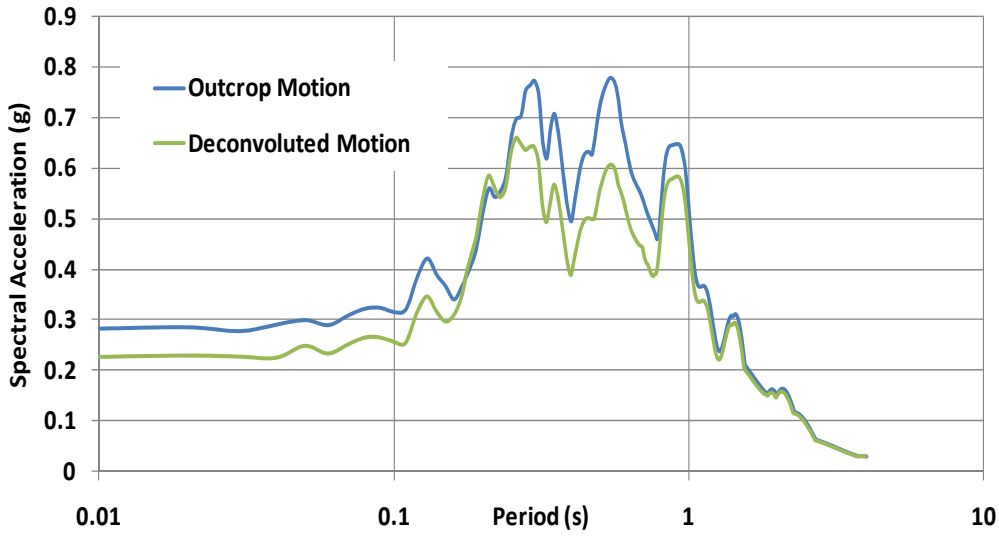

Figure 11-8 Comparison of acceleration response spectra for -360^{o} component at Castaic Dam scaled to 0.28 g versus the deconvoluted motion

11.2.6 **2D finite difference models for Chiquita Canyon landfill**

A finite difference mesh was developed to back analyze the seismic response of cross section C1-C1 as presented in Figure 11-9 (a). The mesh for cross section C1-C1 has more than 9,000 zones, with a higher density of zones towards the waste body. Another finite difference mesh developed to back analyze the seismic response of cross section D1-D1 as presented in Figure 11-9 (b). The mesh for cross section D1-D1 has more than 4,000 zones and also has a higher density of zones towards the waste body. In both finite difference models the geomembrane was modeled as a beam element with interface elements on both sides. In cross section D1-D1, an HDPE geomembrane is deployed only on the side slope while in cross section C1-C1 a geomembrane is deployed on both the side slope and the base of the landfill.

Interface elements were attached to the top and bottom of the beam element to model the geomembrane / foundation soil and geomembrane / leachate collection layer interfaces. However, the low permeability soil layer beneath the base geomembrane in cross section C1-C1 was not included in the model and the leachate collection layer on top of the base geomembrane was also ignored in the analyses to simplify the model. This configuration allows for different interface shear strengths on either side of the geomembrane liner element. The beam element was fixed at the top of the slope in the x and y direction to simulate the anchor trench in the analyses reported in this chapter.

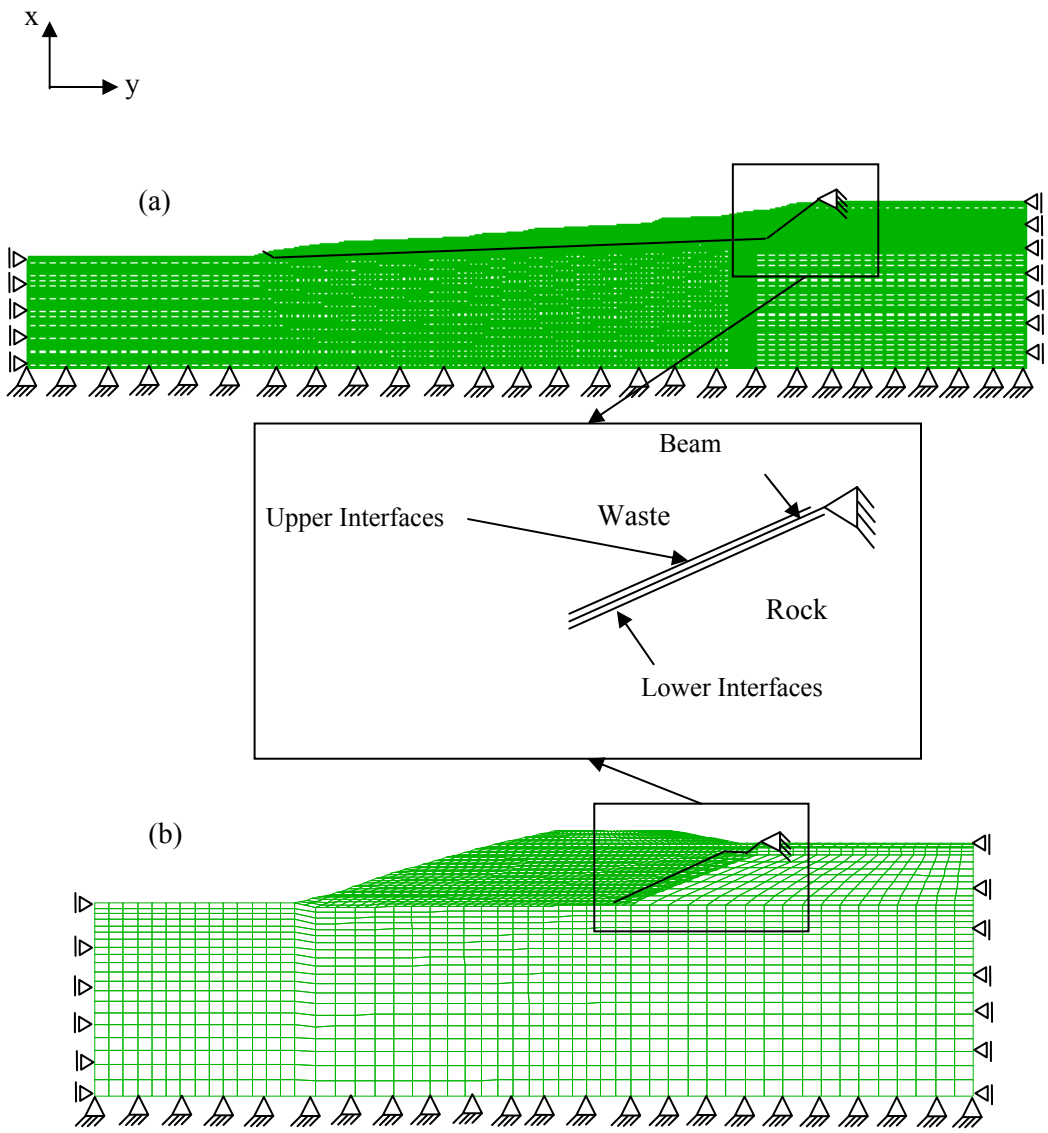

Figure 11-9 Finite difference mesh for Chiquita Canyon landfill cross sections: (a) cross section C1-C1 (b) cross section D1-D1.

11.2.7 **Initial static analyses**

A procedure mimicking as closely as practical the assumed waste placement scenario in the field was used to initialize the stresses in the waste and on the liner before the seismic analyses was conducted. In this procedure, waste material was placed in 3 meters

horizontal lifts, similar to the assumed method of field operation. The Modified Cam-Clay (MCC) material model was used for the waste. The MCC parameters used for the waste material were established using the results of oedometer tests conducted by GeoSyntec (1995) on OII landfill waste material. The MCC properties for the waste are summarized in Table 11-4. Figure 11-10 illustrates the stratigraphy of cross section C1-C1 and cross section D1-D1after building the lifts of waste.

Table 11-4 Modified Cam-Clay parameters used for the Chiquita Canyon landfill waste material

	Initial void Ratio (e_o)	Slope of the consolidation line (λ)	Slope of swelling line (κ)	Preconsolidation Pressure (Pc) (kPa)	M	Unit weight (kN/m3)
MSW	2.0	0.182	0.0182	40	1.3	10.5

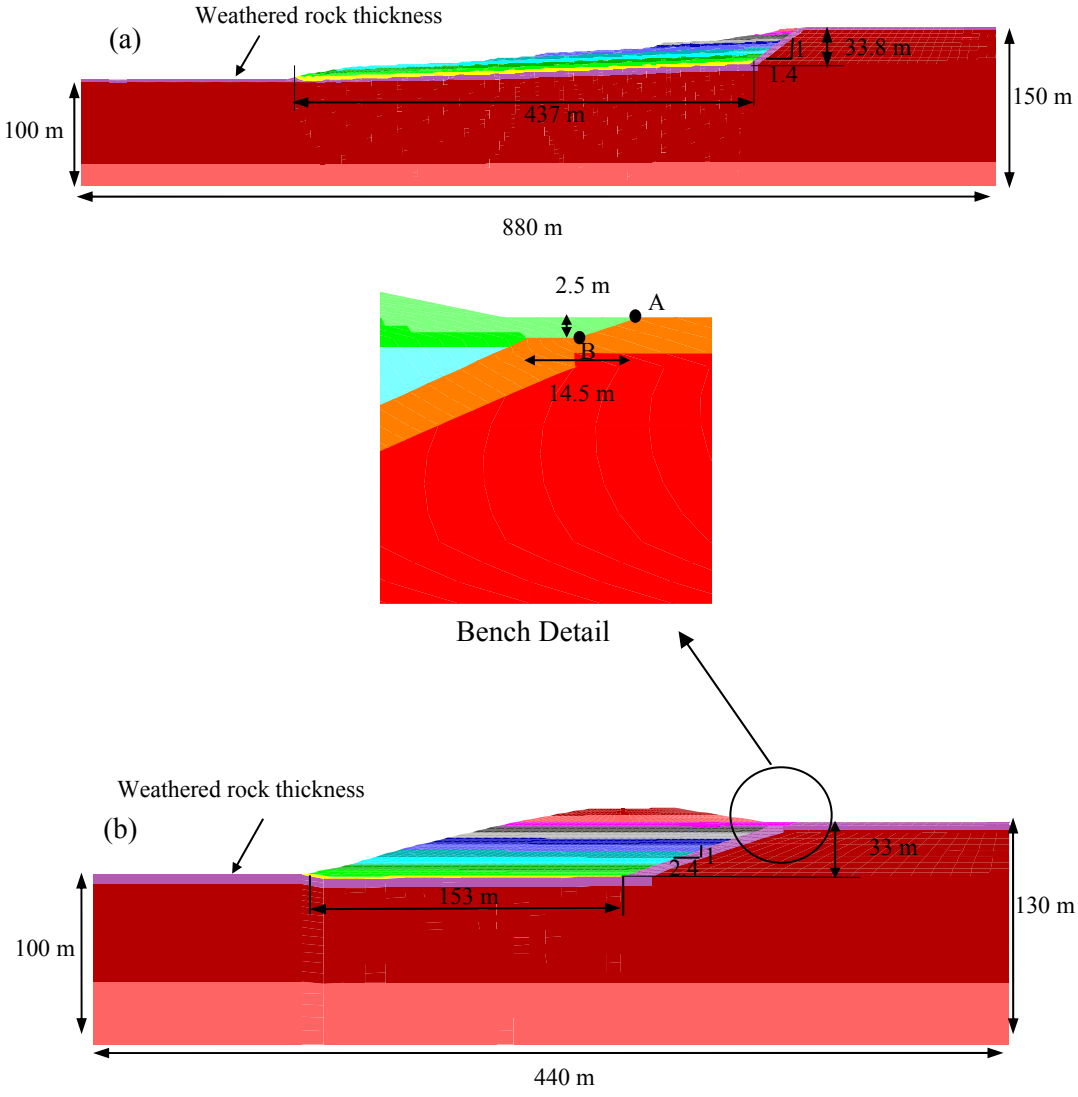

Figure 11-10 waste lift layering for the Chiquita landfill seismic analysis (a) cross section C1-C1 (b) cross section D1-D1.

11.2.8 **Non-Linear 2-D seismic analyses for the Chiquita Canyon landfill**

Waste and foundation material properties used in the seismic analyses for the cross sections C1-C1 and D1-D1 are summarized in Table 11-5. The waste layering is different in the seismic stage of the analysis than it was for the initial static stage. The initial shear modulus and bulk modulus of the waste increases with depth according to the assumed unit weight and shear wave velocity profiles and Poisson's ratio described earlier. Figure 11-11 shows the finite difference models for cross sections C1-C1 and D1-D1 for the seismic analyses.

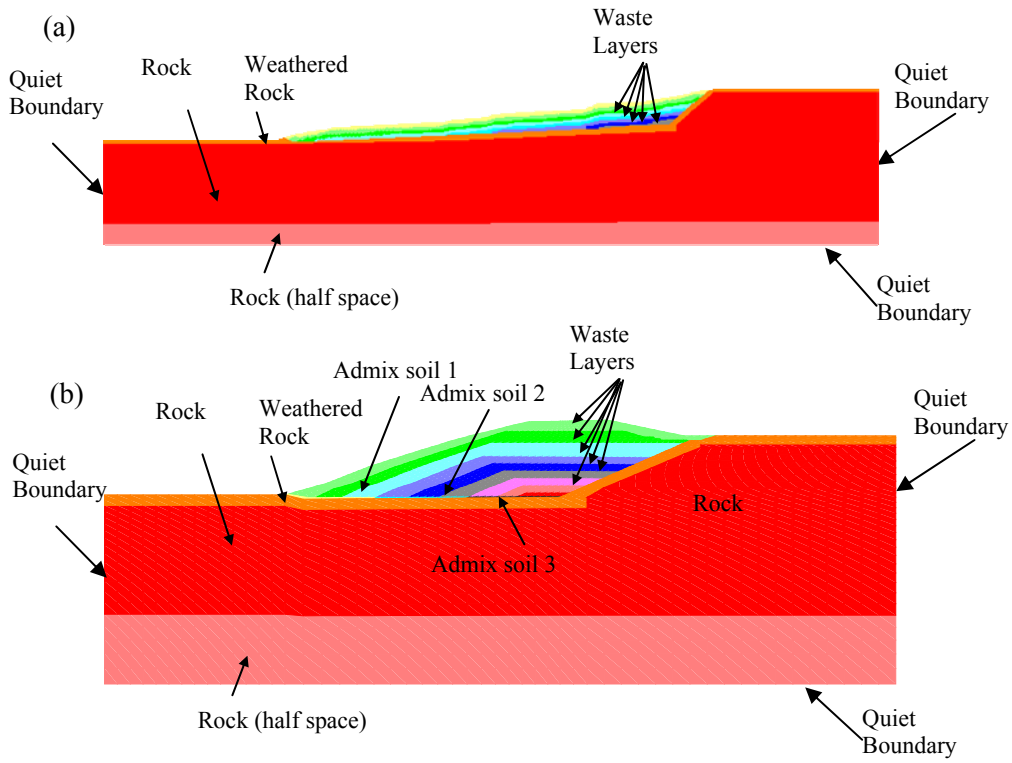

Figure 11-11 Finite difference model with boundary conditions for seismic analyses: (a) cross section C1-C1, (b) cross section D1-D1.

The initial elastic modulus and unit weight values assigned to the waste layers as a function of the depth below the surface of the landfill are presented in Table 11-5. The waste is treated in this stage of the analysis as a Mohr-Coulomb material rather than as a MCC material as it was in the initial static loading step. The waste was assigned a cohesion of 24 kPa and a friction angle of 0 for the top 3 meters and a friction angle of 33^{o} with 0 cohesion at greater depths, consistent with the bi-linear shear strength model described earlier. The rock foundation was modeled as a linear elastic material. In the seismic analysis quiet boundaries were used for the vertical side boundaries and the bottom boundary of the model to absorb the outgoing (downward and outward propagating) seismic waves instead of reflecting them back into the model.

Table 11-5 Waste and foundation material properties

	Layer	Thickness (m)	Unit weight (kN/m^3)	Shear wave velocity (m/s)	Poison's ratio
MSW	Layer 1	3	10.5	170	0.33
	Layer 2	3	11.1	190	0.33
	Layer 3	3	12.7	210	0.33
	Layer 4	3	12.8	240	0.33
	Layer 5	3	13	260	0.33
	Layer 6	3	13.1	275	0.33
	Layer 7	3	13.3	300	0.33
	Layer 8	3	13.6	315	0.33
	Layer 9	3	14	340	0.33
Clay Liner	Admixture base 1	1	18.9	240	0.33
	Admixture base 2	1	18.9	350	0.33
	Admixture base 3	1	18.9	450	0.33
Rock	Weathered Rock	5	16.5	500	0.25
	Rock	86	16.5	900	0.25
	Rock (half space)	23	18.8	1200	0.25

The waste and the low permeability admixture soil in the FLAC 6.0 seismic analyses were treated as nonlinear hysteretic materials using back bone curves. The back bone curves used in the seismic analyses for these materials are cited in Table 11-6. The small strain modulus in each element (or mesh zone) was based upon the shear wave velocity and unit weight.

Table 11-6 Backbone curves used in the seismic analyses for the Chiquita Canyon landfill

	ϕ degree	Modulus reduction and damping curves
MSW	33	ASU curve shown in Figure 10-25
Admixture base clay	30	Vucetic and Dobry (1991) (PI =15)

As illustrated in Figure 11-9, the geomembranes in cross sections C1-C1 and D1-D1 were modeled as beam elements with interface elements on both sides to attach them to finite difference mesh. FLAC 6.0 treats the beam element as a linear elastic material. However, Giroud (2005) showed that geomembranes exhibit nonlinear hyperbolic stress-strain behavior in tension up to yield, as discussed in Chapter 3. Therefore, in order to model the nonlinear behavior of the geomembrane beam elements in FLAC 6.0, the subroutine, JP_E_BeamVariable.fis, presented in Appendix D, was developed. This subroutine degrades the initial tangent modulus, E_G, with the axial tensile strain of the geomembrane according the equation derived by Giroud (1994) for the tangent modulus of a hyperbolic stress-strain curve presented in Chapter 3 as Eq. (4). Figure 11-12 shows the axial force versus axial strain curve for a geomembrane beam element as calculated by the subroutine, JP_E_BeamVariable.fis.

The lower interface elements are attached to the foundation soil and the upper interface elements are attached to the waste in the geomembrane beam model. The in-plane stress-strain behavior of interface elements in FLAC 6.0 are defined using two parameters: the initial stiffness, E_i, and the Mohr-Coulomb shear failure parameters (c and ϕ). The stiffness assigned to the interface elements in the back analysis was $1x10^9$ Pa/m. The upper and lower interface were assigned peak and residual friction angles using the constitutive model for GCL/GM in-plane peak and residual shear strength developed in Chapter 5. Because GM/GCL cyclic behavior was governed by interface behavior rather than internal shear behavior of the GCL at all but the lowest normal stresses, this was considered to be a reasonable assumption. The measured peak and residual friction angles for the upper and lower interfaces were used in the constitutive model along with a residual cumulative displacement, δ_r^p, of 300 mm and k of 0.52 in the constitutive model.

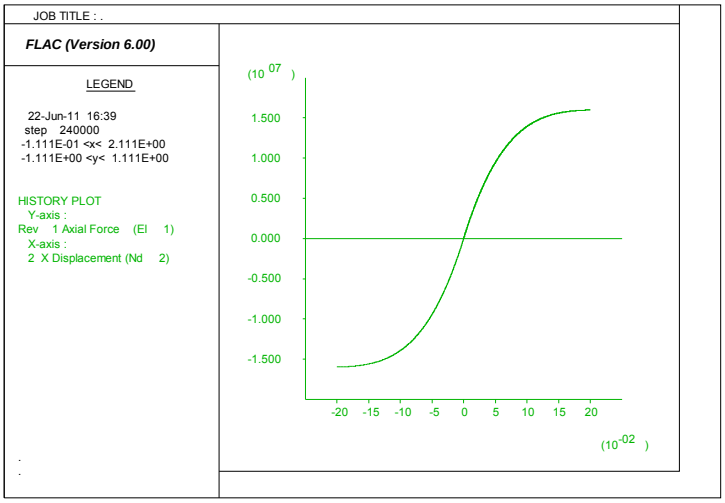

Figure 11-12 Geomembrane stress-strain curve according to Giroud (1994), with equal modulus in tension and compression

Chapter 12 includes a parametric study in which the stiffness of the geomembrane and the stiffness of the upper and lower interfaces along with their failure parameters were varied to test the effect of these parameters on the seismic performance of the landfill. However, only best estimate parameters are used in the back analyses presented in this chapter.

11.2.9 **Geomembrane Strains in cross section C1-C1**

The two strong motion records (090 & 360) from the Castaic Dam station, scaled to 0.28 g, were used in the back analysis. The parameters defining the behavior of the upper and lower interfaces and the geomembrane input parameters for cross section C1-C1 are presented in Table 11-7.

Table 11-7 also presents a summary of the maximum tensile strain in the geomembrane from the analyses for cross section C1-C1. The maximum tensile strains for the two strong motion records were 4.3% to 3.8%. In both cases, the maximum tensile strain was at the anchor point at the top of the slope.

Table 11-7 Tensile strain in the geomembrane for cross section C1-C1

Case*	Input motion	Lower Interface phi (degree)		Upper Interface phi (degree)		GM Max. Tensile Strain (%)	FS
		Φ_p	Φ_r	Φ_p	Φ_r		
1	090-0.28 g	24	22	27	24	4.3	0.45
2	360-0.28 g	24	22	27	24	3.8	0.56

* interface stiffness used $1x10^9$ pa/m and $4.8x10^8$ pa/m geomembrane initial stiffness

While the tensile strains calculated in the back analysis were well below the yield strain of the intact geomembrane, Giroud (2005) showed that failure in geomembranes in the field can occur in cases where the tensile strains are well below the yield strain due to

strain concentration. Therefore, the procedure proposed by Giroud (2005) to estimate the strain concentration due to seams and scratches in the geomembrane was followed to estimate the strain concentration and factor of safety for the geomembrane in cross section C1-C1.

Giroud (2005) presented several correction factors that should be applied to the nominal yield strain of a geomembrane from uniaxial tensile testing to estimate the yield strain in the field. First, Giroud (2005) showed that the yield strain under plain strain conditions is lower than yield strain in uniaxial tensile tests by a factor depending on Poisson's ratio and calculated according to Eqn. (6) in Chapter 3. Assuming a Poisson's ratio of 0.46 and a uniaxial yield strain of 12% for the geomembrane, the yield strain in case of plane strain conditions will decrease to 10.9% according to Eqn. (6). Giroud (2005) also showed that the yield strain will decrease due to scratches in the geomembrane according to the depth of the scratch, as illustrated in Figure 3-25. Assuming that the ratio of the depth of the scratch to the geomembrane thickness is 0.2, the ratio of the yield strain of scratched geomembrane, ε_{SY}, to the intact geomembrane yield strain is 0.35 according to Figure 3-25. This means the yield strain for a geomembrane with a scratch that penetrates 20% of the thickness of the geomembrane under plain strain conditions, ε_{SYps}, is 3.8%.

Giroud (2005) also showed that in the case of a seam in a geomembrane perpendicular to the loading direction, strain concentrations will be developed in the geomembrane right next to the seam. In case of cross section C1-C1 the fillet weld at the top of the patch shown in Figure 11-3 may be considered to be a seam perpendicular to the loading direction. According to the Giroud (2005) procedure, Figure 3-24 can be

used to estimate the additional strain due to bending at the seam knowing the seam type and thickness. The type of the seam in case of the cross section C1-C1 was extrusion fillet with an assumed thickness of between 5 mm. According to Figure 3-24, an additional strain due to bending at the seam was estimated to be 3.0%. Adding the calculated strain at in geomembrane due to the earthquake loading (3.8%) to the bending strain due to the seam stress concentration, a total tensile strain in the geomembrane in the vicinity of the seam of 6.8% was calculated. This total calculated tensile strain can be compared to the reduced yield strain to calculate the factor of safety due to earthquake loading. The factor of safety (FS) due to the earthquake loading can be estimated in this manner as follows:

$$FS = \frac{\varepsilon_{SYps}}{\varepsilon_e + \varepsilon_b} = \frac{3.8}{6.8} = 0.56 \tag{89}$$

where ε_{SYps} is the scratched geomembrane yield strain in plain strain, ε_e is the maximum tensile strain from earthquake, and ε_b is the bending strain due in the seam. A FS of 0.59 means that a tear will be initiated at the seam location in the earthquake, which is what happened at this location in the 1994 Northridge earthquake. A similar calculation for the 090 component of the strong motion record yielded a factor of safety of 0.45 due to the larger earthquake-induced strain (4.3%) for that record. Furthermore, analyses conducted with scratch depth as low as 0.025 times the geomembrane thickness also resulted in a factor of safety less than one for both motions for this cross section. However, as reported subsequently, a scratch depth of 0.2 times the geomembrane thickness was necessary to calculate a FS less than one for cross section D1-D1 for the records scaled to the mean PGA.

One interesting note here is that the geomembrane was not pulled from the anchor trench even though the anchor was designed as a yielding anchor, i.e. an anchor which allows that geomembrane to be pulled out of the anchor trench before yielding. However, in this case as the geomembrane did not reach the assumed tensile force at yield before tearing due to strain concentration. Therefore, the force in the geomembrane was not enough to pull out the geomembrane from the anchor.

Figure 11-13 shows the distribution of axial strain in the geomembrane predicted for the side slope liner in cross section C1-C1 at the end of the earthquake record, which is when the maximum tensile strain occurred, for the 360 strong motion component. As shown in the Figure 11-13, the geomembrane at the crest of the side slope experiences tensile strains while geomembrane at the toe of the slope was subjected to compression strains. The strain distribution at the end of the earthquake for the 090 component of the strong motion record showed a similar pattern. This means that failure in the geomembrane in these cases is most likely to occur in the vicinity of the anchor trench and not further down the slope.

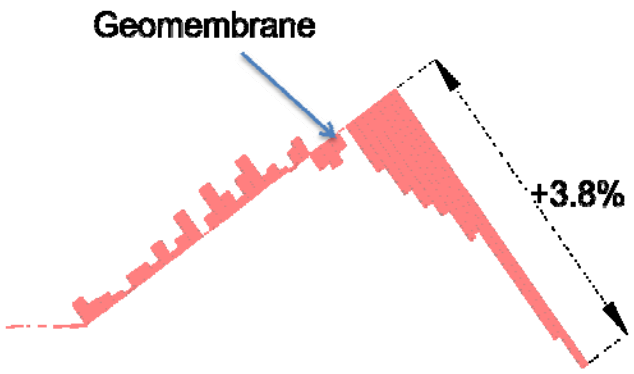

Figure 11-13 Axial strains in the geomembrane for cross section C1-C1 at the end of the Castaic Dam 360 earthquake record

11.2.10 **Geomembrane Strains in cross section D1-D1**

The two strong motion records (090 & 360), scaled to 0.28 g, from the Castaic Dam station were also used as input motions in the back analysis of cross section D1-D1. The parameters defining the behavior of the upper and lower interfaces and the geomembrane input parameters are presented in Table 11-8. As in the analysis of cross section C1-C1, the GM/GCL peak and residual shear strength constitutive model presented in Chapter 5 was used to model the upper and lower interfaces, the residual friction angle was assumed to be reached at a cumulative displacement of δ_r^p, of 300 mm, and the fitting parameter, *k*, was assumed to be 0.5. The beam element representing the geomembrane was pinned at the top of the slope to account for anchoring and the stress-strain curve for the geomembrane proposed by Giroud (1994) for geomembranes under tensile loading was employed, as in the analysis for cross section C1-C1.

Table 11-8 presents a summary of the maximum tensile strain the cross section D1-D1 geomembrane for two strong motion records used in the analyses. The maximum

tensile strains in these analyses were 2.15% and 1.9%, as presented in Table 11-8, and again occurred at the anchor trench. The largest factor of safety against failure of the geomembrane occurs in the case where the maximum tensile strain was 2.3%, i.e. for the 090 record. As for cross section C1-C1, the procedure proposed by Giroud (2005) to estimate the strain concentration due to seams and scratches was followed to estimate the strain concentration and factor of safety for cross section D1-D1.

Table 11-8 Tensile strain in the geomembrane for cross section D1-D1

Case*	Input motion	Lower Interface phi (degree)		Upper Interface phi (degree)		GM Max. Tensile Strain (%)	FS
		Φ_p	Φ_r	Φ_p	Φ_r		
1	090-0.28 g	29	28	26	24	2.15-Bench 1.28- Anchor	0.9
2	360-0.28 g	29	28	26	24	1.9- Bench 0.9-Anchor	0.98

* interface stiffness used $1x10^9$ pa/m and $4.8x10^8$ pa/m geomembrane initial stiffness

In cross section D1-D1, there was horizontal bench 3 m below the crest of the slope where the geomembrane was anchored. In the numerical analysis, the maximum tensile on the bench was slightly greater than the value at the anchor. Consistent with these analyses results, one end of the stair-stepped tear at this location illustrated in Figure 11-4 was on the bench. Assuming a Poisson's ratio of 0.46 and yield strain of 13% for the geomembrane, the yield strain in case of plane strain condition for cross section D1-D1 was 11.8%. Furthermore, assuming the ratio of the depth of the scratch to the geomembrane thickness is 0.2, the ratio of the yield strain of scratched geomembrane, ε_{SY}, to that of the intact geomembrane is estimated to be 0.35 according to Figure 3-25. This means the yield strain for a scratched geomembrane at cross section D1-D1 under plain strain conditions, ε_{SYps}, was 4.1%. Figure 3-24 was used to estimate the additional

strain due to the bending at the seam knowing the seam type and thickness. The type of the seam in case of the cross section D1-D1 was extrusion fillet with an assumed thickness of 5 mm. As in the analysis of cross section C1-C1, the fillet weld at the top of the patch was considered to be a seam perpendicular to the direction of loading. According to Figure 3-24 an additional strain due to bending at the seam was estimated to be 2.25 %. Adding the calculated strain at in geomembrane due to the earthquake loading (1.9 %) to the bending strain due to the seam stress concentration, a total tensile strain in the geomembrane in the vicinity of the seam of 4.15% was calculated. The factor of safety (FS) after the earthquake loading can then be estimated as follows:

$$FS = \frac{\varepsilon_{SYps}}{\varepsilon_e + \varepsilon_b} = \frac{4.1}{4.15} = 0.98 \tag{90}$$

where ε_{SYps} is the scratched geomembrane yield strain in plain strain, ε_e is the maximum tensile strain from earthquake and ε_b is the bending strain due to the seam. A FS of less than one means that a tear will be initiated at the seam location in the earthquake, which is what happened in the 1994 Northridge earthquake. Scratch with a depth less than 0.2 times the geomembrane thickness would not result in a factor of safety less than one at this location for the ground motions used in the analysis. However, this is a 50% probability that the ground motion PGA was greater than the mean value from the NGA relationship of 0.28g used in this study.

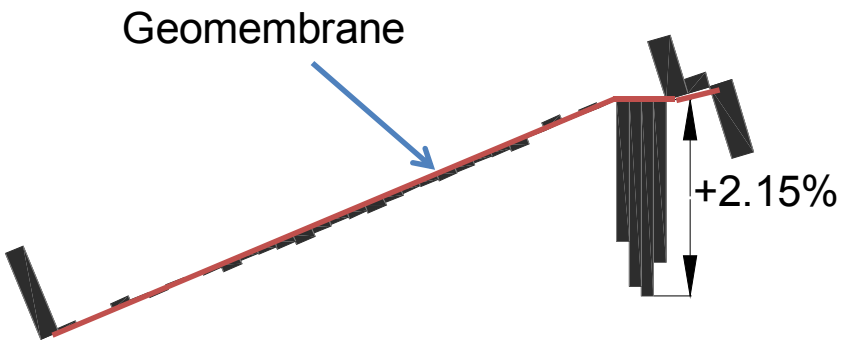

Figure 11-14 Axial strains in the geomembrane on the bench for cross section D1-D1 at the end of the Castaic Dam 090 earthquake record

11.2.11 **Maximum Permanent seismic displacement from 2-D Analysis**

The maximum permanent displacement calculated in case of cross section C1-C1 was at the top of the slope. The maximum permanent displacement ranged from 18 to 29 mm in cross section C1-C1, as presented in Table 11-9. In cross section D1-D1, the maximum permanent displacement was calculated between the slope crest and the bench 3 m below the waste surface. The maximum permanent displacement in case of cross section D1-D1 ranged from 146 to 122 mm, as presented in Table 11-9.

Table 11-9 Calculated maximum permanent seismic displacement from 2-D analysis

Cross section	Input motion	Maximum permanent displacement (mm)
C1-C1	090-0.28 g	29
C1-C1	360-0.28 g	18
D1-D1	090-0.28 g	146
D1-D1	360-0.28 g	122

11.2.12 **Decoupled Newmark displacement analyses for the Chiquita Canyon landfill**

A conventional 1-D decoupled seismic displacement analysis was conducted to evaluate the seismic performance of the Chiquita Canyon landfill according to the criterion presented in the 1995 EPA RCRA Subtitle D seismic design guidance (Richardson et al. 1995). Consistent with the 1995 EPA guidance and the current state of practice, the decoupled procedure described by Bray et al. (1998) for seismic analysis of lined landfills was employed to evaluate liner performance. First, the 1-D equivalent linear seismic response analyses required for a conventional decoupled seismic displacement analyses were conducted for both cross section C1-C1 and D1-D1 at the Chiquita Canyon landfill using SHAKE2000. The equivalent linear site response analyses were conducted for the five columns shown in Figure 11-15 (a) for cross section C1-C1 and for the four columns shown in Figure 11-15 (b) for cross section D1-D1. Each column extends from the bottom of the foundation rock in the FLAC 6.0 model to the top deck of the landfill. The properties presented in Table 11-5 were employed in the equivalent linear analyses along with the modulus reduction and damping curves cited in Table 11-6. As equivalent linear analysis do not consider interface behavior, no interface properties were required for the equivalent linear analysis. Both the 090 and 360 strong motion records were input as free field bedrock outcrop motions in the equivalent linear analyses at the interface between the rock and the waste material. For each column, the time history of shear stress at the liner level from the SHAKE2000 equivalent linear response analysis was converted to an average acceleration time history for the waste mass by dividing the shear stress by the normal stress acting on the geomembrane.

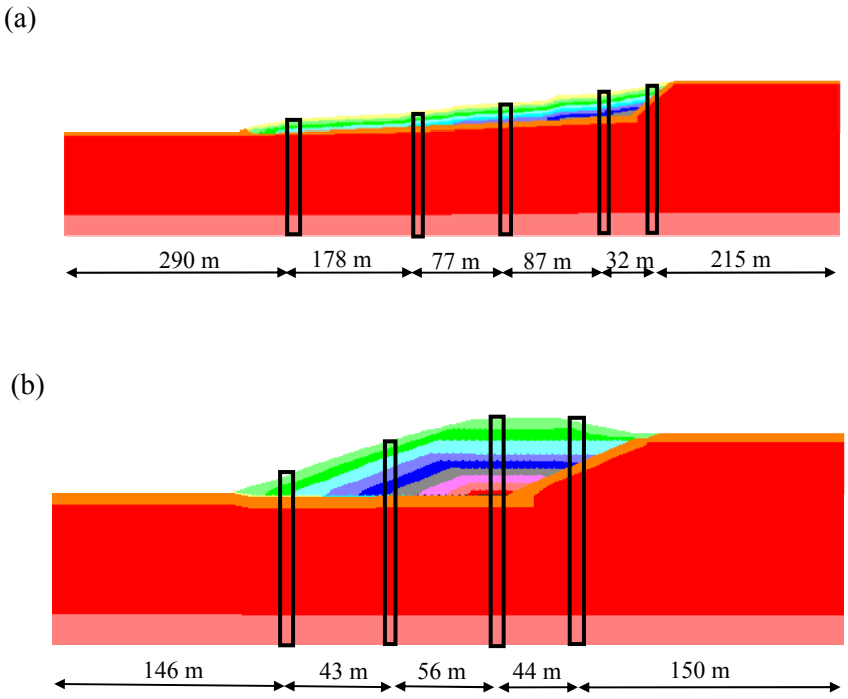

Figure 11-15 Columns used in 1D equivalent linear SHAKE2000 analyses (a) cross section C1-C1, (b) cross section D1-D1

Next, limit equilibrium analysis was used to determine the yield acceleration waste mass / liner system using SLIDE 5.0 (Rockscience 2005). Consistent with current practice, the large displacement friction angle (22 degrees for cross section C1-C1 and 24 degrees for cross section D1-D1) was employed for the geomembrane interfaces. An undrained shear strength of 62.4 kPa from the EMCON Associates (1994) report was used for the shear strength of the low permeability base liner in Section D1-D1. These shear strength values and the associated static factor of safety and yield acceleration for each section are presented in Table 11-10.

Table 11-10 Static FS and yield acceleration for cross sections C1-C1 and D1-D1

Cross section	Large Displacement Interface Friction Angle (degree)	Base Undrained Shear strength (kPa)	Static FS	Yield acceleration (k_y)
C1-C1	22	-	4.6	0.315
D1-D1	24	62.4	1.81	0.14

Excursions of one side of the average acceleration time history above the yield acceleration were then double-integrated (using a sub-routine in the SHAKE2000 program) to calculate the permanent seismic displacement for the decoupled analysis method for each column and for each input motion. Table 11-11 presents the average maximum permanent displacement (PD), calculated using decoupled method, from the five columns for cross section C1-C1 and the four columns for cross section D1-D1. The calculated maximum PDs from different columns and different records in the same cross section were very similar.

For cross section C1-C1, with a relatively high yield acceleration of 0.315 g, the Newmark displacement was zero for both records. For cross section D1-D1, with a much lower yield acceleration of 0.14 g, the calculated Newmark seismic displacement was 12 mm for the 090 record and 40 mm for the 360 record. According to the 1995 EPA guidance document, if the calculated seismic displacement in a Newmark-type analysis is less than between 150 to 300 mm, the design is considered adequate. Therefore, according to this criterion, the seismic performance of landfill cross section C1-C1 with a minimum interface shear strength represented by the critical friction angle should have been satisfactory. The results of the analyses are consistent with the findings of Augello et al. (1995) who concluded that conventional Newmark analyses could not predict the damage to the liner at the Chiquita Canyon landfill in the Northridge earthquake.

Table 11-11 Summary of decoupled displacement analyses for the Chiquita Canyon landfill

Cross Section	Motion	PGA (g)	k_y (g)	Average permanent displacement (mm)
C1-C1	90	0.28	0.315	0
	360	0.28	0.315	0
D1-D1	90	0.28	0.14	12.0
	360	0.28	0.14	40.0

11.2.13 **Summary of the Chiquita Canyon landfill Case History**

Two-dimensional non-linear numerical analyses were conducted of the seismic response of two cross sections at the Chiquita Canyon landfill were tears are reported to have occurred at the crest of the slope in the Northridge earthquake. The analyses were conducted using interface elements that allow for slip at the geomembrane interface and a beam element representing the geomembrane to allow for computation of liner strains. Analyses were conducted using both components of the Castaic Dam record from the M_w 6.7 Northridge earthquake scaled to a peak ground acceleration of 0.28 g. This peak ground acceleration was the mean value calculated for a bedrock outcrop at the site using four NGA relationships. The analyses were conducted using the best-estimate properties for the waste, the liner system material, and the foundation material.

The 2-D non-linear analyses indicated that the tensile strains in the geomembrane were below the yield strain from uniaxial tensile tests. However, when strain concentration factors due scratches and seams from Giroud (2005) were applied and the yield strain was adjusted for plain strain conditions, the factor of safety against geomembrane yield dropped below 1.0 for both cross sections. The permanent displacement calculated from conventional Newmark-type analysis was significantly

lower than 150 mm, indicating that a conventional Newmark-type analysis was not able to predict geomembrane failure in the case of the Chiquita Canyon landfill subject to Northridge earthquake ground motions.

11.3 Back Analysis of Lopez Canyon Landfill Performance in the Northridge Earthquake

11.3.1 Landfill description

The Lopez Canyon landfill is located in the foothills of the San Gabriel Mountains, approximately 30 km north-northwest of downtown Los Angeles. The landfill began operations in 1975 as a municipal solid waste with a total capacity of 16.9 million metric tons of waste. This landfill consists of four disposal areas designated Areas A, B, AB+, and C, as shown in Figure 11-16. Disposal Areas A, B, and AB+ were no longer accepting waste at the time of Northridge Earthquake. Disposal Areas A and B, unlined and cover about 30 hectares of land, were the initial landfill units. Disposal Area C was the newest waste unit and included a geosynthetic liner system on the base and on some of the side slopes. Figure 11-16 shows the most critical cross sections in terms of the stability of Area C according to GeoSyntec Consultant, the engineer of record for Disposal Area C (GeoSyntec 1994). The performance of Disposal Area C in the Northridge earthquake is the subject of this case history.

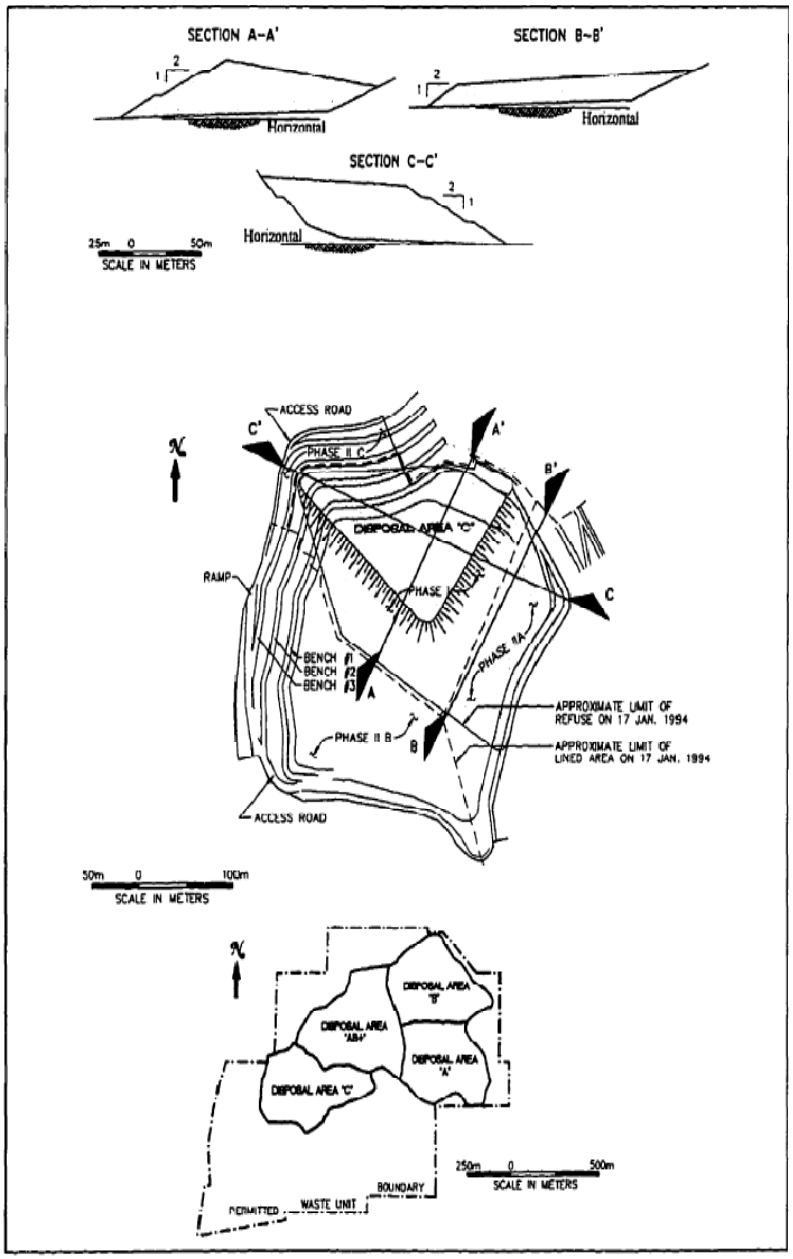

Figure 11-16 Plan view and cross sections through the Lopez Canyon landfill at the time of the Northridge Earthquake (GeoSyntec 1994)

Canyon C's native side slopes are up to 90 m high and were graded to provide slopes of between IH:IV to 1.5H:IV, with 5 m wide benches every 12 m in height. The base and the native side slopes were lined with a Subtitle D composite liner system (GeoSyntec

1994). The base liner system conforms to the prescriptive requirements of Subtitle D and consist of a 0.3 m thick granular leachate collection layer overlying a composite liner. The composite liner consists of a 0.6 m low permeability native soil-bentonite admixture (4% bentonite by weight) layer overlain by a 2.0 mm (80 mil)-thick double-sided textured high density polyethylene (HDPE) geomembrane. There is a 545 g/m^2 non-woven cushion geotextile between the geomembrane and the leachate collection layer and a 410 g/m^2 nonwoven filter geotextile overlain by 0.6 m of protective soil cover on top of the leachate collection layer (Derian et al. 1993). Figure 11-17 shows the cross section for the base lining system for Area C at the Lopez Canyon landfill (GeoSyntec 1994).

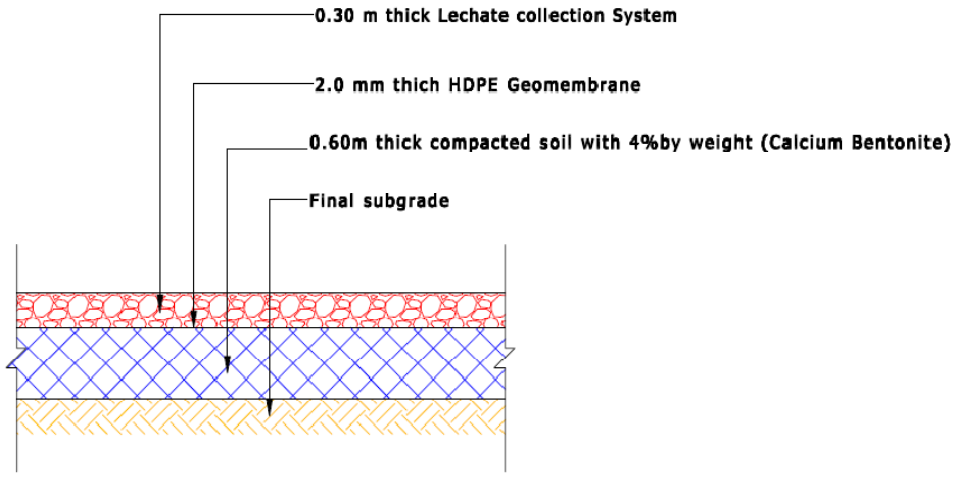

Figure 11-17 Lopez Canyon Landfill Area C base lining system (Derain et al. 1993)

The side slope liner system in Disposal Area C at Lopez Canyon is an alternative liner system designed in conformance with the performance standards of Subtitle D (GeoSyntec 1994). The side slope liner consists of, from top to bottom, a 0.6 m thick protective soil layer, a 410 g/m^2 filter geotextile, a geonet drainage layer, a 2.0 mm-thick

HDPE single-sided textured geomembrane (textured side down), a stitch-bonded geosynthetic clay liner (GCL), and an air-sprayed slope veneer of concrete averaging 75 - 100 mm thick and reinforced with 17-gauge wire hexagonal netting (Derian et al. 1993). The details for the side slope lining system for Area C at the Lopez Canyon are presented in Figure 11-18. Construction of the liner system for Disposal Area C was divided into two phases. Phase I , shown in Figure 11-16, was filled to a height of about 30 m at the time of the Northridge Earthquake. Phase II was not started at the time of the earthquake.

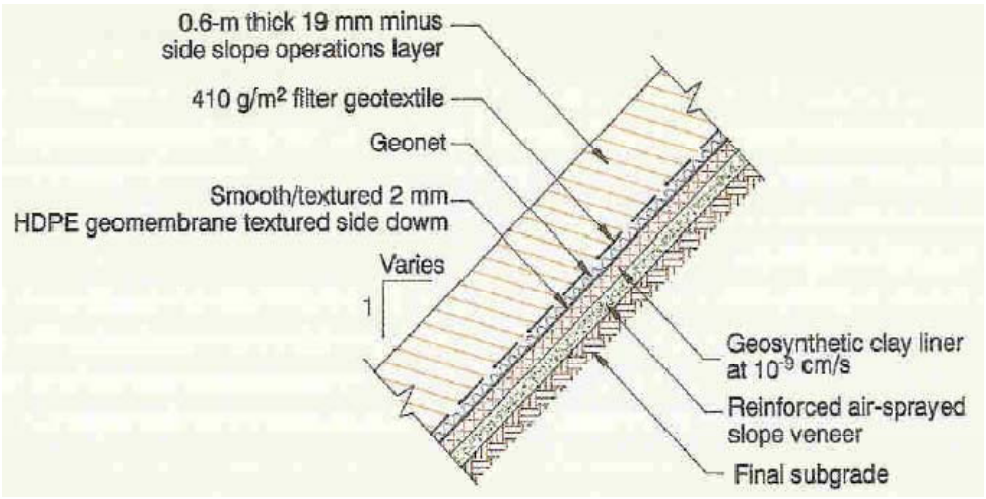

Figure 11-18 Lopez Canyon Landfill Area C side slope lining system (Derian et al. 1993)

11.3.2 **Properties of MSW for Lopez Canyon**

At the Lopez Canyon landfill, four SASW tests were performed after the Northridge earthquake to characterize the shear wave velocity of the solid-waste in the different areas of the landfill (Kavazanjian et al. 1996). The first three arrays (LP1 through LP3) measured the shear wave velocity profiles of the waste fill in the older inactive areas of the landfill. Array LPI was in Disposal Area A and arrays LP2 and LP3 were in Disposal

Area B. The final SASW array (LP4) was located in Disposal Area C, which was the active area of the landfill at the time of the Northridge Earthquake. Figure 11-19 shows the median of all four shear wave velocity SASW arrays profiles measurements. This median V_s profile was used in the dynamic back analysis of Area C.

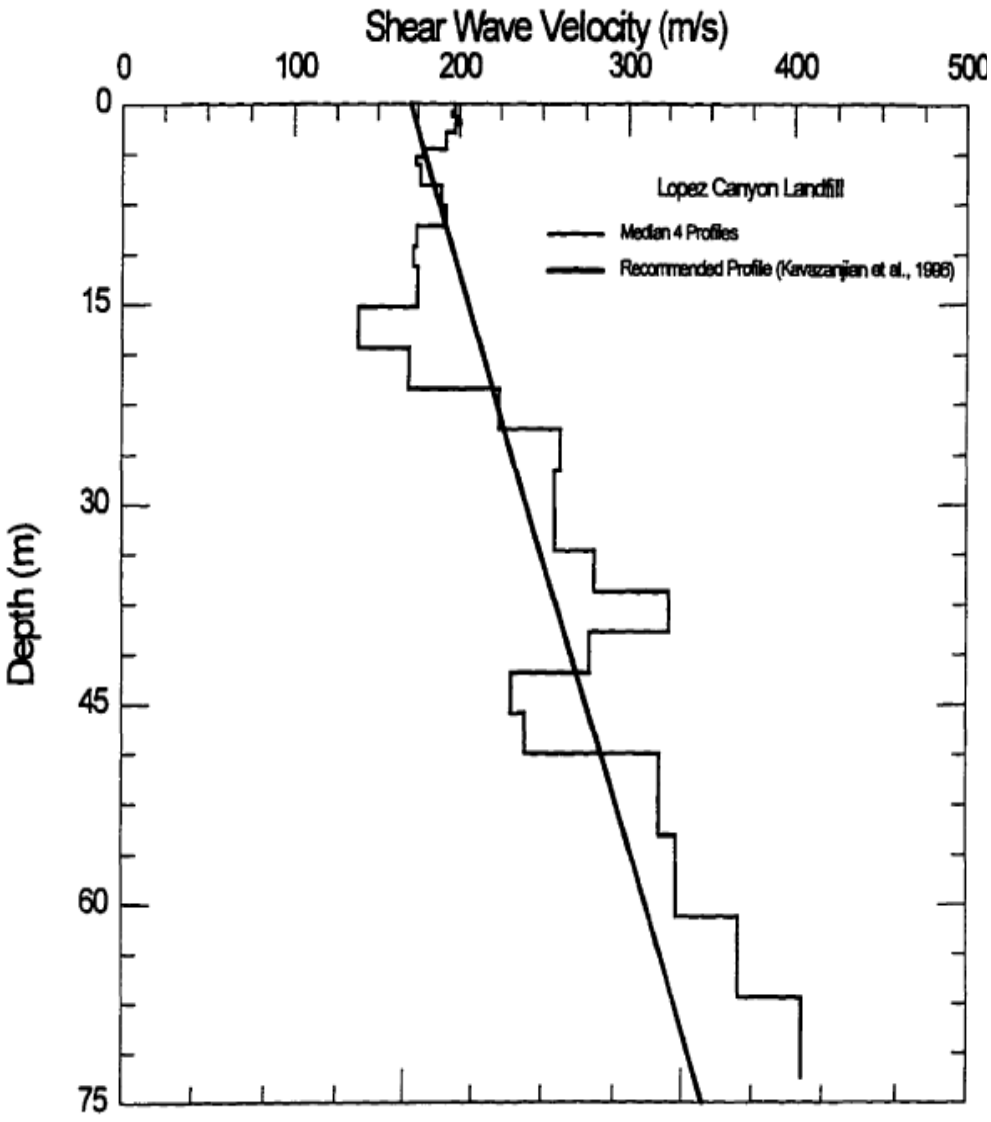

Figure 11-19 shear wave velocity measured in Lopez Canyon landfill (Kavazanjian et al. 1996).

11.3.3 **Interface direct shear testing**

As part of design for Disposal Area C at the Lopez Canyon Landfill, direct shear testing on various geosynthetic interfaces was conducted (GeoSyntec 1994). In this testing program six different interfaces of the lining system were tested. For the base liner, interface direct shear tests were conducted on the low permeability soil/textured geomembrane interface. For the side slope liner system, four interface direct shear tests were conducted, including two "sandwich" tests that included multiple interfaces. The first sandwich test was conducted on a specimen consisting of the following 5 layers of material from top to bottom:

- Stitch-bonded GCL;

- 2.0mm textured/smooth HDPE geomembrane, with the textured side upward (in contact with the GCL);

- Geonet;

- Nonwoven Geotextile;

-site-derived operations layer soil.

The second sandwich test was conducted on a specimen composed of the following 3 layers of side slope material, from top to bottom:

-Geotextiles;

-Geonet;

-2.0mm HDPE geomembrane with the textured side upward (toward the geonet)

The third test was conducted on a GCL hydrated by soaking with the textured side of the geomembane facing the GCL. The results of the interface direct shear tests on elements of the liner system for Area C at the Lopez Canton Landfill are presented in Table 11-12. The failure envelopes for the various side slope interfaces reported in Table 11-11 are shown in Figure 11-20. Figure 11-20 shows that the governing mimium friction angle for the side slope is the geotextile/site soil interface with a friction angle of 5.9 degrees and a cohesion of 25.2 kPa. This means if slip occurs, it will occur only between the geotextile and the operations soil, and thus tensile stresses should only develop in the geotextile.

Table 11-12 Direct shear test results for Lopez Canyon landfill geosynthetic elements (GeoSyntec 1994)

Test Number	Interface tested	Peak strength		Residual strength	
		Friction Angle (degrees)	Cohesion (kPa)	Friction Angle (degrees)	Cohesion (kPa)
1	Base (low permeability soil/GM)	24	65.3	24	65.3
2	GCL/GM/geonet/geotextile/ site soil	7	7.2	5	12.2
3	Geotextile/Geonet/GM	13	20.8	14	16.5
4	Soaked GCL/soaked GM	6.66	28.7	5.9	25.2

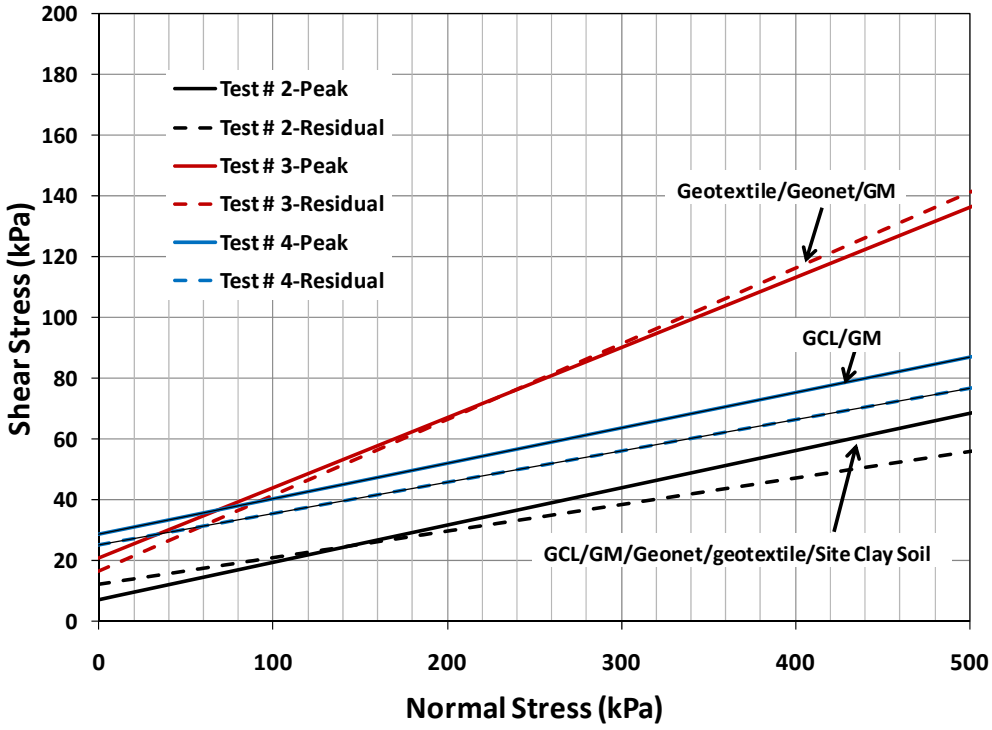

Figure 11-20 Failure envelopes for side slope geosynthetic interfaces in Lopez Canyon landfill (GeoSyntec 1994)

11.3.4 **Input motions**

The Lopez Canyon landfill is located fairly close to the Pacioma Dam Downstream strong motion recording station, so the recorded Pacioma Dam Downstream motions from the 1994 Northridge earthquake were used for the back-analyses. However, the accelerograms were rotated to obtain the motion corresponding to an azimuth of 60 degrees to coincide with the direction of the cross section A-A' and to obtain the motion corresponding to an azimuth of 290 degrees to coincide with the direction of the cross section C-C'. Figure 11-21 shows the response spectra for the motion at Pacioma Dam rotated to azimuths of 60 degrees and 290 degrees.

The strong motion records from Pacoima Dam Downstream station were assumed to represent rock outcrop motions at the landfill site. Based upon the proximity of the site to the Pacoima Dam Downstream station, the ground motions at the site were assumed to have the same PGA as recorded at the Pacoima Dam Downstream station. These values were 0.49 g and 0.33 g for the 60 degree and 290 degree azimuth records, respectively. A deconvolution analysis using SHAKE2000 was performed to calculate the upward propagating motion at the base of the FLAC 6.0 landfill models according to the procedure recommended by Mejia and Dawson (2006) illustrated in Figure 11-6.

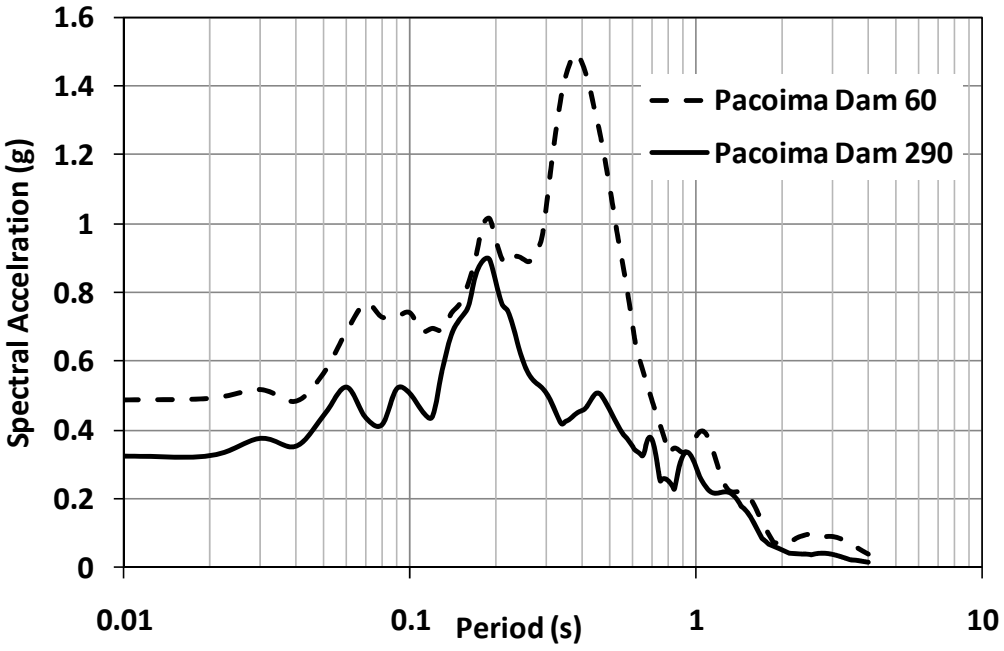

Figure 11-21 Response spectra of motions records at Pacioma Dam Downstream station from 1994 Northridge earthquake rotated to azimuths of 60 degrees and 360 degrees.

11.3.5 **2D finite difference models**

Lopez Canyon Landfill cross sections A-A' and C-C' were chosen for back analysis as these sections both had a lower static factor of safety and yield acceleration than cross section B-B'. The finite difference mesh developed to back analyze the seismic response of cross section A-A' is presented in Figure 11-22 (a). The mesh has more than 3,700 zones, with a higher density towards the waste body. The finite difference mesh developed to back analyze the seismic response of cross section C-C' is presented in Figure 11-22 (b). The mesh for cross section C-C' has more than 8,600 zones, with higher density towards the waste body. Lateral boundaries of the both models were extended beyond the boundaries of the waste fill and quiet boundaries were used to minimize the influence of the lateral boundaries on the computed seismic response. In both cross sections, the side slope geotextiles and base geomembrane were modeled as beam elements.

Interface elements were attached to the top and bottom of the beam elements. This configuration allows for different interface shear strengths on either side of a liner element. On the side slope, the layers of GCL and geomembrane were ignored for simplicity. The beam element was pinned at the in the x and y direction at the top of the slope to simulate the anchor trench at the crest of the slope.

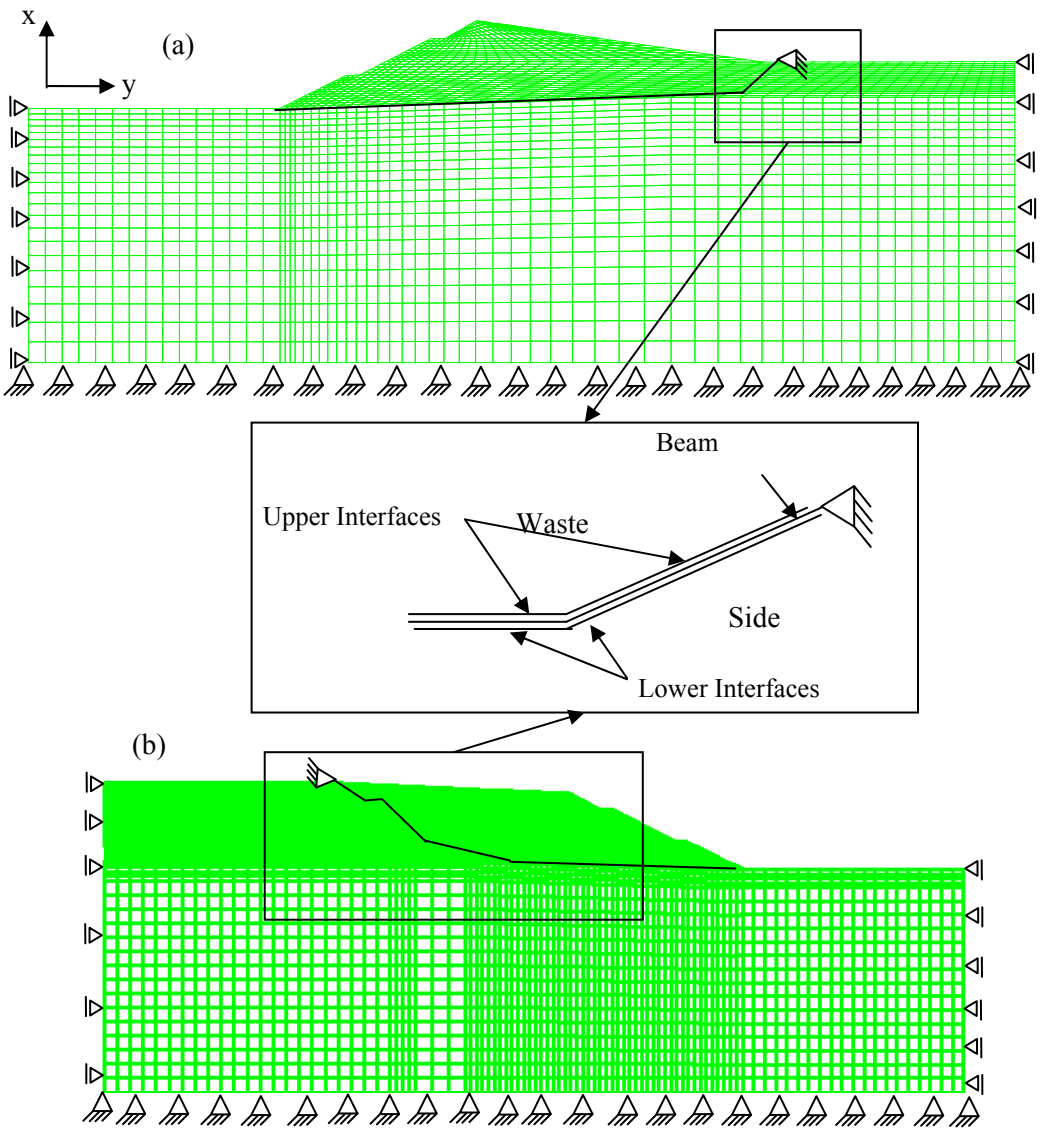

Figure 11-22 Finite difference mesh for Lopez Canyon cross sections: (a) cross section A-A', (b) cross section C-C'.

11.3.6 **Initial static analyses for Lopez Canyon landfill**

To establish the initial stresses for the seismic analyses a procedure intended to simulate the waste placement sequence in the field was employed. A gravity turn-on analyses was done assuming the waste material was built in 3 meters lifts, similar to the field operation. Each lift was deployed (gravity was turned on) and initial stresses were established before the next lift was deployed. The Modified Cam-Clay (MCC) model was used for to simulate the waste. The MCC parameters used for the waste material were established using the results of the oedometer test results conducted by (GeoSyntec 1996) on reconstituted specimens of OII waste material. The MCC parameters for the Lopez Canyon waste are presented in Table 11-4 same as Chiquita Canyon case history. Figure 11-23 shows the stratigraphy used in the finite element models for section C-C' and section A-A' after building 10 layers of waste.

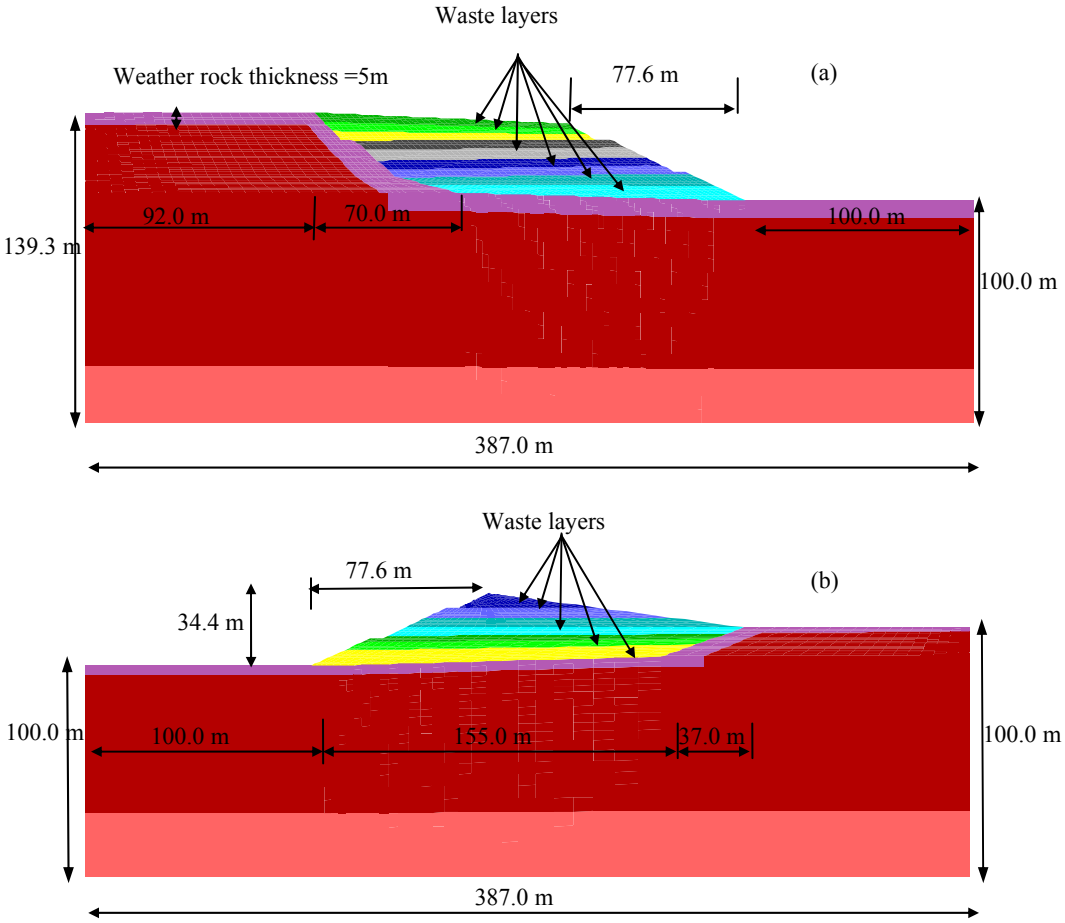

Figure 11-23 Stratigraphy for Lopez Canyon seismic analysis: (a) cross section C-C', (b) cross section A-A'

11.3.7 **Non-Linear 2-D Seismic Analyses**

Waste and foundation material properties used in the seismic analyses for the sections C-C' and A-A' are summarized in Table 11-13. The unit weights assigned to waste layers were based upon the unit weight profile recommended by Zekkos et al. (2006) for typical compaction in landfills in Southern California. The waste is treated in this stage as Mohr-Coulomb material rather than a MCC material as in the initial static step. The waste was assigned cohesion of 24 kPa for the top 3 meters and a friction angle of 33^{o} at greater depths based upon the bi-linear strength envelope of Kavazanjian et al. (1995). The rock foundation was modeled as a linear elastic material.

Figure 11-24 shows the finite difference models for both cross section C-C' and A-A' used in the seismic analyses. The quiet boundaries shown in Figure 11-24 were used in both cross sections to absorb the downward propagating motions (outgoing waves) instead of reflecting them back into the model.

Table 11-13 Waste and foundation material properties for Lopez Canyon Landfill

	Layer	Thickness (m)	Unit weight (kN/m^3)	Shear wave velocity (m/s)	Poison's ratio
MSW	Layer 1	3	10.5	170	0.33
	Layer 2	3	11.1	190	0.33
	Layer 3	3	12.7	210	0.33
	Layer 4	3	12.8	240	0.33
	Layer 5	3	13	260	0.33
	Layer 6	3	13.1	275	0.33
	Layer 7	3	13.3	300	0.33
	Layer 8	3	13.6	315	0.33
Rock	Weathered Rock	5	16.5	500	0.25
	Rock	67	16.5	900	0.25
	Rock (half space)	30.5	18.8	1200	0.25

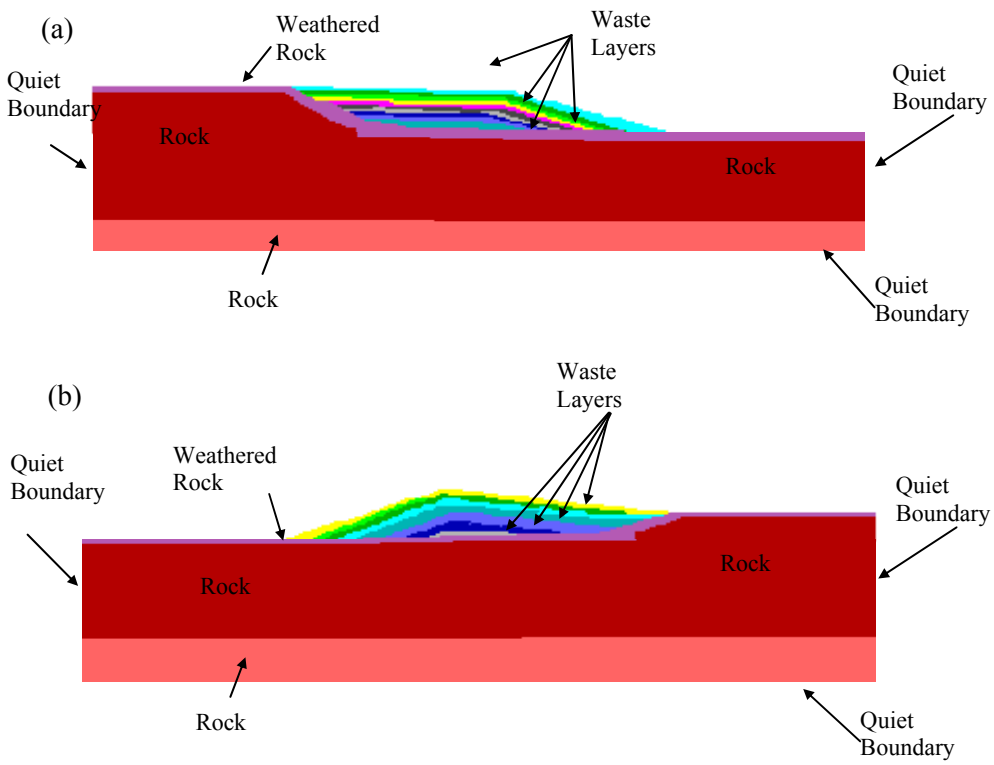

Figure 11-24 Finite difference model with boundary conditions for seismic analyses (a) cross section C-C, (b) cross section A-A

As shown in Figure 11-22, the geotextile in both cross sections C-C' and A-A' was modeled as a beam element with two interface elements to attach it to the finite difference mesh. One face of the geotextile (the lower interface elements) was attached to the foundation and the other face (the upper interface elements) was attached to the waste. The beam elements were treated as elastic materials with an elastic modulus, E_G. The interface element shear response was modeled as elastic-perfectly plastic using three parameters: an initial stiffness, E_i, and the Mohr-Coulomb failure parameters (c and ϕ). The upper interface was assumed to be the geotextile/soil interface and assigned a peak interface strength characterized by a friction angle of 7 degrees and a cohesion of 7.2 kPa and a large displacement shear strength characterized by friction angle of 5 degrees and a

cohesion of 12.2 kPa. The lower interface was assumed to be the geotextile/geonet interface with a friction angle of 13 degrees and a cohesion of 20.8 kPa.

11.3.8 **Geotextile Strains**

In total, four 2-D non-linear analyses were conducted. The two strong motion records from Pacoima Dam Downstream were used. Two analyses were conducted for each cross section, one using the peak interface strength and one using the large displacement interface strength. The record rotated to an azimuth of 60 degrees was used as the input motion for the cross section A-A' while the record rotated to an azimuth of 290 degrees was used as an input motion for the cross section C-C'.

Table 11-14 presents a summary of the maximum tensile strain in the geotextile for the four 2-D non-linear analyses along with the upper and lower interface shear strength and the interface stiffness used in the analyses.

Table 11-14 Tensile strains in the geotextile from nonlinear analyses analysis in Lopez Canyon

case	Side Slope Lower Interface angle (degrees)	Side Slope Lower Interface cohesion (kPa)	Side Slope upper Interface angle (degrees)	Side Slope upper Interface cohesion (kPa)	Max. Geotextile Tensile Strain (%)
Cross Section C-C'					
1	7	7.2	13	20.8	7.3
2	5	12.2	13	20.8	5.9
Cross Section A-A'					
3	7	7.2	13	20.8	0.5
4	5	12.2	13	20.8	0.3

* interface stiffness of $1x10^9$ pa/m and geotextile stiffness of $6x10^8$ pa/m was used in all cases

The calculated tensile strains at the end of the record (which was the maximum tensile strain for the entire earthquake) in cross section C-C' is presented in Figure 11-25. The maximum tensile strain was calculated at the crest of the side slope in the vicinity of the anchor. The values of 7.3% and 5.9% calculated in the analyses for Section C-C' are well below the break strain of the geotextile. The calculated permanent seismic displacements at the top of the slope for cross section C-C' was 100 mm for both cases 1 and 2 at the toe of the waste. The calculated strains and displacements are consistent with observations that the geotextile was stretch tight after the earthquake but that there was no damage to the underlying geonet or geomembrane (GeoSyntec 1994).

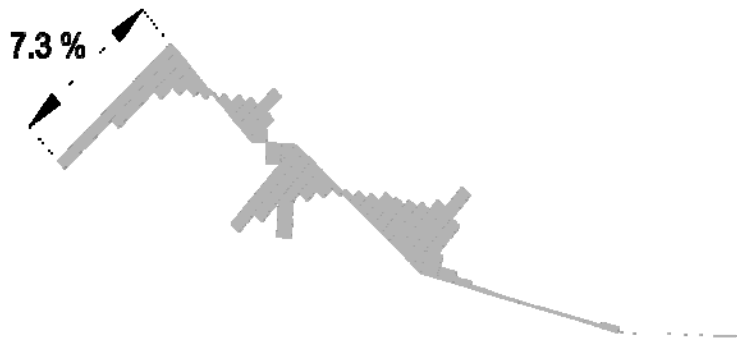

Figure 11-25 Calculated tensile strain at the end of the record for the geotextile in Lopez Canyon cross section C-C' (case 1)

11.4 Summary for Lopez Canyon Case History

Two-dimensional non-linear numerical analyses have been conducted of the seismic response of two cross sections at Lopez Canyon landfill in the Northridge earthquake. The analyses were conducted using interface elements that allow for slip at the geotextile interface on the side slope and the geomembrane interface on the base and beam elements

that allow for computation of strains in these geosynthetic elements. The analyses were conducted using the Pacoima Dam Downstream records from the M_w 6.7 Northridge earthquake, rotated to azimuths of 60 and 390 degrees with PGAs of 0.49 g and 0.33 g, respectively. The non-linear analyses used the interface friction angles measured for the lower and upper geotextile interfaces in tests conducted for design of the waste unit. The critical (lowest peak strength) interface on the side slope was the geotextile/site soil interface. The strains predicted in the geotextile were high but not enough to cause tear in the geotextile. However, the strains were consistent with the observation of tension in the geotextile after the earthquake.

CHAPTER 12 SENSITIVITY ANALYSES

12.1 Introduction

A series of parametric studies was conducted to investigate the influence of the key factors on the tensile strain calculated in geomembrane liner system in of the two Chiquita canyon cross sections. In each study, a baseline case with a typical configuration was employed and then one parameter was changed at a time to investigate the influence of that parameter on the maximum tensile strain in the geomembrane and the seismic response at the top of the landfill. The key factors investigated in these parametric studies were the upper and lower interface shear stiffness, the upper and lower interface shear strength (friction angle), the intensity of the ground motion, the geomembrane stiffness and the anchor at the top of the slope.

In the parametric studies, the 2-D finite difference models shown in Figure 11-10 were loaded with the Castaic Dam 090 and 360 records from the 1994 moment magnitude (M_w) 6.7 Northridge earthquake. In most analyses, these records were scaled to a peak ground acceleration of 0.28 g. However, some analyses were conducted in which the ground motions were scaled to a peak ground acceleration of 0.48 g. Deconvoluted motions calculated as described in Chapter 11 were input at the base of the finite difference models.

12.2 Influence of the interface shear stiffness

The interface shear stiffness is a parameter that is not needed in conventional (i.e. decoupled Newmark) seismic analyses of liner system performance. In advanced (e.g. finite element) numerical analyses of geosynthetics-lined landfill seismic response, numerical modelers typically assume either a large value or perfectly plastic behavior for the interface shear stiffness to enhance the stability of the analyses.

In the parametric study of interface shear stiffness, the baseline case (case I and II) was the same as the case history study reported in the previous chapter except no slip was allowed on the lower interface on the base and side slope (the lower interface was "glued"). The shear stiffness of the upper and lower interface elements was then changed from the value of 1e9 Pa used in the case history analysis in Chapter 11 to 1e7 Pa to investigate the influence of the shear stiffness on the calculated maximum tensile strain of the geomembrane. Table 12-1 presents a summary of maximum tensile strain calculated in the geomembrane for four 2D nonlinear analyses in which the interface shear stiffness was varied. In cases I and II in Table 12-1, cross section C1-C1 was loaded with the Castaic Dam 090 record scaled to 0.28 g and the interface shear stiffness (IS) of both the upper and lower interfaces was changed from 1e9 Pa to 1e7 Pa while not allowing the lower interface to slip (lower interface glued). The maximum geomembrane tensile strain increased from 1.7% for IS=1e9 Pa to 10.6% in case of IS=1e7 Pa. In cases III and IV a similar analysis was conducted on cross section D1-D1: the cross section was loaded with the Castaic Dam 090 record scaled to 0.28 g and the shear stiffness (IS) of both upper and lower interfaces changed from 1e9 Pa to 1e7 Pa while not allowing the lower interface to slip. The geomembrane maximum tensile strain increased from 0.64% for IS=1e9 Pa to 3.2% for IS=1e7 Pa. Clearly, the interface shear stiffness can be an

important parameter if it can change over the range of values used in the parametric study. Decreasing the shear stiffness of the lower interface from 1e9 Pa to 1e7 Pa increased the maximum calculated tensile strain dramatically.

Table 12-1 Influence of the Interface shear stiffness

Case*	Input motion	Lower Interface phi (degree)	Lower Interface IS (pa)	Upper Interface phi (degree)	Upper Interface IS (pa)	GM Max. Tensile Strain (%)
Cross Section C1-C1						
I	090-0.28 g	glued	1e9	27	1e9	1.7
II	090-0.28 g	glued	1e7	27	1e7	10.6
Cross Section D1-D1						
III	90-0.28 g	glued	1e9	26	1e9	0.64-Bench
IV	90-0.28 g	glued	1e7	26	1e7	3.2- Bench

Note: * in all cases the GM was assigned a tensile stiffness of 4.8e8 pa/m

Figure 12-1 compares the ARS from 2-D nonlinear analysis in from cases I and II. The PGA calculated in case I was slightly higher than the PGA calculated the case II. The ARS at short to medium periods (0.01 s-0.4 s) in case I was higher than the ARS in case II, however the ARS in case I was lower than the ARS in case II in long periods (>0.4 s). These results indicate that the landfill has a higher response in the short to medium period range and lower response at longer periods when the interface shear stiffness is decreased.

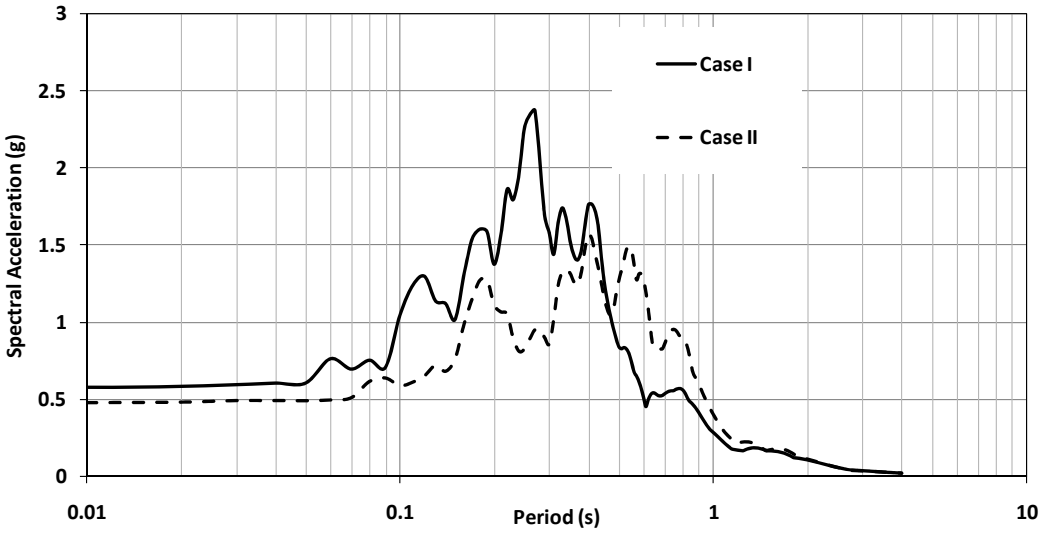

Figure 12-1 ARS at the center of top deck for cross section C1-C1 for an interface stiffness of 1e9 Pa (case I) and 1e7 Pa (case II) for an upper interface friction angle of 27 degrees for the Castaic Dam 090 record scaled to 0.28 g.

A change in the IS had a similar effect on the ARS for cross section D1-D1 as it did for cross section C1-C1 but the difference in the response in the two cases was less pronounced. Figure 12-2 compares the ARS for cross section D1-D1 for case III to the ARS for case IV. The ARS for the lower interface stiffness (case IV) is slightly lower than the ARS for the higher interface stiffness (case III) in the short period and medium period range (up to about 0.6 s). However, the ARS in case IV was slightly higher than the ARS for case III at longer periods (periods higher than 0.6 s). The less pronounced difference in the response due to a change in interface stiffness for cross section D1-D1 compared to cross section C1-C1 may be attributed to the difference in liner system geometry, as cross section D1-D1 has no liner on the base of the cross section.

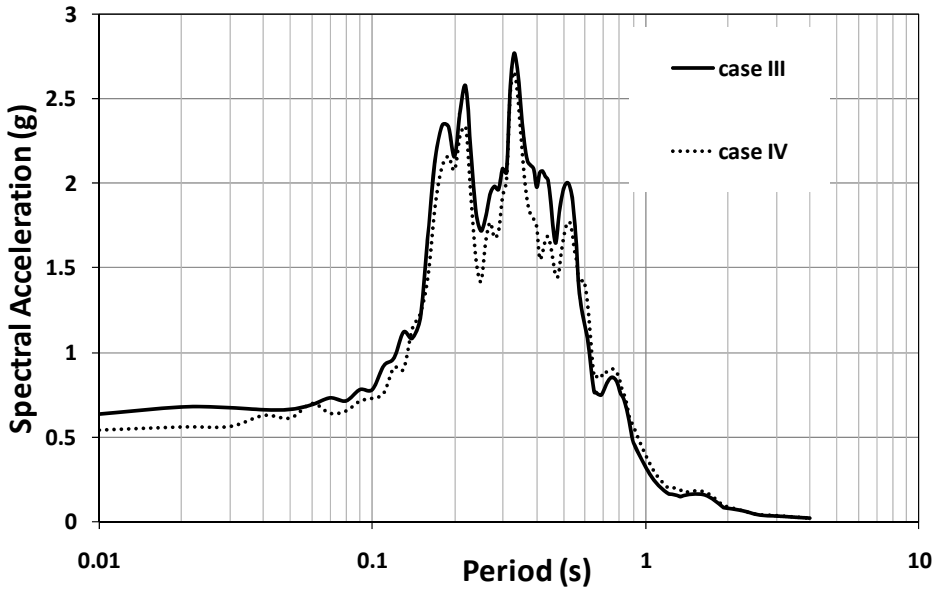

Figure 12-2 ARS at the center of top deck for cross section D1-D1 for an interface stiffness of 1e7 Pa (case III) and 1e9 Pa (case IV) for an upper friction angle of 24 degrees for the Castaic Dam 090 record scaled to 0.28 g.

12.3 Influence of upper interface friction angle

To explore the effect of the upper interface friction angle on the calculated maximum tensile strain was changed from 27 degrees to 12 degrees for cross section C1-C1 with a an interface stiffness of 1e7 Pa and from 24 to12 degrees for cross section D1-D1 with an interface stiffness of 1e9 Pa. In all cases, the Castaic Dam 090 record was used. The interface parameters and maximum tensile strains for these analyses are presented in Table 12-2.

Table 12-2 Influence of the Interface upper friction angle in case of cross section C1-C1

Case*	Input motion	Lower Interface phi (degree)	Lower Interface IS (pa)	Upper Interface phi (degree)	Upper Interface IS (pa)	GM Max. Tensile Strain (%)
Cross Section C1-C1						
V	090-0.28 g	glued	1e7	27	1e7	10.6
VI	090-0.28g	glued	1e7	12	1e7	10.6
Cross SectioD1-D1						
VII	90-0.28 g	glued	1e9	24	1e9	0.64-Bench
VIII	90-0.28 g	glued	1e9	12	1e9	0.4- Bench

Note: * in all cases the GM was assigned a tensile stiffness of 4.8e8 pa/m

Figure 12-3 compares the ARS at the top deck in cross section C1-C1 with an interface stiffness of 1e7 Pa (the softer interface stiffness) for an interface friction angle of 27 degrees (case V) to the ARS calculated when the interface friction angle was decreased to 12 degrees (case VI). The PGA for the case with a friction angle of 12 degrees (case VI) is slightly lower than the PGA for the case with an interface friction angle of 27 degrees (case V). The ARS for the case with the interface friction angle of 12 degrees (case VI) is lower than the ARS for the case with an interface friction angle of 27 degrees (case V) in the mid-period range (from 0.2-0.5 s), while the ARS in are similar at longer periods for these cases.

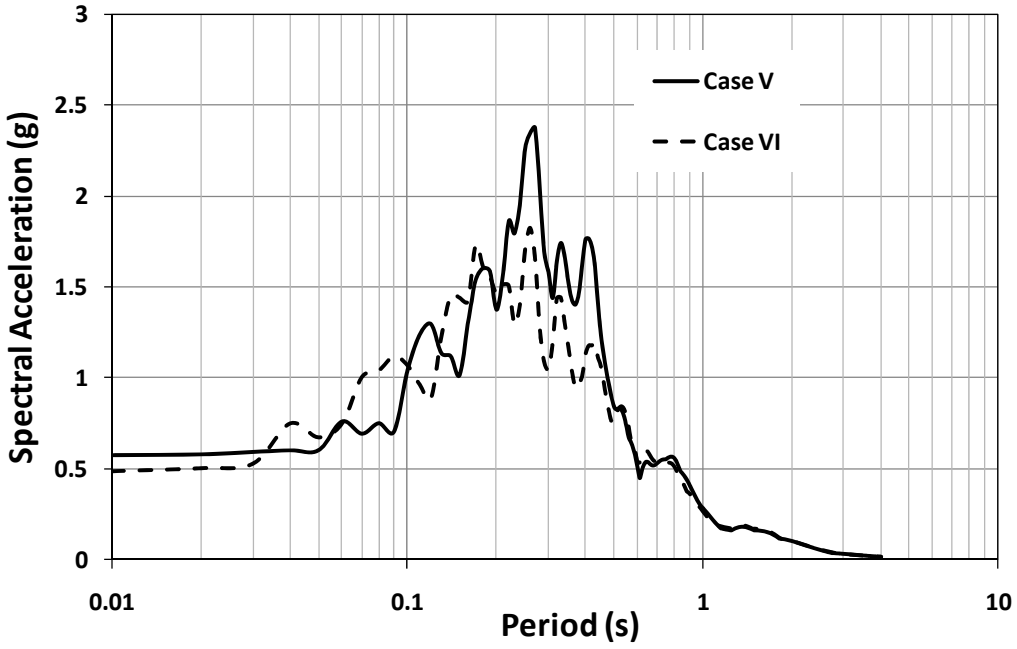

Figure 12-3 ARS at the center of top deck for cross section C1-C1 for an upper interface friction angle of 27 degrees (case V) and 12 degrees (case VI) for the Castaic Dam 090 record scaled to 0.28 g.

Figure 12-4 presents the influence of the interface friction angle on landfill response for cross section D1-D1 with an interface stiffness of 1e9 Pa (the stiffer interface stiffness) for an upper interface friction angle of 24 degrees (case VII) and of 12 degrees (case VIII). The ARS in these cases were almost identical with a slightly lower response in case VIII in the vicinity of the peak spectral acceleration, as illustrated in Figure 12-4.

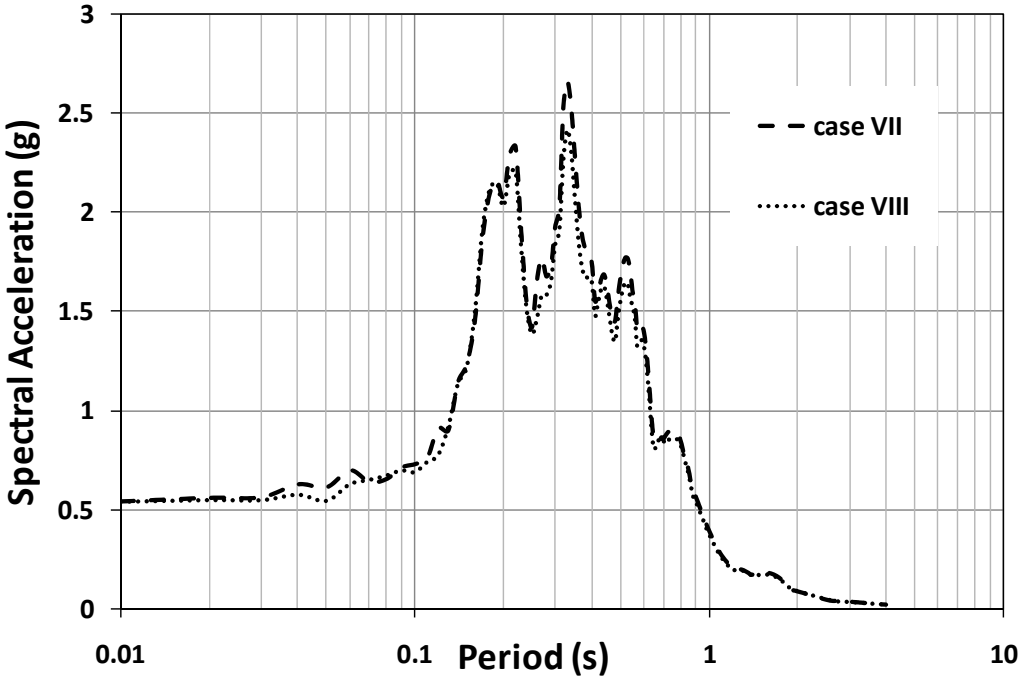

Figure 12-4 ARS at the center of top deck for cross section D1-D1 for an interface friction angle of 24 degrees (case VII) and 12 degrees (case VIII) for the Castaic Dam 090 record scaled to 0.28 g.

In summary, the friction angle of the interface has more pronounced effect of the seismic response of the landfill in case of cross section C1-C1 than in case of D1-D1.

12.4 Influence of the anchor (cross section C1-C1)

In order to investigate the influence of the anchor trench on the calculated maximum tensile strain, analyses were conducted in which the beam element was not pinned at the top of the slope. The geomembrane in cross section C1-C1 was fixed in the x and y direction at the top of the slope in case IX to represent an anchor and was freed in the x and y direction at the crest in case X of. The maximum tensile strain in case IX (with an anchor) was significantly higher in case X (no anchor). The interface parameters and the input motion for both cases IX and X are presented in Table 12-3.

Table 12-3 Influence of the anchor on maximum strain in cross section C1-C1

Case*	Input motion	GM Max. Tensile Strain (%)
IX	090-0.28 g	10.6
X	090-0.28g	0.3

Note: (1) in all cases the GM was assigned a tensile stiffness of 4.8e8 pa/m.
(2) in all cases the interfaces were glued with lower and upper shear stiffness of 1e7 pa/m.

12.5 Influence of ground motion intensity (cross section C1-C1)

To explore the influence of ground motion intensity on the calculated maximum tensile strains, cross section C1-C1 was subject to the Castaic Dam station input motions scaled to 0.48 g. In case XI the Castaic Dam station 090 motion was used resulting in a calculated maximum tensile strain of 1.6% versus 1.3% for the same motion scaled to 0.28 g. In case XII the Castaic Dam station 360 motion was used resulting in a calculated maximum tensile strain of 5.6% versus 5.1% for the same motion scaled to 0.28 g. Cases XI and XII are summarized in Table 12-4.

Table 12-4 Influence of ground motion intensity on geomembrane strain in cross section C1-C1

Case*	Input motion	Lower Interface IS (pa)	Upper Interface IS (pa)	GM Max. Tensile Strain (%)
XI	090-0.48g	1e9	1e7	1.6
XI'	090-0.28g	1e9	1e7	1.3
XII	360-0.48g	1e9	1e7	5.6
XII'	360-0.28g	1e9	1e7	5.1

Note: (1) in all cases the GM was assigned a tensile stiffness of 4.8e8 pa/m.
(2) in all cases the upper and lower interfaces were glued.

12.6 Influence of the geomembrane stiffness

There is no information on geomembrane stiffness in compression in the literature. Some investigators assume that the compressive stiffness of a geomembrane is zero, as the geomembrane wrinkles under compression (Gourc et al. 2004). This is may be true under

low confining pressure. However, in cases when confining pressure (normal stress) on the geomembrane is not zero, the stiffness of the geomembrane in compression will not be zero. Furthermore, by setting the moment of inertia equal to zero and applying the buckling criterion built in to FLAC 6.0 the tendency of the geomembrane to wrinkle is accounted for.

To investigate the influence of having a lower stiffness in compression than tension, a subroutine was written in FLAC 6.0 to make the stiffness of the geomembrane one order of magnitude less in compression than tension. Analyses conducted assuming equal stiffness in compression and tension were compared to analyses with a stiffness in compression one order of magnitude less than in tension. These analyses are presented in Table 12-5. In case XIII, the input parameters were the same as in case XII except that the geomembrane compression stiffness was assumed to be one order of magnitude less than the stiffness of the geomembrane in tension. Results of these analyses, presented in Table 12-5, show that the maximum tensile strain increased from 7.4% to 9.7% when the geomembrane compressive stiffness was degraded. This suggests that if the geomembrane stiffness is actually the same in compression as it is in tension, the conventional assumption that the geomembrane has no stiffness in compression may over-estimate geomembrane tensile strains.

Table 12-5 Influence of the GM stiffness in compression in case of cross section C1-C1

Case	Input motion	Lower interface phi (degree)	Upper interface phi (degree)	GM compressive stiffness (pa/m)	GM tensile stiffness (pa/m)	GM max. tensile strain (%)
C1-C1						
XII*	360-0.28 g	22	27	4.8e8	4.8e8	7.4
XIII*	360-0.28 g	22	27	4.8e7	4.8e8	9.7
XIV**	360-0.28 g	24 to 22	27 to 24	4.8e8	4.8e8	3.8
XV**	360-0.28 g	24 to 22	27 to 24	4.8e8	Giroud (1994)	4.0
XVI	360-0.28 g	24 to 22	27 to 24	4.8e9	4.8e9	1.8

*interface stiffness for upper and lower interfaces in cases XII and XIII is 1e7 pa/m.
**interface stiffness for upper and lower interfaces in cases XIV, XV and XVI is 1e9 pa/m.

In the initial analyses, the geomembrane was assumed to behave linear elastically in tension (fixed tensile stiffness at all tensile strains). However, wide width uniaxial tests on geomembranes show that HDPE geomembranes behave nonlinearly in tension (Giroud 2005). As discussed in Chapter 3, HDPE geomembrane stiffness degrades with increasing of tensile strain. To investigate the effect of the nonlinear stress strain behavior of HDPE on liner performance a subroutine was written to model the stress-strain behavior of the geomembrane beam element as a hyperbola. In case XIV the stiffness of the geomembrane was assumed linear with the stiffness assumed as the initial stiffness of the geomembrane. In case XV the tensile stiffness changed with tensile strain according to the model proposed by Giroud (1994). As presented in Table 12-5, the maximum calculated tensile strain at the end of the record in the geomembrane was higher in case XV, using of the hyperbolic stress-strain curve for the geomembrane in tension, than for case XIV in which a linear stress strain relationship was assumed.

There is no information on geomembrane stiffness under increasing normal stress in the literature. However, investigators have shown that nonwoven geotextile stiffness increases under increasing confining stress (Palmeira 2009). It may be inferred that

geomembranes may show a similar increase in stiffness with increasing confining stress. In case XVI in Table 12-5 the geomembrane stiffness was increased in tension and compression one order of magnitude to explore the effect of a possible increase in geomembrane stiffness due to increasing normal stress. Results of this analysis shows that the maximum tensile strain decreases from 3.8% to 1.8% when the geomembrane stiffness was increased by an order of magnitude. This suggests that if the geomembrane stiffness does actually increase under increasing normal stress, the conventional assumption that the geomembrane stiffness does not increase under normal stress may overestimate geomembrane tensile strains.

12.7 Summary

Parametric studies were conducted in this chapter to investigate the influence of interface parameters, the intensity of the ground motion, and geomembrane stiffness on the seismic response of the Chiquita Canyon landfill. The shear stiffness of the geomembrane interface may have a pronounced effect on both the calculated maximum tensile strain in the geomembrane and the seismic response at the top of the landfill. The appropriate value that should be used for shear stiffness of the interface in a seismic analysis is unknown. Large scale testing is required to calibrate the interface shear stiffness in FLAC interface elements for seismic analysis of lined landfills.

Using anchor to fix the geomembrane at the top of the slope results in stress concentration in the vicinity of the anchor and in this case a tensile strains developed were much higher in case of anchor compared of no anchor at the top of the slope.

Decreasing the earthquake ground motion intensity by decreasing the PGA of the input motion result in decreasing the calculated tensile strains caculated in the geomembrane.

The use of a compressive stiffness for the geomembrane one order of magnitude less than the geomembrane stiffness in tension will lead to higher tensile strains in the geomembrane. The correct compressive stiffness for the geomembrane is unknown. laboratory testing is required to determine the stiffness of the geomembrane in compression. Furthermore, increasing the geomembrane stiffness to account for increased normal stress on the geomembrane can significantly reduce the tensile strain in the geomembrane.

CHAPTER 13 SUMMARY AND CONCLUSIONS

13.1 Summary

The objective of this research was to investigate the conditions under which seismic loading may threaten the integrity of geosynthetic elements of a waste containment barrier system. As demonstrated by the performance of the geosynthetic components of the lining system for the Chiquita Canyon landfill in the Northridge earthquake, the integrity of geosynthetic barrier layers in such systems can be impaired by the tensile forces and strains induced by seismic loading. The tensile forces and strains induced in geosynthetic elements of a waste containment system by seismic loading are not explicitly considered in current landfill design practice. Therefore, the work in this dissertation focused upon developing a method that not only accounted for the effect of interaction between a geosynthetic waste containment system, the overlying waste, and the underlying ground on the seismic response of the landfill but also allowed for explicit calculations of tensile forces and strains developed in the geosynthetic elements of the waste containment system

Comprehensive modeling of the seismic response of landfill liner and cover systems used in waste containment facilities requires suitable constitutive models to model the cyclic shear behavior of the various geosynthetic components of the containment system and their interfaces. In this dissertation, an elastic-perfectly plastic interface model was demonstrated to adequately reproduce the cyclic shear behavior of typical geomembrane-geotextile and geomembrane-geomembrane interfaces provided the appropriate interface strength and stiffness parameters are used. This demonstration was made by comparing numerical results to experimental data from shaking table and centrifuge model tests.

New constitutive models were developed for the in-plane cyclic shear behavior of textured geomembrane/geosynthetic clay liner (GMX/GCL) interfaces (a common interface in landfill practice) and for the in-plane cyclic shear behavior of GCLs for use in seismic response analyses. These models were based upon experimental data from large scale direct shear uniform cyclic tests. The GMX/GCL model was an empirical model that allows for degradation in the cyclic shear resistance from a peak and to a large displacement shear strength. A kinematic hardening multi yield surface plasticity model was employed to model the cyclic in-plane shear behavior of GCLs using Salah-Mars (1989) constitutive model. This model also allowed for degradation of the shear resistance from a peak strength to a large displacement characteristic of GCL cyclic behavior.

One-dimensional (1-D) and two-dimensional (2-D) numerical analyses of the seismic response of a heap leach pad liner system were conducted to demonstrate the ability of the geomembrane-geotextile interface model to account for relative displacement (slip) between the liner system and the overlying and underlying materials. The 1-D analyses included two methods proposed in the literature to model the impact of slip at a geosynthetic liner system interface. The 2-D analyses included interface elements that account for slip at liner system interfaces and beam elements that allow for computation of stresses and strains in liner system components. The 2-D analyses demonstrated the ability of the interface-beam model to predict realistic tensile forces and strains in the geosynthetic elements of a waste containment system.

2-D non-linear time-domain numerical models of two typical landfill configurations were developed to evaluate further investigate the effect of slip at a liner system interface on seismic response and the forces and strains developed in geosynthetic elements of a

liner system subject to seismic loading. These analyses were also used to investigate the adequacy of current methods for the seismic design of geosynthetic liner systems. The two typical landfill configurations analyzed were a symmetrical configuration representative of a quarry fill and an asymmetrical configuration representative of a canyon fill. An important finding from these analyses was that slip at a liner system interface may not always reduce the intensity of the ground motions at the top of the landfill.

Case histories of landfill performance in earthquakes, including the 1994 Northridge earthquake, provided an excellent opportunity to demonstrate the ability of the numerical model to predict the seismic performance of waste fills. A comprehensive back-analysis of the seismic response of the OII landfill (an unlined solid waste landfill), employing strong ground motions recorded at the top and base of the landfill in five different earthquakes, was used to develop appropriate models for the strain dependent shear modulus degradation and damping of solid waste for use in subsequent numerical analysis. Back analyses were then conducted of the performance of two lined landfills in the Northridge earthquake to demonstrate the ability of the numerical model to predict the behavior of lined landfills subject to strong ground shaking in earthquakes. The behavior of the Chiquita Canyon landfill was analyzed to investigate the cause of the tears observed in the geomembrane after the Northridge earthquake at this facility. The behavior of the Lopez Canyon landfill in the Northridge earthquake, wherein the geomembrane appeared to be undamaged and an overlying geotextile appeared to be subject to large tensile strains, was also back analyzed .

13.2 Conclusions

13.2.1 **Geomembrane interface model**

A time-domain finite difference model of a rigid block sliding on a plane using a simple elastic-perfectly plastic constitutive model and the Mohr-Coulomb failure criterion was employed to characterize the load-displacement behavior of a geomembrane interface between a rigid block and an underlying planar surface. This numerical model was shown to accurately reproduce the slip-stick and slip-slip behavior described by Westermo and Udwadia (1983) for frictional sliding of a rigid block on a horizontal plane. The numerical model was also shown to accurately predict shaking table tests of a sliding block on horizontal and inclined planes subject to uniform and non-uniform motions provided the appropriate friction angle was used to characterize the interface. Comparison of physical model test results to the results of best-fit numerical analyses demonstrated that the appropriate friction angle depends upon the velocity of sliding for some geomembrane interfaces. However, the rate dependence appears to be slightly less than deduced in a previous study using a simpler back analysis.

The numerical model was also been shown to predict the main characteristics of shaking table tests of a compliant block on an inclined planes subject to uniform sinusoidal motions provided the appropriate friction angle was used to characterize the interface. It is important to note that, in contrast to the behavior of a rigid block, accelerations in excess of the interface yield acceleration may be induced in both the top and bottom of the compliant soil column on top of a yielding (slipping) interface. Unlike a rigid sliding block, a compliant soil column vibrates during sliding. Therefore, accelerations greater than the yield acceleration may occur within the sliding mass of the

compliant soil column. Also, unlike rigid block dynamic response, the acceleration at the base of a compliant soil column is not constant during sliding, as the limiting force at the sliding interface is not directly related to the acceleration directly above the sliding interface but is instead related to the mass-weighted average of the entire acceleration distribution within the soil column.

13.2.2 **GCL/GM in-plane constitutive model**

An elasto-plastic constitutive model was been developed to simulate the degradation in mobilized shear strength accompanying cyclic loading that exceeds the peak shear strength of the material for the in-plane shear behavior of a textured GM/GCL combination. The model assumes elastic behavior for the interfaces below the peak shear strength and uses the Mohr- Coulomb shear strength criterion for both peak and post-peak shear strength characterization. Comparison of numerical and experimental results indicated that, while the model has some shortcomings with respect to the initial shear stiffness and the shear stress immediately after shear stress reversal, it captured the degradation of the mobilized shear strength once the peaks strength as exceeded, and this degradation considered to be of paramount importance in modeling the behavior of a GMX/GCL combination subject to earthquake loading.

13.2.3 **GCL in-plane constitutive model**

A kinematic hardening multi yield surface plasticity model was employed to model the cyclic in-plane shear behavior of GCLs. The model uses the Drucker-Prager three-dimensional stress space generalization of the Mohr-Coulomb criterion developed from triaxial or direct shear test shear strength criterion for peak shear strength

characterization. The softening in GCL after reaching the peak shear strength mobilized shear strength was captured when implemented in a finite difference computer program. Comparing the numerical results with the experimental results, it was shown that the numerical model does a good job reproducing the key aspects of the cyclic shear behavior of the GCLs, i.e. the computed hysteresis loops reproduced the general patterns of behavior for the measured hysteresis loops and the model exhibited peak and residual behavior similar to the measured behavior.

13.2.4 **Heap leach pad liner system**

Site response analyses were conducted using 2-D nonlinear and 1-D equivalent-linear and nonlinear analyses with and without liner elements. In the 2-D analyses the liner system was modeled 1) solely as a weak interface; and 2) as a beam element with interfaces on each side. In the 1-D non-linear analyses, the liner was modeled as weak soil layer. In the 1-D equivalent linear analyses, the liner was modeled using the recommendations of Yegian et al. (1998) for geosynthetic liners.

Results of the analyses with the 2-D models showed that there are only minor differences in landfill ground motions between the two means of modeling the liner (i.e. interface and beam element with two interfaces). However, the beam model allows for the explicit computation of the stresses and strains in the liner. The 2-D model without a liner element generally produced greater spectral acceleration than the model with a liner, though the difference was usually minor and in one case the model with the liner produced higher spectral acceleration in the 0.1 to 0.3 second spectral period range.

Comparison of the 2-D and 1-D models showed that: 1) based upon comparison to the 2-D analysis with slip elements (which are believed to be more accurate, but which

are also more complicated to perform than 1-D analyses), use of a weak layers in the non-linear 1-D models is an improvement with respect to conventional 1-D analysis without slip elements; 2) additional calibration of the non-linear 1-D models is required to improve the accuracy of this type of modeling; 3) the 1-D equivalent linear model proposed by Yegian et al. (1998) is not reliable; and 4) as the calculated maximum permanent seismic displacement varies along the liner, 1-D models using a weak layer cannot fully account for the impact of slip at a liner interface on seismic response.

The decoupled permanent seismic displacements calculated for different input motion of the heap leach pad system were in excess of 150 – 300 mm, the displacement criteria established by EPA for acceptable seismic performance of geosynthetic liner systems and generally accepted in practice. However, except for one case, the computed maximum tensile strains and forces were well below values at yield for the geomembrane despite calculated decoupled permanent displacements 5 to 10 times the generally accepted limiting value.

13.2.5 **Seismic analysis of two typical landfills configurations**

Two-dimensional non-linear numerical analyses were conducted of the seismic response of idealized quarry-fill and canyon-fill landfills using interface elements that allowed for slip at the geomembrane interface and computation of liner strains and forces. Response analyses were also conducted using conventional 1-D equivalent linear analysis. Analyses were conducted using a record from the M_w 6.7 Coalinga earthquake scaled to 0.4 g. Surprisingly, slip at the liner interface in the non-linear analyses did not significantly reduce the peak ground acceleration or the spectral response for either landfill configuration compared to the results of equivalent linear 1-D analysis which did

not consider slip at the interface. The non-linear analyses indicated that the tensile forces and strains in the geomembrane were minimal when the upper and lower interface shear strength was the same or when the lower interface strength was greater than the upper interface strength. When the interface friction angle was five degree greater on the top than on the bottom of the geomembrane, the seismically-induced tensile stresses were still well within the allowable values.

The calculated permanent displacement was significantly greater in the 2-D non-linear analysis compared to the decoupled analysis for both landfill configurations. The maximum tensile strains and forces for both configurations were well below values at yield. Consistent with these results, in this case the calculated permanent displacement from decoupled analysis for both landfill configurations was well below the allowable permanent deformation of 150 mm.

13.2.6 **OII landfill back analyses**

A comprehensive back-analysis of the OII landfill using five sets of recorded motions was used to establish the appropriate modulus reduction "backbone curve" to model the behavior of solid waste subject to seismic loading. Results of the back analysis indicated that a backbone curve consistent with the ASU modulus reduction curve for 65% ≤ 20mm material used with the Masing rule and 2% Raleigh damping gave the best results for the response at the top deck of the OII landfill compared to the recorded data.

13.2.7 **Chiquita Canyon landfill back analysis**

Back-analysis of two cross sections where geomembrane liner tears were observed in the Chiquita Canyon landfill were conducted using two recorded motions from 1994

Northridge earthquake. The numerical modeling predicted failure in the geomembrane due to strain concentration due to seams and scratches in the geomembrane at the locations of the tears. The decoupled analysis used in current design practice was not able to predict failure in the liner system. The analysis showed that strain concentration due to scratches and seams can cause failure in a geomembrane liner system. One recommendation based upon this finding is that sampling of the geomembrane seam for quality control purposes should be avoided in areas of tensile strains concentration. These areas, as illustrated in the numerical analyses, are likely to be near anchor trenches or in the vicinity of benches.

13.2.8 **Lopez Canyon landfill back analysis**

Back-analysis of the Lopez Canyon landfill was conducted using two recorded motions from 1994 Northridge earthquake. Based upon available laboratory test data, the critical interface on the side slope was determined to be the geotextile/site soil interface. The strains predicted in the geotextile below this interface were high but not enough to cause a tear in the geotextile. The findings from this case history and from the analysis of the two typical landfill configurations suggests that a preferential slip plane may be incorporated into a composite liner system in order to constrain sliding to a specific interface located away from the geomembrane and thereby minimize tensile strains and forces in the geomembrane.

13.3 Future work

Recommendations for future work include:

1) As the interface shear properties (strength and stiffness) of the liner system often represents the critical element for seismic analysis and design, the dynamic properties of interface (i.e. behavior under cyclic and rapid laoding) in composite systems requires better characterization. Cyclic direct shear tests performed on geomembrane/GCL interfaces was done using uniform loading: these tests should be extended to evaluate the response of these interfaces under non-uniform loading (earthquake-like loading). Cyclic direct shear tests were only conducted on geomembrane/GCL: these tests should be extended to evaluate the other geosynthetic components in the landfill liner system.
2) The behavior of confined geomembranes under tensile loading has not been studied. Data in the literature showed that nonwoven geotextile stiffness increase under confinement. Analyses showed that an increase in tensile stiffness of the geomembrane can decrease the tensile strains induced in the geomembrane by seismic loading. Tensile tests on geomembranes under confinement are needed to determine an accurate stiffness for use in numerical analyses.
3) The behavior of geomembranes under compression loading has not been studied. The numerical analysis conducted showed that decreasing the geomembrane compressive stiffness by one order of magnitude can increase the calculated max tensile strains in landfills. Compression tests on geomembranes under confinement are needed to determine an accurate stiffness for use in numerical analyses.
4) Validation and calibration for the numerical models using centrifuge testing is needed to calibrate some parameters required for the numerical model of seismic performance developed herein, most notably to calibrate interface shear stiffness and geomembrane stiffness under service loads.

REFERENCES

AASHTO (2007). AASHTO LRFD Bridge Design Specifications. 4th Edition, American Association of State Highway and Transportation Officials.

Anderson, D. G., and Kavazanjian, E., Jr. (1995) Performance of Landfills Under Seismic Loading. Proc. *3rd International Conference on Recent Advances in Geotechnical Earthquake Engineering and Soil Dynamics*, University of Missouri-Rolla, Rolla, Missouri, Vol. III, pp. 1-30.

Anderson, D. G., Martin, G. R., Lam, I., and Wang, J. N. (2009). Seismic analysis and design of retaining walls, buried structures. slopes, and embankments. NCHRP Rep. 611, Transportation Research Board, Washington, D.C.

Anderson, D.G., Hushmand, S., and Martin, G.R. (1992). Seismic Response of Landfill Slopes. *Proceedings ASCE Specialty Conference on Stability and performance of Slopes and Embankments-II*, Berkeley, California, June 28 -July 1, 973-989.

Arab, G. M., and Kavazanjian, E. Jr., (2010). Time-Domain Analysis of Frictional Base Isolation Using Geosynthetics. 9th International conference on Geosynthetics, Brazil, May 23-27.

Arab, G. M., Kavazanjian, E. Jr., and Matasovic, N. (2010). Nonlinear Time-Domain Analysis of a Sliding Block on a Plane. Proc. 5th International Conference on Recent Advances in Geotechnical Earthquake Engineering and Soil Dynamics, San Diego, California, Paper 4.08 (CD-ROM).

Augello, A. J., Bray, J.D., Abrahamson, N.A., and Seed, R.B. (1998). Dynamic properties of solid waste based on back-analysis of OII landfill. *J. Geotech. Geoenviron. Eng.*, 124(3), 211-222.

Augello, A. J., Matasovic, N., Bray, J.D., Kavazanjian, E., Jr., and Seed, R.B. (1995). Evaluation of Solid Waste Landfill Performance during the Northridge Earthquake, Earthquake Design and Performance of Solid Waste Landfills, ASCE Geotechnical Special Publication No. 54, 17-50.

Bray J.D., Zekkos D., Kavazanjian Jr. E., Athanasopoulos, G.A. and Riemer M.F. (2009) Shear strength of municipal solid waste. *J. Geotech. and Geoenvir. Engrg.*, 135, No. 6, 709-722.

Bray, J. D., A. J. Augello., G. A. Leonards, P. C. Repetto, and R. J. Byrne, (1995). Seismic Stability Procedures for Solid-Waste Landfills. *J. Geotech. Engrg.*, ASCE, , Vol. 121, No. 2, 139-151.

Bray, J. D., and Rathje, E. M. (1998). Earthquake-induced displacements of solid-waste landfills. *J. Geotech. and Geoenvir. Engrg*., ASCE, 124(3), 242–253.

Bray, J. D., Rathje, E. M., Augello, A. J., and Merry, S. M. (1998). Simplified Seismic Design Procedure for Geosynthetic-Lined Solidwaste Landfills. *Geosynthetics International*, Vol. 5, No. 1 and 2, 203–235.

Bray, J. D., Zekkos D., Kavazanjian Jr. E., Athanasopoulos, G.A. and Riemer M.F. (2009). Shear strength of municipal solid waste. *J. Geotech. and Geoenvir. Engrg.*, ASCE, 135(6), 709-722.

Byrne, R. J., Kendall, J., and Brown, S. (1992). Cause and mechanism of failure, Kettleman Hills Landfill B-19, unit IA. Proc., ASCE Spec. Conf. on Perf. and Stability of Slopes and Embankments, , ASCE, New York, N.Y., Vol. (2):1188- 1215.

Byrne, R.J. (1994). Design issues with strain-softening interfaces in landfill liners. Proc. Waste Tech. '94, Charleston, South Carolina, USA, 1-26.

Derian, L., Gharios, K.M., Kavazanjian, E., Jr., and Snow, M.S. (1993). *Geosynthetics Conquer the Landfill Law*. Civil Engineering, ASCE, December.

Desai, C.S., and Fishman, K. L. (1991). Plasticity-based constitutive model with associated testing for joints. *Int. J. Rock Mech. Min. Sci. Geomech. Abstr*., 28, 15–26.

Dixon, N., and Jones, D.R.V. (2005). Engineering Properties of Municipal Solid Waste. *Geotextiles and Geomembranes*, Vol. 23, No. 3, 205-233.

Duncan, J. M., Byrne, P., Wong, K. S., Mabry, P. (1980). Strength, Stress- Strain and Bulk Modulus Parameters for Finite Element Analyses of Stresses and Movements in Soil Masses. University of California at Berkeley, Berkeley.

Elgamal, A. W. M., Scott, R. F., Succarieh, M. F., and Yan, L. (1990). La Villita Dam response during five earthquakes including permanent deformation, *J. of Geotech. Engrg.*, ASCE, 116(10), 1443-1462.

EMCON Associates (1994). Northridge Earthquake Seismic Evaluation, Chiquita Canyon Landfill. April.

Esterhuizen, J.J.B., Filz, G.M., and Duncan, J.M. (2001) Constitutive behavior of geosynthetic interfaces. *J. Geotech. and Geoenvir. Engrg.*, ASCE, 127(10): 834-840.

Fowmes, G.J. (2007). Analysis of Steep sided Landfill Lining System. Eng.D thesis, Department of Civil and Building Engineering, Loughborough University, Loughborough, UK.

Fowmes, G.J., Dixon, N., Jones, D.R.V. (2006). Modelling of Lining System Integrity. Proceedings 8th International Conference on Geosynthetics, Yokohama, Japan, pp207.

Fowmes, G.J., Jones, D.R.V., and Dixon, N. (2005). Analysis of a Landfill Directive Compliant Steepwall Lining System, Proceedings, 10th International Waste Management and Landfill Symposium, Sardinia (CD-ROM).

Fox, P. J., Rowland, M. G. and Scheithe, (1998). Internal Shear Strength of Three Geosynthetic Clay Liners. *J. Geotech. and Geoenvir. Engrg.*, 124(10):933–944.

Fox, P. J., and Stark, T. D. (2004). State-of-the-art report: GCL shear strength and its measurement, *Geosynthetics International*, 11(3), 141-175.

Fox, P.J., and Kim, R.H. (2008). Effect of progressive failure on measured shear strength of geomembrane/GCL interface. *J. Geotech. and Geoenvir. Engrg.*, 134(4), 459-469.

Fox, P.J., and Stark, T.D. (2004). State-of-the-Art Report: GCL Shear Strength and its Measurement. *Geosynthetics International*, Vol. 11, No. 3, 141-175.

Fox, P.J., Nye, C.J., Morrison, T.C., Hunter, J.G., and Olsta, J.T. (2006). Large dynamic direct shear machine for geosynthetic clay liners. *Geotechnical Testing Journal*, 29(5): 392-400.

Franklin, A. G., and Chang, F. K. (1977). Earthquake resistance of earth and rockfill dams. Misc. Paper S-71-17, U.S. Army Wtrwy. Experiment Station, Vicksburg, Miss.

Gazetas, S. G., Uddin, N., (1994). Permanent deformation on pre-existing sliding surfaces in dams. *Journal of Geotechnical Engineering*, ASCE 120, 2041-2061.

GeoSyntec (1994). Assessment of Performance of the Disposal Area C Liner System during the Northridge Earthquake of 17 January 1994 and of Damage to Geotextile and Geonet observed on 18 January 1994, Lopez Canyon Sanitary Landfill, Lake View Terrace, Los Angeles, Memorandum to Solid Waste Management Division, Bureau of Sanitation, City of Los Angeles, GeoSyntec Consultants, Hunting Beach, CA, 6 p.

GeoSyntec. (1996). Seismic site response analyses, Operating Industries, Inc. landfill, Monterey Park, California. Rep. No. SWP-6, GeoSyntec Consultants, Huntington Beach, Calif.

Giroud, J. P. (1984). Analysis of stresses and elongations in geomembranes. Proceedings of the International Conference on Geomembranes, Denver, CO, IFAI Publisher, Vol. 2, pp. 481–486.

Giroud, J. P. (1993). Lessons learned from studying the performance of geosynthetics. Proceedings of Geotextiles-Geomembranes Rencontres 93, Joue´-les-Tours, France, CFG Publisher, Vol. 1, No. 15, pp. 33–46.

Giroud, J. P. (1994). Mathematical model of geomembrane stress-strain curves with a yield peak. *Geotextiles and Geomembranes*, 13 (1), 1-22.

Giroud, J. P. (2005). Quantification of geosynthetic behavior. *Geosynthetics International*, Special Issue on the Giroud Lectures, 12(1), 2-27.

Gourc, J. P., Reyes-Ramirez, R. & Villand, P. (2004). Assessment of Geosynthetics Interface Friction for Slope Barriers of Landfill proceeding of the 3rd Asian Regional Conference on Geosynthetics Seoul, Korea, June, P: 116-149.

GSE (2011). http://www.gseworld.com/.

Hatami, K., Bathurst, R.J., (2005). Parametric analysis of reinforced soil walls with different backfill material properties. NAGS'2006 Conference, Las Vegas, Nevada, USA, p: 1–15.

Hushmand, B., Anderson, D. G., Crouse, C. B., and Robertson, R. J. (1990). Seismic monitoring and evaluation of a solid waste landfill. Proc., 4th U.S. Nat. Conf. on Earthquake Engrg., Palm Springs, Calif., 3, 855-863.

Idriss, I.M., Fiegel, G., Hudson, M.B., Mundy, P.K., and Herzig, R. (1995). Seismic response of the Operating Industries landfill. Earthquake design and performance of solid waste landfills, ASCE Geotechnical Special Publication No. 54, *Edited by* M.Y. Yegian, W.D. Liam Finn, 83-118.

Itasca (2008) FLAC version 600 user's guide – Fast Lagrangian analysis of continua, user's manual Itasca Consulting Group, Inc., Minneapolis, MN

Iwan, W. D. (1967). On a class of models for the yielding behavior of continuous and composite systems. *Journal of Applied Mechanics*, 34, 612-617.

Kavazanjian, E., Jr., and Matasovic, N. (1995). Seismic Analysis of Solid Waste Landfills, Geoenvironment 2000, ASCE Geotechnical Special Publication No. 46, Vol. 2, 1066-1080.

Kavazanjian, E., Jr., Dixon, N., Katusmi, Y., Kortegast, A., Legg, P., and Zanzinger, H. (2006). Geosynthetic Barriers for Environmental Protection at Landfills. Proceedings, 8th International Conference on Geosynthetics, J. Kuwano and J. Koseki, eds., Yokohama, Japan, 121-152.

Kavazanjian, E., Jr., Hushmand, B., and Martin, G.R. (1991). Frictional Base Isolation Using a Layered Soil-Synthetic Liner System, Proceedings, 3rd U.S. Conference on Lifeline Earthquake Engineering, ASCE Technical Council on Lifeline Earthquake Engineering Monograph Vol. 4:1139-1151.

Kavazanjian, E., Jr., Matasovic, N. Bonaparte, R. and Schmertmann, G.R. (1995). Evaluation of MSW Properties for Seismic Analysis. IGeoenvironment 2000, ASCE Geotechnical Special Publication, 2(46), 1126-1141.

Kavazanjian, E., Jr., Matasovic, N., and Caldwell, J.A. (1998). Seismic Design and Performance Criteria for Landfills. Proceedings, 6th US National Conference on Earthquake Engineering, Seattle, Washington (CD-ROM).

Kavazanjian, E., Jr., Matasovic, N., Stokoe, K.H., II, and Bray, J.D. (1996). In-Situ Shear Wave Velocity of Solid Waste from Surface Wave Measurements. Proc. 2nd International Congress Environmental Geotechnics, Osaka, Ja98pan, Balkema, Vol. 1, pp. 97-104

Kim, J., Riemer, M., and Bray, J.D. (2005). Dynamic properties of geosynthetic interfaces. *Geotechnical Testing Journal*, 28(3), 1-9.

Kramer, S. L., and Smith, M. W. (1997). Modified Newmark model for seismic displacements of compliant slopes, *J. Geotech. and Geoenvir. Engrg.*, 123(7), 635–644.

Lin, J.S., Whitman, R.V., (1983). decoupled approximation to the evalutation of earthquake-induced plastic slip in earth dams. *Earthquacke Engrg. and Struct. Dyn.*, 11, 667–678.

Lin, J.S., Whitman, R.V., (1986). Earthquake-induced displacements of sliding block. *J. Geotech. Engrg.*, ASCE 105, 1427–1434.

Linda Al Atik, (2009). Excel File of NGA Models University of California, Berkeley.

Lo Grasso, S.A., Massimino, M.R., and Maugeri, M. (2002) Dynamic analysis of geosynthetic interfaces by shaking table tests. Proc. 7th International Con ference on Geosynthetics, P. Delmas and J. P. Gourc, eds., Nice, 4, 1335-1338.

Makdisi, F. I., and Seed, H. B. (1978). ‘‘Simplified procedure for estimating dam and embankment earthquake-induced deformations’’, *J. Geotech. Engrg. Div.*, ASCE, 104(7), 849–867.

Masing, G. (1926). Eigenspannungen and verfertigung beim messing, Proc. 2nd Int. Congress on Applied Mechanics, Zurich.

Matasovic N. (1993). Seismic Response of Composite Horizontally-Layered Soil Deposits, *Ph.D. Dissertation*, Civil Engineering Dept., Univ. of California, Los Angeles, Calif., 483 p.

Matasovic, N. (2010). D-MOD2000 - A Computer Program for Seismic Response Analysis of Horizontally Layered Soil Deposits, Earthfill Dams, and Solid Waste Landfills, User's Manual, GeoMotions, LLC (www.GeoMotions.com), Lacey, Washington.

Matasovic, N. and M. Vucetic (1993). Cyclic characterization of liquefiable sands. *J. of Geotech. Engrg.*, ASCE, 119 (11), 1805-1822.

Matasovic, N. and M. Vucetic (1995). Generalized cyclic degradation-pore pressure generation model for clays. J. *of Geotech. Engrg.*, ASCE, 121 (1), 33-42.

Matasovic, N., and Kavazanjian, E., Jr. (1998). Cyclic Characterization of OII Landfill Solid Waste, *J. Geotech. and Geoenvir. Engrg.*, 124 (3), 197-210.

Matasovic, N., Kavazanjian, E., Jr., and Giroud, J.P. (1998). Newmark Seismic Deformation Analysis for Geosynthetic Covers, *Geosynthetics International*, Journal of the IGS, 5 (2), 237-264.

Matasovic, N., Kavazanjian, E., Jr., Augello, A.J., Bray, J.D. and Seed, R.B. (1995). Solid Waste Landfill Damage Caused by 17 January 1994 Northridge Earthquake, In: Woods, Mary C. and Seiple, Ray W., Eds., *The Northridge, California, Earthquake of 17 January 1994*: California Department of Conservation, Division of Mines and Geology Special Publication 116, Sacramento, Calif., 221-229, (*Invited Paper*).

McCartney, J.S., Zornberg, J.G., and Swan, R.H., Jr. (2009). Analysis of a large database of GCL geomembrane interface shear strength results. *J. Geotech. and Geoenvir. Engrg.*, 134(2), 209-223.

McGown, A., Andrawes, K.Z., Kabir, M.H. (1982). Load-extension testing of geotextiles confined in soil. 2nd International Conference on Geotextiles, Las Vegas, USA, vol. 3: 793–798.

Mejia, L. H., and E. M. Dawson. (2006). Earthquake Deconvolution for FLAC. Proceedings of the 4th International FLAC Symposium, Madrid, Spain, May 2006, pp. 211-219.

Merry, S.M. and Bray, J.D. (1996). Geomembrane response in the wide strip tension test. *Geosynthetics international*, 3 (4), 517–536.

Mroz, Z. (1967). On the description of anisotropic work hardening. *Journal of the Mechanics and Physics of Solids*, 15, 163-175.

Newmark, N.M., (1965). Effects of earthquakes on dams and embankments. *Geotechnique*, 15, 139–160.

Nye C. J. and Fox, P. J. (2007). Dynamic Shear Behavior of a Needle-Punched Geosynthetic Clay Liner. *J. Geotech. and Geoenvir. Engrg.*, 133(8), 973–983.

Ordonez, G. A. (2010). SHAKE2000 -A Computer Program for the 1-D Analysis of Geotechnical Earthquake Engineering Problems, User's Manual, Geomotions, LLC (www.geomotions.com), Lacey, Washington.

Palmeira, E. M. (2009). Soil-geosynthetic interaction: Modelling and analysis. *Geotextiles and Geomembranes*, 27 (5), 368-390.

Phillips, C. and Hashash, Y. (2009). Damping formulation for nonlinear 1D site response analyses. *Soil Dynamics and Earthquake Engineering*, 29(7), 1143-1158.

Prevost, J. H. (1985). A simple plasticity theory for frictional cohesionless soils. *Soil Dynamics and Earthquake Engineering*, 4 (1), 9-17.

Rathje, E. M., and Bray, J. D. (2000). Nonlinear Coupled Seismic Sliding Analysis of Earth Structures, *J. Geotech. and Geoenvir. Engrg.*, ASCE, 126(11), 1002–1014.

Rathje, E. M., and Bray, J. D. (2001). One and two dimensional seismic analysis of solid-waste landfills, *Can Geotech J.*, 38, 850–62.

Rathje, E.M., Abrahamson, N.A., and Bray, J.D. (1998). Simplified Frequency Content Estimates of Earthquake Ground Motions, *J. Geotech. and Geoenvir. Engrg.*, ASCE, 124(2), 150-159.

Richardson, G.N., Kavazanjian, E., Jr., and Matasovic, N. (1995). RCRA Subtitle D (258) Seismic Design Guidance for Municipal Solid Waste Landfill Facilities, EPA/600/R- 95/051, United States Environmental Protection Agency, Cincinnati, Ohio, 143 p.

Rocscience (2005). Slide v5.0 - 2-D Limit Equilibrium Slope Stability Analysis, Rocscience, Inc. (www.rocscience.com), Toronto, Ontario.

Ross J.D., Fox P. J. and Olsta, J. T. (2010). Dynamic shear testing of a geomembrane/geosynthetic clay liner interface. 9th International Conference on Geosynthetics, IGS-Brazil, 2, 649-652.

Ross, J.D. (2009). Static and dynamic shear strength of a geomembrane/geosynthetic clay liner interface. M.S. thesis, Department of Civil and Environmental Engineering and Geodetic Science, The Ohio State University, Columbus, Ohio, USA.

Salah-Mars, S. (1989). A multiple yield surface plasticity of dry soil to impact loading. Ph.D. Dissertation, Stanford Univ., Stanford, California.

Salah-Mars, S., and Kavazanjian, E., Jr. (1992). A Virtual Surface Concept for Nested Yield Surface Plasticity. *International Journal for Numerical and Analytical Methods in Geomechanics*, 16, 779-796.

Seed, R.B., and Bonaparte, R. (1992). Seismic Analysis and Design of Lined Waste Fills: Current Practice. Proceedings, Stability and Performance of Slopes and Embankments - II, ASCE Geotechnical Special Publication No. 31, Vol. 2, 1521-1545.

Shibuya, S., Kong, X. J., and Tatsuoka, F. (1990). Deformation characteristics of gravels subjected to monotonic and cyclic loading. Proc., 8th Japan Earthquake Engrg. Symp., 771-776.

Siriwardane, H. J. and Desai, C. S., (1983). Computational Procedures for Nonlinear Three-Dimensional Analysis with Some Advanced Constitutive Laws. *Int. J. Num. and Analyt. Meth. in Geomech.*, 7, No. 2.

Stark, T. D. and Poeppel A. R. (1994). Landfill Liner Interface Strengths from Torsional-Ring-Shear Tests. *J. Geotech. Engrg.*, 120(3), 597–615.

Stark, T. D., Williamson, T. A. and Eid, H. T. (1996). HDPE Geomembrane/Geotextile Interface Shear Strength. *J. Geotech. Engrg.*, 122(3),197-203.

Stern, A.N. (2009). Dynamic Shear Behavior of a Needle-Punched Geosynthetic Clay Liner/ Geomembrane Interface at a High Normal Stress. B.S. thesis, Department of Civil and Environmental Engineering and Geodetic Science, The Ohio State University, Columbus, Ohio, USA.

Stewart, J.P., Bray, J.D., Seed, R.B., and Sitar, N. (1994), "Preliminary Report on the Principal Geotechnical Aspects of the January 17, 1994 Northridge Earthquake", Report No. UCB/EERC - 94/08, Earthquake Engineering Research Center, University of California at Berkeley, Berkeley, CA, June.

Sura, J.M. (2009). Monotonic and Cyclic Shear Response of a Needle punched Geosynthetic Clay liner at High Normal Stresses. M.S. thesis, Department of Civil and Environmental Engineering and Geodetic Science, The Ohio State University, Columbus, Ohio, USA.

Thusyanthan, N. I, Madabhushi, S.P.G. and Singh, S. (2007). Tension in geomembranes on landfill slopes under static and earthquake loading – Centrifuge study. Special Issue on Geosynthetics in Harsh Environments, *Geotextiles and Geomembranes*, 25 (2), 78-95.

Triplett, E. J., and Fox, P. J. (2001). Shear strength of HDPE geomembrane/geosynthetic clay liner interfaces. *J. Geotech. and Geoenvir. Engrg.*, 127(6), 543–552.

Vucetic, M. and Dobry, R. (1991). Effect of soil plasticity on cyclic response. *J. Geotech. Engrg.*, 117 (1), 89-107.

Wartman, J. (1999). Physical model studies of seismically induced deformation in slopes. Ph.D. Dissertation, Univ. of California, Berkeley, California.

Wartman, J., Bray, J.D., and Seed, R.B. (2003). *Inclined plane studies of the Newmark sliding block procedure*. *J. Geotech. and Geoenvir. Engrg.*, ASCE, 129(8), 673–684.

Wartman, J., Seed, R. B., and Bray, J. D. (2005). Shaking table modeling of seismically induced deformations in slopes. *J. Geotech. and Geoenvir. Engrg.*, 131(5), 610–622.

Westermo, B. and Udwadia, F. (1983). Periodic response of a sliding oscillator system to harmonic excitation. *Earthquake Engrg. Struct. Dyn.,* 11, 135-146.

Yan, L. (1998). Nonlinear load-deformation characteristics of bridge abutments and footings under cyclic loading. Ph.D. Dissertation, Univ. of Southern California, Los Angeles, California.

Yan, L., Matasovic, N. and Kavazanjian, E., Jr. (1996). Seismic Response of Rigid Block on Inclined Plane to Vertical and Horizontal Ground Motions Acting Simultaneously, Proc. 11th ASCE Engineering Mechanics Conf., Fort Lauderdale, Florida, Vol. 2, pp. 1110-1113.

Yazadini, R., Campbell, J.L., Koerner, G.R., (1995). Long-term in situ strain measurements of a high density polythylene geomembrane in a municipal solid waste landfill. Geosynthetics ’95 Conference Proceedings, Nashville, TN, pp. 893–906.

Yegian, M. K., and Lahlaf, A. M. (1992). Dynamic interface shear strength properties of geomembranes and geotextiles. *J. Geotech. Engrg.*, 118(5), 760–779.

Yegian, M.K. and Kadakal, U. (2004). Foundation Isolation for Seismic Protection Using a Smooth Synthetic Liner , *J. Geotech. and Geoenvir. Engrg.*, 130(11), 1121-1130.

Yegian, M.K., and Kadakal, U. (1998a). Modeling Geosynthetic Liners in Dynamic Response Analysis of Landfills, Geotechnical Earthquake Engineering and Soil Dynamics III, ASCE Geotechnical Special Publication, 2 (75), 986-992.

Yegian, M.K., and Kadakal, U. (1998b). Geosynthetic Interface Behavior under Dynamic Loading, *Geosynthetics International*, 5 (2), 1- 16.

Yegian, M.K., and Lahlaf, A.M. (1992). Dynamic Interface Shear Strength Properties of Geomembranes and Geotextiles. *J. Geotech. Engrg.*, ASCE, 118 (5), 760-779.

Yegian, M.K., Harb, J.N., and Kadakal, U. (1998). Dynamic Response Analysis Procedure for Landfills with Geosynthetic Liners. *J. Geotech. and Geoenvir. Engrg.*, ASCE, 124 (10), 1027-1033.

Yuan, P., Kavazanjian, E., Chen, W., Seo, B. (2011). Compositional effects on the dynamic properties of municipal solid waste. *Waste Management*.

Zekkos (Zeccos), D. P. (2005). Evaluation of static and dynamic properties of municipal solid-waste. Ph.D. thesis, Dept. of Civil and Environmental Engineering, Univ. of California, Berkeley, Calif.

Zekkos, D., Bray, J. D., and Riemer, M. F. (2008). Shear modulus and material damping of municipal solid waste based on large-scale cyclic triaxial testing. *Can. Geotech. J.*, 45(1), 45−58.

Zekkos, D., Bray, Kavazanjian, J.E, Matasovic, N., Rathje, E.M., Riemer, M.F., and Stokoe, K.H., (2006). Unit weight of municipal solid waste. *J. Geotech. and* Geoenvir. Engrg., 132, No. 10, 1250-1261.

APPENDIX A

INTERFACE SOFTENING SUBROUTINE

SSint_eqn_com.fis

ca int.fin

```
def int_var
  while_stepping
  ip=int_pnt
   loop while ip#0
     n1=imem(ip+$kicapt)         ;address of node block 1
     n2=imem(n1)                 ;address of node block 2
     i1=imem(n1+$kidi)           ;i of node 1
     j1=imem(n1+$kidj)           ;j of node 1
     i2=imem(n2+$kidi)           ;i of node 2
     j2=imem(n2+$kidj)           ;j of node 2
     n1b=imem(n1+$kidseg)        ;address of the nearest node to 1
     i1b=imem(n1b+$kidi)         ;i of the node nearest to 1
     j1b=imem(n1b+$kidj)         ;j of the node nearest to 1
     n2b=imem(n2+$kidseg)        ;address of the nearest node to 2
     i2b=imem(n2b+$kidi)         ;i of the node nearest to 2
     j2b=imem(n2b+$kidj)         ;j of the node nearest to 2
     rat1 = fmem(n1+$kidrat)     ; Ratio of first node contact
     if rat1 = 1.0 then
       rat1 = 0.0
     end_if
     rat2 = fmem(n2+$kidrat)     ; Ratio of second node contact
     if rat2 = 1.0 then
       rat2 = 0.0
     end_if
     ;*** First Node Relative Velocity
     if rat1 = 0.0 then          ; Gridpoint aligned
       vxb = xvel(i1b,j1b)
       vyb = yvel(i1b,j1b)
     end_if
     if rat1 < 0.0 then          ; Use reverse link for second node
       rat = -1.0*rat1
       tar = 1.0 - rat
       nbl = imem(n1b+$kidrlk)   ; Node to interpolate with (link node)
       il  = imem(nbl+$kidi)     ; i index of link node
       jl  = imem(nbl+$kidj)     ; j index of link node
       vxb = (rat*xvel(i1b,j1b))+(tar*xvel(il,jl))  ; interpolation
       vyb = (rat*yvel(i1b,j1b))+(tar*yvel(il,jl))  ;
     end_if
     if rat1 > 0.0 then          ; Use forward link for second node
       rat = rat1
       tar = 1.0 - rat
       nbl = imem(n1b)
       il  = imem(nbl+$kidi)
       jl  = imem(nbl+$kidj)
       vxb = (rat*xvel(i1b,j1b))+(tar*xvel(il,jl))  ; interpolation
       vyb = (rat*yvel(i1b,j1b))+(tar*yvel(il,jl))  ;
     end_if
     rvx1 = xvel(i1,j1) - vxb    ; Node 1 Relative Velocity
     rvy1 = yvel(i1,j1) - vyb

   ;*** Second Node Relative Velocity
   if rat2 = 0.0 then          ; Gridpoint aligned
     vxb = xvel(i2b,j2b)
     vyb = yvel(i2b,j2b)
   end_if
   if rat2 < 0.0 then          ; Use reverse link for second node
```

```
      rat = -1.0*rat2
      tar = 1.0 - rat
      nbl = imem(n2b+$kidrlk)   ; Node to interpolate with (link node)
      il  = imem(nbl+$kidi)     ; i index of link node
      jl  = imem(nbl+$kidj)     ; j index of link node
      vxb = (rat*xvel(i2b,j2b))+(tar*xvel(il,jl))  ; interpolation
      vyb = (rat*yvel(i2b,j2b))+(tar*yvel(il,jl))  ;
    end_if
    if rat2 > 0.0 then          ; Use forward link for second node
      rat = rat2
      tar = 1.0 - rat
      nbl = imem(n2b)
      il  = imem(nbl+$kidi)
      jl  = imem(nbl+$kidj)
      vxb = (rat*xvel(i2b,j2b))+(tar*xvel(il,jl))  ; interpolation
      vyb = (rat*yvel(i2b,j2b))+(tar*yvel(il,jl))  ;
    end_if
    rvx2 = xvel(i2,j2) - vxb    ; Node 2 Relative Velocity
    rvy2 = yvel(i2,j2) - vyb

    ;** First Node Relative Shear Velocity
    usx = -1.0*fmem(n1+$kidun+1)              ; Shear normal vector
    usy = fmem(n1+$kidun)                     ;
    rsv1 = (rvx1*usx) + (rvy1*usy)

    ;** Second Node Relative Shear Velocity
    usx = -1.0*fmem(n2+$kidun+1)
    usy = fmem(n2+$kidun)
    rsv2 = (rvx2*usx) + (rvy2*usy)
;
    if rsv#0.0 then
     signp = rsv/abs(rsv)
    else
     signp = 0.0
    end_if
;;;;;;;;;;;;Absolute Relative Shear Velocity;;;;;;;;;;;;;;;;;;;;;;;;;;;;;;;;;;;;;;;;
    rsv = abs(rsv1+rsv2)*0.5    ; Absolute Relative Shear Velocity
;;;;;;;;;;;;;;;;;;;;;;;;;;;;;;;;Direction of motion ;;;;;;;;;;;;;;;;;;;;;;;;;;;;;;;;;;
    if rsv#0.0 then
     sign = rsv/abs(rsv)  ; sign of the relative velocity
    else
     sign = 0.0
    end_if
;;;;;;;;;;;;;;;;;;;;;;;;;;;;;;;;;;;;relative displacement;;;;;;;;;;;;;;;;;;;;;;;;;;;;;;;;
;
    fmem(ip+$kicext)=fmem(ip+$kicext)+rsv*dytdel  ; comulative displacement
;
    rsd_past = rsd                      ; previous step
;
    rsd      = (fmem(ip+$kicext))         ; comulative displacement
;
    _rdispc  = rsd_past                  ; reverse loading
;
;;;;;;;;;;;;;;;;;;;;;;;;;;equation parameters       ;;;;;;;;;;;;;;;;;;;;;;;;;;;;;;;;;;;;
;
      _xo   = 12.0          ; displacement at residual
;
       _c = 0.521               ; fitting parameter
;
      _phip = 16.5             ; peak friction angle
```

```
;
    _phir = 1.5              ; residual friction angle
;
    _a = 1.0/(_phip)
;
    _r = _phip/_phir         ; residual friction angle
;
    _d = _a*(_r-1.0);
;
    rsdp = 10.66/1000.0        ; displacement at peak (11mm)
;
;;;;;;;;;;;;;;;;;;;direction 1 ll;;;;;;;;;;;;;;;;;;;;;;;;;;;;;;;;;;;;;;;;;;;;;

      if _n1#1 then
        _tanphip = tan(_phip*degrad)
      end_if
;
       if _tanphip # 0.0
      _tanphir = tan(_phir*degrad)*_tanphip/abs(_tanphip)   ; _RFF*_tanphip1
       end_if
;
      rsdm = abs(rsd-rsdp)
;
      if rsd >= rsdp then
;
         _n1      = 1
;
       int_fri = 1.0/(_a+_d*((rsdm/_xo)^_c))
;
         int_frip = abs(atan(_tanphip)/degrad)
;
       fmem(ip+$kictph) = tan(int_fri*degrad) ; store friction coefficient
;
     end_if
;
       if (rsd) < rsdp then
;
       int_fri = abs(atan(_tanphip)/degrad)
;
       fmem(ip+$kictph) = tan(int_fri*degrad) ; store friction coefficient
;
     end_if
;
       if (rsd) >= _xo then
;
       int_fri = _phir
;
       fmem(ip+$kictph) = tan(int_fri*degrad) ; store friction coefficient
;
     end_if


    ip=imem(ip)
;
   end_loop
end


def check_int
 ip=int_pnt
```

```
 loop while ip#0
  inum=imem(ip+$kicid)
  rsd=fmem(ip+$kicext)
  int_fri=fmem(ip+$kicfri)
  str1=string(inum)
  str2=string(rsd)
  message=out('The shear displacement of interface number '+str1+' is '+str2)
  xtable(out_tab,inum)=inum
  ytable(out_tab,inum)=int_fri
  ip=imem(ip)
 end_loop
end
```

```
SSint_eqn_com_beam.fis
; ca int.fin

def int_var
array rsd5(1000)
while_stepping
  ip=int_pnt
   aa=imem(ip+$kicid)
    if aa>=200  then
    loop while ip#0
      n1=imem(ip+$kicapt)
      n2=imem(n1)
      i1=imem(n1+$kidi)
      j1=imem(n1+$kidj)
      i2=imem(n2+$kidi)
      j2=imem(n2+$kidj)
      n1b=imem(n1+$kidseg)
      i1b=imem(n1b+$kidi)
      j1b=imem(n1b+$kidj)
      n2b=imem(n2+$kidseg)
      i2b=imem(n2b+$kidi)
      j2b=imem(n2b+$kidj)
      rat1 = fmem(n1+$kidrat)
      if rat1 = 1.0 then
        rat1 = 0.0
      end_if
      rat2 = fmem(n2+$kidrat)
      if rat2 = 1.0 then
        rat2 = 0.0
      end_if
      ;*** First Node Relative Velocity
      if rat1 = 0.0 then          ; Gridpoint aligned

;Prob a

intref25=0
intref26=0
intref25=i1b
intref26=j1b

intref1 = 0
if j1b#0 then
intref1 = xvel(intref25,intref26)
else
n_a = imem(str_pnt + $ksnode)
loop while n_a # 0
     cur_ida  = imem(n_a + $kndid)
     if cur_ida = intref25 then
       intref1 = fmem(n_a + $kndud1)
     endif
     n_a = imem(n_a)
end_loop
end_if
        vxb = intref1
;Prob b

intref2 = 0
if j1b#0 then
intref2 = yvel(intref25,intref26)
else
```

```
n_b = imem(str_pnt + $ksnode)
loop while n_b # 0
     cur_idb  = imem(n_b + $kndid)
     if cur_idb = intref25 then
       intref2 = fmem(n_b + $kndud2)
     endif
     n_b = imem(n_b)
end_loop
end_if
       vyb = intref2

      end_if
      if rat1 < 0.0 then          ; Use reverse link for second node
        rat = -1.0*rat1
        tar = 1.0 - rat
        nbl = imem(n1b+$kidrlk)   ; Node to interpolate with (link node)
        il  = imem(nbl+$kidi)     ; i index of link node
        jl  = imem(nbl+$kidj)     ; j index of link node

;Prob c

intref27=0
intref28=0
intref27=i1b
intref28=j1b

intref3 = 0
if j1b#0 then
intref3 = xvel(intref27,intref28)
else
n_c = imem(str_pnt + $ksnode)
loop while n_c # 0
     cur_idc  = imem(n_c + $kndid)
     if cur_idc = intref27 then
       intref3 = fmem(n_c + $kndud1)
     endif
     n_c = imem(n_c)
end_loop
end_if

intref17=0
intref18=0
intref17=il
intref18=jl

intref3a = 0
if intref18#0 then
intref3a = xvel(intref17,intref18)
else
n_ca = imem(str_pnt + $ksnode)
loop while n_ca # 0
     cur_idca  = imem(n_ca + $kndid)
     if cur_idca = intref17 then
       intref3a = fmem(n_ca + $kndud1)
     endif
     n_ca = imem(n_ca)
end_loop

end_if
```

```
      vxb = (rat*intref3)+(tar*intref3a)  ; interpolation


;Prob d

intref29=0
intref30=0
intref29=i1b
intref30=j1b

intref4 = 0
if j1b#0 then
intref4=yvel(intref29,intref30)
else
n_d = imem(str_pnt + $ksnode)
loop while n_d # 0
     cur_idd  = imem(n_d + $kndid)
     if cur_idd = intref29 then
       intref4 = fmem(n_d + $kndud2)
     endif
     n_d = imem(n_d)
end_loop
end_if

intref4a = 0
if intref18#0 then
intref4a=yvel(intref17,intref18)
else
n_da = imem(str_pnt + $ksnode)
loop while n_da # 0
     cur_idda  = imem(n_da + $kndid)
     if cur_idda = intref17 then
       intref4a = fmem(n_da + $kndud2)
     endif
     n_da = imem(n_da)
end_loop
end_if

      vyb = (rat*intref4)+(tar*intref4a)  ;

      end_if
      if rat1 > 0.0 then          ; Use forward link for second node
       rat = rat1
       tar = 1.0 - rat
       nbl = imem(n1b)
       il  = imem(nbl+$kidi)
       jl  = imem(nbl+$kidj)

;Prob e

intref31=0
intref32=0
intref31=i1b
intref32=j1b

intref5 = 0
if j1b#0 then
intref5 = xvel(intref31,intref32)
else
n_e = imem(str_pnt + $ksnode)
```

```
loop while n_e # 0
     cur_ide  = imem(n_e + $kndid)
     if cur_ide = intref31 then
       intref5 = fmem(n_e + $kndud1)
     endif
     n_e = imem(n_e)
end_loop
end_if

intref17a=0
intref18a=0
intref17a=il
intref18a=jl

intref5a = 0
if intref18a#0 then
intref5a = xvel(intref17a,intref18a)
else
n_ea = imem(str_pnt + $ksnode)
loop while n_ea # 0
     cur_idea  = imem(n_ea + $kndid)
     if cur_idea = intref17a then
       intref5a = fmem(n_ea + $kndud1)
     endif
     n_ea = imem(n_ea)
end_loop
end_if

       vxb = (rat*intref5)+(tar*intref5a)  ; interpolation

;Prob f

intref33=0
intref34=0
intref33=i1b
intref34=j1b

intref6 = 0
if j1b#0 then
intref6=yvel(intref33,intref34)
else
n_f = imem(str_pnt + $ksnode)
loop while n_f # 0
     cur_idf  = imem(n_f + $kndid)
     if cur_idf = intref33 then
       intref6 = fmem(n_f + $kndud2)
     endif
     n_f = imem(n_f)
end_loop
end_if

intref6a = 0
if intref18a#0 then
intref6a=yvel(intref17a,intref18a)
else
n_fa = imem(str_pnt + $ksnode)
loop while n_fa # 0
     cur_idfa  = imem(n_fa + $kndid)
     if cur_idfa = intref17a then
       intref6a = fmem(n_fa + $kndud2)
```

```
      endif
      n_fa = imem(n_fa)
end_loop
end_if
        vyb = (rat*intref6)+(tar*intref6a)

       end_if

;Prob g

intref19=0
intref20=0
intref19=i1
intref20=j1

intref7 = 0
if intref20#0 then
intref7=xvel(intref19,intref20)
else
n_g = imem(str_pnt + $ksnode)
loop while n_g # 0
      cur_idg  = imem(n_g + $kndid)
      if cur_idg = intref19 then
        intref7 = fmem(n_g + $kndud1)
      endif
      n_g = imem(n_g)
end_loop
end_if

       rvx1 = intref7 - vxb    ; Node 1 Relative Velocity

;Prob h

intref8 = 0
if intref20#0 then
intref8=yvel(intref19,intref20)
else
n_h = imem(str_pnt + $ksnode)
loop while n_h # 0
      cur_idh  = imem(n_h + $kndid)
      if cur_idh = intref19 then
        intref8 = fmem(n_h + $kndud2)
      endif
      n_h = imem(n_h)
end_loop
end_if
       rvy1 = intref8 - vyb

    ;*** Second Node Relative Velocity
    if rat2 = 0.0 then          ; Gridpoint aligned

;Prob i

intref35=0
intref36=0
intref35=i2b
intref36=j2b

intref9 = 0
if j2b#0 then
```

```
intref9 = xvel(intref35,intref36)
else
n_i = imem(str_pnt + $ksnode)
loop while n_i # 0
     cur_idi  = imem(n_i + $kndid)
     if cur_idi = intref35 then
       intref9 = fmem(n_i + $kndud1)
     endif
     n_i = imem(n_i)
end_loop

end_if
vxb = intref9

;Prob j

intref10 = 0
if j2b#0 then
intref10 = yvel(intref35,intref36)
else
n_j = imem(str_pnt + $ksnode)
loop while n_j # 0
     cur_idj  = imem(n_j + $kndid)
     if cur_idj = intref35 then
       intref10 = fmem(n_j + $kndud2)
     endif
     n_j = imem(n_j)
end_loop
end_if
vyb = intref10

   end_if
   if rat2 < 0.0 then          ; Use reverse link for second node
     rat = -1.0*rat2
     tar = 1.0 - rat
     nbl = imem(n2b+$kidrlk)   ; Node to interpolate with (link node)
     il  = imem(nbl+$kidi)     ; i index of link node
     jl  = imem(nbl+$kidj)     ; j index of link node

;Prob k

intref37=0
intref38=0
intref37=i2b
intref38=j2b

intref11 = 0
if j2b#0 then
intref11 = xvel(intref37,intref38)
else
n_k = imem(str_pnt + $ksnode)
loop while n_k # 0
     cur_idk  = imem(n_k + $kndid)
     if cur_idk = intref37 then
       intref11 = fmem(n_k + $kndud1)
     endif
     n_k = imem(n_k)
end_loop
end_if
```

```
intref21=0
intref22=0
intref21=il
intref22=jl

intref11a = 0
if intref22#0 then
intref11a = xvel(intref21,intref22)
else
n_ka = imem(str_pnt + $ksnode)
loop while n_ka # 0
     cur_idka  = imem(n_ka + $kndid)
     if cur_idka = intref21 then
       intref11a = fmem(n_ka + $kndud1)
     endif
     n_ka = imem(n_ka)
end_loop
end_if

       vxb = (rat*intref11)+(tar*intref11a)  ; interpolation

;Prob l

intref39=0
intref40=0
intref39=i2b
intref40=j2b

intref12 = 0
if j2b#0 then
intref12 = yvel(intref39,intref40)
else
n_l = imem(str_pnt + $ksnode)
loop while n_l # 0
     cur_idl  = imem(n_l + $kndid)
     if cur_idl = intref39 then
       intref12 = fmem(n_l + $kndud2)
     endif
     n_l = imem(n_l)
end_loop
end_if

intref12a = 0
if intref22#0 then
intref12a = yvel(intref21,intref22)
else
n_la = imem(str_pnt + $ksnode)
loop while n_la # 0
     cur_idla  = imem(n_la + $kndid)
     if cur_idla = intref21 then
       intref12a = fmem(n_la + $kndud2)
     endif
     n_la = imem(n_la)
end_loop
end_if


     vyb = (rat*intref12)+(tar*intref12a)  ;

   end_if
```

```
   if rat2 > 0.0 then          ; Use forward link for second node
     rat = rat2
     tar = 1.0 - rat
     nbl = imem(n2b)
     il  = imem(nbl+$kidi)
     jl  = imem(nbl+$kidj)

;Prob m

intref41=0
intref42=0
intref41=i2b
intref42=j2b

intref13 = 0
if j2b#0 then
intref13 = xvel(intref41,intref42)
else
n_m = imem(str_pnt + $ksnode)
loop while n_m # 0
     cur_idm  = imem(n_m + $kndid)
     if cur_idm = intref41 then
       intref13 = fmem(n_m + $kndud1)
     endif
     n_m = imem(n_m)
end_loop
end_if

intref21a=0
intref22a=0
intref21a=il
intref22a=jl

intref13a = 0
if intref22a#0 then
intref13a = xvel(intref21a,intref22a)
else
n_ma = imem(str_pnt + $ksnode)
loop while n_ma # 0
     cur_idma  = imem(n_ma + $kndid)
     if cur_idma = intref21a then
       intref13a = fmem(n_ma + $kndud1)
     endif
     n_ma = imem(n_ma)
end_loop
end_if


     vxb = (rat*intref13)+(tar*intref13a)  ; interpolation

;Prob n

intref43=0
intref44=0
intref43=i2b
intref44=j2b

intref14 = 0
if j2b#0 then
intref14 = yvel(intref43,intref44)
```

```
else
n_n = imem(str_pnt + $ksnode)
loop while n_n # 0
     cur_idn  = imem(n_n + $kndid)
     if cur_idn = intref43 then
       intref14 = fmem(n_n + $kndud2)
     endif
     n_n = imem(n_n)
end_loop
end_if

intref14a = 0
if intref22a#0 then
intref14a = yvel(intref21a,intref22a)
else
n_na = imem(str_pnt + $ksnode)
loop while n_na # 0
     cur_idna  = imem(n_na + $kndid)
     if cur_idna = intref21a then
       intref14a = fmem(n_na + $kndud2)
     endif
     n_na = imem(n_na)
end_loop
end_if

     vyb = (rat*intref14)+(tar*intref14a)  ;

   end_if

;Prob o

intref23=0
intref24=0
intref23=i2
intref24=j2

intref15 = 0
if intref24#0 then
intref15=xvel(intref23,intref24)
else
n_o = imem(str_pnt + $ksnode)
loop while n_o # 0
     cur_ido  = imem(n_o + $kndid)
     if cur_ido = intref23 then
       intref15 = fmem(n_o + $kndud1)
     endif
     n_o = imem(n_o)
end_loop
end_if

   rvx2 = intref15 - vxb    ; Node 2 Relative Velocity

;Prob P

intref16 = 0
if intref24#0 then
intref16=yvel(intref23,intref24)
else
n_p = imem(str_pnt + $ksnode)
loop while n_p # 0
```

```
      cur_idp  = imem(n_p + $kndid)
      if cur_idp = intref23 then
        intref16 = fmem(n_p + $kndud2)
      endif
      n_p = imem(n_p)
end_loop
end_if

   rvy2 = intref16 - vyb

   ;** First Node Relative Shear Velocity
   usx = -1.0*fmem(n1+$kidun+1)          ; Shear normal vector
   usy = fmem(n1+$kidun)                 ;
   rsv1 = (rvx1*usx) + (rvy1*usy)

   ;** Second Node Relative Shear Velocity
   usx = -1.0*fmem(n2+$kidun+1)
   usy = fmem(n2+$kidun)
   rsv2 = (rvx2*usx) + (rvy2*usy)
;
   if rsv#0.0 then
    signp = rsv/abs(rsv)
   else
    signp = 0.0
   end_if
;;;;;;;;;;;;;Absolute Relative Shear Velocity;;;;;;;;;;;;;;;;;;;;;;;;;;;;;;;;;;;;;;;;
   rsv = abs(rsv1+rsv2)*0.5    ; Absolute Relative Shear Velocity
   rsv2 = (rsv1+rsv2)*0.5      ; Relative Shear Velocity
;;;;;;;;;;;;;;;;;;;;;;;;;;;;;;;;Direction of motion ;;;;;;;;;;;;;;;;;;;;;;;;;;;;;;;;;;;;
   if rsv#0.0 then
    sign = rsv/abs(rsv)  ; sign of the relative velocity
   else
    sign = 0.0
   end_if
;;;;;;;;;;;;;;;;;;;;;;;;;;;;;;;;;;;;relative displacement;;;;;;;;;;;;;;;;;;;;;;;;;;;;;;;;
;

   fmem(ip+$kicext) =fmem(ip+$kicext) +rsv*dytdel  ; comulative displacement
;
   rsd_past = rsd5(aa)                   ; previous step
;
   rsd5(aa) = fmem(ip+$kicext)           ; comulative displacement

;
   rsd = fmem(ip+$kicext)
;
   _rdispc  = rsd_past                   ; reverse loading
;
;;;;;;;;;;;;;;;;;;;;;;;;;;;;equation parameters       ;;;;;;;;;;;;;;;;;;;;;;;;;;;;;;;;;;;;;;;;
;
      _xo   = 12.0         ; displacement at residual
;
      _c = 0.521              ; fitting parameter
;
      _phip = 16.5           ; peak friction angle
;
      _phir = 1.5            ; residual friction angle
;
      _a = 1.0/(_phip)
;
```

```
      _r = _phip/_phir          ; residual friction angle
;
      _d = _a*(_r-1.0);
;
      rsdp = 10.66/1000.0        ; displacement at peak (11mm)
;
;;;;;;;;;;;;;;;;;;;direction 1 ll;;;;;;;;;;;;;;;;;;;;;;;;;;;;;;;;;;;;;;;;;;;;;;

        if _n1#1 then
          _tanphip = tan(_phip*degrad)
        end_if
;
        if _tanphip # 0.0
        _tanphir = tan(_phir*degrad)*_tanphip/abs(_tanphip)   ; _RFF*_tanphip1
        end_if
;
        rsdm = abs(rsd-rsdp)
;
        if rsd >= rsdp then
;
           _n1      = 1
;
         int_fri = 1.0/(_a+_d*((rsdm/_xo)^_c))
;
          int_frip = abs(atan(_tanphip)/degrad)
;
         fmem(ip+$kictph) = tan(int_fri*degrad) ; store friction coefficient
;
       end_if
;
        if (rsd) < rsdp then
;
         int_fri = abs(atan(_tanphip)/degrad)
;
         fmem(ip+$kictph) = tan(int_fri*degrad) ; store friction coefficient
;
       end_if
;
        if (rsd) >= _xo then
;
         int_fri = _phir
;
         fmem(ip+$kictph) = tan(int_fri*degrad) ; store friction coefficient
;
        end_if


      ip=imem(ip)
;
    end_loop
 end_if
end


def check_int
 ip=int_pnt
 loop while ip#0
   inum=imem(ip+$kicid)
   rsd=fmem(ip+$kicext)
   int_fri=fmem(ip+$kicfri)
```

```
  str1=string(inum)
  str2=string(rsd)
  message=out('The shear displacement of interface number '+str1+' is '+str2)
  xtable(out_tab,inum)=inum
  ytable(out_tab,inum)=int_fri
  ip=imem(ip)
 end_loop
end
```

APPENDIX B

GCL SUBROUTINE

```
; ********************************************************************
;                          m_ini.fis
;
; Version F of FISH function to
; (1) set up backbone curve (divide qq into nysf segments); and
; (2) initialize confining pressure, moduli and yield surfaces.
;
; This function is for Version F of Multiple Yield Plasticity Model
; y_myss_f.fis.
; FEATURES: use arrays instead of tables
;
; STARTED:  01/14/98, by L.Y. from y_ini_m.fis
; MODIFIED:
; 01/14/98:
; 06/13/98: ADD $p_min, $y_min, $b_min, $h_min
;
; ********************************************************************
;
;     xtable                ytable
;    --------              --------
; 1   eq(nysf)              qq(nysf)        ;Backbone curve at Pr
; 2              et(nysf)
; 3    l(nysf)              ysr(nysf2)      ;ytable for Values at P
; 4           alpha(nalpha)
;
; Use the following arrays to replace the above tables:
;
; 1   a_eq(nysf)              a_qq(nysf)
; 2   a_et_r(nysf)            a_et(nysf)
; 3                         a_hp(nysf)
; 4   a_ll_r(nysf)            a_sr(nysf2)
; 5                         a_al(nalpha)
;---------------------------------------------------------------------
;
def set_backbone_init
;.....................................................................
;array a_hp(10) a_sr(19) a_al(76) have been defined in y_myss_f.fis
;.....................................................................
;
float  a_eq     a_qq     a_et_r     a_ll_r     a_et
array  a_eq(10)  a_qq(10)  a_et_r(10)  a_ll_r(10)  a_et(10)
;
float  $s_coh  $s_fric  $rf
float  $p_r    $y_r     $b_r  $n_e  $n_b  $n_h
;
float  $p_p  $y_p  $b_p  $g_p   $g_2p  $e_1p  $e_2p
float  $y_i  $g_r  $cphi $sphi  $tphi  $prag1 $prag2
float  $qqf  $eqf  $qqr  $dqq   $g_hp  $xx    $yy    $zz
float  $s_den  $p_min  $y_min  $b_min  $h_min              ; 06/13/98
float  g_value dmin_value                                  ; 06/13/98
float  $_rs $_ss                                  ;M.A
;
int    $nrowb  $nys  $nys2  $nysj  $nalpha
int    ii  ji  k1i   k2i    k3i    k4i  k5i  k6i  k7i
;
  loop ii (1,izones)
    loop ji (1,jzones)
      if int(model(ii,ji)) = 900 then                      ;M.A
;
;.....set up backbone curve at Pr.....
```

```
;
      $s_coh  =  m_coh(ii,ji)
      $s_fric =  m_fric(ii,ji)
      $s_den  = density(ii,ji)                    ;06/13/98
;
      $cphi   = cos($s_fric*degrad)
      $sphi   = sin($s_fric*degrad)
      $tphi   = $sphi/$cphi
;.....................................................................
;For triaxial test, use the following $prag1 & $prag2
;
      $xx    = sqrt(3.0)*(3.0 - $sphi)
      $prag1 = 6.0*$s_coh*$cphi / $xx
      $prag2 = 2.0*$sphi / $xx
            oo = out(' $prag1 = '+string($prag1 ))
            oo = out(' $prag2 = '+string($prag2))
;.....................................................................
;For plane strain condition, use the following $prag1 & $prag2
;
;      $xx    = sqrt(9.0 + 12.0*$tphi*$tphi)
;      $prag1 = 3.0*$s_coh / $xx
;      $prag2 = $tphi / $xx
;.....................................................................
;
      $p_r   = m_pr(ii,ji)
      $y_r   = m_yr(ii,ji)
      $b_r   = m_br(ii,ji)
      $n_e   = m_ne(ii,ji)
      $n_b   = m_nb(ii,ji)
      $n_h   = m_nh(ii,ji)
      $rf    = m_rf(ii,ji)
       $_rss  = m_rss(ii,ji)
       $_ss   = m_ss(ii,ji)
;
      $nrowb  = 4
      $nys   = int(m_nys(ii,ji))
      $nys2  = 2*$nys - 1
      $nysj  = $nys - 1
      $nalpha = $nys2 * $nrowb
;
      $qqf = 2.0*($s_coh*$cphi+$p_r*$sphi)/(1.0-$sphi)
;
      $eqf = 2.8*$qqf / ($y_r*(1.0 - $rf))
;
      $qqr = $rf*$y_r/$qqf
      $dqq = $qqf / float($nysj)
;.....................................................................
;debuging statements.....................................................
;.....................................................................
            oo = out(' y_r = '+string($y_r))
            oo = out(' qqf = '+string($qqf))
            oo = out(' eqf = '+string($eqf))
;.....................................................................
;.....................................................................
;surface nys-1...........................................................
;.....................................................................
      a_eq($nysj) = $eqf                    ; eq(n-1)
      a_qq($nysj) = $qqf                    ; qq(n-1)
;.....................................................................
;surface nys.............................................
```

```
;.....................................................................
      a_eq($nys) = $eqf * $_ss                    ; eq(n) M.A
      a_qq($nys) = $qqf * $_rss                    ; qq(n) M.A
;
a_qq(1) = 140
a_qq(2) = 200
a_qq(3) = 220
a_qq(4) = 230
a_qq(5) = 235
a_qq(6) = 240
a_qq(7) = 260
a_qq(8) = 300
      loop k1i (1,$nysj-1)
        $xx      = float(k1i) * $dqq
;         a_qq(k1i) = $xx
;.....................................................................
;debuging statements.....................................................
;.....................................................................
               oo = out(' (i) = '+string(k1i))
               oo = out(' a_qq(k1i) = '+string(a_qq(k1i)))
;.....................................................................
        a_eq(k1i) = 2.8*$xx / ($y_r - $xx * $qqr)      ; eq(.)
;.....................................................................
;debuging statements.....................................................
;.....................................................................
               oo = out(' a_eq(k1i) = '+string(a_eq(k1i)))
;.....................................................................
      end_loop
;.....................................................................
;debuging statements.....................................................
;.....................................................................
               oo = out(' a_qq(nys-1) = '+string(a_qq($nysj)))
               oo = out(' a_eq(nys-1) = '+string(a_eq($nysj)))
               oo = out(' a_qq(nys) = '+string(a_qq($nys)))
               oo = out(' a_eq(nys) = '+string(a_eq($nys)))
;.....................................................................
;
;.....set material constants.....
;
      $y_i = a_qq(1)/a_eq(1)
;
      $g_r = 3.0*$y_i*$b_r/(9.0*$b_r-$y_i)
;
;.....calculate Et and l of yield surface at Pr.....
;
      a_et_r($nys)  = 0.0                        ;   et(n)
      a_ll_r($nys)  = a_qq($nys) / $qqf           ;M.A
;.....................................................................
;debuging statements.....................................................
;.....................................................................
               oo = out(' a_et_r(nys) = '+string(a_et_r($nys)))
               oo = out(' a_ll_r(nys) = '+string(a_ll_r($nys)))
;.....................................                          ;    l(n)
;
      loop k2i (1,$nysj)
        $xx        = a_eq(k2i+1) - a_eq(k2i)
        $yy        = a_qq(k2i+1) - a_qq(k2i)
        a_et_r(k2i) = $yy / $xx                    ;   et(.)
        a_ll_r(k2i) = a_qq(k2i) / $qqf             ;    l(.)
;.....................................................................
```

```
;debuging statements.....................................................
;.........................................................................
                oo = out(' (i) = '+string(k2i))
                oo = out(' a_et_r(i) = '+string(a_et_r(k2i)))
                oo = out(' a_ll_r(i) = '+string(a_ll_r(k2i)))
;.........................................................................                    ;    l(n)
;
      end_loop
;
;INITIALIZATION: calculate initial modulii and surface radii.....
;
      $p_min = $s_den*g_value*dmin_value              ;06/13/98
      $y_min = $y_i*($p_min/$p_r)^$n_e                ;06/13/98
      $b_min  =$b_r*($p_min/$p_r)^$n_b                ;06/13/98
      $h_min  =     ($p_min/$p_r)^$n_h                ;06/13/98
;
      $p_p =-(sxx(ii,ji)+syy(ii,ji)+szz(ii,ji))/3.0
;
      if $p_p > 0.0 then
        $y_p  = max($y_i*($p_p/$p_r)^$n_e,$y_min)       ;06/13/98
        $b_p  = max($b_r*($p_p/$p_r)^$n_b,$b_min)       ;06/13/98

        $g_p  = 3.0*$y_p*$b_p/(9.0*$b_p-$y_p)
        $g_2p = 2.0 * $g_p
        $e_1p = $b_p + 4.0 * $g_p / 3.0
        $e_2p = $b_p - 2.0 * $g_p / 3.0
;
        loop k3i (1,$nys)
          $xx = a_et_r(k3i)*max(($p_p/$p_r)^$n_h,$h_min) ;06/13/98
          $yy       = 6.0*$prag2*$prag2*a_ll_r(k3i)*a_ll_r(k3i)
          $zz       = sqrt(1.0+$yy)*2.0/3.0
          a_et(k3i) = $xx                         ; Et at P
          a_hp(k3i) = $xx/(1.0-$xx/$y_p)*$zz        ; H' at P
;.........................................................................
;debuging statements.....................................................
;.........................................................................
                oo = out(' i = '+string(k3i))
                oo = out(' Etc = '+string(a_et(k3i)))
                oo = out(' H" = '+string(a_hp(k3i)))
;.........................................................................
        end_loop
;
      else
        nerr  = 170
        error = 1
      end_if
;
;.....calculate initial radii at P.....
;
      $xx = sqrt(2.0)*($prag1+3.0*$prag2*$p_p)
                oo = out(' $xx = '+string($xx))
      loop k4i (1,$nys)
        a_sr(k4i) = $xx*a_ll_r(k4i)               ; ysr(.) at P
;.........................................................................
;debuging statements.....................................................
;.........................................................................
                oo = out(' i = '+string(k4i))
                oo = out(' Radii" = '+string(a_sr(k4i)))
;.........................................................................
      end_loop
```

```
;
;.....calculate virtual radii at P.....
;
      $g_hp       = $g_2p/a_hp(1)                ; 2G/h'
      $xx         = (a_sr(2)-a_sr(1))*(1.0+$g_hp)
      a_sr($nys+1) = a_sr(1) + $xx
;.....................................................................
;debuging statements.....................................................
;.....................................................................
               oo = out(' i = '+string(1))
               oo = out(' Radii V" = '+string(a_sr($nys+1)))
;.....................................................................
;
      if $nys > 2 then
        loop k5i (2,$nysj)
          $g_hp = $g_2p/a_hp(k5i)
          $xx   = a_sr($nys+k5i-1)
          $yy   = (a_sr(k5i+1)-a_sr(k5i))*(1.0+$g_hp)
;.....................................................................
;debuging statements.....................................................
;.....................................................................
          a_sr($nys+k5i) = $xx + $yy              ; vsr(.)
               oo = out(' i = '+string(k5i))
               oo = out(' Radii V" = '+string(a_sr($nys+k5i)))
;.....................................................................
;
        end_loop
      end_if
;
;.....initialize back stresses: put alpha(.) into zero.....
;
      loop k6i (1,$nys2)
        loop k7i (1,$nrowb)
          a_al($nrowb*(k6i-1)+k7i) = 0.0
;.....................................................................
;debuging statements.....................................................
;.....................................................................
               oo = out(' i = '+string(($nrowb*(k6i-1)+k7i)))
               oo = out(' alfa" = '+string(a_al($nrowb*(k6i-1)+k7i)))
;.....................................................................
        end_loop
      end_loop
;
;.....put table values back to state variables.....
;
      m_prag1(ii,ji) = $prag1
      m_prag2(ii,ji) = $prag2
;
         m_pp(ii,ji) = $p_p
          m_y(ii,ji) = $y_p
          m_b(ii,ji) = $b_p
          m_g(ii,ji) = $g_p
         m_g2(ii,ji) = $g_2p
         m_e1(ii,ji) = $e_1p
         m_e2(ii,ji) = $e_2p
;
      case_of $nys
;For nys=2:
        case 2
;
```

```
            m_hp1(ii,ji) = a_hp(1)
            m_hp2(ii,ji) = a_hp(2)
;
            m_yr1(ii,ji) = a_sr(1)
            m_yr2(ii,ji) = a_sr(2)
;
            m_vr1(ii,ji) = a_sr(3)
;
            m_1a11(ii,ji) = a_al(1)
            m_1a22(ii,ji) = a_al(2)
            m_1a33(ii,ji) = a_al(3)
            m_1a12(ii,ji) = a_al(4)
;
            m_2a11(ii,ji) = a_al(5)
            m_2a22(ii,ji) = a_al(6)
            m_2a33(ii,ji) = a_al(7)
            m_2a12(ii,ji) = a_al(8)
;
            m_1v11(ii,ji) = a_al( 9)
            m_1v22(ii,ji) = a_al(10)
            m_1v33(ii,ji) = a_al(11)
            m_1v12(ii,ji) = a_al(12)
;
;For nys=4:
        case 4
;
            m_hp1(ii,ji) = a_hp(1)
            m_hp2(ii,ji) = a_hp(2)
            m_hp3(ii,ji) = a_hp(3)
            m_hp4(ii,ji) = a_hp(4)
;
            m_yr1(ii,ji) = a_sr(1)
            m_yr2(ii,ji) = a_sr(2)
            m_yr3(ii,ji) = a_sr(3)
            m_yr4(ii,ji) = a_sr(4)
;
            m_vr1(ii,ji) = a_sr(5)
            m_vr2(ii,ji) = a_sr(6)
            m_vr3(ii,ji) = a_sr(7)
;
            m_1a11(ii,ji) = a_al(1)
            m_1a22(ii,ji) = a_al(2)
            m_1a33(ii,ji) = a_al(3)
            m_1a12(ii,ji) = a_al(4)
;
            m_2a11(ii,ji) = a_al(5)
            m_2a22(ii,ji) = a_al(6)
            m_2a33(ii,ji) = a_al(7)
            m_2a12(ii,ji) = a_al(8)
;
            m_3a11(ii,ji) = a_al( 9)
            m_3a22(ii,ji) = a_al(10)
            m_3a33(ii,ji) = a_al(11)
            m_3a12(ii,ji) = a_al(12)
;
            m_4a11(ii,ji) = a_al(13)
            m_4a22(ii,ji) = a_al(14)
            m_4a33(ii,ji) = a_al(15)
            m_4a12(ii,ji) = a_al(16)
;
```

```
            m_1v11(ii,ji) = a_al(17)
            m_1v22(ii,ji) = a_al(18)
            m_1v33(ii,ji) = a_al(19)
            m_1v12(ii,ji) = a_al(20)
;
            m_2v11(ii,ji) = a_al(21)
            m_2v22(ii,ji) = a_al(22)
            m_2v33(ii,ji) = a_al(23)
            m_2v12(ii,ji) = a_al(24)
;
            m_3v11(ii,ji) = a_al(25)
            m_3v22(ii,ji) = a_al(26)
            m_3v33(ii,ji) = a_al(27)
            m_3v12(ii,ji) = a_al(28)
;
;For nys=6:
        case 6
;
            m_hp1(ii,ji) = a_hp(1)
            m_hp2(ii,ji) = a_hp(2)
            m_hp3(ii,ji) = a_hp(3)
            m_hp4(ii,ji) = a_hp(4)
            m_hp5(ii,ji) = a_hp(5)
            m_hp6(ii,ji) = a_hp(6)
;
            m_yr1(ii,ji) = a_sr(1)
            m_yr2(ii,ji) = a_sr(2)
            m_yr3(ii,ji) = a_sr(3)
            m_yr4(ii,ji) = a_sr(4)
            m_yr5(ii,ji) = a_sr(5)
            m_yr6(ii,ji) = a_sr(6)
;
            m_vr1(ii,ji) = a_sr( 7)
            m_vr2(ii,ji) = a_sr( 8)
            m_vr3(ii,ji) = a_sr( 9)
            m_vr4(ii,ji) = a_sr(10)
            m_vr5(ii,ji) = a_sr(11)
;
            m_1a11(ii,ji) = a_al(1)
            m_1a22(ii,ji) = a_al(2)
            m_1a33(ii,ji) = a_al(3)
            m_1a12(ii,ji) = a_al(4)
;
            m_2a11(ii,ji) = a_al(5)
            m_2a22(ii,ji) = a_al(6)
            m_2a33(ii,ji) = a_al(7)
            m_2a12(ii,ji) = a_al(8)
;
            m_3a11(ii,ji) = a_al( 9)
            m_3a22(ii,ji) = a_al(10)
            m_3a33(ii,ji) = a_al(11)
            m_3a12(ii,ji) = a_al(12)
;
            m_4a11(ii,ji) = a_al(13)
            m_4a22(ii,ji) = a_al(14)
            m_4a33(ii,ji) = a_al(15)
            m_4a12(ii,ji) = a_al(16)
;
            m_5a11(ii,ji) = a_al(17)
            m_5a22(ii,ji) = a_al(18)
```

```
        m_5a33(ii,ji) = a_al(19)
        m_5a12(ii,ji) = a_al(20)
;
        m_6a11(ii,ji) = a_al(21)
        m_6a22(ii,ji) = a_al(22)
        m_6a33(ii,ji) = a_al(23)
        m_6a12(ii,ji) = a_al(24)
;
        m_1v11(ii,ji) = a_al(25)
        m_1v22(ii,ji) = a_al(26)
        m_1v33(ii,ji) = a_al(27)
        m_1v12(ii,ji) = a_al(28)
;
        m_2v11(ii,ji) = a_al(29)
        m_2v22(ii,ji) = a_al(30)
        m_2v33(ii,ji) = a_al(31)
        m_2v12(ii,ji) = a_al(32)
;
        m_3v11(ii,ji) = a_al(33)
        m_3v22(ii,ji) = a_al(34)
        m_3v33(ii,ji) = a_al(35)
        m_3v12(ii,ji) = a_al(36)
;
        m_4v11(ii,ji) = a_al(37)
        m_4v22(ii,ji) = a_al(38)
        m_4v33(ii,ji) = a_al(39)
        m_4v12(ii,ji) = a_al(40)
;
        m_5v11(ii,ji) = a_al(41)
        m_5v22(ii,ji) = a_al(42)
        m_5v33(ii,ji) = a_al(43)
        m_5v12(ii,ji) = a_al(44)
;
;For nys=8:
      case 8
;
        m_hp1(ii,ji) = a_hp(1)
        m_hp2(ii,ji) = a_hp(2)
        m_hp3(ii,ji) = a_hp(3)
        m_hp4(ii,ji) = a_hp(4)
        m_hp5(ii,ji) = a_hp(5)
        m_hp6(ii,ji) = a_hp(6)
        m_hp7(ii,ji) = a_hp(7)
        m_hp8(ii,ji) = a_hp(8)
;
        m_yr1(ii,ji) = a_sr(1)
        m_yr2(ii,ji) = a_sr(2)
        m_yr3(ii,ji) = a_sr(3)
        m_yr4(ii,ji) = a_sr(4)
        m_yr5(ii,ji) = a_sr(5)
        m_yr6(ii,ji) = a_sr(6)
        m_yr7(ii,ji) = a_sr(7)
        m_yr8(ii,ji) = a_sr(8)
;
        m_vr1(ii,ji) = a_sr( 9)
        m_vr2(ii,ji) = a_sr(10)
        m_vr3(ii,ji) = a_sr(11)
        m_vr4(ii,ji) = a_sr(12)
        m_vr5(ii,ji) = a_sr(13)
        m_vr6(ii,ji) = a_sr(14)
```

```
        m_vr7(ii,ji) = a_sr(15)
;
        m_1a11(ii,ji) = a_al(1)
        m_1a22(ii,ji) = a_al(2)
        m_1a33(ii,ji) = a_al(3)
        m_1a12(ii,ji) = a_al(4)
;
        m_2a11(ii,ji) = a_al(5)
        m_2a22(ii,ji) = a_al(6)
        m_2a33(ii,ji) = a_al(7)
        m_2a12(ii,ji) = a_al(8)

        m_3a11(ii,ji) = a_al( 9)
        m_3a22(ii,ji) = a_al(10)
        m_3a33(ii,ji) = a_al(11)
        m_3a12(ii,ji) = a_al(12)
;
        m_4a11(ii,ji) = a_al(13)
        m_4a22(ii,ji) = a_al(14)
        m_4a33(ii,ji) = a_al(15)
        m_4a12(ii,ji) = a_al(16)
;
        m_5a11(ii,ji) = a_al(17)
        m_5a22(ii,ji) = a_al(18)
        m_5a33(ii,ji) = a_al(19)
        m_5a12(ii,ji) = a_al(20)
;
        m_6a11(ii,ji) = a_al(21)
        m_6a22(ii,ji) = a_al(22)
        m_6a33(ii,ji) = a_al(23)
        m_6a12(ii,ji) = a_al(24)
;
        m_7a11(ii,ji) = a_al(25)
        m_7a22(ii,ji) = a_al(26)
        m_7a33(ii,ji) = a_al(27)
        m_7a12(ii,ji) = a_al(28)
;
        m_8a11(ii,ji) = a_al(29)
        m_8a22(ii,ji) = a_al(30)
        m_8a33(ii,ji) = a_al(31)
        m_8a12(ii,ji) = a_al(32)
;
        m_1v11(ii,ji) = a_al(33)
        m_1v22(ii,ji) = a_al(34)
        m_1v33(ii,ji) = a_al(35)
        m_1v12(ii,ji) = a_al(36)
;
        m_2v11(ii,ji) = a_al(37)
        m_2v22(ii,ji) = a_al(38)
        m_2v33(ii,ji) = a_al(39)
        m_2v12(ii,ji) = a_al(40)
;
        m_3v11(ii,ji) = a_al(41)
        m_3v22(ii,ji) = a_al(42)
        m_3v33(ii,ji) = a_al(43)
        m_3v12(ii,ji) = a_al(44)
;
        m_4v11(ii,ji) = a_al(45)
        m_4v22(ii,ji) = a_al(46)
        m_4v33(ii,ji) = a_al(47)
```

```
        m_4v12(ii,ji) = a_al(48)
;
        m_5v11(ii,ji) = a_al(49)
        m_5v22(ii,ji) = a_al(50)
        m_5v33(ii,ji) = a_al(51)
        m_5v12(ii,ji) = a_al(52)

        m_6v11(ii,ji) = a_al(53)
        m_6v22(ii,ji) = a_al(54)
        m_6v33(ii,ji) = a_al(55)
        m_6v12(ii,ji) = a_al(56)
;
        m_7v11(ii,ji) = a_al(57)
        m_7v22(ii,ji) = a_al(58)
        m_7v33(ii,ji) = a_al(59)
        m_7v12(ii,ji) = a_al(60)
;
;For nys=10:
      case 10
;
        m_hp1(ii, ji) = a_hp( 1)
        m_hp2(ii, ji) = a_hp( 2)
        m_hp3(ii, ji) = a_hp( 3)
        m_hp4(ii, ji) = a_hp( 4)
        m_hp5(ii, ji) = a_hp( 5)
        m_hp6(ii, ji) = a_hp( 6)
        m_hp7(ii, ji) = a_hp( 7)
        m_hp8(ii, ji) = a_hp( 8)
        m_hp9(ii, ji) = a_hp( 9)
        m_hp10(ii,ji) = a_hp(10)
;
        m_yr1(ii, ji) = a_sr( 1)
        m_yr2(ii, ji) = a_sr( 2)
        m_yr3(ii, ji) = a_sr( 3)
        m_yr4(ii, ji) = a_sr( 4)
        m_yr5(ii, ji) = a_sr( 5)
        m_yr6(ii, ji) = a_sr( 6)
        m_yr7(ii, ji) = a_sr( 7)
        m_yr8(ii, ji) = a_sr( 8)
        m_yr9(ii, ji) = a_sr( 9)
        m_yr10(ii,ji) = a_sr(10)
;
        m_vr1(ii,ji) = a_sr(11)
        m_vr2(ii,ji) = a_sr(12)
        m_vr3(ii,ji) = a_sr(13)
        m_vr4(ii,ji) = a_sr(14)
        m_vr5(ii,ji) = a_sr(15)
        m_vr6(ii,ji) = a_sr(16)
        m_vr7(ii,ji) = a_sr(17)
        m_vr8(ii,ji) = a_sr(18)
        m_vr9(ii,ji) = a_sr(19)
;
        m_1a11(ii,ji) = a_al(1)
        m_1a22(ii,ji) = a_al(2)
        m_1a33(ii,ji) = a_al(3)
        m_1a12(ii,ji) = a_al(4)
;
        m_2a11(ii,ji) = a_al(5)
        m_2a22(ii,ji) = a_al(6)
        m_2a33(ii,ji) = a_al(7)
```

```
        m_2a12(ii,ji) = a_al(8)

        m_3a11(ii,ji) = a_al( 9)
        m_3a22(ii,ji) = a_al(10)
        m_3a33(ii,ji) = a_al(11)
        m_3a12(ii,ji) = a_al(12)
;
        m_4a11(ii,ji) = a_al(13)
        m_4a22(ii,ji) = a_al(14)
        m_4a33(ii,ji) = a_al(15)
        m_4a12(ii,ji) = a_al(16)
;
        m_5a11(ii,ji) = a_al(17)
        m_5a22(ii,ji) = a_al(18)
        m_5a33(ii,ji) = a_al(19)
        m_5a12(ii,ji) = a_al(20)
;
        m_6a11(ii,ji) = a_al(21)
        m_6a22(ii,ji) = a_al(22)
        m_6a33(ii,ji) = a_al(23)
        m_6a12(ii,ji) = a_al(24)

        m_7a11(ii,ji) = a_al(25)
        m_7a22(ii,ji) = a_al(26)
        m_7a33(ii,ji) = a_al(27)
        m_7a12(ii,ji) = a_al(28)
;
        m_8a11(ii,ji) = a_al(29)
        m_8a22(ii,ji) = a_al(30)
        m_8a33(ii,ji) = a_al(31)
        m_8a12(ii,ji) = a_al(32)
;
        m_9a11(ii,ji) = a_al(33)
        m_9a22(ii,ji) = a_al(34)
        m_9a33(ii,ji) = a_al(35)
        m_9a12(ii,ji) = a_al(36)
;
        m_10a11(ii,ji) = a_al(37)
        m_10a22(ii,ji) = a_al(38)
        m_10a33(ii,ji) = a_al(39)
        m_10a12(ii,ji) = a_al(40)
;
        m_1v11(ii,ji) = a_al(41)
        m_1v22(ii,ji) = a_al(42)
        m_1v33(ii,ji) = a_al(43)
        m_1v12(ii,ji) = a_al(44)
;
        m_2v11(ii,ji) = a_al(45)
        m_2v22(ii,ji) = a_al(46)
        m_2v33(ii,ji) = a_al(47)
        m_2v12(ii,ji) = a_al(48)
;
        m_3v11(ii,ji) = a_al(49)
        m_3v22(ii,ji) = a_al(50)
        m_3v33(ii,ji) = a_al(51)
        m_3v12(ii,ji) = a_al(52)
;
        m_4v11(ii,ji) = a_al(53)
        m_4v22(ii,ji) = a_al(54)
        m_4v33(ii,ji) = a_al(55)
```

```
          m_4v12(ii,ji) = a_al(56)
;
          m_5v11(ii,ji) = a_al(57)
          m_5v22(ii,ji) = a_al(58)
          m_5v33(ii,ji) = a_al(59)
          m_5v12(ii,ji) = a_al(60)
;
          m_6v11(ii,ji) = a_al(61)
          m_6v22(ii,ji) = a_al(62)
          m_6v33(ii,ji) = a_al(63)
          m_6v12(ii,ji) = a_al(64)
;
          m_7v11(ii,ji) = a_al(65)
          m_7v22(ii,ji) = a_al(66)
          m_7v33(ii,ji) = a_al(67)
          m_7v12(ii,ji) = a_al(68)

          m_8v11(ii,ji) = a_al(69)
          m_8v22(ii,ji) = a_al(70)
          m_8v33(ii,ji) = a_al(71)
          m_8v12(ii,ji) = a_al(72)
;
          m_9v11(ii,ji) = a_al(73)
          m_9v22(ii,ji) = a_al(74)
          m_9v33(ii,ji) = a_al(75)
          m_9v12(ii,ji) = a_al(76)
;
       end_case
;
     end_if
   end_loop
  end_loop
end
set echo on
;opt set_backbone_init
;
;**********************END OF FUCTION*****************************
```

```
; ********************************************************************
;                       y_myss_M.fis
;
; FISH Version F of Multiple Yield Plasticity Model with 2 TO 10
;                       Yield Surfaces
;
; Modification for y_mys_f.fis:  by Liping
; ------------------------------------------------------------------
; STARTED:  03/1/10, by M.A. from y_mys_f.fis
;------------------------------------------------------------------
; 08/06/98: put back stress pressure dependance, alpha*fac
; ------------------------------------------------------------------
; Input Model Parameters:
; (1) m_coh  (2) m_fric (3) m_ten (4) m_rf (5 ) m_nys
; (6) m_pr   (7) m_yr   (8) m_br  (9) m_ne (10) m_nb   (11) m_nh
; ********************************************************************
;             a_hp(nys)    Plastic modulus
;             a_sr(nys2)   radii
;             a_al(nalpha) alfa
;------------------------------------------------------------------
;
set echo off
def y_myss                                  ;M.A y_myss instead of y_mys
  constitutive_model 900                        ; M.A 900 instead of 200
;
  float a_hp     a_sr     a_al     a_sr_l     a_al_l     $sum_al
  array a_hp(10) a_sr(19) a_al(76) a_sr_l(19) a_al_l(76) $sum_al(76)
;
  f_prop  m_coh m_fric m_rf m_nys m_pr m_yr m_br m_ne m_nb m_nh
;
  f_prop  m_ten m_prag1 m_prag2 m_pp m_y m_b m_g m_g2 m_e1 m_e2
;
  f_prop  m_hp1 m_hp2 m_hp3 m_hp4 m_hp5           ;for ytable 3 or a_hp(.)
  f_prop  m_hp6 m_hp7 m_hp8 m_hp9 m_hp10
;
  f_prop  m_rss m_ss                            ;M.A
;
  f_prop  m_yr1 m_yr2 m_yr3 m_yr4 m_yr5         ;for ytable 4 or a_sr(.)
  f_prop  m_yr6 m_yr7 m_yr8 m_yr9 m_yr10
  f_prop  m_vr1 m_vr2 m_vr3 m_vr4 m_vr5
  f_prop  m_vr6 m_vr7 m_vr8 m_vr9
;
  f_prop  m_1a11 m_1a22 m_1a33 m_1a12           ;for ytable 5 or a_al_l(.)
  f_prop  m_2a11 m_2a22 m_2a33 m_2a12
  f_prop  m_3a11 m_3a22 m_3a33 m_3a12
  f_prop  m_4a11 m_4a22 m_4a33 m_4a12
  f_prop  m_5a11 m_5a22 m_5a33 m_5a12
  f_prop  m_6a11 m_6a22 m_6a33 m_6a12
  f_prop  m_7a11 m_7a22 m_7a33 m_7a12
  f_prop  m_8a11 m_8a22 m_8a33 m_8a12
  f_prop  m_9a11 m_9a22 m_9a33 m_9a12
  f_prop  m_10a11 m_10a22 m_10a33 m_10a12
;
  f_prop  m_1v11 m_1v22 m_1v33 m_1v12
  f_prop  m_2v11 m_2v22 m_2v33 m_2v12
  f_prop  m_3v11 m_3v22 m_3v33 m_3v12
  f_prop  m_4v11 m_4v22 m_4v33 m_4v12
  f_prop  m_5v11 m_5v22 m_5v33 m_5v12
  f_prop  m_6v11 m_6v22 m_6v33 m_6v12
  f_prop  m_7v11 m_7v22 m_7v33 m_7v12
```

```
 f_prop  m_8v11 m_8v22 m_8v33 m_8v12
 f_prop  m_9v11 m_9v22 m_9v33 m_9v12
;
 float   $s11i $s22i $s33i $s12i $smi
 float   $s11d $s22d $s33d $s12d $x11i $x22i $x33i $x12i $xim
 float   $xim1 $hp_m1 $g_hp_m1 $temp_2 $temp_3              ;M.A
 float   $temp_4 $temp_5                                    ;M.A
 float  $hp_mj1 $temp_1 $g_hp_mj1 $g_hp_mj $hp_mj          ;M.A
 float   $x11n $x22n $x33n $x12n $amu11 $amu22 $amu33 $amu12
 float   $apex $p_o  $sum_p $sp $am  $alamda $amroz
 float   $g_hp $g_hp_m $hp_m $lcoef $xx $yy $zz $fi $fr $fratio
 float   $hp_mjjj $g_hp_mjjj
;
 int     $nrowb $nys $nys2 $nysj $nalpha $nysm
 int     i1m i2m i3m i4m i5m k1m k2m k3m k4m k5m k6m k7m k8m k9m
 int     kal kal_m kal_p1 kal_m1 kal_p1m kal_m1m
 int     $nbysj1 i6m i7m i8m $nbysj _i8m $_j100 _i9m
;
;*************************************************************************
 CASE_OF  MODE
;*************************************************************************
 CASE 1
; ----------------------
; Initialization section
; ----------------------
;
   $nrowb  = 4
;
;.....set tension to cone apex if larger than apex.....
;
   $apex = m_ten
   if m_prag2 # 0.0 then
     $apex = m_prag1 / (3.0*m_prag2)
   end_if
   m_ten = min($apex, m_ten)
;
;*************************************************************************
 CASE 2
; ---------------
; Running section
; ---------------
;
   zvisc = 1.0
;
   $nys    = int(m_nys)
   $nys2   = 2*$nys  - 1
   $nysj   =   $nys  - 1
   $nalpha =   $nys2 * $nrowb
;
;.....put state variables into tables.....
;
   Case_of $nys
;
;For nys = 2:
     case 2
;
       a_hp(1) = m_hp1
       a_hp(2) = m_hp2
;
       a_sr(1) = m_yr1
```

```
        a_sr(2) = m_yr2
;
        a_sr(3) = m_vr1
;
        a_al(1) = m_1a11
        a_al(2) = m_1a22
        a_al(3) = m_1a33
        a_al(4) = m_1a12
;
        a_al(5) = m_2a11
        a_al(6) = m_2a22
        a_al(7) = m_2a33
        a_al(8) = m_2a12
;
        a_al( 9) = m_1v11
        a_al(10) = m_1v22
        a_al(11) = m_1v33
        a_al(12) = m_1v12
;
;For nys = 4:
     Case 4
;
        a_hp(1) = m_hp1
        a_hp(2) = m_hp2
        a_hp(3) = m_hp3
        a_hp(4) = m_hp4
;
        a_sr(1) = m_yr1
        a_sr(2) = m_yr2
        a_sr(3) = m_yr3
        a_sr(4) = m_yr4
;
        a_sr(5) = m_vr1
        a_sr(6) = m_vr2
        a_sr(7) = m_vr3
;
        a_al(1) = m_1a11
        a_al(2) = m_1a22
        a_al(3) = m_1a33
        a_al(4) = m_1a12
;
        a_al(5) = m_2a11
        a_al(6) = m_2a22
        a_al(7) = m_2a33
        a_al(8) = m_2a12
;
        a_al( 9) = m_3a11
        a_al(10) = m_3a22
        a_al(11) = m_3a33
        a_al(12) = m_3a12
;
        a_al(13) = m_4a11
        a_al(14) = m_4a22
        a_al(15) = m_4a33
        a_al(16) = m_4a12
;
        a_al(17) = m_1v11
        a_al(18) = m_1v22
        a_al(19) = m_1v33
        a_al(20) = m_1v12
```

```
      a_al(21) = m_2v11
      a_al(22) = m_2v22
      a_al(23) = m_2v33
      a_al(24) = m_2v12
;
      a_al(25) = m_3v11
      a_al(26) = m_3v22
      a_al(27) = m_3v33
      a_al(28) = m_3v12
;
;For nys = 6:
    Case 6
;
      a_hp(1) = m_hp1
      a_hp(2) = m_hp2
      a_hp(3) = m_hp3
      a_hp(4) = m_hp4
      a_hp(5) = m_hp5
      a_hp(6) = m_hp6
;
      a_sr(1) = m_yr1
      a_sr(2) = m_yr2
      a_sr(3) = m_yr3
      a_sr(4) = m_yr4
      a_sr(5) = m_yr5
      a_sr(6) = m_yr6
;
      a_sr( 7) = m_vr1
      a_sr( 8) = m_vr2
      a_sr( 9) = m_vr3
      a_sr(10) = m_vr4
      a_sr(11) = m_vr5
;
      a_al(1) = m_1a11
      a_al(2) = m_1a22
      a_al(3) = m_1a33
      a_al(4) = m_1a12
;
      a_al(5) = m_2a11
      a_al(6) = m_2a22
      a_al(7) = m_2a33
      a_al(8) = m_2a12
;
      a_al( 9) = m_3a11
      a_al(10) = m_3a22
      a_al(11) = m_3a33
      a_al(12) = m_3a12
;
      a_al(13) = m_4a11
      a_al(14) = m_4a22
      a_al(15) = m_4a33
      a_al(16) = m_4a12
;
      a_al(17) = m_5a11
      a_al(18) = m_5a22
      a_al(19) = m_5a33
      a_al(20) = m_5a12
;
      a_al(21) = m_6a11
```

```
        a_al(22) = m_6a22
        a_al(23) = m_6a33
        a_al(24) = m_6a12
;
        a_al(25) = m_1v11
        a_al(26) = m_1v22
        a_al(27) = m_1v33
        a_al(28) = m_1v12
;
        a_al(29) = m_2v11
        a_al(30) = m_2v22
        a_al(31) = m_2v33
        a_al(32) = m_2v12
;
        a_al(33) = m_3v11
        a_al(34) = m_3v22
        a_al(35) = m_3v33
        a_al(36) = m_3v12
;
        a_al(37) = m_4v11
        a_al(38) = m_4v22
        a_al(39) = m_4v33
        a_al(40) = m_4v12
;
        a_al(41) = m_5v11
        a_al(42) = m_5v22
        a_al(43) = m_5v33
        a_al(44) = m_5v12
;
;For nys = 8:
    Case 8
;
        a_hp(1) = m_hp1
        a_hp(2) = m_hp2
        a_hp(3) = m_hp3
        a_hp(4) = m_hp4
        a_hp(5) = m_hp5
        a_hp(6) = m_hp6
        a_hp(7) = m_hp7
        a_hp(8) = m_hp8
;
        a_sr(1) = m_yr1
        a_sr(2) = m_yr2
        a_sr(3) = m_yr3
        a_sr(4) = m_yr4
        a_sr(5) = m_yr5
        a_sr(6) = m_yr6
        a_sr(7) = m_yr7
        a_sr(8) = m_yr8
;
        a_sr( 9) = m_vr1
        a_sr(10) = m_vr2
        a_sr(11) = m_vr3
        a_sr(12) = m_vr4
        a_sr(13) = m_vr5
        a_sr(14) = m_vr6
        a_sr(15) = m_vr7
;
        a_al(1) = m_1a11
        a_al(2) = m_1a22
```

```
      a_al(3) = m_1a33
      a_al(4) = m_1a12
;
      a_al(5) = m_2a11
      a_al(6) = m_2a22
      a_al(7) = m_2a33
      a_al(8) = m_2a12
;
      a_al( 9) = m_3a11
      a_al(10) = m_3a22
      a_al(11) = m_3a33
      a_al(12) = m_3a12
;
      a_al(13) = m_4a11
      a_al(14) = m_4a22
      a_al(15) = m_4a33
      a_al(16) = m_4a12
;
      a_al(17) = m_5a11
      a_al(18) = m_5a22
      a_al(19) = m_5a33
      a_al(20) = m_5a12
;
      a_al(21) = m_6a11
      a_al(22) = m_6a22
      a_al(23) = m_6a33
      a_al(24) = m_6a12
;
      a_al(25) = m_7a11
      a_al(26) = m_7a22
      a_al(27) = m_7a33
      a_al(28) = m_7a12
;
      a_al(29) = m_8a11
      a_al(30) = m_8a22
      a_al(31) = m_8a33
      a_al(32) = m_8a12
;
      a_al(33) = m_1v11
      a_al(34) = m_1v22
      a_al(35) = m_1v33
      a_al(36) = m_1v12

      a_al(37) = m_2v11
      a_al(38) = m_2v22
      a_al(39) = m_2v33
      a_al(40) = m_2v12
;
      a_al(41) = m_3v11
      a_al(42) = m_3v22
      a_al(43) = m_3v33
      a_al(44) = m_3v12
;
      a_al(45) = m_4v11
      a_al(46) = m_4v22
      a_al(47) = m_4v33
      a_al(48) = m_4v12
;
      a_al(49) = m_5v11
      a_al(50) = m_5v22
```

```
        a_al(51) = m_5v33
        a_al(52) = m_5v12
;
        a_al(53) = m_6v11
        a_al(54) = m_6v22
        a_al(55) = m_6v33
        a_al(56) = m_6v12
;
        a_al(57) = m_7v11
        a_al(58) = m_7v22
        a_al(59) = m_7v33
        a_al(60) = m_7v12
;
;For nys = 10:
    Case 10
;
        a_hp( 1) = m_hp1
        a_hp( 2) = m_hp2
        a_hp( 3) = m_hp3
        a_hp( 4) = m_hp4
        a_hp( 5) = m_hp5
        a_hp( 6) = m_hp6
        a_hp( 7) = m_hp7
        a_hp( 8) = m_hp8
        a_hp( 9) = m_hp9
        a_hp(10) = m_hp10
;
        a_sr( 1) = m_yr1
        a_sr( 2) = m_yr2
        a_sr( 3) = m_yr3
        a_sr( 4) = m_yr4
        a_sr( 5) = m_yr5
        a_sr( 6) = m_yr6
        a_sr( 7) = m_yr7
        a_sr( 8) = m_yr8
        a_sr( 9) = m_yr9
        a_sr(10) = m_yr10
;
        a_sr(11) = m_vr1
        a_sr(12) = m_vr2
        a_sr(13) = m_vr3
        a_sr(14) = m_vr4
        a_sr(15) = m_vr5
        a_sr(16) = m_vr6
        a_sr(17) = m_vr7
        a_sr(18) = m_vr8
        a_sr(19) = m_vr9
;
        a_al(1) = m_1a11
        a_al(2) = m_1a22
        a_al(3) = m_1a33
        a_al(4) = m_1a12
;
        a_al(5) = m_2a11
        a_al(6) = m_2a22
        a_al(7) = m_2a33
        a_al(8) = m_2a12
;
        a_al( 9) = m_3a11
        a_al(10) = m_3a22
```

```
      a_al(11) = m_3a33
      a_al(12) = m_3a12
;
      a_al(13) = m_4a11
      a_al(14) = m_4a22
      a_al(15) = m_4a33
      a_al(16) = m_4a12
;
      a_al(17) = m_5a11
      a_al(18) = m_5a22
      a_al(19) = m_5a33
      a_al(20) = m_5a12
;
      a_al(21) = m_6a11
      a_al(22) = m_6a22
      a_al(23) = m_6a33
      a_al(24) = m_6a12
;
      a_al(25) = m_7a11
      a_al(26) = m_7a22
      a_al(27) = m_7a33
      a_al(28) = m_7a12
;
      a_al(29) = m_8a11
      a_al(30) = m_8a22
      a_al(31) = m_8a33
      a_al(32) = m_8a12
;
      a_al(33) = m_9a11
      a_al(34) = m_9a22
      a_al(35) = m_9a33
      a_al(36) = m_9a12
;
      a_al(37) = m_10a11
      a_al(38) = m_10a22
      a_al(39) = m_10a33
      a_al(40) = m_10a12
;
      a_al(41) = m_1v11
      a_al(42) = m_1v22
      a_al(43) = m_1v33
      a_al(44) = m_1v12

      a_al(45) = m_2v11
      a_al(46) = m_2v22
      a_al(47) = m_2v33
      a_al(48) = m_2v12
;
      a_al(49) = m_3v11
      a_al(50) = m_3v22
      a_al(51) = m_3v33
      a_al(52) = m_3v12
;
      a_al(53) = m_4v11
      a_al(54) = m_4v22
      a_al(55) = m_4v33
      a_al(56) = m_4v12
;
      a_al(57) = m_5v11
      a_al(58) = m_5v22
```

```
      a_al(59) = m_5v33
      a_al(60) = m_5v12
;
      a_al(61) = m_6v11
      a_al(62) = m_6v22
      a_al(63) = m_6v33
      a_al(64) = m_6v12
;
      a_al(65) = m_7v11
      a_al(66) = m_7v22
      a_al(67) = m_7v33
      a_al(68) = m_7v12
;
      a_al(69) = m_8v11
      a_al(70) = m_8v22
      a_al(71) = m_8v33
      a_al(72) = m_8v12
;
      a_al(73) = m_9v11
      a_al(74) = m_9v22
      a_al(75) = m_9v33
      a_al(76) = m_9v12
;
   End_case
;.....................................................................
;STEP 1: get new trial stresses from old, assuming elastic increments..
;
   $s11i = zs11 + zde11 * m_e1 + (zde22 + zde33) * m_e2
   $s22i = zs22 + zde22 * m_e1 + (zde33 + zde11) * m_e2
   $s33i = zs33 + zde33 * m_e1 + (zde11 + zde22) * m_e2
   $s12i = zs12 + zde12 * m_g2
;
;.....mean normal trial stress.....
;
   $smi = ($s11i + $s22i + $s33i) / 3.0
;
;.....update stresses for plastic process.....
;.....................................................................
;STEP 2: check for isotropic extension.....
;
   if $smi > m_ten then
     $s11i = $s11i - ($smi-m_ten) - 1.0e-12          ;10/07/97
     $s22i = $s22i - ($smi-m_ten) - 1.0e-12
     $s33i = $s33i - ($smi-m_ten) - 1.0e-12
     $smi  = m_ten - 1.0e-12                        ;10/07/97
   end_if
;
;.....deviatoric trial stresses.....
;
   $s11d = $s11i - $smi
   $s22d = $s22i - $smi
   $s33d = $s33i - $smi
   $s12d = $s12i
;.....................................................................
;STEP 3: calculate radii at current pressure.....
;(yield surfaces correction for pressure dependancy)  ;12/28/97
;
   $fi = m_prag1 - 3.0*$smi*m_prag2
   $fr = m_prag1 + 3.0*m_pp*m_prag2
;
```

```
   $fratio = $fi/$fr
;
   loop k7m (1,$nys2)
    a_sr_l(k7m) = a_sr(k7m)*$fratio                ; ysr(.) at P
   end_loop
;
;.....put back stresses into a localized array.....
   loop k8m (1,$nys2)
    loop k9m (1,$nrowb)
      kal_m1        = $nrowb*(k8m-1)+k9m
      a_al_l(kal_m1) = a_al(kal_m1)*$fratio    ;08/06/98, alpha(.) at P!!
    end_loop
   end_loop
;.....................................................................
;STEP 4: calculate trial xi stresses w.r. to the 1st Y.S.....
;
   $x11i = $s11d - a_al_l(1)
   $x22i = $s22d - a_al_l(2)
   $x33i = $s33d - a_al_l(3)
   $x12i = $s12d - a_al_l(4)
;
   $xim  = $x11i*$x11i+$x22i*$x22i+$x33i*$x33i+2.0*$x12i*$x12i
   $xim  = sqrt($xim)
;
;.....check if elastic process really occurs.....
;---------------------------------------------------------------------
   Section
    if $xim <= a_sr_l(1) then
; --- no failure, elastic process---
      zs11 = $s11i
      zs22 = $s22i
      zs33 = $s33i
      zs12 = $s12i
;
      exit section
    end_if
;.....................................................................
;STEP 5: loop over V.S. to find the active Y.S.....
;
    $nysm = 1
;
    loop k2m (1,$nysj)
;
;..... calculate xi, xi dev. and norm, w.r. to V.S.'s
;
      kal_m1 = $nrowb*($nys+k2m-1)
;
      $x11i = $s11d - a_al_l(kal_m1+1)
      $x22i = $s22d - a_al_l(kal_m1+2)
      $x33i = $s33d - a_al_l(kal_m1+3)
      $x12i = $s12d - a_al_l(kal_m1+4)
;
      $xim = $x11i*$x11i+$x22i*$x22i+$x33i*$x33i+2.0*$x12i*$x12i
      $xim = sqrt($xim)
;
;.....check which yield surface is active.....
;
      if $xim >= a_sr_l($nys+k2m) then
        $nysm = k2m + 1
      end_if
```

```
;
    end_loop

;STEP 6: calculate xi stresses and unit normal for the active Y.S.....
;
    kal_m1m = $nrowb*($nysm-1)
;
    $x11i = $s11d - a_al_l(kal_m1m+1)
    $x22i = $s22d - a_al_l(kal_m1m+2)
    $x33i = $s33d - a_al_l(kal_m1m+3)
    $x12i = $s12d - a_al_l(kal_m1m+4)
;
    $xim = $x11i*$x11i+$x22i*$x22i+$x33i*$x33i+2.0*$x12i*$x12i
    $xim = sqrt($xim)
;
    $x11n = $x11i / $xim
    $x22n = $x22i / $xim
    $x33n = $x33i / $xim
    $x12n = $x12i / $xim
;.....
;STEP 7: perform the intermediate stress update
;
;.....loop over inner Y.S., update trial stresses & outer V.S.'s...
;
;
    if $nysm > 1 then
;
      loop i1m (1,$nysm-1)
;
;.....calculate mu.....
;
        kal    =  $nrowb*i1m
        kal_m1 =  $nrowb*(i1m-1)
;
        $xx    = a_al_l(kal+1)    + $x11n*a_sr_l(i1m+1)
        $yy    = a_al_l(kal_m1+1) + $x11n*a_sr_l(i1m)
        $amu11 = $xx - $yy
;
        $xx    = a_al_l(kal+2)    + $x22n*a_sr_l(i1m+1)
        $yy    = a_al_l(kal_m1+2) + $x22n*a_sr_l(i1m)
        $amu22 = $xx - $yy
;
        $xx    = a_al_l(kal+3)    + $x33n*a_sr_l(i1m+1)
        $yy    = a_al_l(kal_m1+3) + $x33n*a_sr_l(i1m)
        $amu33 = $xx - $yy
;
        $xx    = a_al_l(kal+4)    + $x12n*a_sr_l(i1m+1)
        $yy    = a_al_l(kal_m1+4) + $x12n*a_sr_l(i1m)
        $amu12 = $xx - $yy
;
;.....intermediate update of trial stresses.....
;
        $g_hp = m_g2/a_hp(i1m)
;
        $am = $amu11*$x11n+$amu22*$x22n+$amu33*$x33n+2.0*$amu12*$x12n
        $am = $g_hp*$am
;
        $s11i = $s11i - $am*$x11n
        $s22i = $s22i - $am*$x22n
        $s33i = $s33i - $am*$x33n
```

```
        $s12i = $s12i - $am*$x12n
;
;.....intermediate update of outer V. S.'s.....
;
        if $nysm < $nysj then
          loop k3m ($nysm, $nysj-1)
            kal_m1 = $nrowb*($nys+k3m-1)
;
            a_al_l(kal_m1+1) = a_al_l(kal_m1+1) - $g_hp*$amu11
            a_al_l(kal_m1+2) = a_al_l(kal_m1+2) - $g_hp*$amu22
            a_al_l(kal_m1+3) = a_al_l(kal_m1+3) - $g_hp*$amu33
            a_al_l(kal_m1+4) = a_al_l(kal_m1+4) - $g_hp*$amu12
;
          end_loop
        end_if
;
      end_loop
;
    end_if
;.....
;STEP 8: final update of active Y.S. & outer V.S.'s.....
;
;.....mean normal trial stress.....
;
;     $smi = ($s11i + $s22i + $s33i) / 3.0
;
;.....deviatoric stress.....
;
    $s11d = $s11i - $smi
    $s22d = $s22i - $smi
    $s33d = $s33i - $smi
    $s12d = $s12i

;.....calculate lambda.....
;
    kal_m1m = $nrowb*($nysm-1)
;
    $x11i = $s11d - a_al_l(kal_m1m+1)
    $x22i = $s22d - a_al_l(kal_m1m+2)
    $x33i = $s33d - a_al_l(kal_m1m+3)
    $x12i = $s12d - a_al_l(kal_m1m+4)
;
    $xim = $x11i*$x11i+$x22i*$x22i+$x33i*$x33i+2.0*$x12i*$x12i
    $xim = sqrt($xim)
;
    $hp_m = a_hp($nysm)
;
    if $nysm = $nys then
      $g_hp_m = 0.0
    else
      $g_hp_m = m_g2/$hp_m
    end_if
;
    $lcoef = 1.0/(m_g2+$hp_m)
;
    $alamda = $lcoef*($xim-a_sr_l($nysm))
;.....
;.....
;
;STEP 8.2: one of the inner surfaces is active
```

```
;
   if $nysm < $nysj then                ;M.A
;
      kal_m = $nrowb*$nysm
;
      $xx = a_al_l(kal_m  +1) + $x11n*a_sr_l($nysm+1)
      $yy = a_al_l(kal_m1m+1) + $x11n*a_sr_l($nysm)
      $amu11 = $xx - $yy
      $xx = a_al_l(kal_m  +2) + $x22n*a_sr_l($nysm+1)
      $yy = a_al_l(kal_m1m+2) + $x22n*a_sr_l($nysm)
      $amu22 = $xx - $yy
      $xx = a_al_l(kal_m  +3) + $x33n*a_sr_l($nysm+1)
      $yy = a_al_l(kal_m1m+3) + $x33n*a_sr_l($nysm)
      $amu33 = $xx - $yy
      $xx = a_al_l(kal_m  +4) + $x12n*a_sr_l($nysm+1)
      $yy = a_al_l(kal_m1m+4) + $x12n*a_sr_l($nysm)
      $amu12 = $xx - $yy
;
      $xim = $x11n*$amu11+$x22n*$amu22+$x33n*$amu33
      $xim = $xim + 2.0*$x12n*$amu12
;
      $amroz  = $hp_m*$alamda/$xim
;
;.....update active back stress of the active surface
;
      a_al_l(kal_m1m+1) = a_al_l(kal_m1m+1) + $amroz*$amu11
      a_al_l(kal_m1m+2) = a_al_l(kal_m1m+2) + $amroz*$amu22
      a_al_l(kal_m1m+3) = a_al_l(kal_m1m+3) + $amroz*$amu33
      a_al_l(kal_m1m+4) = a_al_l(kal_m1m+4) + $amroz*$amu12
;
;.....update active back stress of the outer V.S.'s
;
      loop k4m ($nysm,$nysj)
        kal_m1 = $nrowb*($nys+k4m-1)
;
        a_al_l(kal_m1+1)=a_al_l(kal_m1+1)-$g_hp_m*$amroz*$amu11
        a_al_l(kal_m1+2)=a_al_l(kal_m1+2)-$g_hp_m*$amroz*$amu22
        a_al_l(kal_m1+3)=a_al_l(kal_m1+3)-$g_hp_m*$amroz*$amu33
        a_al_l(kal_m1+4)=a_al_l(kal_m1+4)-$g_hp_m*$amroz*$amu12
;
      end_loop
;
;STEP 8.2.1: update unit normal for the active Y.S.....
;
      $x11n = $s11d - a_al_l(kal_m1m+1)
      $x22n = $s22d - a_al_l(kal_m1m+2)
      $x33n = $s33d - a_al_l(kal_m1m+3)
      $x12n = $s12d - a_al_l(kal_m1m+4)
;
      $xim = $x11n*$x11n+$x22n*$x22n+$x33n*$x33n
      $xim = $xim + 2.0*$x12n*$x12n
      $xim = sqrt($xim)
;
      $x11n = $x11n / $xim
      $x22n = $x22n / $xim
      $x33n = $x33n / $xim
      $x12n = $x12n / $xim
;STEP 9: final update of trial stresses.....
;
      zs11 = a_al_l(kal_m1m+1) + a_sr_l($nysm)*$x11n + $smi
```

```
      zs22 = a_al_l(kal_m1m+2) + a_sr_l($nysm)*$x22n + $smi
      zs33 = a_al_l(kal_m1m+3) + a_sr_l($nysm)*$x33n + $smi
      zs12 = a_al_l(kal_m1m+4) + a_sr_l($nysm)*$x12n

    end_if


;.....................................................................
;STEP 5-1: the softening surface is active, i.e., m = nys-1                ; by M.A 03/17/10
;.....................................................................
;
if  $nysm = $nysj then
;.....................................................................
;STEP 5-1.3: ;..Update the radius of the active yield surface update the stress....      ; by M.A 03/17/10
;.....................................................................
;
   a_sr_l($nysm) = a_sr_l($nysm) + $hp_m * $alamda

;STEP 9: final update of trial stresses.....
;
   if a_sr_l($nysm) <= a_sr_l($nys) then
            a_sr_l($nysm) = a_sr_l($nys)
            $nysm = $nys
   end_if
;
   if  $nysm = $nysj then
     zs11 =  a_sr_l($nysm)*$x11n + $smi
     zs22 =  a_sr_l($nysm)*$x22n + $smi
     zs33 =  a_sr_l($nysm)*$x33n + $smi
     zs12 =  a_sr_l($nysm)*$x12n
;
;.....................................................................
;STEP 5-1.5: ;..; search for the biggest yeidl surface j, such that Rj< Rm          ; by M.A 03/17/10
;.....................................        ; update the radius MA
;
            loop i6m (1,$nysm-1)
              if a_sr_l(i6m) < a_sr_l($nysm) then
          $nbysj1 = i6m
               end_if
             end_loop
;
;
;.....................................................................
;STEP 5-1.6: ;..; Update virtuial radius coressponding to yield surface $nbysj1....        ; by M.A 03/17/10
;.....................................        ; update the radius MA
;
            if $nbysj1 = 1 then
;
                  $hp_m1   = a_hp(1)
                  $g_hp_m1 = m_g2/$hp_m1
;
                  $temp_2 = ( a_sr_l($nysm) - a_sr_l(1) )*(1.0+$g_hp_m1)
                  a_sr_l($nbysj1+$nys) = a_sr_l(1) + $temp_2
            else
                  $hp_mj1   = a_hp($nbysj1)
                  $g_hp_mj1 = m_g2/$hp_mj1
;
                  $temp_1   = (a_sr_l($nysm)-a_sr_l($nbysj1))*(1.0+$g_hp_mj1)
                  a_sr_l($nbysj1+$nys) = a_sr_l($nbysj1+$nys-1) + $temp_1
;
```

```
            end_if
;.....
;STEP 5-1.7: Collapse all yield surfaces that are bigger than the active one   ....      ; by M.A 03/17/10
;.....        ; update the radius MA
;
            if $nbysj1 < $nysm-1 then
;
                loop i7m ($nbysj1+1 , $nysm-1)
                  a_sr_l(i7m) = a_sr_l($nysj)
                  a_sr_l(i7m+$nys) = a_sr_l($nbysj1+$nys)
            end_loop
;
            end_if
;
;.....
;STEP 5-1.8: Update the virtuial surface nys -1                    ....      ; by M.A 03/17/10
;.....
;
            $temp_3 = (a_sr_l($nysm+1)-a_sr_l($nysm))*(1.0+$g_hp_m)                ;M.A
            a_sr_l($nysm+$nys) = a_sr_l($nysm+$nys-1) + $temp_3
;

    end_if
end_if
;.....
;STEP 5-2.: the outer most surface is active, i.e., m = nys              .....          ; by M.A 03/17/10
;.....
;
            if $nysm = $nys then
;.....
;STEP 5-2.2: final update of trial stresses                        .....      ; by M.A 03/17/10
;.....
;
                zs11 = a_sr_l($nysm)*$x11n + $smi
                zs22 = a_sr_l($nysm)*$x22n + $smi
                zs33 = a_sr_l($nysm)*$x33n + $smi
                zs12 = a_sr_l($nysm)*$x12n
;
;.....
;STEP 5-2.3: search for the biggest yeidl surface j, such that Rj< Rm              ; by M.A 03/17/10
;.....
;
                loop _i8m (1,$nysj)
;
                    if a_sr_l(_i8m) < a_sr_l($nys) then
;
                        $_j100 = _i8m
;
                     end_if
                end_loop
;.....
;STEP 5-2.4: Update last virtuial surface                    .....      ; by M.A 03/17/10
;.....
;
                if $_j100 = 1 then
;
                    $hp_m1 = a_hp(1)
;
                    $g_hp_m1 = m_g2/$hp_m1
;
```

```
                        $temp_4 = (a_sr_l($nysm)-a_sr_l(1))*(1.0+$g_hp_m1)
;
                        a_sr_l($_j100+$nys) = a_sr_l(1) + $temp_4
;
                    else
                        $hp_mjjj = a_hp($_j100)
;
                        $g_hp_mjjj = m_g2/$hp_mjjj
;
                        $temp_5 = (a_sr_l($nysm)-a_sr_l($_j100))*(1.0+$g_hp_mjjj)
;
                        a_sr_l($_j100+$nys) = a_sr_l($_j100+$nys-1) + $temp_5
;
                    end_if
;.....................................................................
;STEP 5-2.4: Collapse all yield surfaces that are bigger than the active one   ....  .        ; by M.A 03/17/10
;.....................................................................
;
                    loop _i9m ($_j100+1,$nys-1)
;
                        a_sr_l(_i9m) = a_sr_l($nys)
;
                        a_sr_l(_i9m +$nys) = a_sr_l($_j100+$nys)
                    end_loop
                end_if
;
;
;.....................................................................
;.....................................................................
;
;
;.....calculate active back stresses evolution.....
;
;STEP 10: update back stresses for inner Y. and V. surfaces .....
;
    if $nysm > 1 then
      loop i5m (1,$nysm-1)
        $xx = a_sr_l($nysm)   -a_sr_l(i5m)
        $yy = a_sr_l($nys+i5m)-a_sr_l($nysm)
;
        kal_m1 = $nrowb*(i5m-1)
        kal_p1 = $nrowb*(i5m-1+$nys)
;
        a_al_l(kal_m1+1) = a_al_l(kal_m1m+1) + $xx*$x11n
        a_al_l(kal_p1+1) = a_al_l(kal_m1m+1) - $yy*$x11n
;
        a_al_l(kal_m1+2) = a_al_l(kal_m1m+2) + $xx*$x22n
        a_al_l(kal_p1+2) = a_al_l(kal_m1m+2) - $yy*$x22n
;
        a_al_l(kal_m1+3) = a_al_l(kal_m1m+3) + $xx*$x33n
        a_al_l(kal_p1+3) = a_al_l(kal_m1m+3) - $yy*$x33n
;
        a_al_l(kal_m1+4) = a_al_l(kal_m1m+4) + $xx*$x12n
        a_al_l(kal_p1+4) = a_al_l(kal_m1m+4) - $yy*$x12n
;
      end_loop
;
 end_if
;
;.....end of plastic correction
```

```
;
    if $nysm = $nys then        ;add on 05/10/97
      zvisc = 0.0
    end_if                      ;add on 05/10/97
;
   End_section
;---------------------------------------------------------------------
;STEP 11: update zone parameters:
;
;.....calculate new average confining pressure.....
;
   $sp    =-(zs11 + zs22 + zs33) / 3.0
   $sum_p = $sum_p + $sp
;
;    loop k8m (1,$nys2)
;      loop k9m (1,$nrowb)
;        kal          = $nrowb*(k8m-1) + k9m
;        $sum_al(kal) = $sum_al(kal)   + a_al_l(kal)
;      end_loop
;    end_loop
;
   if zsub > 0.0 then
    $p_o = m_pp
    m_pp  = $sum_p  / zsub
;
;.....calculate radii at new average confining pressure.....
;
    $fi = m_prag1 + 3.0*m_pp*m_prag2
    $fr = m_prag1 + 3.0*$p_o*m_prag2
;
    loop k7m (1,$nys2)
      a_sr_l(k7m) = a_sr_l(k7m)/$fratio                ; ysr(.) at P
    end_loop
;
    $fratio = $fi/$fr
;
    loop k7m (1,$nys2)
      a_sr_l(k7m) = a_sr_l(k7m)*$fratio                ; ysr(.) at P
    end_loop
      a_sr ($nys) = a_sr ($nys)*$fratio
;
;.....calculate average back stresses.....      ;12/29/97:
;
;      loop k8m (1,$nys2)
;        loop k9m (1,$nrowb)
;          kal       = $nrowb*(k8m-1) + k9m
;          a_al(kal) = $sum_al(kal) / zsub
;        end_loop
;      end_loop

;---------------------------------------------------------------------
;.....reset for next zone.....
;
    $sum_p   = 0.0
;
;      loop k8m (1,$nys2)
;        loop k9m (1,$nrowb)
;          kal          = $nrowb*(k8m-1) + k9m
;          $sum_al(kal) = 0.0
;        end_loop
```

```
;      end_loop
;
;.....put table values back to model properties and state variables.....
;
     Case_of $nys
;
;For nys=2:
       Case 2
;
         m_yr1 = a_sr_l(1)
         m_yr2 = a_sr(2)
;
         m_vr1 = a_sr_l(3)
;
         m_1a11 = a_al_l(1)
         m_1a22 = a_al_l(2)
         m_1a33 = a_al_l(3)
         m_1a12 = a_al_l(4)
;
         m_2a11 = a_al_l(5)
         m_2a22 = a_al_l(6)
         m_2a33 = a_al_l(7)
         m_2a12 = a_al_l(8)
;
         m_1v11 = a_al_l( 9)
         m_1v22 = a_al_l(10)
         m_1v33 = a_al_l(11)
         m_1v12 = a_al_l(12)
;
;For nys=4:
       Case 4
;
         m_yr1 = a_sr_l(1)
         m_yr2 = a_sr_l(2)
         m_yr3 = a_sr_l(3)
         m_yr4 = a_sr(4)
;
         m_vr1 = a_sr_l(5)
         m_vr2 = a_sr_l(6)
         m_vr3 = a_sr_l(7)
;
         m_1a11 = a_al_l(1)
         m_1a22 = a_al_l(2)
         m_1a33 = a_al_l(3)
         m_1a12 = a_al_l(4)
;
         m_2a11 = a_al_l(5)
         m_2a22 = a_al_l(6)
         m_2a33 = a_al_l(7)
         m_2a12 = a_al_l(8)
;
         m_3a11 = a_al( 9)
         m_3a22 = a_al(10)
         m_3a33 = a_al(11)
         m_3a12 = a_al(12)
;
         m_4a11 = a_al(13)
         m_4a22 = a_al(14)
         m_4a33 = a_al(15)
         m_4a12 = a_al(16)
```

```
;
        m_1v11 = a_al_l(17)
        m_1v22 = a_al_l(18)
        m_1v33 = a_al_l(19)
        m_1v12 = a_al_l(20)
;
        m_2v11 = a_al_l(21)
        m_2v22 = a_al_l(22)
        m_2v33 = a_al_l(23)
        m_2v12 = a_al_l(24)
;
        m_3v11 = a_al(25)
        m_3v22 = a_al(26)
        m_3v33 = a_al(27)
        m_3v12 = a_al(28)
;
;For nys=6:
      Case 6
;
        m_yr1 = a_sr_l(1)
        m_yr2 = a_sr_l(2)
        m_yr3 = a_sr_l(3)
        m_yr4 = a_sr_l(4)
        m_yr5 = a_sr_l(5)
        m_yr6 = a_sr(6)
;
        m_vr1 = a_sr_l( 7)
        m_vr2 = a_sr_l( 8)
        m_vr3 = a_sr_l( 9)
        m_vr4 = a_sr_l(10)
        m_vr5 = a_sr_l(11)
;
        m_1a11 = a_al_l(1)
        m_1a22 = a_al_l(2)
        m_1a33 = a_al_l(3)
        m_1a12 = a_al_l(4)
;
        m_2a11 = a_al_l(5)
        m_2a22 = a_al_l(6)
        m_2a33 = a_al_l(7)
        m_2a12 = a_al_l(8)
;
        m_3a11 = a_al_l( 9)
        m_3a22 = a_al_l(10)
        m_3a33 = a_al_l(11)
        m_3a12 = a_al_l(12)
;
        m_4a11 = a_al_l(13)
        m_4a22 = a_al_l(14)
        m_4a33 = a_al_l(15)
        m_4a12 = a_al_l(16)
;
        m_5a11 = a_al(17)
        m_5a22 = a_al(18)
        m_5a33 = a_al(19)
        m_5a12 = a_al(20)
;
        m_6a11 = a_al(21)
        m_6a22 = a_al(22)
        m_6a33 = a_al(23)
```

```
        m_6a12 = a_al(24)
;
        m_1v11 = a_al_l(25)
        m_1v22 = a_al_l(26)
        m_1v33 = a_al_l(27)
        m_1v12 = a_al_l(28)
;
        m_2v11 = a_al_l(29)
        m_2v22 = a_al_l(30)
        m_2v33 = a_al_l(31)
        m_2v12 = a_al_l(32)
;
        m_3v11 = a_al_l(33)
        m_3v22 = a_al_l(34)
        m_3v33 = a_al_l(35)
        m_3v12 = a_al_l(36)
;
        m_4v11 = a_al_l(37)
        m_4v22 = a_al_l(38)
        m_4v33 = a_al_l(39)
        m_4v12 = a_al_l(40)
;
        m_5v11 = a_al(41)
        m_5v22 = a_al(42)
        m_5v33 = a_al(43)
        m_5v12 = a_al(44)
;
;For nys=8:
      Case 8
;
        m_yr1 = a_sr_l(1)
        m_yr2 = a_sr_l(2)
        m_yr3 = a_sr_l(3)
        m_yr4 = a_sr_l(4)
        m_yr5 = a_sr_l(5)
        m_yr6 = a_sr_l(6)
        m_yr7 = a_sr_l(7)
        m_yr8 = a_sr(8)
;
        m_vr1 = a_sr_l( 9)
        m_vr2 = a_sr_l(10)
        m_vr3 = a_sr_l(11)
        m_vr4 = a_sr_l(12)
        m_vr5 = a_sr_l(13)
        m_vr6 = a_sr_l(14)
        m_vr7 = a_sr_l(15)
;
        m_1a11 = a_al_l(1)
        m_1a22 = a_al_l(2)
        m_1a33 = a_al_l(3)
        m_1a12 = a_al_l(4)
;
        m_2a11 = a_al_l(5)
        m_2a22 = a_al_l(6)
        m_2a33 = a_al_l(7)
        m_2a12 = a_al_l(8)
;
        m_3a11 = a_al_l( 9)
        m_3a22 = a_al_l(10)
        m_3a33 = a_al_l(11)
```

```
        m_3a12 = a_al_l(12)
;
        m_4a11 = a_al_l(13)
        m_4a22 = a_al_l(14)
        m_4a33 = a_al_l(15)
        m_4a12 = a_al_l(16)
;
        m_5a11 = a_al_l(17)
        m_5a22 = a_al_l(18)
        m_5a33 = a_al_l(19)
        m_5a12 = a_al_l(20)
;
        m_6a11 = a_al_l(21)
        m_6a22 = a_al_l(22)
        m_6a33 = a_al_l(23)
        m_6a12 = a_al_l(24)
;
        m_7a11 = a_al(25)
        m_7a22 = a_al(26)
        m_7a33 = a_al(27)
        m_7a12 = a_al(28)
;
        m_8a11 = a_al(29)
        m_8a22 = a_al(30)
        m_8a33 = a_al(31)
        m_8a12 = a_al(32)
;
        m_1v11 = a_al_l(33)
        m_1v22 = a_al_l(34)
        m_1v33 = a_al_l(35)
        m_1v12 = a_al_l(36)
;
        m_2v11 = a_al_l(37)
        m_2v22 = a_al_l(38)
        m_2v33 = a_al_l(39)
        m_2v12 = a_al_l(40)
;
        m_3v11 = a_al_l(41)
        m_3v22 = a_al_l(42)
        m_3v33 = a_al_l(43)
        m_3v12 = a_al_l(44)
;
        m_4v11 = a_al_l(45)
        m_4v22 = a_al_l(46)
        m_4v33 = a_al_l(47)
        m_4v12 = a_al_l(48)
;
        m_5v11 = a_al_l(49)
        m_5v22 = a_al_l(50)
        m_5v33 = a_al_l(51)
        m_5v12 = a_al_l(52)
;
        m_6v11 = a_al_l(53)
        m_6v22 = a_al_l(54)
        m_6v33 = a_al_l(55)
        m_6v12 = a_al_l(56)
;
        m_7v11 = a_al(57)
        m_7v22 = a_al(58)
        m_7v33 = a_al(59)
```

```
        m_7v12 = a_al(60)
;
;For nys=10:
      Case 10
;
        m_yr1  = a_sr_l( 1)
        m_yr2  = a_sr_l( 2)
        m_yr3  = a_sr_l( 3)
        m_yr4  = a_sr_l( 4)
        m_yr5  = a_sr_l( 5)
        m_yr6  = a_sr_l( 6)
        m_yr7  = a_sr_l( 7)
        m_yr8  = a_sr_l( 8)
        m_yr9  = a_sr_l( 9)
        m_yr10 = a_sr(10)
;
        m_vr1 = a_sr_l(11)
        m_vr2 = a_sr_l(12)
        m_vr3 = a_sr_l(13)
        m_vr4 = a_sr_l(14)
        m_vr5 = a_sr_l(15)
        m_vr6 = a_sr_l(16)
        m_vr7 = a_sr_l(17)
        m_vr8 = a_sr_l(18)
        m_vr9 = a_sr_l(19)
;
        m_1a11 = a_al_l(1)
        m_1a22 = a_al_l(2)
        m_1a33 = a_al_l(3)
        m_1a12 = a_al_l(4)
;
        m_2a11 = a_al_l(5)
        m_2a22 = a_al_l(6)
        m_2a33 = a_al_l(7)
        m_2a12 = a_al_l(8)
;
        m_3a11 = a_al_l( 9)
        m_3a22 = a_al_l(10)
        m_3a33 = a_al_l(11)
        m_3a12 = a_al_l(12)
;
        m_4a11 = a_al_l(13)
        m_4a22 = a_al_l(14)
        m_4a33 = a_al_l(15)
        m_4a12 = a_al_l(16)
;
        m_5a11 = a_al_l(17)
        m_5a22 = a_al_l(18)
        m_5a33 = a_al_l(19)
        m_5a12 = a_al_l(20)
;
        m_6a11 = a_al_l(21)
        m_6a22 = a_al_l(22)
        m_6a33 = a_al_l(23)
        m_6a12 = a_al_l(24)
;
        m_7a11 = a_al_l(25)
        m_7a22 = a_al_l(26)
        m_7a33 = a_al_l(27)
        m_7a12 = a_al_l(28)
```

```
;
      m_8a11 = a_al_l(29)
      m_8a22 = a_al_l(30)
      m_8a33 = a_al_l(31)
      m_8a12 = a_al_l(32)
;
      m_9a11 = a_al(33)
      m_9a22 = a_al(34)
      m_9a33 = a_al(35)
      m_9a12 = a_al(36)
;
      m_10a11 = a_al(37)
      m_10a22 = a_al(38)
      m_10a33 = a_al(39)
      m_10a12 = a_al(40)
;
      m_1v11 = a_al_l(41)
      m_1v22 = a_al_l(42)
      m_1v33 = a_al_l(43)
      m_1v12 = a_al_l(44)
;
      m_2v11 = a_al_l(45)
      m_2v22 = a_al_l(46)
      m_2v33 = a_al_l(47)
      m_2v12 = a_al_l(48)
;
      m_3v11 = a_al_l(49)
      m_3v22 = a_al_l(50)
      m_3v33 = a_al_l(51)
      m_3v12 = a_al_l(52)
;
      m_4v11 = a_al_l(53)
      m_4v22 = a_al_l(54)
      m_4v33 = a_al_l(55)
      m_4v12 = a_al_l(56)
;
      m_5v11 = a_al_l(57)
      m_5v22 = a_al_l(58)
      m_5v33 = a_al_l(59)
      m_5v12 = a_al_l(60)
;
      m_6v11 = a_al_l(61)
      m_6v22 = a_al_l(62)
      m_6v33 = a_al_l(63)
      m_6v12 = a_al_l(64)
;
      m_7v11 = a_al_l(65)
      m_7v22 = a_al_l(66)
      m_7v33 = a_al_l(67)
      m_7v12 = a_al_l(68)
;
      m_8v11 = a_al_l(69)
      m_8v22 = a_al_l(70)
      m_8v33 = a_al_l(71)
      m_8v12 = a_al_l(72)
;
      m_9v11 = a_al(73)
      m_9v22 = a_al(74)
      m_9v33 = a_al(75)
      m_9v12 = a_al(76)
```

```
;
     End_case
;
   end_if
;
;*********************************************************
;
  CASE 3
; ----------------------
; Return maximum modulus
; ----------------------
;
    cm_max = (m_b + 4.0 * m_g / 3.0)*2.0          ;04/29/98
    sm_max = m_g*2.0                              ;04/29/98
;
  END_CASE
end
opt y_myss
```

APPENDIX C

BEAM ELEMNT SUBROUTINE

```
JP_E_BeamVariable.fis
;Name:
;Diagram:
ca str.fin
def s_s_beam
   while_stepping
   ip=imem(str_pnt+$ksels)
   loop while ip # 0
        el_ac=imem(ip+$keln2)
        el_ad=imem(el_ac+$kndid);node1 id
        if el_ad < 100 then;
              gta_val=0
              gta_val=fmem(ip+$keleax)   ; axial strain
              if gta_val>0. then         ; tension
                 Etan=4*16.0e6/0.125*((1-gta_val/0.125)^3) ;MA J.P. Giroud 1994
                 astr_prop=Etan                    ;
               str_see=imem(ip+$keltad)
               fmem(str_see+$ktype)=astr_prop
              else                              ;compression
               gta_val=-1*gta_val               ;correction for strain <0
              Etanc=4*16.0e6/0.125*((1-gta_val/0.125)^3)  ;/10.0 ;MA less 1 order of magnitude than ten
                astr_prop=Etanc                 ;
              str_see=imem(ip+$keltad)          ; pointer to properties
              fmem(str_see+$ktype)=astr_prop     ; pointer to elastic modulus
              end_if
      end_if
   ip = imem(ip)
   end_loop
end
;
;to implement ;MA
;ca JP_E_BeamVariable.fis
```